

Bangor University

DOCTOR OF PHILOSOPHY

Age, growth and reproductive assessment of the whelk, *Buccinum undatum*, in coastal shelf seas

Hollyman, Philip

Award date:
2017

Awarding institution:
Bangor University

[Link to publication](#)

General rights

Copyright and moral rights for the publications made accessible in the public portal are retained by the authors and/or other copyright owners and it is a condition of accessing publications that users recognise and abide by the legal requirements associated with these rights.

- Users may download and print one copy of any publication from the public portal for the purpose of private study or research.
- You may not further distribute the material or use it for any profit-making activity or commercial gain
- You may freely distribute the URL identifying the publication in the public portal ?

Take down policy

If you believe that this document breaches copyright please contact us providing details, and we will remove access to the work immediately and investigate your claim.



PRIFYSGOL
BANGOR
UNIVERSITY

Age, growth and reproductive assessment of the whelk,
Buccinum undatum, in coastal shelf seas

Philip R. Hollyman MMBiol
School of Ocean Sciences, Bangor University, Menai Bridge, Anglesey, UK, LL59 5AB

Submitted in accordance with the requirements for the degree of Doctor of Philosophy
March, 2017

Declaration and Consent

Details of the Work

I hereby agree to deposit the following item in the digital repository maintained by Bangor University and/or in any other repository authorized for use by Bangor University.

Author Name:

Title:

Supervisor/Department:

Funding body (if any):

Qualification/Degree obtained:

This item is a product of my own research endeavours and is covered by the agreement below in which the item is referred to as “the Work”. It is identical in content to that deposited in the Library, subject to point 4 below.

Non-exclusive Rights

Rights granted to the digital repository through this agreement are entirely non-exclusive. I am free to publish the Work in its present version or future versions elsewhere.

I agree that Bangor University may electronically store, copy or translate the Work to any approved medium or format for the purpose of future preservation and accessibility. Bangor University is not under any obligation to reproduce or display the Work in the same formats or resolutions in which it was originally deposited.

Bangor University Digital Repository

I understand that work deposited in the digital repository will be accessible to a wide variety of people and institutions, including automated agents and search engines via the World Wide Web.

I understand that once the Work is deposited, the item and its metadata may be incorporated into public access catalogues or services, national databases of electronic theses and dissertations such as the British Library’s EThOS or any service provided by the National Library of Wales.

I understand that the Work may be made available via the National Library of Wales Online Electronic Theses Service under the declared terms and conditions of use (<http://www.llgc.org.uk/index.php?id=4676>). I agree that as part of this service the National Library of Wales may electronically store, copy or convert the Work to any approved medium or format for the purpose of future preservation and accessibility. The National Library of Wales is not under any obligation to reproduce or display the Work in the same formats or resolutions in which it was originally deposited.

Statement 1:

This work has not previously been accepted in substance for any degree and is not being concurrently submitted in candidature for any degree unless as agreed by the University for approved dual awards.

Signed (candidate)

Date

Statement 2:

This thesis is the result of my own investigations, except where otherwise stated. Where correction services have been used, the extent and nature of the correction is clearly marked in a footnote(s).

All other sources are acknowledged by footnotes and/or a bibliography.

Signed (candidate)

Date

Statement 3:

I hereby give consent for my thesis, if accepted, to be available for photocopying, for inter-library loan and for electronic repositories, and for the title and summary to be made available to outside organisations.

Signed (candidate)

Date

NB: Candidates on whose behalf a bar on access has been approved by the Academic Registry should use the following version of **Statement 3:**

Statement 3 (bar):

I hereby give consent for my thesis, if accepted, to be available for photocopying, for inter-library loans and for electronic repositories after expiry of a bar on access.

Signed (candidate)

Date

Statement 4:

I agree to deposit an electronic copy of my thesis (the Work) in the Bangor University (BU) Institutional Digital Repository, the British Library ETHOS system, and/or in any other repository authorized for use by Bangor University and where necessary have gained the required permissions for the use of third party material.

In addition to the above I also agree to the following:

1. That I am the author or have the authority of the author(s) to make this agreement and do hereby give Bangor University the right to make available the Work in the way described above.
2. That the electronic copy of the Work deposited in the digital repository and covered by this agreement, is identical in content to the paper copy of the Work deposited in the Bangor University Library, subject to point 4 below.
3. That I have exercised reasonable care to ensure that the Work is original and, to the best of my knowledge, does not breach any laws – including those relating to defamation, libel and copyright.
4. That I have, in instances where the intellectual property of other authors or copyright holders is included in the Work, and where appropriate, gained explicit permission for the inclusion of that material in the Work, and in the electronic form of the Work as accessed through the open access digital repository, *or* that I have identified and removed that material for which adequate and appropriate permission has not been obtained and which will be inaccessible via the digital repository.
5. That Bangor University does not hold any obligation to take legal action on behalf of the Depositor, or other rights holders, in the event of a breach of intellectual property rights, or any other right, in the material deposited.
6. That I will indemnify and keep indemnified Bangor University and the National Library of Wales from and against any loss, liability, claim or damage, including without limitation any related legal fees and court costs (on a full indemnity bases), related to any breach by myself of any term of this agreement.

Signature: Date :

Summary

The whelk, *Buccinum undatum*, is a commercially important shellfish species found throughout the North Atlantic. Many problems face fisheries scientists attempting to assess and monitor populations of this species, due to several life history traits such as highly variable growth rates and sizes at maturity both between and within populations. One major problem has been the lack of a reliable ageing tool, limiting the ability of scientists to develop accurate population age structure estimates for stock assessments. This thesis focuses on three major areas of research: the reproductive assessment, growth and age of *Buccinum undatum* collected from three geographically distinct populations from the Shetlands, North Wales and the Jersey Islands.

Reproductive assessments of several *B. undatum* populations across the UK were undertaken by utilising several previously published maturity estimation techniques to ascertain the most accurate and reliable methods. It was found that size (total shell length) at maturity was highly variable, even over relatively small geographical distances. The timing of the reproductive cycle was assessed in a whelk population from the Menai Strait (North Wales, UK) to investigate changes in maturity assessments over an annual seasonal cycle. It was discovered that size at maturity varied throughout an annual cycle, suggesting an optimal season for maturity assessments.

Spatial variations in shell morphology between populations highlighted clear differences driven by the shape of the aperture and the angle of the shell apex. The crystalline structure of *B. undatum* shells was also investigated for the first time; using a combination of analytical techniques a multi-layered aragonite shell structure was uncovered. The shells of *B. undatum* were also assessed for their potential as environmental recorders. The oxygen isotope ratio contained within *B. undatum* shells was found to be a reliable proxy for seawater temperature, allowing the development of a species-specific palaeotemperature equation that will greatly aid future studies of this species where seawater temperature reconstructions are required. Population growth rates were also assessed, using the isotope data, uncovering clear differences in patterns of shell growth between populations.

A novel age determination technique for *B. undatum* was developed that utilised growth rings present in a pair of calcium carbonate statoliths contained within the foot matrix of each whelk. An annual periodicity of the growth rings was determined by measuring growth in monthly samples of statoliths removed from laboratory reared juvenile whelks of known provenance and age. Cutting edge analytical techniques were also used to assess the structure and seasonal variations in the chemical composition of the statoliths. Following this, the use of statolith growth rings for fisheries monitoring purposes was assessed and compared to the currently used age determination method, operculum growth rings. Using data on size at age, population growth curves were constructed for a range of whelk populations across the U.K. It was confirmed that counting the annual rings in statoliths provide a more reliable assessment of the age of *B. undatum*, delivering a new more reliable tool for fisheries scientists to assess population age structure.

Acknowledgements

There is a long list of people I would like to thank, each of whom has been instrumental in helping me complete this PhD. Firstly my biggest thanks go to my supervisory team. Prof. Chris Richardson, for his unending support and enthusiasm, from the beginning of the project to the very end. His constant feedback and encouragement allowed me to create a body of work which I am very proud to present. I thank Dr. Simon Chenery (BGS), whose endless knowledge of all things geochemical allowed us to try new things with the samples and push the boundaries of what we thought was originally possible. I am also grateful for the generosity he and his wife Carolyn showed in allowing me to stay with them whilst I was completing my work at BGS. I also thank Dr. Vlad Laptikhovsky (CEFAS), whilst he only became an 'official' supervisor towards the end of the project, he has been there from the start giving valuable feedback with his inexhaustible enthusiasm and fisheries knowledge, for which I am very grateful. I would like to thank Bangor University, the Centre for Environment, Fisheries and Aquaculture Sciences (CEFAS) and the British Geological Survey (BGS) for the funding opportunity, allowing me to undertake this project.

Within Ocean sciences, I would like to thank Gwynne Jones and Berwyn Roberts for their help with sample collection (usually in terrible weather) and all of the aquarium work thereafter. I'd also like to thank a long list of colleagues and students who helped with husbandry over the three years, Rich Patton, Alejandro Román González, Charlotte Colvin, Hélène Bonici, Devaney Werrin and Anton Antonov. I would also like to give a special thanks to Dr. Jodie Haig, whose help at the start of the project (and the end) helped me to develop the initial experiments and analyse the data.

I would like to thank Prof. Melanie Leng (BGS) whose help in developing and undertaking all of the isotopic analysis throughout this project cannot be overstated. Without her help in applying for facility funding, a crucial part of this project would have likely never happened. Also at BGS, I would like to thank Hilary Sloane for putting up with my endless shell samples. Dr. Lorraine Fields and Dr. Andy Marriott provided me with some fantastic SEM images for which I am very grateful. There are several people at CEFAS who also deserve my thanks, Dr. Ewan Hunter, Dr. Dave Righton and Andy Lawler have all helped me a great deal over the course of the PhD and given me valuable feedback on chapters and manuscripts. I would also like to thank the teams at the many geochemistry facilities I have been lucky enough to work at. Dr. Richard Hinton and Dr. John Craven (Edinburgh Ion Microprobe Facility), Dr. Konstantin Ingatyev (Diamond light source) and the whole team at the Interface Analysis Unit at Bristol University.

I also thank Dr. Jon Shrives (DoE, Jersey) and Mark Hamilton (NAFC, Shetland) for helping me with the collection of samples from close to their respective institutions. I would also like to thank them, Dr. Bee Berx (Marine Scotland) and Pete Hughes (Bangor) for helping me to source environmental data from each of my study sites. Big thanks also go to Dr. John Grahame (Leeds University) who helped immensely with morphometric data analysis, which would have likely been impossible otherwise.

I would like to thank all of my friends from Menai, for the constant support (even if that was just a drink after work). Having such a great group of people in the same situation really was a pleasure.

I would like to lastly thank my family, whose never-ending encouragement, not just throughout this project, but for the last 27 years has been a constant source of motivation, for which I am eternally grateful.

Finally, my wife Abi, whose unwavering support and love has driven me for the last 10 years. Her constant willingness to read the next version of a manuscript and put up with my stats-related grumpiness is what pulled me through the final weeks of this thesis. Thank you.

Table of Contents

Declaration	i
Summary	iv
Acknowledgements	v
1. Chapter 1: General introduction	1
1.1. The Ecology of <i>Buccinum undatum</i>	2
1.2. Fisheries	5
1.2.1. Active <i>Buccinum undatum</i> fisheries	5
1.2.2. Fisheries regulations and management	7
1.2.3. Fishery declines	9
1.3. Age determination of <i>Buccinum undatum</i>	10
1.3.1. Age estimates based on the operculum	11
1.3.2. Age estimates based on the statolith	13
1.4. Gaps in the literature and structure of the thesis	14
1.4.1. The structure of this thesis	15
1.5. References	17
2. Chapter 2: Spatial variation in shell morphology and reproductive assessment of the whelk, <i>Buccinum undatum</i> in U.K. waters	25
2.1. Introduction	26
2.1.1. Seasonal reproductive cycle of <i>Buccinum undatum</i>	27
2.1.2. Shell morphology	30
2.2. Materials and methods	32
2.2.1. Field collection	32
2.2.2. Timing of the reproductive cycle	34
2.2.2.1. Body and maturity measurements	34
2.2.3. Morphometric study	37
2.2.3.1. Shell measurements	37
2.3. Results	39
2.3.1. Reproductive studies	39
2.3.1.1. Timing of the reproductive cycle and L₅₀ calculations	39
2.3.1.2. Estimates of maturity using penis length	45

2.3.2.	Shell morphology	48
2.3.2.1.	Between site shell morphology comparison	48
2.3.2.2.	Between sex morphology comparison	51
2.3.2.3.	Allometric analyses	52
2.4.	Discussion	56
2.4.1.	Timing of <i>Buccinum undatum</i> reproduction in the Menai Strait	56
2.4.2.	Size at maturity estimations	57
2.4.3.	Penis length as an alternative measure of maturity	58
2.4.4.	Shell morphology	60
2.4.4.1.	Sexual dimorphism of shell morphology	62
2.5.	References	64
3.	Chapter 3: Micro-structure and mineralogy of the shells of <i>Buccinum undatum</i>	69
3.1.	Introduction	70
3.1.1.	Calcium carbonate	70
3.1.2.	Mollusc shell formation	72
3.1.2.1.	The chemical process of mollusc (bivalve) calcification	73
3.1.2.2.	Transport of Ca²⁺ across membranes	75
3.1.2.3.	Sources of carbon and oxygen	76
3.1.2.4.	Organic matrix	78
3.1.3.	Gastropod shell structure	79
3.2.	Materials and methods	81
3.2.1.	Thin sections	81
3.2.2.	Scanning Electron Microscopy (SEM)	82
3.2.3.	Micro-Raman spectroscopy (MRS)	82
3.3.	Results	83
3.3.1.	Layered shell structure	83
3.3.2.	Scanning Electron Microscopy (SEM)	85
3.3.3.	Shell boring organisms	88
3.3.4.	Shell damage repair	92
3.3.5.	Shell mineralogy	92
3.4.	Discussion	96
3.4.1.	Shell structure of <i>Buccinum undatum</i>	96

3.4.2.	Shell erosion and boring organisms	96
3.4.3.	Shell damage and repair	98
3.4.4.	Shell mineralogy	99
3.5.	References	101
4.	Chapter 4: Growth rate and environmental reconstructions from shells of <i>Buccinum undatum</i> using stable isotopes and trace elements	109
4.1.	Introduction	110
4.1.1.	The use of oxygen and carbon isotopes in mollusc shells	110
4.1.2.	The use of trace elements as environmental proxies	114
4.1.2.1.	Strontium and magnesium	115
4.1.2.2.	‘Vital’ effects	116
4.1.2.3.	Barium	117
4.1.2.4.	Lithium	118
4.1.2.5.	Manganese and iron	118
4.1.2.6.	Uranium	119
4.1.2.7.	Sodium	119
4.2.	Materials and Methods	120
4.2.1.	Shell drill sampling	120
4.2.2.	Solution Inductively Coupled Plasma–Mass Spectrometry (Solution ICP–MS)	123
4.2.3.	Isotope Ratio Mass Spectrometry (IRMS)	125
4.2.3.1.	Palaeotemperature equation calibration	126
4.2.3.2.	Average isotope profiles	127
4.2.4.	Growth rate analyses	128
4.3.	Results	128
4.3.1.	Calibration of the palaeotemperature equation	128
4.3.2.	Seawater temperature reconstructions from field collected <i>Buccinum undatum</i>	129
4.3.3.	Growth rate analysis	136
4.3.4.	Trace element profiles from shell carbonate	149
4.3.4.1.	Shetland	141
4.3.4.2.	Jersey	142

4.3.4.3.	Menai Strait	142
4.3.4.4.	Laboratory reared <i>Buccinum undatum</i>	142
4.3.4.5.	Trace element vs. trace element relationships	149
4.3.4.6.	Differential strontium incorporation in male and female whelks	150
4.3.4.7.	Iron and manganese incorporation into shells	150
4.3.4.8.	Productivity	150
4.3.4.9.	Salinity	155
4.4.	Discussion	156
4.4.1.	Palaeotemperature equation calibration	156
4.4.2.	Reconstruction of palaeotemperature from field collected shells	157
4.4.3.	Growth rate analysis	158
4.4.4.	Trace element analyses	159
4.5.	References	165
5.	Chapter 5: Visualisation and validation of <i>Buccinum undatum</i> statolith growth rings	175
5.1.	Introduction	176
5.2.	Materials and methods	178
5.2.1.	Field collection	178
5.2.2.	Statolith extraction and ageing	178
5.2.3.	Statolith visualisation	180
5.2.4.	Laboratory statolith ring formation	181
5.3.	Results	181
5.3.1.	Statolith location and morphology	181
5.3.2.	Statolith ring visualisation	185
5.3.2.1.	Issues with statolith clarity	185
5.3.3.	Hatching ring and growth ring formation	191
5.4.	Discussion	193
5.4.1.	Statolith extraction and preparation	193
5.4.2.	Statolith growth	194
5.4.3.	Scarcity of wild collected juveniles	194
5.4.4.	Statolith growth ring formation	196
5.5.	References	197

6.	<u>Chapter 6: Micro-scale analysis of trace element incorporation and structure of <i>Buccinum undatum</i> statoliths</u>	199
6.1.	<u>Introduction</u>	200
6.2.	<u>Materials and methods</u>	203
6.2.1.	<u>Scanning Electron Microscopy (SEM)</u>	203
6.2.2.	<u>Micro-Raman Spectroscopy (MRS)</u>	203
6.2.3.	<u>Secondary Ion Mass Spectrometry (SIMS)</u>	204
6.2.3.1.	<u>Embedding</u>	204
6.2.3.2.	<u>Grinding</u>	206
6.2.3.3.	<u>SIMS analysis</u>	206
6.2.3.4.	<u>Issues with resin</u>	207
6.2.4.	<u>Transmission micro X Ray Diffraction (μXRD)</u>	208
6.3.	<u>Results</u>	211
6.3.1.	<u>Statolith composition and structure</u>	211
6.3.2.	<u>Statolith microchemistry</u>	215
6.3.3.	<u>Crystal structure and composition of statoliths</u>	227
6.3.4.	<u>Anomalous sample</u>	234
6.3.5.	<u>Comparison of shell isotopes and statolith chemistry</u>	235
6.4.	<u>Discussion</u>	238
6.4.1.	<u>Statolith structure</u>	238
6.4.2.	<u>SIMS analysis</u>	240
6.4.3.	<u>Geochemical validation of statolith growth rings</u>	244
6.5.	<u>References</u>	248
7.	<u>Chapter 7: A comparison of growth curve estimations from the statoliths and opercula of the whelk <i>Buccinum undatum</i></u>	251
7.1.	<u>Introduction</u>	252
7.1.1.	<u>Stock assessment of <i>Buccinum undatum</i></u>	252
7.1.2.	<u>Growth of the operculum</u>	253
7.2.	<u>Materials and methods</u>	255
7.2.1.	<u>Statolith sampling and ageing</u>	255
7.2.2.	<u>Operculum growth ring formation</u>	255
7.2.3.	<u>Assessment of growth ring and adventitious layer clarity</u>	256

7.2.4.	Growth curve construction	258
7.3.	Results	260
7.3.1.	Statolith and operculum growth line formation	260
7.3.2.	Growth ring clarity	260
7.3.3.	Growth curve equation choice	264
7.3.4.	Site growth curve construction	264
7.3.5.	Direct comparison of statolith rings and operculum growth lines	267
7.4.	Discussion	275
7.4.1.	Clarity of growth rings	275
7.4.2.	Growth modelling	275
7.4.3.	Growth curve comparisons	277
7.4.4.	Comparison of statolith and operculum ages	278
7.5.	References	281
8.	Chapter 8: General discussion	285
8.1.	Overview and integration of findings	286
8.1.1.	Chapter 2 - Spatial variation in shell morphology and reproductive assessment of the whelk, <i>Buccinum undatum</i> in U.K. waters.	286
8.1.2.	Chapter 3 - Micro-structure and mineralogy of the shells of <i>Buccinum undatum</i>.	288
8.1.3.	Chapter 4 - Growth rate and environmental reconstructions from shells of <i>Buccinum undatum</i> using stable isotopes and trace elements.	289
8.1.4.	Chapter 5 - Visualisation and validation of <i>Buccinum undatum</i> statolith growth rings.	291
8.1.5.	Chapter 6 - Micro-scale analysis of trace element incorporation and structure of <i>Buccinum undatum</i> statoliths.	291
8.1.6.	Chapter 7 - A comparison of growth curve estimations from the statoliths and opercula of the whelk <i>Buccinum undatum</i>.	292
8.2.	Synthesis of Findings	293
8.2.1.	Reproductive assessment	293
8.2.2.	Growth	294
8.2.3.	Age	297
8.3.	References	299

Appendix list	301
A: Dispensation for the landing of undersized whelks	302
B: Statistical analysis outputs from shell morphology analysis in Chapter 2	306
C: Overview of analytical techniques	310
C.1. Raman Spectroscopy	311
C.2. Solution Inductively Coupled Plasma – Mass Spectrometry	313
C.3. Isotope Ratio Mass Spectrometry (IRMS)	318
C.4. Secondary Ion Mass Spectrometry (SIMS)	320
C.5. Micro-X-Ray Diffraction (μXRD)	324
D: List of elemental standards used for Solution ICP-MS analysis	328
E: NERC Isotope Geosciences Facility Steering Committee (NIGFSC) application for stable isotope support. Successful - £87,500 in analyses awarded	330
F: Custom MATLAB script used to create average oxygen isotope profiles from multiple individual shell profiles	338
G: Elemental relationship plots from <i>Buccinum undatum</i> shell analyses	342
H: Whelk statolith removal and mounting Standard Operating Procedure (SOP), written for statolith workshop at CEFAS	350
I: NERC Edinburgh Ion Microprobe Facility (EIMF) application. Successful, resulted in 8 days of access to the Cameca IMS-4f Ion microprobe - £15,000 in analyses	360
J: Rapid access request to the I-18 beamline at the Diamond Light Source synchrotron facility. Resulted in 24 hours of I-18 beam time with access to Raman microscope and support labs	367
K: X-Ray Diffraction (XRD) profiles from quality control sampling during XRD analysis	370
L: Plots of raw magnesium and calcium from statoliths analysed using SIMS	373
M: Outputs from Gompertz growth equations calculated for operculum growth lines at each site without juvenile statolith and ‘2’ clarity operculum data	375
N: Journal article validating the periodicity of statolith growth line formation. Accepted pending minor revisions at Marine Ecology Progress Series. Title - ‘Statoliths of the whelk <i>Buccinum undatum</i>: a novel age determination tool’	378

Chapter 1:

General introduction

In this introduction to my PhD I discuss the general biology and ecology of the common European Whelk, *Buccinum undatum* (Linnaeus, 1758). I also review both the fisheries practices for this species and the problems that have arisen using these practices. I will then outline the focus of each chapter and how they relate to current research gaps in the existing literature.

1.1 The Ecology of *Buccinum undatum*

The common whelk (*Buccinum undatum*) (referred to as whelks throughout the introduction) also known as a 'buckie' or the 'waved whelk', is a boreal species of marine gastropod with a widespread distribution throughout the North Atlantic, as well as Greenland, the North Sea and Norwegian Sea (Golikov, 1968; Magnúsdóttir, 2010). It has a range stretching from Hudson Bay and the North Eastern shores of North America to the Bay of Biscay, and as far north as Svalbard (Figure 1.1) (Taylor & Taylor, 1977; Atkinson & Wacasey, 1989; Gunnarson & Einarsson, 1995; Hayward *et al.*, 1995; Ten Hallers-Tjabbes *et al.*, 1996; Gulliksen *et al.*, 1999; Włodarska-Kowalczyk, 2007; Smith & Thatje, 2013). Smith & Thatje (2013), claim the range of *B. undatum* extends between 38°N and 79°N, however the Food and Agriculture Organisation (FAO) report populations extending above 80°N to the top of Greenland (Figure 1.1).

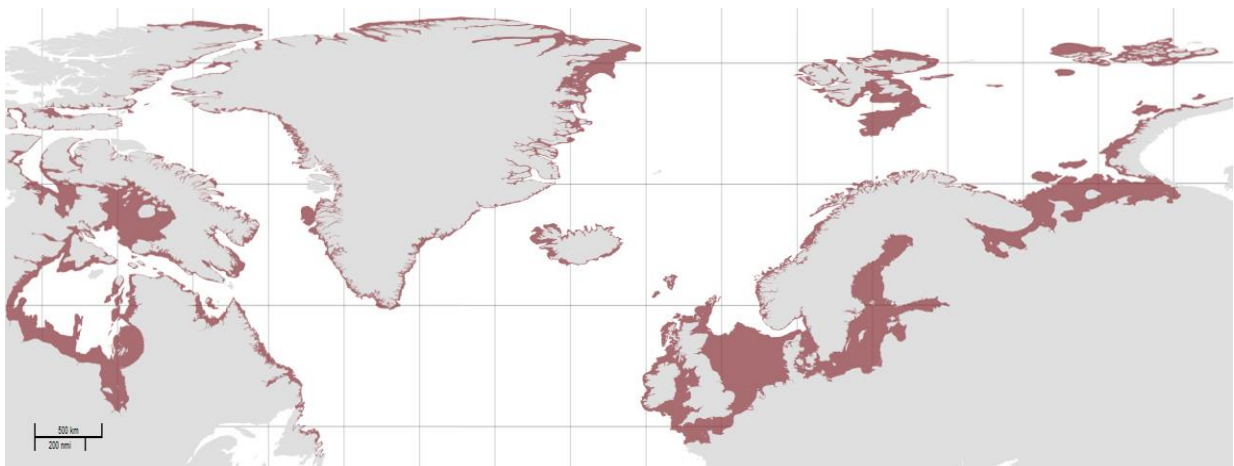


Figure 1.1. Global distribution map of *Buccinum undatum* (FAO, 2014). Presence of *Buccinum undatum* indicated by red shading.

The neogastropod *B. undatum* belongs to a clade of advanced higher gastropods from the subclass Orthogastropoda; the full scientific classification of *B. undatum* is shown in Table 1.1. As such, *B. undatum* has many biological traits common to the majority of other neogastropods. It is a scavenging predatory gastropod, with a diet of both live organisms such as bivalves and

polychaetes (Hancock, 1960; Nielsen, 1975; Taylor, 1978; Scolding *et al.*, 2007) and also carrion (Hunt, 1925; Taylor, 1978; Scolding *et al.*, 2007). They have also been observed displaying kleptoparasitic behaviour i.e. stealing food from other scavengers and predators such as starfish (Rochette *et al.*, 2001; Brokordt *et al.*, 2003). *Buccinum undatum* can locate its prey through a highly developed chemosensory system (Bailey & Laverack, 1966; Ten Hallers-Tjabbes *et al.*, 1993), which it may also use to detect and avoid predators (Mackie *et al.*, 1968). *Buccinum undatum* is gonochoric, displaying two distinct sexes, which is another trait common to the Neogastropoda (Ruppert *et al.*, 2004).

Table 1.1. Scientific classification of *Buccinum undatum* (Bouchet *et al.*, 2005; WoRMS, 2016).

Kingdom:	Animalia
Phylum:	Mollusca
Class:	Gastropoda
Subclass:	Orthogastropoda (formerly Prosobranchia & Opisthobranchia)
Clade (unranked)	Sorbeoconcha
Clade (unranked)	Hypsogastropoda
Clade (unranked)	Neogastropoda
Superfamily:	Buccinoidea
Family:	Buccinidae
Subfamily:	Buccininae
Tribe:	Buccinini
Genus:	<i>Buccinum</i>
Species:	<i>undatum</i>

The external morphology of adult *B. undatum* shells consists of ≈ 7 -8 whorls, which can reach a maximum shell length of around 140mm with a relatively slow growth rate (Figure 1.2) (Fretter & Graham, 1985), reaching a maximum age of around 12 years (Santarelli *et al.*, 1986).

Buccinum undatum has been reported from a varying range of depths between 180m (Ten Hallers-Tjabbes *et al.*, 1993) to over 1000m (Nielson, 1975). However, they are most abundant in the shallower waters in the depth range between 5 and 100m (Nielsen, 1975; Hansson, 1998; Morel & Bossy, 2004; Smith *et al.*, 2013), with densities of between 0.2 and 4.5 m⁻² found across its range (Himmelman, 1988; Jalbert *et al.* 1989; Valentinsson *et al.* 1999). It is a slow moving species, covering a maximum of 50m a day⁻¹ (Hancock, 1960; Himmelman, 1988; Himmelman

and Hamel, 1993). Reports of a salinity tolerance for the species differ within the literature with a minimum limit reported between 2 ppt (Nielsen, 1975) and 15 ppt (Staaland, 1972).

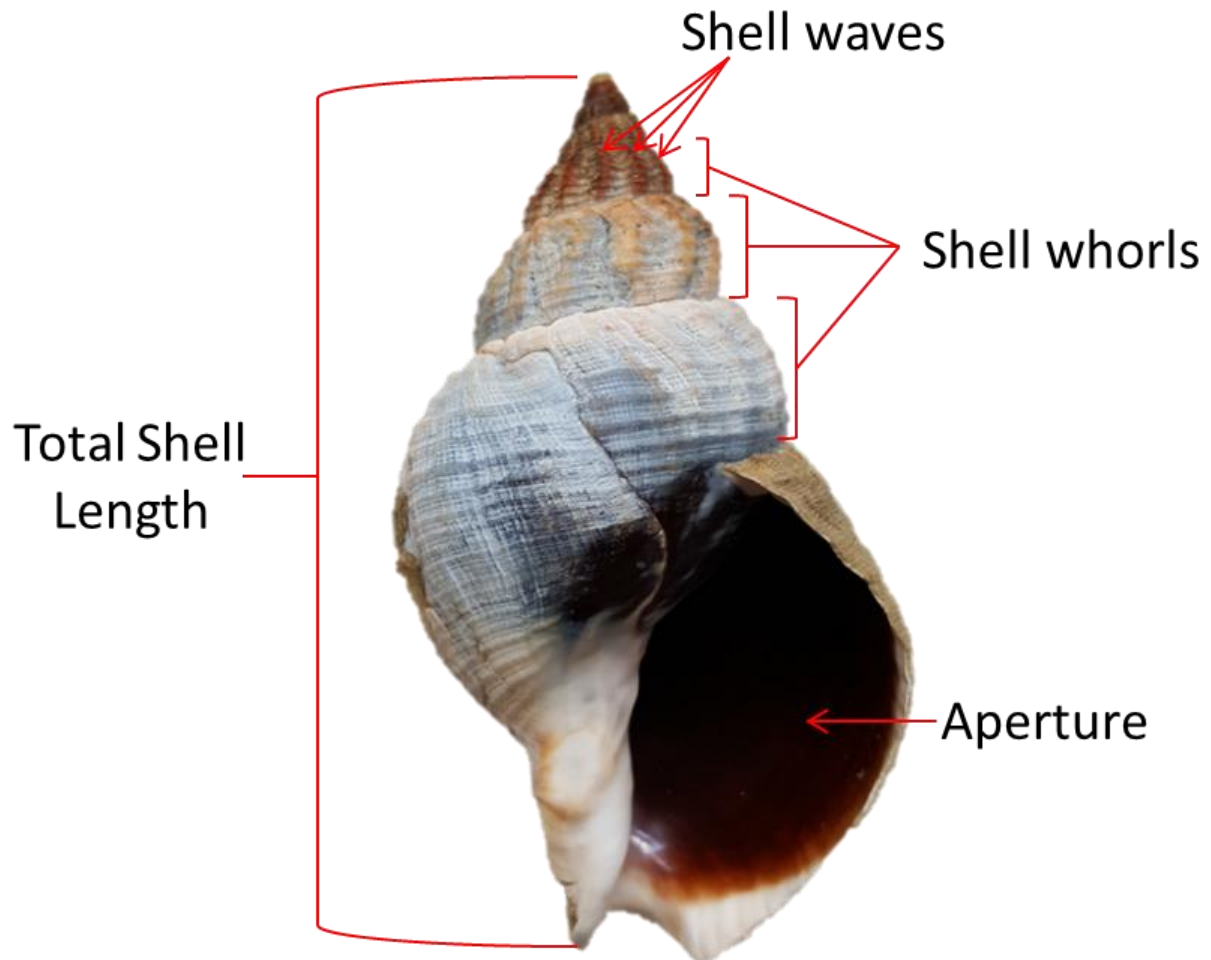


Figure 1.2. The external morphology of a *Buccinum undatum* shell, highlighting the characteristic shell waves.

As *B. undatum* is a boreal species, temperate to cold seawater temperatures are preferential for its survival and growth (Ten Hallers-Tjabbes *et al.*, 1993). Gowanloch (1927) showed that temperatures above 29°C are fatal, with the metabolism and feeding and reproductive abilities likely compromised well before this elevated temperature is reached. At lower seawater temperatures Hancock (1960) showed that *B. undatum* can survive temperatures down to at least -1 °C. *Buccinum undatum* is found in almost all habitat types, preferring sandy and stony substratum (Schäfer, 1956; Nielsen, 1975).

1.2 Fisheries

1.2.1 Active *Buccinum undatum* fisheries

Buccinum undatum is of commercial interest in several countries throughout northern Europe including the U.K. The U.K. has the greatest landings of whelks from commercial fisheries in Europe (Heude-Berthelin *et al.*, 2011) (see also Figure 1.3a). In 2015, 20,858 tonnes of *B. undatum* were landed in the UK by UK vessels with a market value of £18.7 million; this accounted for roughly 14.8% of the total UK shellfish landings by weight and 7% of the total UK shellfish landings by value, highlighting that whelks are a comparatively low value shellfish species (Figure 1.3b). The increasing size of the UK whelk fishery has not only resulted in higher landings but also in higher prices being paid for whelk with the average price per tonne increasing from £230 in 1990 to £890 in 2015 (Figure 1.3b). Throughout Europe, several key fisheries occur in the coastal waters around Belgium, England, France, Ireland and Holland (Fahy *et al.*, 1995, 2000, 2005; Nasution & Roberts, 2004; Shelmerdine *et al.*, 2007). However there are many other smaller fisheries in Europe e.g. around the Shetland Islands (since 1980) (Shelmerdine *et al.*, 2007), the Island of Jersey and the Channel Islands (Morel & Bossy, 2004) and Iceland (Magnúsdóttir, 2010). Sweden has proposed a fishery for whelks in the mid North Sea (Valentinsson *et al.*, 1999). Outside of Europe there is an active fishery in the Gulf of St Lawrence, Canada (Jalbert *et al.*, 1989) and an emerging fishery in the Gulf of Maine in North America (Maine.gov, 2016). The total global landings of *B. undatum* since 1950 are shown in Figure 1.3. A rapid increase in whelk landings can be seen both in the U.K. and worldwide, beginning in the early 1990s. The increase in demand for whelks from Asian markets such as Japan and South Korea has caused an increase in fishing intensity in many areas beginning in ~1994, with one southern Irish exporter stating that 100% of his exports went to East Asia (Fahy *et al.*, 1995 & 2000). Whilst the increase in both the 'per tonne' value and total landings of whelks is good from an economic standpoint, it is as yet unclear what impact this increase in fishing pressure is having on whelk populations. There are several aspects of the life histories of *B. undatum* that make it particularly vulnerable to overfishing, including its sedentary existence and slow growth rate, coupled with the lack of a planktonic life cycle stage leading to 'closed' populations (Valentinsson, 1999; Shelmerdine *et al.*, 2007). It is because of these reasons that it is of the utmost importance to be able to regulate and manage *B. undatum* fisheries to ensure sustainability. Aside from the obvious ecological concerns of removing an important scavenger and predator from the food chain, a troubling, but not uncommon market trend was observed

when economic circumstances in East Asia coupled with heavy import levies imposed by the South Korean Government, led to a decline in this particular market from 1998 onwards. This highlighted the potential boom and bust nature of whelk fisheries. This decline can be seen in Figure 1.3 (see also Fahy *et al.*, 2000 & 2005).

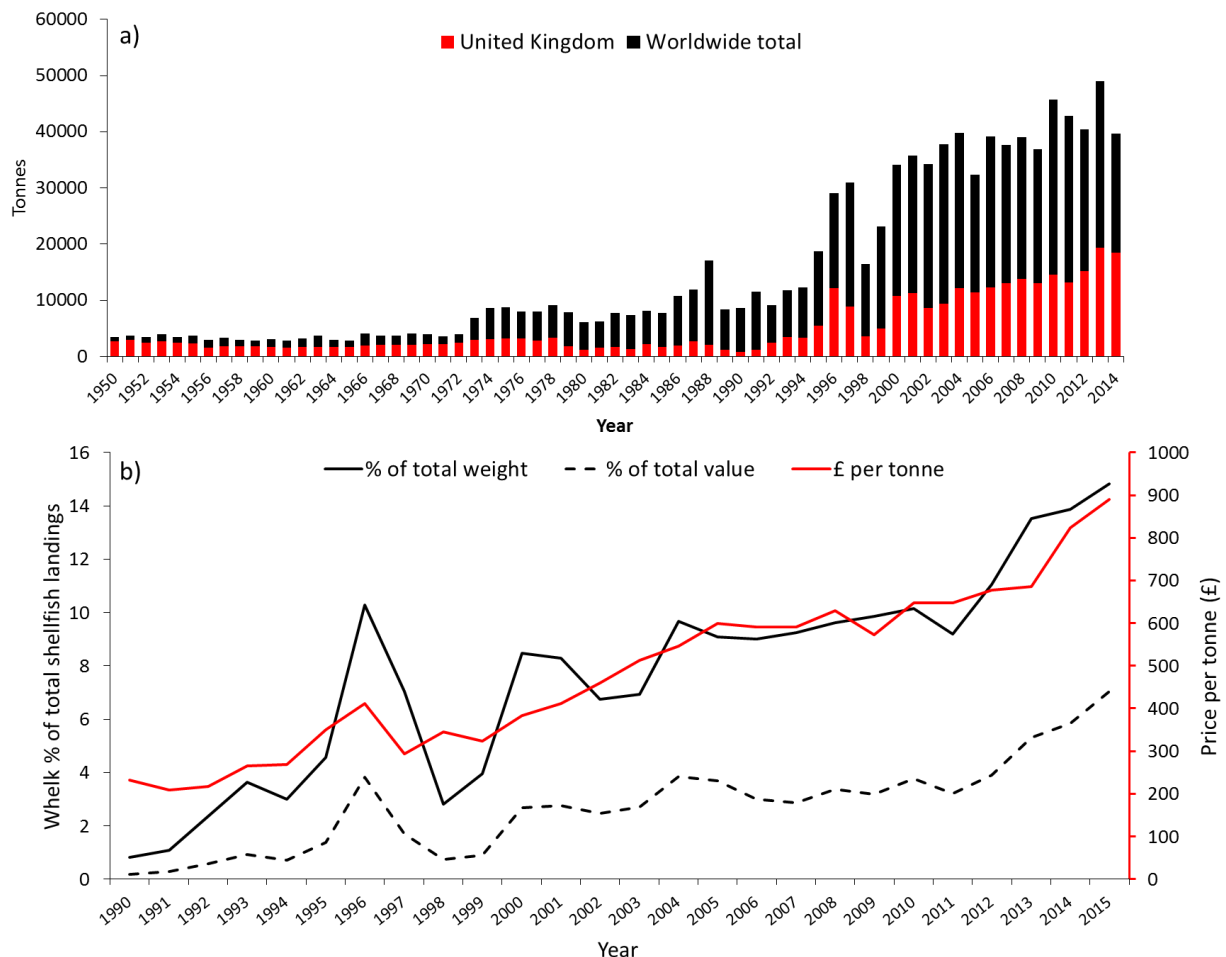


Figure 1.3. a) Total worldwide annual landings of *Buccinum undatum*, between 1950 & 2014, highlighting the market share of the U.K. (FAO FishstatJ, 2016). b) changes in the UK whelk fishery from 1990 to 2014. The % share of total shellfish landings accounted for by whelk is shown for both total weight (solid black line) and total value (dotted black line). The average price per tonne of whelk in the UK fishery is also shown (solid red line). Data for b) were compiled from annual Marine Management Organisation (MMO) sea fishery reports (1990 – 2015) as well as freedom of information requests to the MMO.

The majority of fisheries for *B. undatum* use static pots as a means of catching whelks. These pots come in two common forms: 'lay down' and 'inkwell' (Figure 1.4). 'Laydown' pots are the cheaper option as they are often made from discarded plastic containers (usually 25 litre volume) and weighted with a layer of concrete in the base of the pot. By comparison, 'inkwell'

pots are purpose built and are therefore more expensive. Strings of pots, often hundreds at a time, are laid out (soaked) for periods of 24 to 36 hours and baited with various types of crab and fish which attract whelks (Moore & Howarth, 1996; Jennings *et al.*, 2001). The risk of bycatch with this fishery is low, with the main non-target species including starfish (*Asterias rubens*) and various crab species (mainly *Carcinus maenas*). It has been shown that using *C. maenas* as bait in the pots may also reduce the number of *C. maenas* caught (Moore & Howarth, 1996).

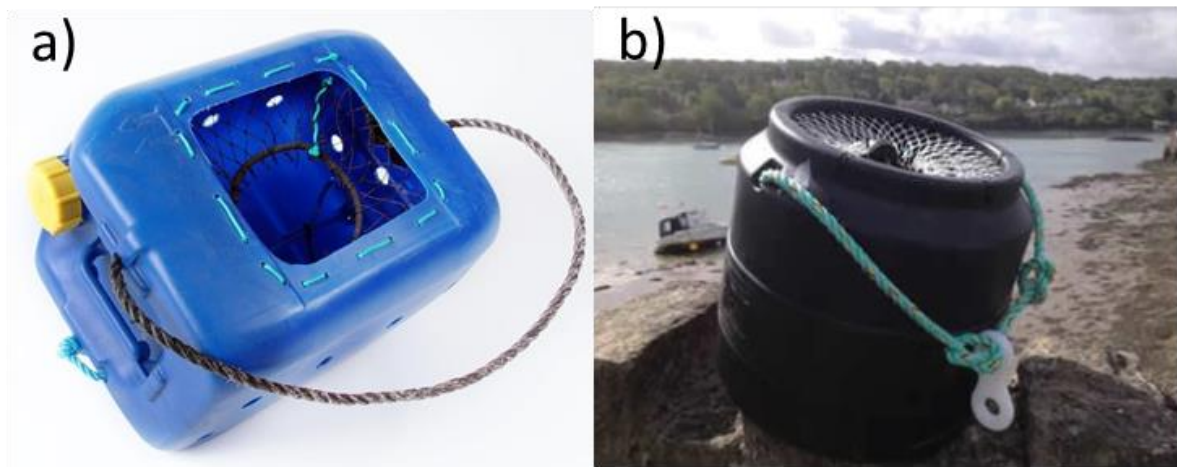


Figure 1. 4. a) 'laydown' whelk pot made from a 25 litre plastic container (coastalnets.co.uk) and b) Fish-Tec scientific 'inkwell' pot. (Image courtesy of Dr. Jodie Haig).

1.2.2 Fisheries regulations and management

Few management strategies exist for whelk fisheries within the U.K. The only routinely enforced regulation is a Minimum Landing Size (MLS) of 45mm shell length. The use of a MLS as a tool for protecting the immature portion of a population until they have spawned has been shown to be effective especially with crustacean species (Jennings *et al.*, 2001). A MLS is set by studying a population to determine the size at which 50% of the population exhibits mature developed gonads (L_{50} ; Heude-Berthelin *et al.*, 2011). For whelk fishermen, the whelk MLS can be adhered to by changing the size of the drainage holes in whelk pots and setting the size of the sorting riddle once the catch has been harvested to remove undersize individuals. A riddle is a device used by fishermen to sort catch by size (Figure 1.5), the catch is placed into a tray, the base of which is made from metal bars spaced at a set width.



Figure 1.5. A commercial whelk riddle in use, whelks below the Minimum Landing Size (MLS) can be seen collecting in the red container beneath the riddle. Whelks above the MLS are seen caught between and on the riddle bars. (<http://www.kentandessex-ifca.gov.uk/>).

Undersized whelks fall through the spaces between the bars and the retained whelks above the MLS are then removed. The width of the riddle bar spacing and whelk pot drainage holes are determined by the length-width ratio of whelks with a shell height of 45 mm. The minimum width of the whelk is used to set gear restrictions as this is the narrowest part of their shell and if they are above the MLS they will not fall through the bar spacings (Figure 1.5). The variation in shell shape and dimensions of whelk shells has raised concerns amongst fisheries regulatory authorities raising concerns over the effectiveness of a MLS regulation that encompasses large geographical areas and different whelk populations with likely different age structures.

For the majority of European populations the MLS of 45 mm was enacted in a 1998 EU regulation (Council regulation 850/98, Annex XII), which has been shown in many studies to be insufficient for protecting the immature portion of many *B. undatum* populations (Fahy *et al.*, 2000; Shelmerdine *et al.*, 2007; Heude-Berthelin *et al.*, 2011). For this reason, many local fisheries authorities have increased the MLS in their particular fisheries following a 'size at maturity' study. For example, the Shetland Isles increased the MLS from 45mm to 75mm within a 6 mile radius of Shetland (Henderson & Simpson, 2006; Shelmerdine *et al.*, 2007). It is the difference in size at age between populations that makes it difficult to impose a blanket MLS. It is unclear what exactly causes the differences in size at age but several theories have been suggested, such as fishing pressure and predation pressure (Thomas & Himmelman, 1988; Gendron, 1992; Fahy *et al.*, 1995). A large MLS would be needed to cover slow maturing

populations. However, a large MLS would be extremely damaging to the profitability of a fishery (Fahy *et al.*, 1995). Recommendations made by Kenchington & Glass (1998) and Shelmerdine *et al.*, (2007) include micro-management within a fishery, i.e. differing MLS limits for different fishing areas. This could go some way to solving the problem of a 'one size fits all' MLS to control whelk catches. However, this would require considerable detailed local studies on the reproductive development and age of local whelk populations and the policing of the MLS might be difficult and costly to implement.

Other methods of fisheries management such as permits that restrict fishing on certain grounds and limit the number of pots have been used in Quebec (Gendron, 1992). More recently, several of the Inshore Fisheries and Conservation Authorities (IFCAs) in the U.K. have implemented emergency byelaws such as permits to fish which charge on a per-pot basis (Eastern IFCA, 2016) and pot restriction permits restricting permit holders to 300 pots per boat (Kent and Essex IFCA, 2013). Since these restrictions have only been recently implemented their effectiveness in controlling the fishery remains as yet unclear.

1.2.3 Fishery declines

Some *B. undatum* fisheries have recently experienced declines in catches and a decrease in whelk numbers in their populations. The whelk fishery in the Dutch Wadden Sea has seen the most drastic declines. Cadée *et al.* (1995) concluded that *B. undatum* had become extinct in the Wadden Sea as of 1991 (see also Ten Hallers-Tjabbes *et al.*, 1993), potentially due to the impact of fisheries practices between the 1920s and 1970s. However the exact reason remains unclear (de Vooy & van der Meer, 2010). The Dutch fishery used dredges and trawls as opposed to pots, and this fishing gear likely caused additional damage through chips and breakages to the shells and disorientation of any un-retained whelks making them more vulnerable to predation (Kaiser & Spencer 1995; Ramsay & Kaiser, 1998).

The situation in the Dutch Wadden Sea population is especially pertinent today as many populations of *B. undatum* in European coastal waters have declined over recent decades including those in the coastal waters of the southern North sea (Ten Hallers-Tjabbes *et al.*, 1996; Nicholson and Evans, 1997; Mensink *et al.*, 2000) and Southern Ireland (Fahy *et al.*, 2005). The Southern Irish fishery is an important case study as a fishery that has experienced bouts of 'boom and bust' with complete collapses after intensive periods of unregulated fishing. The history of the fishery was documented in three reports by Fahy *et al.*, in 1995, 2000 and 2005.

The fishery expanded rapidly in the early 1990s from 56t in 1990 to a peak of over 9000t in 2003. However, the quality of the whelks deteriorated resulting in lower meat yields, and smaller size classes became more prevalent in the catch. The 1995 report highlighted the differences in maturation of males between heavily fished and lightly fished areas and showed that in heavily fished areas whelk maturation sizes were $\approx 20\%$ lower than the least exploited populations, this in part led to the introduction of a minimum landing size (MLS) of 50 mm in 1994. However, the report in 2000 highlighted the problems with a MLS size of 50 mm as it had already been shown that 50 mm was insufficient to protect maturing individuals in less exploited populations. Fahy estimated that 60% of males would not be protected with the 50 mm MLS. Additionally 20-33% of the landings assessed in the study were below the legal MLS, highlighting the need for better enforcement of the regulations. The final report in 2005 highlighted two major collapses of the fishery in 1997 and 2004 through mismanagement by a mix of overfishing and poor regulation and enforcement of the MLS. The report showed declines in some areas of up to 90% and suggested that the damage to some of the fished areas was now irreversible.

It is clear from the published literature that proper management of whelk stocks is a priority to ensure the future of the fishery. Many studies have suggested that improvements can be made by calculating the size at maturity for populations to set regulatory MLS, this has been undertaken by several research groups across the UK in recent years (Haig *et al.*, 2015; McIntyre *et al.*, 2015). It is also apparent that for robust age-based stock assessment of this species, as well as an improvement in the understanding of spatial and temporal changes in size-at-age and age-at-maturity, a new and more reliable age determination technique is urgently required (Haig *et al.*, 2015).

1.3 Age determination of *Buccinum undatum*

Bivalve shells display rings on their surface that have been used to determine their age although it is often difficult to distinguish between annual rings and those caused by disturbance e.g. damage from fishing (Gaspar *et al.*, 1994; Ramsay *et al.*, 2000). Many bivalve shells contain annually-resolved growth lines visible in polished and etched shell sections that have been used to determine their age (Richardson, 2001). The lines form as a result of seasonal changes in shell growth rates linked to the seasonal availability of food and changes in seawater temperature.

Colder winter seawater temperatures and limited food supply cause the slowing of shell growth and deposition of a growth line (see Richardson 2001 for general review). The gastropod shell rarely displays external surface rings, although the shells of some species e.g. *Phorcus lineatus*, do have surface growth rings (Williamson & Kendall, 1981). In many species the visible external growth lines do not correspond with predictable growth cycles in the shell e.g. *Gibbula cineraria* (Schöne *et al.*, 2007). Similarly the shells of *B. undatum* neither display clear external rings nor contain growth lines (Santarelli & Gros, 1986). Even if the rings on *B. undatum* shells were clear, the damage from fishing, predation and intermittent feeding would likely remove the ability to distinguish between annual and disturbance rings/lines in many populations (Thomas & Himmelman, 1988; Mensink, *et al.*, 2000). An alternative method for ageing gastropods has been to use the operculum rings (Santarelli & Gros, 1986) or rings in the statolith (Barroso *et al.*, 2005; Richardson *et al.*, 2005a & b; Chatzinikolaou & Richardson 2007). The possible application of both these methods for determining the age of *B. undatum* will now be discussed.

1.3.1 Age estimates based on the operculum

The gastropod operculum is an organic shield like structure found attached to the dorsal side of the foot. It is used by the gastropod to close off its aperture when the head and foot are retracted into the shell, providing protection from both predators and desiccation (Checa & Jiménez-Jiménez, 1998). There are several different kinds of opercula found amongst the Gastropoda, such as the calcified spiral shaped operculum found in turbinid snails (Vermeij & Williams, 2007) and concentric opercula found in *B. undatum*. The operculum is formed from a protein based secretion from the foot (Hunt, 1969), which in *B. undatum* is laid down in concentric rings emanating from a nucleus (Santarelli & Gros, 1985).

Growth rings are present on the dorsal surface of the operculum of *B. undatum* and have been counted to estimate their age. The rings are thought to form as a result of the slowing of operculum growth at some point during the annual seasonal cycle (Santarelli & Gros, 1985). Secretion of protein layers in the operculum either stop or become closer together, giving the impression of a distinct band in the operculum (Figure 1.6).

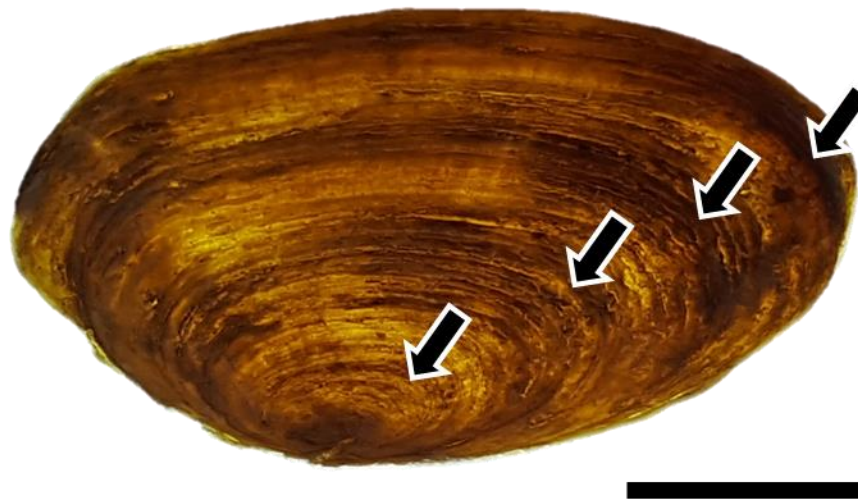


Figure 1.6. The surface growth rings (black arrows) of a good clarity *Buccinum undatum* operculum imaged using transmitted light. Scale bar represents 0.5 cm.

Research published by Santarelli & Gros (1985) suggested that rings on the operculum were annually-deposited although an annual deposition was largely assumed as no growth experiments or direct chemical analysis of the opercula were undertaken. They chose three *B. undatum* shells and drilled (≈ 100 mg) powdered samples of shell calcium carbonate at regular intervals around the shell spiral. These samples were then analysed using Isotope Ratio Mass Spectrometry (IRMS) which was used to determine the stable oxygen isotope profiles along the growth axis of the shells, which are a known proxy for seawater temperature (Epstein *et al.*, 1953; Grossman & Ku, 1986). The reconstructed isotope profiles highlighted three annual cycles in the stable oxygen isotopic content of the shell which were then related to the number of operculum rings. In the three shells analysed the number of operculum growth rings matched the number of stable oxygen isotope annual cycles. On the basis of this, an annual periodicity of formation was concluded. However, no laboratory or field experiments were undertaken to validate the periodicity of the rings.

The conclusions of this work have been extended to other studies on whelk populations. However, the use of the operculum growth rings is confounded by several common problems. The problems with determining the age of whelks using the opercula mainly centre on the difficulty in identifying and reading the rings. A study by Kideys (1996), exemplified this. He found in a sample of >10,000 opercula, collected from whelks from the coastal waters of the Isle of Man, that only 16% had clear readable rings, a further 36% had readable rings that he could use to estimate the age and growth rate of the populations and the remainder (48%) were

unreadable. A study on whelk age undertaken at the Centre for Environment, Fisheries and Aquaculture Science (CEFAS) found a similar result: only 13% of opercula were readable (with all four readers agreeing) plus 28.3% were of 'conventional agreement' when three of four readers provided the same estimate (Lawler, 2013). The operculum can be removed during attacks from predatory crabs and fishing impacts. When the operculum grows back the number of rings or adventitious layers may give a false impression of the actual age of the organism (Richardson *et al.*, 2005a).

1.3.2 Age estimates based on the statolith

Gastropod statoliths are small structures of calcium carbonate found within statocysts that are located in the foot of a gastropod in the locality of the pedal ganglion (Fretter & Graham, 1994; Richardson, 2001). They are used in equilibrium and to assist the animal in determining the direction of gravity (Dorsett, 1986), much like the role of otoliths in the head of fish. Statoliths have been shown to contain distinct growth rings that may have a daily periodicity in veliger larvae (Bell, 1984), but more commonly have an annual periodicity in adult gastropods e.g. *Nassarius reticulatus* (Barroso, *et al.*, 2005; Chatzinikolau & Richardson, 2007), *Neptunea antiqua* (Richardson *et al.*, 2005a) and *Polinices pulchellus* (Richardson *et al.*, 2005b). The appearance of the statolith from *Neptunea antiqua* and the clear annual growth rings are shown in Figure 1.7.

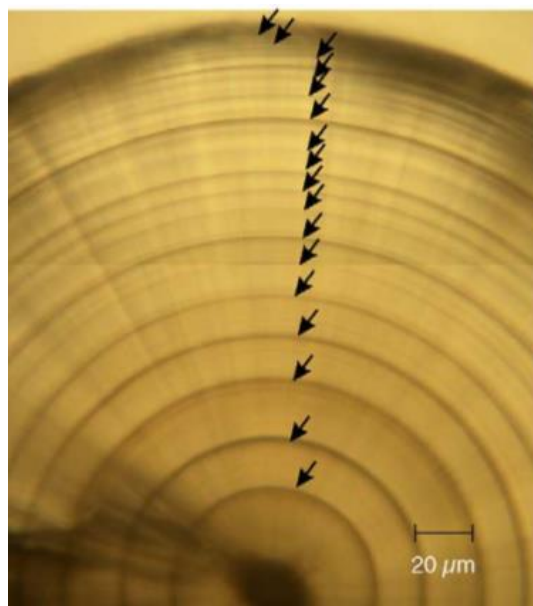


Figure 1.7. Photomicrograph showing the growth rings in the statolith of the gastropod *Neptunea antiqua*. The black arrows indicate the growth increments (taken from Richardson *et al.*, 2005a).

Growth rings in statoliths are much clearer than those found in the operculum and they are likely to be a high resolution archive of the growth of the gastropod throughout ontogeny. Chatzinikolau & Richardson (2007), were able to identify rings in the statoliths of *N. reticulatus* that formed at the time of settlement and at the first year (Figure 1.8). Statoliths are also present in cephalopod squid and cuttlefish species, although statoliths from octopods are not readable (Jackson, 1994). Cephalopod statoliths have shown great potential following geochemical analyses to highlight differences in element uptake in the statolith of the cuttlefish *Sepia apana* at different life history stages using laser ablation (LA-ICP-MS) (Gillanders *et al.*, 2013). Previous literature on statoliths from other gastropod species has highlighted their potential usefulness for age determination of *B. undatum* and their possible advantage over the opercula.

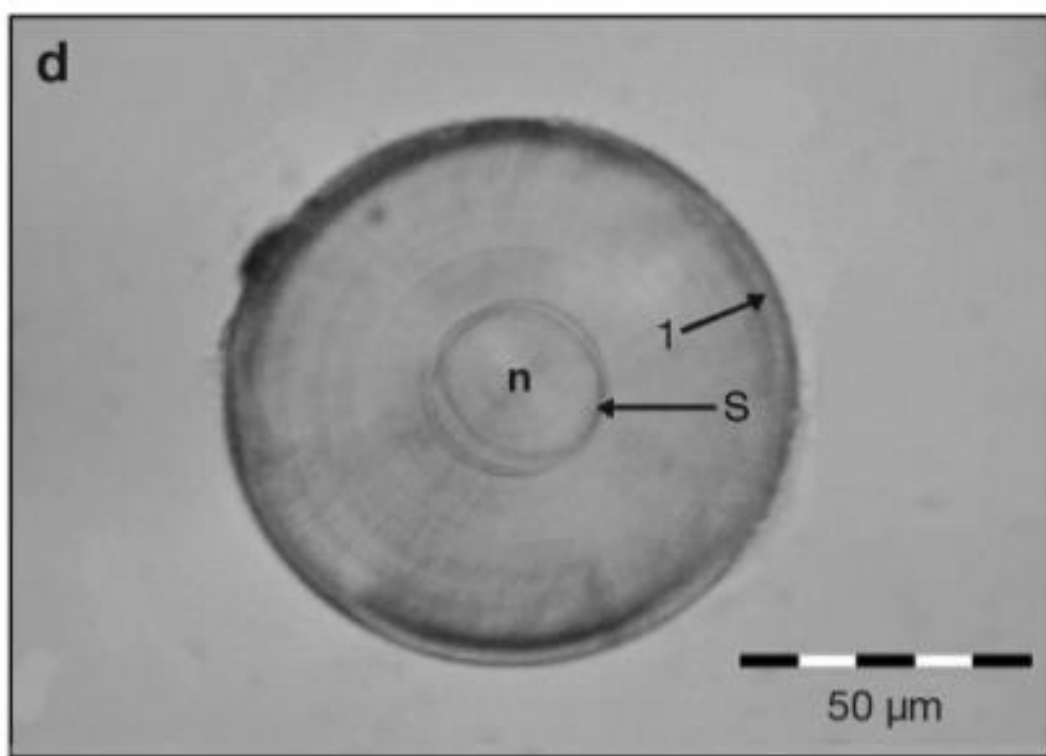


Figure 1.8. The statolith from a 500 day old juvenile *Nassarius reticulatus*, clearly showing the nucleus (n), settlement ring (S) and 1st annual ring (1). (Taken from Chatzinikolau & Richardson, (2007).

1.4 Gaps in the literature and structure of the thesis

Difficulties arise with the management of *B. undatum* fisheries due to the spatial variability in size of individuals from different fisheries and their growth rates and therefore size-at-age and

age-at-maturity. It is clear, from the observed fisheries declines in some commercially important fisheries that new management practices need to be implemented but unfortunately the inability of fisheries scientists to accurately undertake age based stock assessments limits their ability to set informed exploitation rates. The only current method of determining the age of *B. undatum* is through the use of putative annual growth rings on the operculum, serious concerns have been raised in several publications over the reliability and accuracy of the opercular rings (e.g. Kideys, 1996; Shelmerdine *et al.*, 2007, Lawler, 2013). This thesis will investigate in depth the validation of the rings in the common whelk statolith, and highlight their potential as a fisheries management tool. Each whelk possess a pair of statoliths and once removed from the whelk, a series of clear growth rings can be observed in each one. Throughout this thesis, I will investigate their structure and geochemistry. I will also investigate the periodicity of formation of the growth rings in field collected and laboratory-reared animals in order to use the statolith rings to estimate the age of the whelks. This validation of a new age determination technique will allow fisheries scientists to undertake more informed management of whelk fisheries.

As well as investigating the potential of statoliths as age determination tools, several other key issues will be examined. No information currently exists regarding the composition or structure of *B. undatum* shells, or the potential of the shells to record environmental conditions. The shells will be investigated in detail which will also aid the validation of statolith growth rings by allowing accurate age determination from shell carbonate. The size at maturity of several *B. undatum* populations will also be investigated, several recent studies have focussed on reproductive assessment of *B. undatum* populations (e.g. Haig *et al.*, 2015; McIntyre *et al.*, 2015). The methods used in these studies will be replicated and applied to key populations around the UK to contribute to the overall understanding of *B. undatum* size at maturity.

1.4.1 The structure of this thesis

Chapter 1: General introduction

Chapter 2: In this chapter I present data regarding the timing of the reproductive cycle of *B. undatum* in the Menai Strait (the principle study site for this project), as well as measures of size at maturity for six populations around the UK. This will add to existing literature concerning the timing and size at maturity of whelks and the spatial variation of these two metrics across the UK. This chapter will also present a study of differences in the shell morphometrics between the

same six populations. This will add to the currently little understood differences in shell shape between different populations.

Chapter 3: This chapter will present the results of a study looking at the micro-structure of *B. undatum* shells. *B. undatum* shell structure has never before been studied and this chapter presents essential data on both the crystalline structure and composition of *B. undatum* shells.

Chapter 4: This chapter presents elemental data from the shells of *B. undatum*. These data are used to understand differences in seasonal growth rates between sites as well as assessing the suitability of *B. undatum* shells as archives of historical environmental data. This is the first time growth rates of *B. undatum* have been studied between sites using geochemical analyses. It is also the first time that concurrent trace element and stable isotope profiles have been constructed from the shells of *B. undatum*.

Chapter 5: In this chapter I present the development of statolith growth ring visualisation techniques as well as analysis of statoliths from laboratory reared populations to determine the timing of growth line formation. This will represent the first part of the validation process for the use of statolith growth rings as an age determination tool, and represents a novel investigation into *B. undatum* statoliths.

Chapter 6: In this chapter I present the geochemical analyses undertaken on statoliths of *B. undatum*, taken from three populations across the U.K. These analyses are used to further validate the periodicity of the growth rings which lends support to the findings from Chapter 5. The robust ages determined using stable isotopes from the shells in Chapter 4 will also be used as an extra validation of age.

Chapter 7: This chapter presents the results of a study reconstructing growth dynamics from five different populations from across the UK, using statolith growth rings as an age determination tool. The growth curves that are generated are compared both between sites and to growth curves constructed from opercular growth rings as a final validation of the technique and comparison to existing methods.

Chapter 8: The general discussion will draw together and synthesise all the findings from the different chapters in this thesis to highlight how they relate to existing literature with implications for future research and policy management.

1.5 References

- Atkinson EG, Wacasey JW (1989) Benthic invertebrates collected from Hudson Bay, Canada, 1953 to 1965. Can Data Rep Fish Aquat Sci 744:121p
- Bailey DF, Laverack MS (1966) Aspects of the neurophysiology of *Buccinum undatum* L. (Gastropoda). Central responses to stimulation of the osphradium. J Exp Mar Biol Ecol 44:131-148
- Barroso CM, Nunes M, Richardson CA, Moreira MH (2005) The gastropod statolith: a tool for determining the age of *Nassarius reticulatus*. Mar Biol 146:1139–1144
- Bell JL (1984) Statoliths as age indicators in gastropod larvae: application to measurement of field growth rates. Pac Sci 38:357
- Bouchet P, Rocroi JP, Frýda J, Hausdorf B, Ponder W, Valdés Á, Warén A (2005) Classification and nomenclator of gastropod families. Malacologia 47(1-2):1–397
- Brokordt K, Guderley H, Guay M, Gaymer CF, Himmelman JH (2003) Sex differences in reproductive investment: maternal care reduces escape response capacity in the whelk *Buccinum undatum*. J Mar Biol Assoc UK 291:161–180
- Cadée GC, Boon JP, Fischer CV, Mensink BP, Ten Hallers-Tjabbes CC (1995). Why the whelk (*Buccinum undatum*) has become extinct in the Dutch Wadden Sea. Neth J Sea Res 34:337–339
- Chatzinikolaou E, Richardson CA (2007) Evaluating growth and age of netted whelk *Nassarius reticulatus* (Gastropoda: Nassariidae) using statolith growth rings. Mar Ecol Prog Ser 342:163–176
- de Vooy CGN, van der Meer J (2010) The whelk (*Buccinum undatum* L.) in the western Dutch Wadden Sea in the period 1946–1970: Assessment of population characteristics and fishery impact. J Sea Res 63:11–16
- Department for Environment, Food & Rural affairs, Fisheries statistics unit (2001). UK Sea Fisheries statistics, 1999 and 2000. Office for National Statistics, London
- Department for Environment, Food & Rural affairs, Fisheries statistics unit (2002). UK Sea Fisheries statistics, 2001. Office for National Statistics, London.
- Department for Environment, Food & Rural affairs, Fisheries statistics unit (2003). United Kingdom Sea Fisheries statistics, 2002. Office for National Statistics, London
- Department for Environment, Food & Rural affairs, Fisheries statistics unit (2004). United Kingdom Sea Fisheries statistics, 2003. Office for National Statistics, London
- Dorsett DA (1986) Brains to cells: the neuroanatomy of selected gastropod species. In: Willow DAO (eds.) The Mollusca. Neurobiology & behaviour, part II. Academic Press, New York
- Eastern IFCA (2016). <http://www.eastern-ifca.gov.uk/>. Accessed on 1/7/16
- Epstein S, Buchsbaum JR, Lowenstam HA, Ukey HC (1953) Revised carbonate-water isotopic temperature scale. Bull Geol Soc Am 64:1315-1326

- Fahy E, Carroll J, O'Toole M, Barry C, Hother-Parkes L (2005) Fishery associated changes in the whelk *Buccinum undatum* stock in the southwest Irish Sea, 1995-2003. Ir Fish Invest, 15
- Fahy E, Masterson E, Swords D, Forrest N (2000) A second assessment of the whelk fishery *Buccinum undatum* in the southwest Irish Sea with particular reference to its history of management by size limit. Ir Fish Invest 6
- Fahy E, Yalloway G, Gleeson P (1995) Appraisal of the whelk *Buccinum undatum* fishery of the Southern Irish Sea with proposals for a management strategy. Ir Fish Invest Ser B 42
- Fisheries and aquaculture software. FishStatJ - software for fishery statistical time series. In: FAO Fisheries and Aquaculture Department [online]. Rome. Updated 21 July 2016. Accessed 12/8/2016
- Food and Agriculture Organization species distribution maps.
<http://www.fao.org/figis/geoserver/factsheets/species.html>. Accessed 1/7/14
- Fretter V, Graham A (1985) *Buccinum undatum* Linnaeus, 1758, whelk or buckie. J Mollus Stud 51(Supplement 15):486-489
- Fretter V, Graham A (1994) British Prosobranch Molluscs: their functional anatomy and ecology. Printed for the Ray Society, London. Revised and updated edition
- Gaspar MB, Richardson CA, Monteiro CC (1994) The effects of dredging on shell formation in the razor clam *Ensis siliqua* from Barrinha, Southern Portugal. J Mar Biol Assoc UK 74:927-938
- Gendron L (1992) Determination of the size at sexual maturity of the waved whelk *Buccinum undatum* Linnaeus, 1758, in the Gulf of St Lawrence, as a basis for the establishment of a minimum catchable size. J Shellfish Res 11:1-7
- Gillanders BM, Wilkinson LM, Munro AR, de Vries MC (2013) Statolith chemistry of two life history stages of cuttlefish: Effects of temperature and seawater trace element concentration. Geochim Cosmochim Acta 101:12-23
- Global Biodiversity Information Facility.
http://www.gbif.org/occurrence/search?TAXON_KEY=2305073&COUNTRY=GL and reference to Paleobiology Database herein). Accessed 07/12/2016
- Golikov AN (1968) Distribution, variability of long-lived benthic animals as indicators of currents and hydrological conditions. Sarsia 34:199-208
- Gowanloch JN (1927) Contribution to the study of marine gastropods: the intertidal life of *Buccinum undatum*, a study in non-adaptation. Contrib Can Biol Fish 3:167-178
- Grossman EL, Ku T (1986) Oxygen and carbon isotope fractionation in biogenic aragonite: Temperature effects. Chem Geol 59:59-74
- Gulliksen B, Palerud R, Brattegard T & Sneli J (1999) Distribution of marine benthic macro-organisms at Svalbard (including Bear Island) and Jan Mayen. - Research Report for DN 1999-4. Directorate for Nature Management
- Gunnarson K, Einarsson S (1995) Observations on the whelk populations (*Buccinum undatum*) in Breidifjörður, western Iceland. ICES C M 1995/K:20
- Haig JA, Pantin, JR, Murray LG, Kaiser MJ (2015) Temporal and spatial variation in size at maturity of the common whelk (*Buccinum undatum*). ICES J Mar Sci 72 (9):2707-2719

- Hancock DA (1960) The ecology of the molluscan enemies of the edible mollusc. *Proc Malacol Soc Lond* 34:123-143
- Hansson HG (1998) NEAT (North East Atlantic Taxa) database. Tjärnö Marine Biological Laboratory. <http://www.tmbi.gu.se/libdb/taxon/taxa.html>. Accessed 15/8/16
- Hayward PJ, Wigham GD, Yonow N (1995) Molluscs (Phylum Mollusca). In: Hayward PJ, Ryland JS (eds.) *Handbook of the marine fauna of north-west Europe*. Oxford University Press, Oxford
- Henderson S, Simpson C (2006) Size at sexual maturity of the Shetland Buckie *Buccinum undatum*. NAFC, Shetland Marine Centre Fisheries Development, Note 20
- Heude-Berthelin C, Hégron-Macé L, Legrand V, Jouaux A, Adeline B, Mathieu M, Kellner K (2011) Growth and reproduction of the common whelk *Buccinum undatum* in west Cotentin (Channel), France. *Aquat living resour* 24:317–327
- Himmelman JH (1988). Movement of whelks (*Buccinum undatum*) towards a baited trap. *Mar Biol* 97:521-531
- Himmelman JH, Hamel JR (1993) Diet, behaviour and reproduction of the whelk *Buccinum undatum* in the northern Gulf of St Lawrence, eastern Canada. *Mar Biol* 116:423-430
- Hunt OD (1925). The food of the bottom fauna of the Plymouth fishing ground. *J Mar Biol Assoc UK* 13:560–599
- Hunt S (1969) Characterization of the operculum of the gastropod mollusc *Buccinum undatum*. *Biochim Biophys Acta* 207:347-360.
- Jalbert P, Himmelman JH, Bélan P, Thomas B (1989) Whelks (*Buccinum undatum*) and other subtidal invertebrate predators in the Northern Gulf of St Lawrence. *Can Nat* 116:1–15
- Jennings S, Kaiser MJ, Reynolds JD (2001) *Marine fisheries ecology*. Blackwell science ltd
- Kaiser MJ, Spencer BE (1995) Survival of by-catch from a beam trawl. *Mar Ecol-Prog Ser* 126:31-38
- Kenchington E, Glass A (1998) Local adaptation and sexual dimorphism in the waved whelk (*Buccinum undatum*) in Atlantic Nova Scotia with applications to fisheries management. *Can Tech Rep Fish Aquat Sci* 2237:1–42
- Kent & Essex IFCA (2016) <http://www.kentandessex-ifca.gov.uk/>. Accessed 1/7/16
- Kideys AE (1996) Determination of age and growth of *Buccinum undatum* L. (Gastropoda) off Douglas, Isle of Man. *Helgolander Meeresun* 50:353–368
- Lawler A (2013) Determination of the size of maturity of the whelk *Buccinum undatum* in English waters – Defra Project MF0231
- Linnaeus C (1758) *Systema Naturae per regna tria naturae, secundum classes, ordines, genera, species, cum characteribus, differentiis, synonymis, locis*. Editio decima, reformata. Laurentius Salvius: Holmiae.
- Mackie AM, Lasker R, Grant PT (1968) Avoidance reactions of a mollusc *Buccinum undatum* to saponin-like surface-active substances in extracts of the starfish *Asterias rubens* and *Marthasterias glacialis*. *Comp Biochem and Phys* 26:415-428

- Magnúsdóttir H (2010) The common whelk (*Buccinum undatum* L.): Life history traits and population structure. Magister Scientiarum degree thesis, University of Iceland
- Marine and Fisheries Agency (2005). United Kingdom Sea Fisheries statistics, 2004. Office for National Statistics, London
- Marine and Fisheries Agency (2006). United Kingdom Sea Fisheries statistics, 2005. Office for National Statistics, London
- Marine and Fisheries Agency (2007). United Kingdom Sea Fisheries statistics, 2006. Office for National Statistics, London
- Marine and Fisheries Agency (2008). United Kingdom Sea Fisheries statistics, 2007. Office for National Statistics, London
- Marine and Fisheries Agency (2009). United Kingdom Sea Fisheries statistics, 2008. Office for National Statistics, London
- Marine Management Organisation (2010). United Kingdom Sea Fisheries statistics, 2009. Office for National Statistics, London
- Marine Management Organisation (2011). United Kingdom Sea Fisheries statistics, 2010. Office for National Statistics, London
- Marine Management Organisation (2012). United Kingdom Sea Fisheries statistics, 2011. Office for National Statistics, London
- Marine Management Organisation (2013). United Kingdom Sea Fisheries statistics, 2012. Office for National Statistics, London
- Marine Management Organisation (2014). United Kingdom Sea Fisheries statistics, 2013. Office for National Statistics, London
- Marine Management Organisation (2015) UK Sea Fisheries Statistics 2014. Office for National Statistics, London
- Marine Management Organisation (2016) UK Sea Fisheries Statistics 2015. Office for National Statistics, London
- McIntyre R, Lawler A, Masefield R (2015) Size of maturity of the common whelk, *Buccinum undatum*: Is the minimum landing size in England too low? Fish Res 162:53–57
- Mensink BP, Fischer CV, Cadée GC, Fonds M, Ten Hallers-Tjabbes CC, Boon JP (2000) Shell damage and mortality in the common whelk *Buccinum undatum* caused by beam trawl fishery. J Sea Res 43:53-64
- Ministry of Agriculture, Fisheries and Food (1992) Sea Fisheries statistical tables 1990. Government statistical service, HMSO
- Ministry of Agriculture, Fisheries and Food (1994) Sea Fisheries statistics, 1991 and 1992. Government statistical service, HMSO
- Ministry of Agriculture, Fisheries and Food (1995) Sea Fisheries statistic, 1993. Government statistical service, HMSO

- Ministry of Agriculture, Fisheries and Food (1995) United Kingdom Sea Fisheries statistics, 1994. Government statistical service, HMSO
- Ministry of Agriculture, Fisheries and Food (1996) United Kingdom Sea Fisheries statistics, 1995. The Stationery Office, London
- Ministry of Agriculture, Fisheries and Food (1997) United Kingdom Sea Fisheries statistics, 1996. The Stationery Office, London
- Ministry of Agriculture, Fisheries and Food (1998) United Kingdom Sea Fisheries statistics, 1997. The Stationery Office, London
- Ministry of Agriculture, Fisheries and Food (1999) United Kingdom Sea Fisheries statistics, 1998. The Stationery Office, London.
- Moore PG, Howarth J (1996) Foraging by marine scavengers: effects of relatedness, bait, damage and hunger. *J Sea Res* 36(3/4):267-273
- Morel GM, Bossy SF (2004) Assessment of the whelk (*Buccinum undatum* L.) population around the Island of Jersey, Channel Isles. *Fish Res* 68:283-291.
- Nasution S, Roberts D (2004) Laboratory trials on the effects of different diets on growth and survival of the common whelk, *Buccinum undatum* L. 1758, as a candidate species for aquaculture. *Aquacult Int* 12:509-521
- Nicholson GJ, Evans SM (1997) Anthropogenic impacts on the stocks of the common whelk *Buccinum undatum* (L.). *Mar environ Res* 44:305-314
- Nielsen C (1975) Observations on *Buccinum undatum* attacking bivalves and on prey responses with a short review on attack methods of other prosobranchs. *Ophelia* 13:87-108
- Ramsay K, Kaiser M J, Richardson CA, Veale LO, Brand AR (2000) Can shell scars on dog cockles (*Glycymeris glycymeris* L.) be used as an indicator of fishing disturbance? *J Sea Res* 43:167-176
- Ramsay K, Kaiser MJ (1998) Demersal fishing disturbance increases predation risk for whelks (*Buccinum undatum* L.). *J Sea Res* 39:299-304
- Richardson CA (2001) Molluscs as archives of environmental change. *Oceanogr Mar Biol Annu Rev* 39:103-164
- Richardson CA, Kingsley-Smith PR, Seed R, Chatzinikolau E (2005a) Age and growth of the naticid gastropod *Polinices pulchellus* (Gastropoda: Naticidae) based on length frequency analysis and statolith growth rings. *Mar Biol* 148:319-326
- Richardson CA, Saurel C, Barroso CM, Thain J (2005b) Evaluation of the age of the red whelk *Neptunea antiqua* using statoliths, opercula and element ratios in the shell. *J Exp Mar Biol Ecol* 325:55-64
- Rochette R, T  treault F, Himmelman JH (2001) Aggregation of whelks, *Buccinum undatum*, near feeding predators: the role of reproductive requirements. *Anim Behav* 61:31- 41
- Ruppert EE, Fox RS, Barnes RD (2004) Invertebrate Zoology: a functional evolutionary approach. Thomson, Brooks/Cole, Belmont

- Santarelli L, Gros P (1985) Age and growth of the whelk *Buccinum undatum* L. (Gastropoda: Prosobranchia) using stable isotopes of the shell and operculum striae. *Oceanol Acta* 8:221–229
- Santarelli L, Gros P (1986) Modélisation bioéconomique de la pêche de Buccin (*Buccinum undatum* L.: Gastropoda) du port de Granville (Manche Ouest). *Revue Travaux de l'Institut Pêches maritimes* 48:23-32
- Santarelli L, Véron G, Huet J (1986) Exploitation du buccin dans le Golfe Normano-Breton. *La pêche maritime* 65:48-52
- Schäfer W (1956) Wirkungen der Benthos-Organismen auf den jungen Schichtverband. *Senckenbergiana Leth* 37:183-263
- Schöne BR, Rodland DL, Wehrmann A, Heidel B, Oschmann W, Zhang Z, Fiebig J, and Beck L (2007) Combined sclerochronologic and oxygen isotope analysis of gastropod shells (*Gibbula cineraria*, North Sea): life-history traits and utility as a high-resolution environmental archive for kelp forests. *Mar Biol* 150(6):1237-1252
- Scolding JWS, Richardson CA, Luckenbach MJ (2007) Predation of cockles (*Cerastoderma edule*) by the whelk (*Buccinum undatum*) under laboratory conditions. *J Mollus Stud* 73(4):333-337
- Shelmerdine RL, Adamson J, Laurenson CH, Leslie B (2007) Size variation of the common whelk, *Buccinum undatum*, over large and small spatial scales: Potential implications for micro-management within the fishery. *Fish Res* 86:201-206
- Smith KE, Thatje S (2013) Nurse egg consumption and intracapsular development in the common whelk *Buccinum undatum* (Linnaeus 1758). *Helgoland Mar Res* 67:109-120
- Smith KE, Thatje S, Hauton C (2013) Thermal tolerance during early ontogeny in the common whelk *Buccinum undatum* (Linnaeus 1785): Bioenergetics, nurse egg partitioning and developmental success. *J Sea Res* 79:32-39
- Staaland H (1972) Respiratory rate and salinity preference in relation to the ecology of three marine prosobranchs, *Buccinum undatum* (L), *Neptunea antiqua* (L), and *Neptunea despecta* (L). *Norw J Zool* 20:35-51
- State of Maine, department of marine resources (2016). <http://www.maine.gov/dmr/science-research/species/whelks.html>. Accessed 10/5/16
- Taylor J (1978) The diet of *Buccinum undatum* and *Neptunea antiqua* (Gastropoda: Buccinidea). *J Conchol* 29:309-318
- Taylor JD, Taylor CN (1977) Latitudinal distribution of predatory gastropods on the eastern Atlantic shelf. *J Biogeogr* 4:73-81
- Ten Hallers-Tjabbes CC, Boon JP, Lindenboom H, de Vooy C (1993) Ecoprofile of the Whelk, *Buccinum undatum* L. Report for Ministry of the Environment, Dutch Government, NIOZ
- Ten Hallers-Tjabbes CC, Everaarts JM, Mensink BP, Boon JP (1996) The decline of the North Sea whelk (*Buccinum undatum* L.) between 1970 and 1990: a natural or human-induced event? *Mar Ecol* 17:333–343
- Thomas MLH, Himmelman JH (1988) Influence of predation on shell morphology of *Buccinum undatum* L. on Atlantic coast of Canada. *J Exp Mar Biol Ecol* 115:221 – 236

- Valentinsson D, Sjödin F, Jonsson PR, Nilsson P, Wheatley C (1999) Appraisal of the potential for a future fishery on whelks (*Buccinum undatum*) in Swedish waters: CPUE and biological aspects. *Fish Res* 42:215–227
- Vermeij GT, Williams ST (2007) Predation and the geography of opercular thickness in turbinid gastropods. *J Mollus Stud* 73(1):67–73
- Williamson P, Kendall MA (1981) Population age structure and growth of the trochid *Monodonta lineata* determined from shell rings. *J Mar Biol Assoc UK* 61:1011–1026.
- Włodarska-Kowalczyk M (2007) Molluscs in Kongsfjorden (Spitsbergen, Svalbard): a species list and patterns of distribution and diversity. *Polar Res* 26:48–63
- WoRMS, World Register of Marine Species. *Buccinum undatum* taxon details (2016) <http://www.marinespecies.org/aphia.php?p=taxdetails&id=138878>. Accessed on 2/2/2016

Chapter 2:

Spatial variation in shell morphology and reproductive assessment of the whelk, *Buccinum undatum* in U.K. waters.

2.1 Introduction

An understanding of the reproductive cycle is key to predicting effects of impacts on the variability and abundance of a given species, especially from anthropogenic activities such as changes in fishing pressure. As with most other prosobranch gastropod species, *Buccinum undatum* is gonochoric and reproduces via sexual reproduction (Hayward & Ryland, 2000; Ruppert *et al.*, 2004). The first comprehensive overviews of the reproductive cycle of this species were conducted to the west of its range in Canada by Martel *et al.* (1986a & b). Until then, only the physical structures involved in *B. undatum* reproduction had been investigated; this was completed as a practice in anatomy rather than the investigation of reproductive cycles or behaviours (e.g. Fretter 1941 & 1953; Johansson, 1957; Price & Hunt, 1976). In recent years, many aspects of *B. undatum* reproduction and early development have been investigated, from reproductive investment, egg development and maternal care (Brokordt *et al.*, 2003; Nasution & Roberts, 2004) to the effects of Tri-Butyl Tin (TBT) and castrating nematodes on reproductive success (Tétreault *et al.*, 2000; Mensink *et al.*, 2002). Diagrammatic representations of the male and female reproductive systems can be seen in Figure 2.1.

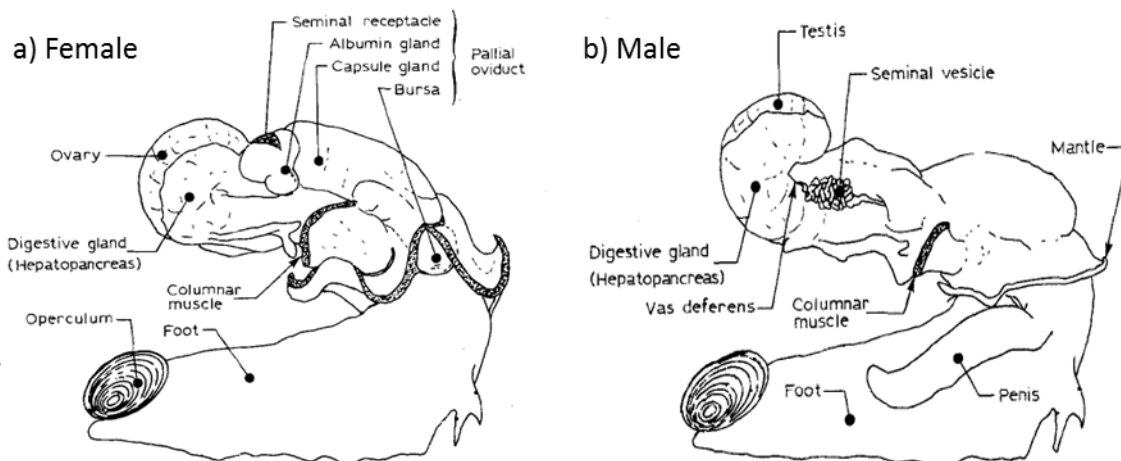


Figure 2.1. The reproductive organs of female a) and male b) *Buccinum undatum*. (Taken from Martel *et al.*, 1986a).

The monitoring of *B. undatum* stocks is often marred by problems arising from inter-population differences in important life history metrics such as size at maturity. In recent years there has been considerable focus in determining size at maturity for many *B. undatum* populations, as it is an important tool for assessing the efficacy of certain management measures such as Minimum Landing Sizes (MLS). The size at maturity is generally measured as the size at which

50% of the population is mature (L_{50}). Maturity itself can be confirmed in several ways such as visual inspection of the gonads, comparison of penis length, weight of gonad tissue and gonad histology. A recent study by McIntyre *et al.* (2015), investigated *B. undatum* from 12 sites, mainly across the south coast of England and found markedly different sizes at maturity across their sample sites (46.4–76.2mm shell height in males and 44.8–77.8mm in females). A similar study undertaken by Haig *et al.* (2015) at 8 sites in Welsh waters found differences across sites for both males and females. A summary of size at maturity studies can be seen in Table 2.1.

Table 2.1. Summary of variations in L_{50} for male and female *Buccinum undatum* and minimum landing sizes (MLS) for populations compiled from existing literature. PL = Penis Length, GSI = Gonado-somatic Index (Adapted from Haig *et al.*, 2015).

Location	L_{50} male	L_{50} female	Method	Study period	MLS	Reference
England	46.4–76.2	44.8–77.8	Visual	Jan–Mar	45	Hancock & Urquhart (1959); McIntyre <i>et al.</i> (2015)
Ireland	63.2–83.2	–	PL	–	50	Fahy <i>et al.</i> (2000)
Shetland	86	101	–	–	75	Shelmerdine <i>et al.</i> (2007)
France	49	52	Histology	–	45	Heude-Berthelin <i>et al.</i> (2011)
Canada	49–76	60–81	PL/GSI	Apr & May	70	Gendron (1992); Santarelli (1985)
Iceland	45–75	–	PL	May and Sep	45	Gunnarsson & Einarsson (1995)
Sweden	53.5–71.9	51.5–71.5	Microscopy	Oct–Nov	45	Valentinsson <i>et al.</i> (1999)
Wales	57.9–74.8	57.5–66.2	PL/GSI	Feb–May (18 Months)	45	Haig <i>et al.</i> (2015)

It is clear from the summary table that even with an increased minimum landing size (MLS) in several areas, large proportions of immature whelks are being caught and may not be protected by the current regulations. This may have severe implications for future fisheries regulations and management.

2.1.1 Seasonal reproductive cycle of *Buccinum undatum*

As a result of conflicting findings in early studies of the reproductive cycle of *B. undatum*, Thorson (1946) assumed that spawning occurred all year round. It is now clear that the timing of reproduction varies with location and this is most likely controlled by seawater temperature. In Canada (Gulf of St. Lawrence), mating begins in early May with egg laying occurring soon after and is completed by mid-summer (July). The eggs hatch 5–8 months later (Martel, 1986a & b; Himmelman & Hamel, 1993). In the Menai Strait, North Wales, U.K. the cycle of egg laying occurs in the autumn (November and December) (pers. obs.) and the juveniles hatch from the eggs several months later from January – March. Generally in the Irish Sea the height of maturity occurs in autumn with egg laying around September – February and hatching in early April after

a much shorter development period of 3-4 months than in the Gulf of St. Lawrence (Martel, 1986a; Kideys *et al.*, 1993). In Swedish waters where egg laying occurs in October new hatchlings appear between January and April (Valentinsson, 2002). An overview of egg laying and hatching by area are summarised in Table 2.2.

Table 2.2. Summary of copulation period, development seawater temperature, egg laying and time to hatching from fifteen studies on *Buccinum undatum*. Adapted and updated from Smith & Thatje, (2013).

Study	Location	Reproduction period (copulation)	Egg Laying Period	Development Temperature (°C)	Time to Hatching (Months)
Cunningham (1899)	Falmouth, UK	n/a	Nov-Feb	n/a	n/a
Fretter and Graham (1985)	n/a	n/a	Nov-Feb	n/a	3–9
Hancock (1967)	Burnham on Crouch, UK	n/a	Nov	n/a	3–4
Kideys <i>et al.</i> (1993)	Douglas, Isle of Man	n/a	Sep-Feb	n/a	3–5
Lebour (1937)	Plymouth, UK	n/a	Oct-May	n/a	n/a
Martel <i>et al.</i> (1986a)	Gulf of St Lawrence, Canada	May-July	May-July/Aug	2–3	5–8
Moore (1937)	Isle of Man, UK	n/a	Nov-Apr	n/a	n/a
Nasution & Roberts (2004)	Irish Sea, Northern Ireland	n/a	n/a	8–11	2.5–3
Nasution <i>et al.</i> (2010)	Irish Sea, Northern Ireland	n/a	n/a	10	3
Portmann (1925)	Roscoff, France	n/a	n/a	5–9	n/a
Smith <i>et al.</i> (2013)	Southampton Water, UK	n/a	Dec - Feb	6	4.5–5
Smith & Thatje (2013), Magnúsdóttir (2010)	Breiðafjörður, Iceland		Oct-Mar	0-5	n/a
Valentinsson (2002)	Skagerrak, Sweden	n/a	Oct	4–8	3–4
Heude-Berthelin <i>et al.</i> (2011)	Cotentin, France		Oct-Dec	n/a	n/a

Martel *et al.*, (1986a) investigated the timings of gonad development in both male and female whelks from the Gulf of St. Lawrence (Canada) and documented the first example of inverse testes/ovary development in a marine invertebrate. They found that males produced sperm for use in the following year's reproductive cycle around the same time as copulation, and stored it in the seminal vesicle. This is different from the females that did not begin oogenesis until 2-3 months later, possibly triggered by the depletion of oocytes during egg laying. Martel *et al.*, (1986a) measured gonad weight after dissection of the gonad tissue from the digestive gland to find the period of maximum sexual maturity, along with measuring the development of several other sexual organs the same way (pallial oviduct in females and testes and seminal vesicle in males). They found clear seasonality in the development of the pallial oviduct, testes, and seminal vesicle over two years, indicating a peak in gonad size in June with maximum local seawater temperatures. However, the cycle of gonad development for both sexes was less clear. For females the peak in GSI was found in June in the first year and peaked in March the

following year, however it is unclear what caused the difference. It was estimated that the female reproductive effort was approximately 6 times that of the male owing to the production of large lipid rich oocytes and egg capsules, this heavy energetic expenditure may leave the females more vulnerable to predation immediately following the egg laying period (Kideys *et al.*, 1993; Borkordt *et al.*, 2003). A later study by Heude-Berthelin *et al.* (2011) employed histological techniques to assess gonad maturity. They attempted to more accurately track the reproductive cycle in *B. undatum* samples from Granville Bay in the North of France by monitoring gametogenesis; it was hypothesised that the histological methods would allow them to also monitor imposex within the population, although no cases were found. Their study showed that in both sexes, gametogenesis begins in the winter and reaches a peak in October, prior to spawning between October and December. Haig *et al.* (2015) found a peak in the gonadosomatic index (GSI; gonad weight/body weight * 100) between September and October for all eight sites studied across Wales. Martel *et al.* (1986a & b) concluded that the spawning season in Europe was different to the Gulf of St. Lawrence i.e. a summer reproductive season in Canada and an Autumn/Winter reproductive season in Europe. It was suggested that because *B. undatum* is a boreal species, its temperature tolerance does not favour an energetically costly reproduction period in Europe over the summer. This theory was questioned by Laptikhovsky (2014) who highlighted that the reproductive cycle of *B. undatum* in Breiðafjörður (Iceland) was similar to that in Europe (October – March) but the seawater temperature during that period was roughly the same as the Gulf of St. Lawrence (0-5°C; Magnúsdóttir, 2010). He suggested instead, that the seasonality of breeding of European whelk populations was timed upon hatching to allow juveniles to benefit from the rising temperatures during the spring season thus facilitating rapid growth when ample food reserves were present. In Canada however, it was suggested that the reproductive cycle was tied to that of a major predator of *B. undatum*, the starfish *Lepasterias polaris*. Females of *L. polaris* cease feeding during their brooding period in Autumn that coincides with hatching of juvenile *B. undatum* from their egg cases. There are no predators of *B. undatum* with an equivalent cycle of reproduction in European waters.

2.1.2 Shell morphology

Several aspects of the morphology of *B. undatum* have been shown to vary with location (Golikov, 1968; Thomas & Himmelman, 1988; Gendron, 1992; Shelmerdine *et al.*, 2007). In some areas, these differences are thought to be related to predation pressure via repeated damage and repair of the shell, causing a thickening of the shell structure (Thomas & Himmelman, 1988; Gendron, 1992). The plasticity inherent in the morphology of *B. undatum* has been clear for many years, with early scientific exploration trips finding a wide variety of shell morphologies for this species (Figure 2.2; Dautzenberg & Fischer, 1912). Gender differences in shell morphology have been shown by Ten Hallers-Tjabbes (1979) and Kenchington & Glass (1998), specifically the shape of the most recent whorl and aperture in whelks from the North Sea and Canadian Pacific respectively. However, this has proven to be inconclusive for many study areas as the morphological differences governed by geographical location seem to negate any effect of gender (e.g. Thomas & Himmelman, 1988). More recently Magnúsdóttir (2010) found significant differences between several morphometric measurements over a single bay (~100 km) in the west of Iceland (Breiðafjörður). They concluded that the variability observed across the populations likely arose from a combination of environmental and genetic factors. An understanding of differences in shell morphology between geographical locations will aid in the interpretation of size at age data through an inference of how changes in environmental conditions affect shell growth.

In this chapter I focus on the seasonal reproductive cycle of a *B. undatum* population in the Menai Strait. It is hypothesised that mating and egg laying in this location will occur between September and February and occur at a similar time to that seen in Isle of Man waters, Irish Sea by Kideys *et al* (1993). I also investigate whether there are morphological differences in shape of shells from 6 geographically separated locations around the British Isle. It is hypothesised that there will be clear differences in shell morphology of *B. undatum* between sites due to differing environmental conditions.



Figure 2.2. A plate showing morphological differences in the shells of *B. undatum*, made from samples collected during scientific campaigns by Albert I sovereign Prince of Monaco on his research yachts 'Hirondelle' & 'Princess Alice' (Taken from Dautzenberg & Fischer, 1912).

2.2 Materials and methods

2.2.1 Field collection

Eighteen monthly samples of 50 whelks were collected from the Menai Strait using a string of 3 scientific inkwell pots (baited with green shore crab (*Carcinus maenas*) and mackerel (*Scomber scombrus*)) soaked for 24 hours. This was done to assess the timing of the reproductive cycle of whelks in the Menai Strait. The drainage holes in the pots were covered with 3mm mesh and the whelk catch was not riddled (the process used by fishermen to remove undersized whelks) to ensure all size classes were retained for analysis. Dispensation for the landing of undersized whelks (<45mm) was granted by the Welsh Government (disp#004, [Appendix A](#)). Once collected, whelks were frozen in labelled bags until required.

In addition to the monthly samples collected from the Menai Strait, whelks were obtained between February 2014 and July 2015 from 5 additional locations and 7 additional sites across the UK (see Figure 2.3) to assess differences in various key shell morphometrics. As three sites were sampled within the location of Jersey, 8 sites were sampled in total from 6 locations. For a full description of site details see Table 2.3. All whelk samples from Shetland, Nefyn, Holyhead and Amlwch were purchased from local fishermen and the exact locations are not reported at the request of the fishermen. Whelk samples from the three sites within the location of Jersey (JE4, JE5 & JD5) were donated by the Jersey Department of the Environment (DoE) and were collected during their annual whelk survey. The sites around North Wales (Amlwch, Holyhead & Nefyn) were chosen to investigate differences in *B. undatum* populations over small linear distances, whilst the populations in Jersey and Shetland were chosen to investigate differences over large geographical distances in areas with differing environmental conditions (i.e. seawater temperature). The populations of *B. undatum* in both Jersey and Shetland are actively exploited and have been studied previously (Shrives *et al.*, 2015 – Jersey; Shelmerdine *et al.*, 2007 – Shetland). Although three separate sites within the location of Jersey were sampled, for the maturity studies and many of the morphometric analyses, all of these sites were grouped together. This was because the small sample size at each individual site often produced insignificant results.

Table 2.3. A summary of the location, collection dates and number of whelks collected.

Site name	Latitude	Longitude	Date	Depth (m)	Number of whelks
Menai Strait	53.2338889	-4.143055556	Feb '14 - Jul '15	10 - 11.5	50/month (900)
Jersey E4	49.193889	-1.858611	Feb '15	14	91
Jersey E5	49.025	-1.934722	Feb '15	13	100
Jersey D5	49.192884	-1.9925	Feb '15	7	86
Shetland	-	-	Feb '15	18 - 20	218
Nefyn	-	-	Jul '15	≈12	107
Amlwch	-	-	Jul '15	≈12	151
Holyhead	-	-	Jul '15	≈13	107



Figure 2.3. Map illustrating the eight sample sites for *Buccinum undatum* collected from the U.K.

2.2.2 Timing of the reproductive cycle

2.2.2.1 Body and maturity measurements

Frozen whelk samples were thawed in ambient temperature fresh water for 3 – 4 hours until fully defrosted. Any large epiphytes were scrapped from the outside of the shell using a blunt knife, patted dry on a piece of absorbent blue roll and weighed on a top-loading balance to the nearest 0.01g. Using large forceps, the foot of each whelk was gripped and gently pulled until the collumellar muscle detached, the whelk body mass was eased out of the shell whilst twisting in an attempt to remove it intact. If the whelk broke during removal, the remaining section was extracted from the shell using water pressure from a tap with a spray attachment. A paper label with the sample name was appended to each shell and together with the soft body photographed together. The whelk's gender was assessed and noted. In male whelks the penis was measured using digital Vernier callipers to the nearest 0.01 mm. Females were inspected for the presence of a small penis due to the effects of imposex (Ten Hallers-Tjabbes *et al.*, 1994). To assess gonad maturity, the steps outlined in Haig *et al.* (2015) were followed and involved estimating the proportion of digestive gland taken up by gonad tissue for both males and females to give a percent maturity value (%mat) (Figure 2.4).

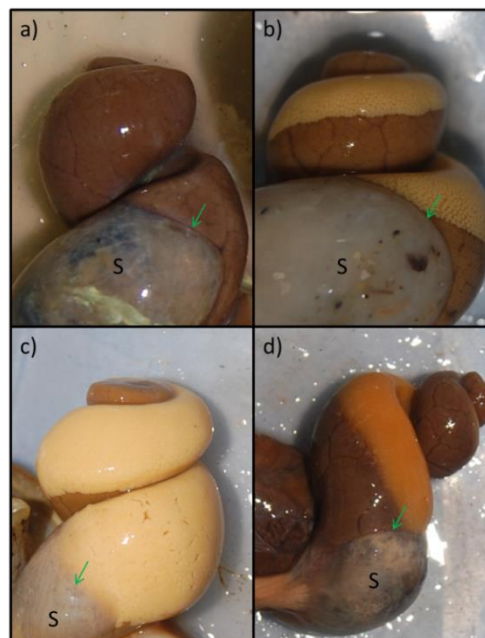


Figure 2.4. Examples of maturity stages of *Buccinum undatum* showing differences in the proportion of the digestive gland to gonad. a) a female whelk showing 0% gonad development, b) a female whelk showing 50% development, pale orange/yellow gonad tissue is visible, c) a female whelk showing 100% development and d) a male whelk showing 50% development. Males exhibit a dark orange and often brown colour to the gonad tissue. S: stomach; green arrows: dissection boundary for weight measurements.

In the case of male whelks, the presence or absence of a vas deferens was also noted as this is a good indicator of sexual maturity (Fretter, 1941). This can however be misleading if the animals have been exposed to Tri-Butyl Tin (TBT) which can lead to the formation of male sex organs in female whelks (imposex), even in juvenile animals (Mensink *et al.*, 2002). The vas deferens is visible as a convoluted tube underneath the base of the digestive gland/gonad (Figure 2.5a) and as a raised line on the dorsal surface of the body, leading to the penis (Figure 2.5b).

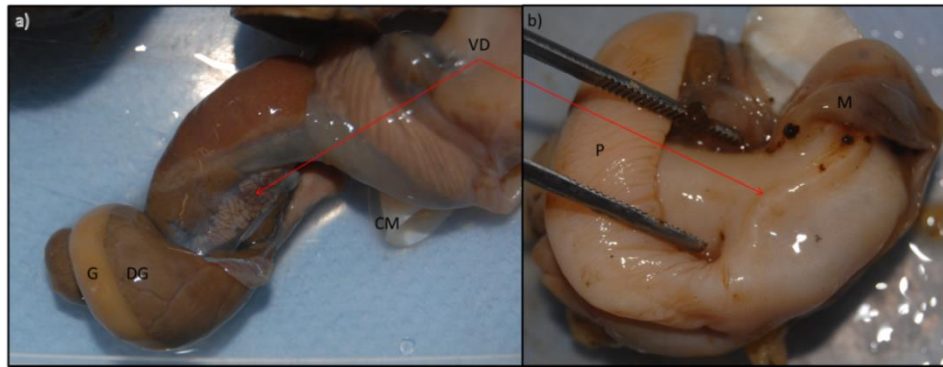


Figure 2.5. Development of the vas deferens (VD) in a mature male *Buccinum undatum*. a) the position of the VD on the underside of the digestive gland/gonad and b) the position of the VD on the dorsal surface of the whelk body. G: gonad, DG: digestive gland, CM: columellar muscle, VD: vas deferens, P: penis and M: mantle.

The complete body was weighed on a top loading balance to the nearest 0.01g. The gonad/digestive gland were removed from the rest of the body mass and the two organs separated after dissection using two pairs of forceps to pull apart the two halves of the body just above the stomach (boundary highlighted by green arrows in Figure 2.5), weighed separately and disposed of. The stomach and viscera were removed from the foot of each whelk, the foot was weighed and placed in a labelled ziplock bag and re-frozen for later study of the statoliths (see Chapter 5). The stomach was not weighed as the type and amount of contents varied between samples and individuals. Both the stomach and viscera were not retained. The labelled shells were dried at room temperature for 48 hours before weighing to the nearest 0.01g.

Following processing, the Gonadosomatic Index (GSI) was calculated by expressing the weight of the gonad/digestive gland as a percentage of the total body weight minus the stomach weight (see Haig *et al.*, 2015). This calculation differs from previous published studies which dissected the gonad and digestive gland tissues from each other to assess the weight of the gonad alone, the time constraints and large sample volume of this project made this approach unsuitable (Martel *et al.*, 1986a; Gendron, 1992). In an attempt to find middle ground between these two approaches, an adjusted GSI (aGSI) was calculated by amending the gonad/digestive gland

weight in relation to the %mat value for each specimen (i.e. a specimen with a %mat. value of 30% would have the gonad/digestive gland weight multiplied by 0.3), and then presenting this as a percentage of the body weight. Bar plots of resulting data were compiled using the ggplot2 package in R- 3.3.2.

Estimates of L_{50} , the size at which 50% of the population is mature, were made using a logistic regression model (Roa *et al.*, 1999; Walker, 2005) to create:

$$P = P_{max} \left(1 + \exp^{-\ln(19) \left[\frac{l - l_{50}}{l_{95} - l_{50}} \right]} \right)^{-1}$$

Where P represents the proportion of the population mature at a given length (l), P_{max} is the maximum proportion of mature animals. Acronyms l_{50} & l_{95} refer to the lengths at which 50% and 95% of the population are mature respectively. Ogives for maturity estimates were constructed using R, the original code was written by Harry (2013) and was also utilised by Haig *et al.* (2015). The parameter estimates and significance of the Generalised Linear Model (GLM, used in the ogive calculation) were tested using Chi-squared tests against a null model. Confidence intervals were calculated by bootstrapping the GLM (x10,000 runs). The values of l_{50} & l_{95} were compared between sites as well as between seasons for the Menai Strait by grouping 3 months together into spring, summer, autumn and winter periods (January, February & March – winter; April, May & June – spring; July, August & September – summer; October, November & December – autumn).

Several calculations were undertaken to determine whether Penis Length (PL) is a good proxy for maturity. Firstly, the size at which PL is greater than 50% of the Total Shell Length (TSL) was calculated by plotting %PL (PL/TSL * 100) against TSL (after Santarelli, 1985). The resulting equation was used to estimate the TSL at which %PL equals 50%. Secondly, ogives for PL_{50} (the penis size at which 50% of the population is mature, after Fahy *et al.* (2005)) and % PL_{50} (the %PL at which 50% of the population is mature after K  ie, 1969) were estimated using the above methods for GLM, where PL and %PL were substituted for TSL in the calculations. Lastly, an iterative search procedure was utilised with the following linear model:

$$TSL = PL * I(x < c) + x * I(x > c)$$

This model was used to estimate an ‘inflection’ in the relationship between TSL and PL, by finding the point with the lowest residual mean standard error to infer a change in allometry (Crawley, 2007; Haig *et al.*, 2015).

2.2.3 Morphometric study

2.2.3.1 Shell measurements

Several metrics were taken from each dried shell; dry shell weight was measured to the nearest 0.01 g and total shell length, maximum shell width, minimum shell width and shell lip thickness were measured using digital vernier callipers to the nearest 0.1 mm (see Figure 2.6a). Shell lip thickness was measured at 4 locations along the shell margin. The ventral surface of each shell was then photographed with a ruler for scale.

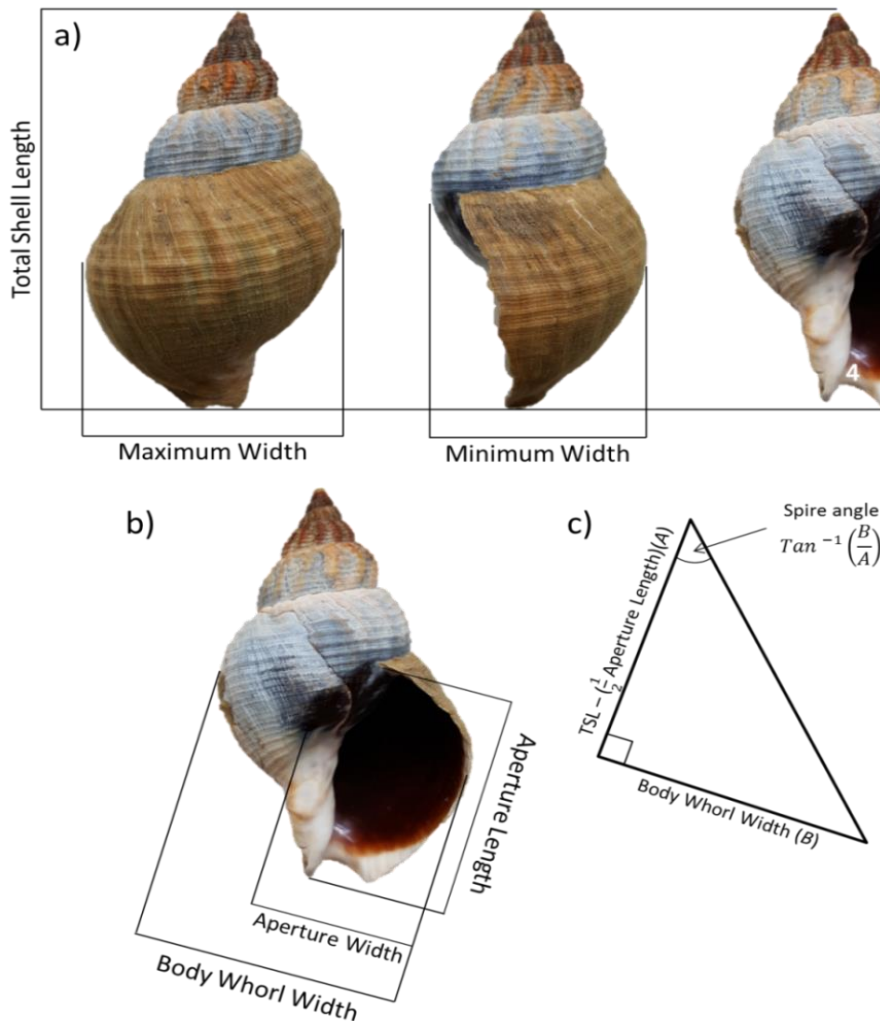


Figure 2.6. A representation of the length measurements taken from all *Buccinum undatum* shells that were used in morphometric analyses. a) the measurements taken with vernier callipers; positions 1, 2, 3 & 4 represent positions where the thickness of the shell lip was measured, b) the measurements taken from photographs of the aperture and body whorls and c) demonstrates how the spire angle measurement was calculated.

Six specimens were photographed at a time allowing the accurate measurement of aperture length and aperture width to be made at a later date using ImageJ (version 1.48, Ferreira & Rasband, 2012; see Figure 2.6b). The method was employed as it was more time-efficient than manual measurements. However a sub-set of shells was first measured using both Vernier callipers and ImageJ and the measurements compared to ensure both methods independently provided accurate and comparable measurements. Trigonometry was used to calculate the angle of the shell spire (see Figure 2.4c), a similar approach used to calculate the shell angle of mussels shells by Beggel *et al.* (2015).

The resulting measurements were initially analysed using Principle Component Analysis (PCA) and Linear Discriminant Analysis (LDA), to investigate whether there were differences between sites as well as between male and female whelks. The data were first transformed using a DM_LOG transformation (Darroch & Mossimann, 1985; Jungers *et al.*, 1995). This transformation involves calculating the geometric mean size (GMS) for each sample from the linear variables ($10^{(\text{sum of the log-normalised variables}/\text{number of variables})}$). The DM_LOG is then performed by dividing the sample values for each variable by the GMS and log transforming the resulting numbers. All DM_LOG outputs were tested for normality by site (Shapiro-Wilk & Kolmogorov-Smirnov tests). The resulting principal components from the PCA were also tested for normality and compared between sites using one-way ANOVA with Tukey *post-hoc* comparisons. All analyses were performed in R (3.3.2), LDA was conducted with the MASS (Modern Applies Statistics with S; Ripley *et al.*, 2016) package. Both LDA and PCA outputs were plotted using the 'ggord' (ordination plots with the ggplot2 package) with 95% confidence intervals.

The PCA and LDA results were used to identify the variables that caused the greatest differences between sites. These differences were then investigated further using the smatr-3 package (Standardised Major Axis Estimation and Testing Routines; Warton *et al.* 2015) to investigate differences in the allometry of variables between sites (Warton *et al.*, 2012). The smatr-3 package fits linear models to logged data and compares the resulting slopes using pairwise comparisons (the analyses are similar to ANCOVA). The slope, elevation (movement on the y-axis) and shift (along the slope) of the lines were compared. Following each analysis the residuals were tested for normality (Shapiro-Wilk test). Variables which did not display allometric change with growth (such as spire angle), were compared using one way ANOVA with Tukey *post-hoc* comparisons following tests for normality (Shapiro-Wilk & Kolmogorov-Smirnov

tests). For the PCA and LDA analyses, any shells with 1 or more missing measurement were removed as neither analysis works with missing data points. The removed samples were included later for the allometric analyses following the PCA and LDA.

2.3 Results

2.3.1 Reproductive studies

2.3.1.1 Timing of the reproductive cycle and L_{50} calculations

Seasonal variation in the Gonado-Somatic Index (GSI) and the timing of the reproductive cycle are shown in Figure 2.7a). There is a clear peak in the female GSI in June and the male GSI in May with the lowest values in March. In contrast to this, Figure 2.7b) shows the adjusted GSI (aGSI) for the same samples. There is a clear peak in both the female and male GSI in September with a complete absence of mature females in November. The ratio of males and females in each monthly sample is shown in Figure 2.8. The lowest number of females was observed in October and November and coincided with the egg-laying period (pers. obs.). Over 18 months of sampling, only 3 clear cases of imposex were identified within the Menai Strait population out of a sample size of 900.

The L_{50} ogives for males and females for all sites are shown in Figures 2.9 & 2.10. The GLMs calculated for the males and females from Nefyn and Amlwch were found to be non-significant, this is likely due to a lack of mature or immature animals. The resulting ogives are still presented for comparison and the reasons for the lack of significance are discussed later. A full summary of the L_{50} and L_{95} values for all sites is shown in Table 2.4. The seasonality of L_{50} was investigated for both males and females by grouping the 18 monthly samples from the Menai Strait into 3-month seasons (January, February & March – winter; April, May & June – spring; July, August & September – summer; October, November & December – autumn). The L_{50} ogives for all seasons are shown in Figures 2.11 & 2.12 and the full results are summarised in Table 2.5.

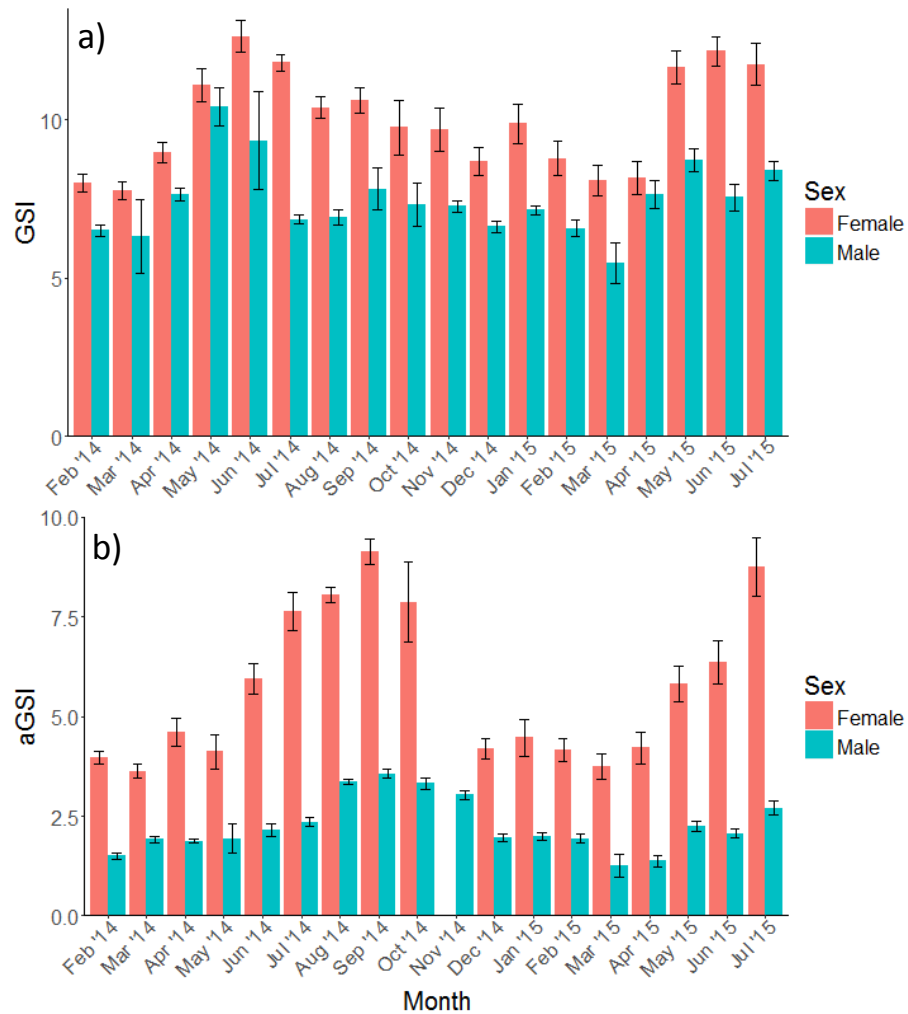


Figure 2.7. a) seasonal variation in the gonadosomatic index (GSI) and b) the adjusted gonadosomatic index (aGSI), for male (blue) and female (pink) *Buccinum undatum* from the Menai Strait over an 18 month period. Error bars represent $\pm 1SE$. Note the absence of mature females in the population during November.

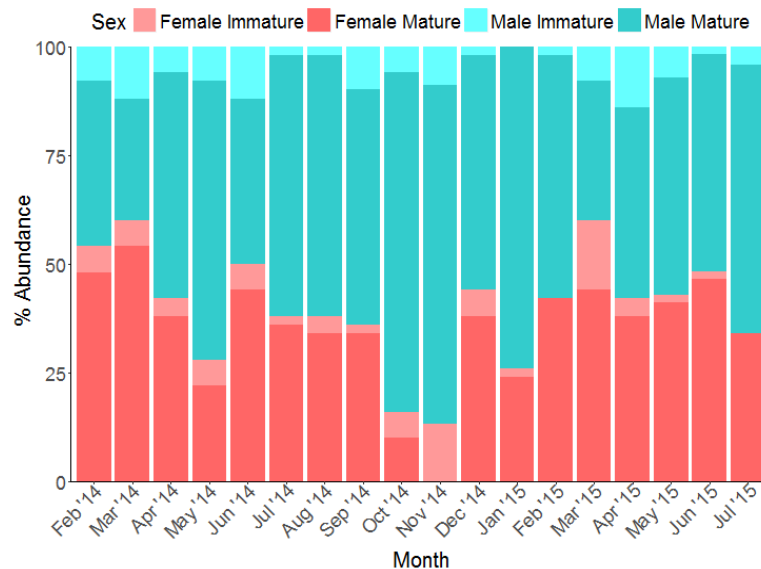


Figure 2.8. Seasonal variation in the ratio between immature and mature male and female *Buccinum undatum* from the Menai Strait over an 18 month sampling period. Note the absence of mature females in the population during November.

#

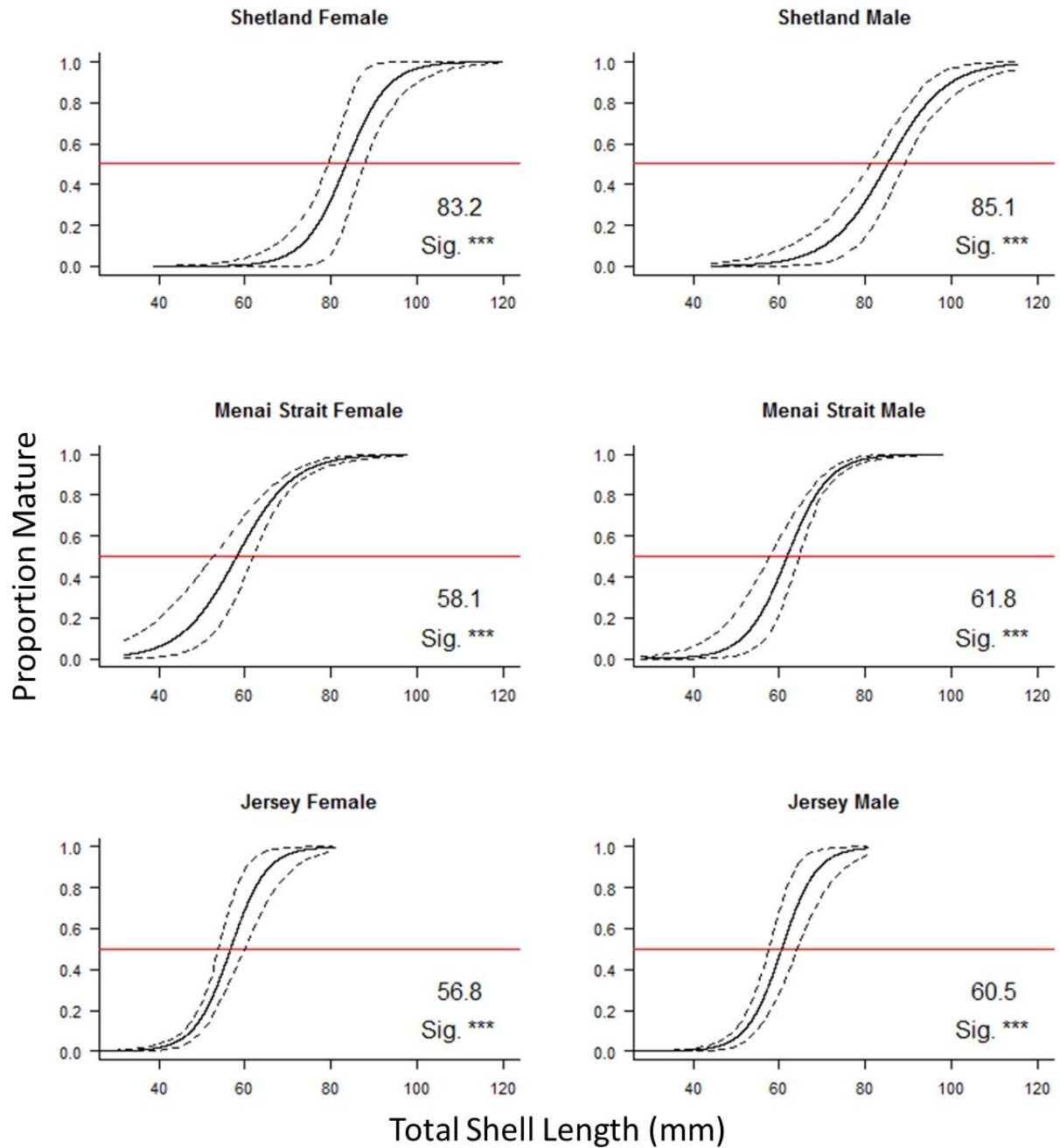


Figure 2.9. Maturity ogives for male and female *Buccinum undatum* populations from the Shetland Isles, Menai Strait and Jersey. The red lines indicate 50% population maturity, insets show L_{50} for each plot. Dotted lines represent upper and lower 95% confidence intervals. Significance codes: '***' < 0.001.

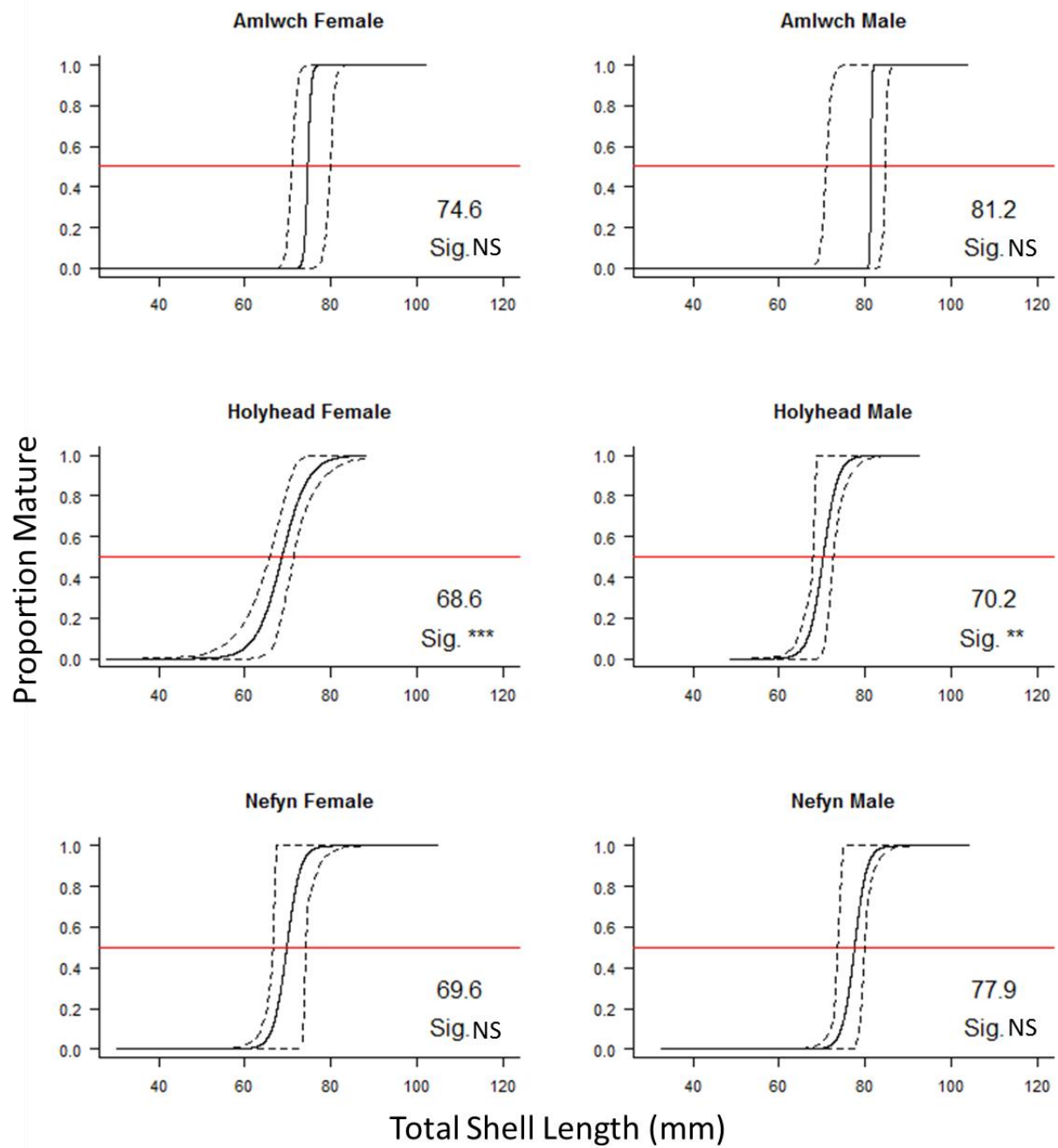


Figure 2.10. Maturity ogives for male and female *Buccinum undatum* populations from Amlwch, Holyhead and Nefyn. The red lines indicate 50% population maturity, insets show L₅₀ for each plot. Dotted lines represent upper and lower 95% confidence intervals. Significance codes: '***' < 0.001, '**' < 0.01, NS - not significant.

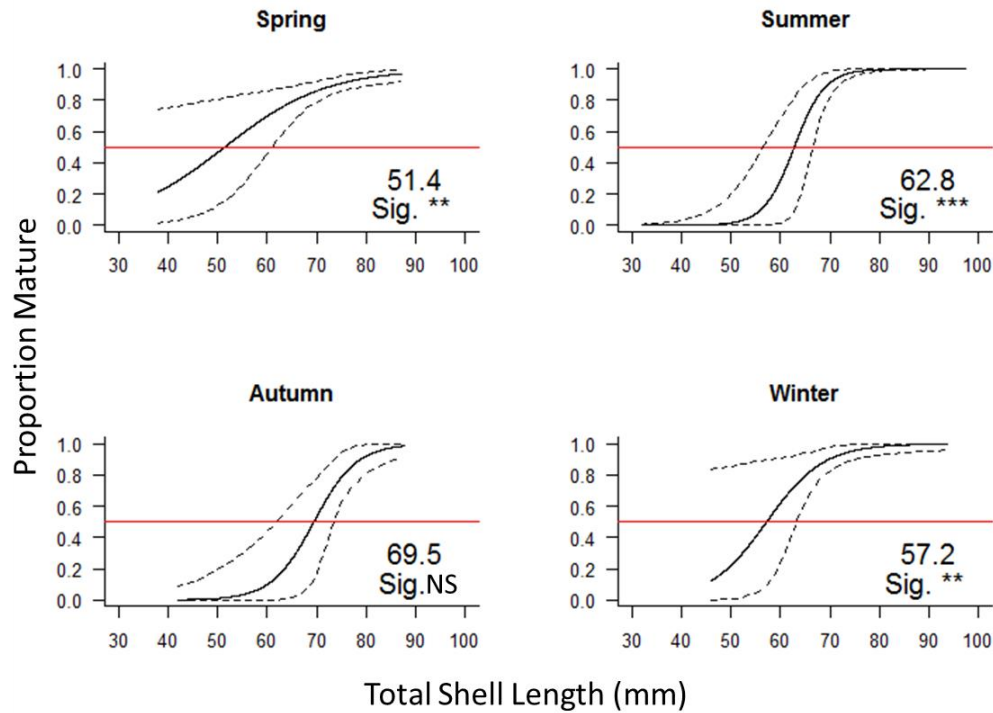


Figure 2.11. Maturity ogives showing seasonal changes in female *Buccinum undatum* populations from the Menai Strait. The red lines indicate 50% population maturity; insets show L₅₀ for each plot. Dotted lines represent upper and lower 95% confidence intervals. Significance codes: '***' < 0.001, '**' < 0.01, NS - not significant.

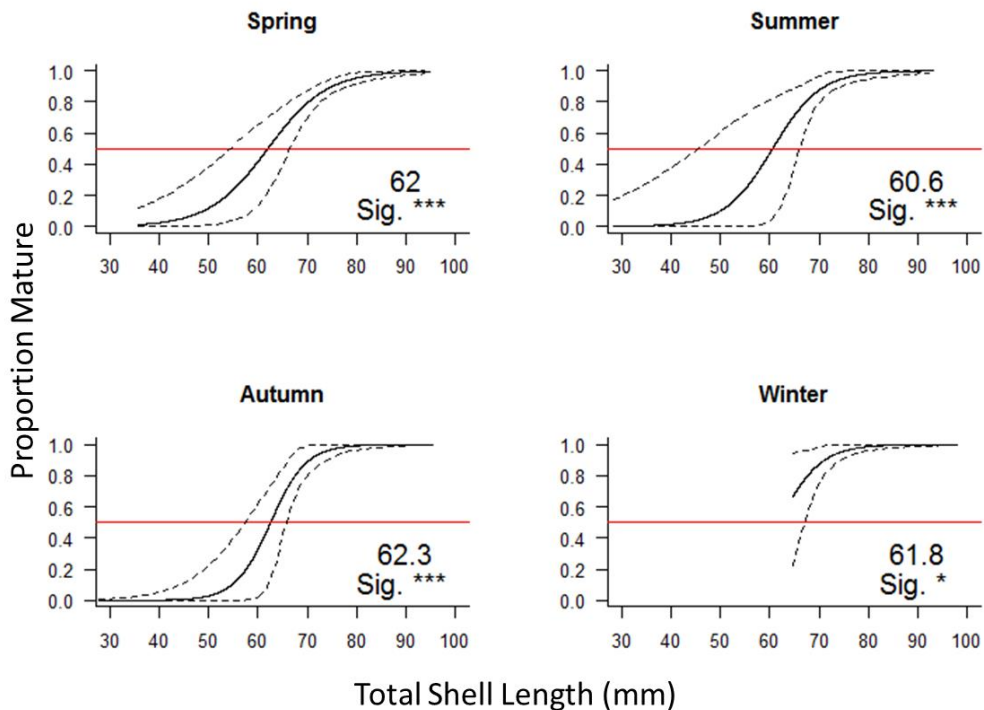


Figure 2.12, Maturity ogives showing seasonal changes in male *Buccinum undatum* populations from the Menai Strait. The red lines indicate 50% population maturity; insets show L₅₀ for each plot. Dotted lines represent upper and lower 95% confidence intervals. Significance codes: '***' < 0.001, '*' < 0.05.

Table 2.4. The estimated L_{50} and L_{95} values (mm) for male, female and combined genders of *Buccinum undatum* collected from six locations. The upper and lower 95% confidence intervals and the significance of the GLM are shown. (** = $p < 0.01$; *** = $p < 0.001$; NS = not significant).

Site	Gender	L_{50}	Upper CI	Lower CI	L_{95}	Upper CI	Lower CI	Sig.	<i>n</i>
Shetland	Female	83.2	87.2	79.3	105	118.5	92.8	***	29
	Male	85.1	89	81.3	105	112.4	97.7	***	171
	Combined	84.4	87.2	81.6	102	107.4	97.2	***	200
Menai Bridge	Female	58.1	61.9	52.7	77.3	80.6	73.9	***	375
	Male	61.8	64.5	57.8	75.9	78.2	73.6	***	535
	Combined	60.3	62.7	57.2	76.4	78.3	74.6	***	910
Jersey	Female	56.6	60.1	53.9	68.8	75.6	62.9	***	136
	Male	60.5	64.4	57.4	72.3	78.9	65.8	***	141
	Combined	58.5	60.9	56.4	71	75.6	66.7	***	277
Amlwch	Female	74.6	79.7	70.8	75.7	81.6	72.4	NS	74
	Male	81.2	84.5	70.9	81.6	85.4	72.7	NS	76
	Combined	80.8	82.9	72	81.2	83.5	73.6	NS	150
Holyhead	Female	68.6	71.2	65.6	77.4	82.1	71.7	***	62
	Male	70.2	72.5	68.1	75.1	78	68.1	**	46
	Combined	69.5	71.1	67.8	76.6	79.4	72.9	***	108
Nefyn	Female	69.7	74.1	66.5	74.3	78.9	66.6	NS	46
	Male	77.9	80.8	75.5	83.7	86.9	76	NS	57
	Combined	74.3	77.9	70	82.8	86.3	74.1	***	103

Table 2.5. Seasonal variation in the estimated L_{50} and L_{95} values (mm) for male and female *Buccinum undatum* collected from the Menai Strait for each of four seasons. The upper and lower 95% confidence intervals and the significance of the GLM are also shown. (** = $p < 0.01$; *** = $p < 0.001$; * = $p < 0.05$; NS = not significant).

Gender	Season	L_{50}	Upper CI	Lower CI	L_{95}	Upper CI	Lower CI	Sig.	<i>n</i>
Female	Spring	51.4	61.2	15.5	81.6	99.9	73.7	**	140
	Summer	62.8	66.6	56.1	71.9	74.6	67.4	***	109
	Autumn	69.5	73.6	61.6	82.1	91.4	75.4	NS	31
	Winter	57.2	65.2	27.2	74	85.5	65.5	**	93
Male	Spring	62	66.5	53.2	79.5	84.5	75.1	***	165
	Summer	60.6	66.2	45	74.8	80.7	69.2	***	147
	Autumn	62.3	65.7	57.3	73.1	77.6	67.1	***	112
	Winter	61.8	67	40.3	74.3	78.3	66.7	*	107

2.3.1.2 Estimates of maturity using penis length

Estimates of the size at maturity calculated from the Penis Length (PL) were attempted using several previously published methods (see summary in Table 2.6) together with the standard L_{50} values calculated from gonad development. The values presented for P_{50} were calculated by substituting PL for Total Shell Length (TSL) in the L_{50} calculations used above (after Haig *et al.*, 2015). The resulting value was in the form of a PL measurement which was converted back to TSL using the logarithmic relationship between TSL and PL for each site. The 50% PL column in Table 2.6 represents the size at which male whelks have a PL > 50% of their TSL, this was one of the methods used to estimate maturity by Santarelli (1985). The %PL was calculated in the same way as P_{50} by substituting the %PL ($PL/TSL \times 100$) for TSL in the calculations. However the results of the %PL were not converted back into TSL and instead represent the %PL at 50% maturity. The final column represents the results of the iterative search procedure (with a linear model) used to identify the inflection point in the relationship between TSL & PL. All of the relationships found during these analyses were significant. The plots produced from this analysis are presented in Figure 2.13.

Table 2.6. Differences in maturity estimates calculated using different published methods. The inflection point (Figure 2.13) and P_{50} (with 95% confidence intervals, CI) were calculated using the methodology of Haig *et al.* (2015). The %PL50 is the variation of the P_{50} with 95% confidence intervals and 50% PL as utilised by Santarelli (1985). (***) = $p < 0.001$; ** = $p < 0.01$; * = $p < 0.05$; NS = not significant).

Site	L_{50}	P_{50}	Upper CI	Lower CI	P_{50} Sig.	50% PL	%PL50	Upper CI	Lower CI	%PL50 Sig.	Inflection point
Shetland	84.0	93.6	97.8	90.5	***	94.3	44.4	49.9	38.7	***	84.7
Jersey	60.5	59.6	61.1	58.3	***	56.6	31.3	39.9	29.0	***	44.0
Menai	61.8	69.0	70.6	66.9	***	73.7	37.1	40.9	32.2	***	61.9
Amlwch	81.2	75.6	81.5	72.1	NS	85.0	40.1	45.6	33.2	NS	83.8
Holyhead	70.2	72.3	74.2	69.8	*	75.5	58.4	65.3	51.2	*	68.4
Nefyn	77.9	79.4	83.7	74.1	**	87.0	36.5	44.5	29.3	**	60.1

The final results of the maturity analyses are shown in Figure 2.14. The histograms show clear differences in population structure between sites, with Shetland having a greater number of large *B. undatum* when compared to sites such as Jersey and the Menai Strait, as well as differences in the size structure of the male and female populations in Shetland. The percentage values placed onto each plot indicate how much of each population is potentially not protected if the results of the L_{50} calculations are accurate and the size histograms accurately represent the population.

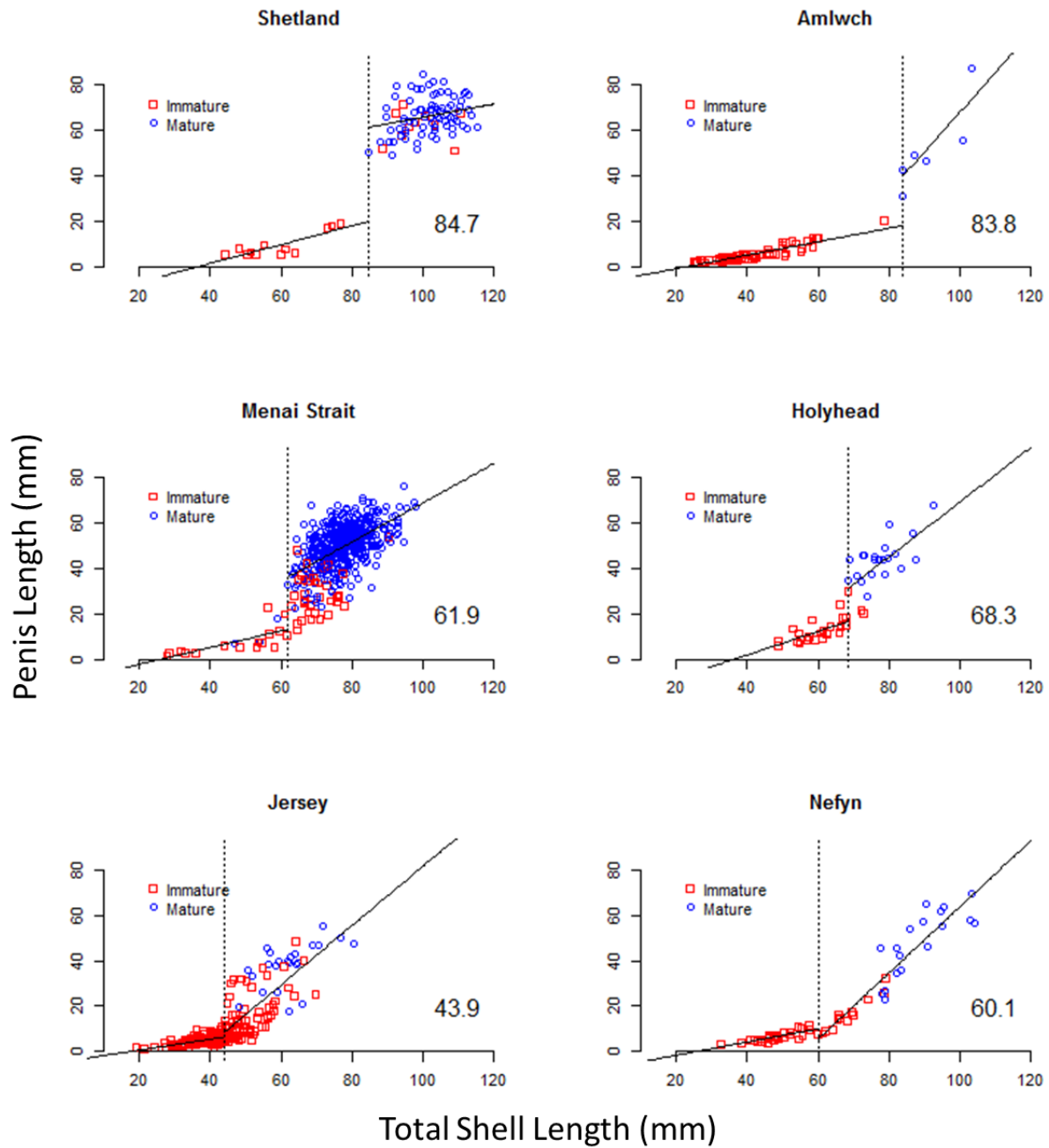


Figure 2.13. Scatter plots of penis length against total shell length for the six locations. 'Inflection points' (vertical dotted lines) were found in the data using an iterative search procedure with a linear model. The inflection point values are shown on each graph. Red squares – immature animals and blue circles – mature whelks.

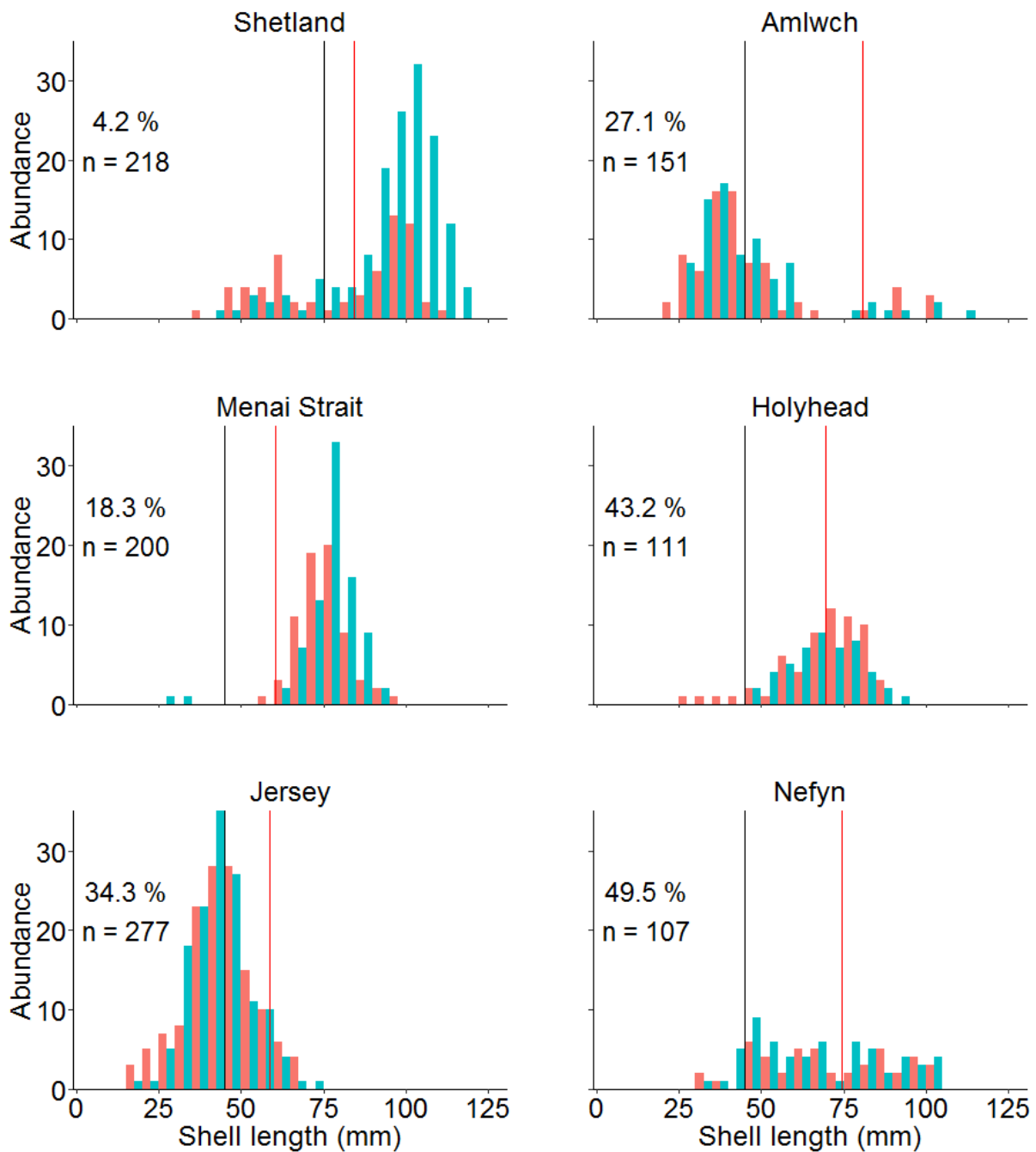


Figure 2.14. Length frequency distributions of *Buccinum undatum* from each of the six locations (5 mm bins). Genders are plotted side by side, blue – male, pink – female. Black vertical lines represent the minimum landing size (MLS) of whelks and the red vertical lines represent the calculated L_{50} (male & female whelks combined) at each location. Numbers on each figure are the % of each catch not protected by the MLS. The histogram for the Menai strait only presents a subsample of data (4 monthly samples, Feb & March 2014 & 2015) due to the large overall sample size.

2.3.2 Shell morphology

2.3.2.1 Between site shell morphology comparison

Following a DM_LOG transformation, data from all six locations were normally distributed (Kolmogorov-Smirnov and Shapiro-Wilk normality tests, [Appendix B](#) - Table B.1). Within the PCA analysis, a clear grouping of sites was observed (Figure 2.15). Principal components 1 & 2 (PC 1 & 2) were identified as representing 67% of the total variance as shown by the scree plot in Figure 2.13a. The full PCA loadings can be seen in [Appendix B](#) (Table B.2). The loadings for PC1 were largely comprised of size measurements (e.g. total shell length, body whorl width, min/max shell width & aperture length) whereas PC2 was comprised of variables such as spire angle and aperture width. The resulting PCs were found to be normally distributed within location (Kolmogorov-Smirnov and Shapiro-Wilk tests, [Appendix B](#) – Table B.3) and significantly different between location using a one-way ANOVA (Table 2.7).

Table 2.7. a significance matrix of the between site differences of PC 1 and PC 2.

PC1	Shetland	Menai Bridge	Jersey	Amlwch	Holyhead	Nefyn
Shetland		0.122	0.418	< 0.000	< 0.000	< 0.000
Menai Bridge			0.015	< 0.000	< 0.000	< 0.000
Jersey				< 0.000	< 0.000	0.013
Amlwch					0.449	0.060
Holyhead						0.456
PC2	Shetland	Menai Bridge	Jersey	Amlwch	Holyhead	Nefyn
Shetland		< 0.000	< 0.000	< 0.000	< 0.000	< 0.000
Menai Bridge			< 0.000	0.944	0.002	< 0.000
Jersey				< 0.000	< 0.000	< 0.000
Amlwch					0.866	0.084
Holyhead						0.208

Following PCA, Linear Discriminant Analysis (LDA) was used to investigate any variations between sites (Figure 2.16). The groupings resulting from the LDA are clearer than those from the PCA. Linear discriminants 1 & 2 (LD1 & 2) explain 91.98% of the between site variation, the full linear discriminant weightings can be seen in [Appendix B](#) (Table B.4). The arrows in Figure 2.16b), highlight the variables driving the variation between sites, namely total shell length, spire angle, body whorl width and min/max shell width.

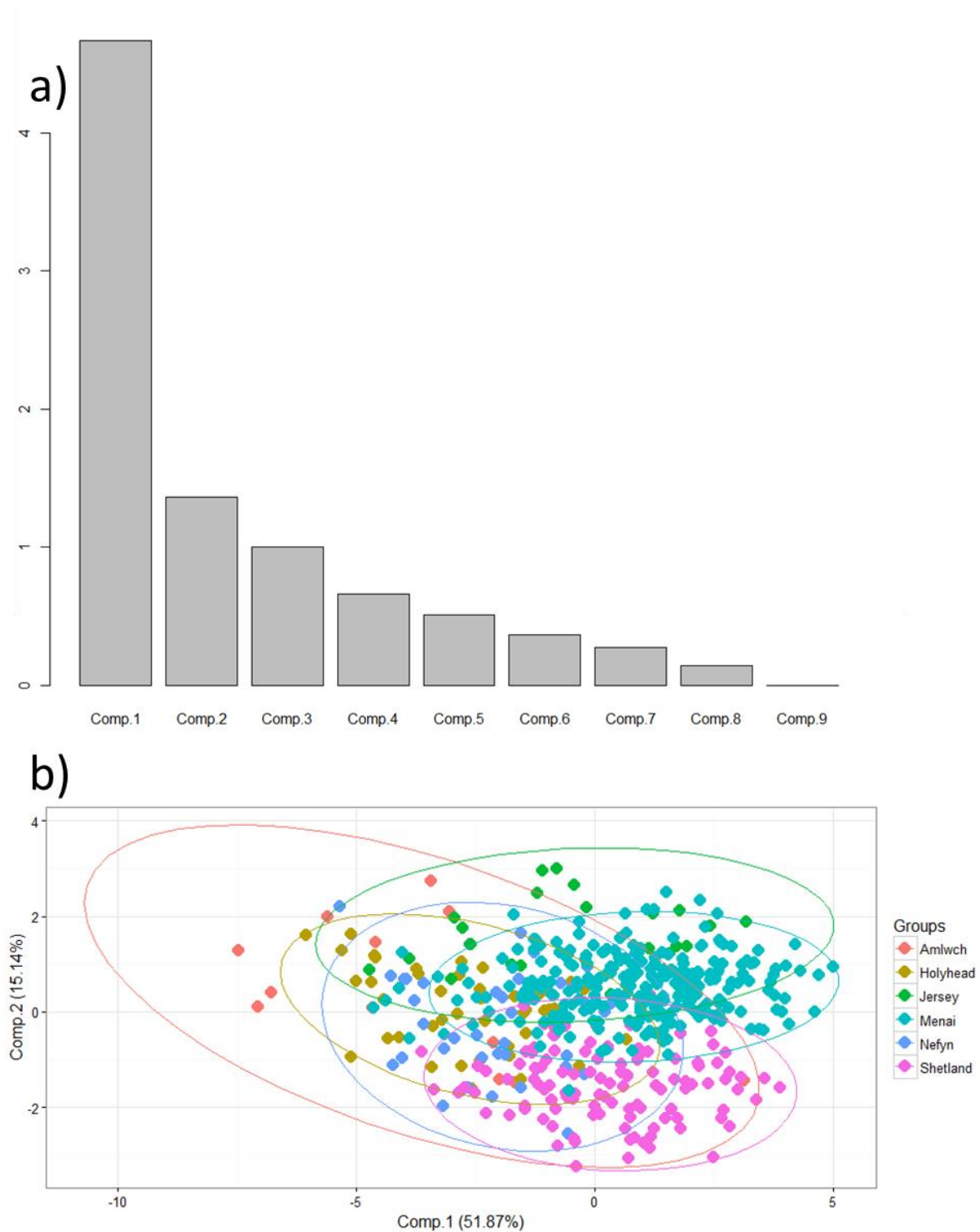


Figure 2.15. a) scree plot of the principal components extracted from the PCA analysis. PC 1, 2 & 3 explain 78% of the variance within the dataset. Comp 1 & 2 alone explain 67% of the variance and b) a plot of PCA 1 against PCA 2, the variance explained by each component is shown in each axis label. Ellipses denote 95% confidence intervals for each site.

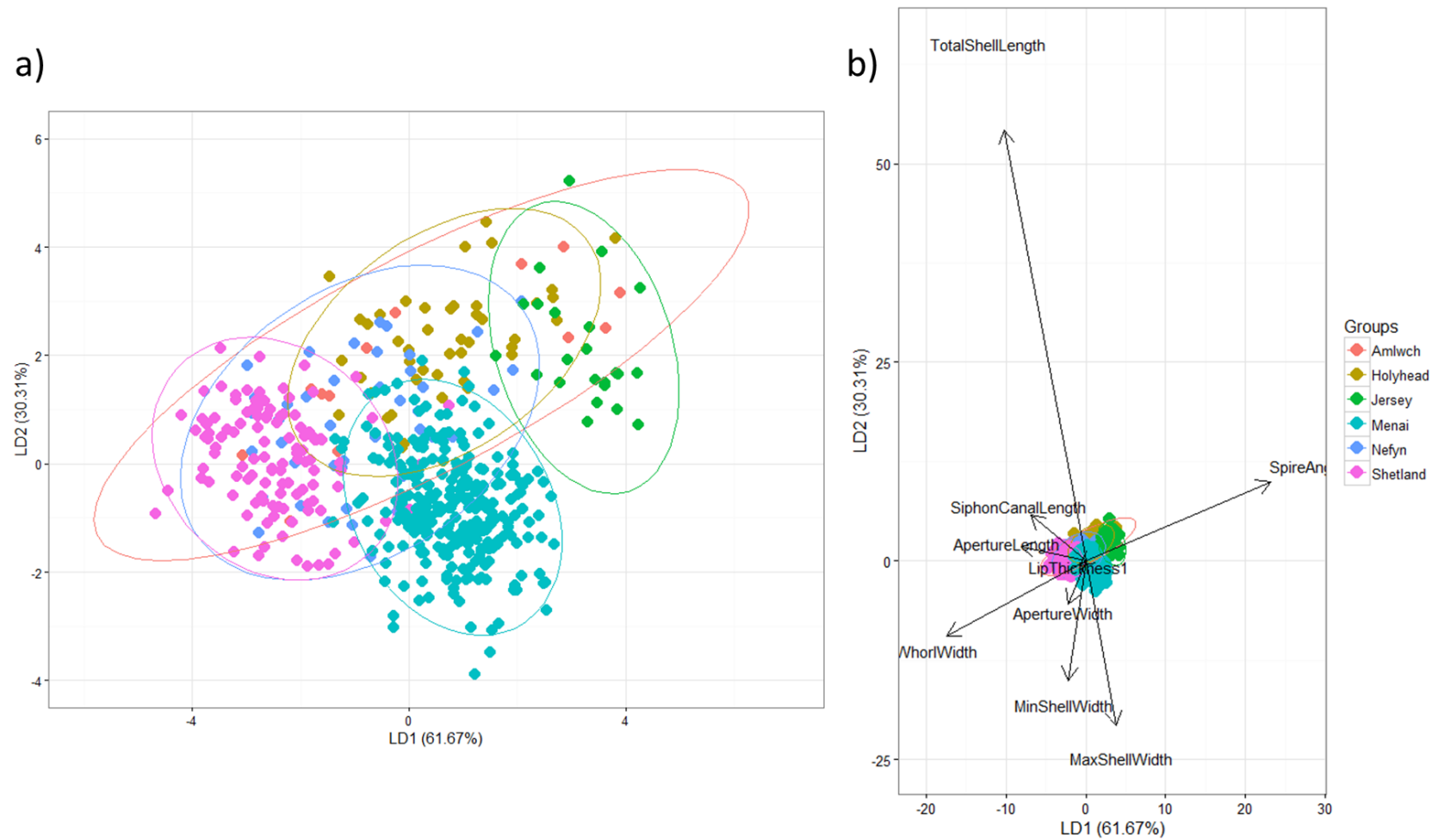


Figure 2.16. a) Plot of LD1 against LD2 from the Linear Discriminant Analysis. The amount of variance explained by each LD is shown in brackets on the axis labels, 95% confidence intervals are denoted by the ellipses drawn around each site and b) plot of LD1 against LD2 with arrows highlighting both the direction of influence and importance (based on the length of the arrow) of each variable.

2.3.2.2 Between sex morphology comparison

Differences between sexes in the Menai Strait were shown by a PCA that found two PCs explaining 62.66% of the total variance. PC1 was related to total shell length and max/min shell width. However, PC2 related to aperture size, with aperture width and length shown to be important in the loading. The resulting principal components were found to be normally distributed between sexes (Kolmogorov-Smirnov & Shapiro-Wilk), the differences between males and females were tested using a one-way ANOVA which found no difference between for PC1 ($p = 0.65$) but a significant difference in PC2 ($p = 0.02$). These results are illustrated in Figure 2.17, with a shift in the 95% confidence interval ellipses along the y-axis which represents PC2.

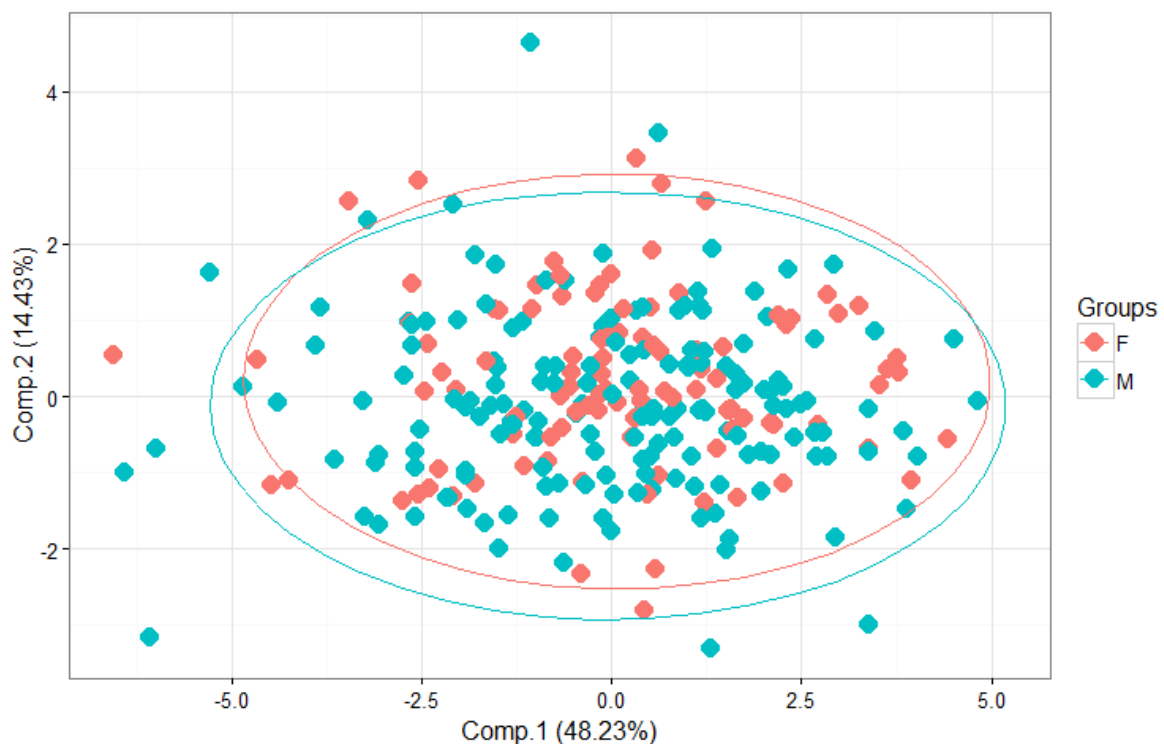


Figure 2.17. Plot of PCA 1 against PCA 2 for male and female *Buccinum undatum* from the Menai Strait. The variance explained by each component is shown on each axis label. Ellipses denote 95% confidence intervals for each gender.

2.3.2.3 Allometric analyses

The results of the PCA and LDA highlighted several shell dimensions driving differences in shell morphology between locations. Allometric analyses of several of these measurements between sites were undertaken using the *smatr*-3 package in R, which was used to compare linear relationships of log-transformed data (e.g. total shell length vs. aperture length) between sites and significant differences in slope and elevation were investigated between sites. Any shifts along the slope were also examined, however this frequently gave the same result due to the differences in size structure between populations, the only comparisons which did not have a significant shift along the slope were Amlwch vs. Jersey and Nefyn vs. Holyhead. Several weight measurements i.e. dry shell weight and eviscerated body weight that were not included in the PCA/LDA analyses were also investigated using *smatr*. Tables 2.8 & 2.9 show summaries of all of the pairwise comparisons of both elevation and slope for the six different metric assessments.

The PCA analysis between sexes in the Menai Strait (Figure 2.17) highlighted differences in aperture size that indicated there were differences between male and female whelks. Gender differences at the other five locations were further investigated using *smatr*-3. Comparisons of both elevation and slope between males and females for each site are summarised in Table 2.10. Three separate analyses were undertaken, Aperture Length Vs. Total Shell Length (ApL Vs. TSL), Aperture Width Vs. TSL (ApW V. TSL) and ApW Vs. ApL. As with the between-site analyses the shift along the slope was the same for all analyses, it is clear that there are shell dimension differences between males and females in the Menai Strait and Shetland.

Spire angle was found to be a major driver of inter-site difference in the PCA and LDA analyses with a horizontal linear relationship between spire angle and TSL indicating that spire angle stays constant through ontogeny. Instead of using linear analyses, ANOVA was used to assess differences in spire angle between sites, the summary of which can be seen in Table 2.11. Data from all sites analysed using ANOVA were found to be normally distributed (Shapiro-Wilk & Kolmogorov-Smirnov tests)

Table 2.8. Significance matrix of pairwise comparisons between all locations following allometric analysis of variables related to aperture size. Significance codes: *** < p = 0.001, ** = p < 0.01, * = p < 0.05.

<u>Elevation</u>							<u>Slope</u>						
	Amlwch	Jersey	Menai Strait	Shetland	Holyhead	Nefyn		Amlwch	Jersey	Menai Strait	Shetland	Holyhead	Nefyn
Aperture Width Vs. Aperture Length													
Amlwch	-			***	**	***		-	*		*	*	
Jersey		-		***	***	.		*	-	*	***		.
Menai			-	***	*	**			*	-		*	
Shetland	***	***	***	-				*	***		-	***	*
Holyhead	**	***	*		-			*		*	***	-	.
Nefyn	***	.	**			-			.		*	.	-
Aperture Length Vs. Total Shell Length													
Amlwch	-	*	***	***	***	*		-	***				.
Jersey	*	-	***	**	***	***		***	-	***	***	***	***
Menai	***	***	-	***	***	***			***	-			.
Shetland	***	**	***	-		***			***		-		
Holyhead	***	***	***		-	***			***			-	
Nefyn	*	***	***	***	***	-		.	***	.			-
Aperture Width Vs. Total Shell Length													
Amlwch	-		*					-			*	**	
Jersey		-	***						-				
Menai	*	***	-		***	***				-			
Shetland				-				*			-		*
Holyhead			***		-			**				-	**
Nefyn			***			-					*	**	-

Table 2.9. Significance matrix of pairwise comparisons between all locations following allometric analysis of variables related to shell width and weight. Significance codes: *** = $p < 0.001$, ** = $p < 0.01$, * = $p < 0.05$.

	<u>Elevation</u>						<u>Slope</u>					
	Amlwch	Jersey	Menai Strait	Shetland	Holyhead	Nefyn	Amlwch	Jersey	Menai Strait	Shetland	Holyhead	Nefyn
Max Shell Width Vs. Total Shell Length												
Amlwch	-	*	***		***		-					
Jersey	*	-	***		***			-				
Menai	***	***	-	***	***	***			-		*	
Shetland			***	-	**					-		
Holyhead	***	***	***	**	-	***		.	*		-	*
Nefyn			***		***	-					*	-
Min Shell Width Vs. Total Shell Length												
Amlwch	-	***	***	**		*	-	***			*	
Jersey	***	-	***		***		***	-	***	***	**	***
Menai	***	***	-	***	***	***		***	-			
Shetland	**		***	-	***			***		-		
Holyhead		***	***	***	-	**	*	**			-	
Nefyn	*		***		**	-		***				-
Dry Shell Weight Vs. Total Shell Length												
Amlwch	-	***	***	***	***	***	-	**	**		***	*
Jersey	***	-	***	***	***	***	**	-			.	
Menai	***	***	-	**	***	***	**		-		**	
Shetland	***	***	**	-	***	***				-	**	
Holyhead	***	***	***	***	-	***	***	.	**	**	-	***
Nefyn	***	***	***	***	***	-	*				***	-

Table 2.10. Significance of comparisons between male and female *Buccinum undatum* from the six locations following allometric analysis. ApL = Aperture length; ApW = Aperture Width; TSL = Total shell length. Significance codes: *** = $p < 0.001$, ** = $p < 0.01$, * = $p < 0.05$.

	ApL Vs. TSL		ApW Vs. TSL		ApW Vs. ApL		Shift
	Elevation	Slope	Elevation	Slope	Elevation	Slope	
Menai Strait	***		*	*	***		**
Shetland	**	*		*			***
Jersey	**						
Nefyn							
Holyhead	***						
Amlwch							

Table 2.11. Significance of pairwise comparisons between sites following an ANOVA of spire angle between sites. Significance codes: *** = $p < 0.001$, ** = $p < 0.01$, * = $p < 0.05$.

	Holyhead	Jersey	Menai Strait	Nefyn	Shetland
Amlwch	***	***	***		**
Holyhead		*	***	***	*
Jersey			***		
Menai				***	***
Nefyn					
Shetland					

2.4 Discussion

2.4.1 Timing of *Buccinum. undatum* reproduction in the Menai Strait

The peak period of gonad development of *B. undatum* from the Menai Strait was different depending on whether reproductive development was assessed as the Gonadosomatic Index (GSI) or adjusted GSI (aGSI). In calculating the GSI the weight of the digestive gland from each whelk is included resulting in gender differences in the peak of development i.e. the GSI peaks for females in June and males in May. This appears to be early in the season as egg capsule laying in the Menai Strait occurs five months later between November and January (Pers. Obs.). Using GSI as an estimate of the peak in reproductive development, whelk populations in the English Channel have maximum gonadal development in October, 1 - 2 months prior to egg laying between October and December (Heude-Berthelin *et al.*, 2011). When the seasonal change in the aGSI (which takes into consideration the amount of digestive gland comprising the gonad tissue) was calculated for the Menai Strait population, the peak in gonad development occurred later in September for both male and female whelks. This is 1 - 2 months prior to the start of the egg laying period; a similar duration between maximum reproductive condition and egg laying was observed in the English Channel whelk population studied by Heude-Berthelin *et al.*, (2011). However, the Welsh and English Channel populations were sampled at a different resolution, every 2 months in the Heude-Berthelin *et al.*, (2011) study whereas the Menai Strait population was sampled monthly. It is possible that the maximum period of gonadal development in whelks from the English Channel could also have occurred in September and did not appear in the data owing to the absence of sampling. Comparisons of exact timings of reproduction in different whelk populations can be problematic if the frequency of data collection is substantially different in different studies. The peaks in GSI in May and June for males and females respectively in the Menai Strait population likely does not represent the maximum period of reproduction. It is probably due to a factor other than reproduction and arises from an increase in the size of the digestive gland. This likely occurs due to an increase in feeding activity during a period of fast growth in the spring, between April and June, to accumulate nutrients for the consecutive release of egg masses during the spawning. In November the aGSI and frequency of ratios of female to male whelk data showed that no mature female whelks were collected in baited pots deployed in the Menai Strait. The observed appearance of egg capsules in the population during November and the absence of mature females in pots indicates that they are likely egg-laying during this period and not feeding (i.e.

not attracted to baited pots). For future studies which are time limited, the aGSI technique used here is a viable alternative to time-consuming dissection and histological techniques for assessing maturity (e.g. Martel *et al.*, 1986; Gendron, 1992; Heude-Berthelin, 2011). aGSI shows a seemingly more accurate representation of the reproductive season than using the unadjusted GSI alone. Future work should look to further validate this method with a histology based comparison study.

2.4.2 Size at maturity estimations

Estimates of L_{50} , values indicating the shell length where 50% of the whelks in the population are sexually mature, showed variation between locations and gender. In all cases the L_{50} calculated for males was larger than that of females, suggesting that females reach maturity at a smaller size. Haig *et al.*, (2015) reported that the size at maturity of *B. undatum* from North Wales (sites L1 & L2 - the sample locations were commercially confidential and were presented as general areas) was 64.5 mm and 63.2 mm for females and males respectively from L1 and site L2 reported 66.2 mm and 74.8 mm for females and males respectively. The estimated L_{50} values for whelks from the Menai Strait are lower than those found by Haig *et al.* (2015) at both L1 & L2 (58.1 mm & 61.8 mm for females and males respectively in this study). The values reported in the current study for Holyhead (in the same general area as L1) were closer to the reported values seen in both L1 and L2 by Haig *et al.* (2015) (68.6 mm & 70.2 mm for females and males respectively). Seasonal changes in L_{50} for both males and females from the Menai Strait were also observed with maximum values for both genders in autumn. It is unclear why this is the case, however, a similar pattern was reported by Haig *et al.* (2015). It is possible that the increase in L_{50} coincides with the peak in the reproductive cycle (see Haig *et al.* 2015). The finding that season, location and gender specific differences in L_{50} occur has implications for the management of whelk fisheries in coastal waters. Therefore any future whelk size at maturity studies should aim to incorporate a seasonal aspect and a detailed local study of populations to properly assess maturity at each location.

The estimated L_{50} values for Nefyn and Amlwch are unreliable as the GLM model used to predict the L_{50} value was non-significant. This was most likely due to differences in the population structures at the six locations. Amlwch and Nefyn have populations skewed towards the smaller immature sizes and likely reduced the number of whelks around the actual L_{50} causing a rapid increase in the ogives from immature to mature (cf. Figure 2.10). The L_{50} value of the combined males and females from Nefyn (74.3 mm) was significant and close to the L_{50} reported by Haig *et*

al. (2015) for sample site L2a (L_{50} - 76 mm) which is in the same area where the Nefyn sample was collected. Shelmerdine *et al.* (2007) reported L_{50} values from the Shetlands of 101 mm and 86 mm for females and males respectively. It is unclear how many samples they used for this analysis as the data are unpublished, however in the current study the size at maturity is considerably smaller for females although similar for males (i.e. 83.2 & 85.1 mm respectively). This could have been due to the size of sample studied by Shelmerdine *et al.* (2007), or possibly due to the samples being drawn from different populations (the values reported from Shelmerdine *et al.* were from two combined populations). Likewise, for the sample from Jersey, Heude-Berthelin *et al.* (2011) sampled sites close to those sampled during the current study from the location of Jersey. Their reported L_{50} values for female and male whelks were 52 mm and 49 mm respectively, values that are smaller than those reported here (56.6 mm & 60.5 mm). The L_{50} values for Jersey reported in this study are more similar to those from the Menai Strait which is ≈ 400 miles away. It is clear from the current study and previously published studies that comparison of L_{50} values is difficult as the different studies were likely conducted at different times of the year and from general areas rather than specific sample locations. Differences in population structure, location and gender bias all complicate any comparisons. Therefore it is unhelpful to speculate as to the causes of the differences without access to factors such as water depth, month of collection and population size structure etc. Future studies will need to take into account all these factors when comparisons are made.

2.4.3 Penis length as an alternative measure of maturity

As an alternative tool for determining seasonality of breeding and spawning, the efficacy of maturity estimates based on Penis Length (PL) was tested, using three different methods of analysis i.e. P_{50} , 50%PL and the inflection point. The accuracy of these methods varied between locations. The P_{50} estimates were relatively accurate when compared to the L_{50} values. Estimates from the Shetland and Menai Strait populations showed some deviation with the P_{50} overestimating maturity by 7-10 mm whilst the other sites only differed by ≈ 2 mm. This differed from Haig *et al.*'s, (2015) study where they reported that the P_{50} method considerably overestimated the size at maturity at each location by between as much as ± 5 to ± 15 mm. 50%PL measurements were first used by K  ie (1969) who noticed that penis length increased above 50% of the body length around the time of maturity and this metric has since been used in several studies to estimate maturity (e.g. Santarelli, 1985; Martel *et al.*, 1986a; Gendron, 1992; Fahy *et al.*, 2000; McIntyre *et al.*, 2015). A recent study by McIntyre *et al.* (2015) reported

that the estimates determined by using the 50% PL were similar to those of the L_{50} (determined via visual inspection of gonads, ± 1.5 mm). The use of 50% PL in this study overestimated the size at maturity at all locations by between 4 & 11 mm except for Jersey where 50% PL underestimated the size by ≈ 4 mm.

The size of the penis length at 50% maturity (%PL50) was estimated by replacing the TSL with the %PL measurement in maturity estimations. However penis length at maturity was highly variable across locations and ranged between 31.3% of the TSL in Jersey to 58.4% of the TSL in Holyhead. This wide variation indicates that more accurate methods of maturity estimation should be used in place of 50%PL, unless the %PL50 is known, in which case it could potentially be accurate. This would change the 50%PL to the %PL as the value would change between locations. The final maturity estimate from the PL was calculated using the inflection point in the relationship between PL and TSL (Gunnarsson & Einarsson, 1995; Haig *et al.*, 2015). Again, the accuracy of this technique varied, however for 4 out of 6 locations it predicted a size at maturity within ± 2.5 mm of the L_{50} . The estimates for both Jersey and Nefyn were 14-17 mm lower. However the L_{50} from Nefyn was non-significant for males so this is liable to be different to the reported value. The value for Jersey ($L_{50} = 44$ mm) is much closer to the L_{50} reported by Heude-Berthelin *et al.*, (2011) for males collected ≈ 10 miles from Jersey. Thus it is possible that the sample collected from Jersey used in this study was not representative of the actual population structure (the sample was collected by a third party during an annual monitoring program). If this is the case then the L_{50} may well be lower and in line with both the inflection point and the value reported by Heude-Berthelin *et al.* (2011).

The accuracy of the inflection point method is untested in the literature for individual sites. Haig *et al.* (2015) pooled all male samples from all sites and found an inflection point of 65 mm which was only slightly higher than the pooled L_{50} of 61.8 mm for all males. Gunnarsson and Einarsson (1995) were unable to compare the accuracy of their results as they did not perform any other type of maturity assessment on their populations. This also means that no estimates were made for female whelks which have been shown in this study to have different L_{50} estimates to males from the same population. It is clear that estimates of maturity calculated from penis length are variable between locations so where possible a more accurate maturity assessment such as visual gonad inspection should be undertaken in parallel in a combined approach. In cases where the gonad tissue is not suitable for assessment (such as poor preservation of samples in a freezer), the use of the inflection point and %PL could be used as an alternative measure of

maturity. The %PL has the potential to be more accurate than the inflection point if the %PL₅₀ for the particular site is known from previous assessments as it has been shown that the %PL at maturity varies between sites.

All female whelks in the populations studied were found to mature at a smaller size than their male conspecifics. This finding has not been reported in other size at maturity studies which often found differences across sites, with variation regarding which sex matured at a larger size being found (Gendron, 1992; Haig *et al.*, 2015; McIntyre *et al.*, 2015). The differences between L_{50} and the Minimum Landing Size (MLS) for the different sites is a potentially troubling finding. If the L_{50} estimates and the population structures reported are accurate then many of the populations are not currently protected by regional minimum landing sizes. In all the populations studied even if the MLS was increased to the L_{50} at each site, 50% of the catch taken at the MLS would still be immature, so the fact that the L_{50} is up to ≈ 15 mm lower in most populations suggests that large numbers of immature animals are being caught and landed that fall below the minimum landing sizes set by current fisheries regulations at all the sampled locations. My findings also highlight the flaws of a widespread MLS in general, one size does not protect all populations equally. However, the enforcement of area or population specific MLS is currently unfeasible, especially for a relatively low value species like *Buccinum undatum*.

2.4.4 Shell morphology

Significant differences in shell morphology between locations were identified using PCA and LDA. A dual analysis approach was used as LDA and PCA explain different types of variance within a dataset. PCA can be used to identify sources of total variance as it is blind to prior groupings of data such as location. LDA however is formulated to look for differences between pre-identified groups and can explain between-group variance. Even though the sites were not grouped for PCA analysis the sites were still visibly grouped in the resulting plot of PC1 vs PC2. The difference in these groups was driven largely by the metrics shell width, shell length and aperture length (PC1) as well as differences in spire angle and aperture width (PC2). Varying differences between locations were observed such that Holyhead, Amlwch and Nefyn were not significantly different, for either PC1 or PC2, whereas the Menai Strait whelks were significantly different to all three of these geographically close sites on PC1, PC2 or both. Whelks from Jersey were distinct from all other locations for PC2 whilst for PC1 Jersey whelks were significantly different for all sites except Shetland, suggesting a similarity in the geometric proportions of measurements such as shell width and total length between Shetland and Jersey. Shetland

whelks were also not significantly different from the Menai Bridge whelks for PC1 but significantly different to all sites for PC2. These results suggest that many of the differences seen between Jersey, Shetland and the Menai Strait are driven by differences in spire angle and aperture size. Much clearer groupings were seen between the populations following LDA analysis. The same variables were found to be driving the differences as in the PCA, namely length measurements such as shell width, total shell length and spire angle. The LDA plot is essentially similar to that of the PCA at a 90° angle with greater distinction between locations, leading to the conclusion that the total variance and between-site variance is driven by between location differences in shell morphology.

Spire angle was found to be significantly different between whelks from all sites apart from between Nefyn - Amlwch, Nefyn - Shetland, Nefyn - Jersey and Jersey - Shetland comparisons. This suggests that whilst spire angle is an important difference between the Menai Strait and Shetland whelk populations, it is aperture size driving the differences between Shetland and Jersey as their similarities are related to PC2 (spire angle and aperture size). The summary tables (2.11 & 2.12) highlight differences between locations for several allometric relationships. Significant positive allometric and negatively allometric relationships were observed. Differences in elevation (left hand side of the tables) arise from proportionally larger or smaller values of the measured variable with increasing shell length (most variables were compared against total shell length). Differences in slope (right hand side of the tables) indicate differences in rate of change with increasing shell length. As expected, Shetland and Jersey are significantly different in both slope and elevation for aperture length vs. total shell length (Table 2.11). They are also significantly different in both slope and elevation for the relationship between the aperture length and aperture width. Whilst the Menai Strait showed differences in elevation for aperture measurements against Shetland, the slope remained the same. Minimum shell width varied widely across all sampled locations in both elevation and slope. This particular finding has direct relevance to current fisheries management practices as the relationship between shell length and minimum shell width is used to set the riddle spacings as this is the narrowest part of the whelk morphology. If the differences in minimum shell width/shell height are pronounced enough then the minimum width at which the whelks reach the MLS (45 mm in most places) will differ. As an example, the differences found between the whelks from the Menai Strait and Jersey would constitute a 3 mm difference in riddle size (22 mm in the Menai Strait fishery and 19 mm in Jersey). Dry shell weight length relationships were clearly different in elevation between almost all sites. The differences in slope were also highly variable even across sites

with relative geographic proximity (e.g. Amlwch and Holyhead). The clear difference in shell weight/length relationships may potentially support the conclusions of Thomas and Himmelman (1988), who suggested that differences in shell weight could be attributed to differences in predator abundance causing differences in shell thickness and weight.

2.4.4.1 Sexual dimorphism of shell morphology

Differences in shell morphology related to sexual dimorphism were demonstrated at several locations. Aperture size contributed to differences between male and female whelks from the Menai Strait and was further confirmed from the allometric analyses which found differences in elevation in the relationship between aperture length and shell length between males and females from most locations. A significant difference in elevation was also observed in the relationship between aperture width and aperture length between male and female whelks from the Menai Strait. A significant shift along the slope was also seen between males and females from Shetland and the Menai Strait; this can be explained by the differences in the male and female whelk population structures. The differences in aperture length against shell length resulted in male specimens having longer apertures than females. This could potentially be due to differences in the anatomy of male and female whelks with males needing greater space to store their proportionally large penis. The sexual dimorphism of aperture size has been commented on in earlier studies in whelks from Canada (Gendron, 1992; Kenchington & Glass, 1998) and the North Sea (Ten Hallers-Tjabbes, 1979). However in other studies it has been noted that differences in shell dimensions are often not pronounced enough to distinguish between genders at many sites in Canada (Thomas and Himmelman, 1988; Gendron, 1992). This was similarly observed in the current study.

In conclusion, clear differences were found in both size at maturity and shell morphometry between locations. These differences were seen over both large and small spatial scales, and these findings have several implications for the way in which fisheries scientists monitor and regulate coastal whelk fisheries. Size at maturity was seen to vary widely between locations and seasonally in the Menai Strait. This highlights a need for a prior knowledge of the reproductive cycle and timing of reproduction to accurately assess size at maturity and to understand how size at maturity varies seasonally, as there is an increase in the size at maturity as the reproductive season progresses. Multiple surveys should be undertaken annually or throughout the reproductive season to ensure the most conservative estimate of maximum size at maturity is determined, as catch demographics vary in response to exploitation and seemingly the timing

of the reproductive cycle. With the exception of the regular monthly sampling of the Menai Strait, only one sample of whelks was collected from the other locations, so interpretation of the results from these locations should be made with caution. Variation in size at maturity is a clear issue which has been raised many times previously and there is agreement that the current MLS across much of the UK's coastal waters is insufficient to protect large portions of the immature whelk populations (see Haig *et al.*, 2015; McIntyre *et al.*, 2015). The only way to address this is to increase the minimum landing size, a measure that has been imposed on whelk populations from the Shetland Isles (Shelmerdine *et al.*, 2007) and Ireland (Fahy *et al.*, 2005). This still does not discount the problem of spatial variations in size at maturity as even a UK wide increase in the MLS to 60 mm, for example, might protect some populations whilst still leaving others vulnerable. The possibility of a population by population MLS is something that has been proposed before (e.g. Gendron, 1992). However, in reality this would not be easily enforceable. Variation in the ratio of males to females caught in pots during the 18 month survey of the Menai Strait population highlights a potential problem with a bias in capture of males and above MLS immature females during the reproductive season. Information such as this could be used by fisheries scientists to inform a seasonal closure of whelk fisheries to avoid any disproportionate impacts on a particular gender within a population. If a countrywide MLS can be found, other issues still arise from differences in shell morphometry. The different relationships between minimum shell width and total shell length may potentially require regional variations in the riddle bar spacings needed to effectively enforce a MLS, a need that fisheries scientists may not have been aware of before the current study was undertaken.

The reasons behind the differences in shell morphometry between sites are unclear without further study. It is likely that a combination of factors such as regional differences in seawater temperature, depth, predation pressure (Thomas and Himmelman, 1988) and genetic differences (Magnúsdóttir, 2010) likely combine to drive the observed variation. In the following Chapters 4 and 7, the growth rate of adult *B. undatum* from the Menai Strait, Shetland and Jersey will be investigated to look for differences between sites that can be related back to environmental differences and shell morphology. An investigation into the structure of shells (Chapter 3) from different locations may also help elucidate whether micro-structural differences occur and whether these differences may be driving location-specific differences in metrics such as shell weight.

2.5 References

- Beggel S, Cerwenka AF, Brander J, Geist J (2015) Shell morphological versus genetic identification of quagga mussel (*Dreissena bugensis*) and zebra mussel (*Dreissena polymorpha*). *Aquat Invasions* 10(1):93-99
- Brokordt K, Guderley H, Guay M, Gaymer CF, Himmelman JH (2003) Sex differences in reproductive investment: maternal care reduces escape response capacity in the whelk *Buccinum undatum*. *J Exp Mar Biol Ecol* 291:161–180
- Crawley MJ (2007) *The R Book*. Wiley, Blackwell, West Sussex, UK
- Cunningham JT (1899) Formation of egg-capsules in Gasteropoda. *Nature* 59:557
- Darroch JN, Mosimann JE (1985) Canonical and principal components of shape. *Biometrika* 72(2):241-252
- Dautzenberg P, Fischer H (1912) 'Mollusques provenant des campagnes de l'Hirondelle et de la Princesse-Alice dans les Mers du Nord', Résultats des Campagnes Scientifiques Accomplies sur son Yacht par Albert Ier Prince Souverain de Monaco, Monaco: Imprimerie de Monaco
- Fahy E, Carroll J, O'Toole M, Barry C, Hother-Parkes L (2005) Fishery associated changes in the whelk *Buccinum undatum* stock in the southwest Irish Sea, 1995-2003. *Ir Fish Invest*
- Fahy E, Masterson E, Swords D, Forrest N (2000) A second assessment of the whelk fishery *Buccinum undatum* in the southwest Irish Sea with particular reference to its history of management by size limit. *Ir Fish Invest* 6
- Ferreira T, Rasband W (2012) *ImageJ User Guide*
- Fretter V (1941) The Genital Ducts of Some British Stenoglossan Prosobranchs. *J Mar Biol Assoc UK* 25(1):173–211
- Fretter V (1953) The transference of sperm from male to female prosobranch, with reference, also, to the Pyramidellids. *Proc Linn Soc Lond* 164:217-224
- Fretter V, Graham A (1985) *Buccinum undatum* Linnaeus, 1758, whelk or buckie. *J Mollus Stud* 51 (Supplement 15):486-489
- Gendron L (1992) Determination of the size at sexual maturity of the waved whelk *Buccinum undatum* Linnaeus, 1758, in the Gulf of St Lawrence, as a basis for the establishment of a minimum catchable size. *J Shellfish Res* 11:1–7
- Golikov AN (1968) Distribution and variability of long-lived benthic animals as indicators of currents and hydrological conditions. *Sarsia* 34:199-208
- Gunnarsson K, Einarsson, S (1995) Observations on whelk populations (*Buccinum undatum* L. Mollusca: Gastropoda) in Breiðafjörður, Western Iceland. ICES shellfish committee report, C.M. 1995/K:20
- Haig JA, Pantin, JR, Murray LG, Kaiser MJ (2015) Temporal and spatial variation in size at maturity of the common whelk (*Buccinum undatum*). *ICES J Mar Sci* 72 (9):2707-2719

- Hancock D, Urquhart A (1959) Methods for marking whelks (*Buccinum undatum* L.). J Cons Int Mer 24:494–496
- Hancock DA (1967) Whelks. Ministry of Agriculture, Fisheries and Food, Laboratory Leaflet No. 15, Fisheries Laboratory, Bournemouth, Crouch, Essex
- Harry AV (2013) Maturity ogive R. <https://gist.github.com/alharry/4576675> (last accessed 10/11/2016)
- Hayward PJ, Ryland JS (2000) Handbook of the Marine Fauna of North-West Europe. Oxford University Press, Oxford
- Heude-Berthelin C, Hégron-Macé L, Legrand V, Jouaux A, Adeline B, Mathieu M, Kellner K (2011) Growth and reproduction of the common whelk *Buccinum undatum* in west Cotentin (Channel), France. Aquat living resour 24:317–327
- Himmelman JH, Hamel JR (1993) Diet, behaviour and reproduction of the whelk *Buccinum undatum* in the northern Gulf of St Lawrence, eastern Canada. Mar Biol 116:423–430
- Johansson J (1957) Notes on the littorinacean and stenoglossan genital organs, and a comparison with the Rissoacea. Zoologiska bidrag från Uppsala 32:81–91
- Jungers WL, Falsetti AB, Wall CE (1995) Shape, relative size and size - adjustments in morphometrics. Yearb Phys Anthropol 38:137–161
- Kenchington E, Glass A (1998) Local adaptation and sexual dimorphism in the waved whelk (*Buccinum undatum*) in Atlantic Nova Scotia with applications to fisheries management. Can Tech Rep Fish Aquat Sci 2237:1–42
- Kideys AE, Nash RDM, Hartnoll RG (1993) Reproductive cycle and energetic cost of reproduction of the neogastropod *Buccinum undatum* in the Irish sea. J Mar Biol Assoc UK 73:391–403
- Køie M (1969) On the endoparasites of *Buccinum undatum* L. with special reference to the trematodes. Ophelia 6:251–279
- Laptikhovsky VV (2014) Does starfish predation determine spawning seasonality in the whelk *Buccinum undatum* in the Gulf of St. Lawrence? J Mollus Stud 80(2):219–221
- Lebour MV (1937) The eggs and larvae of the British prosobranchs with special reference to those living in the plankton. J Mar Biol Assoc UK 22:105–166
- Magnúsdóttir H (2010) The common whelk (*Buccinum undatum* L.): Life history traits and population structure. Master thesis. University of Iceland, Reykjavik
- Martel A, Larrivée DH, Himmelman JH (1986a) Behaviour and timing of copulation and egg-laying in the neogastropod *Buccinum undatum* L. J Exp Mar Biol Ecol 96:27–42
- Martel A, Larrivée DH, Klein KR, Himmelman JH (1986b) Reproductive cycle and seasonal feeding activity of the neogastropod *Buccinum undatum*. Mar Biol 92:211–221
- McIntyre R, Lawler A, Masfield R (2015) Size of maturity of the common whelk, *Buccinum undatum*: Is the minimum landing size in England too low? Fish Res 162:53–57
- Mensink BP, Kralt H, Vethaak AD, Ten Hallers-Tjabbes CC, Koeman JH, van Hattum B, Boon JP (2002) Imposex induction in laboratory reared juvenile *Buccinum undatum* by tributyltin (TBT). Environ Toxicol Pharmacol 11(1):49–65

- Moore HB (1937) Marine fauna of the Isle of Man. Proc Trans Liverpool Biol Soc 50:1–293
- Nasution S, Roberts D (2004) Laboratory trials on the effects of different diets on growth and survival of the common whelk, *Buccinum undatum* L. 1758, as a candidate species for aquaculture. Aquacult Int 12(6):509–521
- Nasution S, Roberts D, Farnsworth K, Parker GA, Elwood RW (2010) Maternal effects on offspring size and packaging constraints in the whelk. J Zool 281:112–117
- Portmann A (1925) Der Einfluss der Nöhreier auf die Larven-Entwicklung von *Buccinum* und *Purpura*. Zeitschrift für Morphologie und Ökologie der Tiere 3: 526–541
- Price NR, Hunt C (1976) An unusual type of secretory cell in the ventral pedal gland of the Gastropod mollusc *Buccinum undatum* L. Tissue Cell 8:217–228
- Ripley B, Venables B, Bates DM, Hornik K, Gebhardt A, Firth D (2016) R package ‘MASS’ Modern Applied Statistics with R
- Roa R, Ernst B, Tapia F (1999) Estimation of size at sexual maturity: An evaluation of analytical and resampling procedures. Fishery Bulletin US, 97:570–580
- Ruppert EE, Fox RS, Barnes RD (2004) Invertebrate Zoology: a functional evolutionary approach. Thomson, Brooks/Cole, Belmont
- Santarelli L (1985) Les pecheries de Buccin (*Buccinum undatum* L.: Gastropoda) du Golfe Normand-Breton. Eléments de gestion de la ressource. PhD thesis, L'Universite d'aix-Marseille
- Shelmerdine RL, Adamson J, Laurenson CH, Leslie B (2007) Size variation of the common whelk, *Buccinum undatum*, over large and small spatial scales: potential implications for micro-management within the fishery. Fish Res 86:201–206
- Shrives JP, Pickup SE, Morel GM (2015) Whelk (*Buccinum undatum* L.) stocks around the Island of Jersey, Channel Islands: Reassessment and implications for sustainable management. Fish Res, 167:236–242
- Smith KE, Thatje S (2013) Nurse egg consumption and intracapsular development in the common whelk *Buccinum undatum* (Linnaeus, 1758). Helgo Mar Res 67:109–120
- Smith KE, Thatje S, Hauton C (2013) Thermal tolerance during early ontogeny in the common whelk *Buccinum undatum* (Linnaeus 1785): Bioenergetics, nurse egg partitioning and developmental success. J Sea Res 79:32–39
- Ten Hallers-Tjabbes CC (1979) Sexual dimorphism in *Buccinum undatum* L. Malacologia 18:13–17
- Ten Hallers-Tjabbes CC, Kemp JF, Boon JP (1994) Imposex in whelks (*Buccinum undatum*) from the Open North Sea: relation to shipping traffic intensities. Mar Pollut Bull 28:311–313
- Tétreault F, Himmelman JH, Measures L (2000) Impact of a castrating trematode, *Neophasis* sp., on the common whelk, *Buccinum undatum*, in the Northern Gulf of St. Lawrence. Biol Bull 198:261–271
- Thomas MLH, Himmelman JH (1988) Influence of predation on shell morphology of *Buccinum undatum* L. on Atlantic coast of Canada. J Exp Mar Biol Ecol 115:221 – 236

- Thorson G (1946) Reproduction and larval development of Danish marine bottom invertebrates. Meddelelser fra Kommissionen for Danmarks Fiskeri- og Havundersøgelser Serie Plankton 4. Copenhagen: Commission for Danish Fishery and Marine Research
- Valentinsson D (2002) Reproductive cycle and maternal effects on offspring size and number in the neogastropod *Buccinum undatum* (L.). Mar Biol 140:1139-1147
- Walker TI (2005) Reproduction in fisheries science. In: Hamlett WC (ed.) Reproductive Biology and Phylogeny of Chondrichthyans: Sharks, Batoids, and Chimaeras, pp. 81–127. Science Publishers, Inc., Enfield, New Hampshire
- Warton DI, Duursma RA, Falster DS, Taskinen S (2012) SMATR 3 – an R package for estimation and inference about allometric lines. Methods Ecol Evol 3:257-259
- Warton DI, Duursma RA, Falster DS, Taskinen S (2015) R- Package ‘smatr’ (standardised) Major Axis Estimation and Testing Routines

Chapter 3:

Micro-structure and mineralogy of the shells of
Buccinum undatum.

3.1 Introduction

The introduction to this chapter serves introduces the topics contained within this section, provides a general overview of the physical and chemical properties of calcium carbonate and discusses the general models of molluscan shell formation. These subjects will be important for understanding and interpreting data presented in this and subsequent chapters.

3.1.1 Calcium carbonate

Calcium carbonate (CaCO_3) is a naturally occurring compound found throughout nature in four polymorphic mineral forms, i.e. calcite, aragonite, vaterite as well as Amorphous Calcium Carbonate (ACC) (Carlson, 1983; Gong *et al.*, 2012). Vaterite is rarely seen in biogenic carbonates that are comprised of calcite or aragonite as it is less thermodynamically stable (Lippmann, 1973; Lowenstam & Abbott, 1975; Carlson, 1983). However, vaterite occurs naturally in some molluscan shells such as those of the Antarctic bivalve *Laternula elliptica* (Nehrke *et al.*, 2012) and in the spicules of some ascidians (Lowenstam & Abbott, 1975). ACC is also rarely observed in nature, as it is the least stable polymorph of CaCO_3 and contains no observable crystalline structure, making it difficult to identify (Gong *et al.*, 2012), it readily morphs to a more stable form under the right conditions (Rodriguez-Blanco *et al.*, 2011; Gong *et al.*, 2012). For this reason, only calcite and aragonite will be discussed further. The differences between these minerals do not arise from changes in chemical composition, but rather changes in the spatial arrangement of the composite atoms, causing differences in crystal structure. These variances in structure result in differences in the physical properties between calcite and aragonite, including the densities of the two substances (calcite 2.71 g.cm^{-3} and aragonite 2.83 g.cm^{-3} ; Mindat.org). The molecular structures of calcite and aragonite are shown in Figure 3.1. In calcite, the blue Ca atom is bonded to 6 surrounding red O atoms from 6 separate CO_3 groups. Whereas in aragonite the Ca atom is bonded to 9 surrounding O atoms, again from only 6 separate CO_3 groups, with 3 of these groups bonding twice with the same Ca atom. At ambient temperature and pressure, calcite will precipitate from a supersaturated solution of CaCO_3 under thermodynamic equilibrium, as it is the most stable form of CaCO_3 . Aragonite precipitates at higher temperatures (above 85°C) and pressures (Helgeson *et al.*, 1978; Ropp, 2013). Aragonite does however form at ambient temperatures and pressures in many places such as cave mineral deposits (Frisia *et al.*, 2003; Parker *et al.*, 2010) and most notably in seawater and within biologically created carbonate structures such as bivalve and gastropod shells (Parker *et al.*,

2010). When aragonite does preferentially form over calcite it is classed as metastable, meaning that it is in a less than stable state for a prolonged period of time, but over geological time it will revert to its more stable form (calcite) through a solid state reaction (Essene, 1983). The reason for aragonite formation in conditions that would favour calcite deposition has been heavily speculated to involve the magnesium (Mg) content of the precipitating liquid (Morse *et al.*, 1997 & 2007). An increase in Mg leads to a decrease in calcite growth, whereas aragonite is unaffected (Morse *et al.*, 2007, Sun *et al.*, 2015). Mg also leads to disorder and strain of the CaCO_3 lattice (Mucci & Morse, 1983; Paquette & Reader, 1995; Hong *et al.*, 2016). Due to the metastability of aragonite it is more soluble than calcite, causing marine animals with aragonitic hard parts to be more susceptible to ocean acidification (Orr *et al.*, 2005).

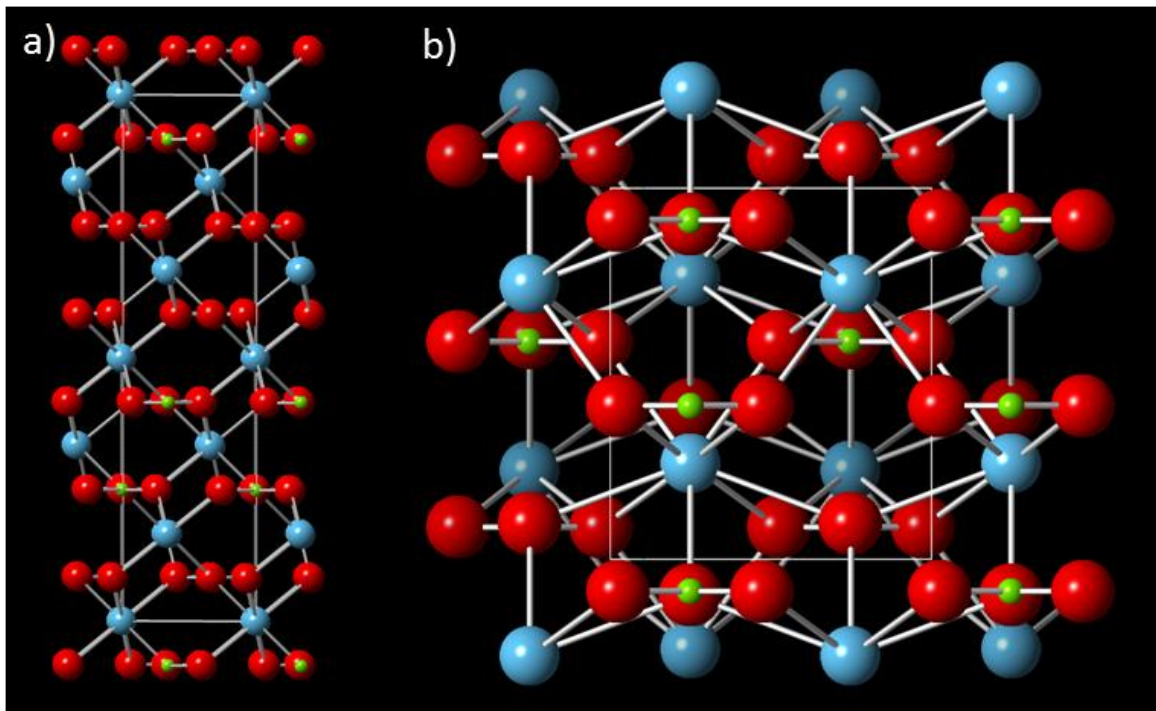


Figure 3.1. the atomic structure of a) calcite and b) aragonite. Red – oxygen, Blue– calcium, green– carbon. (Made using CrystalViewer 9.2.6, 2015).

The differences in molecular structure result in different shaped crystals being formed with different planes of symmetry. Calcite has trigonal-rhombohedral crystal symmetry (Bragg, 1913) and aragonite has orthorhombic crystal symmetry (Bragg, 1924). The differences in crystal symmetry determine the shape of not only the individual crystal units but also the larger overall crystal lattice, as these crystal units are added together like tessellating building blocks. It is these building blocks that are utilised by molluscs to create their shells (Bonucci, 2007).

3.1.2 Mollusc shell formation

Biological calcification (or biomineralisation) is the process by which organisms produce their endo- or exoskeletons, as well as a plethora of other calcified hard tissues (Bonucci, 2007). As such the process has been, and is, a vital component in the existence and evolution of the majority of modern fauna (Mann, 1988; Bonucci, 2007). Whilst its importance is clear, the physical and molecular processes comprising calcification are largely unknown (Wheeler, 1992; Bonucci, 2007). In molluscs, (especially bivalves and gastropods) the process of calcification usually results in the formation of an external shell, a process performed by a soft tissue covering the inside of the shell - the mantle margin and epithelium (Ruppert *et al.*, 2004). The following section will focus on the mechanisms of calcification in bivalve molluscs. Whilst both gastropods and bivalves accrete their shells in much the same way, the formation of the bivalve shell has been studied in more detail (Ruppert *et al.*, 2004).

In the extra-pallial space (EPS), a space enclosed by the edge of the mantle, the mantle epithelium and the growing edge of the shell, calcium carbonate is precipitated over an organic matrix to form the shell structure (Wilbur & Saleuddin, 1983; Wheeler, 1992). During shell formation, both the precipitation of CaCO_3 and the dissolution of CaCO_3 are simultaneously occurring (McConnaughey, 1989), thus it requires a net gain of CaCO_3 precipitation for shell material to be formed and the shell to increase in length. The shell normally comprises at least two distinct layers, an outer prismatic layer and an inner nacreous layer, this general structure varies between species and groups (Ruppert *et al.*, 2004; Barthelat *et al.*, 2006). The resulting shell that is deposited is composed of 95-99% CaCO_3 in the form of either aragonite or calcite and between 1 & 5% organic matter (Kaplan, 1998). The crystal matrices and mechanical characteristics of mollusc shells are often studied by materials scientists because of their physical properties, such as their strength and hardness. For example, calcium carbonate (aragonite & calcite) in shell structures can be up to 1000x tougher than laboratory precipitated counterparts (Wegst & Ashby, 2004; Barthelat *et al.*, 2006). Mollusc shell structures are often emulated in the field of biomimicry, with special focus on the tough 'brick and mortar'- like aragonitic nacreous mother of pearl layers (Jackson *et al.*, 1988) that are found in many mollusc shells, in an attempt to develop strong composite ceramic materials (Wilt, 2005; Barthelat *et al.*, 2006; Barthelat, 2010).

3.1.2.1 The chemical process of mollusc (bivalve) calcification

The following steps outline the general calcification process within bivalves. The first four steps refer to stages which take place within the seawater surrounding a living bivalve (Figure 3.2).

- 1) Atmospheric and respiratory CO_2 are absorbed into seawater at equilibrium.
- 2) CO_2 reacts with water molecules to create Carbonic Acid (H_2CO_3).
- 3) Carbonic Acid undergoes deprotonation to form Bicarbonate (HCO_3^-) and Hydrogen (H^+) ions.
- 4) Molecules and ions enter the pallial cavity and pass into the extrapallial fluid (EPF) by membrane transport across the mantle epithelium, across the bivalve gill surface during respiration and/or during feeding ingestion, digestion and absorption.

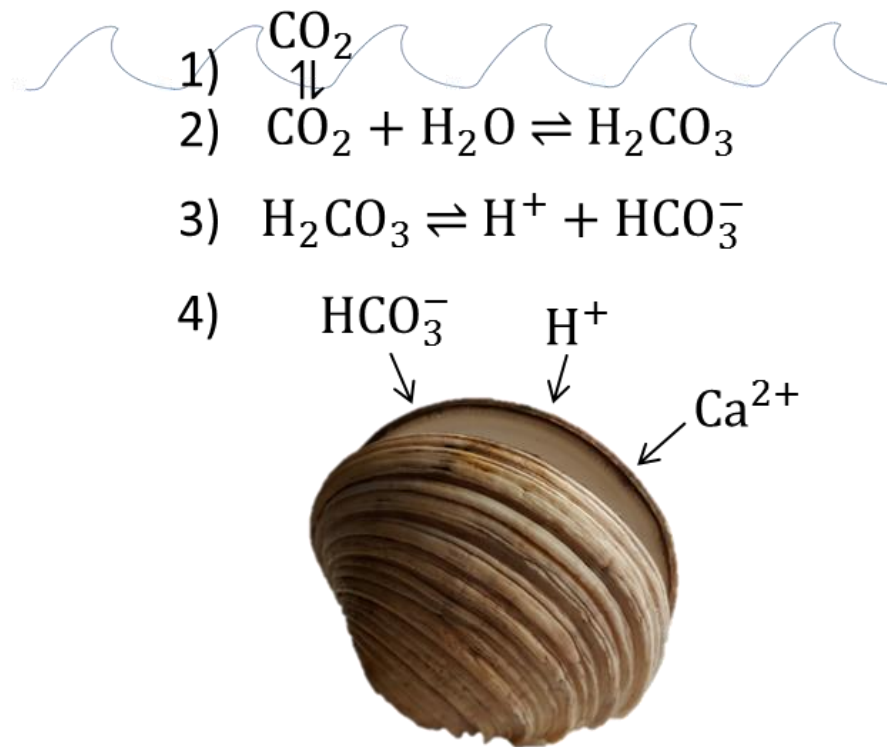


Figure 3.2. Schematic representation of the initial four stages of bivalve shell calcification that occur in the surrounding seawater.

Once inside the pallial cavity, requisite molecules and ions move actively across the mantle epithelium into the EPF (Figure 3.3) of the animal which is contained within the EPS. Within the EPF and across the mantle epithelium, several reactions take place to enable the deposition of Calcium Carbonate. The pH of the EPF increases, becoming alkaline, by removal of H^+ ions, this increase in pH is necessary for calcification to occur (Cohen & McConnaughey, 2003; McConnaughey & Gillikin, 2008). The following 3 steps (5-7) occur within the EPF (Figure 3.4).

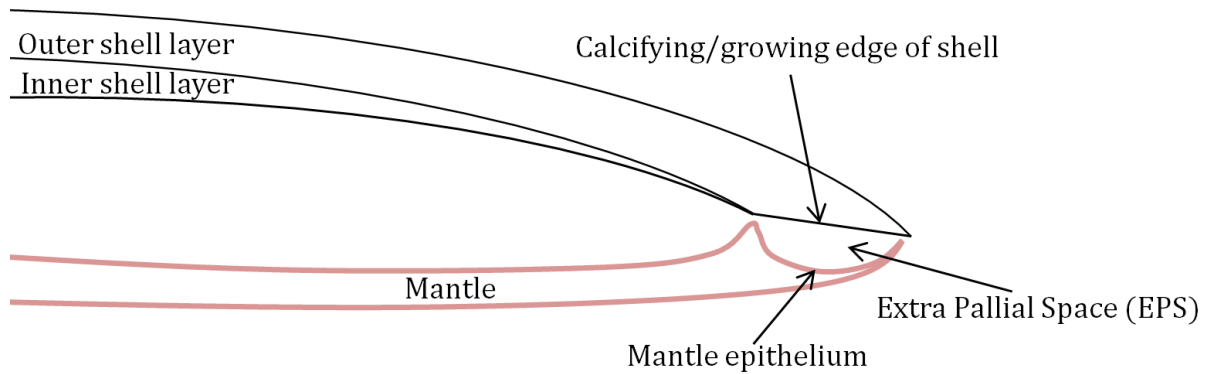


Figure 3.3. A diagrammatic cross sectional drawing of the shell and mantle of a bivalve. The extrapallial space between the mantle and shell has been exaggerated in the drawing.

- 5) With a pH increase in in the EPF, CO_2 is converted into bicarbonate (HCO_3^-) through hydroxylation (the addition of an hydroxide ion (OH^- from water)), causing more CO_2 to be drawn into the EPF via diffusion. The enzyme Carbonic anhydrase (CA) is involved in speeding up (catalysing) the process (Miyamoto *et al.*, 1996, 2005).
- 6) The deprotonation of bicarbonate (HCO_3^-) forms carbonate ions (CO_3^{2-}) and hydrogen (H^+) ions.
- 7) Carbonate ions (CO_3^{2-}) react with Calcium ions (Ca^{2+}) to form Calcium Carbonate (CaCO_3)

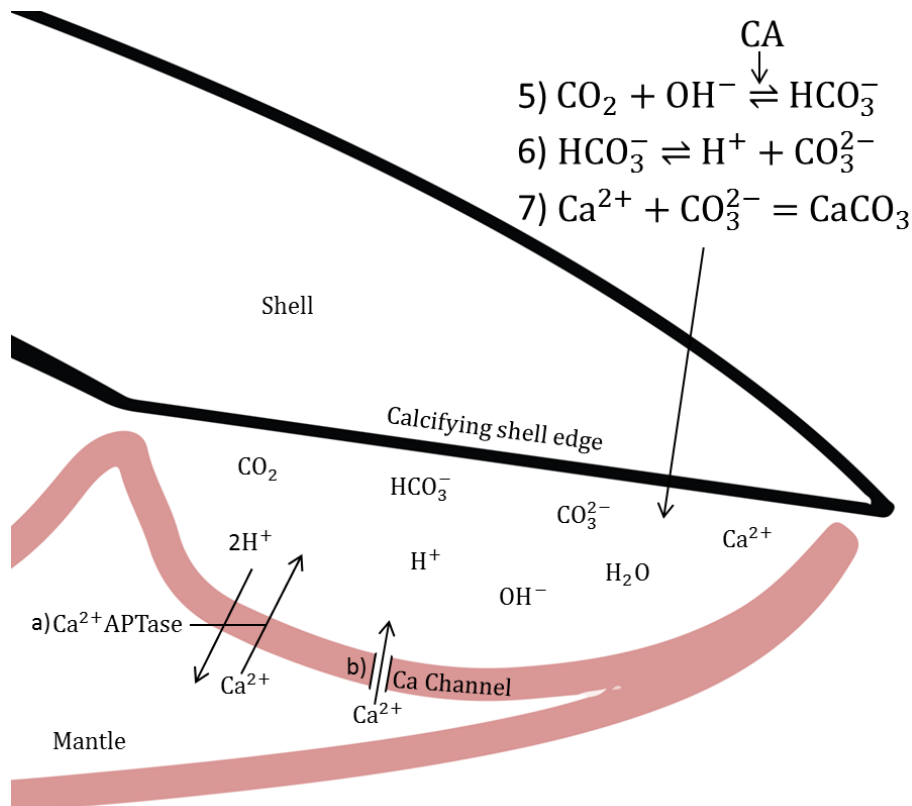


Figure 3.4. Diagrammatic representation of the reactions taking place within the EPF (steps 5, 6 & 7). a) highlights the action of Ca^{2+} ATPase and b) highlights the action of calcium channels in the mantle epithelium. (Adapted from Watson *et al.*, 1971 and McConnaughey, 1988).

Aspects of the processes and mechanisms of ion movements across the mantle epithelium are currently unclear, for example there are uncertainties around several areas, such as how Ca^{2+} ions are transported into the EPF, the source of elements such as carbon and oxygen, how the organic matrix is secreted and how this matrix controls crystallisation and shell growth.

3.1.2.2 Transport of Ca^{2+} across membranes

Certain molecules easily diffuse through the mantle epithelium e.g. CO_2 (Gutknecht *et al.*, 1977) however, the transport of Ca ions across membranes appears to be more difficult (Zhao *et al.*, 2016). There are several theories regarding the transport of Ca^{2+} into the EPF, but the mechanisms and processes are not well understood (Wheeler, 1992). There are two current routes by which Ca^{2+} pass through the mantle epithelium:

- 1) Ca^{2+} specific energy consuming intracellular pathways actively pumping Ca^{2+} across the mantle epithelium (Fan *et al.*, 2007)
- 2) Passive non-specific pathways ('gap junctions' between cells effectively causing diffusion across the mantle) (Crenshaw, 1980; Wheeler, 1992; Gillikin *et al.*, 2005)

Although only a slight elevation in Ca^{2+} is seen within the EPF compared to the external seawater (Wada & Fujinuki 1976; Gillikin, 2005; Gillikin *et al.*, 2006) calcification still occurs owing to saturation of CaCO_3 to a higher level in the EPF than in the external seawater. Therefore it is thought that rather than passive diffusion of Ca^{2+} into the EPF an active pathway for Ca^{2+} plays a more important role during calcification (McConnaughey, 1989; Gillikin, 2005; Carré *et al.*, 2006; Gillikin *et al.*, 2006). To strengthen the argument for active transport of Ca^{2+} across the mantle, Fan *et al.*, (2007) isolated calcium-ATPase (Ca^{2+} -ATPase) from the mantle of the bivalve *Pinctada fucata*. Calcium-ATPase is a transport protein which moves Ca^{2+} across biological membranes exchanging 2 hydrogen ions (H^+) in the process (Figure 3.4a, Watson *et al.*, 1971; McConnaughey, 1988). Not only does the presence of Ca^{2+} -ATPase account for the increase in Ca^{2+} needed for calcification, importantly it also raises the pH through the removal of H^+ ions which is necessary for calcification to occur (Cohen & McConnaughey, 2003; McConnaughey & Gillikin, 2008).

Carré *et al.* (2006) suggested that whilst Ca^{2+} -ATPase clearly plays a role in the transport of Ca^{2+} into the EPF there is physically no way for the membrane to contain enough of the transport protein to account for the amount of Ca that is contained within the final structure of the shell.

This same problem has been highlighted by Addadi *et al.* (2006), who stated that the volume of CaCO_3 saturated EPF needed for aragonite formation far exceeded the volume of the extrapallial space. Instead, they suggested the presence of calcium channels in the mantle epithelium (Figure 3.4b), which are known to increase membrane permeability to Ca^{2+} (Hagiwara & Byerly, 1981). They differ from the active and passive pathways for Ca^{2+} transport as they are selective for Ca^{2+} whilst also being passive and able to account for high fluxes of Ca^{2+} (Sather & McCleskey 2003). Sather and McCleskey (2003) postulate that as biomineralisation occurs, the Ca^{2+} concentration in the EPF is lowered, which sets a diffusion gradient that is supplied by the calcium channels. Due to the difficulty of sampling and observing *in-situ* the EPF during the calcification process and identifying transport mechanisms in mantle tissues, it is still unclear which of these mechanisms actually controls Ca^{2+} transport into the EPF.

Several studies have suggested alternative hypotheses to explain the discrepancy between the amount of CaCO_3 secreted and the amount of CaCO_3 available within the EPF, through the utilisation of crystallogenic cells (Mount *et al.*, 2004) or storage vesicles containing CaCO_3 in the form of unstable vaterite (Neff, 1972; Watabe *et al.*, 1976) or Amorphous Calcium Carbonate (ACC) (Addadi *et al.*, 2006). It is hypothesised that ACC is formed elsewhere (potentially in the haemolymph) and either transported to the EPF or directly to the mineralisation site where it spontaneously crystallises on an organic matrix to form the desired calcite or aragonite structure. Amorphous Calcium Carbonate as an initial formation phase has been observed in other organisms such as echinoderms (Politi *et al.*, 2004; Beniash *et al.*, 1997), corals (Meibom *et al.*, 2004) and crustaceans (see Raz *et al.*, 2002; Dillaman *et al.*, 2005).

3.1.2.3 Sources of carbon and oxygen

An increase in EPF pH is critical for a number of reasons that relate to the fluid's ability to precipitate CaCO_3 . A higher pH causes more CO_2 to be converted into bicarbonate (HCO_3^-) through hydroxylation (the addition of a hydroxide ion (OH^- from water)), causing more CO_2 to be drawn into the EPF via a diffusion gradient. The HCO_3^- ion is then deprotonated owing to the higher pH to form carbonate ions (CO_3^{2-}) that are required for the formation of CaCO_3 . The diffusion gradient of CO_2 into the EPF then becomes the major factor behind the accumulation of CO_3^{2-} and the saturation, and subsequent precipitation, of CaCO_3 (Cohen & McConnaughey, 2003; McConnaughey & Gillikin, 2008). Carbon dioxide concentrations are easily accounted for within the EPF as biological membranes are highly permeable to CO_2 (Gutknecht *et al.*, 1977),

however it is the origin of the CO₂ that is of scientific interest as it has many implications in the interpretation of stable carbon and oxygen isotope ratios in molluscan shells (McConnaughey, 1989; McConnaughey & Gillikin, 2008). During shell formation the calcification sites and exposed crystal surface of the mineralising shell are in equilibrium with the EPF. This means that through precipitation and dissolution of the forming crystals, the isotopic ratios of carbon (¹³C/¹²C) and oxygen (¹⁸O/¹⁶O) within the crystal matrix and the EPF will be similar. As seawater temperature changes, the ambient concentrations of these two naturally occurring isotopes of oxygen, ¹⁸O and ¹⁶O, change in a predictable way. Evaporation of seawater during warmer periods favours water molecules formed from the lighter ¹⁶O, therefore during warm periods the ratio of ¹⁶O to ¹⁸O, known as δ¹⁸O, changes i.e. the residual water is heavier in ¹⁸O (Epstein *et al.*, 1953). This change in O isotope ratio is reliable and reflected within the CaCO₃ of shell forming organisms as they form under equilibrium with external seawater and the ratios normally appear to be unaffected by metabolic ('vital') effects within the animal (Epstein *et al.*, 1953; Mook & Vogel, 1968; Klein *et al.*, 1996). Although there are exceptions to this pattern where metabolic CO₂ is incorporated into rapidly mineralising scallop *Pecten maximus* shell (see Owen *et al.*, 2002a & b). This topic will be discussed in detail in Chapter 4. The isotopic composition of shell material is determined using Isotope Ratio Mass Spectrometry (IRMS) allowing the reconstruction of historical isotope ratios. Due to the physio-chemical relationship between seawater temperature, salinity and δ¹⁸O, it is possible to calculate the seawater temperature at the time of formation by using a palaeotemperature equation (Epstein *et al.*, 1953; Grossman & Ku, 1986). Oxygen isotope ratios as proxies for seasonal temperature changes have been used successfully to reconstruct past seawater temperatures from shell carbonate (e.g. Sosdian *et al.*, 2006; Gentry *et al.*, 2008; Prendergast *et al.*, 2013; Bušelić *et al.*, 2015); as shells grow incrementally at tidal and annual resolution they are powerful tools for environmental and climatic reconstructions of bottom seawater temperatures.

The interpretation of carbon isotopes in molluscan shells has been shown to be more complex than the interpretation of oxygen isotopes as the former can reflect both internal and external sources of carbon. External carbon comes from Dissolved Inorganic Carbon (DIC) which is in approximate equilibrium with seawater and comes from seawater CO₂, bicarbonate and carbonate ions, which in turn reflect cycles in ocean productivity (Mook & Vogel, 1968; Mook, 1971; Donner & Nord, 1986). Internal sources of carbon can be derived through metabolic processes such as digestion and respiration, and the subsequent diffusion of CO₂ from these

processes into the EPF from the haemolymph (Borchardt, 1985; Tanaka *et al.*, 1986; Klein *et al.*, 1996; Gillikin *et al.*, 2006 & 2007). This mixing of carbon sources can make interpretation of Carbon isotopes within mollusc shells difficult if the sources of carbon are unknown, or very powerful if they can be properly understood (McConnaughey & Gillikin, 2008).

3.1.2.4 Organic matrix

When calcium carbonate is precipitated in the shell, the crystals must be added in a regimented way, as the shell crystal structure can be complex. Different crystal orientation and crystal size between different layers is common, as are the abundance and proportion of calcite and aragonite, that are both commonly seen in the shells of a single mollusc shell. In some vaterite is also deposited (Wilt, 2005; Nehrke *et al.*, 2012). It is currently understood that during or before calcification occurs, the mantle epithelium secretes an organic matrix; the composition of which likely varies between species (Addadi *et al.*, 2006; Furuhashi *et al.*, 2009). The CaCO_3 crystals then nucleate and are precipitated within the organic matrix, the constituents of which are speculated to control the formation of the intricate crystal structures seen within the shells of different molluscs. Many aspects of the morphology of the crystal matrix are determined by the organic matrix, from the polymorph of CaCO_3 (aragonite or calcite) and the shape of the subsequent crystal growth, to the initial nucleation, placement and alignment of crystals (Weiner & Traub, 1980; Mann *et al.*, 1989; Addadi *et al.*, 1991; Addadi & Weiner, 1997; Levi-Kalishman *et al.*, 2001). In the resulting shell structure, the organic matrix can often be found in different places amongst the crystals depending on the type of structure that is formed, for example in Nacre it can be seen as layers between crystal sheets (Figure 3.5a & b).

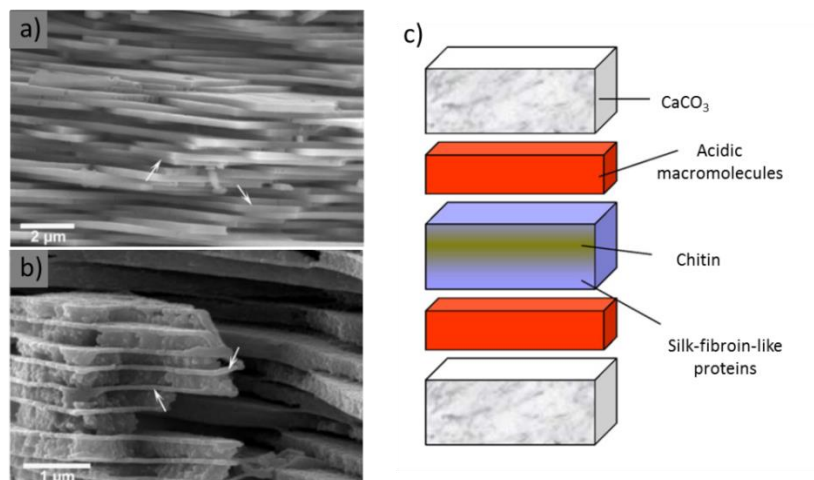


Figure 3.5. Scanning electron microscopy images from fractured mollusc shells. a) Nacreous plates from the bivalve *Atrina rigida*, b) the cephalopod *Nautilus pompilius* showing the visible organic matrix (white arrows) between the shell layers (adapted from Addadi *et al.*, 2006) and c), a simplified diagrammatic model of shell organic matrix structure, taken from Furuhashi *et al.*, 2009 (modified from Weiner and Traub, 1984).

There have been several proposed models of organic matrix formation and structure which vary in complexity but revolve around a layered structure composed from a mixture of chitin, silk fibroin proteins and acidic macromolecules (Figure 3.5c), all of which play different roles in regimenting the crystallisation process (Weiner & Traub, 1984; Levi-Kalisman *et al.*, 2001; Nudelman *et al.*, 2007; Furuhashi *et al.*, 2009). The exact mechanisms of organic matrix secretion, the structure and composition of the matrices and how these matrices control crystal deposition is largely unknown (Barthelat *et al.*, 2006). This is due to the difficulties arising from isolating and analysing organic components of differing solubility within a CaCO_3 matrix (Furuhashi *et al.*, 2009). A large body of work has been dedicated to a better understanding of this process and large advances in understanding have been made (e.g. see Barthelat *et al.*, 2009; Furuhashi *et al.*, 2009).

3.1.3 Gastropod shell structure

The class Gastropoda represents a highly diverse collection of molluscan species with highly varied shell shapes (Bouchet *et al.*, 2005). The shell of *Buccinum undatum* is asymmetrical and conispirally coiled around the columella, giving them a characteristic cone shape common to many neogastropods (Figure 3.6) (see Fretter & Graham, 1994, Ruppert *et al.*, 2004).



Figure 3.6. Internal view of a laterally sectioned *Buccinum undatum* shell. The coiled shell structure is clearly visible revolving around the central columella (c).

The internal microstructure of mollusc shells is composed of distinct crystal layers. In gastropods the shell is frequently composed of at least four distinct layers (Figure 3.7) that usually consist

of:

- 1) outer organic periostracum
- 2) Prismatic layer with crystals orientated perpendicular to the shell surface
- 3) one or more crossed-lamellar layers with crystals orientated parallel to the shell surface
- 4) Nacreous layers are often found on the internal surface of the shell

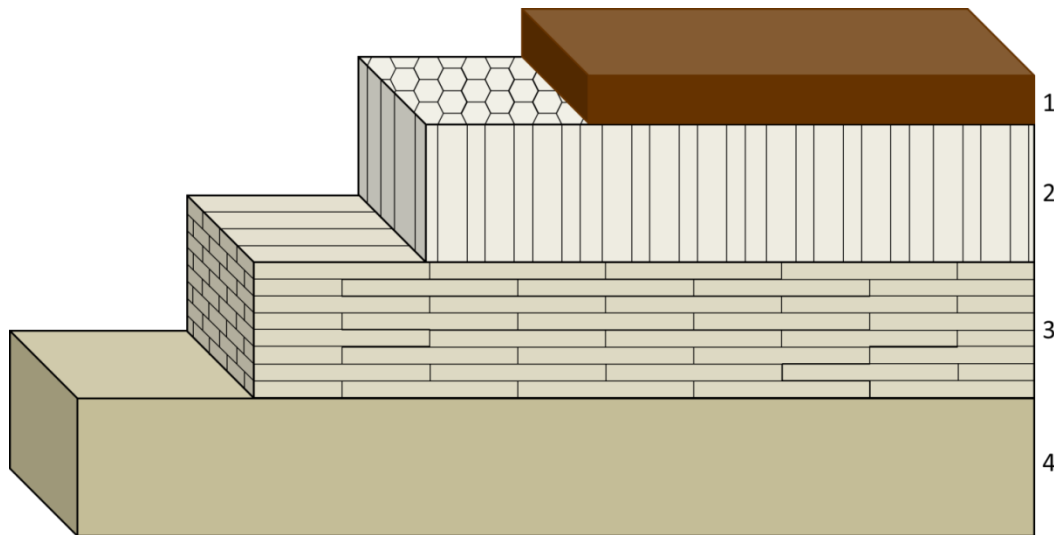


Figure 3.7. Generalised model of gastropod shell structure showing 1) the outer organic periostracum, 2) the prismatic shell layer, 3) a crossed-lamellar layer and 4) an internal nacreous layer (Hawkes *et al.*, 1996; Dauphin & Denis, 2000; Pokroy & Zolotoyabko, 2003).

An understanding of the shell structure of *B. undatum* is necessary prior to undertaking any geochemical analyses of the crystal layers. A knowledge of the cross sectional structure is key to knowing where to take samples for elemental analysis as well as a knowledge of the polymorph (aragonite or calcite) of calcium carbonate present in the shell. The calcium carbonate polymorph can affect the interpretation of geochemical data such as trace element concentrations as some trace elements e.g. magnesium (Mg) and strontium (Sr) are differentially incorporated into aragonite and calcite (Speer, 1983; Lloyd *et al.*, 2008). If the shell layers differ in their calcium carbonate polymorph it is crucial to know where these changes occur before undertaking any further analyses. The internal micro-structure of *B. undatum* shells has not been studied previously. In the following chapters, several different kinds of geochemical analyses are undertaken on the shells of *B. undatum* collected from three study sites. The initial exploration of *B. undatum* shell structure outlined in this chapter is vital for the development of a sampling methodology and interpretation of the data. It is hypothesised that *B. undatum* shells will fit the general model of gastropod shell growth outlined above at each sampled site.

3.2 Materials and methods

As the internal structure of the *B. undatum* shell had not been studied previously several methods were applied to shells collected from the Menai Strait, Shetland and Jersey (see Chapter 2, Figure 2.3). Shell sections were prepared to give an overview of the shell structure in both recent and older shell growth to look for differences in the width and preservation of the calcium carbonate shell layers over time. Damaged areas on the outer surface of *B. undatum* shells were frequently observed in shells collected from the Menai Strait. Areas of the shell that displayed clear damage close to the shell margin and along the shell whorls were removed using a hand-held Dremel 4000 multitool with attached cutting wheel to investigate shell growth during and following a damage event.

Seven whelk egg masses that had been laid naturally in an intertidal location at Tal-y-Foel (53.158512, -4.279493) in the Menai Strait were collected in November 2013 and 2014. Egg masses were transported to the laboratory and held in aquaria supplied with flowing ambient seawater. Approximately 2 months later juvenile whelks hatched directly from the egg capsules and were reared for 1 year (2014 cohort) and 2 years (2013 cohort) under an approximate 10:14hr light/dark cycle and fed regularly thrice weekly with small pieces of frozen and thawed mackerel (*Scomber scombrus*). As a comparison to field collected whelks, 10 2 year old juveniles were artificially damaged by cutting a $\approx 1\text{cm}^2$ area from the shell using the Dremel and attached cutting disk. Over the following 7 days, the shells were allowed to repair before being damaged again and allowed to recover for a further 7 days. The structure of the naturally damaged and repaired shell was investigated in shell sections to study the crystal structure during shell repair.

3.2.1 Thin sections

Pieces of shell were removed from the field collected and laboratory repaired shells using the Dremel and cutting wheel, embedded in Kleerset polyester resin and left to cure for 72 hours. The resulting resin blocks and embedded shell pieces were sectioned parallel to the direction of shell growth using a Buehler Isomet 4000 precision saw to expose the internal structure of the embedded shell fragments. The surface of each sectioned block was then ground smooth using successive grades of silicon carbide grinding paper (400 down to 4000 grit) lubricated with fresh water to remove all visible scratches from the sectioned surface. The ground surface was polished using a 3 μm diamond suspension polish on a rotating pad. The ground and polished surface was attached to a standard glass microscope slide using super glue. The block was then

sectioned again, this time cutting off the attached microscope slide with a thin slice (1-2 mm) of resin and shell still attached. The thin slice was then ground and polished as before until the thickness had been reduced to 30 to 80 μm , to allow light to pass through the thin shell section. Photomicrographs of thin shell sections illuminated in transmitted light at 20x magnification were taken using a Lumenera Infinity 3 microscope camera mounted on a Meiji Techno MT8100 microscope. Montage images of serial photographs taken along the thin shell sections were assembled using Image Pro Premier software.

3.2.2 Scanning Electron Microscopy (SEM)

To view the crystal structure of the *B. undatum* shell, several shells collected from the Menai Strait, Shetland and Jersey were broken using a bench vice. Fragments from the shell lip and the shell apex that displayed a break both parallel to the growth axis and perpendicular to it were selected and attached to 1 inch diameter aluminium SEM stubs using Electrodag[®] and sputter coated with gold. Shell fragments were imaged using a Zeiss Sigma VP field emission SEM at the Interface Analysis Centre at the School of Physics, Bristol University. Images of interest were taken as secondary electron images at an accelerating voltage of 10 kV with working distances from 4.8 – 12.5 mm.

3.2.3. Micro-Raman spectroscopy (MRS)

The structure and composition of the shell layers of *B. undatum* were investigated using MRS. Raman spectroscopy allows differentiation between the polymorphs of CaCO_3 (amorphous CaCO_3 (ACC), calcite, aragonite and vaterite) by focusing a laser light onto the sample surface. Inelastic scattering of the light occurs after interacting with the sample structure due to the vibrational levels of the composite molecules. This causes a shift in the wavelength of a proportion of the measured scattered photons (Raman shift) (Higson, 2006). An overview of the Raman spectroscopy technique can be found in [Appendix C](#). The wavelength shifts of the spectra are predictable in position and relative intensity for different substances. For CaCO_3 , two main sections of the spectra are of interest, peaks in the 100–350 cm^{-1} range pertain to interaction with features of the external lattice structure, whereas peaks in the 600–1800 cm^{-1} range relate to interactions with the internal molecular planes (Parker *et al.*, 2010). To determine the shell composition, sectioned shell layers of resin embedded *B. undatum* shell fragments were analysed using a Reinshaw InVia Raman-Microscope, located at the Diamond Light Source facility in Didcot, Oxfordshire. This was to determine whether the polymorph structure of the different shell layers was aragonite or calcite. A 473 nm laser at a power of 15

mW was employed at a magnification of 20x; a grating with 2400 lines.mm⁻¹ and a pinhole size of 100 µm were used for spectra acquisition between 100 and 3200 cm⁻¹. Three sample spots were analysed from each visible layer on thin sections of 1 shell from the Menai Strait, Shetland and Jersey. Synthetic calcite and speleothem aragonite standards (Brinza *et al.*, 2014) were sampled prior to and after shell analyses for comparison. The resulting Raman spectra were adjusted using a polynomial background correction. The spectra from the three sample spots in each layer were then averaged for comparison between layers.

3.3 Results

3.3.1 Layered shell structure

The internal layered structure of a sectioned and polished *Buccinum undatum* shell is shown in Figure 3.8. Four clearly distinct layers are visible - an outer prismatic layer, two inner crossed-lamellar layers and an internal nacreous layer. The colour difference between the layers is possibly due to the differential incorporation of organic matter. There are visible structural differences between the layers due to different crystal structures at the microscopic level. The organisation of these layers was observed to be consistent in all the sampled shells from the three locations.

The shell section shown in Figure 3.8 is from approximately three quarters of the way along an adult whelk shell and parallel to the growth axis. To investigate the orientation of the crystal structures in the separate layers, Figure 3.9 shows a shell section from close to the lip of an adult *B. undatum* shell taken perpendicular to the growth axis. The positions of the two internal crossed-lamellar layers are switched, implying that the layers are the same at a 90° plane to each other. The outer layer in Figure 3.9 is harder to differentiate, likely because the sample is not thin enough to allow sufficient light to pass through. However, there are clear laminations present which are not immediately visible in Figure 3.8. The positions of the two Crossed-lamellar layers are reversed from the positions seen in Figure 3.8. The nacreous layer is absent from Figure 3.9 probably because the shell section was taken close to the lip of the newly formed shell and the nacreous layer is only deposited later and away from the shell edge (c.f. at the pallial line in a bivalve shell). As the gastropod grows older nacre is deposited to thicken and strengthen the shell during ontogeny (Wilbur & Saleuddin, 1983; Hawkes *et al.*, 1996).

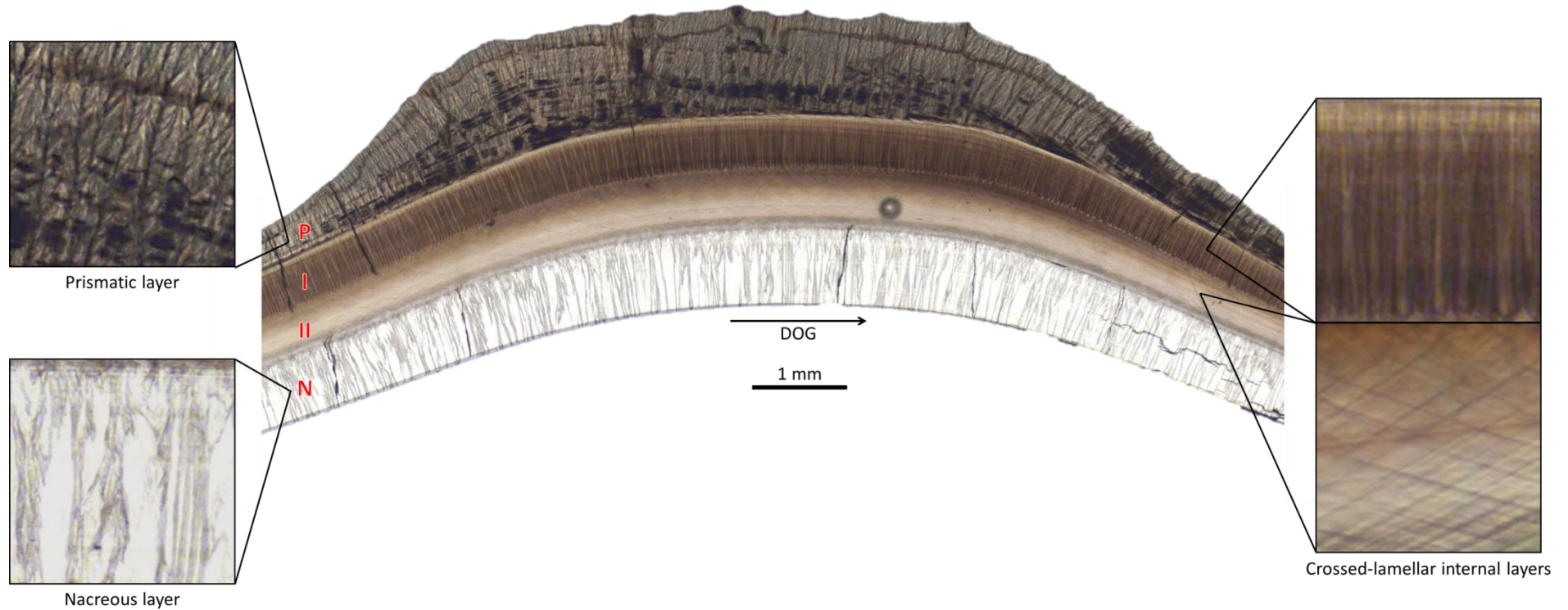


Figure 3.8. Photomicrograph montage of a thin shell section from approximately three quarters of the way along an adult *Buccinum undatum* shell collected from the Menai Strait. The section has been prepared parallel to the growth axis. The thin section was taken over a characteristic outer shell 'wave' (Chapter 1, Figure 3.2) which results in thickening of the outer prismatic layer only in the centre of the image. There are distinctive differences in crystal structure visible between the four different layers observable in the inset images. DOG = Direction of Growth. P = prismatic Layer, I = crossed-lamellar layer 1, II = crossed-lamellar layer 2, N = nacreous layer.

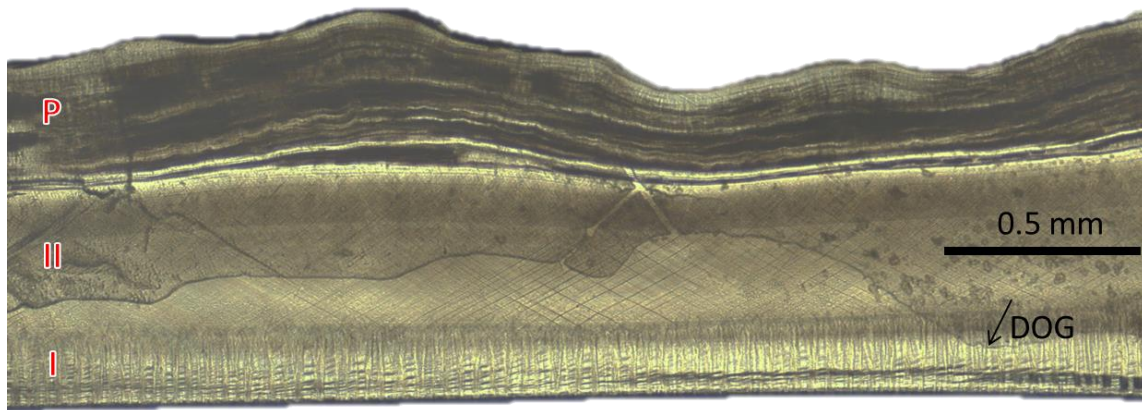


Figure 3.9. Photomicrograph montage of a thin shell section from close to the tip of an adult *Buccinum undatum* from the Menai strait. The section was taken at 90° to the growth axis. Here, only the upper three shell layers seen in Figure 3.8 are visible i.e. the prismatic layer and two crossed-lamellar layers. The nacreous layer is absent. The positions of the two crossed-lamellar layers are also switched around. P = prismatic Layer, I = crossed-lamellar layer 1, II = crossed-lamellar layer 2, DOG = Direction of Growth.

3.3.2 Scanning Electron Microscopy (SEM)

The detailed images shown in Figure 3.10 highlight the differences in crystal structure found between the visible growth layers of the shell. The four layers can be seen in Figure 3.10a and the prismatic layer in more detail in Figure 3.10b. Figures 3.10c & d, show the crossed-lamellar layers that are visible in Figures 3.8 & 3.9. In Figure 3.10c the view of the crystals is end on, with repeated units of roughly $10\ \mu\text{m}$ across the image. In Figures 3.10d, a side on view of the repeated crystal units observed from the 1st crossed-lamellar layer can be seen (3.10c), which are at 90° to the crystals seen in Figure 3.10c, shows long thin crystals layered together. The nacreous layer shown in Figure 3.10e, is composed of flattened crystals and has the least regimented and organised crystal structure of all the four layers.

Figure 3.11a & b, show the same area (a) parallel to the growth axis and (b) perpendicular to it. The distinctive crystal patterns of the internal growth layers seen in Figure 3.10c & d can be seen in the same order in (a), but with reversed positions in (b) which is positioned 90° to the original break. This confirms the idea of two identical crossed-lamellar layers that are seen in Figures 3.8 & 3.9. Higher magnifications of these layers in Figure 3.11c & d (layer I in (c), and layer II in (d)) where the distinction of individual crystals is possible, appear to show thin flattened crystals. During fracturing of the shell, the shell layers occasionally sheared away from each other revealing the interface between them. The boundary between layers I, II and the nacreous layer can be seen in Figure 3.11e. The crossed-lamellar structure of layers I & II can be

clearly seen here and the clear ridges seen on the surface of the layers may give an indication of how the layers are tessellated together. Finally, Figure 3.11f, shows the same nacreous layer to that in Figure 3.10e, but in a perpendicular plane to the original break and the structure now appears far more regular and regimented.

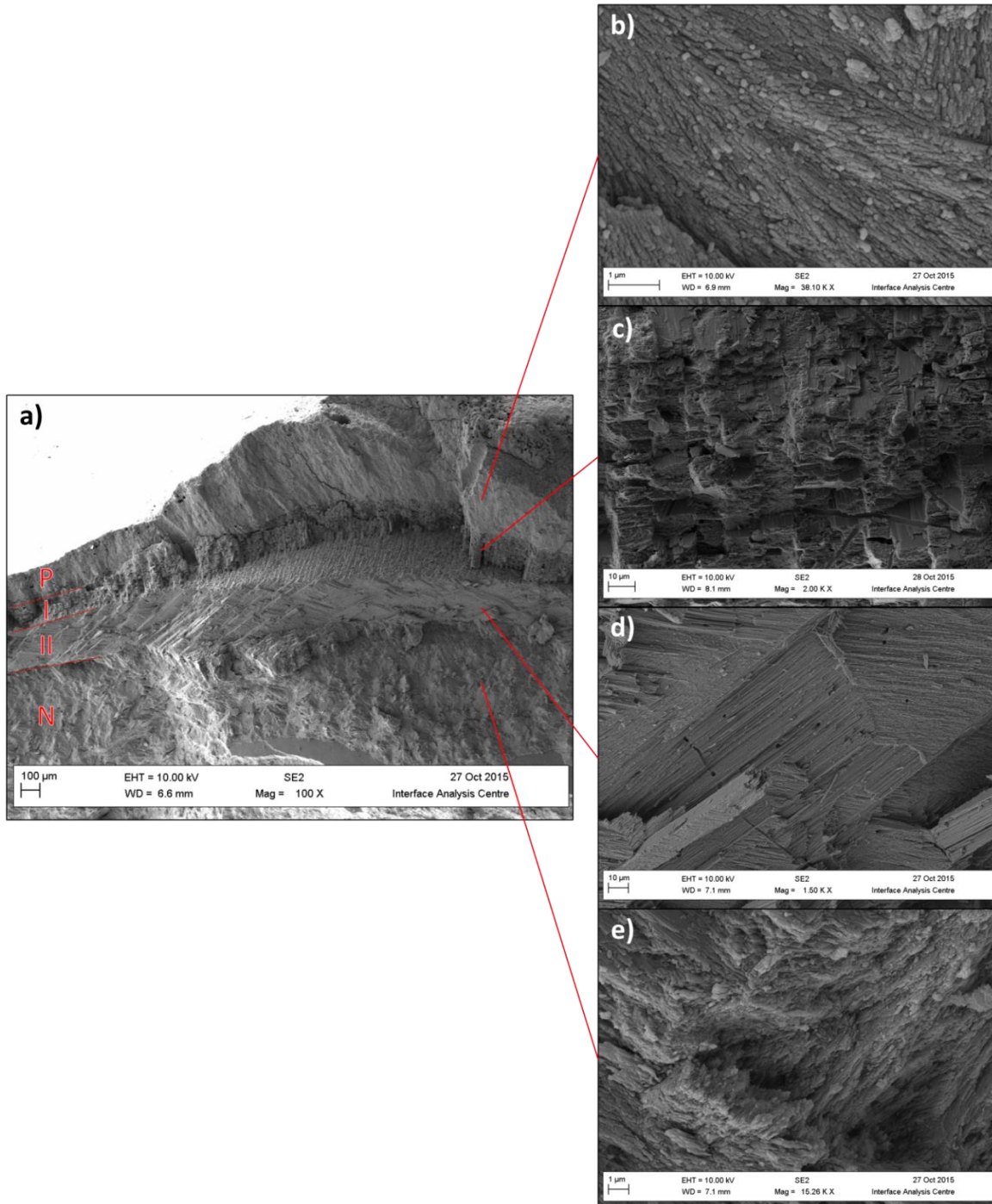


Figure 3.10. Scanning electron microscope images of the fractured surfaces of unetched shell fragments from close to the apex of a *Buccinum undatum* shell from Shetland taken at various magnifications. a) a broken shell edge parallel to the growth axis with the four layers in Figure 3.8 visible. b, c, d & e) magnified images of the four visible shell layers, the prismatic layer, the 1st crossed-lamellar layer, the 2nd crossed-lamellar layer and the nacreous layer respectively. P = prismatic Layer, I = crossed-lamellar layer 1, II = crossed-lamellar layer 2, N = nacreous layer.

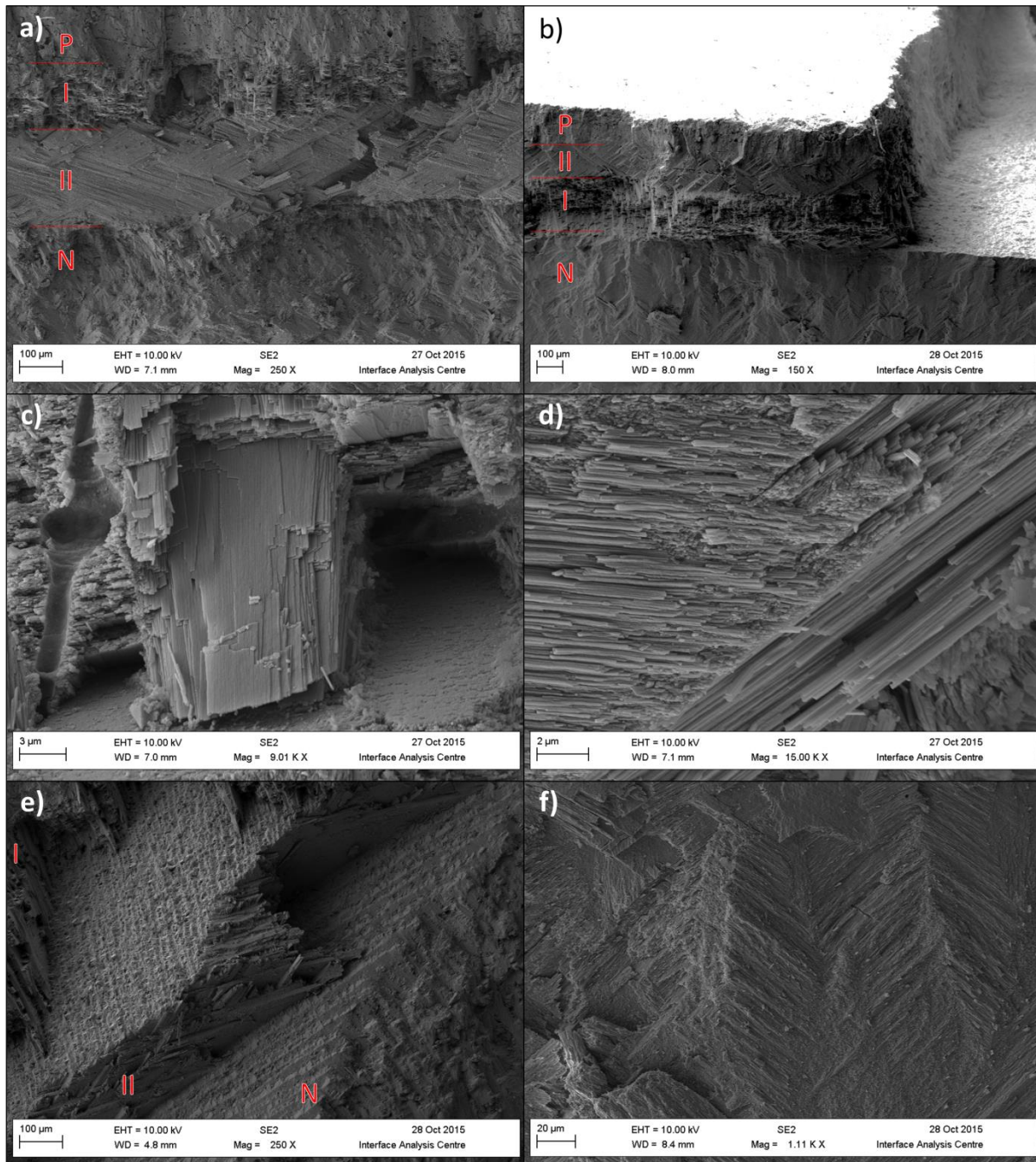


Figure 3.11. Scanning electron microscope images of unetched shell fragments from close to the apex of a *Buccinum undatum* shell from Shetland taken at varying magnifications. a & b) show the same shell area parallel to a) and perpendicular to b) the growth axis. The crossed-lamellar layers (labelled I & II) noticeably switch in b) at 90° to the original break seen in a). (P – prismatic layer, N – nacreous layer, red lines indicate layer boundaries). c & d), show magnified images of the crossed-lamellar layers (I & II respectively). e), shows the interface between the two crossed-lamellar layers (1 & 2) and the underlying nacreous layer (N) and f), shows the crystal structure of the nacreous layer perpendicular to the growth axis.

3.3.3 Shell boring organisms

During shell processing many whelks from Shetland and several from Jersey had a green colouration to their shell exteriors that could not be removed with brisk scrubbing and visible erosion between the shell 'waves' (inset Figure 3.12). The green colouration could be removed with immersion in sodium hydroxide (NaOH) which was undertaken for a separate experiment. Thin sections of these shells showed that the upper shell layer was eroded between the 'waves' with a concomitant thickening of the inner nacreous layer (Figure 3.12). Scrutiny with the SEM revealed hundreds of small holes ($\approx 2 \mu\text{m}$ in diameter) (Figure 3.13a) that extended from the shell surface through the outer prismatic and crossed-lamellar layers into the inner nacreous layer. Closer inspection revealed they had been bored by either worms, diatoms or fungi (Akpan & Farrow, 1984) with evidence that there was either crystallisation of the tube formations or more likely, deposition of organic material inside the bore hole (Figure 3.13b). In a thin section of the shell margin (Figure 3.13c) the black lines visible throughout the structure are the bore holes visible throughout the shell. The bore holes are visible (white arrows) in Figure 3.12, although they obscure much of the details of the shell structure. The shell margin in Figure 3.13c is of interest as the crossed-lamellar layers that have been seen previously are harder to distinguish in section and there appears to be a switch between the upper crossed-lamellar layer and the prismatic outer layer. An unidentified boring sponge was found in several adult whelk shells from Jersey that had inflicted damage to the shell structure (Figure 3.14). The sponge species could not be identified from the visible spicules which were barbed in appearance (Figure 3.14c & d).

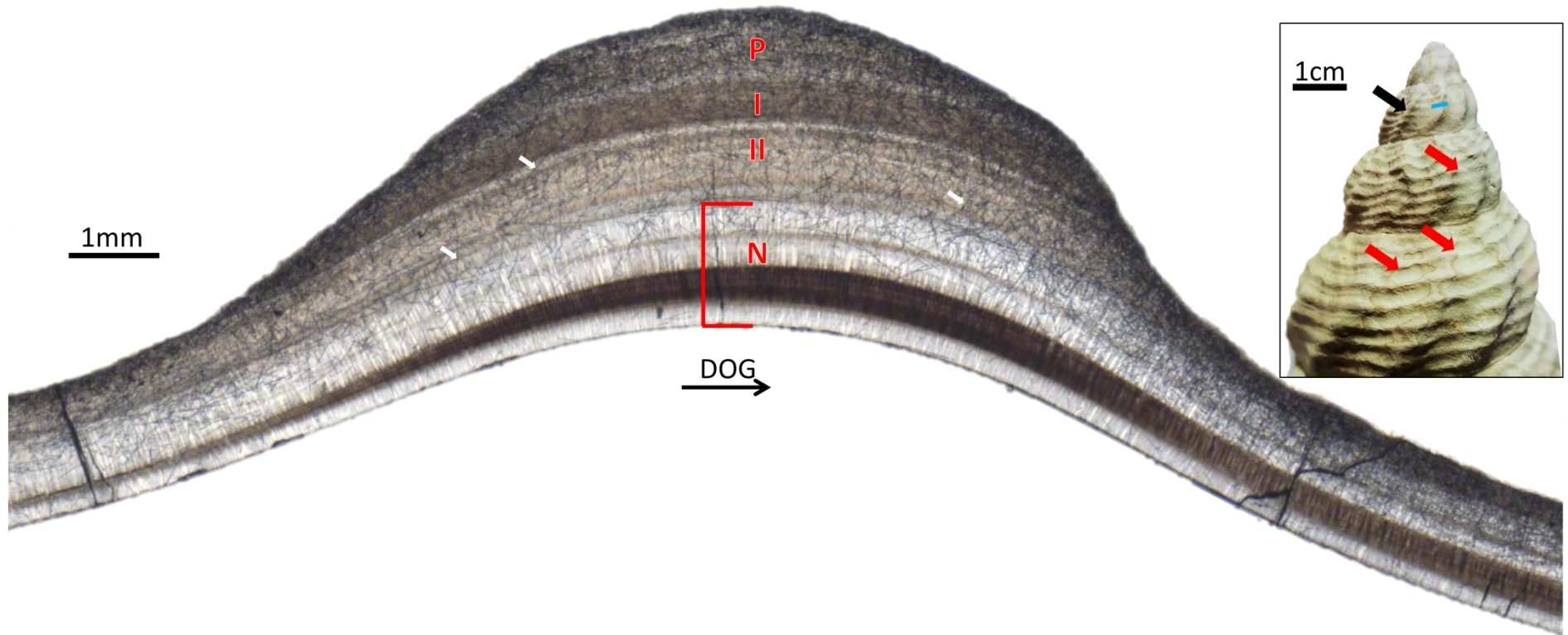


Figure 3.12. Photomicrograph montage of a thin section from a *Buccinum undatum* shell from Shetland. The section is parallel to the growth axis and taken over a visible shell 'wave' (see inset, large black arrow). The blue line on the shell in the inset represents the visible sectioned area shown in the montage image. The four main shell layers are numbered, however, layers 1, 2 and 3 have been eroded away on either side of the 'wave'. The nacreous layer (4) is similarly thickened, the entire shell structure is ramified throughout with black lines (white arrows). The inset highlights areas of shell erosion between shell whorls of another whelk shell from Shetland (red arrows), a green hue is also noticeable. P = prismatic Layer, I = crossed-lamellar layer 1, II = crossed-lamellar layer 2, N = nacreous layer, DOG = Direction of Growth.

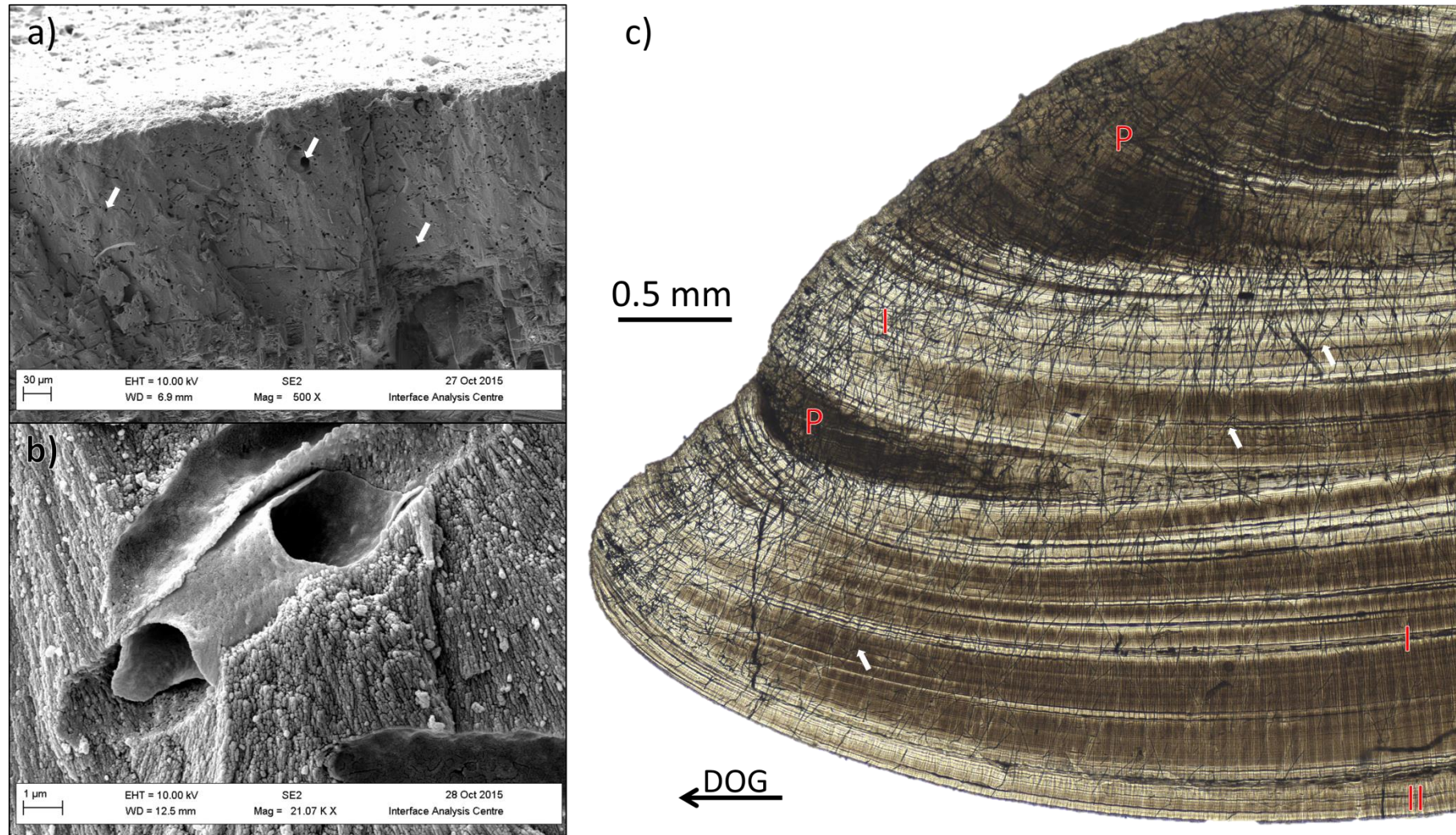


Figure 3.13. a & b) scanning electron microscope images of bore holes found in the outer prismatic shell layer (white arrows) of a *Buccinum undatum* shell from Shetland. a) small black dots represent individual bore holes. b) shows a magnified image of a bore hole in the prismatic layer, a tube, not part of the shell crystal matrix can be seen. c) Photomicrograph montage of the margin edge from a whelk shell from Shetland. The bore holes are clearly visible ramifying throughout the structure, reaching down into the inner Crossed-lamellar layer (II). P = prismatic Layer, I = crossed-lamellar layer 1, II = crossed-lamellar layer 2, DOG = Direction Of Growth.

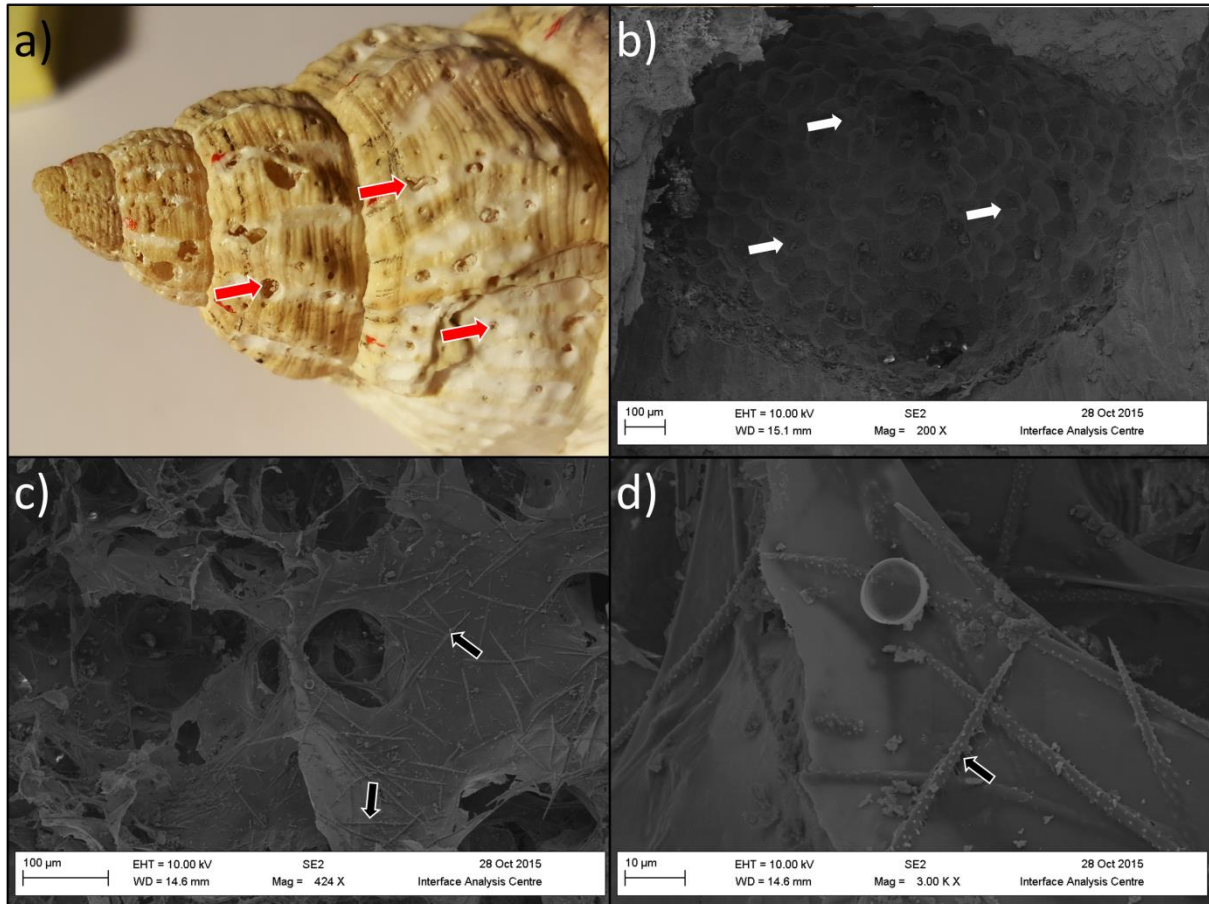


Figure 3.14. a) appearance of the shell spire of a *Buccinum undatum* shell from Jersey. Large (~1mm diameter) pits (red arrows) can be clearly seen on the shell surface, b) a SEM image of a pit left by a boring sponge; the individual pits made by the sponges acid secretions can be seen (white arrows) and c & d) SEM images of the remains of a dried sponge in a hole in the shell structure photographed at different magnifications. The dried sponge tissue containing spined spicules can be clearly seen (black arrows).

3.3.4 Shell damage repair

Figure 3.15a shows the shell increment and layered structure deposited when the *B. undatum* shell was repaired following damage in a field collected specimen. The outer shell layers present before the shell was damaged are similarly deposited following damage. Shell deposition begins up to 2 mm back from the damage site (Figures 3.15a & b) and with the start of repair, prismatic shell (layer P) nucleate onto the inner crossed-lamellar layer (layer II; Figure 3.15a). This is then followed by rapid extension of a thin 'finger' of newly deposited shell that begins to thicken to reinforce the shell in this region. Several millimetres of shell form before shell deposition thickens the shell to its original pre-damage thickness (Figure 3.15a). Similarly Juvenile *B. undatum* shells were successfully repaired following consecutive artificial damage events (Figure 3.15b). However when the juveniles repaired their shells the thickness of the repaired shell was thinner than in the adult repaired shell and only two shell layers were deposited i.e. prismatic and 1st crossed-lamellar layers (compare Figures 3.15a & b). It is possible following the first damage incident that shell deposition may have been disrupted even further by the second damage incident and this resulted in the formation of a thinner repaired shell than during the 1st repair. Understanding of the mechanism of shell repair requires considerably more work and was outside the scope of this thesis.

3.3.5 Shell mineralogy

The average Raman spectra for three sample spots from each of the four shell layers from the Menai Strait whelk shell are shown in Figure 3.16. The spectra from shell layers in those from the other two sites, Jersey and Shetland, were essentially similar to the Menai Strait shell. Comparison of these spectra with the spectra from the calcite and aragonite standards demonstrated that all four shell layers are composed of aragonite (see Figure 3.16). The spectra acquired between 1000 and 3100 cm⁻¹ showed clear coincidences in peaks between the prismatic and the two crossed-lamellar layers whereas the Raman spectra from the nacreous layer were different to the other three layers (see Figure 3.17).

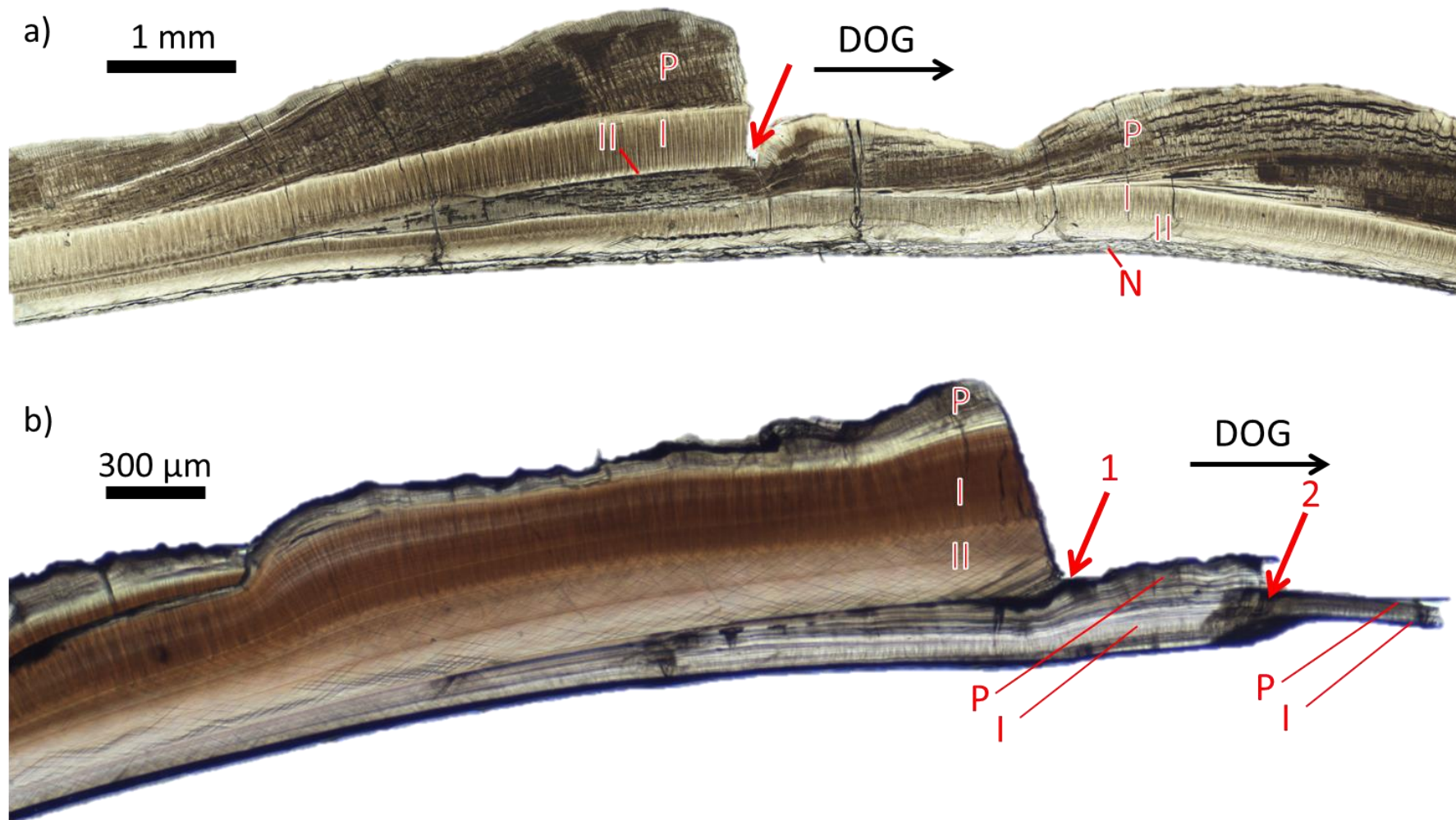


Figure 3.15. a) Photomicrograph montage of a thin section from an adult *Buccinum undatum* shell from the Menai strait that was experimentally damaged (large red arrow) and allowed to repair its shell. Three shell layers (P = prismatic Layer, I = crossed-lamellar layer 1, II = crossed-lamellar layer 2) are visible before the damage event, however four layers (P, I, II & N = nacreous layer) are deposited in the subsequent repaired shell. b) Photomicrograph montage of a thin shell section from a laboratory reared 1 year old juvenile *Buccinum undatum* that was experimentally damaged on two occasions (red arrows; 1 & 2). Three shell layers are visible (P, I & II) prior to damage and in the repaired shell only the outer prismatic layer and crossed-lamellar layer 1 (P & I respectively) are visible. DOG = Direction of Growth.

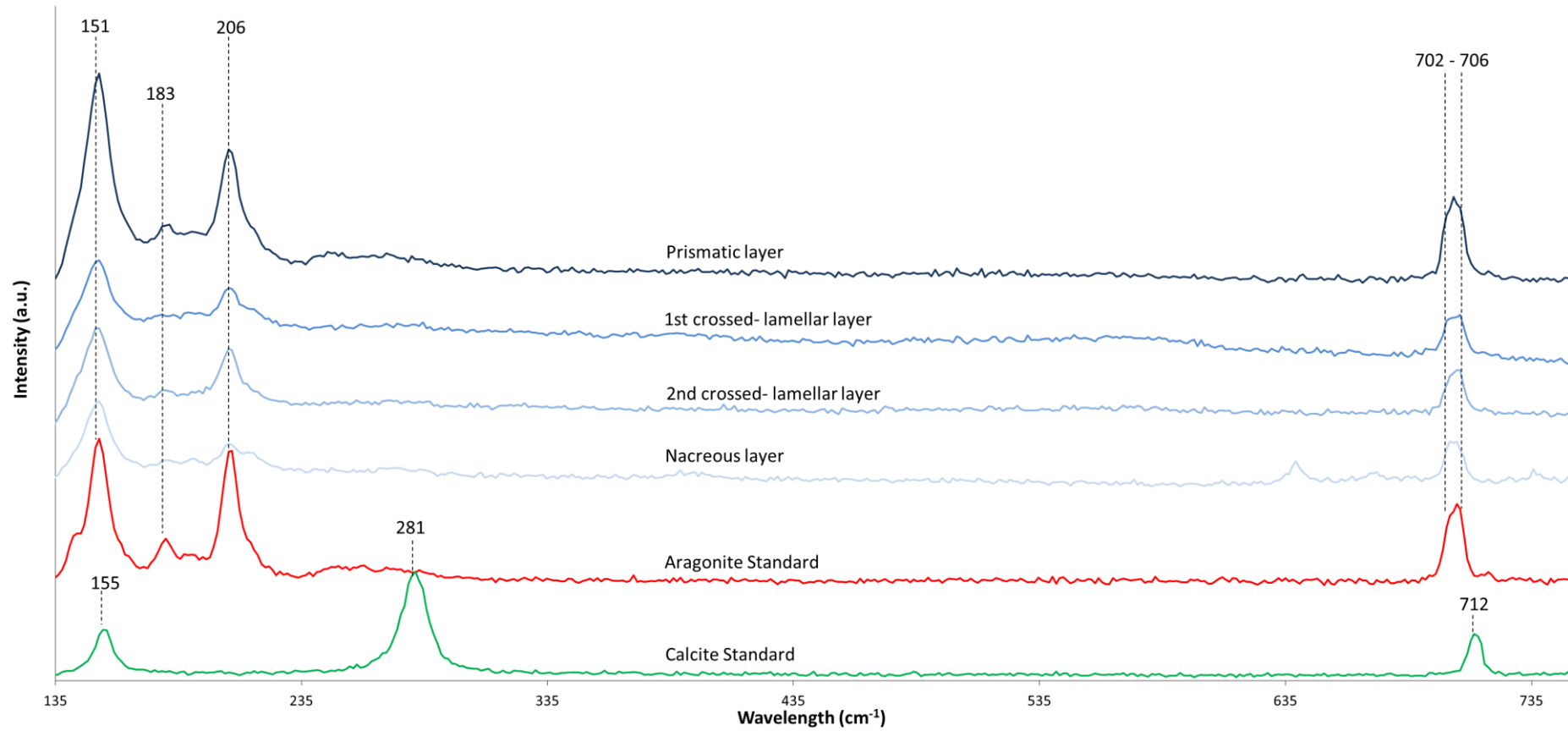


Figure 3.16. Raman spectra between 135 and 750 cm⁻¹ for four shell layers, the prismatic layer, 1st and 2nd crossed-lamellar layers and nacreous layers from a shell section of *Buccinum undatum* from the Menai Strait. Characteristic peaks in the spectra are indicated (dotted lines) for both calcite and aragonite. There is clear agreement between the four shell layers and the aragonite standard. Y axis = arbitrary units.

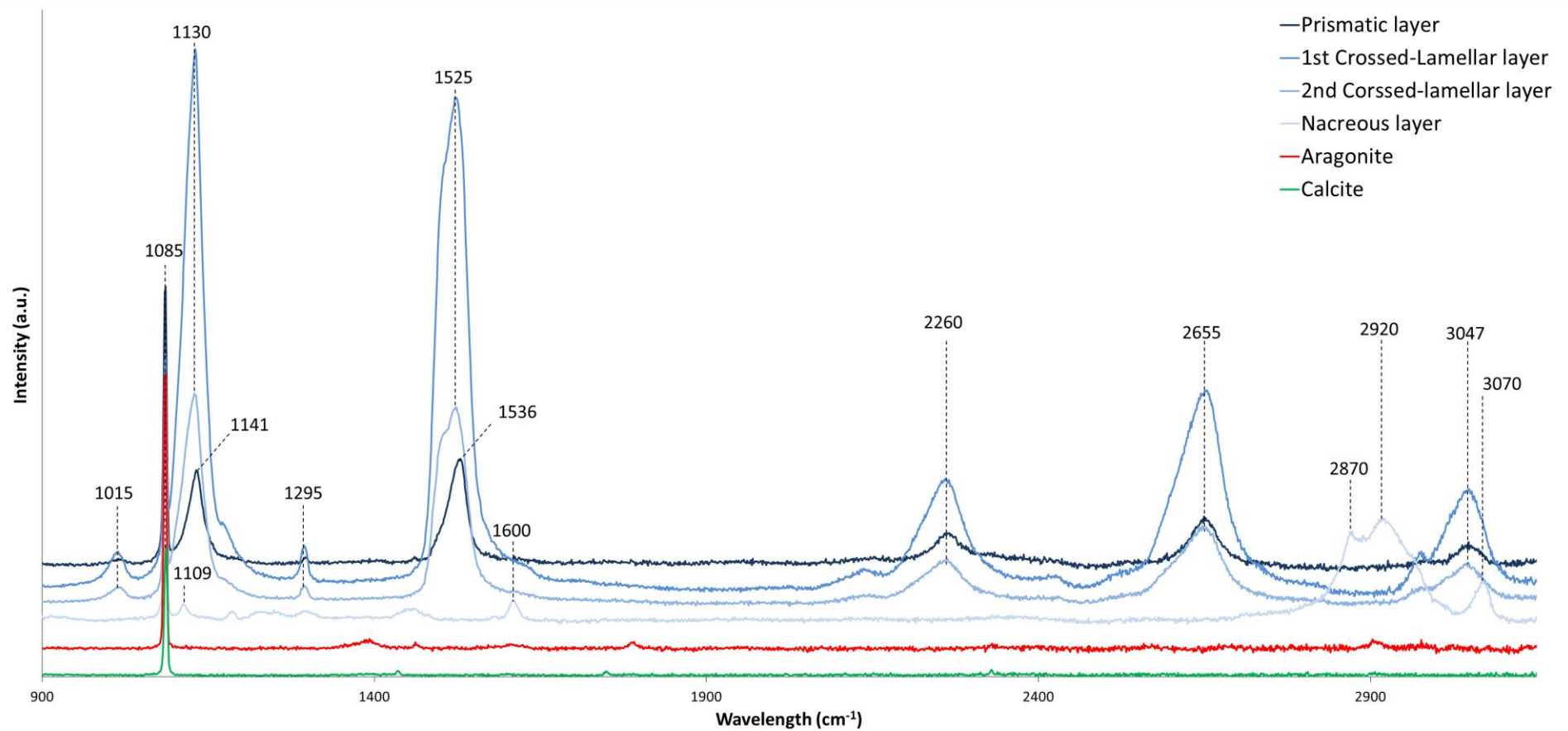


Figure 3.17. Raman spectra between 1000 and 3150 cm⁻¹ for four shell layers, the prismatic layer, 1st and 2nd crossed-lamellar layers and nacreous layers from a shell section of *Buccinum undatum* from the Menai Strait. There is a characteristic peak in the spectra at 1085 cm⁻¹ for both aragonite and calcite (dotted lines) and several clear coincidences in the spectra peaks between the prismatic and 1st and 2nd crossed-lamellar layers. However the nacreous layer shows Raman shifts at different wavelengths. Y axis = arbitrary units

3.4 Discussion

3.4.1 Shell structure of *Buccinum undatum*

The structure of the shell of *Buccinum undatum* has been determined from thin shell sections and SEM images and is comprised of 4 distinct layers: an outer prismatic layer, an inner 1st crossed-lamellar layer, a 2nd inner crossed-lamellar layer deposited perpendicular to the 1st and an internal nacreous layer, normally only visible in older parts of the shell, sometimes as multiple layers. The outer organic periostracum layer was observed although it was thin, and was scrubbed off prior to resin embedding. This visible structure in Figure 3.8 fits the general model of a layered crystal structure outlined in the introduction. In the thin shell sections it appears as though the 1st crossed-lamellar layer has a structure perpendicular to the surface, however, the SEM images in Figure 3.10c & 3.11c show that the structure is parallel to the surface but is being viewed end-on; it is also identical and perpendicular to the 2nd crossed-lamellar layer. The plywood like structure of the crossed-lamellar layer in the whelk shell sections is a common feature seen in other gastropod shells, for example in *Strombus decorus* (Pokroy & Zolotoyabko, 2003), *Strombus gigas*, *Cypraea leviathan* and *Phalium granulatum* (Dauphin & Denis, 2000). It is also clear that during the growth of the characteristic shell waves, it is only the prismatic layer which thickens; all of the other layers maintain their thickness. When shell sections were taken from approximately halfway up the spire of the shell an inner nacreous layer was apparent, however close to the shell lip the nacreous layer was absent. A similar situation exists in bivalve shells where nacre is deposited on the inner shell surface inside the pallial line (the site of attachment of the mantle margin epithelium), and absent from the growing shell edge i.e. outside of the pallial line. The nacreous layer forms an important role in maintaining the integrity of the shell's structure, particularly in regions of the shell where there is external wear as is seen in the earliest (oldest) parts of the shell.

3.4.2 Shell erosion and boring organisms

Frequently whelk shells from the Shetlands were eroded, particularly in the older parts of the shell (i.e. first deposited as juveniles) and between the shell 'waves' forming the outer sculpture. These shells also displayed bore holes often visible to the naked eye that in SEM images and thin shell sections were visible ramifying throughout the shell structure. Many of the adult shells from Shetland (70% >65mm shell length) had a greenish hue on the outer surface. Thin sections taken close to the shell apex through the outer shell sculpture of 'shell waves' showed that in the troughs of these waves the outer shell surface was heavily eroded and the inner shells layers

extensively bored with $\approx 2\ \mu\text{m}$ diameter tubes. The likely explanation for the erosion of the outer surface is a boring alga and/or fungi within the shell structure giving rise to a greenish hue to the shells. When these green shells were placed in NaOH for cleaning for a separate experiment, the green colouration leached out of the shells, possibly implying that the chlorophyll in the algae was being drawn out as the micro-algal cells were broken down. Due to the small size of the tubes it is unlikely that worms were the cause of the bore holes. It is likely that small microalgae caused the damage, alternatively, fungi are also known to bore into mollusc shells with boreholes roughly the same size as those observed here (Akpan & Farrow, 1984; Golubic *et al.*, 2005). It has also been recorded that both algal and fungal infestations can co-occur within a single shell (Akpan & Farrow, 1984). The response of the whelk to this infestation appears to be an increase in deposition of nacreous layer on the inner shell surface resulting on occasions in the formation of at least four separate nacreous layers. No reference to micro-algal or fungal infestations of whelk shells was found but the occurrence of boring algae in mollusc shells in U.K. coastal waters is well documented (e.g. intertidal limpets and littorinid gastropods - Wilkinson & Burrows, 1972; multiple infaunal bivalves such as *Venerupis spp.* - Akpan & Farrow, 1984). The microalga *Coccomyxa parasitica* bores into mussel *Mytilus edulis chilensis* shells from the Falkland Isles (Gray *et al.*, 1999) and a microalga causes extensive damage to the outer shell layer of limpet *Cellana toreuma* shells from the intertidal shore of Hong Kong (Richardson & Liu, 1994). Although not investigated, several whelk shells from Jersey also displayed green colouration to the exterior of the shells. Similar looking tubes, 'microtubules', were been reported by Böhm *et al.* (2016) in *Glycymeris glycymeris* shells and have been suggested to serve as a connection between the inner shell surface and the outer shell surface to act as structural 'crack arrestors'. They hypothesised that the micro-tubules were formed by specialised mantle cells etching channels through the shell layers as organic material was found to be coating the inside of the tubules. This organic material bears a striking resemblance to the possible organic material found within the bore holes of this study (Figure 3.13b). It is not discussed why the shells would need extra 'crack arrestors' as it is well documented that the layered and organised structure of mollusc carbonates can mitigate and 'arrest' damage (Kamat *et al.*, 2000; Kuhn-Spearing *et al.*, 1996). It is therefore unlikely that is the cause of the tubes in their case. A more likely explanation is that the shells in their study were infested with a similar boring organism which entered the pallial fluid of the external shell and bored their way through the structure.

Whilst the outer shell layers of Shetland whelks were extensively damaged by microalgae older whelk shells from Jersey ($\approx 30\%$ $> 50\text{mm}$ shell height) displayed boring sponge infestations. The

globally distributed boring sponge *Cliona celata* (Hayward & Ryland, 2000) is thought to be the only species of boring sponge in U.K. waters inhabiting calcified structures (Ackers *et al.*, 2007). The barbed spicules seen in the sponge boring into *B. undatum* shells in this study are different from the spicules of *Cliona celata* (see Ackers *et al.* 2007). It is therefore likely that the sponge that inhabits whelk shells from Jersey is not *Cliona celata* but another species or even genus of boring sponge that inhabits the warmer southern waters of the British Isles. The damage to the whelk shells caused by boring algae and boring sponges potentially poses a risk to the whelk populations that are infected through erosion and weakening of the shells and this could leave the shells weakened and potentially more susceptible to damage, either from direct impacts of fishing trawling or predatory attacks (see Mensink *et al.*, 2000).

3.4.3 Shell damage and repair

Whelks from all the populations studied had some form of shell damage (see Chapter 2) but until now the mechanism by which damage to the shells was repaired is unclear. Immediately following shell damage the shell begins to repair several millimetres back from the site of damage. Nucleation of the crystals takes place on the inner nacreous layer and a thin projection of shell with narrow outer prismatic layer and two crossed-lamellar layers is rapidly deposited but without an inner nacreous layer. With time the shell directly preceding the damage becomes thickened and likely contributes to a heavier and more protected shell in the area. Several millimetres of shell deposition occur beyond the damaged area before all 3 shell layers thicken to the pre-break shell thickness. Repairing a damaged juvenile shell did not occur as quickly following a second damage event. Colvin (2016) (unpublished Master of Marine Biology (MMBiol) dissertation) showed that juvenile whelks can repair shell damage quickly. For example during autumn (September to October) under ambient Menai Strait seawater temperatures, 2 year old whelks proficiently repaired an experimentally damaged 1 cm² area of shell in 2 weeks. The speed of shell repair is likely a response to protect themselves quickly from predator attacks. Currently the only published data on shell repair in *B. undatum*, is from Mensink *et al.* (2000) who timed the repair rates of adult whelks damaged by trawl fishing. No measurements were taken of the initial damage or of the actual rates of repair, damage was just classed as light or severe. Only the mortality rates and total growth were measured with all surviving animals repairing all damage within the 6 week experiment time. It is known from studies in Canada that whelks living in areas with large predatory crab populations have heavier shell weights than whelks from areas with low crab populations because they are repeatedly

repairing their predator-damaged shells (Thomas & Himmelman, 1988). Whelk shells damaged by trawled fishing gears (Mensink *et al.*, 2000) or riddling of the catch (See chapter 1) will similarly require repair. Thus with repeated anthropogenic and natural impact damage to whelk shells it is likely that their shells will be significantly heavier than undamaged shells of the same size. Future work should focus on developing an accurate damage assessment for *B. undatum* shells and applying this to heavily damaged and relatively undamaged populations to look for relationships between damage frequency and shell weight.

3.4.4 Shell mineralogy

Investigation using Micro-Raman spectroscopy of the shell of *B. undatum* revealed that the four shell layers are composed entirely of aragonite. For wavelengths between 135 and 750 cm^{-1} there was close agreement between the aragonite standard and the averaged sample spots in each of the 4 shell layers. Several of the reported Raman spectra peaks differed by 1-3 cm^{-1} compared with those published in the literature in both the aragonite standard and the shell layers (see Parker *et al.*, 2010). There are two possible reasons for this shift, firstly the Raman microscope may not have been correctly calibrated. Studies often use a material with easily identifiable Raman shifts such as Silicon to reduce the signal to noise ratio and compare data to published literature as opposed to standard materials (see Galante-Oliveira *et al.*, 2014). In this study, *in lieu* of a calibrant, standards of speleothem aragonite and synthetic calcite were used for direct comparison of Raman spectra. However it is highly unlikely that the Raman microscope was incorrectly calibrated as only the aragonite samples displayed a shift, importantly the calcite standard displayed all of the expected peaks. A second possible reason for the difference may be the presence of trace elements such as Mg^{2+} substituting for Ca^{2+} within the lattice and distorting it (Parker *et al.*, 2010). This could explain why the synthetic calcite standard exhibited all of the expected peaks whereas the sample spots and the speleothem aragonite standard (which can contain trace elements, Finch *et al.*, 2001) did not. The spectra across the entire sampled range gave an expected peak for both calcite and aragonite at 1085 cm^{-1} (see Wehrmeister *et al.*, 2010a & b). No vaterite was detected as there was no evidence of a triple peak between 1074 and 1091 cm^{-1} (see Wehrmeister *et al.*, 2010a & b). Variation in composition between layers became apparent when comparing the spectra between 1100 and 3100 cm^{-1} . The presence of peaks at 1015, ≈ 1130 , 1295 and ≈ 1500 cm^{-1} have been shown to be due to the presence of pigments in shell carbonate (Hedegaard *et al.*, 2006). Spectra between 1100-1150 cm^{-1} and 1500-1530 cm^{-1} represent the presence of single (C-C) and

double (C=C) Carbon to Carbon bonds respectively within pigments commonly seen within mollusc carbonates (Hedegaard *et al.*, 2006; Karampelas *et al.*, 2007 & 2009). Hedegaard *et al.* (2006) demonstrated two separate types of pigments were present in the calcium carbonate matrix of a range of mollusc shells, Polyenes and Carotenoids. The difference in position of the C-C and C=C bands in the Raman spectra allowed them to differentiate between the two pigment types (see Figure 3.19). From the Raman spectra shifts it appears that the prismatic and crossed-lamellar layers of *B. undatum* contain Polyene pigments. The difference between the crossed-lamellar layers and the prismatic layer is likely due to the presence of different polyene pigments (Hedegaard *et al.*, 2006).

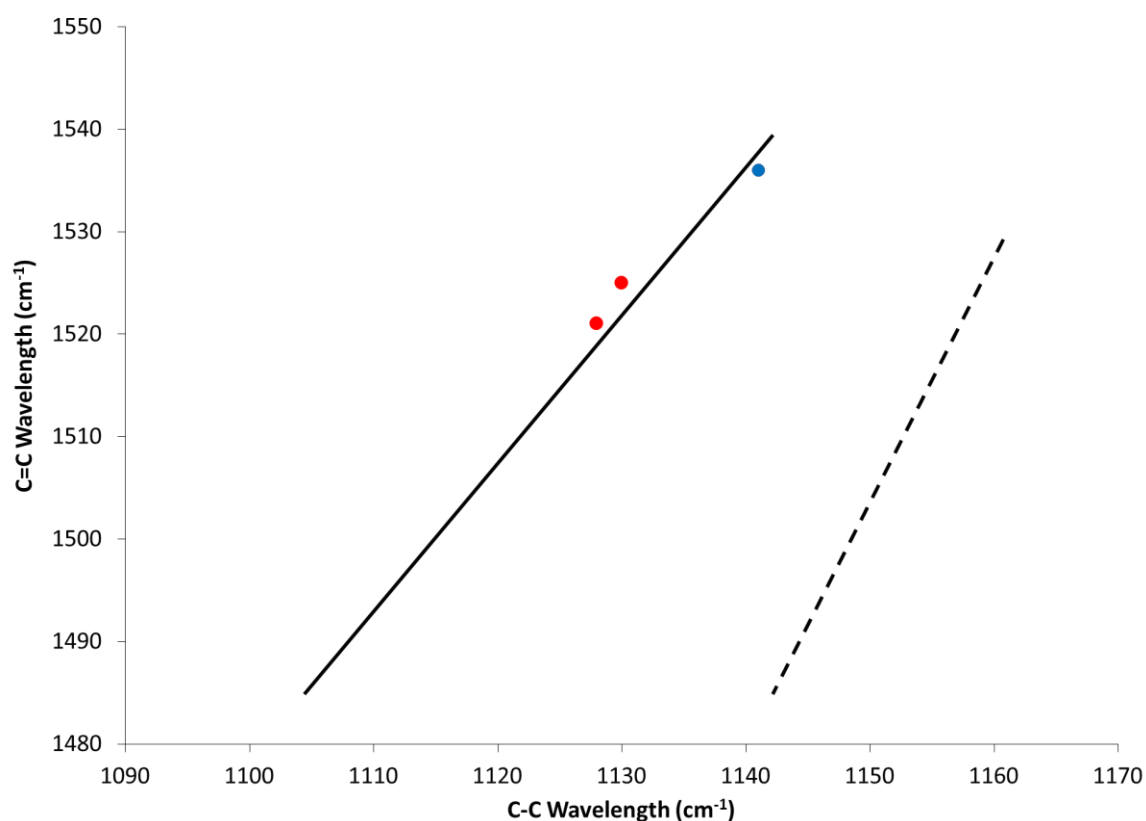


Figure 3.19. Scatter plot of the relationship between the wavelength positions of C-C and C=C Raman shifts for the shell layers of *Buccinum undatum*. The prismatic layer is represented by a blue symbol and the crossed-lamellar layers by red symbols. The lines represent lines of best fit taken from Hedegaard *et al.* (2006) for a range of standards of Polyene pigments (solid line) and Carotenoid pigments (dashed) line.

The nacreous shell layer does not show any of the characteristic peaks for Polyene pigments. The observed colouration of the prismatic and crossed-lamellar shell layers contrasts with the colourless nacreous layer. There are other coinciding peaks in the spectra between 200 and

3100, the spectra in this region are often representative of organic molecules (Dollish *et al.*, 1974; Socrates, 2001). This suggests that the compositions of the 3 uppermost shell layers are more similar to each other than to the nacreous layer. This is perhaps not surprising as the nacreous layer appears to be deposited at the shell margin at a later time than the outer layers. It is believed that the organic matrix controls the deposition of the shell crystals (Weiner & Traub, 1980; Mann *et al.*, 1989; Addadi & Weiner, 1997; Levi-Kalisman *et al.*, 2001) thus it is highly likely that the organic matrices found within the layers are different and in turn control the different crystal structures observed in the shell layers. It is speculated here that different combinations of lipids and proteins may be required to produce the different crystal matrixes seen between layers, resulting in the differing Raman spectra related to organic compounds (200-3100 cm^{-1}).

In conclusion, this chapter has detailed for the first time the microscopic and sub-crystalline structure of the shell of *Buccinum undatum* using standard microscopic study (light microscope and SEM) and cutting edge analytical tools such as Micro-Raman spectroscopy. The shell is wholly composed of aragonite and there are demonstrable differences in the structure and composition not only of the different visible shell layers, but also between the organic components within the shell layers. This initial study was undertaken to fully understand the shell structure before embarking on a geochemical analyses of the prismatic and crossed-lamellar layers that are laid down contemporaneously. Several structural problems were observed in the shells of the whelks collected from the Shetlands and Jersey that appear to have been caused by boring organisms such as fungi and microalgae that could potentially modify, through shell dissolution and remineralisation, the elemental composition of the shell layers. The structural damage inflicted by these organisms on the shells of whelks from Shetland and Jersey could render them more susceptible to predator attacks and impacts with fishing gear through weakening of the shell.

3.5 References

- Ackers RG, Moss D, Picton BE, Stone SMK, Morrow CC (2007) Sponges of the British Isles ('Sponge V'). Marine Conservation Society
- Addadi L, Berman A, Weiner S (1991) Intracrystalline proteins from a sea urchin and a mollusk: A comparison. In: Suga S, Nakahara H (eds.), Mechanisms and Phylogeny of Mineralization in Biological Systems, pp. 29–33, Springer- Verlag, Tokyo

- Addadi L, Weiner S (1997) Design Strategies in mineralized biological materials. *J Mater Chem* 7:689-702
- Addadi L, Joester D, Nudelman F, Weiner S (2006) Mollusk shell formation: a source of new concepts for understanding biomineralization processes. *Chemistry–Eur J* 12:980–87
- Akpan EB, Farrow GE (1984) Depth of deposition of Early Holocene raised sediments at Irvine deduced from algal borings in mollusc shells. *Scott J Geol* 20(2): 237-247
- Barthelat F (2010) Nacre from mollusk shells: a model for high-performance structural materials. *Bioinsp Biomim* 5(3):035001
- Barthelat F, Li CM, Comi C, Espinosa HD (2006) Mechanical properties of nacre constituents and their impact on mechanical performance. *J Mater Res* 21:1977–1986
- Barthelat F, Rim JE, Espinosa HD (2009) A Review on the Structure and Mechanical Properties of Mollusk Shells – Perspectives on Synthetic Biomimetic Materials. In: Bhushan B, Fuchs H (eds.) *Applied Scanning Probe Methods XIII, Biomimetics and Industrial Applications*. Springer, New York
- Beniash E, Aizenberg J, Addadi L, Weiner S (1997) Amorphous calcium carbonate transforms into calcite during sea urchin larval spicule growth. *Proc R Soc Lond B Biol Sci* 264:461-465
- Böhm CF, Demmert B, Harris J, Fey T (2016) Structural commonalities and deviations in the hierarchical organization of crossed-lamellar shells: A case study on the shell of the bivalve *Glycymeris glycymeris*. *J Mater Res* 31(5):536-546
- Bonucci E (2007) *Biological calcification. Normal and pathological processes in the early stages*. Springer-Verlag, Berlin, Germany
- Borchardt T (1985) Relationship between carbon and cadmium uptake in *Mytilus edulis*. *Mar Biol* 85:233-244
- Bouchet P, Rocroi JP, Frýda J, Hausdorf B, Ponder W, Valdés Á, Warén A (2005) Classification and nomenclator of gastropod families. *Malacologia* 47(1-2):1–397
- Bragg WL (1913) The structure of some crystals as indicated by their diffraction of X-rays. *Proc R Soc Lond A* 89:248–277
- Bragg WL (1924) The structure of aragonite. *Proc R Soc Lond A* 105:16–39
- Brinza L, Schofield PF, Mosselmans JFW, Donner E, Lombi E, Paterson D, Hodson ME (2014) Can earthworm-secreted calcium carbonate immobilise Zn in contaminated soils? *Soil Biol Biochem* 74:1-10
- Bušelić I, Peharda M, Reynolds DJ, Butler PG, González AR, Ezgeta-Balić D, Vilibić I, Grbec B, Hollyman P, Richardson CA (2015) *Glycymeris bimaculata* (Poli, 1795) — A new sclerochronological archive for the Mediterranean? *J Sea Res* 95:139-148
- Carlson WD (1983) The polymorphs of CaCO₃ and the aragonite-calcite transformation. *Rev Mineral Geochem* 11:191–225
- Carré M, Bentaleb I, Bruguier O, Ordinola E, Barrett NT, Fontugne M (2006) Calcification rate influence on trace element concentrations in aragonitic bivalve shells: evidences and mechanisms. *Geochim Cosmochim Acta* 70:4906-4920

- Cohen AL, McConnaughey TA (2003) Geochemical perspectives on coral mineralization. *Biom mineralization* 54:151–187
- Colvin CN (2016) Timing of Shell Growth and Repair in the Whelk *Buccinum undatum* under Experimental Conditions. Master of Marine Biology thesis, Bangor University
- Crenshaw MA (1980) Mechanisms of shell formation and dissolution. In: Rhoads DC, Lutz R (eds.) *Skeletal growth of aquatic organisms. Topics in geobiology*. Plenum, New York
- CrystalViewer 9.2.6. CrystalMaker® software (2015)
- Dauphin Y, Denis A (2000) Structure and composition of the aragonitic crossed lamellar layers in six species of Bivalvia and Gastropoda. *Comp Biochem Physiol A* 126:367–377
- Dillaman R, Hequembourg S, Gay M (2005) Early pattern of calcification in the dorsal carapace of the blur crab, *Callinectes sapidus*. *J Morphol* 263:356–374
- Dollish FR, Fateley WG, Bentley FF (1974) *Characteristic Raman frequencies of organic compounds*. John Wiley & Sons Ltd, New York
- Donner J, Nord AG (1986) Carbon and oxygen stable isotope values in shells of *Mytilus edulis* and *Modiolus modiolus* from Holocene raised beaches at the outer coast of the Varanger Peninsula, North Norway. *Palaeogeogr Palaeoclim Palaeoecol* 56:35–50
- Epstein S, Buchsbaum JR, Lowenstam HA, Ukey HC (1953) Revised carbonate-water isotopic temperature scale. *Bull Geol Soc Am* 64:1315–1326
- Essene EJ (1983) Solid solutions and solvi among metamorphic carbonates with applications to geologic thermobarometry. *Rev Mineral Geochem* 11:77–96
- Fan W, Li C, Li S, Feng Q, Xie L, Zhang R (2007) Cloning, characterization, and expression patterns of three sarco/endoplasmic reticulum Ca^{2+} -ATPase isoforms from pearl oyster (*Pinctada fucata*). *Acta Bioch Bioph Sin* 39:722–730
- Finch AA, Shaw PA, Weedon GP, Holmgren K (2001) Trace element variation in speleothem aragonite: potential for palaeoenvironmental reconstruction. *Earth and Planet Sci Lett* 186:255–267
- Fretter V, Graham A (1994) *British Prosobranch Molluscs*. The Ray Society, London
- Frisia S, Borsato A, Preto N, McDermott F (2003) Late Holocene annual growth in three Alpine stalagmite record the influence of solar activity and the North Atlantic Oscillation on winter climate. *Earth Planet Sci Lett* 216:411–424
- Furuhashi T, Schwarzhinger C, Miksik I, Smrz M, Beran A (2009) Molluscan shell evolution with review of shell calcification hypothesis. *Comp Biochem Physiol B* 154:351–71
- Galante-Oliveira S, Marçal R, Guimarães F, Soares J, Lopes JC, Machado J, Barroso CM (2014) Crystallinity and microchemistry of *Nassarius reticulatus* (Caenogastropoda) statoliths: towards their structure stability and homogeneity. *J Struct Biol* 186:292–301
- Gentry DK, Sosdian S, Grossman EL, Rosenthal Y, Hicks D, Lear CH (2008) Stable isotope and Sr/Ca profiles from the marine gastropod *Conus ermineus*: testing a multiproxy approach for inferring paleotemperature and Paleosalinity. *Palaios* 23:195–209

- Gillikin DP (2005) Geochemistry of marine bivalve shells: the potential for paleoenvironmental reconstructions. PhD Thesis, Vrije Universiteit Brussel, Belgium
- Gillikin DP, Dehairs F, Lorrain A, Steenmands D, Baeyens W, Andre L (2006) Barium uptake into the shells of the common mussel (*Mytilus edulis*) and the potential for estuarine paleo-chemistry reconstruction. *Geochim Cosmochim Acta* 70:395–407
- Gillikin DP, Lorrain A, Meng L, Dehairs F (2007) A large metabolic carbon contribution to the $\delta^{13}\text{C}$ record in marine aragonitic bivalve shells. *Geochim Cosmochim Acta* 71:2936–2946
- Gillikin DP, Lorrain A, Navez J, Taylor JW, André L, Keppens E, Baeyens W, Dehairs F (2005) Strong biological controls on Sr/Ca ratios in aragonitic marine bivalve shells. *Geochim Geophys Res* 10:Q05009
- Golubic S, Radtke G, Campion-Alsumard T (2005) Endolithic fungi in marine ecosystems. *Trends in Microbiology* 13(5):229-235
- Gong YUT, Killian CE, Olson IC, Appathurai NP, Amasino AL, Martin MC, Holt LJ, Wilt FH, Gilbert PUPA (2012) Phase transitions in biogenic amorphous calcium carbonate. *Proc Natl Acad Sci USA* 109(16):6088-6093
- Gray AP, Lucas IAN, Seed R, Richardson CA (1999) *Mytilus edulis chilensis* infested with *Coccomyxa parasitica* (Chlorococcales, Coccomyxaceae). *J Mollusc Stud* 65:289-294
- Grossman EL, Ku TL (1986) Oxygen and carbon isotope fractionation in biogenic aragonite: Temperature effects. *Chem Geol* 59:59-74
- Gutknecht J, Bisson MJ, Tosteson FC (1977) Diffusion of carbon dioxide through lipid bilayer membranes: effects of carbonic anhydrase, bicarbonate, and unstirred layers. *J Gen Physiol* 55:1–17
- Hagiwara S, Byerly L (1981) Calcium Channel. *Ann Rev Neurosci* 4:69-125
- Hawkes GP, Day RW, Wallace MW, Nugent KW, Bettiol AA, Jamieson DN, Williams MC (1996) Analyzing the growth and form of mollusc shell layers, in situ, by Cathodoluminescence and Raman spectroscopy. *J Shellfish Res* 3:659-666
- Hayward PJ, Ryland JS (2000) Handbook of the Marine Fauna of North-West Europe. Oxford University Press, Oxford.
- Hedegaard C, Bardeau J-F, Chateigner D (2006) Molluscan shell pigments: an in situ resonance Raman study. *J Molluscan Stud* 72:157–162
- Helgeson HC, Delany JM, Nesbitt HW, Bird DK (1978) Summary and critique of the thermodynamic properties of rock-forming minerals. *Am J Sci* 278A:1-229
- Hong M, Xu J, Teng HH (2016) Evolution of calcite growth morphology in the presence of magnesium: Implications for the dolomite problem. *Geochim Cosmochim Acta* 172:55-64.
- Jackson AP, Vincent JFV, Turner RM (1988) The mechanical design of nacre. *Proc R Soc Lond B Biol Sci* 234:415–440
- Kamat S, Su X, Ballarini R, Heuer AH (2000) Structural basis for the fracture toughness of the shell of the conch *Strombus gigas*. *Nature* 405:1036–1040

- Kaplan D (1998) Mollusc shell structures: Novel design strategies for synthetic materials. *Curr Opin Solid State Mater Sci* 3:232-236
- Karampelas S, Fritsch E, Mevellec J-Y, Gauthier J-P, Sklavounos S, Soldatos T (2007): Determination by Raman scattering of the nature of pigments in cultured freshwater pearls from the mollusk *Hyriopsis cumingi*. *J Raman Spectrosc* 38:217–230
- Karampelas S, Fritsch E, Mevellec J-Y, Sklavounos S, Soldatos T (2009) Role of polyenes in the coloration of cultured freshwater pearls. *Eur J Mineral* 21:85-97
- Klein RT, Lohman KC, Thayer CW (1996) Sr/Ca and $^{13}\text{C}/^{12}\text{C}$ ratios in skeletal calcite of *Mytilus trossulus*: covariation with metabolic rate, salinity and carbon isotopic composition of sea water. *Geochim Cosmochim Acta* 60:4207-4221
- Kuhn-Spearing LT, Kessler H, Chateau E, Ballarini R, Heuer AH, Spearing SM (1996) Fracture mechanisms of the *Strombus gigas* conch shell: implications for the design of brittle laminates. *J Mater Sci* 31:6583–6594
- Levi-Kalishman Y, Falini G, Addadi L, Weiner S (2001) Structure of the nacreous organic matrix of a bivalve mollusk shell examined in the hydrated state using cryo- TEM. *J Struct Biol* 135:8–17
- Lippmann F (1973) *Sedimentary Carbonate Minerals*. Springer-Verlag, New York.
- Lloyd DC, Zacherl DC, Walker S, Paradis G, Sheehy M, Warner RR (2008) Egg source, temperature and culture seawater affect elemental signatures in *Kelletia kelletii* larval statoliths. *Mar Ecol Prog Ser* 353:115–130
- Lowenstam HA, Abbott DP (1975) Vaterite: A mineralization product of hard tissues of a marine organism (Ascidacea). *Science* 188:363–365
- Mann S (1988) Molecular recognition in biomineralization. *Nature* 332:119–124
- Mann S, Webb J, Williams RJP (1989) *Biomineralization: Chemical and Biochemical Perspectives*. VCH, Weinheim
- McConnaughey TA (1988) Biomineralization mechanisms. In: Crick FC (ed.) *The Origin, Evolution, and Modern Aspects of Biomineralization in Animals and Plants*. Elsevier.
- McConnaughey TA (1989) ^{13}C and ^{18}O isotopic disequilibrium in biological carbonates: I Patterns *Geochim Cosmochim Acta* 53:151–162
- McConnaughey TA, Gillikin DP (2008) Carbon isotopes in mollusc shell carbonates. *Geo-Mar Lett* 28:287–99
- Meibom A, Cuif J-P, Hillion F, Constanz BR, Juliet-Leclerc Am Dauphin Y, Watanabe T, Dunbar RB (2004) Distribution of magnesium in coral skeleton. *Geophys Res Lett* 31:L23306
- Mensink BP, Fischer CV, Cadée GC, Fonds M, Ten Hallers-Tjabbes CC, Boon JP (2000) Shell damage and mortality in the common whelk *Buccinum undatum* caused by beam trawl fishery. *J Sea Res* 43:53-64
- Mineral Database. www.mindat.org (accessed 5/10/16)
- Miyamoto H, Miyashita T, Okushima M, Nakano S, Morita T, Matsushiro A (1996) A carbonic anhydrase from the nacreous layer in oyster pearls. *P Natl Acad Sci* 93(18):9657–9660

- Miyamoto M, Miyoshi F, Kohno J (2005) The Carbonic Anhydrase Domain Protein Nacrein is Expressed in the Epithelial Cells of the Mantle and Acts as a Negative Regulator in Calcification in the Mollusc *Pinctada fucata*. *Zool Sci* 22(3):311-315
- Mook WG (1971) Paleotemperatures and chlorinities from stable carbon and oxygen isotopes in shell carbonate: *Palaeogeogr Palaeoclimatol Palaeoecol* 9: 245-263
- Mook WG, Vogel JC (1968) Isotopic Equilibrium between Shells and Their Environment. *Science* 159:874-875
- Morse JW, Wang Q, Tsio MY (1997) Influences of temperature and Mg:Ca ratio on CaCO_3 precipitates from seawater. *Geology* 25(1):85-87
- Morse JW, Arvidson RS, Luttge A (2007) Calcium carbonate formation and dissolution. *Chem Rev* 107:342-381
- Mount AS, Wheeler AP, Paradkar RP, Snider D (2004) Hemocyte-mediated shell mineralization in the eastern oyster. *Science* 304:297-300
- Mucci A, Morse JW (1983) The incorporation of Mg^{2+} and Sr^{2+} into calcite overgrowths – influences of growth-rate and solution composition. *Geochim Cosmochim Acta* 47(2):217-233
- Neff JM (1972) Ultrastructure of the outer epithelium of the mantle in the clam *Mercenaria mercenaria* in relation to calcification of the shell. *Tiss Cell* 4:591600
- Nehrke G, Poigner H, Wilhelms-Dick D, Brey T, Abele D (2012) Coexistence of three calcium carbonate polymorphs in the shell of the Antarctic clam *Laternula elliptica*. *Geochem Geophys* 13:106
- Nudelman F, Chen HH, Goldberg HA, Weiner S, Addadi L (2007) Spiers memorial lecture: Lessons from biomineralization: comparing the growth strategies of mollusc shell prismatic and nacreous layers in *Atrina rigida*. *Faraday Discussions* 136:9-25
- Orr JC, Fabry VJ, Aumont O, Bopp L, Doney SC, Feely RA, Gnanadesikan A, Gruber N, Ishida A, Joos F, Key RM, Keith L, Maier-Reimer E, Matear R, Monfray P, Mouchet A, Najjar RG, Plattner G-K, Rodgers KB, Sabine CL, Sarmiento JL, Schlitzer R, Slater RD, Totterdell IJ, Weirig M-F, Yamanaka Y, Yool A (2005) Anthropogenic ocean acidification over the twenty-first century and its impact on calcifying organisms. *Nature* 437:681-686
- Owen R, Kennedy HA, Richardson CA (2002a) Experimental investigation into partitioning of stable isotopes between scallop (*Pecten maximus*) shell calcite and sea water. *Palaeogeogr Palaeoclimatol Palaeoecol* 185(1-2):163-174
- Owen R, Kennedy HA, Richardson CA (2002b) Isotopic partitioning between scallop shell calcite and sea water: effect of shell growth rate. *Geochim Cosmochim Acta* 66:1727-1737
- Paquette J, Reeder R J (1995) Relationship between surface structure, growth-mechanism, and trace-element incorporation in calcite. *Geochim Cosmochim Acta* 59(4):735-749
- Parker JE, Thompson SP, Lennie AR, Potter J, Tang CC (2010) A study of the aragonite-calcite transformation using Raman spectroscopy, synchrotron powder diffraction and scanning electron microscopy. *Cryst Eng Comm* 12:1590-1599

- Pokroy B, Zolotoyabko E (2003) Microstructure of natural plywood-like ceramics: a study by high-resolution electron microscopy and energy-variable X-ray diffraction. *J Mater Chem* 13:682-688
- Politi Y, Arad T, Klein E, Weiner S, Addadi L (2004) Sea urchin spine calcite forms via a transient amorphous calcium carbonate phase. *Science* 306:1161–1164
- Prendergast AL, Azzopardi M, O'Connell TC, Hunt C, Barker G, Stevens RE (2013) Oxygen isotopes from *Phorcus (Osilinus) turbinatus* shells as a proxy for sea surface temperature in the central Mediterranean: A case study from Malta. *Chem Geol* 354:77-86
- Raz S, Testiniere O, Hecker A, Weiner S, Luguet G (2002) Stable amorphous calcium carbonate is the main component of the calcium storage structures of the crustacean, *Orchestria cavimana*. *Biol Bull* 203:269–274
- Richardson CA, Liu JH (1994) Tidal microgrowth bands in the shell of the intertidal limpet *Cellana toreuma* (Reeve 1855) from the shores of Cape d'Aquilar, Hong Kong. In: Morton B (ed.), *Proceedings of the 3rd International Workshop on the Malacofauna of Hong Kong and southern China 1993* 445-465
- Rodriguez-Blanco JD, Shaw S, Benning LG (2011) The kinetics and mechanisms of amorphous calcium carbonate (ACC) crystallization to calcite, via vaterite. *Nanoscale* 3:265-271
- Ropp RC (2013) *Encyclopedia of the alkaline earth compounds*. Elsevier, Oxford, UK
- Ruppert EE, Fox RS, Barnes RD (2004) *Invertebrate Zoology: a functional evolutionary approach*. Thomson, Brooks/Cole, Belmont
- Sather WA, McCleskey EW (2003) Permeation and selectivity in calcium channels. *Annu Rev Physiol* 65:133–159
- Socrates G (2001) *Infrared and Raman Characteristic Group Frequencies: Tables and Charts*, 3rd Edition. John Wiley & Sons Ltd. Chichester, England
- Sosdian S, Gentry DK, Lear CH, Grossman EL, Hicks D, Rosenthal Y (2006) Strontium to calcium ratios in the marine gastropod *Conus ermineus*: growth rate effects and temperature calibration. *Geochem Geophys* 7(11):1525-2027
- Speer JA (1983) Crystal chemistry and phase relations of the orthorhombic carbonates. *Rev Mineral Geochem* 11:145–190
- Sun W, Jayaraman S, Chen W, Persson KA, Ceder G (2015) Nucleation of metastable aragonite CaCO₃ in seawater. *PNAS* 112(11):3199-3204
- Tanaka N, Monaghan M, Rye D (1986) Contribution of metabolic carbon to mollusc and barnacle shell carbonate. *Nature* 320:520–523
- Thomas MLH, Himmelman JH (1988) Influence of predation on shell morphology of *Buccinum undatum* L. on Atlantic coast of Canada. *J Exp Mar Biol Ecol* 115:221–236
- Wada K, Fujinuki T (1976) Biomineralization in bivalve molluscs with emphasis on the chemical composition of the extrapallial fluid. In: Bryan NM, Wilbur KM (eds.), *Mechanisms of Mineralization in the Invertebrates and Plants*. University of South Carolina Press, Georgetown
- Watabe N, Meenakshi VR, Blackwelder PL, Kurtz EM, Dunkelberger DG (1976) Calcareous spherules in the gastropod, *Pomacea paludosa*. In: Watabe N, Wilbur KM (eds.), *The Mechanisms of*

- Mineralization in the Invertebrates and Plants 283-308, Univ. of South Carolina Press, Columbia
- Watson EL, Vincenzi FF, Davis PW (1971) Ca^{2+} -activated membrane ATPase: selective inhibition by ruthenium red. *Biochim Biophys Acta* 249:606-610
- Wegst UGK, Ashby MF (2004) The mechanical efficiency of natural materials. *Philos Magazine* 84:2167–2181
- Wehrmeister U, Jacob DE, Soldati AL, Loges N, Häger T, Hofmeister W (2010b) Amorphous, nanocrystalline and crystalline calcium carbonates in biological materials. *J Raman Spectrosc* 42:926–935
- Wehrmeister U, Soldati AL, Jacob DE, Häger T, Hofmeister W (2010a) Raman spectroscopy of synthetic, geological and biological vaterite: a Raman spectroscopic study. *J Raman Spectrosc* 41:193–201
- Weiner S, Traub W (1980) X-ray diffraction study of the insoluble organic matrix of mollusk shells. *FEBS Lett* 111:311–316
- Weiner S, Traub W (1984) Macromolecules in mollusc shells and their function in biomineralization. *Phil Trans R Soc London* 304B:425–434
- Wheeler AP (1992) Mechanisms of molluscan shell formation. In: Bonucci E (ed.) *Calcification in biological systems*. CRC Press, Boca Raton
- Wilbur KM, Saleuddin AS (1983) Shell formation. In: Wilbur KM (ed.) *The Mollusca - physiology*. Vol. 4. Academic Press, New York
- Wilkinson M, Burrows EM (1972) The distribution of marine shell-boring green algae (1972) *J Mar Biol Ass UK* 52:59-65
- Wilt FH (2005) Developmental biology meets materials science: Morphogenesis of biomineralized structures. *Dev Biol* 280:15-25
- Zhao L, Schöne BR, Mertz-Kraus R (2016) Delineating the role of calcium in shell formation and elemental composition of *Corbicula fluminea* (Bivalvia). *Hydrobiologia* 790:259–272

Chapter 4:

Growth rate and environmental reconstructions from shells of *Buccinum undatum* using stable isotopes and trace elements.

4.1 Introduction

There are many ways to reconstruct life history events and some environmental histories using different hard parts of molluscan specimens such as statoliths (squid–Arkhipkin, 2004; gastropods– Galante–Oliveira *et al.*, 2015), opercula (Vasconlecos *et al.*, 2012; Bökenhans *et al.*, 2016) and beaks (Cherel & Hobson, 2005). However, the molluscan shell is the most used and reliable tool from palaeontological to modern specimens (e.g. Latal *et al.*, 2004; Prendergast *et al.*, 2013; Prendergast *et al.*, 2015). The value of mollusc shells as environmental monitors is well known (see Richardson, 2001 for review). Environmental and physiological information can be reconstructed through the use of stable isotopes of major elements such as oxygen and carbon and the relative values of trace elements such as strontium and magnesium.

4.1.1 The use of oxygen and carbon isotopes in mollusc shells

The use of oxygen isotope compositions from mollusc shells for reconstructing past seawater temperature (also known as palaeothermometry or stable isotope thermometry) is a common and widely used technique in the field of sclerochronology in both bivalve and gastropod shells (Leng & Lewis, 2016) and in molluscan palaeontology and palaeoecology (Latal *et al.*, 2004). Isotopes are atoms of the same element with the same atomic number and the same number of electrons and protons, but different numbers of neutrons giving them different atomic mass. Because of their differences in mass, isotopes of a single element have slightly different chemical and physical properties. These differences cause fractionation (change in relative abundances of isotopes) under certain conditions. For stable oxygen isotopes (^{16}O & ^{18}O) in water there are two main factors which combine to control the changes in isotopic composition, equilibrium and kinetic fractionation (Kendall & McDonnell, 1998; Krumbiegel, 2012). Equilibrium fractionation occurs in a closed system as isotopes are exchanged between two substances, as that system moves from one equilibrium state to another after perturbation (such as by a change in temperature). During chemical/thermodynamic equilibrium the lowest energy state of a system is reached and results in the heavier isotopes being distributed to the substance or compound which is most stably bound (Kendall & McDonnell, 1998). As an example, at 100% air humidity within a closed system, air can be in chemical and isotopic equilibrium with a water body. As a liquid, water is more stable than water vapour so more of the heavier ^{18}O will be distributed within the water body as opposed to the water vapour in the air (Kendall & McDonnell, 1998). Likewise, water molecules in vapour containing ^{18}O are more

likely to condense first with decreases in air temperature (Kendall & McDonnell, 1998). Kinetic isotope fractionation can occur when different amounts of energy are required to break bonds that hold molecules together. As molecules composed of heavier isotopes require more energy to break apart, lighter ^{16}O is preferentially evaporated from a water body with increases in temperature as less energy is required to separate the water molecules containing ^{16}O , this leaves ^{18}O enriched water behind. The combination of these types of fractionation causes changes in the isotopic signature of the water, not only through direct evaporation but also through the influx of fresh water from precipitation (which is generally enriched in lighter ^{16}O following evaporation, Figure 4.1). The mixing of two water masses with different oxygen isotopic compositions can also change the isotopic composition of seawater (McKenna *et al.*, 2016; Rohling, 2013). Due to the depletion of ^{18}O in freshwater inputs, there is often also a strong relationship between the salinity of a water mass and its isotopic composition. This may allow the prediction of water isotope values using salinity alone when the relationship between the two is known; this is determined using a salinity mixing line equation for a particular site (e.g. MacLachlan *et al.*, 2007; Cage & Austin, 2010).

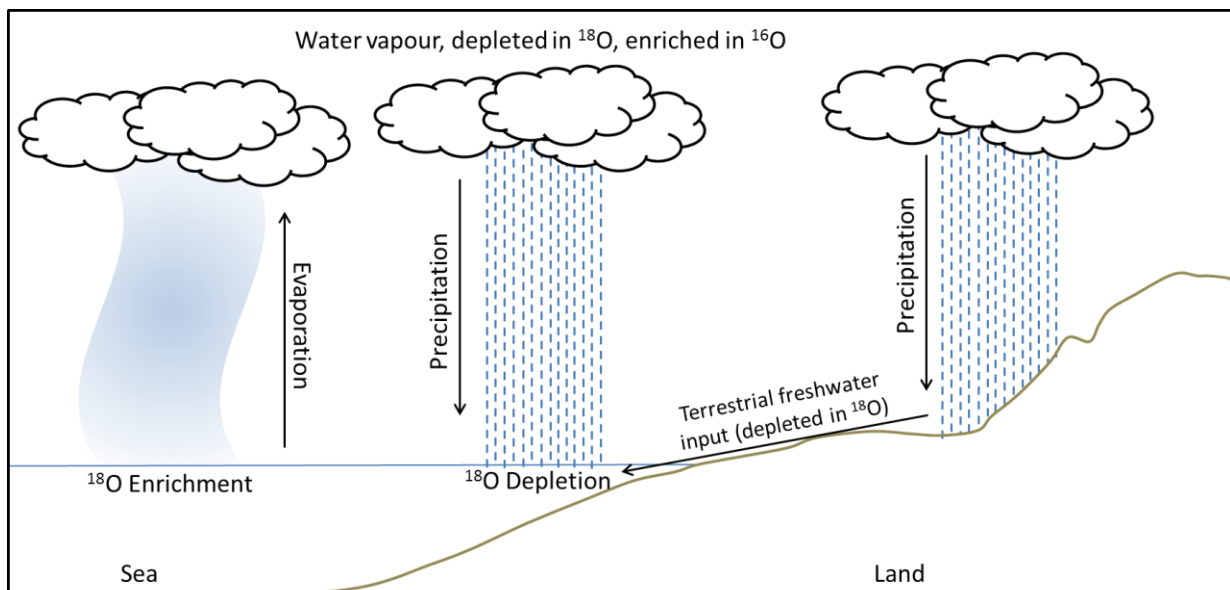


Figure 4.1. The processes of ^{18}O enrichment and depletion in seawater (Adapted from Rohling, 2013).

The incorporation of stable isotopes during the formation of mollusc shell carbonates is also under the influence of fractionation, much like seawater. Both equilibrium and kinetic fractionation control the incorporation of stable isotopes during calcification, both of which are in turn controlled by temperature. This combination of controls gives rise to an annual cycle in the oxygen isotope composition within shell carbonates observed repeatedly over more than 60 years (Epstein *et al.*, 1953; Grossman & Ku, 1986; Colonese *et al.*, 2017). Due to the predictable

relationship between the isotopic value of the water, isotope fractionation during calcification and water temperature, the water temperature at the time of shell mineralisation can be calculated from the isotopic composition of the shell carbonate. This is often measured using a technique called Isotope Ratio Mass Spectrometry (IRMS).

IRMS is used to determine the abundances of the common isotopes of target elements. The resulting ratios between isotopes are frequently expressed as delta values (δ) which represent per mille (mil) (‰, parts per thousand) deviations from internationally recognised standards. For palaeoclimate reconstructions, the reference carbonate standard used currently is Vienna Pee Dee Belemnite (VPDB; International Atomic Energy Agency (IAEA), 1993) and for water samples it is Vienna Standard Mean Ocean Water 2 (VSMOW2) and Standard Light Antarctic Precipitation 2 water (SLAP2; IAEA, 2009). VPDB and VSMOW2 represent newer versions of standards used in early isotope work which have since been depleted (PDB & SMOW). As these newer standards were calibrated to be identical to the originals, data resulting from their usage is directly comparable with data calibrated against PDB and SMOW (Leng & Lewis, 2016). The calculation used to determine the δ value for each samples is as follows:

$$(\text{‰}) = (\text{isotope ratio in sample} / \text{isotope ratio in standard} - 1) * 1000$$

Once the $\delta^{18}\text{O}$ of a shell carbonate sample has been determined, the seawater temperature at the time of formation can be retroactively calculated using a palaeotemperature equation. For calcium carbonate, the relationship between shell $\delta^{18}\text{O}$ ($\delta^{18}\text{O}_{\text{shell}}$) and seawater temperature was first established by Epstein *et al.* (1953) and modified into the first palaeotemperature equation by Craig (1965):

$$t(^{\circ}\text{C}) = 16.5 - 4.2 * (\delta^{18}\text{O}_{\text{shell}} - \delta^{18}\text{O}_{\text{water}}) + 0.13 * (\delta^{18}\text{O}_{\text{shell}} - \delta^{18}\text{O}_{\text{water}})^2$$

Where t is seawater temperature, $\delta^{18}\text{O}_{\text{shell}}$ and $\delta^{18}\text{O}_{\text{water}}$ represent the isotopic ratios of the carbonate and water samples respectively. The values of 16.5 and -4.2 represent the intercept and slope respectively of the linear relationship between seawater temperature and $\delta^{18}\text{O}_{\text{shell}} - \delta^{18}\text{O}_{\text{water}}$. This original equation was calibrated using a mix of aragonitic and calcitic marine shells over a wide range of temperatures. In the years since this initial equation was produced, many studies have found that an amendment to the equation has been necessary to account for differences in fractionation factors between calcite and aragonite (Leng & Lewis, 2016). Well known examples of this were produced by Kim & O'Neil, (1997) for laboratory precipitated

calcite (later established as an equation by Leng & Marshall, 2004; L&M reorganisation of K&ON):

$$t(^{\circ}\text{C}) = 13.85 - 4.58 * (\delta^{18}\text{O}_{\text{shell}} - \delta^{18}\text{O}_{\text{water}}) + 0.08 * (\delta^{18}\text{O}_{\text{shell}} - \delta^{18}\text{O}_{\text{water}})^2$$

And by Grossman & Ku, (1986) for aragonitic mollusc shells:

$$t(^{\circ}\text{C}) = 20.6 - 4.34 * (\delta^{18}\text{O}_{\text{shell}} - (\delta^{18}\text{O}_{\text{water}} - 0.27))$$

These two equations are commonly used in studies investigating biogenic calcite and aragonite respectively (Leng & Lewis, 2016). Even though these equations are widely used, species specific palaeotemperature equations are calibrated for more accurate reconstructions (Bemis *et al.*, 2002; Wejnert *et al.*, 2013). An example of a species specific palaeotemperature equation from mollusc shell material was calculated by Wanamaker *et al.* (2007) for the blue mussel (*Mytilus edulis*), whilst the calibrated equation was novel, it was shown to be insignificantly different to the calculations of Kim and O'Neil (1997).

Carbon isotope ratios of mollusc shells ($\delta^{13}\text{C}_{\text{shell}}$) are analysed concurrently with oxygen isotope ratios during IRMS of shell carbonates and also have the potential to be important recorders of environmental conditions. As previously discussed in chapter 3, $\delta^{13}\text{C}_{\text{shell}}$ has been shown to be strongly linked to dissolved inorganic carbon in the water column and therefore it can be a proxy for ocean productivity (Mook & Vogel, 1968; Mook, 1971; Donner & Nord, 1986; Goodwin *et al.*, 2013). However, the interpretation of $\delta^{13}\text{C}_{\text{shell}}$ is often confounded, as internal sources of C (from respiration and digestion) can be included during shell calcification, resulting in mixed signals (Figure 4.2; Borchardt, 1985; Tanaka *et al.*, 1986; Klein *et al.*, 1996; Gillikin *et al.*, 2006 & 2007). The incorporation of internally generated sources of carbon was shown in the rapidly mineralising scallop (*Pecten maximus*) shell which appeared to be incorporating metabolic CO_2 into the shell matrix (Figure 4.2; Owen *et al.*, 2002a & b).

The heavier isotopes of both oxygen and carbon (^{18}O & ^{13}C) can also be discriminated against during growth due to kinetic fractionation in which lighter isotopes are preferentially included during the formation of mineralising calcium carbonate (CaCO_3 ; McConnaughey, 1988). This is seen during periods of fast shell deposition and growth, which can potentially make the interpretation of $\delta^{13}\text{C}$ and $\delta^{18}\text{O}_{\text{shell}}$ difficult (McConnaughey, 1988). Even though there are acknowledged potential issues with the use of $\delta^{13}\text{C}$ and $\delta^{18}\text{O}_{\text{shell}}$, they remain a widely used tool in the field of sclerochronology (Carré *et al.*, 2006; Mettam *et al.*, 2014; Colonese *et al.*, 2017).

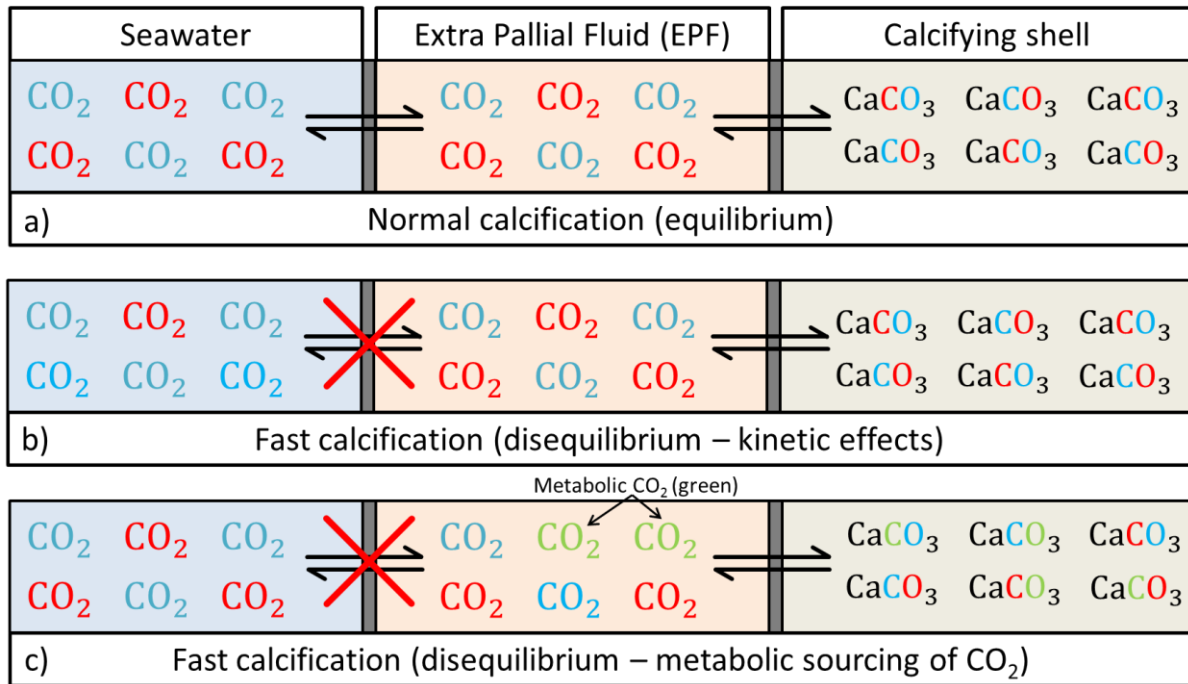


Figure 4.2. A simplified diagrammatic representation of isotopic incorporation into molluscan shell carbonate of isotopically light (blue) and isotopically heavy (red) CO₂. a) normal calcification with representative levels of C and O found in the EPF and shell matrix as equilibrium between seawater and the EPF is reached. b) shows what can happen under fast calcification conditions, ratios of C and O in the seawater are not represented in the shell as it is growing too fast for the EPF and seawater to re-equilibrate. c) a similar fast calcification situation to b), however, in this case metabolic CO₂ (green) is incorporated as the EPF and seawater do not equilibrate fast enough causing a deficit of CO₂ which is supplemented by metabolically sourced CO₂.

4.1.2 The use of trace elements as environmental proxies

Similar to the use of oxygen isotopes in the shell to reconstruct past seawater temperatures, trace elements within the shell matrix have been studied extensively as proxies for reconstructing past environmental conditions. Several elements have been targeted for various types of reconstruction within marine mollusc shells, such as seawater temperature (e.g. strontium – Zhao *et al.*, 2017a; magnesium – Freitas *et al.*, 2005), salinity (e.g. barium – Poulain *et al.*, 2015; sodium – Findlater *et al.*, 2014), pollution events (e.g. lead – Bourgoin, 1990; Richardson *et al.*, 2001; Krause-Nehring *et al.*, 2012; cadmium & chromium – Moloukhia & Sleem, 2011; complex elements – McClintock *et al.*, 2014) and productivity (e.g. barium – Elliot *et al.*, 2009; Goodwin *et al.*, 2013). The efficacy of many trace element proxies is heavily contested with large discrepancies being seen between species, polymorphs of CaCO₃ and even intra-specific reliability (Klein *et al.*, 1996; Gillikin *et al.*, 2006).

It is likely that trace elements use the same pathways discussed in Chapter 3 to enter the Extra Pallial Fluid (EPF) and be incorporated into the mineralising CaCO₃ lattice as substitutes for Ca²⁺

(Zhao *et al.*, 2016). Trace element incorporation may occur within the crystal matrix in two main ways:

- 1) Divalent ions of trace elements (with the same 2+ charge as Ca^{2+}) of similar size (ionic radius) are substituted for Ca^{2+} within the CaCO_3 crystals during precipitation (Speer, 1983)
- 2) Trace elements are incorporated into the organic matrix (Schöne *et al.*, 2010)

The first method of incorporation requires the trace metal ions to have similar electrochemical properties to Ca^{2+} such as being divalent ($^{2+}$) and with a similar ionic radius. Trace metal ions of a different charge but similar ionic radius may be included but this requires incorporation of other non-divalent species to retain the charge balance, i.e. addition of one Fe^{3+} ion can be balanced by incorporation of singly charge Na^+ or K^+ . The second method of incorporation may potentially make the interpretation of trace elements (if they are organically bound) more difficult as the concentrations of trace elements will increase in areas of the shell with increased organic matter such as growth lines (Schöne *et al.*, 2010).

4.1.2.1 Strontium and magnesium

The two most widely studied trace elements in biogenic carbonates are strontium (Sr) and magnesium (Mg) (Schöne *et al.*, 2010). As concentrations of Mg and Sr in seawater are fairly constant over time (Broecker & Peng, 1982; Kastner, 1999), it is thought that they are incorporated into the CaCO_3 lattice at equilibrium and therefore any changes in the ratio of Sr–Ca ratios (Sr/Ca) and Mg–Ca ratios (Mg/Ca) reflect a change in seawater temperature which controls the calcification equilibrium. Trace element abundance in carbonates is always presented as a ratio to Ca as the concentration of Ca in a CaCO_3 matrix is fairly constant, giving a universal baseline for comparison between structures. Ions with a smaller ionic radius to Ca^{2+} such as Mg^{2+} appear to be more readily incorporated into the rhombohedral crystal structure of calcite, whereas ions with a larger ionic radius than Ca^{2+} such as Sr^{2+} appear to be more readily incorporated into the orthorhombic crystal structure of aragonite (Speer, 1983; Schöne *et al.*, 2010). This can often result in aragonite containing several orders of magnitude more Sr than calcite (Dietzel *et al.*, 2004; Schöne *et al.*, 2010), although Sr and Mg concentrations in both calcite and aragonite may still reflect seawater temperature. It has been shown that in abiogenic aragonite Sr/Ca and Mg/Ca have a negative relationship to seawater temperature (i.e. with increasing temperature the concentration of Sr and Mg decreases) (Kinsman & Holland, 1969;

Gaetani & Cohen, 2006); the opposite of this is seen in abiogenic calcite (Katz, 1973; Mucci, 1987). With this knowledge it should be expected that the concentrations of Sr and Mg within a biogenic carbonate should also reflect seawater temperature at the time of mineralisation, provided that they are incorporated at equilibrium.

The use of strontium as a proxy for seawater temperature has been shown to be reliable in several species groups, however, the relationship between seawater temperature and Sr differs within the literature. The relationship has been shown to be negative in several species groups with aragonitic structures such as freshwater bivalves (Zhao *et al.*, 2016), marine bivalves (Dodd, 1965; Schöne *et al.*, 2011; Yan *et al.*, 2013), sclerosponges (Rosenheim *et al.*, 2005) and corals (Beck, *et al.*, 1992; Chen *et al.*, 2013). In biogenic calcite, Sr/Ca is often found to display a positive relationship with temperature, a relationship which is often exploited in temperature reconstructions from calcitic foraminiferal tests (Martin *et al.*, 1999; Andreasen & Delaney, 2000; Elderfield *et al.*, 2002). An experiment by Dodd (1965), neatly showed the calcite prismatic layer and aragonitic nacreous layer in *Mytilus californianus* and *M. edulis* shells to have negatively correlated Sr/Ca profiles. The aragonite layer was negatively correlated to seawater temperature and the calcite layer positively correlated. However, this pattern of Sr/Ca is not always seen in nature, it has also been shown to have the opposite relationship with temperature in aragonitic shells of marine gastropods such as *Conus ermenius* where it has been shown to be positively correlated (Sosdian *et al.*, 2006; Gentry *et al.*, 2008). Magnesium has also been shown to reflect seawater temperature in several species groups such as marine bivalves (Dodd, 1965; Freitas *et al.*, 2005—during early ontogeny), and corals (Mitsuguchi *et al.*, 1996; Sinclair *et al.*, 1998; Fallon *et al.*, 1999). Synthesising this evidence suggests that a species specific ‘calibration’ between trace element content and temperature would normally be required (e.g. Sosdian *et al.*, 2006).

4.1.2.2 ‘Vital’ effects

For marine molluscs in particular, strong relationships (positive or negative) between Sr/Ca, Mg/Ca ratios and seawater temperature are not always found, with concentrations of Sr and Mg within shells sometimes differing from predicted values calculated from the concentrations of Sr and Mg in the water (assuming chemical equilibrium during formation) (Buchardt & Fritz, 1978; Palacios *et al.*, 1994). This has caused a debate over the reliability of trace element proxies within mollusc shells (Gillikin *et al.*, 2006). These issues are thought to arise from biological

control over the calcification process also known as ‘vital’ effects (e.g. Klein *et al.*, 1996; Purton *et al.*, 1999; Gillikin *et al.*, 2005). As an example, it has been suggested that the relationships often seen between Sr/Ca and seawater temperature are in fact related to growth rate, which is often controlled by temperature but liable to change with ontogeny i.e. a vital effect, e.g. *Saxidomus giganteus* (Gillikin *et al.*, 2006) and *Conus ermenius* (Sosdian *et al.*, 2006). However, a relationship with growth rate is not always found in cases where there is a poor correlation between Sr/Ca and seawater temperature (e.g. *Mercenaria mercenaria* - Gillikin *et al.*, 2006 and *Arctica islandica* - Foster *et al.*, 2009). In these cases the profiles in trace elements are often ascribed to a range of metabolic factors i.e. vital effects (e.g. Schöne *et al.*, 2011; Hahn *et al.*, 2012). Intra-specific differences in the abundance of trace elements within a single species from the same site are frequently observed (e.g. Klein *et al.*, 1996), further confounding the use of trace elements in mollusc shells. The potential extent of vital effects was shown by Dick *et al.* (2007) who found no correlation in the shells of *Laternula elliptica*, between the element/Ca ratios and the concentrations of the elements in the surrounding seawater or sediment, implying a tight biological control over their incorporation into the mineralising shell of the species.

Other widely studied trace element proxies in bivalve shells include barium (Ba), lithium (Li), manganese (Mn) and to a lesser extent iron (Fe), uranium (U) and sodium (Na).

4.1.2.3 Barium

Ba/Ca profiles often have a low background concentration punctuated with characteristic spikes (Gillikin *et al.*, 2008). The true cause of Ba/Ca variation within mollusc carbonates is a debated topic with several main theories including:

- 1) Background Ba is a proxy for salinity (e.g. Poulain *et al.*, 2015–*Ruditapes philippinarum*)
- 2) Ba spikes are a proxy for productivity (e.g. Elliot *et al.*, 2009–*Tridacna gigas*; Thébault *et al.*, 2009a–*Comptopallium radula*; Goodwin *et al.*, 2013–*Crassostrea gigas*)
- 3) Ba spikes are a proxy for barite ingestion from phytoplankton flocs with the background being a proxy for ambient Ba/Ca in the water column (Gillikin *et al.*, 2006–*Mytilus edulis*)

It is clear that there are many possible causes for the variation of Ba within bivalve shells. Gillikin *et al.* (2008) concluded that the cause of spikes in Ba/Ca profiles is likely due to some as yet undescribed environmental forcing, following the discovery of synchronous Ba peaks in several

Saxidomus giganteus from the same site which could not be matched to any environmental perturbations.

4.1.2.4 Lithium

The incorporation of Li into the shells of several bivalves has been shown to have a weak correlation with seawater temperature and strong correlation with growth rate (Thébault *et al.*, 2009b – *Arctica islandica*; Thébault & Chauvaud, 2013 – *Pecten maximus*). It has also been postulated that Li/Ca correlates with phytoplankton blooms in *Pecten maximus* (Thébault & Chauvaud, 2013). Interestingly, it has shown promise as a palaeotemperature proxy when Sr is used in place of Ca for the elemental ratio (i.e. Sr/Li instead of Sr/Ca), seemingly overcoming the influence of vital effects in animals grown in brackish environments (Füllenbach *et al.*, 2015 – *Cerastoderma edule*).

4.1.2.5 Manganese and iron

Whilst there is a paucity of research regarding the incorporation of Fe into mollusc shells, in the shells of the long lived bivalve *Arctica islandica*, Fe was shown to decrease with ontogeny (Holland, *et al.*, 2014). This was attributed to the shells recording a decrease in bioavailable iron over time as land use changed resulting in a reduction of iron rich fertilizer run off (Holland, *et al.*, 2014). It is likely that trace elements such as Fe and Mn are introduced into the sediments and pore waters in marine environments through the breakdown of organic matter and sulphides in redox reactions (Pinto & Rivera, 2003; Lourino–Cabana *et al.*, 2014). With seasonal variations in the downflux of organic matter (i.e. plankton blooms) it is possible that these events may be recorded in the shells of molluscs in the same environment as Fe^{2+} and Mn^{2+} are released during redox reactions which take place during the decomposition of phytoplankton blooms (Pinto & Rivera, 2003). The controlling factors behind Mn incorporation into mollusc shells are also little understood. Freitas *et al.* (2006) suggested a cyclicity to Mn/Ca in the shells of *Pecten maximum*, controlled by Mn^{2+} concentrations in the seawater. However, later work on the mussel *Mytilus edulis* showed no such correlation with either particulate Mn or dissolved Mn^{2+} in the water column (Freitas *et al.*, 2016).

4.1.2.6 Uranium

Uranium has also been found in the shells of some mollusc species, however this is often within the context of its use as a dating tool in fossil shells, for which the concentration of uranium present is thought to be an indicator of diagenesis (Kaufman *et al.*, 1996; McLaren & Rowe, 1996; Labonne & Hillaire-Marcel, 2000). Studies on U in modern molluscs have related it to pollution in both marine and freshwater settings and granite weathering in the marine environment (Price & Pearce, 1997; Markich *et al.*, 2002). A more recent study by Gillikin and Dehairs (2013), aimed to relate U in the shells of *Saxidomus giganteus* to ocean pH, as it is found to correlate in deepwater corals (Shen & Dunbar, 1995; Anagnostou *et al.*, 2011). In shallow water corals, it is also shown to be strongly temperature controlled (Min *et al.*, 1995; Shen & Dunbar, 1995). They found no correlation with temperature or pH, however there was a decrease in U/Ca with ontogeny, they concluded from this that the presence of U was an early indicator of shell diagenesis.

4.1.2.7 Sodium

Unlike most of the other trace elements already discussed, the ionic form of Na most commonly found within seawater is monovalent Na^+ , which differs in charge from the divalent Ca^{2+} . The incorporation of Na into the CaCO_3 matrix must therefore somehow overcome this difference in charge. Even so, the concentration of Na^+ in the EPF has been shown to directly relate to the amount of Na within the shell matrix in *Mytilus edulis* (Lorens & Bender, 1980). The presence of Na in mollusc shells is often related to salinity (Pilkey & Harriss, 1966; Gordon *et al.*, 1970), with concentrations >2000 ppm often attributed to marine environments (Findlater *et al.*, 2014). In support of this theory, strong relationships between Na/Ca and road salting events have been found in the freshwater bivalve *Elliptio complanata* (O'Neil & Gillikin, 2014). It has also been suggested that Na/Ca may be under physiological control as variation is seen in historical samples between mollusc species from the same environments (Land & Hoops, 1973). In more recent publications, the importance of Na^+ in mitigating the effects of ocean acidification have been explored. The Na^+/H^+ membrane pump found within the mantle (which has been shown to play an important role in maintaining the correct pH within the EPF for calcification to occur (Li *et al.*, 2016)), was suggested by Zhao *et al.* (2017b) to increase Na^+ in the EPF and therefore Na/Ca with decreasing pH in the shells of *Mytilus edulis*. However, this pattern was not replicated in the shells of the scallop *Patinopecten yessoensis*.

It is clear that the use of trace elements as environmental proxies in mollusc shells is frequently beset with issues, especially vital effects influencing trace element incorporation (e.g. Dick *et al.*, 2007). However, with proper validation, they remain a potentially powerful tool in historical environmental reconstructions. The primary aim of this study was to investigate the potential use of *Buccinum undatum* shells as recorders of environmental change using stable isotope and trace element analysis of shells from several locations. *B. undatum* are often found in archaeological samples from the Mesolithic to recent centuries (Mannino & Thomas, 2001; Campbell, 2011; Campbell & Russell, 2014); the ability to reconstruct past environmental conditions from their shells could be greatly beneficial in the field of archaeology. The chemical analysis of *B. undatum* shells has only been undertaken once before by Santarelli and Gros, (1985) who reconstructed $\delta^{18}\text{O}_{\text{shell}}$ profiles from the shells of *B. undatum* from the English Channel. This was undertaken with the sole intention of ascribing an age to the samples by counting the number of annual cycles in the $\delta^{18}\text{O}_{\text{shell}}$ profiles, no further investigation has been done in this area. Based on the findings of Santarelli and Gros, it was hypothesised that shell $\delta^{18}\text{O}$ would reflect seawater temperatures at the time of calcification.

A secondary aim of the work was to use the reconstructed $\delta^{18}\text{O}_{\text{shell}}$ profiles to accurately age several individual specimens of *B. undatum* from geographically distinct sites. Through the use of a set sampling resolution, the aim was to determine the season of maximum growth for this species at each site; it was hypothesised that whelks would grow fastest during the warmest period of the year. This type of information could be essential for fisheries scientists attempting to determine population dynamics and potentially calculate the most appropriate closed seasons for the fishery as a management strategy.

4.2 Materials and Methods

4.2.1 Shell drill sampling

Due to the spiral nature of a *Buccinum undatum* shell, standard analytical techniques usually used for trace element analysis in mollusc shells, such as Laser Ablation–Inductively Coupled Plasma–Mass Spectrometry (LA–ICP–MS) (e.g. Schöne *et al.*, 2010), were unsuitable as a single complete growth axis could not be obtained via embedding and sectioning the shell. For this reason, solution Inductively Coupled Plasma–Mass Spectrometry (Solution ICP–MS) was used to

determine trace element concentrations along the growth axis of each sampled shell. Alongside this, Isotope Ratio Mass Spectrometry (IRMS) was undertaken to sample $\delta^{18}\text{O}_{\text{shell}}$, $\delta^{13}\text{C}_{\text{shell}}$ to determine the number of seasonal seawater temperature cycles. In a pilot study $\delta^{18}\text{O}_{\text{shell}}$, $\delta^{13}\text{C}_{\text{shell}}$ and trace element concentrations were analysed from the shell of an adult female whelk (75 mm) from the Menai Strait. The results obtained raised minor concerns about potential vital effects on the trace element signatures. During the reproductive cycle female whelks have a much higher energetic input during mating and egg laying (Brokordt *et al.*, 2003) and several trace element concentrations within the shell may therefore reflect vital effect controls on their incorporation. Following the pilot study, shells from a further two adult female whelks (78.5 & 81.5 mm) from the Menai Strait were analysed to investigate the observed possible vital effects in females. Since male whelks have a lower energetic input during the mating and breeding season (Brokordt *et al.*, 2003) shells of male whelks were similarly investigated to see if the trace element profiles within their shells displayed any clear sign of vital effects. The $\delta^{18}\text{O}_{\text{shell}}$ profiles were also constructed to determine the number of seawater temperature cycles. Overall, the shells of three adult male whelks (>70 mm) were selected for analysis from three populations, the Menai Strait, the Shetland Isles and Jersey for an inter-site comparison (see chapter 3 for details of collection), alongside the three adult females from the Menai Strait. Whelk shells were chosen based on their condition, the largest shells with low damage and fouling were used to avoid confusion arising from damage repaired sections of shells.

Shells were scrubbed clean with a stiff bristled plastic brush and soapy hot water to remove loose fragments of the organic periostracum as well as any attached debris or epiphytes and then left to air dry. To maintain consistency, a sampling track of 2 mm increments was measured around the shell whorls using a fabric tape measure and their position, located roughly 5 mm from the shoulder of the shell whorl, drawn onto the shell using a fine pencil (Figure 4.3a). Although this distance varied depending on the size of each shell the same area and resolution were sampled each time. A 1mm diamond burr drill was used attached to a Dremel™ 4000 precision drill to remove any surface contaminants and obtain powder samples. Considerable care was taken to only sample the outer prismatic layer of the shells as differences in both structure and composition exist between the shell layers (see Chapter 3). Powder samples were removed with the diamond burr from 1 cm long trenches every 2 mm along the whole whorl of the shell from the lip backwards, starting at the second millimetre to avoid interference from the shell lip structure (Figure 4.3a). Sample trenches were made in line with visible striations on the surface of the shell structure (Figure 4.3b). The diamond burr was used

at a slow speed (≈ 5000 rpm) to drill each trench whilst held over a 10 x 10 cm sheet of greaseproof paper; this paper was then used to transfer the powder to a labelled 0.5 ml Eppendorf™ tube. Following analysis of the single shell from the female whelk during the pilot study the sampling resolution was reduced to 4 mm over the central portion of the shell (between the 2nd and 3rd shell whorls) as the growth was fast over this region. For all subsequent shells the resolution was reduced to sampling at 4 mm intervals over the central section but kept at 2 mm for the body whorl and shell apex (Figure 4.3a).

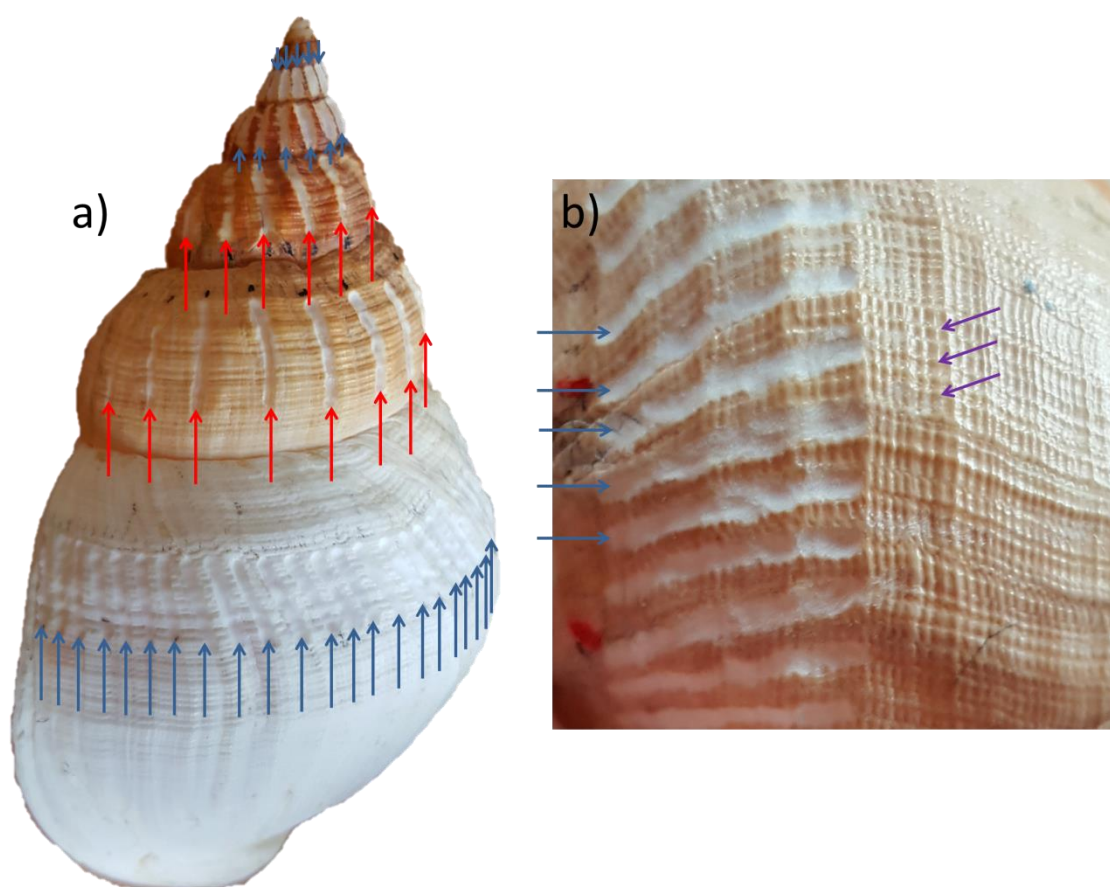


Figure 4.3. a) a *Buccinum undatum* shell following drill sampling. Blue arrows represent a 2 mm sampling resolution whilst the red arrows represent a 4 mm sampling resolution. b) magnified image of the 2 mm resolution samples tracks (blue arrows) along visible shell striations (purple arrows).

Where shell damage was obvious, the sample track was continued into the repaired area, although additional drilled samples were taken from the undamaged shell either side of the shell repair to compare with the $\delta^{18}\text{O}_{\text{shell}}$ from the damaged shell. Using this sampling strategy the maximum amount of growth history was captured (see Figure 4.4). The shell powder samples from each drilled groove were split into two portions for trace element and stable

isotope analyses to ensure that trace element and stable isotope ratio profiles could be directly compared.

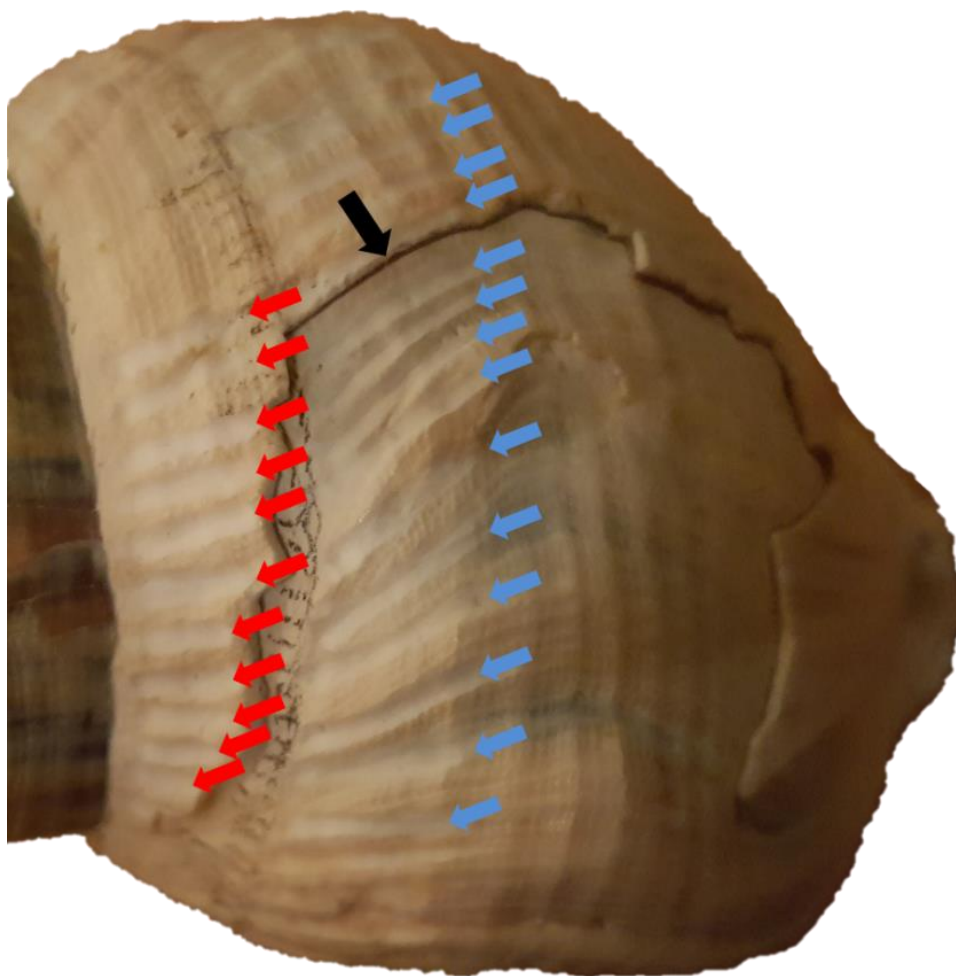


Figure 4.4. The drill sampling strategy employed at damage incidences (black arrow). Blue arrows–main sample track. Red arrows–samples taken from pre–damage shell.

4.2.2. Solution Inductively Coupled Plasma–Mass Spectrometry (Solution ICP–MS)

This technique allows high precision analyses of trace element concentrations contained within a liquid sample. Shell powder samples ($100\ \mu\text{g} \pm 20\ \mu\text{g}$) were weighed into individual 1.5 ml sample tubes and the following digestion and dilution procedure was applied:

- 1) 0.2 ml of 10% nitric acid (HNO_3) added to sample to digest it.
- 2) 0.2 ml of internal standard solution added. This solution was added to all sample, blank and standard vials. It contained several uncommon elements spread across the mass range (scandium– ^{45}Sc , rhodium– ^{103}Rh , indium– ^{115}In & iridium– ^{193}Ir) at set concentrations which were used to standardise all samples and check for anomalous data points.

- 3) 0.6 ml of Mili-Q water was added to dilute the sample and make a total of 1 ml giving a dilution factor of 10,000.

The resulting aliquots were analysed using a combination of three devices: an auto-sampler, a nebuliser, and a mass spectrometer. All of the solution ICP-MS work for this project was undertaken at the British Geological Survey (BGS) using a Teledyne Cetac MVX-7100 low volume auto-sampler (LVA) coupled to a Teledyne Cetac Agilent II desolvating nebulizer which fed into a SPECTRO MS mass spectrometer (an overview of all equipment used can be seen in [Appendix C](#)). The combination of this equipment allowed the sampling of small powdered shell samples. This is the first time that this combination of equipment has been used to sample biogenic carbonate samples (Chenery, 2015).

In addition to the shell samples, several carbonate standards were also prepared and analysed in the same manner, two synthetic calcium carbonate standards (CAPPT-0a & CAPPT-1b) and an otolith carbonate sample (FEBS-1, Sturgeon *et al.*, 2005). Several steps were taken to detect machine drift and contamination over the sample runs. Firstly, the samples were run out of order, odd numbered and even numbered samples were split into two separate runs. This ensured that when the data were combined during post processing, any anomalous samples or machine drift could be detected. It also ensured that in the event of a machine failure, an entire shells-worth of samples were not lost. Secondly, calibration samples (separate to the carbonate standards) consisting of a range of different element combinations at known concentrations were analysed at the beginning and end of each sample run (full list of analytical standards can be found in [Appendix D](#)). Finally, the carbonate standards (CAPPT-0a, CAPPT-1b & FEBS-1) as well as calcium standards (containing the same concentration of Ca as the CaCO₃ samples) were interspersed throughout each sample run, along with blanks (containing nothing except the internal standard, Mili-Q and HNO₃). The combination of the sample running order, calibration, standard and blank samples ensured confidence in the resulting data.

To investigate whether the trace elements contained within the shells of *B. undatum* reflect any environmental conditions, several elements were chosen to explore their potential as different environmental proxies. Strontium (⁸⁸Sr), magnesium (²⁴Mg) and lithium (⁷Li) were chosen to investigate any potential seawater temperature signal. Sodium (²³Na) and barium (¹³⁸Ba) were chosen to investigate the potential of a salinity signal. Ba was also used to look for cycles which may be related to productivity, along with lithium (⁷Li), manganese (⁵⁵Mn) and iron (Fe). Fe

profiles were also assessed for their potential use as recorders of pollution, along with uranium (^{238}U).

4.2.3 Isotope Ratio Mass Spectrometry (IRMS)

This technique is also based on mass spectrometric detection similar to solution ICP-MS (see [Appendix C](#) for overview), however instead of analysing the abundance of trace elements within a sample, the ratios of carbon and oxygen isotopes were analysed. Thus the ratio of the isotopes of each of these elements, in this case carbon ($^{12}\text{C}/^{13}\text{C}$) ($\delta^{13}\text{C}_{\text{shell}}$) and Oxygen ($^{16}\text{O}/^{18}\text{O}$) ($\delta^{18}\text{O}_{\text{shell}}$) could be determined in each drilled shell sample. All stable isotope sampling was undertaken following a successful facility grant application to the NERC Isotope Geosciences Facilities Steering Committee (NIGSFC) (IP-1527-0515, [Appendix E](#)). For this analysis an IsoPrime dual inlet mass spectrometer and Multiprep device were used at the BGS facility in Keyworth, UK. 50–100 μg of the powdered sample was weighed, added to a glass vial and sealed with a rubber septa and lid. The sample vials were evacuated and anhydrous phosphoric acid (H_3PO_4) added to each sample at 90°C . The samples were left to digest for 15 minutes and the expressed gas (mainly comprised of CO_2) was collected, cryogenically cleaned to remove any moisture and passed into a mass spectrometer using a bellows. After ionisation, the positively charged ions were focussed into a magnetic field sector where they were sorted by mass. The three most common carbon dioxide ion molecular masses were then analysed ($44 - ^{12}\text{C} + ^{16}\text{O} + ^{16}\text{O}$; $45 - ^{13}\text{C} + ^{16}\text{O} + ^{16}\text{O}$ and $46 - ^{12}\text{C} + ^{16}\text{O} + ^{18}\text{O}$). The ratios between the abundances of these masses were then used to deduce the abundance of the respective O and C isotopes. As with the solution ICP-MS, machine drift was accounted for by analysing standards before, during and after each run. The standard used was a laboratory standard (KCM) which had been calibrated against a well-known international standard (NBS-19-Friedman *et al.*, 1982). Isotope values ($\delta^{18}\text{O}_{\text{shell}}$ and $\delta^{13}\text{C}_{\text{shell}}$) are reported as deviations from the isotopic ratios ($^{18}\text{O}/^{16}\text{O}$, $^{13}\text{C}/^{12}\text{C}$) calculated against the VPDB (Vienna Pee Dee Belemnite) standard, by using the calibrated within run laboratory standard. The resulting isotopic ratios of the samples are then expressed in delta units, $\delta^{13}\text{C}$ and $\delta^{18}\text{O}$ (‰, parts per mille). The reproducibility of the laboratory standard (KCM) is $<0.1\text{‰}$ for $\delta^{13}\text{C}$ and $\delta^{18}\text{O}$.

The Craig correction (Craig, 1957) was applied to account for low concentrations of ^{17}O which can contribute to the molecular masses of CO_2 described above ($45 - ^{12}\text{C} + ^{16}\text{O} + ^{17}\text{O}$ and $46 - ^{13}\text{C} + ^{16}\text{O} + ^{17}\text{O}$). The correction is comprised of standard values which remove any effect of ^{17}O :

$$\delta^{13}\text{C} = 1.0676 \delta (45/44) - 0.0338 \delta^{18}\text{O}$$

$$\delta^{18}\text{O} = 1.0010 \delta (46/44) - 0.0021 \delta^{13}\text{C}$$

Finally a fractionation factor was applied to the data. During H_3PO_4 digestion of the carbonate samples roughly 1 mole of oxygen is left behind in the solution. Fractionation factors are derived from the difference in the isotopic values of O_2 and CO_2 produced during digestion at a constant temperature and the total oxygen content of the CaCO_3 (Sharma & Clayton, 1965). Fractionation factors are both temperature and mineral dependant, the factor for aragonite at 90°C is 1.00855 (Sharma & Clayton, 1965; Kim *et al.*, 2007). The fractionation factor must be applied to a value that represents a solid, values that result from the analysis are for gas so they were converted and corrected as follows:

$$\text{Solid aragonite value} = \frac{\text{Craig corrected gas value} + 1000}{1.00855 (\text{fractionation factor for aragonite})} - 1000$$

Due to the high sampling frequency per annual cycle the data from all trace element and stable isotope profiles were treated with a 9-point Savitsky–Golay smoothing filter (Savitsky & Golay, 1964; Steiner *et al.*, 1972) and the data plotted using Microsoft Excel.

4.2.3.1 Palaeotemperature equation calibration

The Palaeotemperature equation was calibrated using juvenile *B. undatum* that had been hatched from egg masses and reared for a period of 2 years in a laboratory aquarium, using the methods outlined in Chapter 3 (section 3.2). Seawater temperatures within the aquarium were monitored throughout the 2-year experiment at three hourly intervals using a Tinytag™ Aquatic 2 temperature logger. Monthly, three replicate seawater samples were removed from the centre of the aquarium in 25 ml PTFE bottles. Seawater samples were processed using the CO_2 equilibration method with an Isoprime 100 mass spectrometer plus Aquaprep device to determine monthly the $\delta^{18}\text{O}$ of the seawater ($\delta^{18}\text{O}_{\text{water}}$) during growth and development of the whelks. 200 μl of each seawater sample was pipetted into a Labco Exetainer® vial and heated to 40°C in a sample tray. Any gas present in the vials was removed, flushed with CO_2 and left to equilibrate for 12 hours. A cryogenic water trap was then used to remove any moisture from each equilibrated gas sample. The dry sample gas was analysed using the IRMS. Two laboratory standards (CA–HI and CA–LO) plus up to two secondary standards were analysed in each run. Each laboratory standard had been calibrated against reference materials (VSMOW2, SLAP2 and

GISP) so the resulting $^{18}\text{O}/^{16}\text{O}$ ratios of the samples ($\delta^{18}\text{O}_{\text{water}}$) were calculated and expressed in delta units, $\delta^{18}\text{O}$ (‰, parts per mille). Errors are typically ± 0.05 per mil.

In February 2016 three of the largest 2-year old whelks (47, 42 & 51 mm, samples T1, T2 & T3) were randomly selected from the aquarium to investigate seasonal variations in $\delta^{18}\text{O}_{\text{shell}}$ and $\delta^{13}\text{C}_{\text{shell}}$. The largest whelk shells allowed more room for the 2 mm resolution drill sampling around the whole shell (apex to lip margin). The shells were sampled and analysed using the methods described above for IRMS of shell carbonate. Using the measured seawater temperatures and determined $\delta^{18}\text{O}_{\text{water}}$ and $\delta^{18}\text{O}_{\text{shell}}$ a species specific palaeotemperature equation (after Craig, 1965 and Grossman & Ku, 1986) was calculated for *B. undatum*. Trace element concentrations were also analysed in the carbonate samples from two of the juvenile laboratory reared animals.

4.2.3.2 Average isotope profiles

Each individual whelk isotope profile was aligned to the seasonal cycle of the site-specific seawater temperature by manually pinning the dates of the maxima and minima of the seawater temperature profile to the minima and maxima in the $\delta^{18}\text{O}_{\text{shell}}$ profile respectively (as $\delta^{18}\text{O}_{\text{carbonate}}$ is inverse to seawater temperature). Dates were then interpolated between the pinned dates using the fill series (trend) function in Microsoft Excel. Next, average isotope profiles were created for each site by compiling all the isotope profiles from a single site into one average profile. This was achieved using a custom script in MATLAB (ver. 9.0) (written by Ben Marchant, BGS, [Appendix F](#)). The script used Excel files that contained fitted date and isotope data for several shells from the same site. Firstly it converted all the dates to decimal dates, data were interpolated onto the first day of each calendar week (or each day depending on the resolution required) using a cubic spline, and all the isotope values for the same interpolated date were averaged. The resulting site isotope profiles were converted to temperature values using the newly calibrated palaeotemperature equation and plotted against the measured SST from each site using Excel.

For comparisons between the resulting trace element and stable isotope profiles with environmental conditions, historical daily sea surface temperature (SST) data were sourced from deployed temperature loggers at each of the 3 locations, (Menai Bridge, Shetland Isles and Jersey). The seawater temperature data were not collected during the course of the study but were obtained from governmental organisations for each location (CEFAS–The Menai Strait,

Marine Scotland–Shetland, Jersey Department of the Environment–Jersey). High resolution salinity data were only available from waters around the Shetland Isles (from Marine Scotland), none were available for the Menai Strait or Jersey. No chlorophyll data or $\delta^{18}\text{O}_{\text{water}}$ samples during the period of interest were available from any of the 3 locations.

4.2.4 Growth rate analyses

For growth rate analyses, the Total Lip Extension (TLE) was measured by coiling a length of cotton around the whorls of each shell (i.e. the full growth axis) from the lip backwards to the apex. The cotton was then cut and measured against a ruler to the nearest 1mm. This measurement was then compared to the Total Shell Length (TSL, see Chapter 2 Figure 2.6) to calculate the relationship between TLE and TSL. The aim of this was the determination of a relationship between TSL and TLE which would allow the distances covered by the drill sampling for trace element and isotope analyses to be converted into growth distances in terms of TSL.

4.3 Results

4.3.1 Calibration of the palaeotemperature equation

The $\delta^{18}\text{O}_{\text{shell}}$ profiles from each of the three laboratory reared 2 year old *B. undatum* shells were averaged in Matlab to form a single isotope profile. This process also interpolated the data to a daily resolution. These data were matched to $\delta^{18}\text{O}_{\text{water}}$ values with the same dates ($n = 40$) and together with tank seawater temperature data were used to create the linear plot of $\delta^{18}\text{O}_{\text{shell}} - \delta^{18}\text{O}_{\text{water}}$ against seawater temperature shown in Figure 4.5. This linear relationship was used to create the following palaeotemperature equation:

$$t(^{\circ}\text{C}) = 14.061 - 5.031 * (\delta^{18}\text{O}_{\text{shell}} - \delta^{18}\text{O}_{\text{water}})$$

The calibrated *B. undatum* equation was then compared to both the observed tank water temperature and several other palaeotemperature equations used for mollusc species in the literature (Figure 4.6 & Table 4.1). Figure 4.6 shows that the calibrated equation from this current study results in a more accurate seawater temperature reconstruction than the other published equations. Similarly the seawater temperature reconstructions using the equation from Leng & Marshal (2004) (a reorganisation of the Kim & O'Neil (1997) equation; L&M reorganisation of K&ON) show close agreement with the observed seawater temperature. This

is confirmed further in Table 4.1, which shows the average deviation (sum of reconstructed seawater temperature – actual seawater temperature / n) of each reconstruction, with only 0.004°C deviation the new calibration displays the best fit. The absolute range of the reconstructed temperatures was also $\approx 13\%$ better with the calibrated *B. undatum* equation than with the L&M reorganisation of K&ON. However, as the instrumental error of the points in Figure 4.5 is 0.11, there is likely no statistical difference between the equation calculated for *B. undatum* and the L&M reorganisation of K&ON.

4.3.2 Seawater temperature reconstructions from field collected *Buccinum undatum*

Seasonal sea surface temperature (SST) profiles from the Menai Strait, Jersey and Shetland covering a 4.5 year period are shown in Figure 4.7. The northerly most Shetland was the coldest of the three sites. The Menai Strait and Jersey have a more similar seasonal temperature cycle, although the Menai Strait reached lower temperatures in the winter (4°C) (comparable to Shetland) than Jersey (7°C). Jersey coastal waters reached slightly higher maximum temperatures (18.5°C) and stayed warmer for longer between the summer maximum and the winter minimum (7°C).

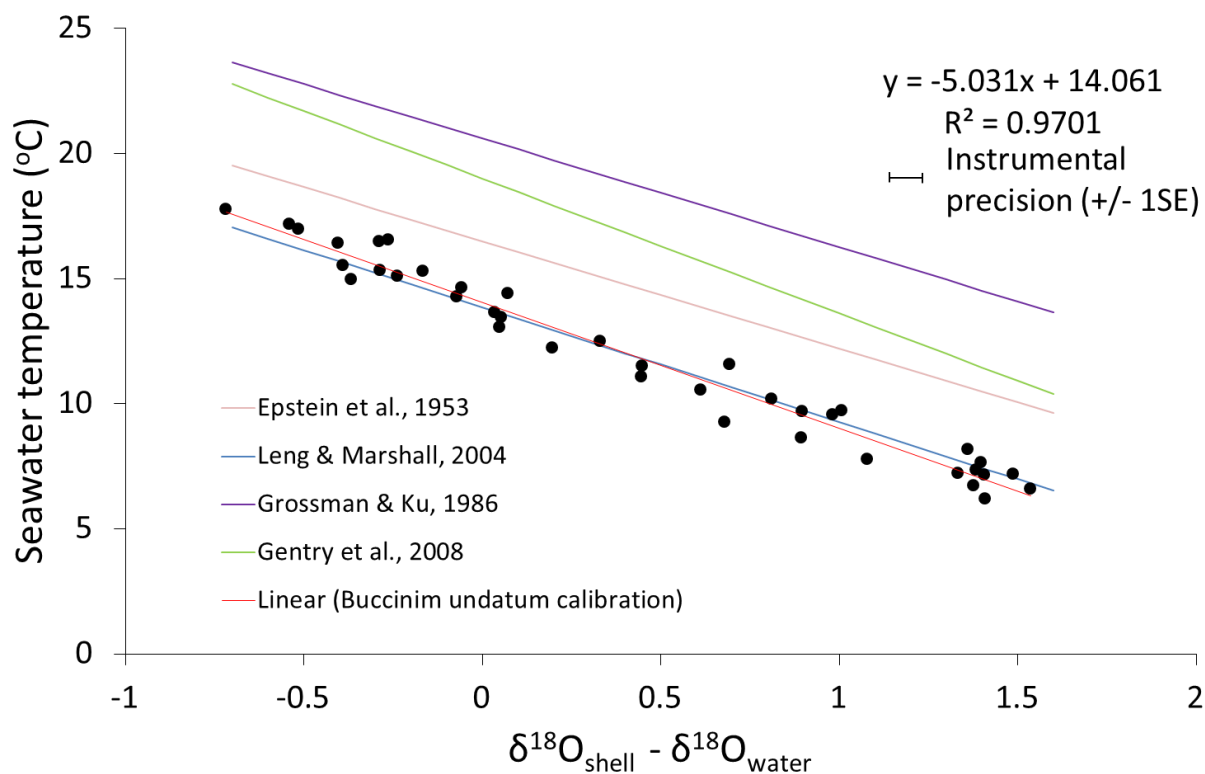


Figure 4.5. Plot of $\delta^{18}\text{O}_{\text{shell}} - \delta^{18}\text{O}_{\text{water}}$ against seawater temperature highlighting a strong linear relationship between the two data series ($R^2 = 0.97$). The standard error of the data points is 0.11.

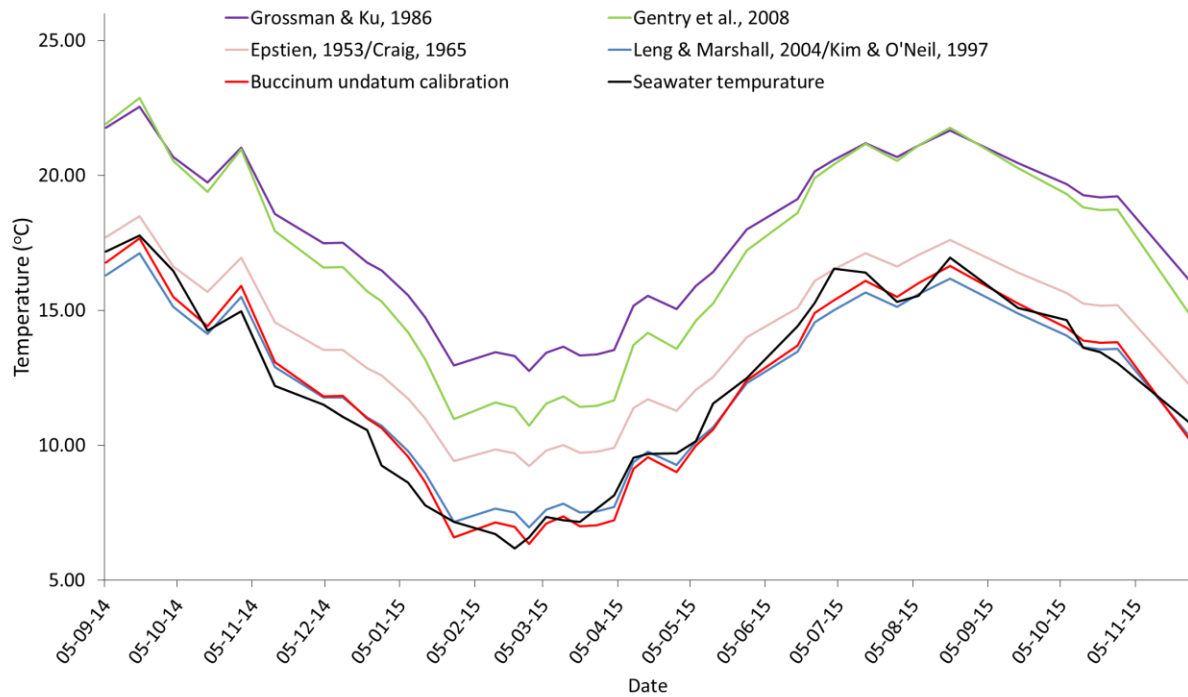


Figure 4.6. Observed tank seawater temperatures over the growth period (black line) overlaid with temperature reconstructions (from $\delta^{18}\text{O}_{\text{shell}}$) calculated using a range of palaeotemperature equations sourced from the literature as well as the calibrated equation from this study (red line).

Table 4.1. A comparison of the average reconstructed seawater temperature deviation from the recorded seawater temperature over the period of growth during the *Buccinum undatum* calibration with relevant equations taken from the literature ($\pm 1\text{SE}$). The % of the observed SST range reconstructed by each equation is also shown.

Source of equation	Calibration material	Average deviation from temperature ($^{\circ}\text{C}$)	% of observed temperature range reconstructed
Epstien, 1953/Craig, 1965	Mixture of aragonite & calcite mollusc shell	3.30 ± 0.14	80.0
Grossman & Ku, 1986	Aragonitic mollusc shell	5.67 ± 0.12	84.5
Leng & Marshall, 2004/Kim & O'Neil, 1997	Inorganic calcite	0.03 ± 0.11	87.8
Gentry <i>et al.</i> , 2008	Aragonitic gastropod shell	4.76 ± 0.1	104.9
<i>B. undatum</i> calibration (this study)		0.004 ± 0.09	97.7

In situ $\delta^{18}\text{O}_{\text{water}}$ values for each site over the 4.5 year reconstructions was unavailable. To compensate for the absence of actual data a sensitivity analysis was undertaken to determine the most likely values of $\delta^{18}\text{O}_{\text{water}}$ to use in the seawater temperature reconstructions at each site. Table 4.2 shows the results of the analysis, a $\delta^{18}\text{O}_{\text{water}}$ range from -1 to 1 with 0.25 steps was chosen based on $\delta^{18}\text{O}_{\text{water}}$ values from the palaeotemperature equation used in this study as well as those in the literature (Hermoso *et al.*, 2016; McKenna *et al.*, 2016). For each 0.25

step the average deviations of the reconstructed temperature ($^{\circ}\text{C}$) from recorded seawater temperature over the whole period of growth were calculated, these values were then compared to find the lowest deviation. The values with the lowest deviation were used in the palaeotemperature reconstructions. An average $\delta^{18}\text{O}_{\text{water}}$ value for Menai Strait water of 0.01, calculated from all of the $\delta^{18}\text{O}_{\text{water}}$ data from the palaeotemperature equation calibration, was also used in the sensitivity analysis. As expected, when this value was used in the palaeotemperature equation it gave the most accurate reconstruction for data from the Menai Strait.

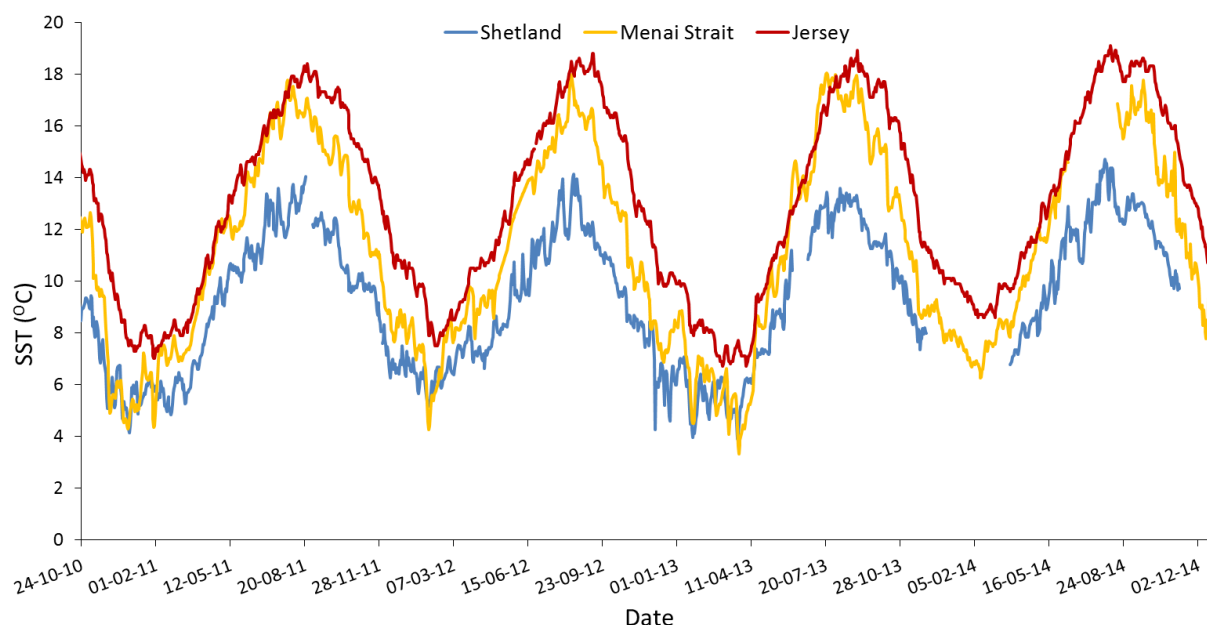


Figure 4.7. Daily recorded sea surface temperature (SST) records between October 2010 and February 2014 from the three main study sites. Gaps in the Shetland and Menai Strait data were due to temperature logger failures. Data were obtained from Marine Scotland (Shetland), Department of the Environment (Jersey) and CEFAS (Menai Strait).

Table 4.2. Results of a sensitivity analysis to determine the most likely $\delta^{18}\text{O}_{\text{water}}$ values to use in the seawater temperature reconstructions from Jersey, the Menai Strait and Shetland. Values stated are average deviations of the reconstructed temperature ($^{\circ}\text{C}$) from recorded seawater temperature during the period of growth of *Buccinum undatum* in the experimental aquaria. The values with the lowest deviation are highlighted in bold. The 0.01 value (in *italics*) was calculated from $\delta^{18}\text{O}_{\text{water}}$ values from Menai Strait derived seawater samples.

	$\delta^{18}\text{O}_{\text{water}}$									
	-1	-0.75	-0.5	-0.25	0	<i>0.01</i>	0.25	0.5	0.75	1
Jersey	8.78	7.52	6.26	5.01	3.75	3.70	2.50	1.24	-0.02	-1.27
Menai Strait	5.33	4.08	2.82	1.57	0.31	0.26	-0.95	-2.20	-3.46	-4.71
Shetland	6.09	4.83	3.58	2.32	1.07	1.02	-0.19	-1.44	-2.70	-3.96

The seawater temperature reconstructions for the three sites are shown in Figures 4.8, 4.9 & 4.10 (Jersey, The Menai Strait and Shetland respectively). The black bars above each plot

represent the number of shells included in the average profile at any one point, portions of the average profile which only represent a single shell are not presented. It is clear from the plots that the reconstructions from Jersey and the Menai Strait have roughly the same temperature range as their observed SST counterparts (89.75% and 80.63% of the same range respectively). However, the reconstruction for Shetland has a temperature range that only covers 63.5 % of the SST range which is clearly visible in Figure 4.10.

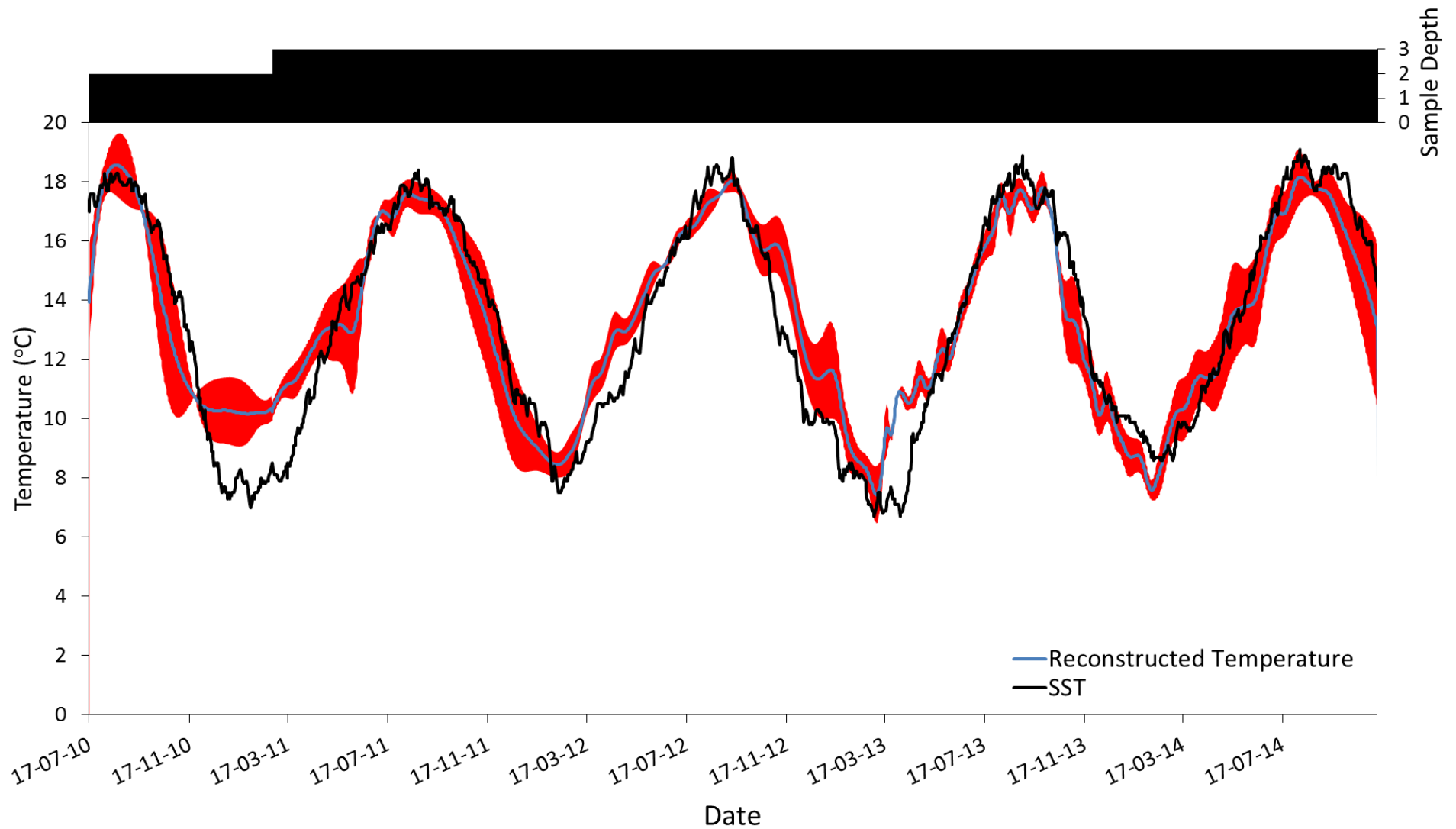


Figure 4.8. Daily observed seawater temperature from Jersey (black line) overlaid with the reconstructed temperature from the average Jersey isotope profile (blue line). Shaded red areas indicate $\pm 1SE$. The sample depth (i.e. number of samples averaged at any point over the analysis) is shown at the top.

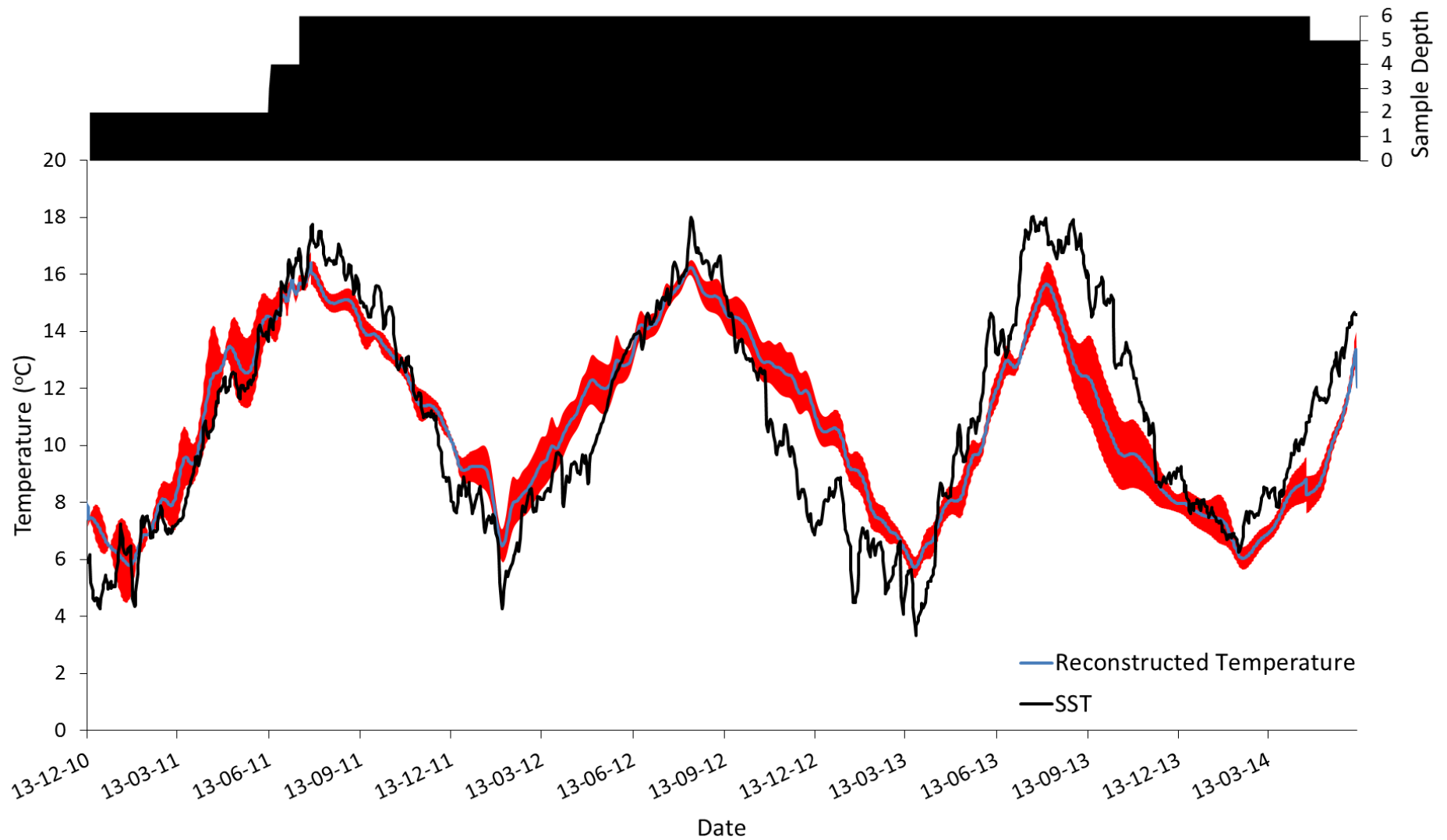


Figure 4.9. Daily observed seawater temperature from the Menai Strait (black line) overlaid with the reconstructed temperature from the average Menai Strait isotope profile (blue line). Shaded red areas indicate ± 1 SE. The sample depth (i.e. number of samples averaged at any point over the analysis) is shown at the top.

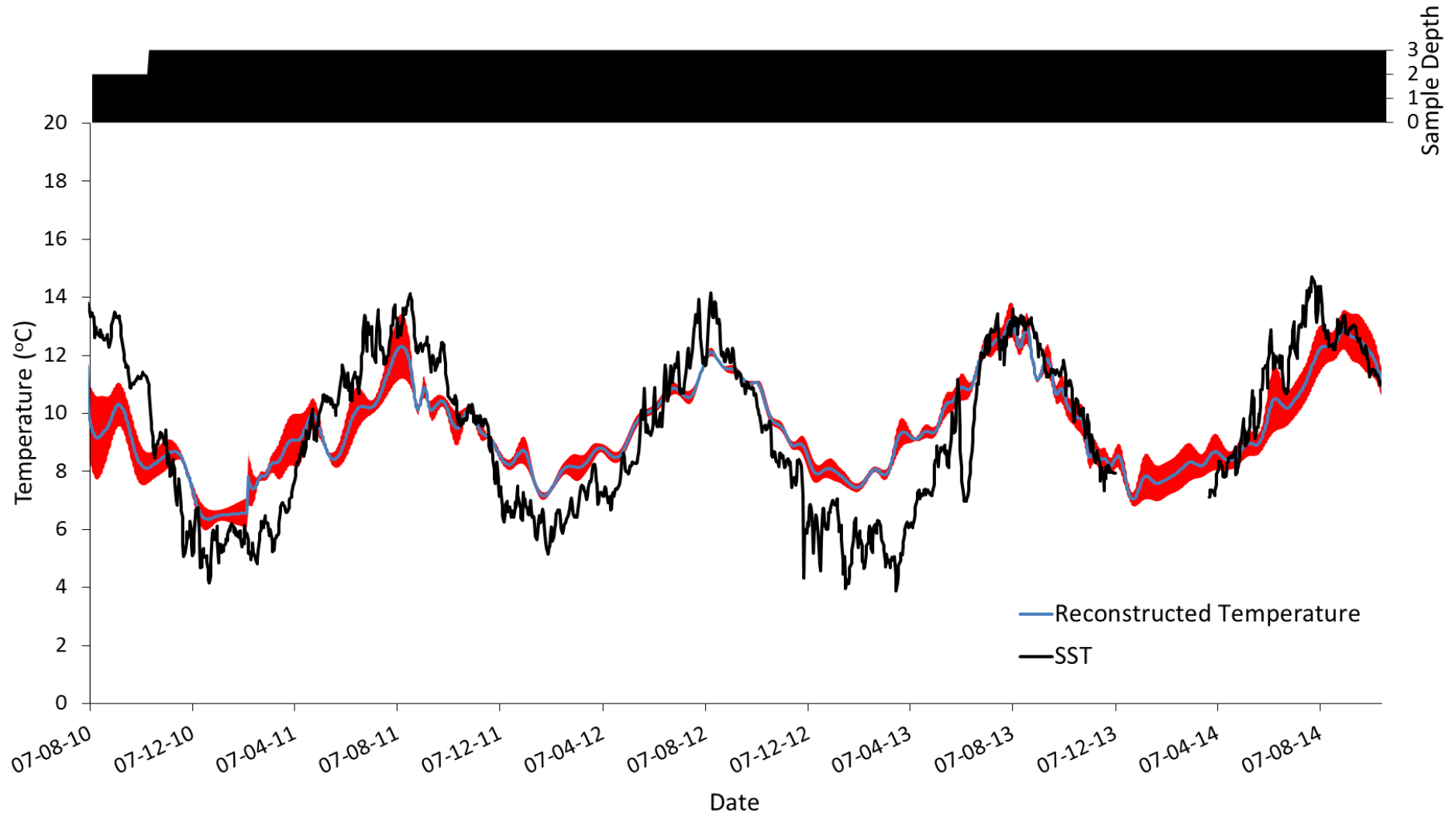


Figure 4.10. Daily observed seawater temperature from Shetland (black line) overlaid with the reconstructed temperature from the average Shetland isotope profile (blue line). Shaded red areas indicate ± 1 SE. The sample depth (i.e. number of samples averaged at any point over the analysis) is shown at the top.

4.3.3 Growth rate analysis

A strong linear relationship exists between Total Shell Length (TSL) and Total Lip Extension (TLE) i.e. $TSL = 0.2421 \times TLE + 2.7766$ (Figure 4.11). This equation allowed the conversion of distances covered during the isotope sampling (along the maximal growth axis from the shell lip backwards) to the TSL measurements. Figure 4.12 shows the annual growth (in TSL measurements) of all shells sampled for $\delta^{18}O$ analysis. Annual seasonal cycles in shell length were determined from the cycles in the $\delta^{18}O_{shell}$ profiles. The distance sampled during each annual cycle was converted from TLE to TSL using the above equation. Individuals from the Menai Strait have the fastest annual growth in their 2nd year of life, whilst Shetland samples display the same in the 3rd year. Jersey appears to have similar fast rates of growth in both the 1st and 4th years of life. Menai Strait and Shetland appear to grow faster than whelks from Jersey. Three individuals (one male and two females) from the Menai Strait show growth in their second year above 35mm.year⁻¹.

Due to the method used to assign dates to the $\delta^{18}O_{shell}$ profiles (i.e. pinning the dates of the SST maxima and minima with the minima and maxima of the $\delta^{18}O_{shell}$ cycles), seasonal growth analysis was limited to two 'seasons' as no dates could be ascribed to values between the temperature minima and maxima:

- 1) Season 1: winter temperature minimum–summer temperature maximum
- 2) Season 2: summer temperature maximum–winter temperature minimum

The bar plots shown in Figures 4.13 – 4.15 represent the % of the total annual growth occurring in seasons 1 and 2 for each individual animal. Year 1 is missing for most of the field collected whelks as shell sampling could not be extended far enough along the shell to capture the full first year of growth. Figure 4.13 illustrates the seasonal growth bar plots for three male (a, b & c) and 3 female (d, e & f) whelks from the Menai Strait. There is no clear difference in the seasonal growth of males and females apparent from these plots. Figure 4.14 shows similar plots for three male specimens from Jersey (a, b & c) and Shetland (d, e & f). It appears from these plots that in all years in all shells from Jersey the majority of growth is completed during season 1 whereas the reverse is true for Shetland where the majority of growth is undertaken following the summer maximum in season 2. For the laboratory reared whelks (Figure 4.15), as with the field collected whelks from the Menai Strait (Figure 4.14) there is no clear pattern

across years, however all the juveniles showed increased growth in season 2 in year 1 and conversely season 1 in year 2. The correlation between environmental variables and growth rate is discussed further in Chapter 8.

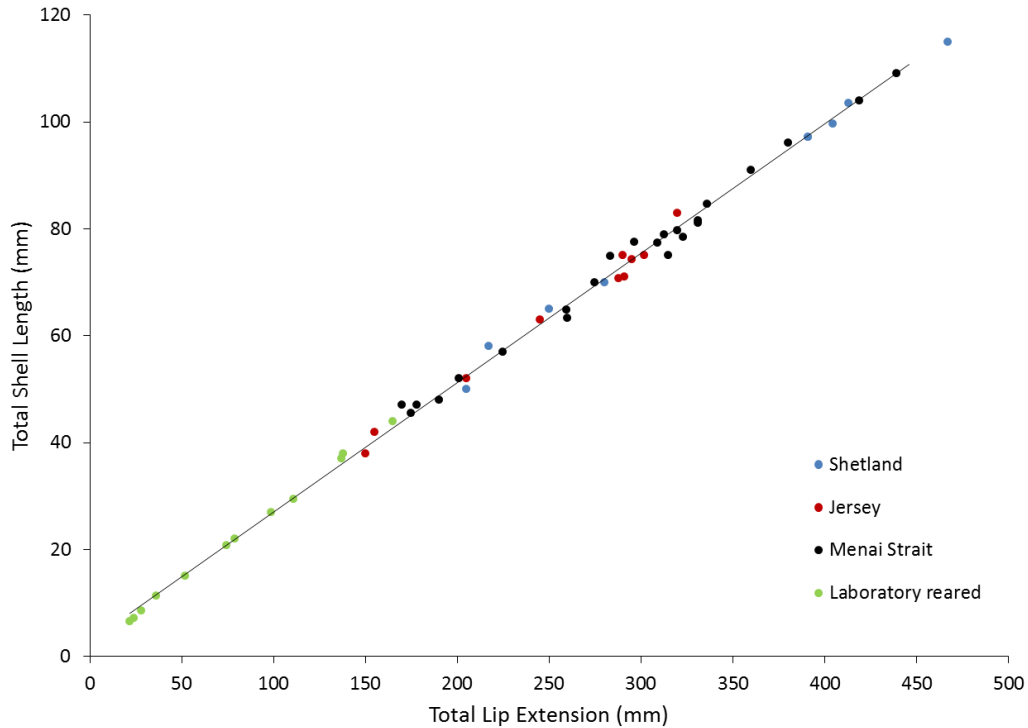


Figure 4.11. The significant linear relationship ($y = 0.2421x + 2.7766$, $R^2 = 0.99$) between Total Shell Length (TSL) and Total Lip Extension (TLE) determined from the shells from a range of laboratory reared and field collected *Buccinum undatum*, $n = 60$.

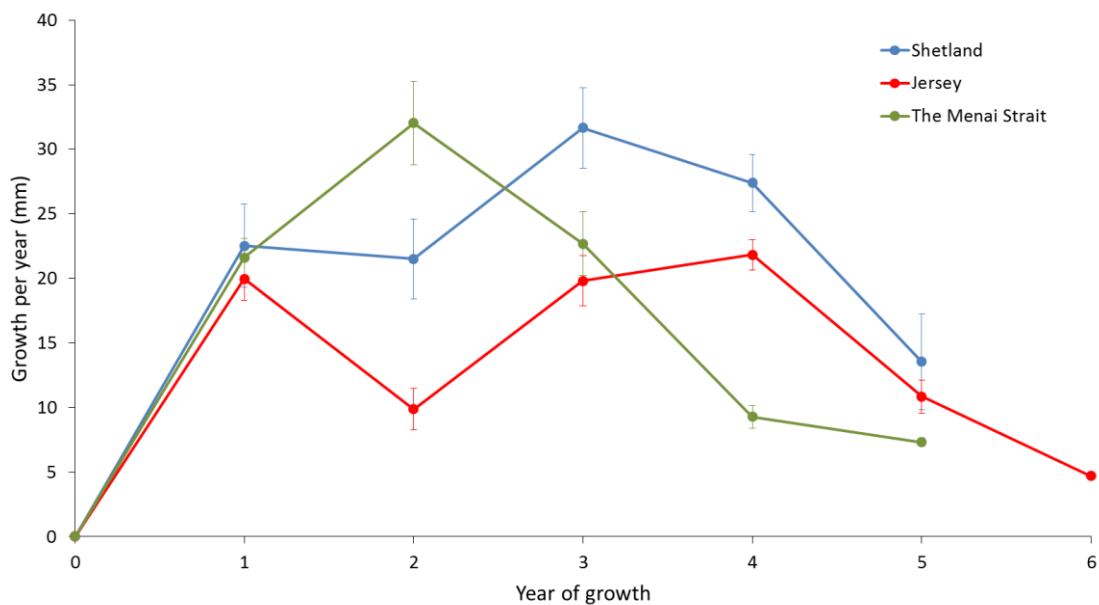


Figure 4.12. Annual growth rates of individual field collected whelks from Jersey, the Menai Strait and Shetland whelks. Average profiles are shown from all sampled shells from each site, error bars represent ± 1 SE.

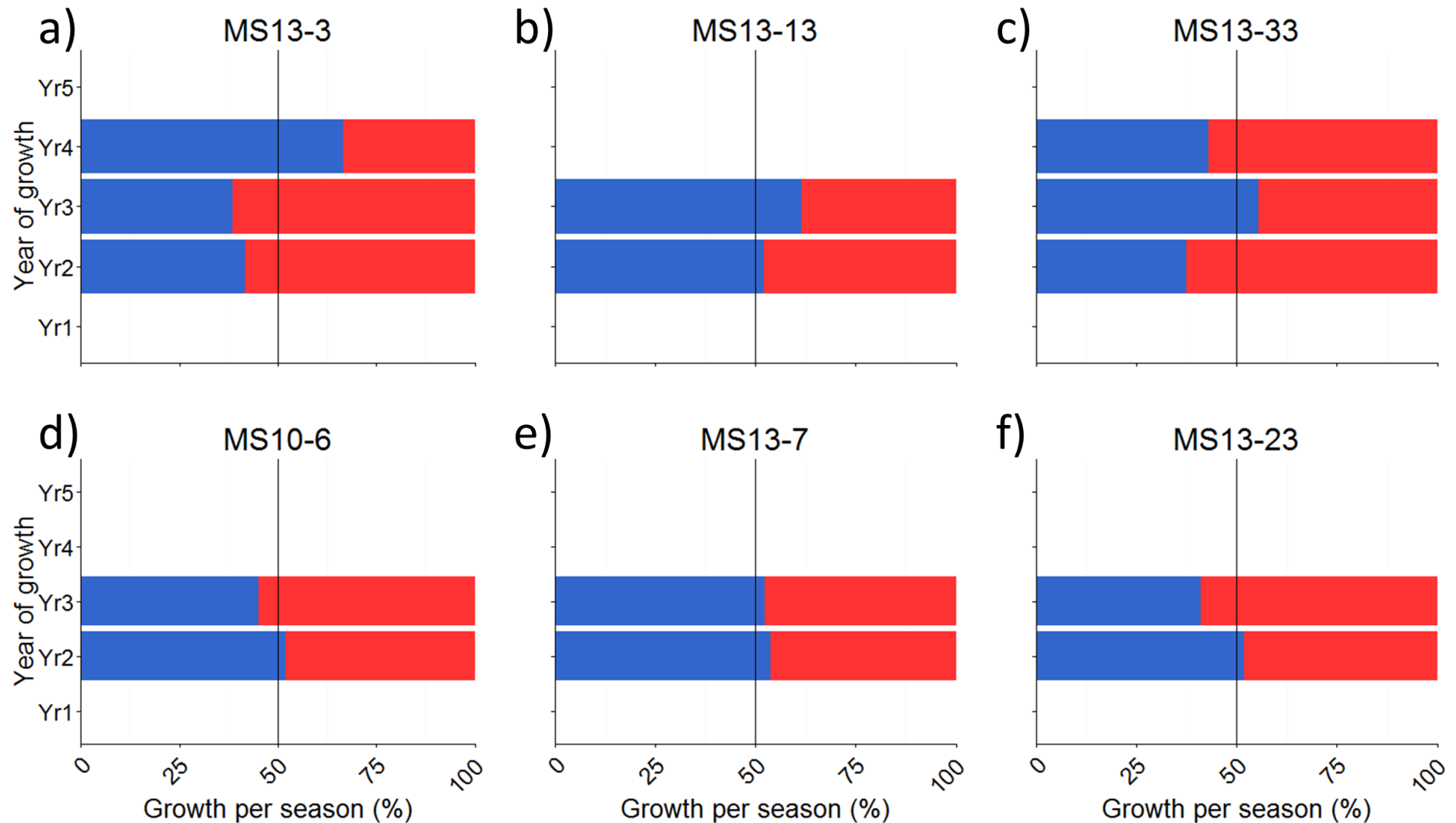


Figure 4.13. Bar plots showing the percentage of annual growth per 'season' for each year of growth for male (a, b & c) and female (d, e & f) *Buccinum undatum* from the Menai Strait. Season 1 is shown by the blue portion of each bar and season 2 is represented by the red portion. The vertical black line on each plot indicates the 50% point.

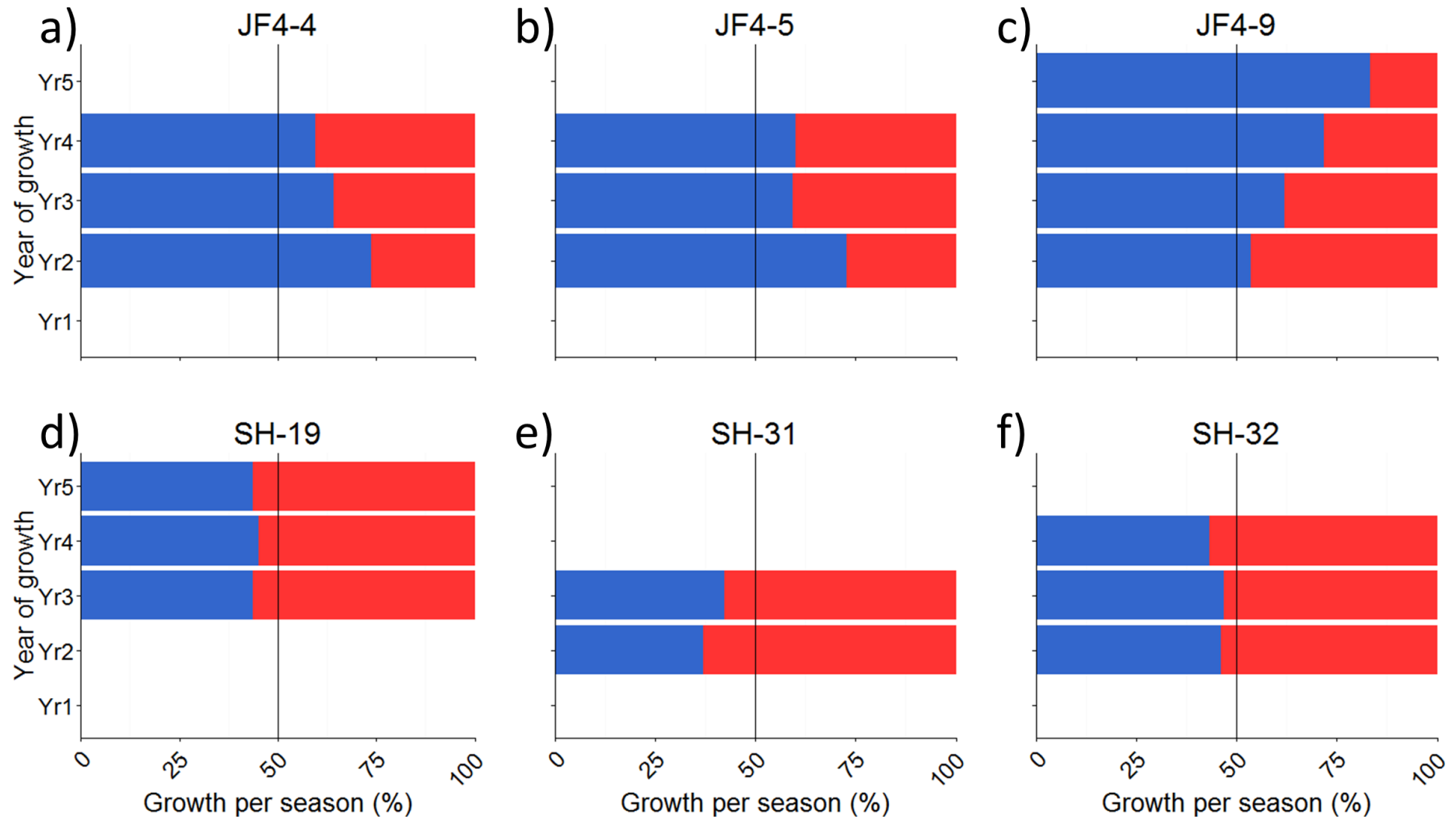


Figure 4.14. Bar plots showing the percentage of annual growth per 'season' for each year of growth for *Buccinum undatum* from Jersey (a, b & c) and Shetland (d, e & f). Season 1 is shown by the blue portion of each bar and season 2 is represented by the red portion. The black line on each plot highlights the 50% point.

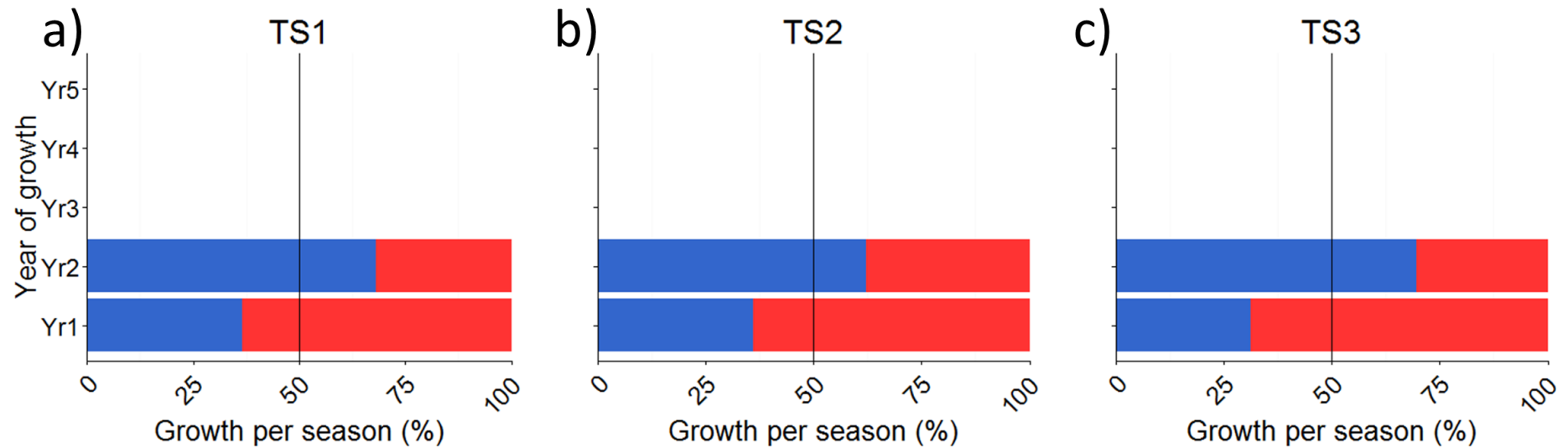


Figure 4.15. Bar plots showing the percentage of annual growth per 'season' for each year of growth for individual laboratory reared *Buccinum undatum*. Season 1 is shown by the blue portion of each bar and season 2 is represented by the red portion. The black line on each plot highlights the 50% point.

4.3.4 Trace element profiles from shell carbonate

Following data processing, all trace element concentrations are presented as ratios to ^{44}Ca in milligrams of trace element to kilograms of Ca (mg.kg^{-1}). For ease of reading throughout this section and the following discussion, trace element to Ca ratios will be referred to only using elements symbols (e.g. Sr) as opposed to the full ratio (e.g. Sr/Ca). Also, $\delta^{18}\text{O}_{\text{shell}}$ and $\delta^{13}\text{C}_{\text{shell}}$ will be referred to as $\delta^{18}\text{O}$ and $\delta^{13}\text{C}$ respectively for ease of reading.

The data presented in Figures 4.16 to 4.18 show the relationship between $\delta^{18}\text{O}$ and $\delta^{13}\text{C}$ (Figures 4.16a, 4.17a & 4.18a) as well as the trace element profiles of Sr (Figure 4.16b, 4.17b & 4.18b), Mg (Figure 4.16c, 4.17c & 4.18c) and Na (Figure 4.16d, 4.17d & 4.18d) for a single shell from Jersey (Figure 4.16), the Menai Strait (Figure 4.17) and Shetland (Figure 4.18). $\delta^{18}\text{O}$ is used as a proxy for seawater temperature. However, it should be noted that the relationship between $\delta^{18}\text{O}$ and seawater temperature is negative, for this reason, the axes of $\delta^{18}\text{O}$ are inverted. Differences in elemental concentrations between sites are clear, Figure 4.19 shows the relationship between Sr and $\delta^{18}\text{O}$ in each shell, the relationships are visibly different not only between sites but also between shells from a single site, similar figures for several other elemental relationships can be found in [Appendix G](#). Tables 4.4, 4.5 & 4.6 summarise the correlations between all trace elements of interest and $\delta^{18}\text{O}$ and $\delta^{13}\text{C}$ for all of the sampled shells from both experimental sites and laboratory reared specimens. There are clear differences between sites seen for almost all elements. The strength of the correlations has been categorised as follows (based on Fowler *et al.*, 1998):

0–0.19 = very weak; 0.2–0.39 = weak; 0.4–0.69 = moderate; 0.7–0.89 = strong; 0.9–1 = very strong.

4.3.4.1 Shetland

Sr shows no clear relationship with $\delta^{18}\text{O}$ for any of the specimens. There are only moderate correlations whenever relationships are found throughout the trace elements and shells at this site. Moderate positive correlations were found between $\delta^{18}\text{O}$ and Na in all shells, this was the only moderate relationship found across the 3 shells at this site. Negative relationships between Mg and $\delta^{18}\text{O}$ were found in two of the shells along with weak negative relationships between lighter elements (Li, Na & Mg) and $\delta^{13}\text{C}$ (aside from Li in SH–31). The data for Mn and Fe are missing from sample SH–31, because the data are below detection limits.

4.3.4.2 Jersey

Strong and moderate positive relationships were found between Sr and $\delta^{18}\text{O}$ as well as U and $\delta^{18}\text{O}$ in all shells. Li also showed weak, moderate and strong positive correlations with $\delta^{18}\text{O}$. Weak and moderate negative relationships were seen between Na and $\delta^{18}\text{O}$, Mg also showed weak positive relationships with $\delta^{18}\text{O}$, however, not all of these relationships were significant. A moderate negative relationship was found between Mn and $\delta^{13}\text{C}$ in samples JF4–9 and JF4–5 (very weak negative in JF4–4). Fe and $\delta^{13}\text{C}$ showed a strong negative relationship in JF4–9 and a weak negative relationship in JF4–4.

4.3.4.3 Menai Strait

Strontium and $\delta^{18}\text{O}$ showed strong positive correlations in all shells, the average concentrations of Sr in each shell ranged between 1800 & 2400 mg.kg^{-1} . Aside from MS13–3, there are strong and moderate negative correlations between Na and $\delta^{18}\text{O}$ for all specimens from the Menai Strait (excluding MS13–3). Mg against $\delta^{18}\text{O}$ shows no consistent pattern with some shells showing weak positive relationships and some showing weak negative relationships, there are also much lower values of Mg in each shell when compared to Sr and Na. In all the male whelks (top row of Table 4.4) there is a moderate correlation between U and $\delta^{18}\text{O}$ and also between Ba and $\delta^{18}\text{O}$ in two of the male specimens. It is clear that the patterns seen in the trace elements are not consistent from shell to shell within the same site. There are also strong and moderate negative correlations between $\delta^{13}\text{C}$ and several trace elements in two of the female shells (MS13–7 & MS13–23).

4.3.4.4 Laboratory reared *Buccinum undatum*

Strong and moderate positive relationships were seen between several trace elements (Li, Sr, Ba & U) and $\delta^{18}\text{O}$ as well as $\delta^{18}\text{O}$ and $\delta^{13}\text{C}$ in whelk T1. A moderate negative relationship between Na and $\delta^{18}\text{O}$ and a weak negative relationship between Mg and $\delta^{18}\text{O}$ were also found in this whelk. Most of the relationships were also seen between trace elements and $\delta^{18}\text{O}$ in whelk T2, with the exception of Na, Mg where the relationship between $\delta^{18}\text{O}$ and $\delta^{13}\text{C}$ is much weaker. Unsurprisingly (due to the strong relationship between $\delta^{18}\text{O}$ and $\delta^{13}\text{C}$) similar relationships were also seen between $\delta^{13}\text{C}$ and several of the trace elements. However, after exhibiting a poor relationship against $\delta^{18}\text{O}$, Fe showed moderate and weak positive correlations with $\delta^{13}\text{C}$ in both shells (T1 & T2).

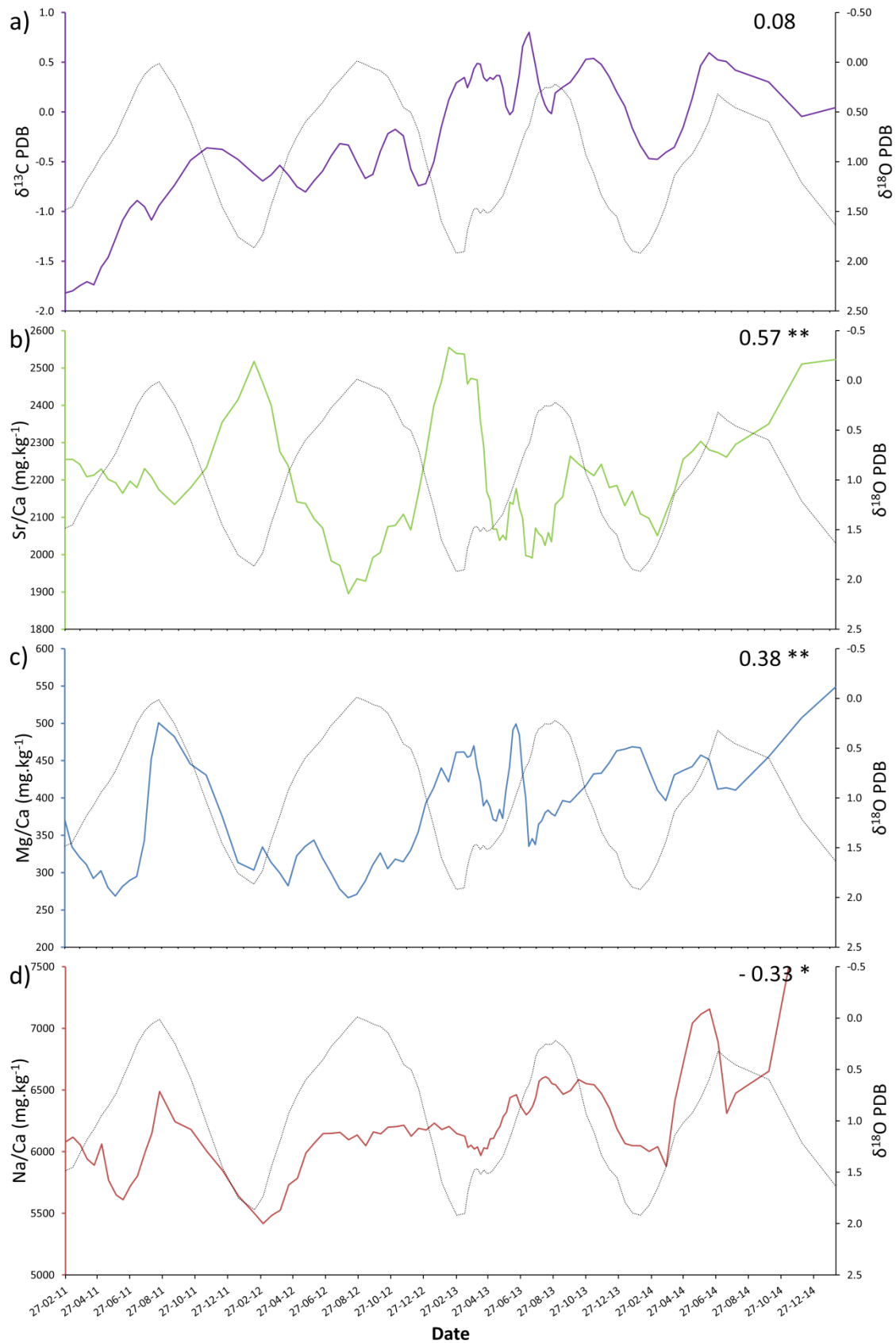


Figure 4.16. Profiles of $\delta^{18}\text{O}$ (dotted black lines) from a single specimen of *Buccinum undatum* from Jersey (JF4–9), overlaid with profiles of $\delta^{13}\text{C}$ (a), purple line), Sr (b), green line), Mg (c), blue line) and Na (d), red line) from the same shell. The Pearson correlation coefficient between the two profiles in each plot is shown as an inset, the significance of the correlations are: ** = $p < 0.05$, *** = $p < 0.005$.

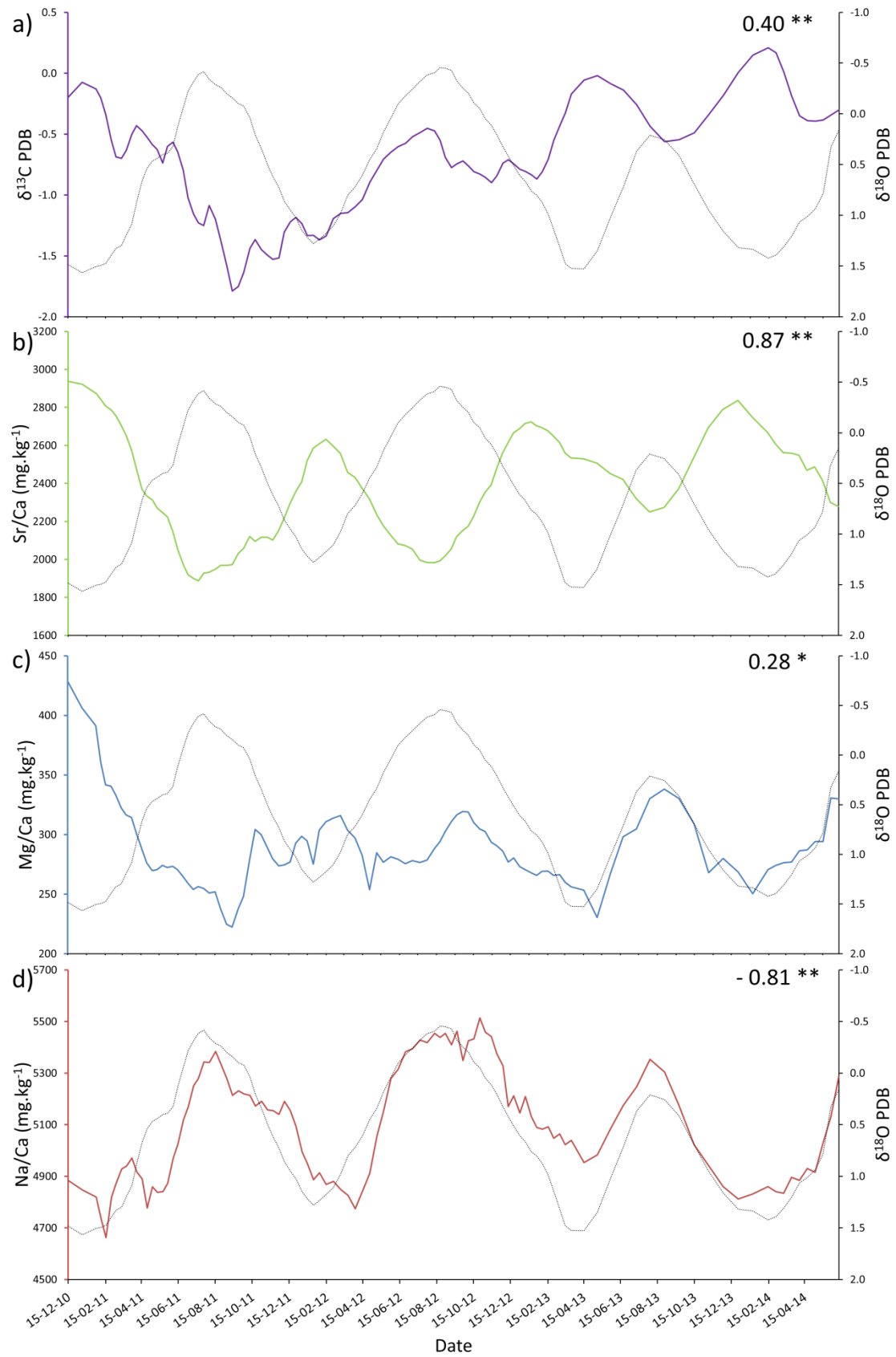


Figure 4.17. Profiles of $\delta^{18}\text{O}$ (dotted black lines) from a single specimen of *Buccinum undatum* from the Menai Strait (MS13–33), overlaid with profiles of $\delta^{13}\text{C}$ (a), purple line), Sr (b), green line), Mg (c), blue line) and Na (d), red line) from the same shell. The Pearson correlation coefficient between the two profiles in each plot is shown as an inset, the significance of the correlations are: * = $p < 0.05$, ** = $p < 0.005$.

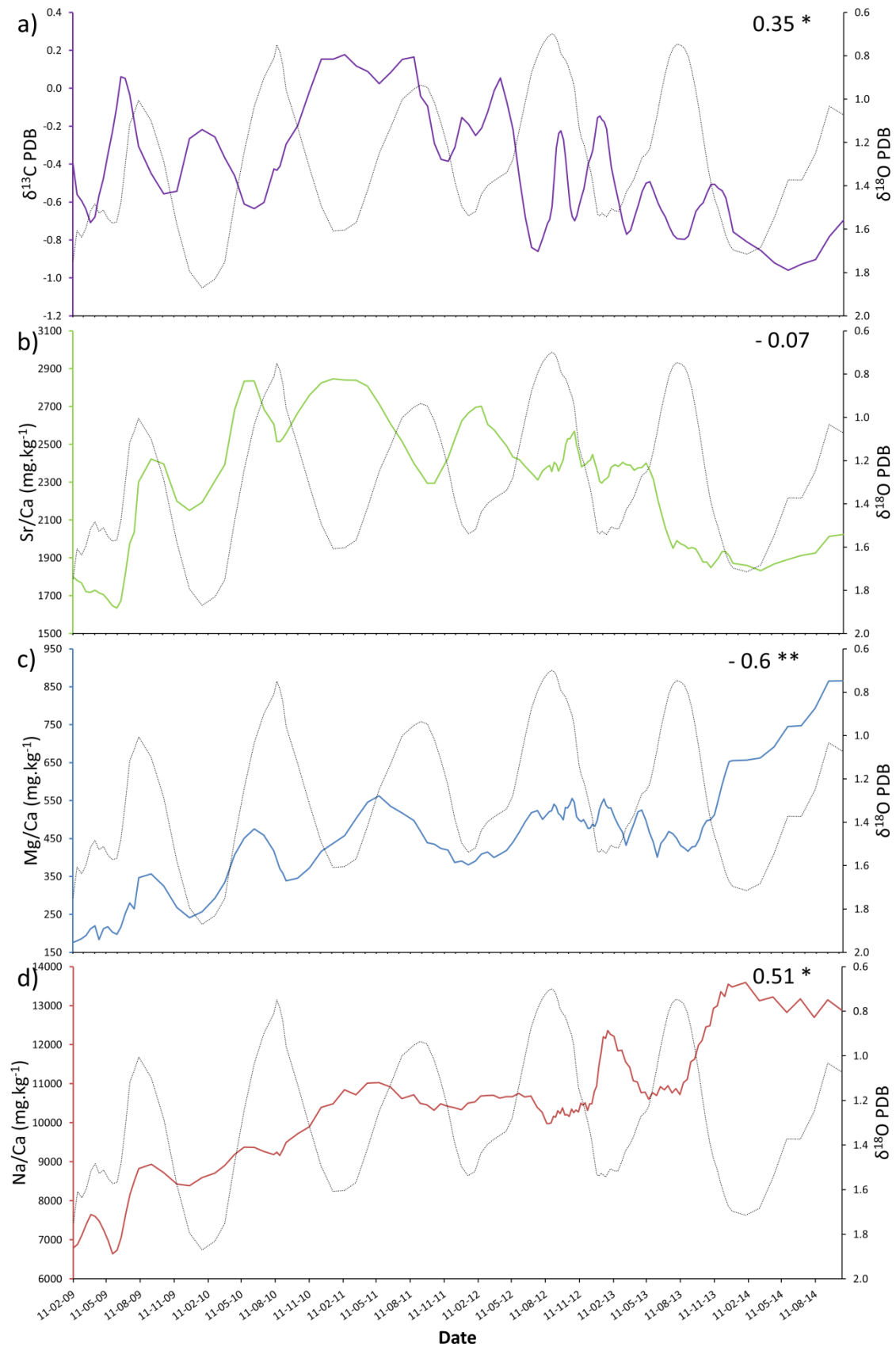


Figure 4.18. Profiles of $\delta^{18}\text{O}$ (dotted black lines) from a single specimen of *B. undatum* from Shetland (SH-32), overlaid with profiles of $\delta^{13}\text{C}$ (a), purple line), Sr (b), green line), Mg (c), blue line) and Na (d), red line) from the same shell. The Pearson correlation coefficient between the two profiles in each plot is shown as an inset, the significance of the correlations are: * = $p < 0.05$, ** = $p < 0.005$.

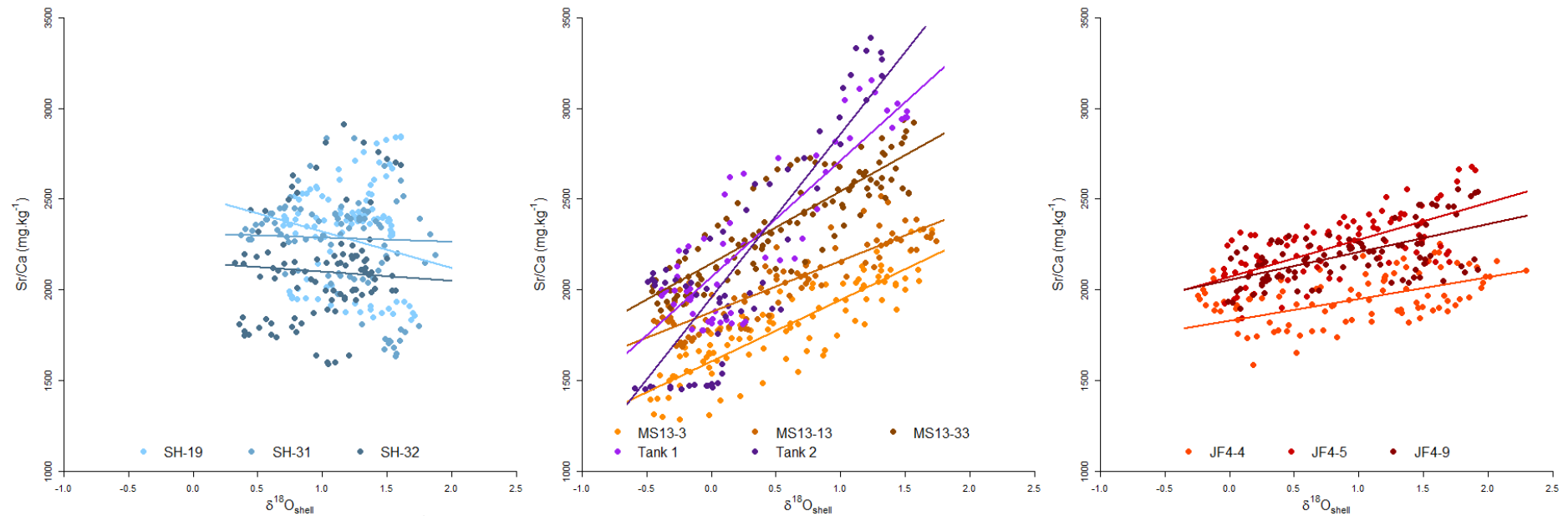


Figure 4.19. Scatter plots of Sr/Ca against $\delta^{18}\text{O}$ for each shell from Shetland (a), male adults from the Menai Strait and laboratory reared juveniles (Tank 1 & 2) (b) and Jersey (c). The data from each shell are fitted with a linear line of best fit of the matching colour.

Table 4.3. Summary data for the trace element and isotopic composition of each of the 3 shells from Shetland (top table) and Jersey (bottom table). The data shown are Pearson correlation coefficients. Coloured cells denote the strength of the correlation, grey – weak, yellow–moderate and orange–strong. Significance of correlations, * = $p < 0.05$, ** = $p < 0.001$.

Shell number			SH-19			SH-31					SH-32				
Elements	Correlation coeff.		Descriptive values (mg.kg ⁻¹)			Correlation coeff.		Descriptive values (mg.kg ⁻¹)			Correlation coeff.		Descriptive values (mg.kg ⁻¹)		
	vs. δ ¹⁸ O	vs. δ ¹³ C	Max.	Min.	Mean	vs. δ ¹⁸ O	vs. δ ¹³ C	Max.	Min.	Mean	vs. δ ¹⁸ O	vs. δ ¹³ C	Max.	Min.	Mean
Li	-0.20*	-0.19*	1.06	0.26	0.77	0.03	-0.22*	2.05	0.62	0.89	-0.45**	0.06	0.98	0.2	0.74
Na	0.54**	-0.27*	13593	6644	10441	0.55**	-0.20	11038	9617	10291	0.51**	-0.24*	13811	10052	11863
Mg	*	-0.31**	849	199	454	0.04	-0.33*	557	402	466	-0.60**	-0.36**	549	200	329
Mn	-0.05	-0.31**	60.63	0.54	6.74	n/a	n/a	n/a	n/a	n/a	n/a	n/a	n/a	n/a	n/a
Fe	-0.46**	0.15	2895	2.1	581	n/a	n/a	n/a	n/a	n/a	0.48**	0.13	140	4.63	32.39
Sr	-0.20*	0.42**	2846	1635	2274	-0.02	-0.22*	3034	2241	2581	-0.07	-0.07	2628	1613	2096
Ba	-0.22*	0.4**	25.54	0.53	6.53	-0.30*	-0.27*	25.85	2.76	7.84	0.29**	0	13.21	2.33	4.73
U	0.05	0.49**	5.95	0.2	2.36	-0.08	0.12	13.67	0.15	2.28	0.36**	-0.07	5.14	2.25	3.64
δ ¹³ C	0.22*	—	0.18	-0.96	-0.44	0.42**	—	0.31	-1.07	-0.52	0.35**	—	-0.26	-1.39	-0.82
δ ¹⁸ O	—	0.22*	1.87	0.7	1.24	—	0.42**	1.63	0.37	1.05	—	0.35**	1.86	0.32	1.09

Shell number			JF4-4			JF4-5					JF4-9				
Elements	Correlation coeff.		Descriptive values (mg.kg ⁻¹)			Correlation coeff.		Descriptive values (mg.kg ⁻¹)			Correlation coeff.		Descriptive values (mg.kg ⁻¹)		
	vs. δ ¹⁸ O	vs. δ ¹³ C	Max.	Min.	Mean	vs. δ ¹⁸ O	vs. δ ¹³ C	Max.	Min.	Mean	vs. δ ¹⁸ O	vs. δ ¹³ C	Max.	Min.	Mean
Li	0.25*	0.16	1	0.39	0.71	0.43**	0.28*	0.58	0.11	0.3	0.69**	0.14	1.07	0.25	0.76
Na	-0.43**	-0.25*	5832	4252	4823	-0.20	-0.11	4835	3370	4128	-0.33*	0.53**	7157	5418	6187
Mg	0.1	-0.06	663	169	350	0.25*	0.44**	543	216	388	0.38**	0.45**	536	273	389
Mn	-0.45**	-0.13	19.96	1.71	11.05	0.23*	-0.49**	51.5	0.64	8.65	-0.23*	-0.69**	73.16	0.9	13.88
Fe	-0.13	-0.31*	434	3.65	95.15	0.18	-0.01	216	4.87	39.11	-0.06	-0.64**	152	6.55	48.53
Sr	0.54**	0.33*	2256	1587	1954	0.71**	-0.08	2677	1845	2221	0.57**	0.04	2555	1895	2198
Ba	-0.14	-0.22*	49	1.18	5.64	0.32*	-0.20	26.77	1.96	5.45	0.56**	-0.26*	11.19	1.15	4.16
U	0.41**	0.11	2.7	0.15	1.14	0.59**	-0.20	3.21	0.29	1.38	0.59**	-0.11	6.18	0.47	2.67
δ ¹³ C	0.03	—	0.94	-1.00	-0.05	0.14	—	0.86	-1.30	-0.12	0.08	—	0.8	-1.82	-0.21
δ ¹⁸ O	—	0.03	2.29	-0.12	1.05	—	0.14	1.9	-0.24	0.73	—	0.08	1.92	-0.01	0.93

Table 4.4. Summary data for the trace element and isotopic composition of each of the 3 analysed shells from the Menai Strait. The top table shows data from the male specimens and the bottom table the female specimens. The data shown are Pearson correlation coefficients. Coloured cells denote the strength of the correlation, grey – weak, yellow–moderate and orange–strong. Significance of correlations, * = $p < 0.05$, ** = $p < 0.001$.

Shell number	MS13–3					MS13–13					MS13–33				
Elements	Correlation coeff.		Descriptive values (mg.kg ⁻¹)			Correlation coeff.		Descriptive values (mg.kg ⁻¹)			Correlation coeff.		Descriptive values (mg.kg ⁻¹)		
	vs. $\delta^{18}\text{O}$	vs. $\delta^{13}\text{C}$	Max.	Min.	Mean	vs. $\delta^{18}\text{O}$	vs. $\delta^{13}\text{C}$	Max.	Min.	Mean	vs. $\delta^{18}\text{O}$	vs. $\delta^{13}\text{C}$	Max.	Min.	Mean
Li	0.49**	0.13	1.94	0.35	0.85	n/a		n/a	n/a	n/a	0.75**	0.2*	0.89	0.43	0.67
Na	0.18	-0.06	4888	2647	3566	-0.69**	0.28*	6243	4656	4997	-0.81*	-0.29*	5515	4663	5098
Mg	0.31*	-0.04	275	102	145	-0.31*	0.21	543	224	324	-0.07*	0.27*	428	222	289
Mn	0.15	0.1	119.16	5.37	43.75	-0.55**	0.13	851.24	6.33	1.49.22	-0.17	-0.21	243	1.4	63.4
Fe	0.18	-0.05	3667	80.12	1291.82	-0.47**	0.25*	3300	63.6	605	0.31*	-0.17*	4599	1.5	1061
Sr	0.87**	0.03	2331	1288	1793	0.88**	-0.04	2518	1687	2031	0.87**	0.48**	2937	1887	2372
Ba	0.41**	-0.10	34.24	2.34	14.74	0.1	-0.31*	16.14	2.33	7.79	0.57**	0	18.23	4.65	8.05
U	0.65**	-0.22*	2.6	0.94	1.45	0.53**	0.11	2.39	0.88	1.6	0.52**	-0.10	4.09	1.24	2.89
$\delta^{13}\text{C}$	-0.01	-	0.07	-1.35	-0.73	-0.13	-	0.37	-1.02	-0.29	0.4*	-	0.21	-1.79	-0.73
$\delta^{18}\text{O}$	-	-0.01	1.71	-0.47	0.54	-	-0.13	1.74	-0.44	0.52	-	0.4*	1.57	-0.46	0.57

Shell number	MS13–7					MS13–23					MS10–6				
Elements	Correlation coeff.		Descriptive values (mg.kg ⁻¹)			Correlation coeff.		Descriptive values (mg.kg ⁻¹)			Correlation coeff.		Descriptive values (mg.kg ⁻¹)		
	vs. $\delta^{18}\text{O}$	vs. $\delta^{13}\text{C}$	Max.	Min.	Mean	vs. $\delta^{18}\text{O}$	vs. $\delta^{13}\text{C}$	Max.	Min.	Mean	vs. $\delta^{18}\text{O}$	vs. $\delta^{13}\text{C}$	Max.	Min.	Mean
Li	0.51**	-0.46**	0.75	0.26	0.51	0.68**	0.16	0.93	0.56	0.73	0.53**	-0.34**	1.95	0.39	1.13
Na	-0.85**	0.14	5387	4583	4915	-0.63**	-0.52**	6369	4819	5351	-0.44**	-0.01	4934	2711	4160
Mg	-0.31*	-0.57**	305	158	227	-0.55**	0.31*	317	174	225	0.43**	-0.04	763	354	520
Mn	-0.09	-0.77**	119	1.61	27.32	-0.21*	-0.33*	46.92	0.92	12.64	-0.02	-0.01	242	1.04	57.58
Fe	-0.07	-0.66**	2767	13.89	8.06	-0.17	-0.64**	2502	1.04	429	-0.11	0.27*	4340	4.08	1084
Sr	0.74**	-0.09	2606	1940	2248	0.46**	0.02	2642	1857	2152	0.47**	-0.03	2637	1634	2115
Ba	0.37**	-0.76**	12.03	5.1	8.06	0.26*	-0.45**	11.82	2.09	5.79	-0.12	0.27*	38.23	7.07	17.02
U	-0.30*	-0.68**	4.05	0.06	1.47	-0.11	-0.52**	4.27	0.37	2.09	0.15	0.27*	2.62	0.31	1.52
$\delta^{13}\text{C}$	0.07	-	0.48	-1.91	-0.54	-0.03	-	0.43	-1.85	-0.30	-0.35**	-	2.06	-0.05	0.88
$\delta^{18}\text{O}$	-	0.07	1.68	-0.46	0.58	-	-0.03	1.79	-0.76	0.73	-	-0.35**	0.2	-2.31	-1.14

Table 4.5. Summary data for the trace element and isotopic composition of 2 analysed shells from the laboratory reared *Buccinum undatum*. The data shown are Pearson correlation coefficients. Coloured cells denote the strength of the correlation, grey – weak, yellow–moderate and orange–strong. Significance of correlations, * = $p < 0.05$, ** = $p < 0.001$.

Shell number	T1					T1				
	Correlation coeff.		Descriptive values (mg.kg ⁻¹)			Correlation coeff.		Descriptive values (mg.kg ⁻¹)		
	vs. $\delta^{18}\text{O}$	vs. $\delta^{13}\text{C}$	Max.	Min.	Mean	vs. $\delta^{18}\text{O}$	vs. $\delta^{13}\text{C}$	Max.	Min.	Mean
Li	0.61**	0.37*	0.68	0.36	0.53	0.54**	0.25*	0.73	0.22	0.53
Na	-0.53**	-0.53**	9660	7082	8276	-0.04	-0.30*	10131	7694	8773
Mg	-0.38*	-0.39*	323	126	223	0.2	-0.16	380	99	203
Mn	0.08	0.15	40.85	0.35	8.23	-0.35*	0.19	11.09	1.07	2.6
Fe	-0.03	0.27*	94.7	2.69	34.33	0.17	0.41*	29.96	5.97	19.57
Sr	0.78**	0.7**	3154	1689	2264	0.75**	0.55**	3390	1452	2135
Ba	0.4*	0.44**	19.14	1.57	6.42	0.47**	0.47**	35.77	0.8	8.82
U	0.65**	0.49**	2.19	0.74	1.45	0.41*	0.16	7.4	3.86	5.27
$\delta^{13}\text{C}$	0.68**	–	-1.17	-1.90	-1.60	0.32*	–	-0.92	-2.19	-1.63
$\delta^{18}\text{O}$	–	0.68**	1.52	-0.39	0.33	–	0.32*	1.58	-0.59	0.26

There were also differential levels of incorporation of elements between sites. Elements such as Mg and Sr had similar average values across all the sites, however Na and Fe did not. Profiles of Na from the Shetland whelks exhibited far higher rates (average $\approx 10,000$ mg.kg⁻¹) when compared with the Jersey and Menai Strait whelks which were quite similar (average between 4000–6200 mg.kg⁻¹). Interestingly, concentrations of Na in laboratory reared shells was elevated (averages of 8200 and 8800 for T1 and T2 respectively) compared with the field collected whelks. Concentrations of Fe also differed between sites with maximum values in the Menai Strait shells that far exceeded those seen in any of the shells from the other two sites or in the laboratory reared shells i.e. a maximum (2500 to 4600 mg.kg⁻¹) for the Menai strait shells was seen compared with between 30 and 250 mg.kg⁻¹ everywhere else. There was one notable exception to this pattern with a single Shetlands specimen (SH-19) exhibiting a high concentration of Fe (maximum 2800 mg.kg⁻¹).

4.3.4.5 Trace element vs. trace element relationships

Table 4.6 summarises the relationships between several trace elements in the whelk shells. There are clear intra- and inter-site differences in the trace elements. For a majority of whelk shells, positive relationships were found between Sr & Ba and Mg & U. The strong and moderate relationships seen between Sr and U across all the sites are shown in Figure 4.20 and it is clear that these relationships are not universally similar. Mostly negative relationships are seen

between Sr and Na (aside from the Shetland samples). Several strong positive relationships are seen between both Na - Mg and Mn - Fe (the latter again excluding Shetland).

4.3.4.6 Differential strontium incorporation in male and female whelks

Figure 4.21 demonstrates the disassociation of the Sr shell profile from the $\delta^{18}\text{O}$ profile in the female whelks from the Menai Strait in the later years of shell growth (i.e. towards the shell lip). The Pearson's correlation coefficients between Sr and $\delta^{18}\text{O}$ for the 2.5 year period shown in Figure 4.21 are summarised in Table 4.7. The correlation coefficients for the female shells without the disassociated periods included and for the disassociated period alone can also be seen. With the removal of the disassociated period the correlations greatly improve.

4.3.4.7 Iron and manganese incorporation into shells

For the six adult shells sampled from the Menai Strait, clear ontogenic decreases in Fe and Mn were observed (Figure 4.22). Whilst the values of Fe were much higher and less variable across whelks (maximum values of 4600–2500 mg.kg^{-1} for Fe and 850–46 mg.kg^{-1} for Mn) the same patterns were observed, resulting in highly correlated Fe and Mn concentrations in whelk shells from the Menai Strait. There appears to be a positive correlation between Fe and $\delta^{18}\text{O}$ during early ontogeny (before winter 2012) for 3 of the shells (MS13–3, MS13–33 & MS10–6 with Pearson's correlations of 0.59, 0.90 and 0.80 respectively). Ontogenetic negative correlations and decreases in Fe were seen in two of the specimens from Jersey although the total concentrations of Fe were much lower than in the Menai Strait shells (maximums of 180 and 140 mg.kg^{-1}). One whelk shell from Shetland exhibited a moderate negative correlation (-0.64) between Fe and $\delta^{18}\text{O}$ before winter 2012 instead of a positive correlation seen in the shells from Menai Bridge.

4.3.4.8 Productivity

To investigate correlations between isotope and trace element profiles and productivity, profiles of $\delta^{13}\text{C}$, Li, Mn and Ba were visually inspected for peaks in concentrations before the summer maximum seawater temperature (April and July) during a typical season for spring algal blooms (Blight, 1996; Freitas *et al.*, 2016; <http://www.foodstandards.gov.scot/>); no consistent patterns could be found in the shells for any of the inspected trace elements for any of the sites.

Table 4.6. Pearson's correlation coefficients of relationships between trace elements for each sampled shell. Coloured cells denote the strength of the correlation, grey – weak, yellow–moderate, orange–strong and red–very strong. SH: Shetlands, J: Jersey, MS: Menai Strait and T1 & T2: Laboratory reared. Significance of correlations, * = $p < 0.05$, ** = $p < 0.001$.

Elements	Sample number					
	SH-19	SH-31	SH-32	JF4-4	JF4-5	JF4-9
Sr vs. Li	0.39**	0.66**	0.39**	0.35**	0.36**	0.09
Sr vs. Na	0.07	0.58**	0.01	-0.36**	-0.23*	-0.20*
Sr vs. Mg	0.16	0.62**	0.2*	0.55**	0.33*	0.42**
Sr vs. Ba	0.7**	0.11	n/a	-0.39**	0.47**	0.57**
Sr vs. U	0.64**	-0.39**	0.36**	0.79**	0.93**	0.73**
Na vs. Mg	0.86**	0.85**	0.68**	-0.08	-0.42**	0.44**
Mn vs. Fe	-0.46**	n/a	n/a	0.62**	0.43**	0.84**

	MS13-3	MS13-13	MS13-33	MS13-7	MS13-23	MS10-6
Sr vs. Li	0.43**	-0.15	0.72**	0.34*	0.35**	0.16
Sr vs. Na	0.42**	-0.38**	-0.66**	-0.85**	-0.41**	-0.56**
Sr vs. Mg	0.14	0.05	0.41**	-0.13	-0.11	0.74**
Sr vs. Ba	0.34**	0.13	0.58**	0.7**	0.67**	0.52**
Sr vs. U	0.58**	0.73**	0.48**	0.45**	0.43**	0.84**
Na vs. Mg	0.46**	0.76**	-0.17	0.25*	0.02	-0.48**
Mn vs. Fe	0.89**	0.85**	0.63**	0.85**	0.78**	0.87**

	T1	T2
Sr vs. Li	0.6**	0.71**
Sr vs. Na	-0.70**	-0.11
Sr vs. Mg	-0.44**	0.19
Sr vs. Ba	0.72**	0.53**
Sr vs. U	0.84**	0.44**
Na vs. Mg	0.82**	0.77**
Mn vs. Fe	0.6**	0.33*

Table 4.7. Correlations between $\delta^{18}\text{O}$ and Sr for the *Buccinum undatum* shells shown in Figure 4.21. For the female shells which exhibit a disassociation, correlations were also performed on the sections excluding the disassociated data, and the disassociated data alone. Coloured cells denote the strength of the correlation, yellow–moderate, orange–strong and red–very strong.

		Full 2.5 years	Excluding Disassociated portion	Disassociated alone
Male	MS13-3	0.915		
	MS13-13	0.913		
	MS13-33	0.851		
Female	MS13-7	0.728	0.822	0.285
	MS13-23	0.406	0.900	0.016
	MS10-6	0.423	0.820	-0.388

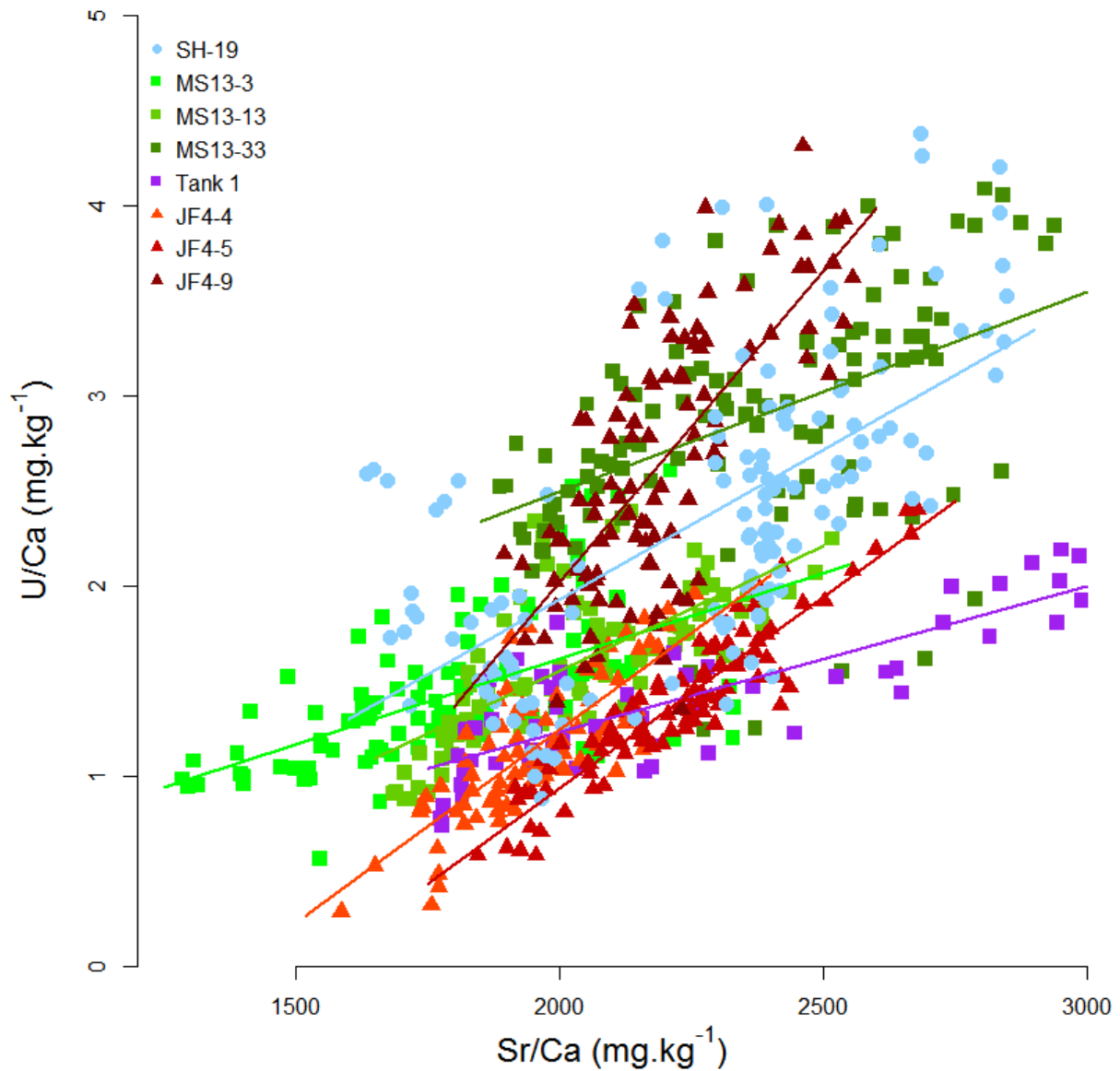


Figure 4.20. A scatter plot of Sr/Ca against U/Ca for all male shells from the Menai Strait, one laboratory reared juvenile shell (Tank 1, squares), Jersey (triangles) and one shell from Shetland (circles). The data from each shell are fitted with a linear line of best fit of the matching colour.

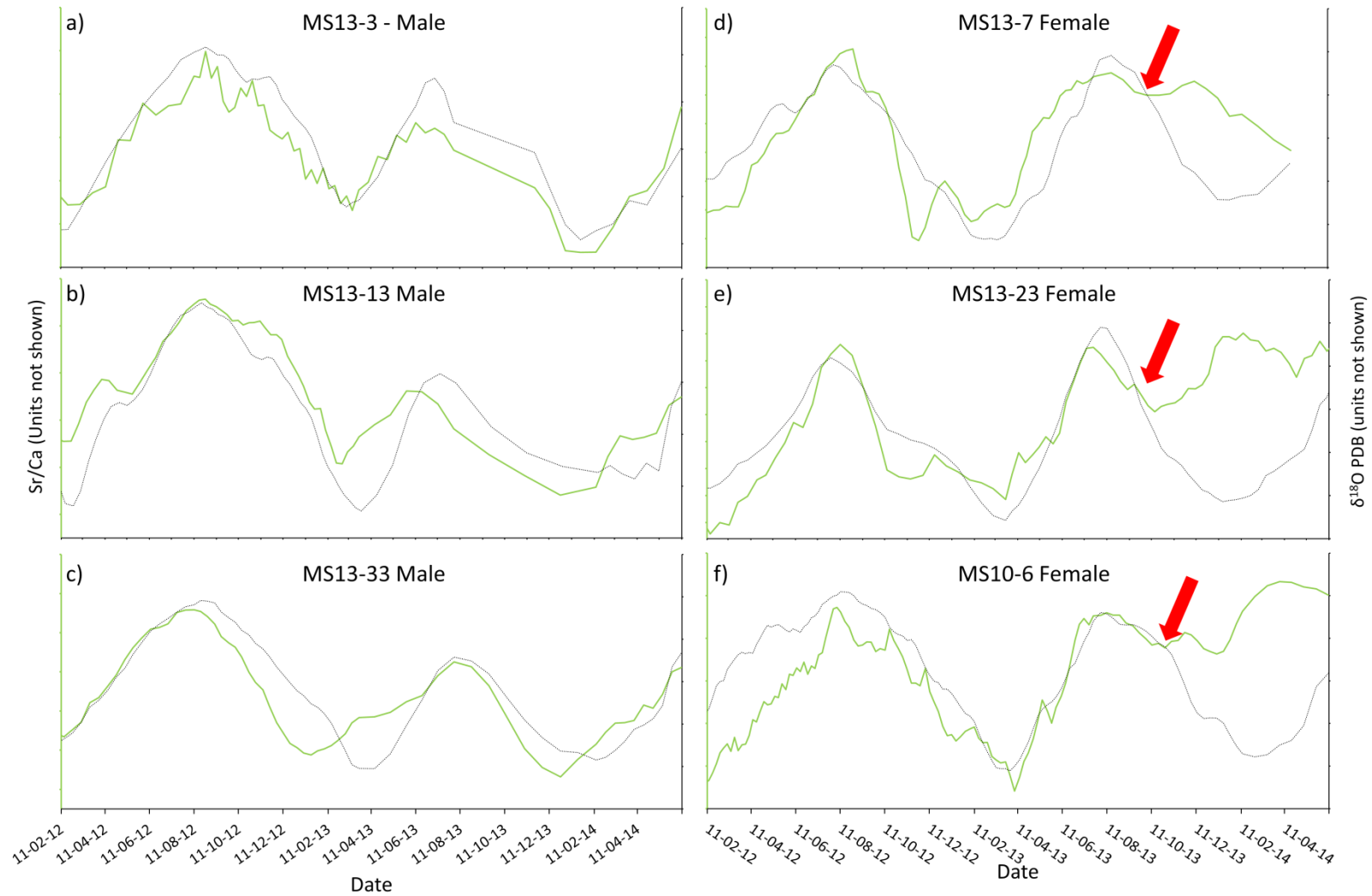


Figure 4.21. Overlaid plots of $\delta^{18}\text{O}$ (dotted black lines) and Sr (green lines) from male (a, b & c) and female (d, e & f) *Buccinum undatum* from the Menai Strait covering the most recent ≈ 2.5 annual cycles of shell growth. The absolute values on the y axis are not shown as different axis limits were needed to achieve the best visual agreement between the two profiles. Red arrows indicate clear disassociation points between the two profiles in the female specimens but not in the males. All y axes are inverse to represent seawater temperature.

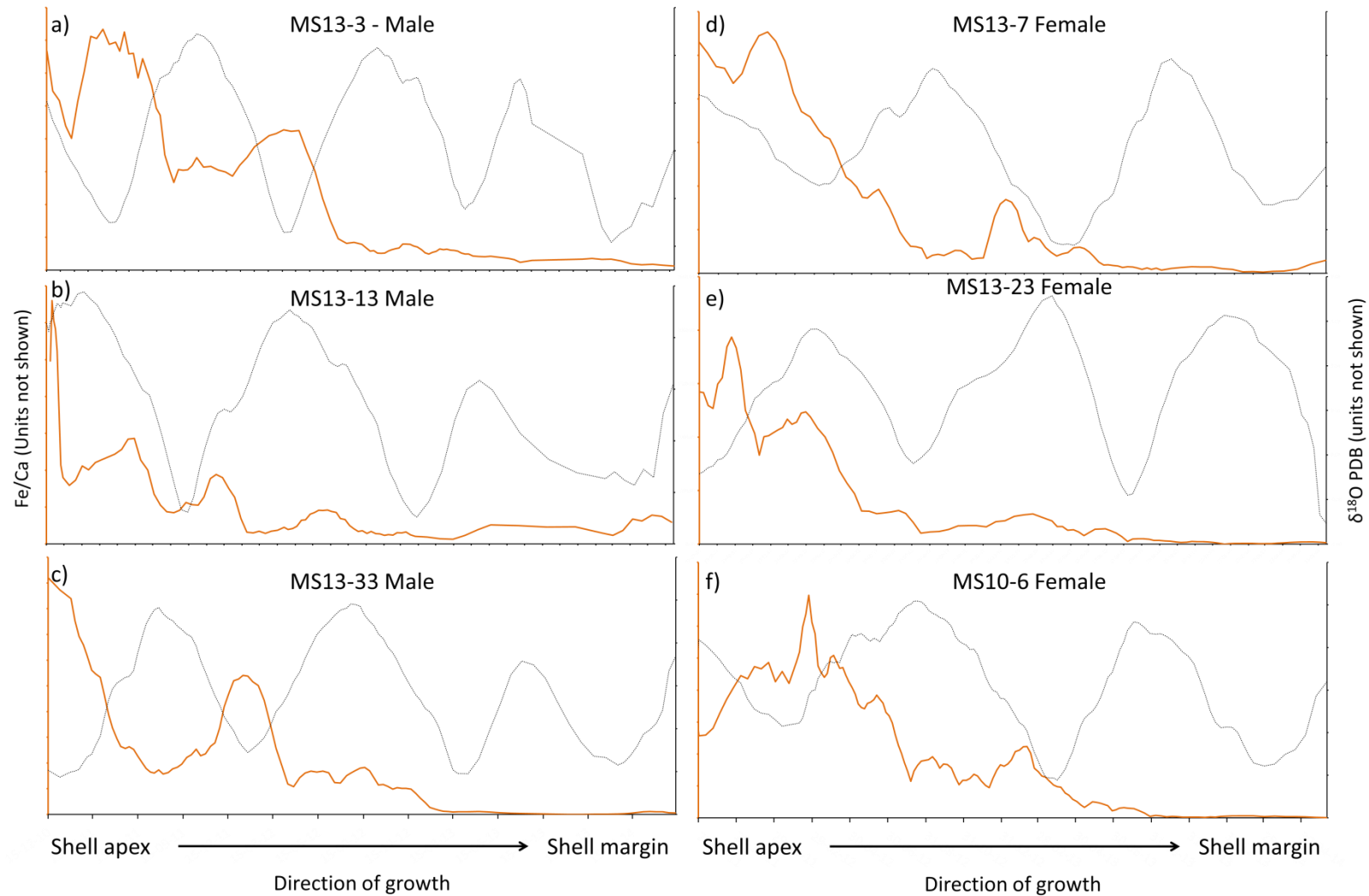


Figure 4.22. Overlaid plots of $\delta^{18}\text{O}$ (dotted black lines) and Fe (orange lines) from male (a, b & c) and female (d, e & f) *Buccinum undatum* from the Menai Strait covering the most recent ≈ 2.5 annual cycles of shell growth. The absolute values on the y axis are not shown as differing axis limits were needed to achieve the best visual agreement between the two profiles. Red arrows indicate clear disassociation points between the two profiles in the female specimens. $\delta^{18}\text{O}$ y axes are inverse to represent water temperature.

4.3.4.9 Salinity

The influence of salinity on Na and Ba were investigated. Sparse salinity data were obtained for the Menai Strait with a range of 32–33.6 PSU (Practical Salinity Unit), and the average salinity value for the waters surrounding Jersey is around 34 PSU (Pers. Comm. Paul Chambers, Jersey Department of the Environment). High resolution salinity data (weekly) were available for the Shetlands (with a range of 33.5–35.3 PSU) and the laboratory reared whelks (range 32.5–33.5 PSU). The correlations between salinity and selected trace elements can be seen in Table 4.8. Moderate negative relationships are clearly visible between salinity and Na in whelks from the Shetlands (-0.48 to -0.53), coupled with weak and moderate positive relationships between Ba and salinity in two of these whelks (0.32 & 0.51). The same relationships were not found in laboratory reared animals with only very weak positive relationships found between Ba and salinity (0.13 & 0.20). Even though moderate negative relationships were found between Na and salinity in Shetland, it is still unclear whether this was the true and/or sole driver behind the variation as there was also a good relationship between Na and $\delta^{18}\text{O}$ of approximately the same magnitude. Salinity and seawater temperature also co-vary over an annual seasonal cycle in whelks from Shetland (Figure 4.25) with a moderate positive correlation (0.50). High resolution (weekly) salinity data for the Menai Strait were available but covered a time period between late 2009 and late 2011, insufficient to compare a large enough sample size with the Menai Strait shell data. However, within these salinity data there was a clear covariation between seawater temperature and salinity in the Menai Strait and a similar salinity range to Shetland (30–34.5 and 31.2–35 respectively).

Table 4.8. Pearson's correlations between salinity and selected trace elements for laboratory reared *Buccinum undatum* (T1 & T2) and field collected whelks (SH-19, SH-31 & SH-32) from Shetland. Coloured cells denote the strength of the correlation, grey – weak, yellow–moderate. Significance of correlations, * = $p < 0.05$, ** = $p < 0.001$.

	SH-19	SH-31	SH-32	T1	T2
Na vs. Salinity	-0.53**	-0.50**	-0.48**	0.09	0.00
Ba vs. Salinity	0.32*	0.03	0.51**	0.13	0.20

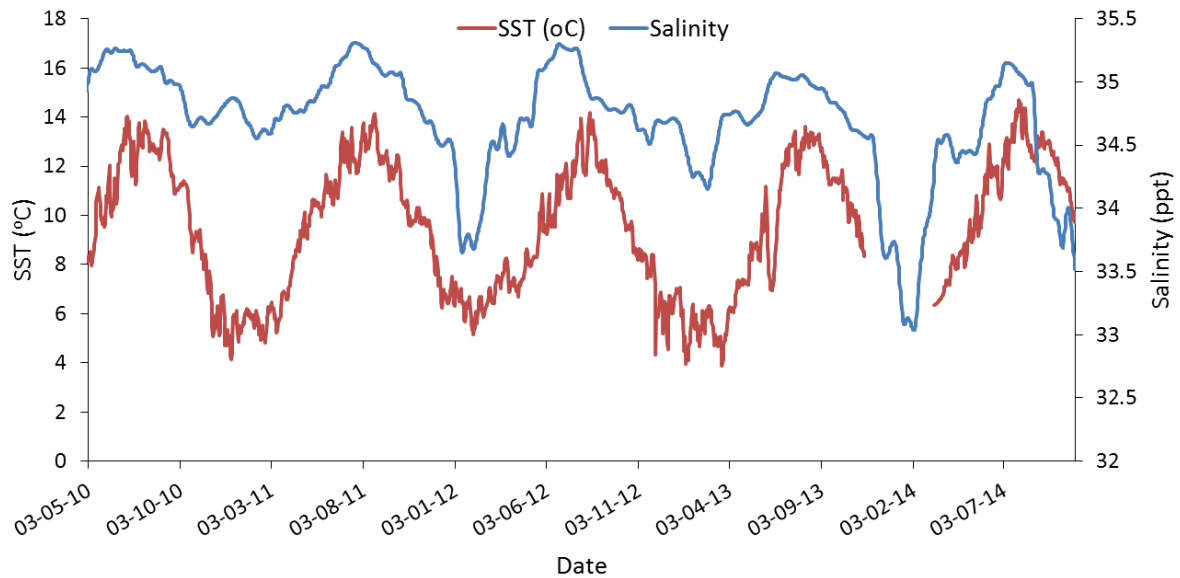


Figure 4.23. The relationship between sea surface salinity (SSS) (blue line) and SST (red line) for the Shetlands. The Pearson's correlation between the two profiles is 0.5.

4.4 Discussion

4.4.1 Palaeotemperature equation calibration

The calibration of the palaeotemperature equation from *B. undatum* shells in the current study resulted in an equation very similar to the Leng and Marshall (2004) reorganisation of Kim and O'Neil (1997). In itself, this result is at odds with much of the published literature as the Kim and O'Neil equation was calibrated using laboratory precipitated calcite and not aragonite. This is a similar finding to Wanamaker *et al.* (2007) who found no difference between their calibrated equation for shells of the mussel (*Mytilus edulis*) and Kim and O'Neil (1997). However, the samples they used for the analysis were from the calcitic portion of *M. edulis* shells. The commonly used equation for aragonite shells (both bivalve and gastropod) is the Grossman and Ku (1986) calibration which was calculated using biogenic aragonite (e.g. Sosdian *et al.*, 2006; Schöne *et al.*, 2007; Reynolds *et al.*, 2013). In the case of the whelks in this study, the Grossman and Ku (1986) equation significantly overestimated the seawater temperatures, as did the original equation of Epstein *et al.* (1953) and Craig (1965), which were calibrated using a mixture of both biogenic aragonite and calcite. This result would normally suggest that the composition of the shell is in fact calcite. However, *Buccinum undatum* shells are composed of aragonite and this has been confirmed using Raman spectroscopy (Chapter 3). The high concentration of Sr and lower concentration of Mg in the shells also support an aragonite composition (Schöne *et*

al., 2010). The unsuitability of the Grossman and Ku (1986) equation is most likely due to a species specific calcification process which overrides the normally seen differences in fractionation between calcite and aragonite. This difference may be due to vital effect(s), but perhaps it is more likely due to a kinetic isotope effect at the site of mineralisation (see Figure 4.2) that is linked to rapid shell calcification seen in *B. undatum* (Colvin, 2016).

4.4.2 Reconstruction of palaeotemperature from field collected shells

The calibrated *B. undatum* equation undoubtedly produced the closest match to the observed seawater temperatures for the laboratory reared whelks with an average 0.004 °C deviation from the observed temperature and a profile which covered 97.74% of the observed seawater temperature range. When this new equation was applied to isotope profiles from field collected *B. undatum* it also accurately reconstructed the observed SST records from shells of the Menai Strait and Jersey whelk populations (covering 80.63% and 89.75% of the observed SST range respectively). However the Shetland reconstruction was not as accurate (63.5% of the observed SST range). There are several possible explanations for this, firstly, the $\delta^{18}\text{O}_{\text{water}}$ calculated during the sensitivity analysis was not accurate. This is unlikely as the calculated value for Shetland (0.25) fell within the range of isotope values in seawater samples from the Faroe–Shetland channel during the period between 2009 and 2013 (0.04–0.6, McKenna *et al.*, 2016; B. Berx, Marine Scotland, Pers. Comm.). The channel is roughly 160 km away from the study site and due to the strong current flows will have an influence on the study site itself. There is therefore, likely an annual periodicity to the $\delta^{18}\text{O}_{\text{water}}$ values, although it is usual practice to use a single $\delta^{18}\text{O}_{\text{water}}$ value during the palaeotemperature reconstruction for a full annual cycle (e.g. Hermoso *et al.*, 2016). However by analogy with other sites, this value will likely change throughout the year. A clear annual periodicity was seen in the salinity of the seawater around Shetland and it is possible to reconstruct $\delta^{18}\text{O}_{\text{water}}$ from salinity values using a salinity mixing line equation. However, this requires a range of $\delta^{18}\text{O}_{\text{water}}$ values from a range of salinities at a single site (e.g. Cage & Austin, 2010), something that was not available during this Ph.D. and so no reconstruction of $\delta^{18}\text{O}_{\text{water}}$ was possible. The measured $\delta^{18}\text{O}_{\text{water}}$ values from the Menai Strait that were used in the palaeotemperature calibration of the whelk shells from this location did not exhibit a clear annual cyclicity. This is similar to the findings of Owen *et al.* (2002a) who found no annual cycle in the $\delta^{18}\text{O}_{\text{water}}$ profile of Menai Strait seawater. Another possible explanation is that the temperature range experienced by the whelks from Shetland was less than that recorded by the SST logger. Significantly, the whelks from Shetland were obtained

from a site deeper than either the Menai Strait or Jersey and may well have been buffered from the temperature extremes recorded in the surface waters, resulting in an isotopic profile with a lower range than the observed SST profile.

The final possible explanation for the poorer seawater temperature reconstruction observed in the Shetland whelks may be because there was a cessation of growth during the winter seawater temperature minima. It is likely that the growth of *B. undatum* slows or even ceases during the cold winter season as their metabolism drops below a critical level. This has been noted in many mollusc species (Lutz & Rhoades, 1977; Schöne *et al.*, 2005) and often results in the formation of a growth line or annulus in the shell (Richardson, 2001). The feeding and growth rates of laboratory reared *B. undatum* (Pers. Obs.) slow at colder seawater temperatures, although it is not yet known whether there is complete cessation of growth during these cold periods or just a decrease. If this is the case, then a gap in the seasonal seawater temperature reconstructions should be inserted to mimic a period of growth cessation that occurs during each winter minima reconstruction. In the Menai Strait, however, the observed seawater temperatures were as cold as those in the Shetlands, yet the seawater temperature reconstructions in the Menai Strait whelks accurately and closely matched the measured seawater temperature, so it is less likely an explanation as it was not apparent at this site.

4.4.3 Growth rate analysis

The annual growth rate of *B. undatum* differed greatly between sites, with the Menai Strait whelks showing the fastest growth in the second year of life. Both the Menai Strait and Shetland whelk shells grew faster than those from Jersey. Seasonal growth rate in the Menai Strait whelks did not follow a clear winter-spring (season 1): summer – autumn (season 2) shell growth pattern. In the 3 Shetland whelks the majority of shell growth occurred following the summer maximum seawater temperature (season 2); the opposite occurred in the Jersey whelks with the majority of growth in the spring early summer (season 1). These observed differences in the season of shell growth are likely related to seawater temperature. As the Shetland whelks grew faster than the Jersey whelks it is probable that there is an optimum temperature range for shell growth to occur, somewhere below the summer maximum for Jersey (19°C). Whelks in Shetland have a larger window of optimum growth as they live in waters with an annual seawater temperature range between 5 and 14°C. *Buccinum undatum* is a boreal species so optimum

shell growth is unlikely to occur at the warmest seawater temperatures during the warmest season of the year (summer). Shell growth is more likely to occur between the winter minimum and summer maximum (season 1). Unlike bivalves which are reliant on food abundance in the water column (which constrains shell growth to particular periods of the year when food is available), food supply for predatory and scavenging gastropods (such as *B. undatum*) is unlikely to be influenced by seawater temperature, minimising the impact of food availability on annual growth rates. Growth rate in the laboratory reared whelks displayed a clear seasonal pattern during the 1st year of growth, with slower growth in season 1 compared to season 2 and explains the slow 1st year of growth seen in adult whelks from the Menai Strait. It is unclear what causes this slow initial growth, but it is likely due to the seawater temperature at the time of hatching which occurs in the Menai Strait at the coldest seawater temperatures during the annual seasonal cycle (see Chapter 2).

4.4.4 Trace element analyses

Clear variations in all trace element shell profiles were found both between sites and between individuals from a single site. As discussed in the introduction, there is much debate surrounding the reliability of most trace element proxies within mollusc carbonates. The picture is further complicated by the highly varied results presented in this chapter. The potentially most promising trace element was Sr, this element showed a strong or moderate positive relationship with $\delta^{18}\text{O}$ (therefore inverse to water temperature) in 11 of the 14 shells sampled. Unfortunately, there was not a universally strong relationship across all samples, making its future use as a water temperature proxy in this species problematic and unreliable. Even within the Menai Strait population where the whelk shells showed the strongest relationship between Sr and seawater temperature, there were clear differences in Sr incorporation between male and female whelk shells. A disassociation between Sr and $\delta^{18}\text{O}$ occurred in the shells of all the female whelks following the summer maximum temperature in their 3rd year of life (i.e. 2.5 years old). When the total distance of shell deposited, covered by the disassociated Sr section, was subtracted from the TLE measurement for each shell, the Sr disassociation was estimated to occur between 65 and 70 mm TSL. Back calculating further to the preceding spring when it is assumed that whelks first show signs of entering the reproductive cycle (see Martel *et al.*, 1986), the TSL drops to 59–62 mm for each female whelk which is close to the size at maturity for females at this site (51.4 – 62.8 mm over a seasonal cycle, 57.2 in winter when these samples were collected, see Chapter 2, section 2.3.1.1). It is possible that the disassociation of Sr and

$\delta^{18}\text{O}$ observed in the shells of the females is indicative of an event in the reproductive cycle, specific to females, that occurs after the summer maximum temperature. It is likely that this time period in the Menai Strait marks the end of the copulation period when the females begin to prepare to lay their egg masses which is likely coupled with a distinct change in their physiology. For example there may be a change in energy allocation when the whelk switches from shell growth to egg capsule production. It is therefore likely that the disassociation between Sr and $\delta^{18}\text{O}$ seen in the Menai Strait female whelk shells is controlled by a physiological response to the egg laying event in the reproductive cycle and this may, with further study, reveal that female whelks from other sites have a similar pattern. Shells from male whelks from the Shetlands did not display a clear relationship between Sr and $\delta^{18}\text{O}$ and the profiles seen in male whelk shells from Jersey were not consistently well correlated over the whole growth period. Strontium and growth rate have been found to correlate in the aragonitic gastropod, *Conus ermenius* (Sosdian *et al.*, 2006; Gentry *et al.*, 2008). Unfortunately, accurate growth rates for *C. ermenius* were not shown on a sample by sample basis due to the methodology used to assign dates to the elemental profiles. Nevertheless an ontogenetic change in Sr occurred as shell growth rate slowed over time (Sosdian *et al.* 2006). There are two major differences between the Sosdian *et al.* (2006) study of *C. ermenius* and this study of *B. undatum* shell biogeochemistry. First, an ontogenetic decline in Sr was not observed in any of the fourteen *B. undatum* shells sampled and second the relationship between Sr and temperature in *C. ermenius* was the inverse of the one described here for *B. undatum*. This clearly demonstrates the difficulty of finding an inter- and intra-species commonality between strontium and seawater temperature amongst gastropod shells.

Correlations between Na and $\delta^{18}\text{O}$ showed strong and moderate positive correlations in 7 out of 14 whelk shells and weak negative correlations in a further 2 shells suggesting a possible relationship between Na and seawater temperature. If an annual seasonal cyclicity in salinity is assumed for each of the 3 locations with more saline coastal waters during the summer periods (as seen in the salinity records from the Menai Strait and Shetlands) then it is highly likely that the annual cyclicity of Na seen in many of the whelk shells may be directly related to salinity. Similar patterns of Na incorporation in mollusc shells have been observed in other studies (e.g. Findlater *et al.*, 2014 – various marine bivalve species; O’Neil & Gillikin, 2014 - *Elliptio complanata*). However, whilst a clear seasonal pattern in salinity is observed at the Shetland site, the pattern of Na incorporation in 2 whelk shells is inverse to that seen in shells from all of

the other sites, with positive relationships with $\delta^{18}\text{O}$ and therefore a negative relationship with both SST and salinity. This scenario is further confused when the total amounts of Na within the shells are considered. Specimens from Shetland exhibited a higher concentration of Na in their shells than any other site with 45–62 % higher maximum values than any whelk shell from the Menai Strait or Jersey. The laboratory reared whelks also exhibited a higher concentration of Na than whelks from the adjacent Menai strait (35–50 % higher maximum values) even though the seawater in which the laboratory reared animals were reared was sourced directly from the Menai Strait and had the same annual salinity range. The only conclusion that can be reached is that Na incorporation is likely under physiological control in the shells of *B. undatum*. The particular physiological driver is unclear as no pattern was seen across sites, instead of an offset at a particular site, a total reversal in incorporation patterns and a large increase incorporation were seen with no discernibly large differences in either the salinity or temperature shell profiles at each site.

No consistent patterns were seen in potential proxies for productivity i.e. Li, Mn/Fe and Ba. Each shell profile from each of these elements was examined for peaks during the spring season that might coincide with the spring algal bloom. It is known that there is a regular seasonal spring algal bloom in the Menai Strait and Shetland (Blight, 1996; Freitas *et al.*, 2016; <http://www.foodstandards.gov.scot/>). Profiles of Li and Ba displayed moderate and strong correlations with $\delta^{18}\text{O}$, indicating some kind of temperature control on Li and Ba incorporation but only in shells from the Menai Strait, Jersey and in the laboratory reared animals. By contrast these elements in the Shetland shells were either weak or negatively correlated with spring temperatures i.e. the reverse of the relationships from the other sites. Interestingly, strong positive relationships were often seen between Li, Ba and Sr at all sites (but not all shells). This suggests that whilst the trace element profiles of Li and Ba are not necessarily correlated with temperature, they appear to be under similar physiological control to Sr, although with no disassociation of Li or Ba was seen in the female specimens from the Menai Strait relating to maturity. This lack of correlation between productivity proxies in the shells of *B. undatum* is not unexpected as they are both carnivorous (Scolding *et al.*, 2007) and scavenging gastropods that do not directly rely on surface water productivity. Productivity proxies have been reported in the shells of bivalves that rely on phytoplankton as a primary food source (e.g. Thébault *et al.*, 2009b). However, it is currently unknown whether the consumed phytoplankton or the environmental chemistry of the seawater associated with primary production are the sources of

Li or Ba that are incorporated into the mineralising shell. The fact that *B. undatum* does not show a productivity signal suggests that it is the phytoplankton that are consumed by suspension feeding bivalves and not the seawater chemistry that are the source of the Li and Ba in the shell.

Manganese and Fe displayed no patterns of note in shells from Jersey and most of the shells from Shetland. However, a single shell from Shetland and all of the shells from the Menai Strait showed a clear ontogenetic decrease in these elements with after the second year of life. The patterns in several shells correlated significantly with $\delta^{18}\text{O}$ before the ontogenetic decrease, indicating some form of temperature control before the decrease began. This pattern does not fit with the theory that the whelk shell may be recording incidences of Fe and Mn release into the surrounding water and sediment due to the breakdown of organic matter, possibly following plankton blooms. Pilkey and Goodell (1963) found an inverse relationship between Fe, Mn and seawater temperature in the shells of the aragonitic gastropod *Busycon contrarium*. No ontogenic decrease in the concentration of either element was observed, however they did also note that Fe and Mn were correlated. This is similar to the observations in this study in which Fe and Mn correlated in 11 of the 14 shells, even when a temperature correlation was not apparent. The shells from Shetland again showed an inverse pattern to this. The decrease in Mn and Fe with ontogeny has potentially two explanations: Firstly, the animals preferentially incorporated less of these elements over time due to some kind of ontogenetic physiological control, such as a decrease in growth rate which in turn is under temperature control and this may explain the initial correlation with seawater temperature. Alternatively, the shells somehow absorb these two elements from the water column with prolonged exposure, explaining the increased concentrations in older parts of the shell. No Information is available on the seasonal concentration of dissolved Fe or Mn in the Menai Strait at the time of this study. However, over an annual cycle, Freitas *et al.* (2016) showed variations in both particulate and dissolved Mn concentrations in the Menai Strait in 2004 relating to plankton blooms; a pattern that is not reflected in the Mn values of the shells of *B. undatum* collected between 2014 and 2015. These findings suggest some kind of physiological control over the incorporation of both Mn and Fe.

Unlike the concentrations of Mn and Fe, the concentrations of U in the shells of *B. undatum* did not display an ontogenetic decrease over time and are in contrast to the findings of Gillikin and Dehairs (2013). They ascribed the ontogenetic decrease in U to the early signs of diagenesis in

the shell of the butter clam *Saxidomus gigantean*. If this was the case with *B. undatum* then the concentration of U would likely mimic that of Fe and Mn. Instead moderate correlations were observed between U and $\delta^{18}\text{O}$ in 8 out of 14 of the shells, excluding all of the Shetland shells and all of the female shells from the Menai Strait. Moderate, strong and very strong positive relationships were found between Sr and U in 12 out of 14 shells. The disassociation seen in the Sr profiles from the female Menai Strait shells was also apparent in the U profiles. The conclusion drawn from these relationships is that the incorporation of U and Sr are likely under very similar physiological controls in the shells of *B. undatum* and that control looks to be seawater temperature related. However, no clear relationships between any of the elements and growth rate are noted suggesting an as yet, unidentified mechanism in operation.

The profiles of $\delta^{13}\text{C}$ often showed poor correlations with the profiles of $\delta^{18}\text{O}$ with only 3 of the sampled 14 shells showing a moderate correlation. In certain specimens (e.g. MS13–23) there is a clear annual cyclicity to the cycles of $\delta^{13}\text{C}$, however, they are offset from the temperature profile with maximums after the summer maximum temperature. Whilst in certain species $\delta^{13}\text{C}$ often appears to reflect the dissolved inorganic carbon concentration of the surrounding water ($\delta^{13}\text{C}_{\text{DIC}}$; Donner & Nord, 1986; Goodwin *et al.*, 2013) which displays a clear annual cycle of ocean productivity, this is not reflected in the shells of *B. undatum*. It is likely instead that these profiles reflect the influence of metabolic C which may be more influential during times of fast growth (McConnaughey, 1988).

There were several possible limitations to this work. Firstly, at 2 out of the 3 sites there is a sample size of 3 shells which makes it difficult to draw meaningful broad scale conclusions due to the unexpectedly inconsistent nature of the results. However, 3–5 individuals is a common sample size for geochemical analyses of mollusc shells (e.g. Sosdian *et al.*, 2006; Yan *et al.*, 2013). With a limited number of samples available through the facility grant, potential differences between sites were prioritised as an important aspect of the investigation (and clear differences between sites were found), leading to the decision to spread the resources across 3 sites. Even so, the total number of samples analysed for both stable isotopes and trace elements was 1470, which represents both a large financial and time-consuming undertaking. Finally, the trace element results of 1 of the Shetland shells (SH–31) were not as clear as the other shells from Shetland with several anomalous data points, especially in the samples from the older parts of the shell. Electron microscope images of shells from Shetland (taken following the geochemical analysis) indicate the possibility of contamination from bore holes left by some

kind of shell inhabiting algae or fungi (see Chapter 3, section 3.3.3). Whilst this was unavoidable, it is strongly advised in future studies involving chemical analyses of *B. undatum* shells that the structural integrity of each shell analysed is initially checked using SEM.

In conclusion, the accuracy of the $\delta^{18}\text{O}$ values in reconstructing seawater temperature using the newly calibrated equation highlight the potential of *B. undatum* shells as recorders of annual seawater temperature. In the context of this study, this information was used to investigate other environmental proxies and growth rates of *B. undatum*. In practice these findings could also greatly increase the potential of archaeological *B. undatum* shells which are regularly found in fossil shell deposits and middens (Campbell & Russel, 2014) in reconstructing past environmental conditions. The use of $\delta^{18}\text{O}$ analysis for sclerochronology of dead collected and archaeological shells often relies on the ability to cross match and absolutely date long lived animals to infer long term trends in environmental conditions (Andrus, 2011; Reynolds *et al.*, 2016). Whilst this would not be possible for *B. undatum*, they do provide an excellent opportunity to reconstruct high resolution 'windows' of seawater temperature data due to the fast growth rates, provided that the general age of the shell deposit or midden is known. If samples are collected from human created shell middens, it would also be possible to infer the season of collection from the $\delta^{18}\text{O}$ values of the most recently deposited shell material, providing information about ancient foraging trends (e.g. Mannino *et al.*, 2003).

Although no clear patterns in trace element or $\delta^{13}\text{C}$ profiles were found, limiting the use of *B. undatum* as an environmental recorder with current understanding; there are clearly physiological and possibly environmental factors at play which warrant further investigation. The fast growth of *B. undatum* (up to 40 mm TSL/150 mm TLE per year), and the ease with which they can be cultured in laboratory aquaria makes them an ideal species for further work investigating the controls of trace element incorporation and stable isotope fractionation under laboratory conditions and opens up exciting prospects for future studies. The differences in growth rate of different *B. undatum* populations shown here also remains an interesting area of study. It is unclear whether these differences are solely temperature driven or if there is also a genetic aspect to the differences between these 3 geographically distinct sites. The seasonal growth rate differences observed between sites could with further work impact potential management options for fisheries. By pinpointing the seasons of maximum and minimum growth for particular sites and coupling this with knowledge of reproductive timings, recommendations could be made regarding the most sustainable seasons for fishing and

potential seasonal fishery closures which are effective in protecting reproductive seasons in commercial fish species (e.g. Halliday, 1988; Somers & Wang, 1997). The seasons of maximum growth could also potentially be avoided to increase the yield of individual *B. undatum* fisheries.

4.5 References

- Anagnostou E, Sherrell RM, Gagnon A, LaVigne M, Field MP, McDonough WF (2011) Seawater nutrient and carbonate ion concentrations recorded as P/Ca, Ba/ Ca, and U/Ca in the deep-sea coral *Desmophyllum dianthus*. *Geochim Cosmochim Acta* 75:2529–2543
- Andreassen GH, Delaney ML (2000) Bulk calcite size fraction distribution and Sr/Ca composition for deep-sea sediments at selected age horizons. *Mar Geol* 169:185
- Andrus CFT (2011) Shell midden sclerochronology. *Quaternary Sci Rev* 30:2892–2905
- Arkhipkin AI, Campana SE, FitzGerald J, Thorrold SR (2004) Spatial and temporal variation in elemental signatures of statoliths from the Patagonian longfin squid (*Loligo gahi*). *Can J Fish Aquat Sci* 61:1212– 1224
- Beck JW, Edwards RL, Ito E, Taylor FW, Recy J, Rougerie F, Joannot P, Henin C (1992) Sea-surface temperature from coral skeletal strontium/calcium ratios. *Science* 257:644–647
- Bemis BE, Spero HJ, Thunell RC (2002) Using species-specific paleotemperature equations with foraminifera: a case study in the Southern California Bight. *Mar Micropaleontol* 46(3–4):405–430
- Blight SP (1996) Microbial metabolism and temperature. PhD thesis. University of Wales, Bangor
- Bökenhans V, Bigatti G, Averbuj A (2016) Age estimation methods in the marine gastropod *Buccinanops globulosus* comparing shell marks and opercula growth rings. *Mar Biol Res* 12:881–887
- Borchardt T (1985) Relationship between carbon and cadmium uptake in *Mytilus edulis*. *Mar Biol* 85:233–244
- Bourgoin BP (1990) *Mytilus edulis* shell as a bioindicator of lead pollution: considerations on bioavailability and variability. *Mar Ecol Prog Ser* 61:253–262
- Broecker WS, Peng TH (1982) Tracers in the sea. Lamont-Doherty Geological Observatory, Columbia University, New York
- Brokordt K, Guderley H, Guay M, Gaymer CF, Himmelman JH (2003) Sex differences in reproductive investment: maternal care reduces escape response capacity in the whelk *Buccinum undatum*. *J Mar Biol Assoc UK* 291:161–180
- Buchardt B, Fritz P (1978) Strontium uptake in shell aragonite from the freshwater gastropod *Limnaea stagnalis*. *Science* 199:291–292
- Cage AG, Austin WEN (2010) Marine climate variability during the last millennium: The Loch Sunart record, Scotland, UK. *Quaternary Sci Rev* 29:1633–1647

- Campbell G (2011) Assessment of the archaeological potential of the sieved middle Saxon molluscs sieved from Lyminge, Kent, University of Reading, internal report available at: <http://www.lymingearchaeology.org/publications/>
- Campbell G, Russell M (2014) Direct Evidence for Bottom-fishing in Archaeological Whelks (*Buccinum undatum*). 'Human Exploitation of Aquatic Landscapes' special issue (Fernandes R, Meadows J eds.). Int Archaeol. <http://dx.doi.org/10.11141/ia.37.6>
- Carré M, Bentaleb I, Bruguier O, Ordinola E, Barrett NT, Fontugne M (2006) Calcification rate influence on trace element concentrations in aragonitic bivalve shells: evidences and mechanisms. Geochim Cosmochim Acta 70:4906-4920
- Chen T, Yu K, Chen T (2013) Sr/Ca–sea surface temperature calibration in the coral *Porites lutea* from subtropical northern South China Sea. Palaeogeogr Palaeoclimatol Palaeoecol 392:98–104
- Chenery SR, Tye A, Hollyman PR, Clarke D, Winship P, Reijnen M (2015) Analysis of Small Sample Volume Geochemistry Samples by Array Detector ICP-MS. Teledyne CETAC technologies application note: MVX7100-004
- Cherel Y, Hobson KA (2005) Stable isotopes, beaks and predators: a new tool to study the trophic ecology of cephalopods, including giant and colossal squids. Proc R Soc B 272:1601–1607
- Colonese AC, Hausmann N, Netto SA, Francisco AS, DeBlasis P, Villagran XS, de Almeida Rocha Ponzoni R, Hancock Y, Eloy de Farias DS, Prendergast A, Schöne BR, da Cruz FW, Giannini PCF (2017) Shell sclerochronology and stable isotopes of the bivalve *Anomalocardia flexuosa* (Linnaeus, 1767) from southern Brazil. Palaeogeogr Palaeoclimatol Palaeoecol. In press 1-15
- Colvin CN (2016) Timing of Shell Growth and Repair in the Whelk *Buccinum undatum* under Experimental Conditions. Master of Marine Biology thesis, Bangor University
- Craig H (1957) Isotopic standards for carbon and oxygen and correction factors for mass-spectrometric analysis of carbon dioxide. Geochim Cosmochim Acta 12:133-149
- Craig H (1965) The measurement of oxygen isotope palaeotemperatures, pp. In: Tongioli E (ed.), Stable Isotopes in Oceanographic Studies and Palaeotemperatures. Pisa: Consiglio Nazionale delle Ricerche Laboratorio di Geologia Nucleare 161–82
- Dick D, Philipp E, Kriews M, Abele, D (2007) Is the umbo matrix of bivalve shells (*Laternula elliptica*) a climate archive? Aquat Toxicol 84:450-456
- Dietzel M, Gussone N, Eisenhauer A (2004) Co-precipitation of Sr^{2+} and Ba^{2+} with aragonite by membrane diffusion of CO_2 between 10 and 50°C. Chem Geol 203:139–151
- Dodd JR (1965) Environmental control of strontium and magnesium in *Mytilus*. Geochim Cosmochim Acta 29:385-398
- Donner J, Nord AG (1986) Carbon and oxygen stable isotope values in shells of *Mytilus edulis* and *Modiolus modiolus* from Holocene raised beaches at the outer coast of the Varanger Peninsula, North Norway. Palaeogeogr Palaeoclimatol Palaeoecol 56:35-50
- Elderfield H, Vautravers M, Cooper M (2002), The relationship between shell size and Mg/Ca, Sr/Ca, $\delta^{18}\text{O}$, and $\delta^{13}\text{C}$ of species of planktonic foraminifera. Geochem Geophys Geosyst 3(8):1052

- Elliot M, Welsh K, Chilcott C, McCulloch M, Chappell J, Ayling B (2009) Profiles of trace elements and stable derived from giant long-lived *Tridacna gigas* bivalves: Potential applications in paleoclimate studies. *Palaeogeogr Palaeoclimatol Palaeoecol* 280(1-2):132–142
- Epstein S, Buchsbaum JR, Lowenstam HA and Ukey HC (1953) Revised carbonate-water isotopic temperature scale. *Bull Geol Soc Am* 64: 1315-1326
- Fallon SJ, McCulloch MT, van Woesik R, Sinclair DJ (1999) Corals at their latitudinal limits: Laser ablation trace element systematics in *Porites* from Shirigai Bay, Japan. *Earth Planet Sci Lett* 172:221-238
- Findlater G, Shelton A, Rolin T, Andrews J (2014) Sodium and strontium in mollusc shells: preservation, palaeosalinity and palaeotemperature of the Middle Pleistocene of eastern England. *P Geologist Assoc* 125(1):14–19
- Food Standards Scotland: <http://www.foodstandards.gov.scot/> (accessed 5/12/2016)
- Foster LC, Allison N, Finch AA, Andersson C (2009) Strontium distribution in the shell of the aragonite bivalve *Arctica islandica*. *Geochem Geophys Geosyst* 10(3):Q03003
- Fowler J, Cohen L, Jarvis P (1998) *Practical stats for field biology*. John Wiley and Sons, Chichester, England
- Freitas P, Clarke LJ, Kennedy H, Richardson C, Abrantes F (2005) Mg/Ca, Sr/Ca, and stable-isotope ($\delta^{18}\text{O}$ and $\delta^{13}\text{C}$) ratio profiles from the fan mussel *Pinna nobilis*: seasonal records and temperature relationships. *Geochem Geophys Geosyst* 6:Q04D14
- Freitas PS, Clarke LJ, Kennedy H, Richardson CA (2016) Manganese in the shell of the bivalve *Mytilus edulis*: Seawater Mn or physiological control? *Geochim Cosmochim Acta* 194:266-278
- Freitas PS, Clarke LJ, Kennedy H, Richardson CA, Abrantes F (2006) Environmental and biological controls on elemental (Mg/Ca, Sr/Ca and Mn/Ca) ratios in shells of the king scallop *Pecten maximus*. *Geochim Cosmochim Acta* 70:5119-5133
- Friedman I, O'Neil J, Cebula G (1982) Two new carbonate stable isotope standards. *Geostand Newslett* 6 1:11-12
- Füllenbach CS, Schöne BR, Mertz-Kraus (2015) Strontium/lithium ratio in aragonitic shells of *Cerastoderma edule* (Bivalvia) — A new potential temperature proxy for brackish environments. *Chem Geol* 417:341-355
- Gaetani GA, Cohen AL (2006) Element partitioning during precipitation of aragonite from seawater: A framework for understanding paleoproxies. *Geochim Cosmochim Acta* 70:4617-4634
- Galante-Oliveira S, Marçal R, Espadilha F, Sá M, Abell R, Machado J, Barroso CM (2015) Detection of periodic Sr-Ca⁻¹ cycles along gastropod statoliths allows the accurate estimation of age. *Mar Biol* 162:1473-1483
- Gentry DK, Sosdian S, Grossman EL, Rosenthal Y, Hicks D, Lear CH (2008) Stable isotope and Sr/Ca profiles from the marine gastropod *Conus ermineus*: testing a multiproxy approach for inferring paleotemperature and Paleosalinity. *Palaios* 23:195-209
- Gillikin DP, Dehairs F (2013) Uranium in aragonitic marine bivalve shells. *Palaeogeogr Palaeoclimatol Palaeoecol* 373:60-65

- Gillikin DP, Dehairs F, Lorrain A, Steenmans D, Baeyens W, André L (2006) Barium uptake into the shells of the common mussel (*Mytilus edulis*) and the potential for estuarine paleo-chemistry reconstruction. *Geochim Cosmochim Acta* 70:395–407
- Gillikin DP, Lorrain A, Meng I, Dehairs F (2007) A large metabolic carbon contribution to the $\delta^{13}\text{C}$ record in marine aragonitic bivalve shells. *Geochim Cosmochim Acta* 71:2936–2946
- Gillikin DP, Lorrain A, Navez J, Taylor JW, André L, Keppens E, Baeyens W, Dehairs F (2005) Strong biological controls on Sr/Ca ratios in aragonitic marine bivalve shells. *Geochem Geophys Geosyst* 6:Q05009
- Gillikin DP, Lorrain A, Paulet YM, André L, Dehairs F (2008) Synchronous barium peaks in high-resolution profiles of calcite and aragonite marine bivalve shells. *Geo-Mar Lett* 28:351–358
- Goodwin DH, Gillikin DP, Roopnarine PD (2013) Preliminary evaluation of potential stable isotope and trace element productivity proxies in the oyster *Crassostrea gigas*. *Palaeogeogr Palaeoclimatol Palaeoecol* 373:88–97
- Gordon CM, Carr RA, Larson RE (1970) Influence of environmental factors on sodium and manganese content of Barnacle shells. *Limnol Oceanogr* 15:461–466
- Grossman EL, Ku TL (1986) Oxygen and carbon isotope fractionation in biogenic aragonite – temperature effects. *Chem Geol* 59:59–74
- Hahn S, Rodolfo-Metalpa R, Griesshaber E, Schmahl WW, Buhl D, Hall-Spencer JM, Baggini C, Fehr KT, Immenhauser A (2012) Marine bivalve shell geochemistry and ultrastructure from modern low pH environments: environmental effect versus experimental bias. *Biogeosciences* 9:1897–1914
- Halliday RG (1988) Use of Seasonal Spawning Area Closures in the Management of Haddock Fisheries in the Northwest Atlantic. *NAFO Scientific Council Studies* 12: 27–36
- Hermoso M, Chan IZX, McClelland HLO, Heuresux AMC, Rickaby REM (2016) Vanishing coccolith vital effects with alleviated carbon limitation. *Biogeosciences* 13:301–312
- Holland HA, Schöne BR, Marali S, Jochum KP (2014) History of bioavailable lead and iron in the Greater North Sea and Iceland during the last millennium – A bivalve sclerochronological reconstruction. *Mar Pollut Bull* 87:104–116
- Hui Y, Da S, Yuhong W, Liguang S (2013) Sr/Ca profile of long-lived *Tridacna gigas* bivalves from South China Sea: A new high resolution SST proxy. *Geochim Cosmochim Acta* 112:52–65
- International Atomic Energy Agency (IAEA) (1993) Reference and inter-comparison materials for stable isotopes of light elements. *Proceeding of consultants meeting, Vienna, Austria*
- International Atomic Energy Agency (IAEA) (2009) Reference sheet for international measurement standards, VSMOW2, SLAP2. *Vienna, Austria*
- Kastner M (1999) Oceanic minerals: Their origin, nature of their environment, and significance. *PNAS* 96:3380–3387
- Katz A (1973) The interaction of magnesium with calcite during crystal growth at 25–90°C and one atmosphere. *Geochim Cosmochim Acta*, 37:1563–1586

- Kaufman A, Ghaleb B, Wehmiller JF, Hillaire-Marcel C, (1996) Uranium concentration and isotope ratio profiles within *Mercenaria* shells: geochronological implications. *Geochim Cosmochim Acta* 60:3735–3746
- Kendall C, McDonnell JJ (eds.) (1998) *Isotope Tracers in Catchment Hydrology*. Elsevier Science, Amsterdam
- Kim S-T, Mucci A, Taylor BE (2007) Phosphoric acid fractionation factors for calcite and aragonite between 25 and 75°C: Revisited. *Chem Geol* 246:135–146
- Kim S-T, O’Neil JR (1997) Equilibrium and nonequilibrium oxygen isotope effects in synthetic carbonates. *Geochim Cosmochim Acta* 61:3461–75
- Kinsman DJJ, Holland HD (1969) The co-precipitation of cations with CaCO₃-IV. The co-precipitation of Sr²⁺ with aragonite between 16° and 96°C. *Geochim Cosmochim Acta* 33:1-17
- Klein RT, Lohmann KC, Thayer CW (1996) Sr/Ca and ¹³C/¹²C ratios in skeletal calcite of *Mytilus trossulus*: Covariation with metabolic rate, salinity, and carbon isotopic composition of seawater. *Geochim Cosmochim Acta* 60:4207-4221
- Krause–Nehring J, Brey T, Thorrold SR (2012) Centennial records of lead contamination in northern Atlantic bivalves (*Arctica islandica*). *Mar Pollut Bull* 64(2):233–240
- Krumbiegel P (2012) Stable isotope terminology. *Isotopes Environ Health Stud* 48(3):384-90
- Labonne M, Hillaire-Marcel C (2000) Geochemical gradients within modern and fossil shells of *Concholepas concholepas* from Northern Chile: an insight into U–Th systematics and diagenetic/authigenic isotopic imprints in mollusk shells. *Geochim Cosmochim Acta* 64:1523–1534
- Land LS, Hoops GK (1973) Sodium in carbonate sediments and rocks: a possible index to the salinity of diagenetic solutions. *J Sediment Petrol* 43:614–617
- Latal C, Piller WE, Harzhauser M (2004) Palaeoenvironmental reconstructions by stable isotopes of Middle Miocene gastropods of the Central Paratethys. *Palaeogeogr Palaeoclimatol Palaeoecol* 211:157-169
- Leng MJ, Lewis JP (2016) Oxygen isotopes in Molluscan shell: Applications in environmental archaeology. *Environmental Archaeology* 21(3):295-306
- Leng MJ, Marshall JD (2004) Palaeoclimate interpretation of stable isotope data from lake sediment archives. *Quaternary Sci Rev* 23(7-8):811-831
- Li S, Liu C, Huang J, Liu Y, Zhang S, Zheng G, Xie L, Zhang R (2016) Transcriptome and biomineralization responses of the pearl oyster *Pinctada fucata* to elevated pCO₂ and temperature. *Sci Rep* 6:18493
- Lorens RB, Bender ML (1980) The impact of solution chemistry on *Mytilus edulis* calcite and aragonite: *Geochim Cosmochim Acta* 44:1265–1278
- Lourino-Cabana B, Billon G, Lesven L, Sabbe K, Gillan D-C, Gao Y, Leermakers M, Baeyens W (2014) Monthly variation of trace metals in North Sea sediments. From experimental data to modeling calculations. *Mar Pollut Bull* 87:237–246

- Lutz RA, Rhoads DC (1977) Anaerobiosis and a Theory of Growth Line Formation. *Science* 198(4323):1222-1227
- MacLachlan SE, Cottier FR, Austin WEN, Howe JA (2007) The salinity: $\delta^{18}\text{O}$ water relationship in Kongsfjorden, western Spitsbergen. *Polar Res* 26:160-167
- Mannino MA, Spiro BF, Thomas KD (2003) Sampling shells for seasonality: oxygen isotope analysis on shell carbonates of the inter-tidal gastropod *Monodonta lineata* (da Costa) from populations across its modern range and from a Mesolithic site in southern Britain. *J Archaeol Sci* 30:667–79
- Mannino MA, Thomas KD (2001) The Bioarchaeology of the Culverwell Shell Midden. Eds: Palmer S. In: Culverwell Mesolithic Habitation Site. British Archaeological Reports, British Series 287, Oxford
- Markich SJ, Jeffree RA, Burke PT (2002) Freshwater bivalve shells as archival indicators of metal pollution from a copper–uranium mine in tropical northern Australia. *Environ Sci Technol* 36:821–832
- Martel A, Larrivée DH, Klein KR, Himmelman JH (1986) Reproductive cycle and seasonal feeding activity of the neogastropod *Buccinum undatum*. *Mar Biol* 92:211-221
- Martin PA, Lea DW, Mashiotta TA, Papenfuss T, Sarnthein M (1999) Variation of foraminiferal Sr/Ca over Quaternary glacial-interglacial cycles: Evidence for changes in mean ocean Sr/Ca. *Geochem Geophys Geosyst* 1:1004
- McClintock JB, Amsler CD, Amsler MO, Duquette A, Angus RA, Hall-Spencer JM, Milazzo M (2014) Trace elements in shells of common gastropods in the near vicinity of a natural CO₂ vent: no evidence of pH-dependent contamination. *Biogeosci Discuss* 11:5215-5237
- McConnaughey TA (1988) Biomineralization mechanisms. In: Crick FC (ed.), *The Origin, Evolution, and Modern Aspects of Biomineralization in Animals and Plants*. Elsevier, Amsterdam
- Mckenna C, Berx B, Austin WEN (2016) The decomposition of the Faroe-Shetland Channel water masses using Parametric Optimum Multi-Parameter analysis. *Deep-Sea Res pt I* 107:9–21
- Mclaren SJ, Rowe PJ (1996) The reliability of uranium-series mollusc dates from the western Mediterranean basin. *Quaternary Sci Rev* 15:709–717
- Mettam C, Johnson ALA, Nunn EV, Schöne BR (2014) Stable isotope ($\delta^{18}\text{O}$ and $\delta^{13}\text{C}$) sclerochronology of Callovian (Middle Jurassic) bivalves (*Gryphaea (Bilobissa) dilobotes*) and belemnites (*Cylindroteuthis puzosiana*) from the Peterborough Member of the Oxford Clay Formation (Cambridgeshire, England): Evidence of palaeoclimate, water depth and belemnite behaviour. *Palaeogeogr Palaeoclimatol Palaeoecol* 399:187–201
- Min GR, Edwards RL, Taylor FW, Recy J, Gallup CD, Beck JW (1995) Annual cycles of U/Ca in coral skeletons and U/Ca thermometry. *Geochim Cosmochim Acta* 59:2025–2042
- Mitsuguchi T, Matsumoto E, Abe O, Uchidam T, Isdale PJ (1996) Mg/Ca thermometry in coral-skeletons. *Science* 274:961–963
- Moloukhia H, Sleem S (2011) Bioaccumulation, Fate and Toxicity of Two Heavy Metals Common in Industrial Wastes in Two Aquatic Molluscs. *J Amerc Sci* 7(8):459-464

- Mook WG (1971) Paleotemperatures and chlorinities from stable carbon and oxygen isotopes in shell carbonate: *Palaeogeogr Palaeoclimatol Palaeoecol* 9:245-263
- Mook WG, Vogel JC (1968) Isotopic Equilibrium between Shells and Their Environment. *Science* 159:874-875
- Mucci A (1987) Influence of temperature on the composition of magnesian calcite overgrowths precipitated from seawater. *Geochim Cosmochim Acta* 51:1977-1984
- O'Neil DD, Gillikin DP (2014) Do freshwater mussel shells record road-salt pollution? *Sci Rep* 4:7168
- Owen R, Kennedy HA, Richardson CA (2002a) Experimental investigation into partitioning of stable isotopes between scallop (*Pecten maximus*) shell calcite and sea water. *Palaeogeogr Palaeoclimatol Palaeoecol* 185(1-2):163-174
- Owen R, Kennedy HA, Richardson CA (2002b) Isotopic partitioning between scallop shell calcite and sea water: effect of shell growth rate. *Geochim Cosmochim Acta* 66:1727-1737
- Palacios R, Orensanz J, Armstrong D (1994), Seasonal and life-long variation of Sr/Ca ratio in shells of *Mya arenaria* from Grays Harbor-an ancillary criterion in demographic studies. *Estuar Coast Shelf S* 39:313–327
- Pilkey OH, Goodell HG (1963) Trace elements in recent mollusk shells. *Limnol Oceanogr* 8:137-148
- Pilkey OH, Harriss RC (1966) The effect of intertidal environment on the composition of calcareous skeletal material. *Limnol Oceanogr* 11:381–385
- Pinto LA, Rivera C (2003) Distribution of Fe(II) and Mn(II) in porewaters of Concepción Bay and continental shelf during the 'El Niño 1997-1998' Event. *J Chil Chem Soc* 48:31-35
- Poulain C, Gillikin DP, Thébault J, Munaron JM, Bohn M, Robert R, Paulet Y-M, Lorrain A (2015). An evaluation of Mg/Ca, Sr/Ca, and Ba/Ca ratios as environmental proxies in aragonite bivalve shells. *Chem Geol* 396:42–50
- Prendergast AL, Azzopardi M, O'Connell TC, Hunt C, Barker G, Stevens RE (2013) Oxygen isotopes from *Phorcus (Osilinus) turbinatus* shells as a proxy for sea surface temperature in the central Mediterranean: A case study from Malta. *Chem Geol* 354:77-86
- Prendergast AL, Stevens RE, Barker G, O'Connell TC (2015) Oxygen isotope signatures from land snail (*Helix melanostoma*) shells and body fluid: Proxies for reconstructing Mediterranean and North African rainfall. *Chem Geol* 409:87–98
- Price GD, Pearce NJG (1997) Biomonitoring of pollution by *Cerastoderma edule* from the British Isles: a laser ablation ICP-MS study. *Mar Pollut Bull* 34:1025–1031
- Purton LMA, Shields GA, Brasier MD, Grime GW (1999) Metabolism controls Sr/Ca ratios in fossil aragonitic mollusks. *Geology* 27:1083–1086
- Reynolds DJ, Richardson CA, Scourse JD, Butler PG, Wanamaker AD, Ridgway I, Sayer MDJ, Gulliver P (2013) The potential of the marine bivalve mollusc *Glossus humanus* (L.) as a sclerochronological archive. *The Holocene* 23(12):1711– 1720
- Reynolds DJ, Scourse JD, Halloran PR, Nederbragt AJ, Wanamaker AD, Butler PG, Richardson CA, Heinemeier J, Eiríksson J, Knudsen KL, Hall IR (2016) Annually resolved North Atlantic marine climate over the last millennium. *Nat Commun* 7:13502

- Richardson CA (2001) Molluscs as archives of environmental change. *Oceanogr Mar Biol* 39:103–164
- Richardson CA, Chenery SRN, Cook JM (2001) Assessing the history of trace metal (Cu, Zn, Pb) contamination in the North Sea through laser ablation ICP-MS of horse mussel *Modiolus modiolus* shells. *Mar Ecol Prog Ser* 211:157–167
- Rohling EJ (2013) Oxygen isotope composition of seawater. *Encyclopedia of Quaternary Science*. Elsevier, Amsterdam
- Rosenheim BE, Swart PK, Thorrold SR (2005) Minor and trace elements in sclerosponge *Ceratoporella nicholsoni*: biogenic aragonite near the inorganic endmember? *Palaeogeogr Palaeoclimatol Palaeoecol* 228:109–129
- Santarelli L and Gros P (1985) Age and growth of the whelk *Buccinum undatum* L. (Gastropoda: Prosobranchia) using stable isotopes of the shell and operculum striae. *Oceanol Acta* 8 (2): 221–229
- Savitsky A, Golay MJE (1964) Smoothing and differentiation of data by simplified least squares procedures. *Anal Chem* 36(8):1627-1639
- Schöne BR, Houk SD, Castro ADF, Fiebig J, Oschmann R, Krönke I, Dreyer W, Gosselck F (2005) Daily Growth Rates in Shells of *Arctica islandica*: Assessing Sub-seasonal Environmental Controls on a Long-lived Bivalve Mollusk. *Palaios* 20(1):78-92
- Schöne BR, Rodland DL, Wehrmann A, Heidel B, Oschmann W, Zhang Z, Fiebig J, Beck L (2007) Combined sclerochronologic and oxygen isotope analysis of gastropod shells (*Gibbula cineraria*, North Sea): life-history traits and utility as a high-resolution environmental archive for kelp forests. *Mar Biol* 150(6):1237-1252
- Schöne BR, Zhang Z, Jacob D, Gillikin DP, Tutken T, Garbe-Schoenberg D, McConnaughey T, Soldati A (2010) Effect of organic matrices on the determination of the trace element chemistry (Mg, Sr, Mg/Ca, Sr/Ca) of aragonitic bivalve shells (*Arctica islandica*)-Comparison of ICP-OES and LA-ICP-MS data. *Geochem J* 44:23-37
- Schöne BR, Zhang ZJ, Radermacher P, Thebault J, Jacob DE, Nunn EV, Maurer AF (2011) Sr/Ca and Mg/Ca ratios of ontogenetically old, long-lived bivalve shells (*Arctica islandica*) and their function as paleotemperature proxies. *Palaeogeogr Palaeoclimatol Palaeoecol* 302:52-64
- Scolding JWS, Richardson CA, Luckenbach MJ (2007) Predation of cockles (*Cerastoderma edule*) by the whelk (*Buccinum undatum*) under laboratory conditions. *J Mollus Stud* 73(4):333-337
- Sharma T, Clayton RN (1965) Measurement of $^{18}\text{O}/^{16}\text{O}$ ratios of total oxygen of carbonates. *Geochim Cosmochim Acta* 56:419–430
- Shen GT, Dunbar RB (1995) Environmental controls on uranium in reef corals. *Geochim Cosmochim Acta* 59:2009–2024
- Sinclair DJ, Kinsley LPJ, McCulloch MT (1998) High resolution analysis of trace elements in corals by laser ablation ICP-MS. *Geochim Cosmochim Acta* 62:1889–1901
- Somers I, Wang Y-G (1997) A Simulation Model for Evaluating Seasonal Closures in Australia's Multispecies Northern Prawn Fishery. *North Am J Fish Mana* 17:114-130

- Sosdian S, Gentry DK, Lear CH, Grossman EL, Hicks D, Rosenthal Y (2006) Strontium to calcium ratios in the marine gastropod *Conus ermineus*: growth rate effects and temperature calibration. *Geochem Geophys Geosyst* 7(11):1525-2027
- Speer JA (1983) Crystal chemistry and phase relations of the orthorhombic carbonates. *Rev Mineral Geochem* 11:145–190
- Steiner J, Termonia Y, Deltour J (1972) Comments on Smoothing and Differentiation of Data by Simplified Least Square Procedure. *Anal Chem* 44:1906-1909
- Sturgeon RE, Willie SN, Yang L, Greenberg R, Spatz RO, Chen Z, Sriver C, Clancy V, Lama JW, Thorrold S (2005) Certification of a fish otolith reference material in support of quality assurance for trace element analysis. *J Anal At Spectrom* 20:1067–1071
- Tanaka N, Monaghan M, Rye D (1986) Contribution of metabolic carbon to mollusc and barnacle shell carbonate. *Nature* 320:520–523
- Thébault J, Chauvaud L (2013) Li/Ca enrichments in great scallop shells (*Pecten maximus*) and their relationship with phytoplankton blooms. *Palaeogeogr Palaeoclimatol Palaeoecol* 373:108-122
- Thebault J, Chauvaud L, L'Helguen S, Clavier J, Barats A, Jacquet S, Pecheyran C, Amouroux D (2009a) Barium and molybdenum records in bivalve shells: Geochemical proxies for phytoplankton dynamics in coastal environments? *Limnol and Oceanogr* 54:1002-1014
- Thébault J, Schöne BR, Hallmann N, Barth M, Nunn EV (2009b) Investigation of Li/Ca variations in aragonitic shells of the ocean quahog *Arctica islandica*, northeast Iceland. *Geochem, Geophys, Geosy* 10(12):Q12008.
- Vasconcelos P, Gharsallah IH, Moura P, Zamouri-Langar L, Gaamour A, Missaoui H (2012) Appraisal of the usefulness of operculum growth marks for ageing *Hexaplex trunculus* (Gastropoda: Muricidae): Comparison between surface striae and adventitious layers. *Mar Biol Res* 8:141-53
- Wanamaker Jr, AD, Kreutz, KJ, Borns Jr, HW, Introne DS, Feindel S, Funder S, Rawson PD, Barber BJ (2007) Experimental determination of salinity, temperature, growth, and metabolic effects on shell isotope chemistry of *Mytilus edulis* collected from Maine and Greenland. *Paleoceanography* 22:PA2217
- Wejnert KE, Thunell RC, Astor Y (2013) Comparison of species-specific oxygen isotope paleotemperature equations: Sensitivity analysis using planktonic foraminifera from the Cariaco Basin, Venezuela. *Mar Micropaleontol* 101:76–88
- Yan H, Shao D, Yuhong W, Sun L (2013) Sr/Ca profile of long-lived *Tridacna gigas* bivalves from South China Sea: a new high-resolution SST proxy. *Geochim Cosmochim Acta* 112:52-65
- Zhao L, Schöne BR, Mertz-Kraus R (2016) Delineating the role of calcium in shell formation and elemental composition of *Corbicula fluminea* (Bivalvia). *Hydrobiologia* 790:259–272
- Zhao L, Schöne BR, Mertz-Kraus R (2017a) Controls on strontium and barium incorporation into freshwater bivalve shells (*Corbicula fluminea*) *Palaeogeogr Palaeoclimatol Palaeoecol* 465:386–394
- Zhao L, Schöne BR, Mertz-Kraus R, Yang F (2017b) Insights from sodium into the impacts of elevated pCO₂ and temperature on bivalve shell formation. *J Exp Mar Biol Ecol* 486:148-154

Chapter 5:

Visualisation and validation of *Buccinum undatum* statolith growth rings.

5.1 Introduction

The reliable assessment of age and longevity of European whelk, *Buccinum undatum*, populations is problematic for fisheries scientists, as this species has several life history traits that make it difficult to monitor at both the individual and population level. The lack of a planktonic larval stage and a relatively inactive adult lifestyle with no apparent seasonal migration (Pálsson *et al.*, 2014), has led to the formation of geographically discrete stocklets which are vulnerable to overexploitation (Fahy *et al.*, 2000). In many studies these stocklets have been observed to show clear genetic and morphological differences (e.g. Weetman *et al.*, 2006; Shelmerdine *et al.*, 2007; Magnúsdóttir, 2010), whilst size at maturity can also differ markedly between sites (McIntyre *et al.*, 2015; Haig *et al.*, 2015).

A reliable method for estimating age needs to be established for *B. undatum* so that accurate population age assessments and accurate stock assessments can be undertaken. The currently accepted method used universally by fisheries scientists and validated in 1985 by Santarelli and Gros, determines the age of whelks by reading the putative annual growth rings on the operculum, an organic ‘shield’ that protects the shell aperture when the animal withdraws into its shell. However, this method traditionally has a low success rate owing to the poor clarity of the rings, a problem that has been highlighted by Kideys (1996), who reported that only 16%, of a total of 10,975 opercula examined in whelks from the Isle of Man, U.K. had clear and readable rings. Similar low readability of opercula was found by Lawler (2013) who studied several sites around the UK. The resultant population growth curves had a high variance that was likely due to the ambiguity of the opercular readings that had only been taken from a small proportion of the whelks where the rings were clear enough to read.

Whelks are becoming increasingly exploited so there is an urgent scientific need to underpin the fisheries stock assessment of their populations with accurate data concerning the age of individuals and their growth rates. For many mollusc species, the age of an individual can be determined by counting the annual growth lines present in shell sections (See Richardson, 2001, for review). This is particularly applicable to bivalve molluscs. However, in the case of many gastropods this is not possible because there are often no obvious annual growth rings on the shell surface or contained within sections of their shells.

Because the factors responsible for the ‘readability’ of the operculum are unknown (for example one might suppose that only fast-growing animals can have clearly readable rings or vice-versa),

the small proportion of available age readings cannot be used to study population parameters without important reservations, unless verified by an alternative aging tool. Therefore, this chapter describes the validation and use of growth rings in the statolith.

Statoparticles, such as statoliths, are structures that are integral to the nervous system of a diverse range of animal groups including the Polychaeta (Beesley *et al.*, 2000), Holothuroidea (Ehlers, 1997), Crustacea (Espeel, 1985) and several classes of the Mollusca e.g. the Bivalvia (Morton, 1985), Gastropoda (Barroso *et al.*, 2005; Chatzinikolaou & Richardson 2007; Galante-Oliveira *et al.*, 2013; Hollyman *et al.*, 2017 (in review)) and Cephalopoda (Arkhipkin, 1997). They are used in gravity perception and are contained within a nerve sac, the statocyst, which detects movement of the statoparticle, and indicates a change in orientation (Chase, 2002). They are frequently composed of calcium carbonate and have a wide ranging morphology across the phyla in which they are found. The statoparticles of gastropods are often single, roughly spherical granules called statoliths, but can also be collections of multiple smaller granules (see Fretter & Graham, 1994; Richardson, 2001). Gastropod statoliths can contain rings that are deposited annually e.g. *Nassarius (=Hinnia) reticulatus* (Barroso *et al.*, 2005), *Neptunea antiqua* (Richardson *et al.*, 2005a) and *Polinices pulchellus* (Richardson *et al.*, 2005b). They are an archive of their life history and contain information about the age and the seasonal temperature cycle (Richardson *et al.*, 2005a, Galante-Oliveira *et al.*, 2015) and the transition from a planktonic pelagic larval lifestyle to a benthic existence (Barroso *et al.*, 2005; Richardson *et al.*, 2005a; Chatzinikolaou & Richardson 2007). Once the rings in the statolith have been deciphered, information about a gastropod's life history can be extracted to understand their ontogenic growth. Thus they are potentially an invaluable resource for fisheries scientists who could use this information to assess commercially important gastropod species such as *B. undatum* whose statoliths and growth rings have never been studied or validated.

This chapter focusses on the initial development of methods used to extract, view and interpret statoliths as well as basic data regarding their morphology. Finally, the annual periodicity of the growth rings is validated using seasonally field collected whelks and laboratory reared juvenile *B. undatum*. It is hypothesised that a statolith growth ring forms during the cold winter period in temperate and boreal latitudes in much the same way as annual growth lines form in the shells of most intertidal and subtidal bivalves.

5.2 Materials and methods

5.2.1 Field collection

Samples collected during the shell morphology study (outlined in Chapter 2) were used for this study. See the methods section from Chapter 2 for details regarding site locations and sampling procedure.

5.2.2 Statolith extraction and ageing

Whelk bodies were thawed in their labelled bags (3 hrs) before removal and bisected using large forceps and dissection scissors (Figure 5.2a). Each half of the whelk was examined under a low power binocular dissecting microscope to locate, dissect and then remove, using fine forceps (0.10 x 0.06 mm tip), a pair of statocyst sacs (left and right side) each containing a statolith along with the surrounding tissue (Figure 5.2b). When bisected through the middle of the body (dotted line Figure 5.1a), a single statolith is revealed in each resulting half.

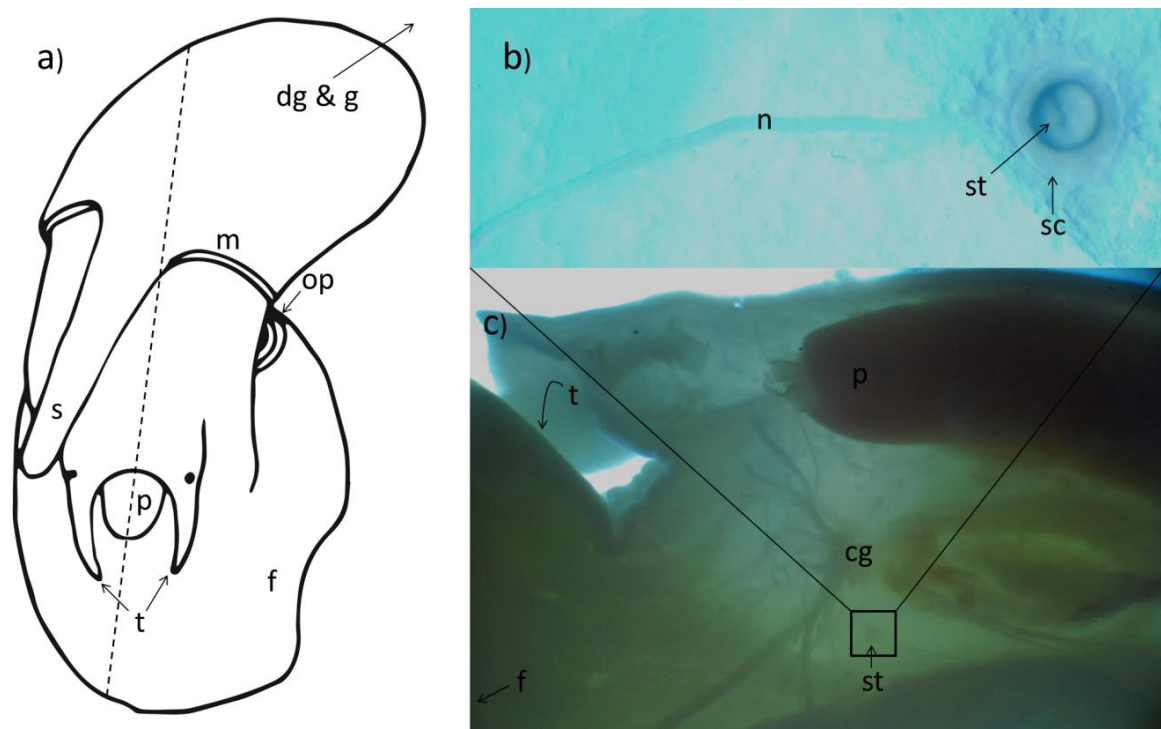


Figure 5.2. a) a ventral view of a female *Buccinum undatum* removed from its shell showing; s - Siphon, m - Mantle, p - Proboscis, op - Operculum, f - Foot and t - Tentacles. dg - Digestive Gland and g - Gonad are out of frame. The dotted line represents the bisection of the whelk, b) a statolith following removal; n - Nerve, st - Statolith and sc - Statocyst and c) half a bisected *B. undatum* illuminated using transmitted light, viewed in a dissecting microscope, showing the cg - Cerebral Ganglion and st - Statolith.

Each statolith position is indicated by a shadow which is visible in each cross section of the whelk body (Figure 5.2c). Once removed, the statocyst was placed in an appropriate watch glass labelled 'left' and 'right' (Figure 5.3a). Incident illumination and transmitted light were used during the dissections and highlighted the statoliths as small shadows beneath the cerebral ganglion (Figure 5.2c). Statoliths were removed with the surrounding tissue as they were liable to fracture when gripped firmly with forceps. The <0.75mm statocysts were transferred to a shallow glass embryo dish with a drop of Mili-Q® ultrapure water (Merck Millipore) (Figure 5.3a), cut open and the statoliths removed using a hypodermic needle (diameter 0.5 mm) and fine forceps, and left to dry (Figure 5.3b). Where necessary, statoliths were cleaned of any adhering tissue by immersion in 20% sodium hydroxide (NaOH) for 30 minutes and rinsed in Mili-Q®, although this was rarely required.

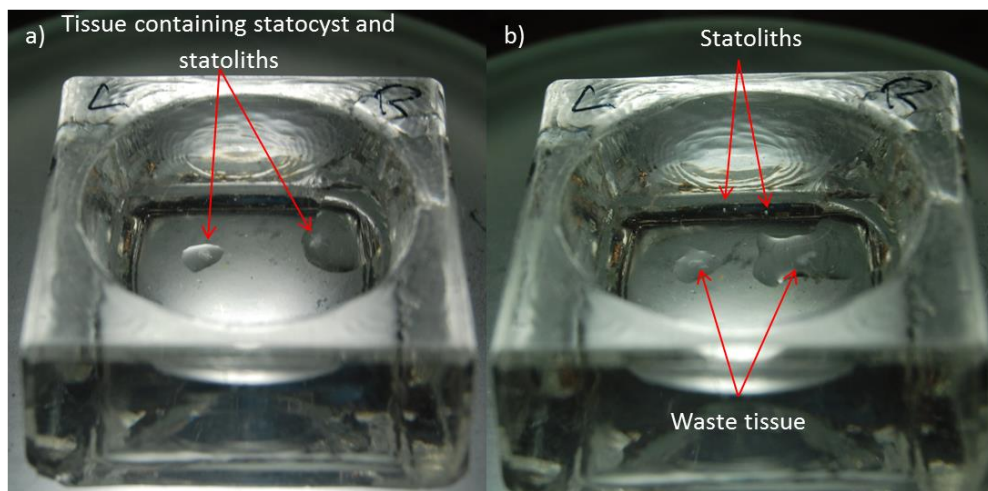


Figure 5.3. a) left and right statocysts from a *Buccinum undatum* specimen placed in a shallow embryo dish in several drops of Mili-Q® water and b) statoliths drying in the glass dish following dissection from the statocyst sacs shown in a).

Once air-dried (30 minutes), the left statolith was mounted on a microscope slide using Crystalbond™ 509 thermoplastic resin. This was achieved by heating a standard microscope slide (75 x 25 x 1 mm) over an open flame (alcohol burner) and melting a small (2 mm³) piece of resin in the centre of the heated slide surface. The statolith was then quickly 'picked up' by dipping the tip of the fine forceps into Mili-Q® water and using the water tension to adhere it, and safely transferred to the molten resin on the slide (Figure 5.4a). The statolith was then covered with a fragment (<1 mm³) of solid resin (Figure 5.4b) and warmed again to melt the resin so as to fully enclose the statolith.

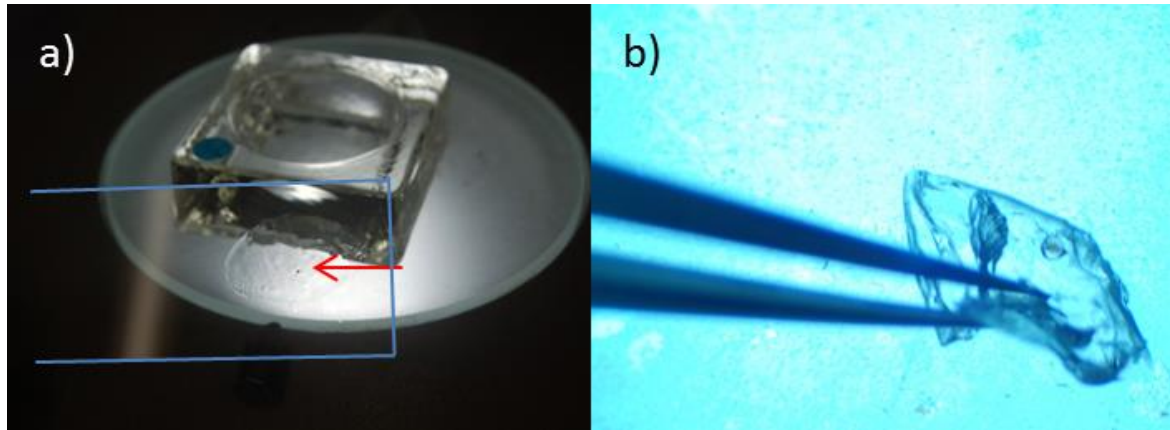


Figure 5.4. a) a *Buccinum undatum* statolith (highlighted by red arrow) immediately following encapsulation in the melted resin on a microscope slide (outlined in blue) and b) a statolith being covered with a fragment of resin to complete the statolith mounting process.

Whilst the resin was still pliable, the statolith was manipulated to ensure the correct orientation and best clarity of the rings. This was achieved by rotating the statolith using the hypodermic needle so that any cracks in the statolith structure (all removed statoliths contain cracks), were aligned perpendicular to the slide surface. The remaining right statolith was stored in 100% Industrial Methylated Spirit (IMS) in a labelled Eppendorf tube until further study. All mounted statoliths were imaged at 20x magnification using transmitted light under a Meiji Techno MT8100 microscope with a Lumenera Infinity 3 microscope camera to visualise the statolith growth rings. The resulting statolith images were measured using ImageJ (ver. 1.48) to assess statolith diameter and these data plotted against shell length. This allometric relationship was compared between sites using the *smatr* package (Warton *et al.* 2012) in R 3.3.2. A standard operating procedure for *B. undatum* statoliths has already been developed and written (by PH) for fisheries agencies and can be found in [Appendix H](#).

5.2.3 Statolith visualisation

In previous studies, statoliths have been ground and polished to visualise the visible growth rings (e.g. Richardson *et al.*, 2005a). In the current study the clarity of the rings was compared in whole and sectioned statoliths from male and female *B. undatum*. The left and right statoliths from selected male and female *B. undatum* from the Menai Strait, Shetland Isles and Jersey were resin mounted. The right statolith was ground by hand on progressively finer 400, 1200, 2500 silicon carbide grinding papers lubricated with Mili-Q®, until the central plane was reached. This required regular microscopical inspection of the statolith during grinding to assess progress of the sectioning to ensure the desired plane of section had been reached. The ground

surface was finally polished on a rotary polisher using a 3 µm diamond suspension. The resulting polished section and the whole-mounted statolith were imaged in both transmitted light and reflected light and statolith composite images were prepared using Adobe Photoshop CC.

5.2.4 Laboratory statolith ring formation

This experiment was designed to study the ontogeny of the whelk statolith and the seasonal timing of growth ring formation. Each month for 24 months, 10 whelks were removed from the 2 year cohorts (2014 & 2013, see Chapter 3 for details, section 3.2) of laboratory reared juvenile whelks and frozen for later statolith extraction, statolith measurement and determination of the timing of ring formation.

5.3 Results

5.3.1 Statolith location and morphology

Each whelk contains two statocysts in the tissues of its foot containing a single roughly spherical statolith (st) (<0.75mm in diameter) (Figure 5.2b). Orientation of the statolith in resin in a dorsal/ventral position shows a circular outline shape and is the optimum position to view and measure the visible growth rings (Figure 5.5a). Laterally the statolith has an oval shape (Figure 5.5b) and has a dorso-ventrally compressed spherical shape where the rings are less clear. Thus, to maintain consistency and to maximise the visibility of the rings, all analyses/images were undertaken from statoliths orientated in a dorsal-ventral view.

Figure 5.6a, shows that Statolith Diameter (StD) and Total Shell Length (TSL) have a strong relationship across all sites ($R^2 = 0.9336$). Figure 5.6b, shows the relative statolith diameter (RStD) (= StD as a % of TSL) plotted against TSL ($R^2 = 0.9623$). The relationships show that the growth of the statoliths is negatively allometric with respect to TSL, with smaller whelks having relatively larger statoliths than large individuals. Whilst it appears that a good relationship is seen between statolith diameter and shell length overall between sites in Figure 5.6, further analysis reveals that there are statistical differences in the relationship between sites. This is summarised in Table 1. The data used for this analysis were log transformed prior to analysis.

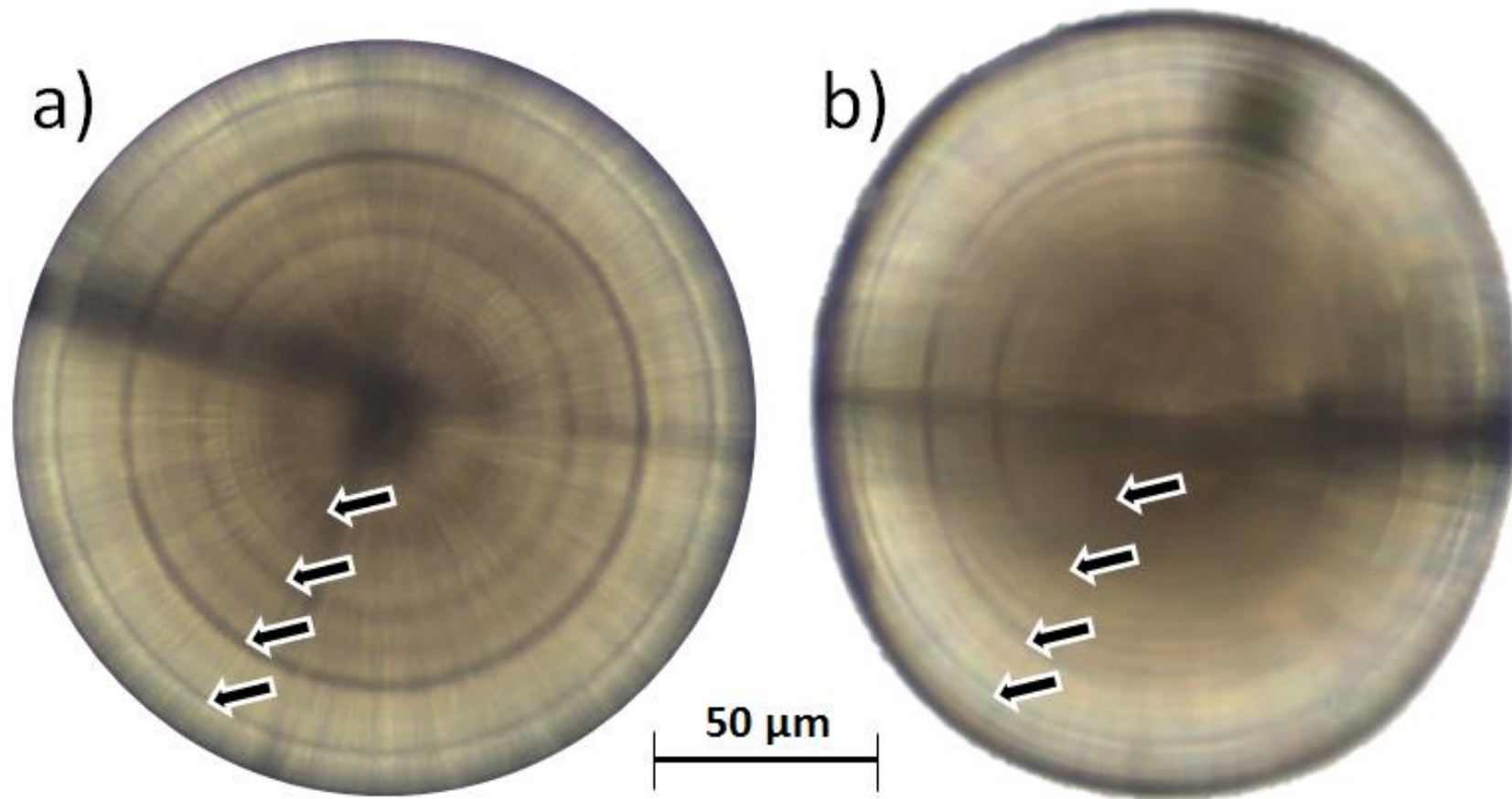


Figure 5.5. Photomicrographs of two statoliths removed from a *Buccinum undatum* from the Menai Strait. a) shows a dorso-ventral view whilst b) shows a lateral view of the statolith. The growth rings are marked with arrows in each statolith orientation.

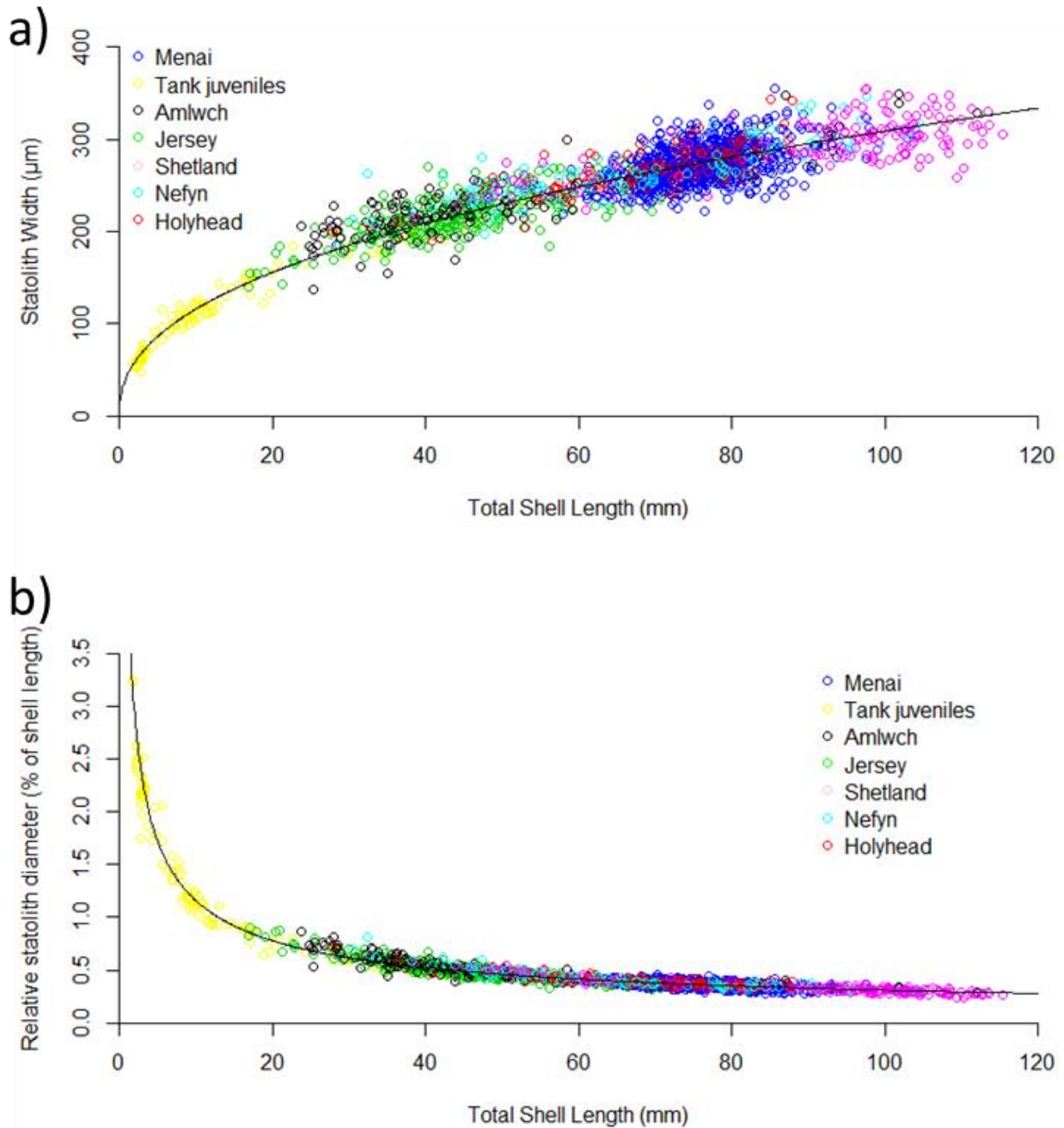


Figure 5.6. a) scatterplot showing the relationship between statolith diameter (StD) and shell length (TSL) from laboratory-reared (Tank juveniles) and field collected *Buccinum undatum* from all sites, the data are fitted with a power trend line ($y = 43.439x^{0.4259}$) $R^2 = 0.9336$. b) The relationship between TSL and relative statolith diameter (RStD = StD as a % of TSL), fitted with a power trend line ($y = 4.3439x^{-0.574}$) $R^2 = 0.9623$. $n = 1719$.

Table 5.1. Significance matrix of pairwise comparisons between all locations following allometric analysis of the relationship between statolith diameter and shell length. LR – Laboratory reared. Significance codes: *** = $p < 0.001$, ** = $p < 0.01$, * = $p < 0.05$.

	<u>Elevation</u>								<u>Slope</u>						
	Amlwch	Nefyn	Jersey	Menai	Holyhead	LR	Shetland		Amlwch	Nefyn	Jersey	Menai	Holyhead	LR	Shetland
	Statolith diameter Vs. Total Shell Length														
Amlwch	-		***	***	*	***	*		-		***	***	*	***	*
Nefyn		-	*	***		*	*			-	*	***		*	*
Jersey	***	*	-	***					***	*	-	***			
Menai	***	***	***	-	***	***	***		***	***	***	-	***	***	***
Holyhead	*			***	-		*		*			***	-	*	
LR	***	*		***		-			***	*		***		-	
Shetland	*	*		***	*		-		*	*		***		*	-

5.3.2 Statolith ring visualisation

The composite images in Figures 5.7 and 5.8 compare and contrast images of statoliths prepared using the 3 different methods for viewing the statolith growth rings. Figure 5.7 a and b compare the appearance of a statolith from a female and a male whelk, whilst Figure 5.8 compares the appearance of the statoliths from Shetlands and Jersey whelks. Figure 5.7a and d and Figure 5.8a and d show a ground statolith imaged with transmitted light, Figure 5.7b and e and Figure 5.8b and e show a resin mounted and ground statolith imaged with reflected light and Figure 5.7c and f and Figure 5.8c & f show a whole statolith imaged with transmitted light. In all images under reflected light the rings have the poorest clarity, especially towards the edge of the statolith. Weakly defined ‘disturbance’ rings are clearly visible in sectioned statoliths (Figures 5.7a and 5.8a). By contrast all images of whole statoliths viewed in transmitted light had the clearest defined rings and for this reason this technique was used in imaging all of the whelks examined in this study (unless otherwise stated).

5.3.2.1 Issues with statolith clarity

Several common issues were encountered during statolith preparation and visualisation of the growth rings. Figure 5.9 illustrates some examples of crystallised and deformed statoliths, the frequency of crystallised and deformed statoliths at each site can be seen in Table 2. Crystallised or deformed statoliths never affected more than 2.4% of a population and in many cases the annual growth rings could still be identified (e.g. Figure 5.9c & d).

Table 5.2. The frequency of crystallised/deformed and opaque statoliths from all sampled sites

Site	% crystalised/deformed statoliths	% opaque statoliths
Amlwch	0.66	59.60
Holyhead	1.80	6.31
Nefyn	0.95	1.90
Jersey (combined)	2.17	13.72
JD5	2.33	3.49
JE4	-	34.07
JE5	2.00	4.00
Shetland	0.92	4.59
Menai Strait	2.38	1.31
Laboratory reared	-	-

Figures 5.9a and b show translucent statoliths with an apparent lack of central pigmentation and discernible growth rings. Figure 5.9c and d show deformed statoliths, c) appears to have a double nucleus (arrows) and d) has had accelerated growth in the top right and bottom left portions of the statolith. Figure 5.9e, shows an apparent crystallised statolith with large crystal formations visible on the outside of its structure and no visible growth rings. The statolith from Shetland (Figure 5.9f), has an external granular appearance. When this statolith was cleaned in 20% NaOH for 30 minutes to remove adhered organic matter the external structures persisted, suggesting they were likely composed of calcium carbonate. Opaque statoliths were a more frequently encountered issue than crystallised statoliths, with most sampled populations having a frequency of $\approx 5\%$, however JE4 and Amlwch had high frequencies (34.07% & 59.6% respectively, Table 5.2) of opaque statoliths. This problem nearly always occurred in both statoliths within an affected animal (95%), these individuals were excluded from any further analyses. Figure 5.10 shows examples of opaque statoliths from whelks collected from various sites. Figure 5.10a & b display fully opaque statoliths, although there are a few visible growth rings in b), it is not possible to discern all of the growth rings. Figure 5.10c & d appear to show statoliths that have opaque regions within their structure that may be caused by discrete events in the life of the whelks that have later been overcome. Figure 5.10e & f show deformed and opaque statoliths from juvenile *B. undatum* from Amlwch.

Immersing opaque statoliths in 20% NaOH for 6 hours to remove any adhering organic matter did not improve the clarity of the statolith growth rings within opaque statoliths. Five opaque statoliths were selected and the different grinding and imaging processes described above were applied to try and improve the clarity of the rings. Whilst passing transmitted light through a ground and polished statolith (Figure 5.11a) increased the visibility of the growth rings, the outermost most recently deposited rings remained invisible. Similarly viewing ground and polished statoliths in reflected light (Figure 5.11b) also did not improve the clarity of the rings. By comparison (Figure 5.11c) shows the opaque appearance of the whole mounted statolith with no visible rings.

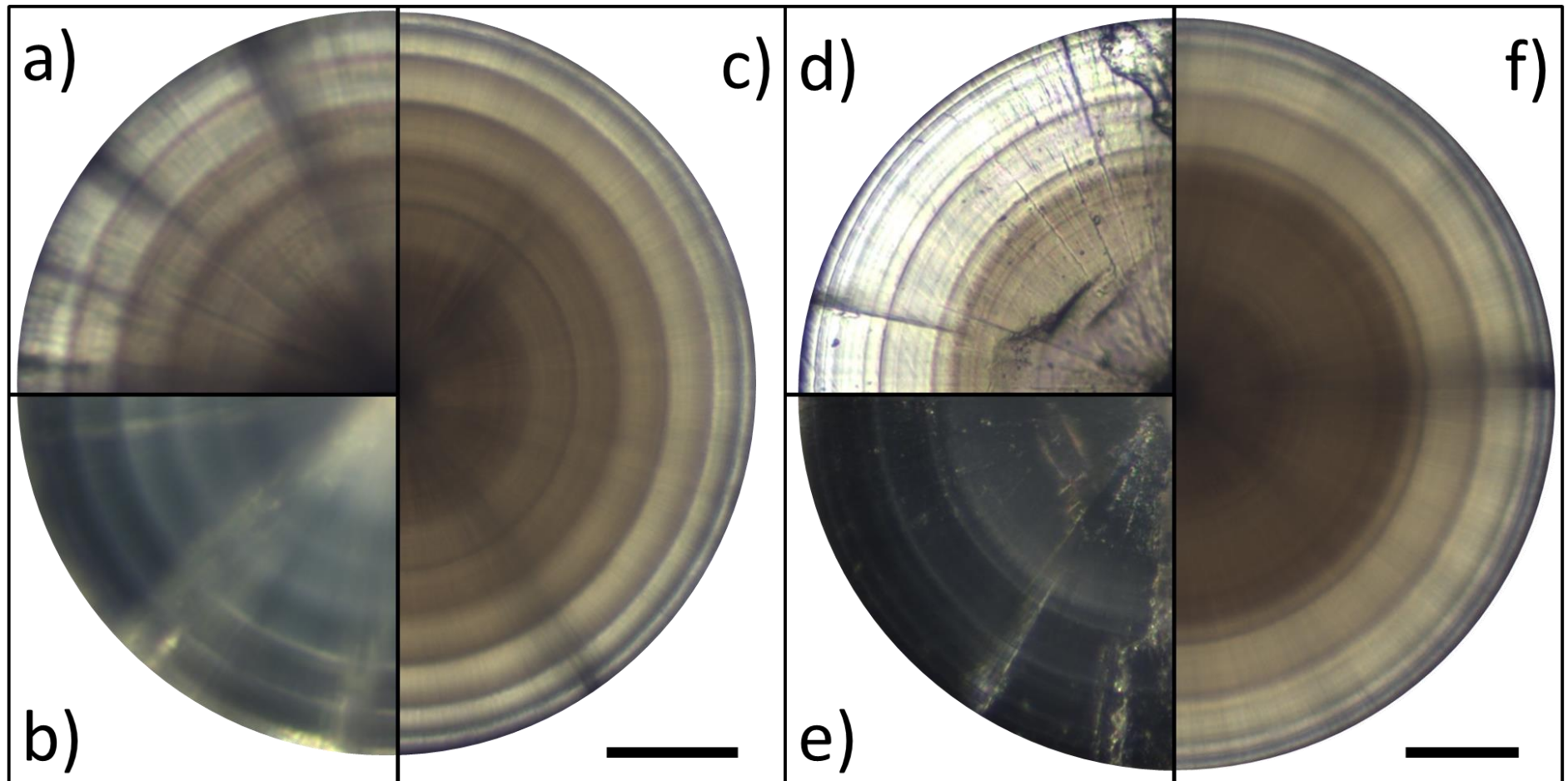


Figure 5.7. Composite images of statoliths taken from whelk specimens from the Menai Strait, showing differences in preparation and imaging techniques. a-c) a statolith from a female specimen, d-f), a statolith from a male specimen. a & d) resin mounted, ground and imaged with transmitted light. b & e) resin mounted, ground and imaged with reflected light. c & f) resin mounted, whole statoliths imaged with transmitted light.

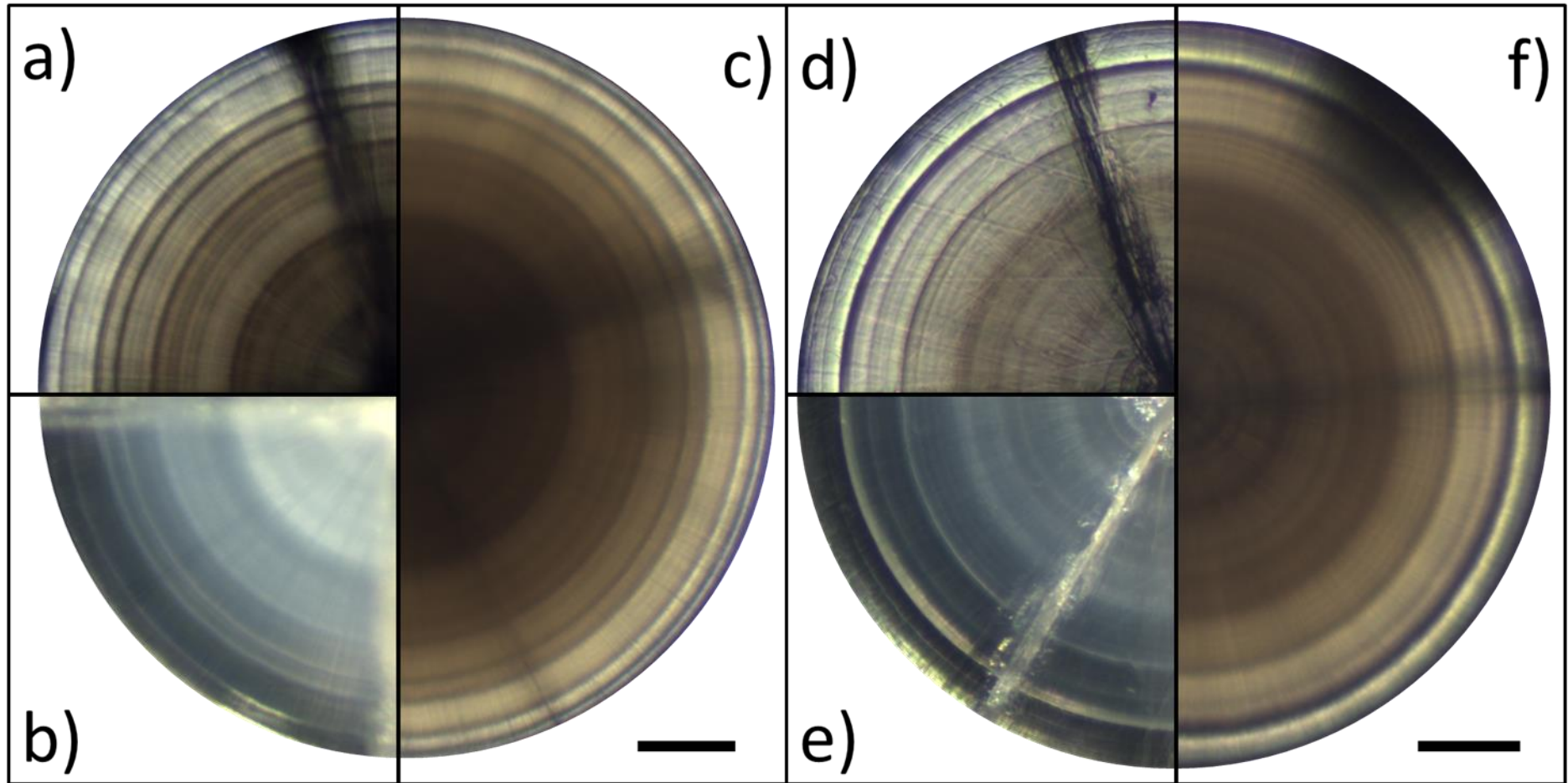


Figure 5.8. Composite images of statoliths taken from male specimens from Shetland (a-c) and Jersey (d-f), showing differences in preparation and imaging techniques. a & d) resin mounted, ground and imaged with transmitted light. b & e) resin mounted, ground and imaged with reflected light. c & f) resin mounted, whole statoliths imaged with transmitted light. Scale bars represent 25 μm .

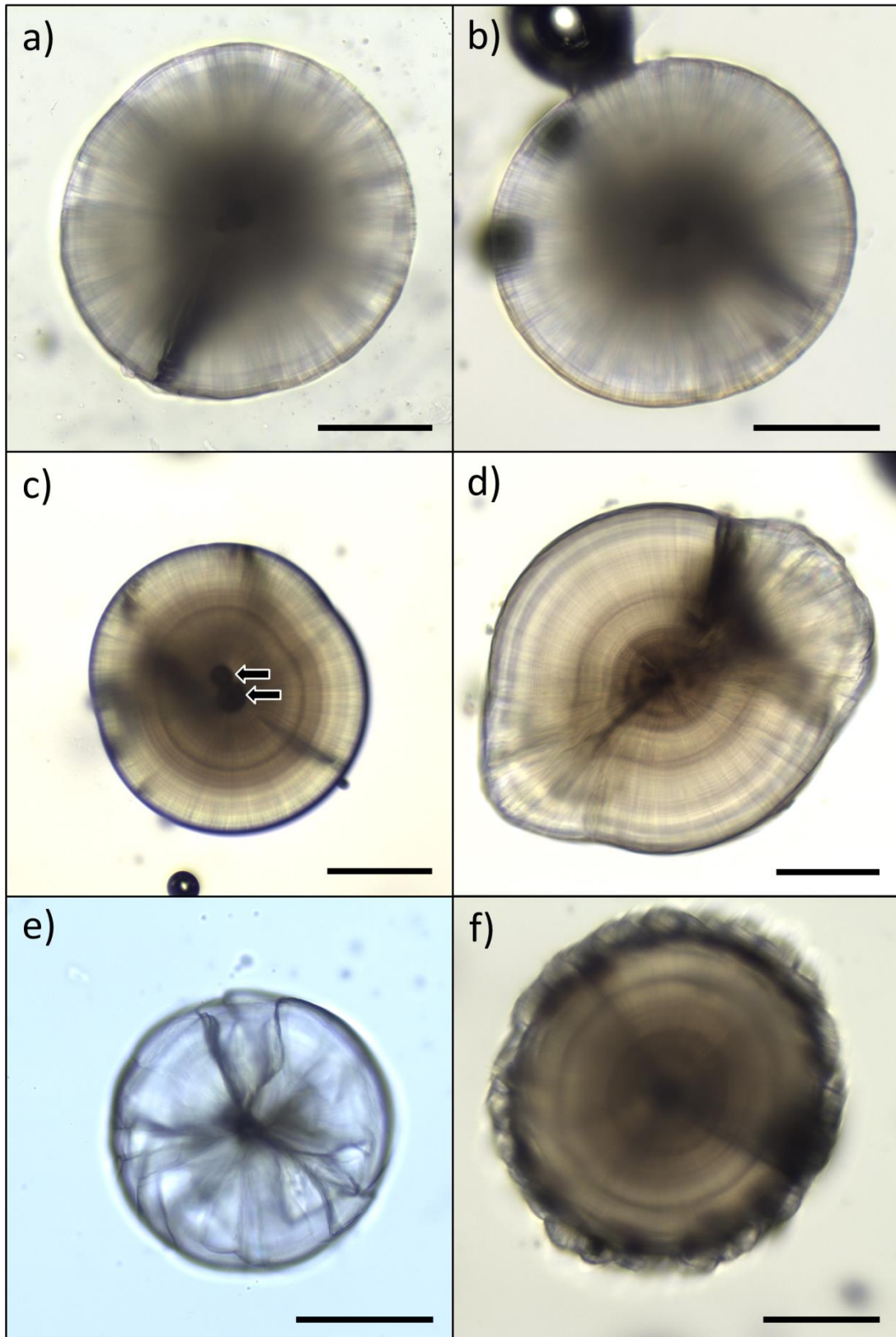


Figure 5.9. Photomicrographs of deformed and ‘crystallised’ statoliths. a & b) statoliths taken from different adult whelk specimens from the Menai Strait lacking the characteristic brown coloured centre with indiscernible growth rings, c & d) statoliths taken from different adult whelks from the Menai Strait showing a deformed growth appearance, c displays a double nucleus (black arrows), e) a statolith from the Menai Strait showing an external crystallised structure and f) a statolith from a Shetland whelk showing granules attached to the outer surface of the statolith. Scale bars represent 50 μm .

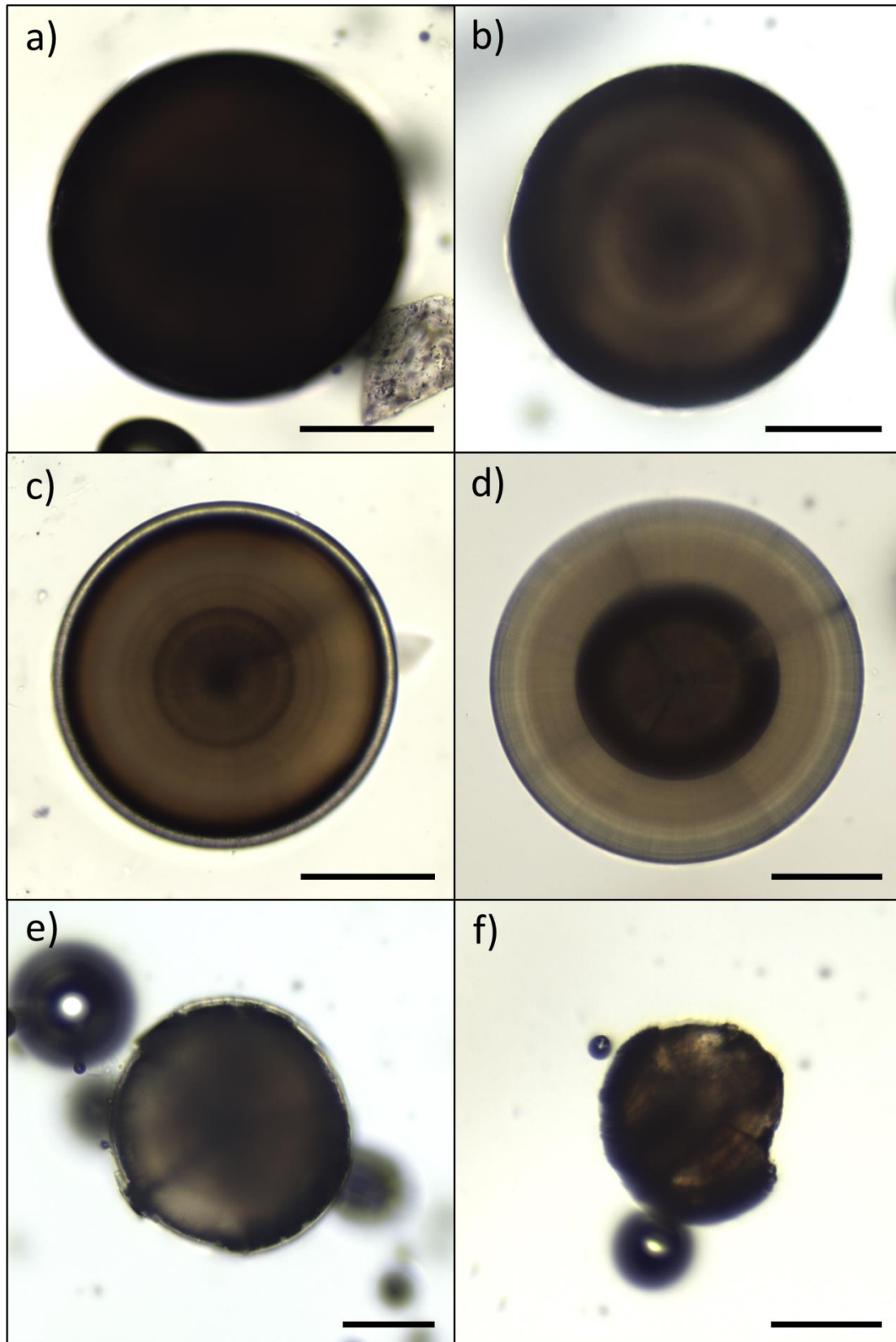


Figure 5.10. Photomicrographs of statoliths with central opaque regions. a & b) completely opaque statoliths taken from adult whelk specimens from the Menai Strait and Shetland respectively, c & d), statoliths taken from adult whelk specimens from the Menai Strait and Holyhead respectively. Both show a central opaque region followed by a normal statolith appearance and e & f) statoliths taken whelks from Amlwch showing a disfigured opaque structure. See Figure 5.1 for location of collection sites. Scale bars represent 50 μm .

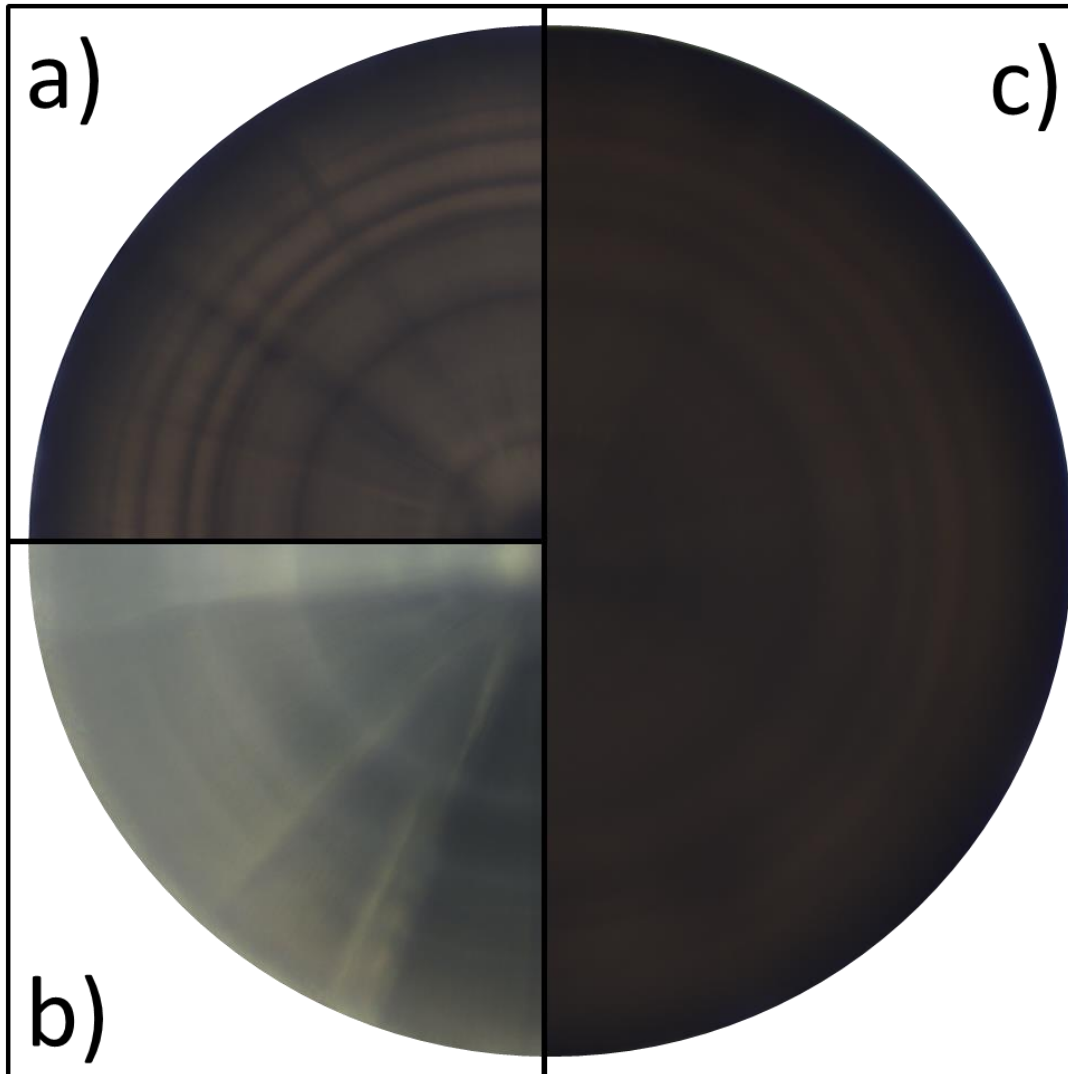


Figure 5.11. Composite image of an opaque statolith taken from a whelk collected from Amlwch, showing improvements to the clarity of the statolith using different preparation and imaging techniques. a) resin mounted, ground and imaged with transmitted light, b) resin mounted, ground and imaged with reflected light and c) resin mounted, whole statoliths imaged with transmitted light.

5.3.4 Hatching ring and growth ring formation

The ontogenetic growth of the juvenile whelk statoliths was monitored over a 24 month period. Growth and timing of deposition of the growth ring was estimated from statoliths extracted from 10 whelks selected randomly each month from the 2 annual cohorts of hatched juvenile whelks (2013 & 2014). The first clearly visible ring in the statoliths is the hatching ring (HR) formed following the whelk's emergence from the egg capsules. This small diffuse ring, $53.6 \pm 3.9 \mu\text{m}$ ($n = 32$ for the 2013 cohort)) and $55.1 \pm 5.9 \mu\text{m}$ ($n = 28$ for the 2014 cohort) is visible in all readable adult statoliths. A pictorial summary of seasonal statolith ring formation over a 24 month period is shown in Figure 5.12. The dark and diffuse hatching ring (HR) is visible in all four

statoliths in Figure 5.12 and the clear year 1 ring (yr 1) in Figure 5.12d is delineated by a colour change from dark brown to light brown and forms around February. In the laboratory-reared whelk statoliths weak disturbance rings are frequently seen but clearly discernible from the annual rings (e.g. yr 1 ring in Figure 5.12d). The colour changes of the hatching ring and year 1 ring can be clearly seen in field collected adult whelks and together with the validation of an annual periodicity of growth ring formation, now enable an accurate estimate of the age of individual whelks and the construction of population growth curves for *B. undatum* to be undertaken.

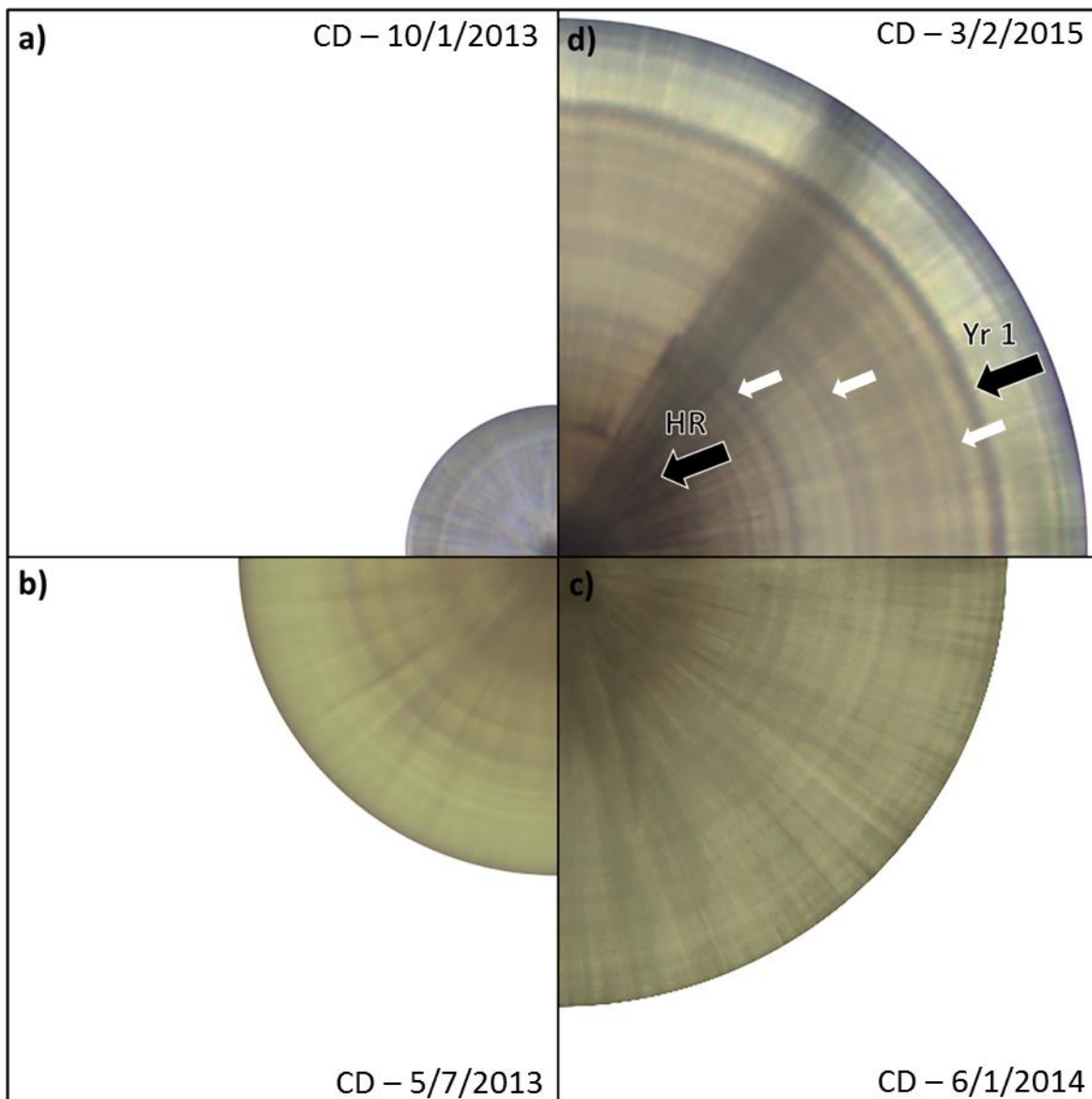


Figure 5.12. a) composite image showing seasonal juvenile statolith development on four collection dates (CD) at a) two weeks following hatching, b) 6 months after hatching, c) 1 year after hatching and d) 2 years after hatch. The hatching ring (HR) appears as a diffuse dark ring with a clearly deposited 1st year ring (Yr 1) that are both clearly visible in the two year old whelk. Suspected disturbance rings are highlighted with white arrows.

5.4 Discussion

5.4.1 Statolith extraction and preparation

The methods employed for gastropod statolith removal reported in this chapter differ from those previously reported for gastropod statolith extractions. Previously, whole animals or the body tissues were digested in sodium hydroxide to dissolve part (in-situ) or all of the body mass to reveal the statoliths (Barroso *et al*, 2005; Richardson *et al.*, 2005a & b). It was found that using the conventional alkali digestion method on *B. undatum* was unsuitable due in part to the large size of the animals that were being dissected and digested. The methods reported here are essentially similar to those employed by Galante-Oliveira *et al.*, (2013), who sectioned the ventral body surface of a range of small species of gastropods and dissected out the statoliths. For the larger *B. undatum* in this study it was easier and quicker to wholly bisect the animal due to the large body size and locate and extract the small diameter statoliths.

In a previous study, following extraction and statolith cleaning, Richardson *et al.* (2005a) hand-ground and polished the statoliths of the neogastropod *Neptunea antiqua* to observe the growth rings. In this study hand grinding and polishing statoliths of *B. undatum* did not improve the clarity of the growth rings when compared to the standard transmitted light images of whole statoliths. Viewed in transmitted light several of the outer most recently deposited growth rings were not clearly visible in sectioned statoliths. When the three different techniques of statolith preparation and illumination were compared the clearly delineated growth rings ‘matched up’ in all preparations seen in the composite image. However whole-mounted statoliths appeared in all cases to contain all the clear growth rings. Sectioning the statoliths increased the visibility of any weakly defined ‘disturbance’ rings. Disturbance rings are likely formed as a result of a temporary cessation in statolith growth, possibly due to changes in food availability or shell damage (these are clearly visible in Figures 5.7a, 5.8a & d). Weak disturbance rings are usually thinner and not as clearly defined and delineated as the annually-resolved rings and are visible in all statolith preparations. However, they were always clearer in the ground statolith sections and frequently observed in the statoliths of faster growing juvenile whelks. In whole statolith preparations viewed in transmitted illumination, weak rings were less apparent and the annually-resolved rings more easily observed. Whole statoliths are much quicker to prepare than grinding each statolith and this will improve the appeal of the method

as a fishery monitoring tool. For these reasons whole statolith preparations were studied in this thesis.

5.4.2 Statolith growth

During ontogenetic development the whelk statolith shows negative allometric growth with respect to shell length; small juvenile whelks had relatively large statoliths compared with large whelks. A similar relationship has been observed in other gastropod (Barroso *et al.*, 2005; Galante-Oliveira *et al.*, 2013) and cephalopod squid species (Arkhipkin & Mikheev 1993; Arkhipkin *et al.*, 1999). This phenomenon is difficult to explain from an ecological or developmental perspective. It might possibly be a consequence of linear growth of the statolith and sigmoid growth of body size throughout ontogeny but this question requires further exploration. Despite the strong relationship between statolith diameter and shell length (Figure 5.3, $R^2=0.9336$), it is not possible to use the relationship reliably to estimate shell length from statolith diameter for adult specimens (but see Chatzinikolaou & Richardson 2007). For example to determine shell length for each ring diameter, particularly in older (larger) whelks, would be difficult as statolith diameter in these individuals is highly variable. Differences in the relationship between StD and TSL was seen between sites for *B. undatum* in this study, this is similar to what is seen in *Nassarius (=Hinnia) reticulatus*, where Barroso *et al.*, (2005) observed differences in the relationship between StD and TSL with location on the west coast of Portugal. The findings of Barroso *et al.* (2005) differ from a study by Chatzinikolaou and Richardson (2007) which also investigated the statoliths of *N. reticulatus*, from 6 locations around Anglesey, North Wales (Chatzinikolaou & Richardson 2007). They found no difference in the relationship between StD and TSL between sites; although the power trend reported for their combined sites had a similar shape and growth pattern to the one presented here (Figure 5.6). It is possible that the differences observed between sites are due to a lack of cross over between size classes, i.e. most sites were missing small size classes and many were missing large size classes. This lack of directly comparable size ranges may account for the observed statistical dissimilarity in the relationship between statolith diameter and shell length between sites.

5.4.3 Scarcity of wild collected juveniles

Both field collected whelks and laboratory reared juveniles were studied to construct the relationship between statolith diameter and shell length. Data from small juvenile whelks were only available from laboratory reared specimens as only rarely were small (<25 mm TSL) whelks

caught in the scientific inkwell whelk pots, even when they were fitted with 3 mm mesh to retain any small whelks that were attracted to the pots. The mackerel bait offered in the pots was not deemed a controlling factor in attracting juvenile whelks to the pots as laboratory reared juveniles readily consumed mackerel when it was offered in the laboratory. Shelmerdine *et al.*, (2007) similarly found that whelks from the lower size classes (below 30 mm TSL) were absent from whelk catches from sites in the Shetlands, (east Shetlands at Scalloway and in the west at Whalsay) and South England (landed at Deal). They attributed this to the possibility of predation pressure acting on the newly hatched and developing juveniles. However, a more plausible explanation is that following emergence from their egg capsules, juvenile whelks congregate in nursery grounds distant from the main adult fished populations. From conversations with local whelk fishermen it appears anecdotally that for some whelk populations in North Wales, U.K., egg laying, juvenile development and juvenile growth of *B. undatum* likely takes place in inshore nursery areas from where the juveniles move and recruit into the adult fished populations.

The laboratory reared juvenile cohorts displayed an average monthly mortality of $\approx 2\%$ during the summer period in 2014 and 2015. Over the same period and at similar seawater temperatures, mortality in field collected adult whelks that were maintained in aquaria in the laboratory with a maximum daily average seawater temperature of 16.9°C , suddenly increased to $\approx 80\%$. The daily average seawater temperature in the tanks and in the field was not drastically different (16.96°C in aquaria and 16.68°C SST in the Menai Strait), however, the temperature in the tanks was monitored 3 hourly and the temperature regularly spiked to over 18°C over the summer. In the summer of 2016, the 2013 cohort of juvenile laboratory reared animals reached a size (and age) when they were likely maturing in natural populations i.e. 35-50mm shell length and 2.5 years of age. During a period of unseasonably elevated high seawater temperatures (tank seawater temperature spiked to $\approx 24^{\circ}\text{C}$ over 48 hours), $\approx 85\%$ mortality of the 2013 cohort of 35-50 mm whelks occurred in the laboratory aquaria. In the younger and smaller 2014 juvenile cohort almost no mortality ($\approx 3\%$) of whelks was observed in the same system. This suggests that small (<35 mm) juvenile animals may have a higher tolerance to warmer seawater temperatures and this may allow them to live and survive in shallower warmer waters in nursery grounds up until a size of 35-50 mm from where they migrate offshore into deeper colder water as the summer seawater temperatures reach their maximum.

Understanding differences in the age, growth rate and distributions of whelks in coastal waters will add immeasurably to understanding how to manage and conserve these important scavengers in coastal zones.

5.4.4 Statolith growth ring formation

This chapter has presented evidence that validates for the first time an annual periodicity of growth ring formation in the statoliths of *B. undatum* by studying the ontogenetic development of statoliths in laboratory reared whelks of known provenance. A growth ring was deposited annually during February and March when seawater temperatures were minimal in the Menai Strait. Female *B. undatum* lay egg capsules in which larvae develop and from which juveniles hatch directly leaving their egg capsules without a planktonic larval stage. The first discernible weakly defined statolith ring deposited was shown to be the ‘hatching ring’, formed as the juveniles emerge from their capsules. The hatching ring has a similar position in the statolith to the settlement ring formed in the statoliths of several gastropod species during metamorphosis from the planktonic larval veliger to the benthic juvenile stage e.g. *Polinices pulchellus* (Richardson *et al.*, 2005b) and *Nassarius reticulatus* (Barroso *et al.*, 2005; Chatzinikolaou & Richardson 2007). Thus these two kinds of juvenile rings in gastropods with different early life strategies represent the same life history event i.e. the transition from a larva to a juvenile. Whilst hatching ring diameters in the statoliths of reared *B. undatum* juveniles are similar (53.6 to 55.1 μm) it has been shown that maternal size directly influences egg capsule size and subsequently juvenile hatching size, which can also be mediated by intra-capsular cannibalism (Nasution, 2003; Nasution *et al.*, 2010, Smith & Thatje, 2013). Therefore, in a population with larger than average sized whelks the hatching ring will be likely larger than the average observed here. A strong relationship exists between statolith diameter and shell length, however with wide variation in statolith diameters in large (>60 mm) and older whelks this means it is not possible to estimate a whelk’s age solely from statolith size. The age of each whelk must be determined by counting the number of annually-resolved statolith rings.

In conclusion, the most appropriate methods for both statolith extraction and statolith visualisation have been detailed. An annually-resolved periodicity of growth ring formation in the statoliths removed from laboratory reared and monthly collected *Buccinum undatum* been validated. The employment of the statolith age determination method will now allow fisheries scientists to successfully sample and interpret statoliths from wild *B. undatum* populations.

5.5 References

- Arkhipkin AI (1997) Age of the micronektonic squid *Pterygioteuthis gemmata* (Cephalopoda: Pyroteuthidae) from the central-east Atlantic based on statolith growth increments. *J Mollus Stud* 63:287-290
- Arkhipkin AI, Laptikhovsky V and Golub A (1999) Population structure and growth of the squid *Todarodes sagittatus* (Cephalopoda: Ommastrephidae) in north-west African waters. *J Mar Biol. Ass UK* 79:467-477
- Arkhipkin AI, Mikheev A (1993) Age and growth of the squid *Sthenoteuthis pteropus* (Oegopsida, Ommastrephidae) from the Central-East Atlantic. *J Exp Mar Biol Ecol* 163:261-276
- Barroso CM, Nunes, M, Richardson CA and Moreira MH (2005) The gastropod statolith: a tool for determining the age of *Nassarius reticulatus*. *Mar Biol* 146:1139–1144
- Beesley PL, Ross GJB, Glasby CJ (eds) Polychaetes & Allies: The Southern Synthesis. Fauna of Australia. Vol. 4A Polychaeta, Myzostomida, Pogonophora, Echiura, Sipuncula. CSIRO publishing, Melbourne
- Chase R (2002) Behaviour & its neural control in gastropod molluscs. Oxford University Press, New York
- Chatzinikolaou E, Richardson CA (2007) Evaluating the growth and age of the netted whelk *Nassarius reticulatus* (gastropoda: nassaridae) from statolith growth rings. *Mar Ecol Prog Ser* 342:163-176
- Ehlers U (1997) Ultrastructure of the Statocysts in the Apodous Sea Cucumber *Leptosynapta inhaerens* (Holothuroidea, Echinodermata). *Acta Zool – Stockholm* 78 (1): 61-68
- Espeel M (1985) Fine structure of the statocyst sensilla of the mysid shrimp *Neomysis integer* (Leach, 1814) (Crustacea, Mysidacea). *J Morphol* 186:149-165
- Fahy E, Masterson E, Swords D, Forrest N (2000) A second assessment of the whelk fishery *Buccinum undatum* in the southwest Irish Sea with particular reference to its history of management by size limit. *Irish Fisheries Investigations* 6
- Fretter V, Graham A (1994) British Prosobranch Molluscs. The Ray Society, London
- Galante-Oliveira S, Marçal R, Espadilha F, Sá M, Abell R, Machado J, Barroso CM (2015) Detection of periodic Sr-Ca⁻¹ cycles along gastropod statoliths allows the accurate estimation of age. *Mar Biol* 162:1473-1483
- Galante-Oliveira S, Marçal R, Ribas F, Machado J, Barroso CM (2013) Studies on the morphology and growth of statoliths in Caenogastropoda. *J Mollus Stud* 79:340–345
- Haig JA, Pantin, JR, Murray LG, Kaiser MJ (2015) Temporal and spatial variation in size at maturity of the common whelk (*Buccinum undatum*). *ICES J Mar Sci* 72 (9):2707-2719
- Hollyman PR, Leng MJ, Chenery SRN, Laptikhovsky VV, Richardson CA (2017) Statoliths of the whelk *Buccinum undatum*: a novel age determination tool. In review with *Mar Ecol Prog Ser*
- Kideys AE (1996) Determination of age and growth of *Buccinum undatum* L. (Gastropoda) off Douglas, Isle of Man. *Helgol Meeresunters* 50(3):353–368

- Lawler A (2013) Determination of the size of maturity of the whelk *Buccinum undatum* in English waters – Defra Project MF0231
- Magnúsdóttir H (2010) The common whelk (*Buccinum undatum* L.): Life history traits and population structure. Master thesis. University of Iceland, Reykjavik
- McIntyre R, Lawler A, Masfield R (2015) Size of maturity of the common whelk, *Buccinum undatum*: Is the minimum landing size in England too low? *Fish Res* 162:53–57
- Morton B (1985) Statocyst structure in the Anomalodesmata (Bivalvia). *J Zool* 206:23–34
- Nasution S (2003) Intra-capsular development in marine gastropod *Buccinum undatum* (Linnaeus 1758). *Jurnal Natur Indonesia* 5:124–128
- Nasution S, Roberts D, Farnsworth K, Parker GA, Elwood RW (2010) Maternal effects on offspring size and packaging constraints in the whelk. *J Zool* 281:112–117
- Pálsson S, Magnúsdóttir H, Reynisdóttir S, Jónsson ZO and Örnólfsson EB (2014) Divergence and molecular variation in common whelk *Buccinum undatum* (Gastropoda: Buccinidae) in Iceland: a trans-Atlantic comparison. *Biol J Linn Soc Lond* 111:145–159
- Richardson CA (2001) Molluscs as archives of environmental change. *Oceanogr Mar Biol* 39:103–164
- Richardson CA, Kingsley-Smith PR, Seed R, Chatzinikolaou E (2005b) Age and growth of the naticid gastropod *Polinices pulchellus* (Gastropoda: Naticidae) based on length frequency analysis and statolith growth rings. *Mar Biol* 148:319–326
- Richardson CA, Saurel C, Barroso CM, Thain J (2005a) Evaluation of the age of the red whelk *Neptunea antiqua* using statoliths, opercula and element ratios in the shell. *J Exp Mar Biol Ecol* 325:55–64
- Santarelli L, Gros P (1985) Age and growth of the whelk *Buccinum undatum* L. (Gastropoda: Prosobranchia) using stable isotopes of the shell and operculum striae. *Oceanol Acta* 8 (2):221–229
- Shelmerdine RL, Adamson J, Laurenson CH, Leslie B (2007) Size variation of the common whelk, *Buccinum undatum*, over large and small spatial scales: potential implications for micro-management within the fishery. *Fish Res* 86:201–206
- Smith KE, Thatje S (2013) Nurse egg consumption and intracapsular development in the common whelk *Buccinum undatum* (Linnaeus, 1758). *Helgo Mar Res* 67:109–120
- Warton DI, Duursma RA, Falster DS, Taskinen S (2012) SMATR 3 – an R package for estimation and inference about allometric lines. *Methods Ecol Evol* 3:257–259
- Weetman D, Hauser L, Bayes MK, Ellis JR, Shaw PW (2006) Genetic population structure across a range of geographic scales in the commercially exploited marine gastropod *Buccinum undatum*. *Mar Ecol Prog Ser* 317:157–169

Chapter 6:

Micro-scale analysis of trace element incorporation
and structure of *Buccinum undatum* statoliths

6.1 Introduction

The structure and composition of gastropod statoliths varies between the species and groups in which they are found. The external morphology of gastropod statoliths is usually roughly spherical and uniform (Galante-Oliveira *et al.*, 2013). However, their internal structure and chemical composition have been seldom studied with only two recent publications on this topic investigating the statoliths of the netted whelk *Nassarius reticulatus* (Galante-Oliveira *et al.* 2014 & 2015). The internal structure of *N. reticulatus* statoliths was investigated by Galante-Oliveira *et al.* (2014), using a combination of Raman spectroscopy, powder X-Ray Diffraction (XRD) and Scanning Electron Microscopy (SEM). They showed a radial crystal structure emanating from a central nucleus containing both calcite and aragonite in a spatially homogenous matrix, with aragonite being the most abundant crystalline structure, although neither the absolute or relative abundances of each polymorph were quantified. Due to the differential preference of calcite and aragonite to incorporate certain trace elements (such as Sr and Mg, White *et al.*, 1977; Speer 1983; Lloyd *et al.*, 2008), there is a possibility that the presence of both of these polymorphs within the same matrix might influence the incorporation of trace elements along the growth axis if the homogeneity of the aragonite-calcite matrix is not constant.

The previous Chapter 5 focussed on the external morphology of *Buccinum undatum* statoliths and determined the periodicity of growth ring formation. Statoliths also have the potential to contain chemical information within their structure that might shed light on the environmental conditions at the time of their formation. It is important to understand how these structures are formed if environmental proxies are to be developed using geochemical analyses. Previous studies focussing on the geochemical analysis of statoliths have often used the statolith as a whole to determine the origins of specimens using trace element fingerprinting (Zacherl *et al.*, 2003a; Zacherl, 2005). Galante-Oliveira *et al.* (2015), using Laser Ablation – Inductively Coupled Plasma – Mass Spectrometry (LA-ICP-MS), identified cycles in the strontium to calcium ratio (Sr/Ca) in the statoliths of *N. reticulatus* at a sub-annual resolution that corresponded with the annual growth rings. Sr/Ca and magnesium to calcium (Mg/Ca) ratios have previously been used in past studies as seawater temperature proxies in mollusc carbonates e.g. mussels (*Pinna nobilis* - Freitas *et al.*, 2005) and cone snails (*Conus ermenius* - Sosidan *et al.*, 2006). However, there are often issues with disassociation of trace element profiles from environmental temperature profiles as discussed in Chapter 4. Trace element incorporation into statoliths potentially has a

much greater chance of being under physiological control as several more biological barriers have to be crossed to reach the calcifying fluid within the statocyst in comparison to the extra pallial fluid, for bivalve and gastropod shell formation. In this way, statoliths can be thought of as analogous to fish otoliths which often show strong biological controls on trace element incorporation (Sturrock *et al.*, 2014 & 2015).

The chemical analysis of small structures such as statoliths has several obvious limitations using conventional surface analysis techniques such as LA-ICP-MS that may require sample spot sizes of >10 μm to maintain a detectable signal of many trace elements (e.g. Galante-Oliveira *et al.*, 2015 – 12 μm spot size used for *N. reticulatus* statoliths). This is a proportionally large spot size when it is considered that some of the growth rings in *B. undatum* statoliths are $\approx 8 \mu\text{m}$ wide and by analogy $\approx 8 \mu\text{m}$ deep. There is a proportional relationship between the mass and volume of sample material analysed and the detection limit of the trace elements. In essence the smaller the volume removed the poorer the detection limit. Importantly, if the diameter of the crater is doubled from 15 to 30 μm and the depth doubled from 15 to 30 μm , the volume has increased by a substantial factor of 8 and the detection limits similarly improve. Therefore, the more common spot sizes of >30 μm are often used for the analysis of mollusc carbonates using LA-ICP-MS (e.g. Pourang *et al.*, 2014; Gomes *et al.*, 2016). However, this is not the only limitation when using quadrupole ICP-MS as this is a sequential analysis technique, albeit a very fast technique. Sequential analysis means that only one element/isotope can be measured at a time. Consequentially, the available material for measurement is divided between the numbers of elements/isotopes analysed. If the number of elements/isotopes counted is reduced from 16 to 4, the time for analysing each is increased, potentially improving detection limits by a factor of 4. The protocol that is adopted if smaller craters are attempted is to reduce the number of elements determined. Analytical techniques with a higher sampling resolution such as Secondary Ion Mass Spectrometry (SIMS) and nanoSIMS which have sample spot sizes of <2 μm have never before been applied to gastropod statoliths. However, they have been used to analyse trace elements and stable isotopes in fish otoliths (e.g. Matta *et al.*, 2013, Sturrock *et al.*, 2015) and trace elements in the statoliths of cephalopods (Zumholz *et al.*, 2007a). SIMS is an analysis technique which uses an instrument, frequently called an ion microprobe, when quantification of elements is required. An ion microprobe can be used to sample the upper few microns of a sample surface. This is achieved using a beam of primary ions (often comprised of O^- or Cs^+) which upon interaction with the sample surface, erode and release secondary ions

comprised of sample material (O'Connor *et al.*, 2003; Higson, 2006). These secondary ions are analysed using a mass spectrometer which filters the ions by mass and/or charge (O'Connor *et al.*, 2003; Higson, 2006). See [Appendix C](#) for an overview of the SIMS technique. Much like analysis using a quadrupole ICP-MS, conventional SIMS can only measure one element at a time so the sampling must be sequential, requiring the same balance of the number of elements analysed against the time taken for each one. The application of high-resolution, high-sensitivity techniques (such as SIMS) to the analysis of gastropod statoliths may allow the reconstruction of high resolution environmental proxies in a more time efficient manner than the analysis of multiple shell carbonate samples (see chapter 4).

Chapter 6 presents findings on the first and only structural chemical analyses of *B. undatum* statoliths and one of the first to sample gastropod statoliths at sub-annual resolution to investigate annual trace element cycles. These findings represent the first time that SIMS has been applied to gastropod statoliths. Firstly, findings on the internal structure of *B. undatum* statoliths explored using both SEM and micro-Raman spectroscopy are presented. Trace element profiles within the statoliths analysed using SIMS will then be presented and discussed. Three main trace elements were analysed, Mg, Sr and Na; it was hypothesised that Sr would provide the best proxy for annual seawater temperature due to previous findings from Galante-Oliveira *et al.* (2015) in the statoliths of *N. reticulatus*. Strontium was also the most promising trace element for temperature reconstructions in the shells of *B. undatum* (presented in Chapter 4). Changes in the calcium carbonate polymorph of statoliths were then investigated at high resolution using synchrotron based (Diamond Light Source) transmission micro XRD (μ XRD) to investigate any effect that a potential mix of calcite and aragonite may have had on trace element incorporation (analysed using SIMS). The results from the μ XRD analyses also allowed conclusions to be made on the crystal structure of the statoliths. Finally, chemical profiles from the statoliths will be compared to chemical profiles from the corresponding shells (analysed in Chapter 4) as a final validation of annual growth ring formation.

6.2 Materials and methods

6.2.1 Scanning Electron Microscopy (SEM)

The left and right statoliths from 3 small and 3 large whelks from the Menai Strait were selected for structural analysis based on the clarity of the growth rings. Three animals with clear statolith growth rings and 3 with less clear growth rings were chosen. Polished and etched statoliths were prepared and imaged as follows. Each statolith was mounted in Kleer-Set resin (Metprep) on a microscope slide and left to cure for 48 hours. The statolith was then ground by hand to the central plane using progressively finer 400, 1200, 2500 & 4000 silicon carbide grinding papers lubricated with Milli-Q® quality water. Each statolith was finally polished with a 1 µm diamond suspension gel and thoroughly cleaned with detergent and water and dried before submersion in 0.1M Hydrochloric acid for 2 minutes to etch the exposed statolith surface. The resin sections containing the statoliths were then carefully removed from the microscope slides using a scalpel, attached to an aluminium SEM stub and gold coated. The exposed and etched statolith surfaces were then imaged using a Phenom-Pro table top SEM (PhenomWorld) with an acceleration voltage of 10kV in charge reduction mode. The 3D surface reconstruction and height measurement was undertaken using the ProSuite software (PhenomWorld). This SEM is located at the Biocomposites centre at Bangor University.

Statolith fragments imaged using SEM were prepared and imaged as follows. Statoliths were placed in a watch glass and broken into fragments using fine tipped forceps (0.10 x 0.06mm tip) and selected pieces mounted on Kapton (poly (4,4'-oxydiphenylene-pyromellitimide)) tape. The statolith fragments were imaged using an FEI QUANTA 600 environmental scanning electron microscope (SEM) operated in low vacuum mode, with an electron beam accelerating voltage of 12.5 - 15 kV, a beam probe current of 0.14 - 0.26 nA, and a working distance of 10.6-10.9 mm. This SEM is located at the British Geological Survey (BGS), Nottingham.

6.2.2 Micro-Raman Spectroscopy (MRS)

Raman spectroscopy was undertaken using the methods and experimental conditions outlined in Chapter 3 (3.2.3). These methods were used to analyse 3 sample spots along the growth axis of 3 broken statoliths to assess their calcium carbonate composition. Statoliths were dissected from adult whelks from the Menai strait and broken in a watch glass using the tip of a pair of forceps.

6.2.3 Secondary Ion Mass Spectrometry (SIMS)

SIMS analysis of statolith sections conducted during this project was possible due to a successful application to the NERC Edinburgh Ion Microprobe Facility (EIMF, grant code: IMF543/1114, [Appendix I](#)). An overview of the Ion microprobe system used for the analysis can be found in [Appendix C](#). A total of 34 whelks from 3 sampling locations as well as aquarium grown animals were chosen based upon their size and sex. The largest sexually mature animals with the least number of serious damage incidences to their shells were chosen from adult populations to reduce the impact of disturbance lines in the statolith caused by shell damage. Adult whelks from Shetland, the Menai Strait and Jersey were selected for analysis. Three male and 3 female specimens were chosen from each of the sites. These comprised all of the specimens analysed in chapter 4 (3 males from Shetland and Jersey as well and 3 males and females from the Menai Strait) plus 3 female specimens from Shetland and Jersey. As well as field collected specimens, immature laboratory reared animals (rearing methods outlined in Chapter 3, section 3.2) of known age were chosen. A selection of 4 above average size and 4 below average size juveniles (2 males and 2 females for each) were selected from the same hatched cohort at year 1 and year 2 time points. Only 6 of the 8 analysed specimens from each year are presented here for clarity (3 large and 3 small) as no differences were found between male and female juvenile specimens.

The chosen whelks were processed for sexual maturity assessment following the methods outlined in Chapter 2 (section 2.2.2.1) and both statoliths were removed using the methods described in Chapter 5 (section 5.2.2). However, neither statolith was embedded immediately, instead both were stored in 70% IMS in labelled 0.5ml Eppendorf™ tubes denoting the sample number and location/position (i.e. left or right hand statolith). Statoliths were sampled from 14 of the 15 specimens for which shell analyses were undertaken in chapter 4 (all samples from the Menai Strait and laboratory reared animals, all male specimens from Jersey and Shetland), aside from the pilot specimen. This was completed with the aim of comparing the geochemical analyses of matching shells and statoliths.

6.2.3.1 Embedding

The sample requirements for SIMS analysis are strict as the sample blocks have to fit into a 1 inch circular sample stage, be of uniform thickness and be able to remain intact in a vacuum of 5×10^{-10} Torr. Due to the nature of the sampling process, a novel method of sample preparation

had to be developed. An individual statolith was embedded using EpoThin™2 resin (Buehler) in a single 1 inch round mould placed on a glass microscope slide. A translucent mould for embedding could not be sourced from a commercial supplier in the size required so instead the upper section of a round plastic histology mould was used (Figure 6.1). Mould translucency was essential as once the resin had been poured the statoliths were manipulated to ensure they were correctly orientated. A circular glass slide of just <26 mm diameter, coated on the underside with silicone grease, was placed in the base of the inside of the histology mould. The silicone grease formed a seal between the underside of the slide and the mould to prevent resin running beneath the slide into the rectangular base of the mould (see Figure 6.1a & b). The sample number of the statolith was scratched into the underside of the slide whilst a crosshatch was scratched onto the upper surface of the slide using a diamond scribe to create a surface for resin attachment and limit the problem of resin detachment during grinding and polishing. Initially a base layer of resin was poured into the mould (≈ 1 mm depth) and left to cure for 72 hours at room temperature.

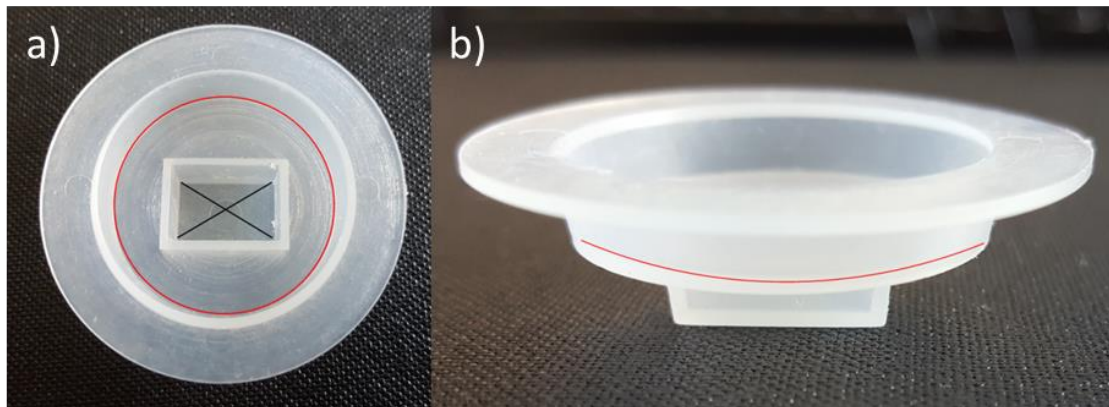


Figure 6.1. Plastic histology moulds used to embed statoliths on 25 mm round slides, a) dorsal view and b) lateral view. The red circle represents a 26 mm diameter circular well that was used to support the circular slides with silicone grease isolating the resin from the rectangular well beneath (denoted by the black X).

The left hand statolith from each of the selected whelks was transferred into the centre of the prepared base layer of resin. This was achieved by decanting the contents of the Eppendorf tube into a watch glass, carefully removing the statolith with fine tipped forceps (0.10 x 0.06 mm tip) and transferring it to the mould under a dissecting microscope. A second layer of resin was used to fully submerge the statolith in a 2-3 mm sheet. Whilst this second layer of resin was still liquid, each block was inspected under a dissecting scope and a hypodermic needle was used to manipulate the statolith into the correct position and orientation, with the dorso-ventral axis of

the statolith perpendicular to the slide. This second layer was then left for 72 hours to cure at room temperature.

6.2.3.2 Grinding

A bespoke sample holder for grinding was constructed from a 2 cm thick block of acrylic sheet with a 1-inch round x 1 mm deep hole machined into the surface, which allowed each block to be held in place and ground by hand. Four grades of silicone carbide wet grinding papers (400, 1200, 2500 & 4000) were used to reach the central plane of each embedded statolith (Figure 6.2). The progression of the grinding was monitored regularly under a dissecting microscope to check progression and avoid over-grinding. 400 and 1200 papers were not used once the statolith itself had been reached as the coarse nature of these papers was liable to fracture the statolith. Once the central plane was reached, two grades of diamond gel polish (3 μm & 1 μm , Presi) were used in conjunction with a Memphis polishing cloth (Metprep) to obtain the smoothest finish possible. Each slide was then imaged using a Meiji Techno MT8100 microscope with a Lumenera Infinity 3 microscope camera at varying magnifications to create maps for the SIMS analysis. Each slide was then gold coated prior to SIMS analysis.

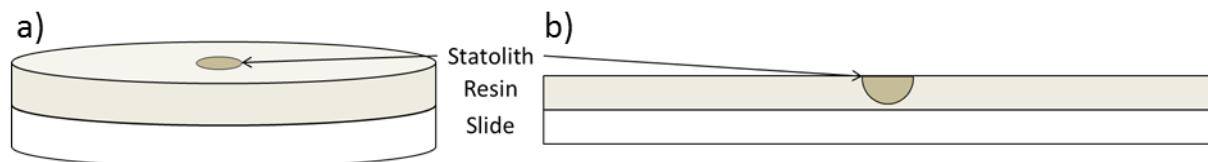


Figure 6.2. Diagrammatic representation of an embedded statolith used in the SIMS analysis. a) Represents a statolith placed in the centre of a circular glass slide and b) shows a lateral view of a cross section through the centre of a whole slide. The statoliths have been enlarged in these diagrams for visibility, representing roughly 2 mm as opposed to the actual size of ≈ 0.25 mm.

6.2.3.3 SIMS analysis

SIMS analysis was carried out at the Edinburgh Ion Microprobe Facility (EIMF) using a CAMECA IMS-4f Ion Microprobe with a primary negative ion beam ($^{16}\text{O}^-$) from a duoplasmatron source. Samples were pumped to a vacuum of 5×10^{-10} Torr and a pre-ablation path was cleaned via a beam current of 6 nA with an input energy of 15 KeV using primary aperture 1 to give a beam size of ≈ 25 μm ; 10 μm steps were used to remove gold and pre-condition the statolith surface. Following this, a continuous sample track was made across the cleared section of each statolith using primary aperture 3 and beam current of 0.06 nA with an input energy of 15 KeV; this gave a spot size of ≈ 1 μm , a 25 μm image field was used and no energy filtering was employed. The 1

μm beam was used with a step size of 2 μm to create the sample track. The positively charged secondary ions were detected using an electron multiplier. Five elements were quantified across the growth axis of each statolith: ^{27}Al (to monitor contamination from polishing compounds), ^{44}Ca (to which all trace elements are compared to create a ratio), ^{23}Na , ^{88}Sr and ^{24}Mg . Initially ^7Li and ^{138}Ba were analysed in a single statolith, however the responses of both elements were low and heavily influenced by noise suggesting quantitative data would not be attainable. Thus these elements were not analysed in other statoliths. Elemental concentrations were defined using working curves based on standards previously analysed by bulk techniques, which included a mixture of inorganic and organically derived carbonates and a magnesium rich dolomite standard. Although no corrections were made, at the concentrations measured the molecular or doubly charged ion species e.g. $^{48}\text{Ca}^{2+}$ overlap on ^{24}Mg were considered negligible from measured standard samples. Doubly charged ions can cause interference during trace element analyses, this occurs when an ion picks up a double charge during ionisation. A doubly charged ion will have the same mass reading as the element with exactly half of its atomic mass (Thomas, 2011). This is overcome by analysing standards with known concentrations of target elements (such as magnesium-rich dolomite). Estimated $^{48}\text{Ca}^{2+}$ at mass 24 was <0.4 ppm wt. This standard analysis confirmed that any ^{24}Mg readings were an artefact of changes in ^{24}Mg concentrations instead of interference from doubly charged Ca species.

Owing to the symmetrical nature of the statoliths, duplicate tracks were taken in reverse from each statolith once the sampling had passed the central nucleus. Following analyses, data were converted from counts per second to a mg.kg^{-1} ratio against ^{44}Ca . The high precision of the technique coupled with the sampling resolution meant that no data smoothing was necessary.

6.2.3.4 Issues with resin

The standard type of casting resin (KLEERSET – Metprep) used in the sclerochronology group in Bangor University School of Ocean Sciences was unsuitable for SIMS analysis as polyester resins react unpredictably in high vacuum, causing interference with the sample signal. For this reason, a suitable epoxy resin was sought. Firstly, EPO-FLO (Metprep) was purchased under advice from the EIMF. Unfortunately, seemingly due to the low volumes of resin being used for this embedding process, a thin layer of unset resin on the surface of the block was always present which made it unfit for purpose. Several attempts were made to rectify this problem after contacting Metprep, including differing mixing times as well as differing ratios of resin and hardener, removing the unset resin with acetone and curing the resin in an oven set to 60°C .

However, none of these resolved the problem so a second resin was sought. The next resin chosen was EpoThin™2 from Buehler which after some initial issues with mixing fixed all of the above problems.

6.2.4 Transmission micro X-Ray Diffraction (μ XRD)

All transmission μ XRD sampling was undertaken following a successful rapid access request to the Diamond Light Source (DLS) synchrotron facility (grant code: sp13616-1, [Appendix J](#)). An overview of the μ XRD technique used can be found in [Appendix C](#). The right hand statolith of 18 whelks from the 3 locations and laboratory reared animals were analysed using μ XRD, following SIMS analysis. This was done to improve on the initial compositional analysis undertaken with MRS by increasing both the sampling resolution and sample number. Individual statoliths were prepared in an identical manner to the SIMS samples, however, they were ground to a final grade of 4000 and no polishing steps were employed. As a transmission technique was used, the sample needed to be both thin enough for the x-rays to pass through the statolith and have a symmetrical thickness with the nucleus in the centre of the section. To achieve this, once the plane of section of one side of the statolith had been ground to $\approx 15\ \mu\text{m}$ from the central nucleus, the resin block was carefully removed from the microscope slide with a scalpel and turned over. The ground surface was then attached to the slide using superglue and the grinding process was repeated to produce a thin statolith section of $\approx 25\text{--}30\ \mu\text{m}$. This thin section was removed from the slide using acetone to dissolve the glue and then cleaned in ethanol and Milli-Q® water. Small squares containing individual statoliths were cut from each of the thin resin sections using a scalpel. Each resin square was then mounted on a custom plastic slide (75 x 25 x 3 mm, laser cut acrylic sheet with a 25 x 18 mm window) and secured in position with Kapton tape, 6 samples to a slide (Figure 6.3). The plastic slides and Kapton tape are non-crystalline plastics and were used to avoid any distortion of the X-ray beam and subsequent sample diffraction. Each sample was imaged using a Meiji Techno MT8100 microscope with a Lumenera Infinity 3 microscope camera at x2.5 and x20 magnifications.

The I18 micro-diffraction beamline at the Diamond Light Source (DLS) has a collimated $2 \times 2\ \mu\text{m}$ X-ray beam. This was used with a step size of $2\ \mu\text{m}$ to create a line profile across the centre of each statolith, to investigate any mineralogical changes in the calcium carbonate phase (Figure 6.4). A beam current of 12 KeV was employed and a Photonics CMOS camera was used to collect the diffraction images. Standards of Silicon and Lanthanum Boride (LaB_6) were analysed to calibrate the beam and synthetic calcite and speleothem aragonite standards were analysed for

direct comparison with sample data (Brinza *et al.*, 2014). To check that no compositional changes had been caused within the statoliths during physical sample preparation, several XRD samples were taken of unmounted, broken statoliths. These were investigated as any heat created during grinding has the potential to cause a polymorph change from aragonite to calcite (Radha *et al.*, 2010; Gong *et al.*, 2012; Galante-Oliveira *et al.*, 2014). To check for potential damage to the statolith structure during μ XRD analysis, prolonged exposure to the X-ray beam was conducted at two points on the same statolith thin section, in the centre and at the outer edge. The beam was held on a single spot for 120 seconds, taking a separate diffraction pattern every 10 seconds to look for changes in structure over time.

All resulting data were converted to d-spacing values for ease of analysis and adjusted using a rolling ball baseline correction; all data processing was done in Dawn 1.9.0 (Basham *et al.*, 2015).

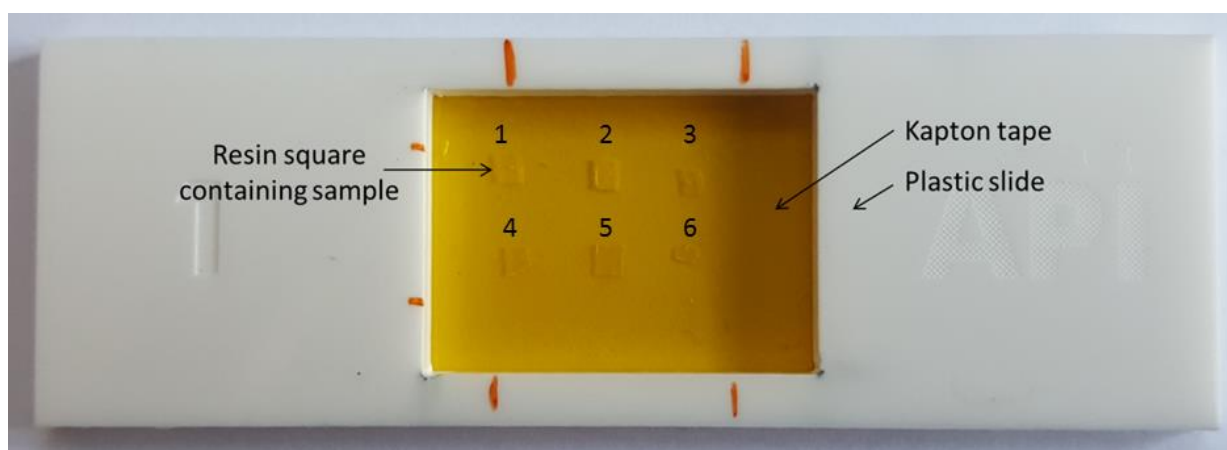


Figure 6.3. A plastic mount used to hold the samples for μ XRD. Adhesive Kapton tape was placed over the back of the window in the centre of the plastic mount to provide an adhesive surface on which to fix the resin squares containing the individual resin squares and statoliths. The slide shown contains 6 samples.

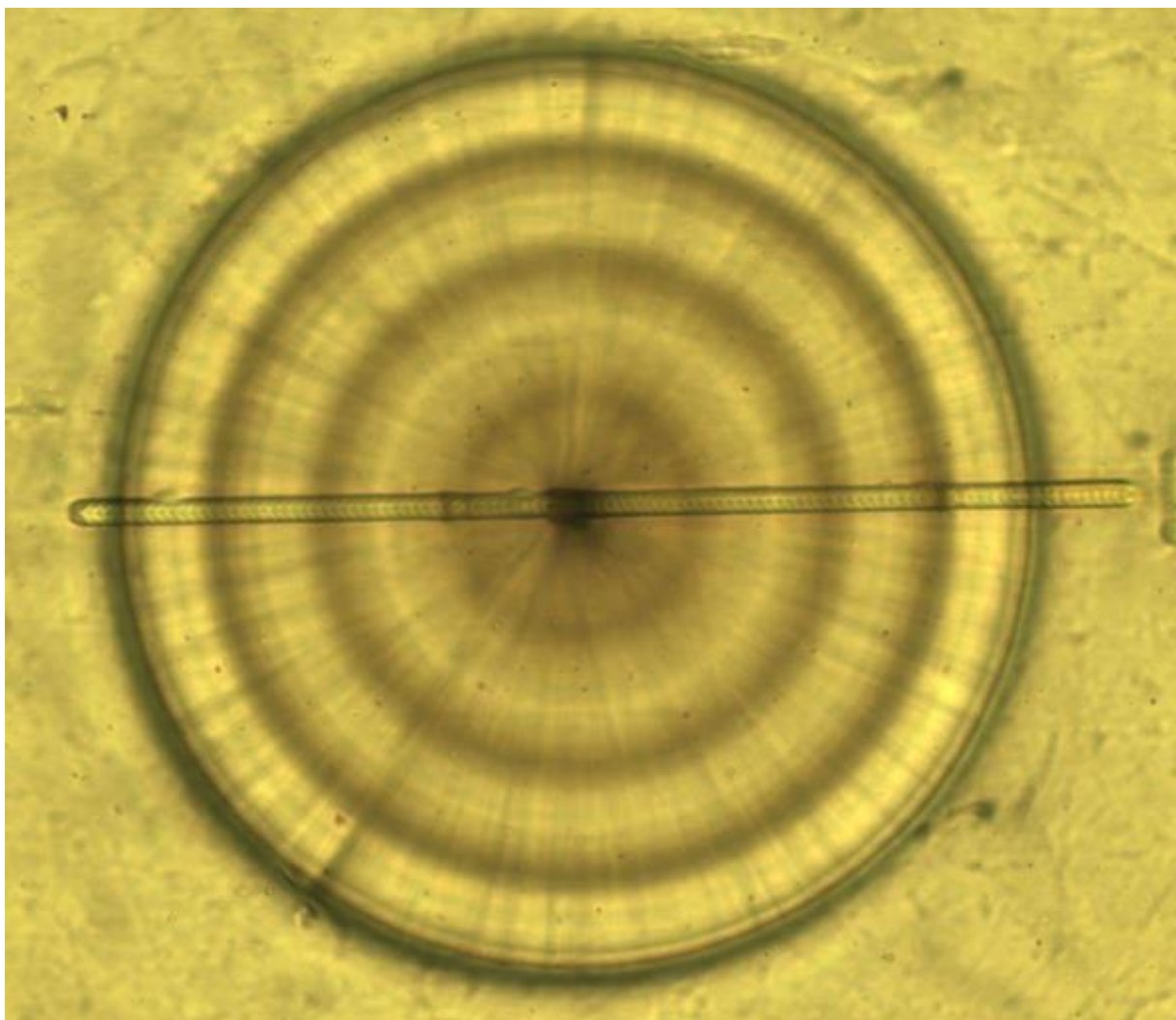


Figure 6.4. Photomicrograph of a post-analysed (μ XRD) statolith mounted in its resin square attached to Kapton tape beneath. The sampling track can be clearly seen across the centre of the statolith with the individual steps visible as regular small check marks within the sample trench. As μ XRD is non-destructive, the visible sample path does not represent damage to the statolith but rather to the Kapton tape.

6.3 Results

6.3.1 Statolith composition and structure

The composite statolith images shown in Figure 6.5 show an agreement between the visible dark rings seen in the optical microscope (OM) image of a whole statolith (left hand side of each image) and the exposed acid etched SEM image of the central plane of the paired statolith (right hand side of each image). The clarity of the rings in the SEM images suggests a clear structural change occurs during growth ring formation. This is further confirmed in Figure 6.6 which shows how the surface of the statolith is differentially etched, with the growth rings appearing more heavily etched than the intervening growth increments between the rings. This differential etching suggests differences in the calcium carbonate matrix between the darker rings and the growth between them, with the rings more susceptible to acid etching.

The broken statolith in Figure 6.7a is seemingly composed of aragonite. The Raman spectra extracted between 100 and 750 cm^{-1} shown in Figure 6.7b demonstrates a coincidence of peaks at 151 cm^{-1} , 183 cm^{-1} , 206 cm^{-1} and a wide peak at 702-706 cm^{-1} for all sample spots from the statolith and the aragonite standard. A shoulder is also visible on the 151 cm^{-1} peak at 143 cm^{-1} . By contrast the calcite standard peaks at 155 cm^{-1} , 281 cm^{-1} and 712 cm^{-1} indicate that this statolith contains no trace of calcite. There is however, a small chance that the low sampling resolution has missed calcite components included within the statolith structure. The only other published assessment of gastropod statolith composition found *Nassarius reticulatus* statoliths to be a homogenous matrix of both aragonite and calcite (Galante-Oliveira *et al.*, 2014). Figure 6.7c shows an additional peak between 2850 and 3000 cm^{-1} for the three sample spots. Peaks in this range are thought to be indicative of CH functional groups found within organic matter (Smith & Dent, 2005) and are thus likely indicative of the presence of an organic component within the crystal matrix.

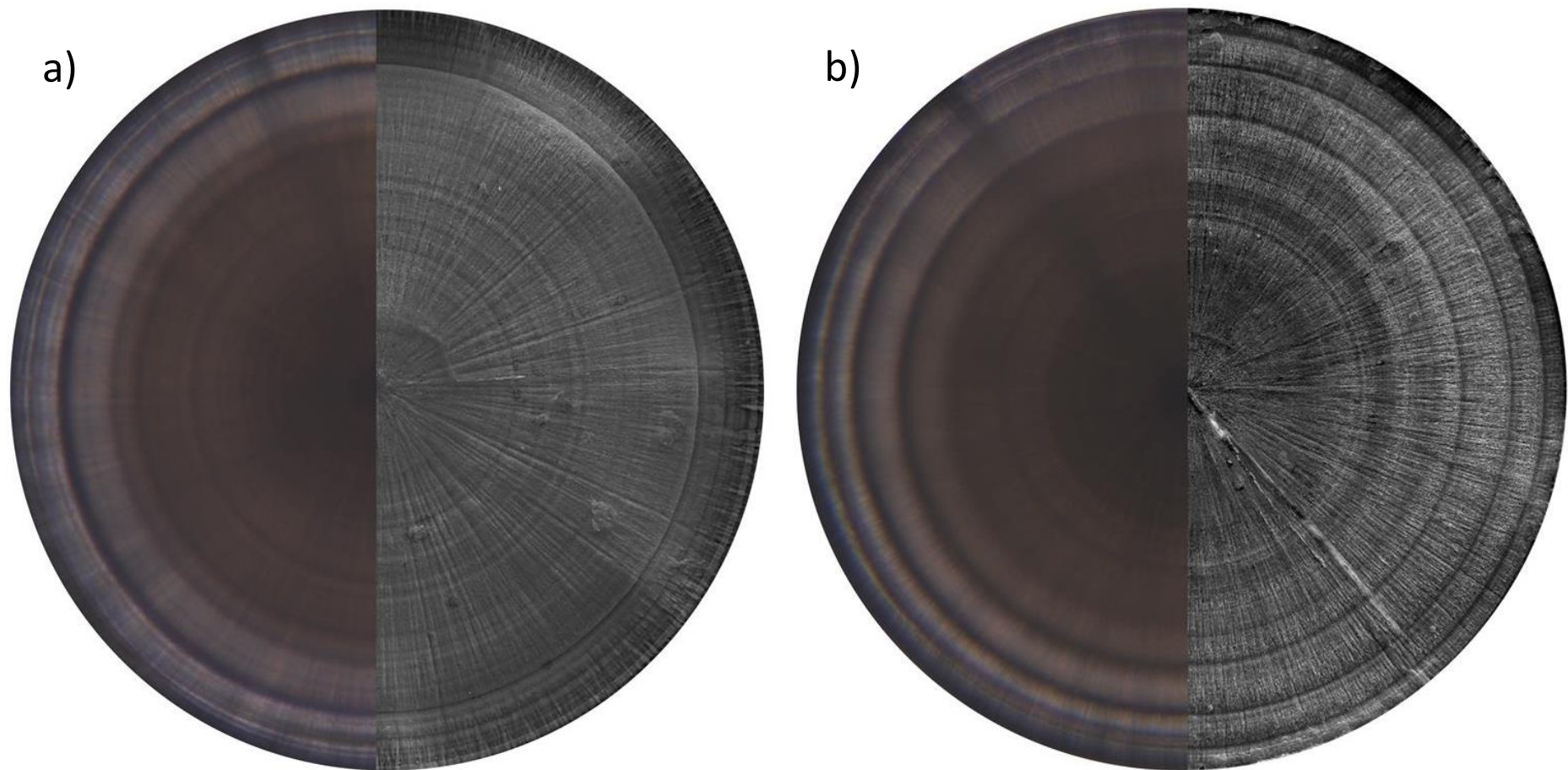


Figure 6.5. Composite images of both statoliths from two separate *B. undatum*, the left side of the image represents the left statolith, imaged whole at 20x magnification with transmitted light in a compound microscope. The right side represents an SEM image of the exposed, polished, and etched central plane of the right hand statolith. a) statoliths from a young (3 year old) whelk and b) statoliths from an older (5 years old) whelk. All statoliths were imaged in line with the dorso-ventral axis.

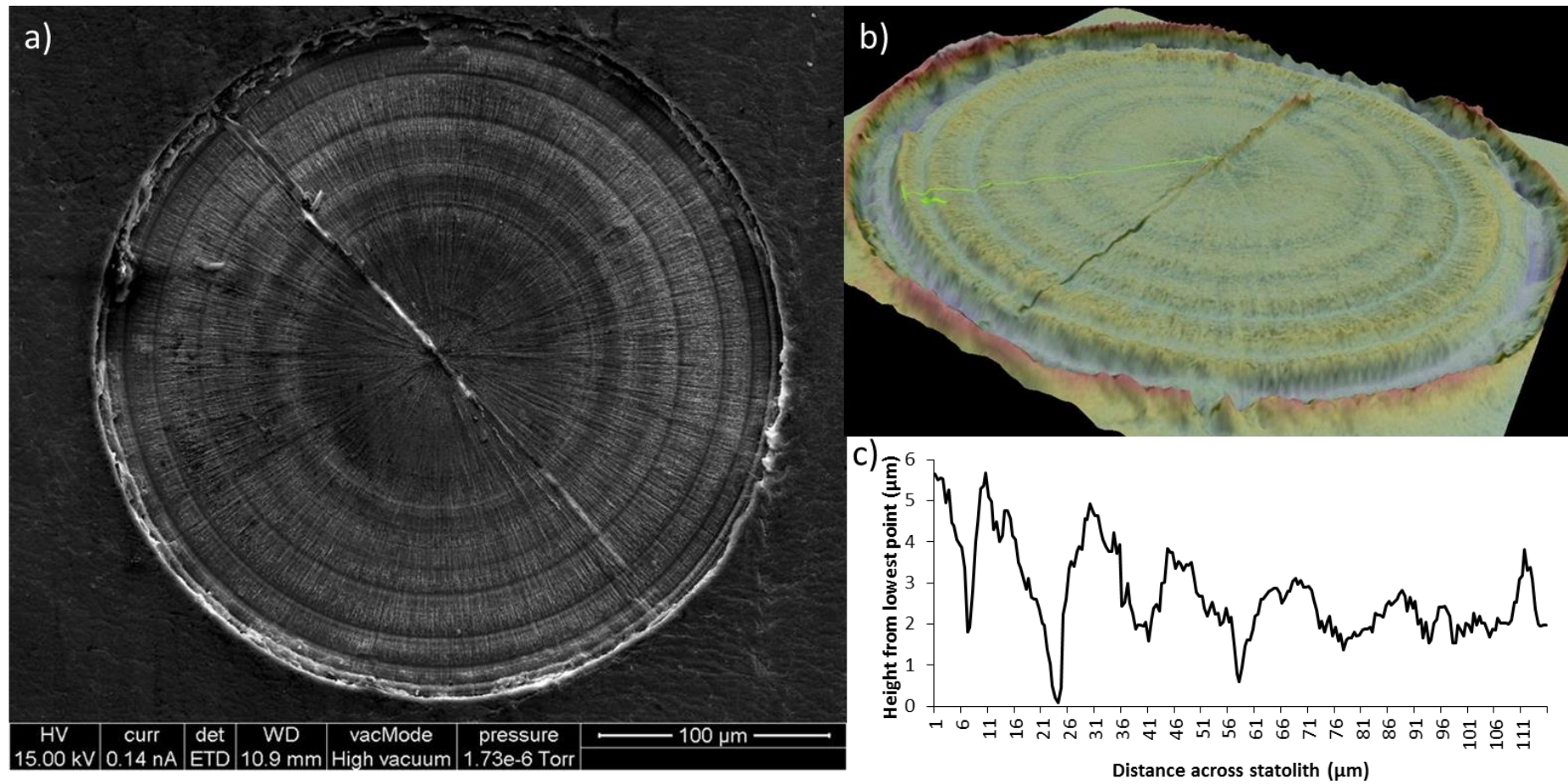
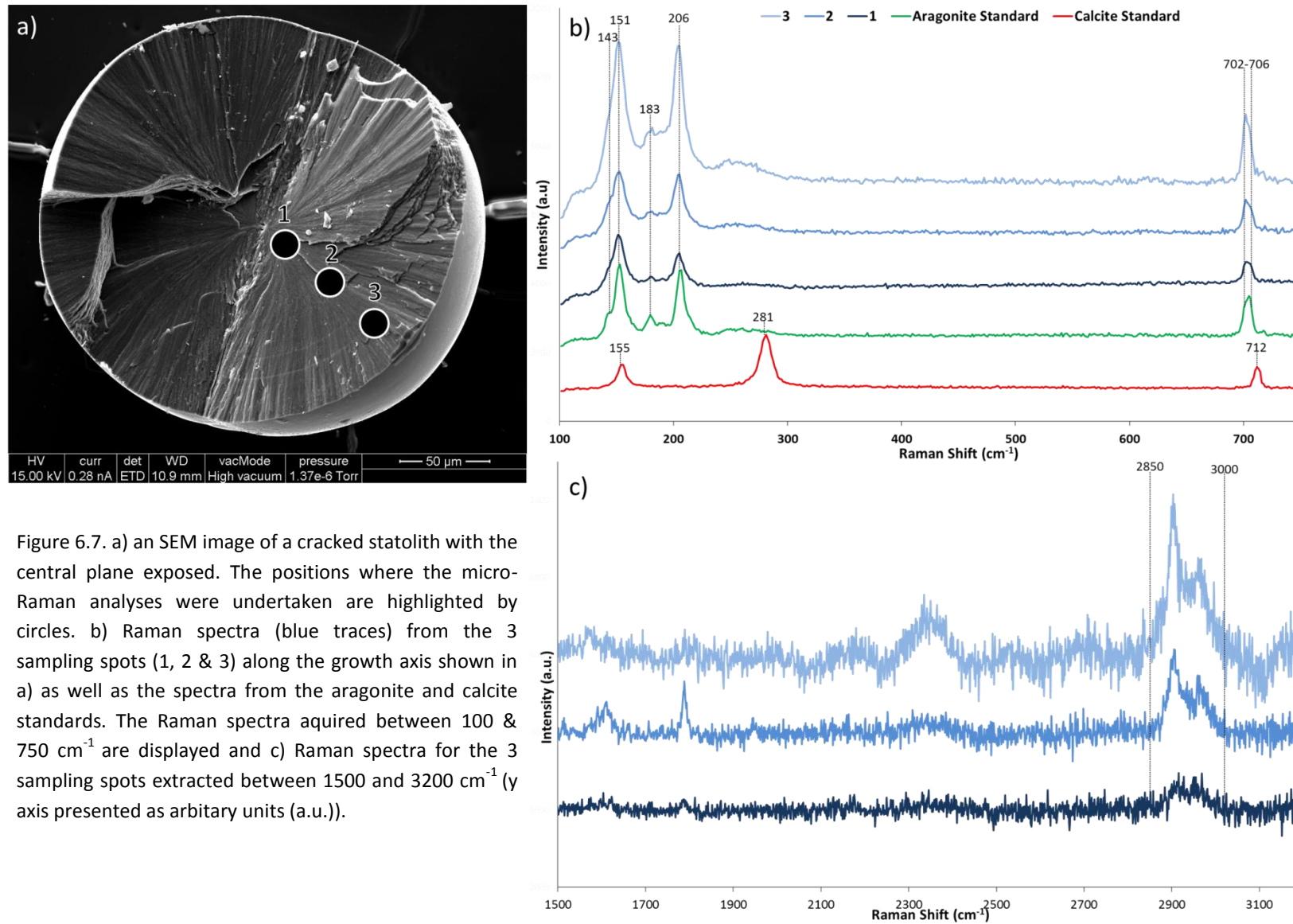


Figure 6.6. a) SEM image of a sectioned and etched statolith. The statolith was sectioned across the lateral plane, perpendicular to the dorso-ventral axis. b) 3D surface reconstruction of the statolith image shown in a). The fluorescent green line represents a 3D surface reconstruction, the results of which are shown in c), the 3D profile of the line transect highlighted in b), the values on the y-axis are displayed as height from the lowest point.



6.3.2 Statolith microchemistry

Whilst several trace elements were analysed with SIMS, Mg had the clearest cycles with minima corresponding to the annual growth rings. Figure 6.8 presents the profiles in Mg/Ca from 1 year old laboratory reared juvenile *B. undatum*. There is 1 clear peak in Mg/Ca outside the dark hatching ring visible in each statolith. The cycle is also present regardless of the size of the whelk, with both large and small animals exhibiting similar peaks. The annual periodicity of the Mg/Ca cycles is further confirmed with two Mg/Ca cycles present in the 2 year old laboratory reared animals of similar age but markedly different size (Figure 6.9). The peak of the second Mg/Ca cycle in each statolith is markedly lower than the peak of the first Mg/Ca cycle. Figures 6.10 – 6.12 show Mg/Ca SIMS profiles in statoliths acquired from field collected male (a & b) and female (c & d) *B. undatum* from the Shetlands (Figure 6.10), the Menai Strait (Figure 6.11) and Jersey (Figure 6.12). There is clear coincidence between the strong dark annual growth rings and the minima of the Mg/Ca cycles. The innermost annual cycle of Mg/Ca concentrations in the 2 year old laboratory reared whelks was always higher than the concentration of the subsequent Mg/Ca ratio cycles (Figure 6.9). The same was generally seen in statoliths from the field collected whelks i.e. the innermost Mg/Ca cycles (outside the hatching ring) were generally elevated compared with the subsequent Mg/Ca cycles (Figures 6.10, 6.11 & 6.12).

Two other elements (Sr and Na) were determined alongside Mg. Figure 6.13 shows the Sr/Ca and Na/Ca profiles from a polished and ground statolith from a Jersey whelk (a & b respectively), plotted together with the Mg/Ca profiles from the same statolith. The overall correlation between Sr and Mg is positive (Pearson's Correlation = 0.36). However, along the profiles in Figure 6.13 the concentrations differ as the 2 profiles are both positively and negatively correlated at different positions (times) along the growth axis and with no consistent pattern. Sr/Ca concentrations in all but one statolith of the 34 statoliths analysed rise towards the outer edges of each statolith on both sides. Profiles of Na/Ca and Mg/Ca are negatively correlated (Pearson's Correlation = -0.75) and suggest that Na concentrations peak during the winter with minima during the summer. Similar to the Sr/Ca ratios, the Na/Ca profiles appear to rise towards the outer part of the statolith, ending the profile $\approx 400 \text{ mg.kg}^{-1}$ higher than in the centre of the statolith but only on the right side of the sample. This was seen in all the adult 18 whelk statoliths and 6 of the 12 juvenile whelk statoliths analysed.

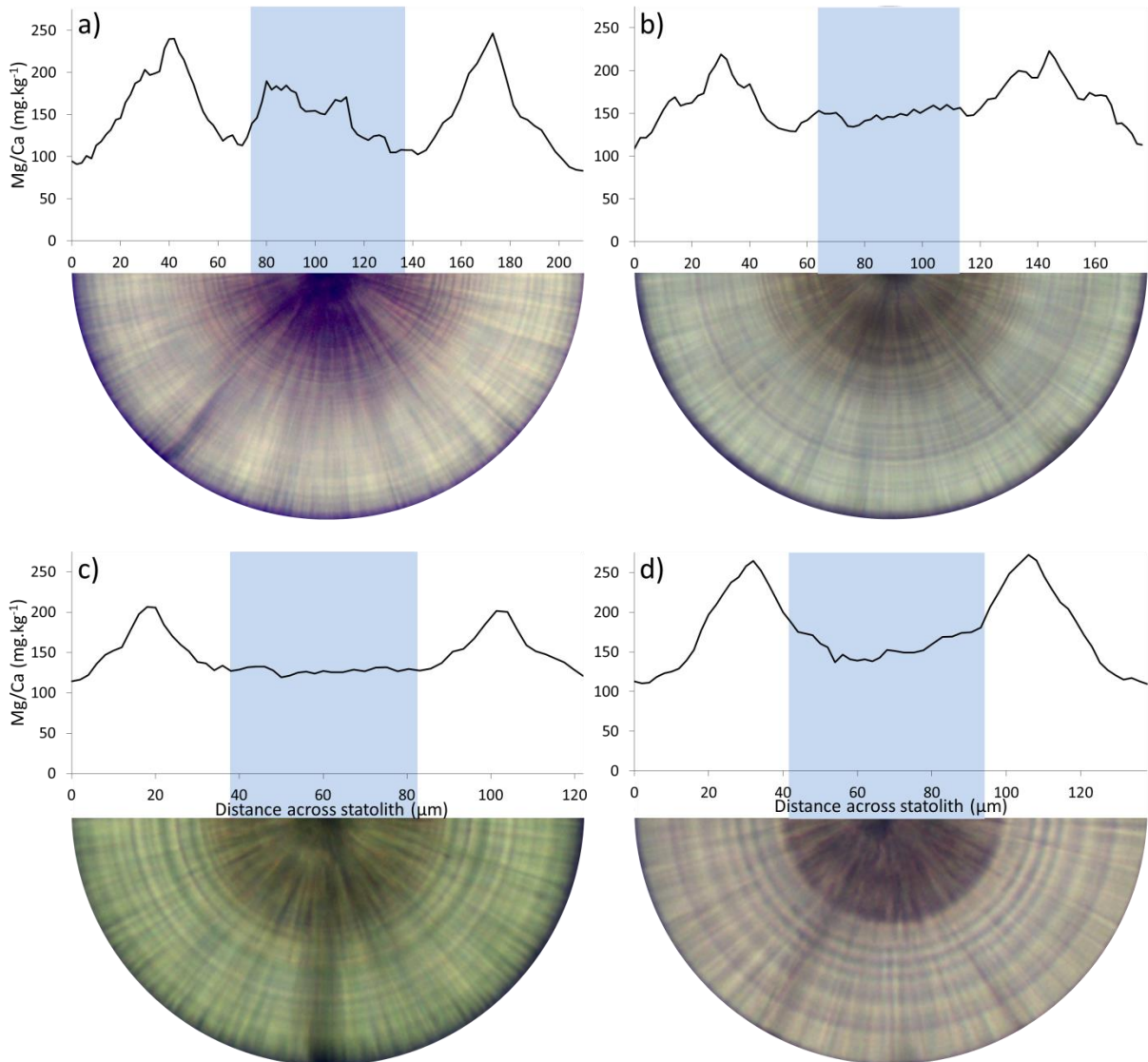


Figure 6.8. Photomicrographs of ground and polished statoliths from 1 year old laboratory reared *Buccinum undatum*, overlaid with profiles of the Mg/Ca ratios determined using SIMS. a & b) are statoliths from the largest male (a) and female (b) whelks (≈ 30 mm TSL) whilst c & d) are statoliths from smaller male (c) and female (d) whelks (≈ 10 mm TSL). Blue areas represent larval growth inside the hatching ring. The first ring is in the process of being formed around the circumference of the statolith.

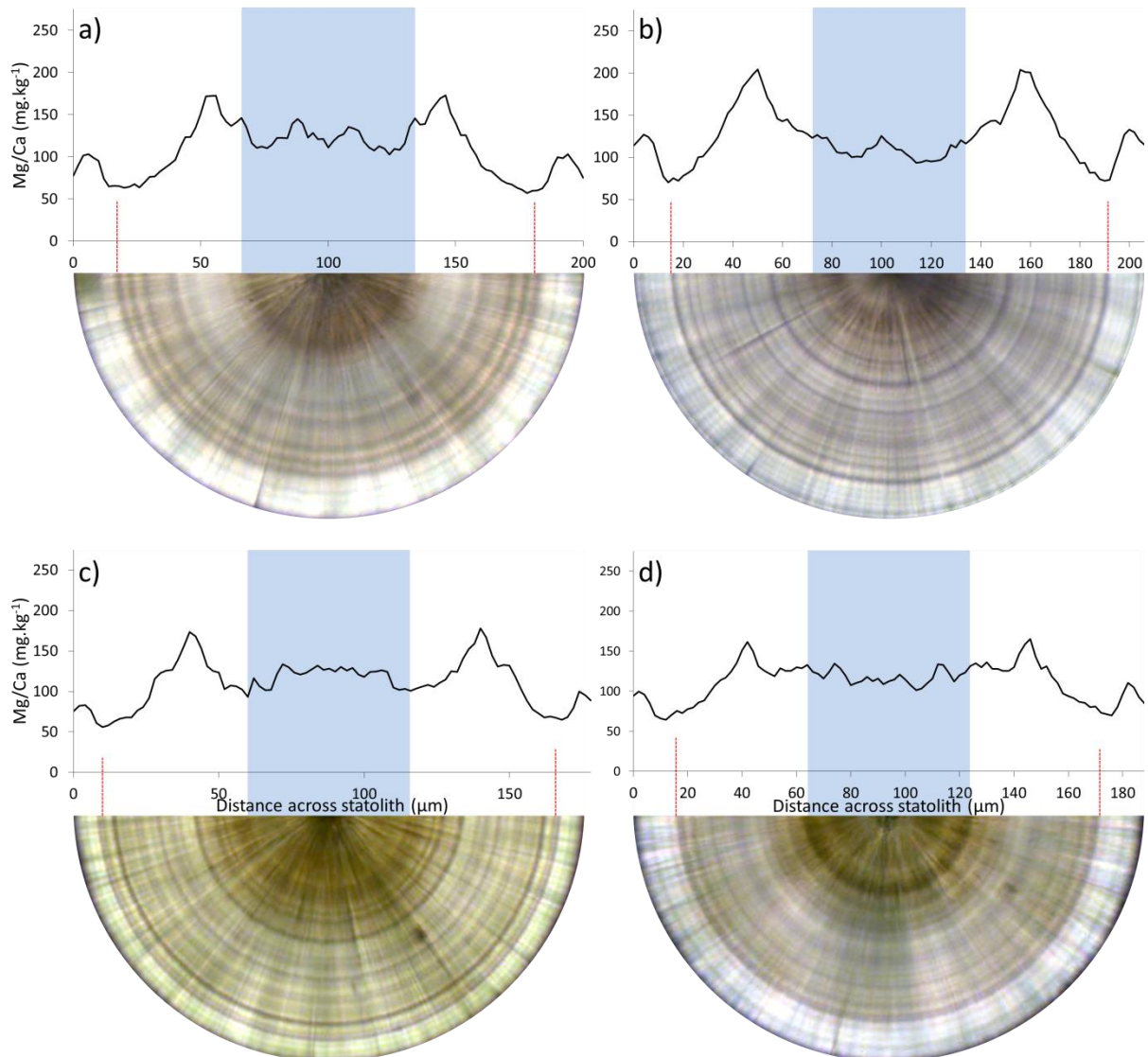


Figure 6.9. Photomicrographs of ground and polished statoliths from 2 year old laboratory reared *Buccinum undatum*, overlaid with profiles of the Mg/Ca ratios determined using SIMS. a & b) are statoliths from the largest male (a) and female (b) whelks (≈ 50 mm TSL) whilst c & d) are statoliths from smaller male (c) and female (d) whelks (≈ 35 mm TSL). Blue areas represent larval growth inside the hatching ring. The vertical red line above the statolith indicates the position of the first growth ring whilst the second ring is forming around the circumference of the statolith.

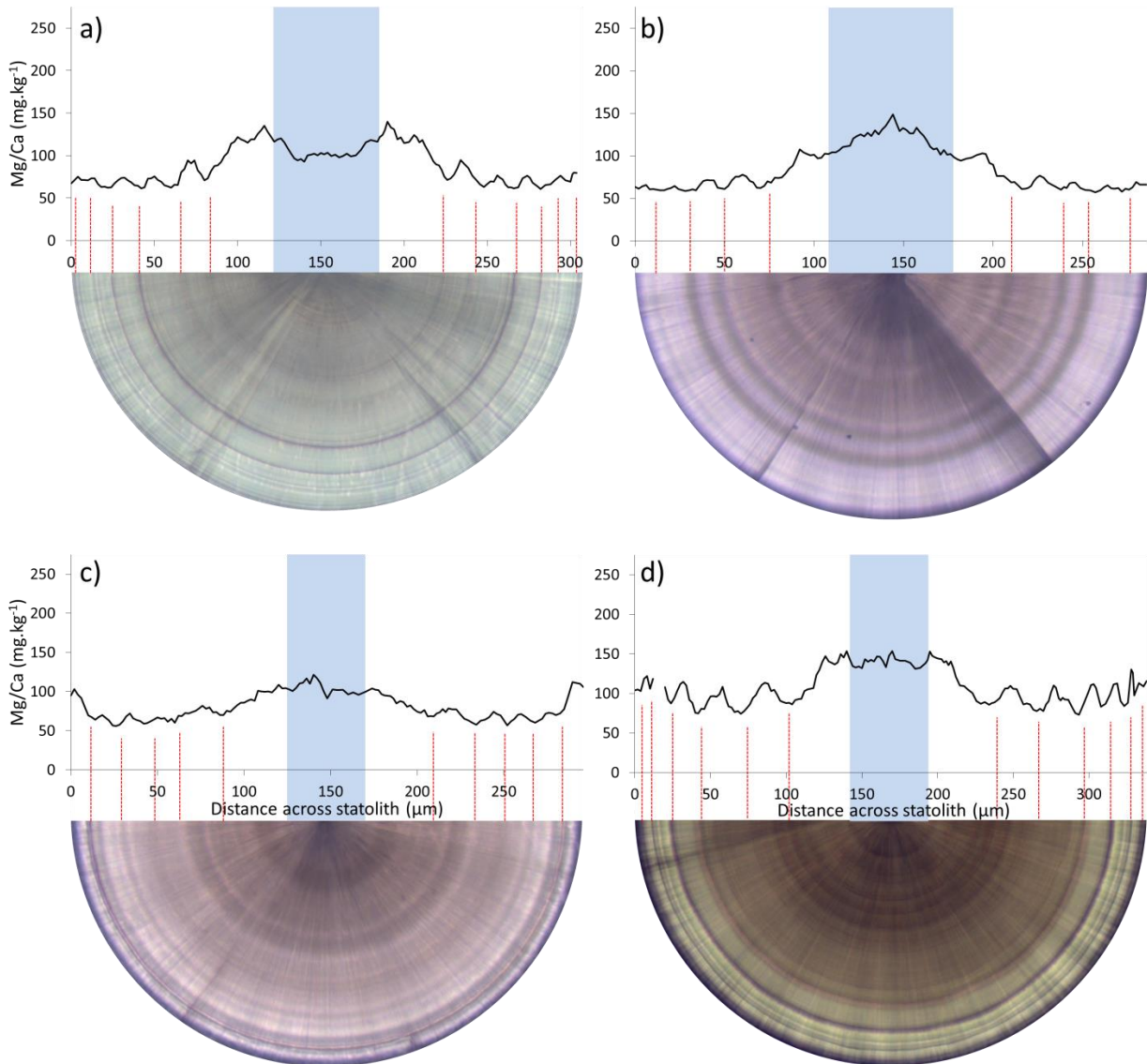


Figure 6.10. Photomicrographs of ground and polished statoliths from field collected *Buccinum undatum* from Shetland, overlaid with profiles of the Mg/Ca ratios determined using SIMS. a & b) are statoliths from mature male whelks whilst c & d) are statoliths from mature female whelks. Blue areas represent larval growth inside the hatching ring. Vertical red lines above the statolith indicate the positions of the growth rings.

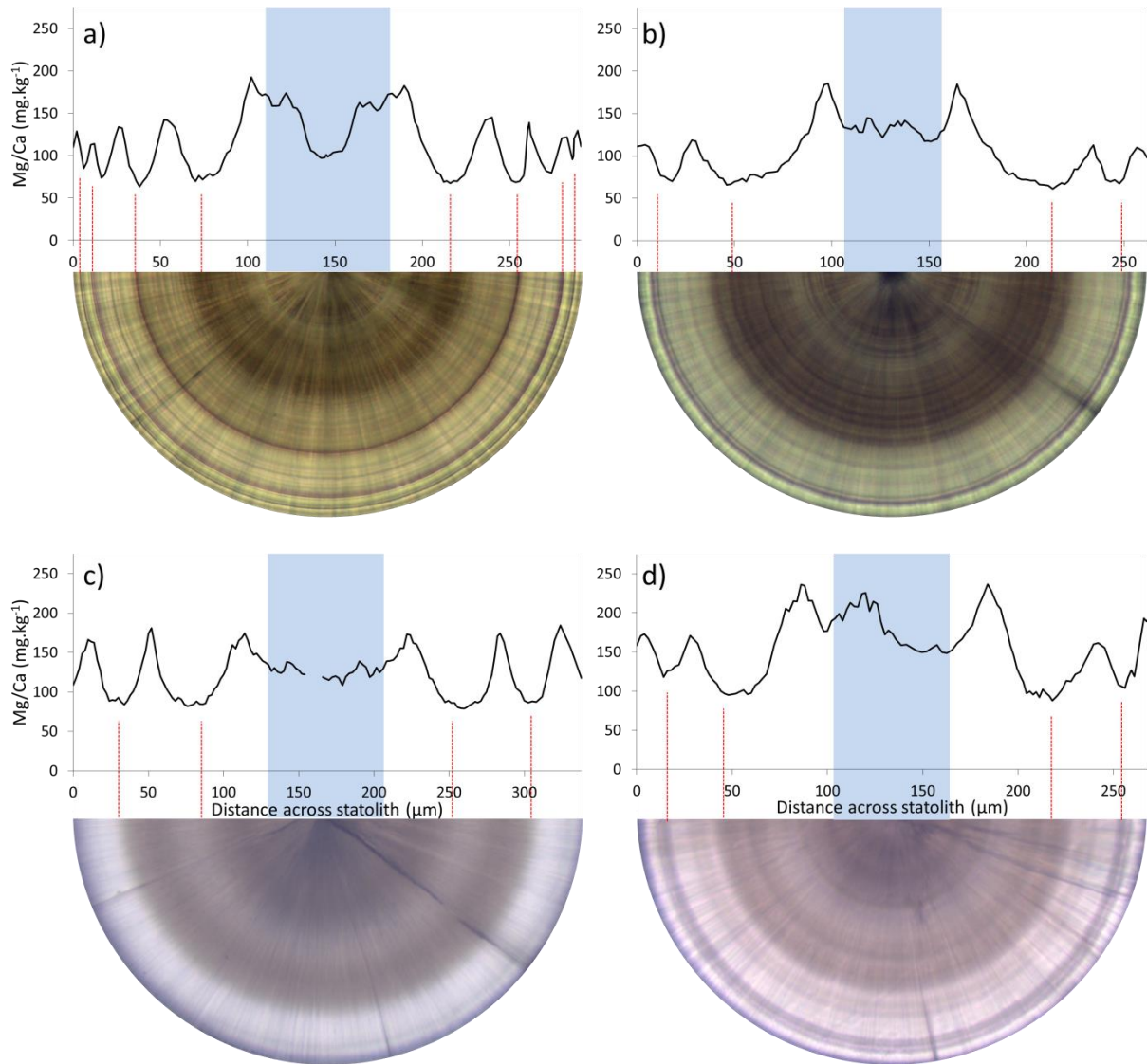


Figure 6.11. Photomicrographs of ground and polished statoliths from field collected *Buccinum undatum* from the Menai Strait, overlaid with profiles of the Mg/Ca ratios determined using SIMS. a & b) are statoliths from mature male whelks whilst c & d are statoliths from mature female whelks. Blue areas represent larval growth inside the hatching ring. Vertical red lines above the statolith indicate the positions of the growth rings.

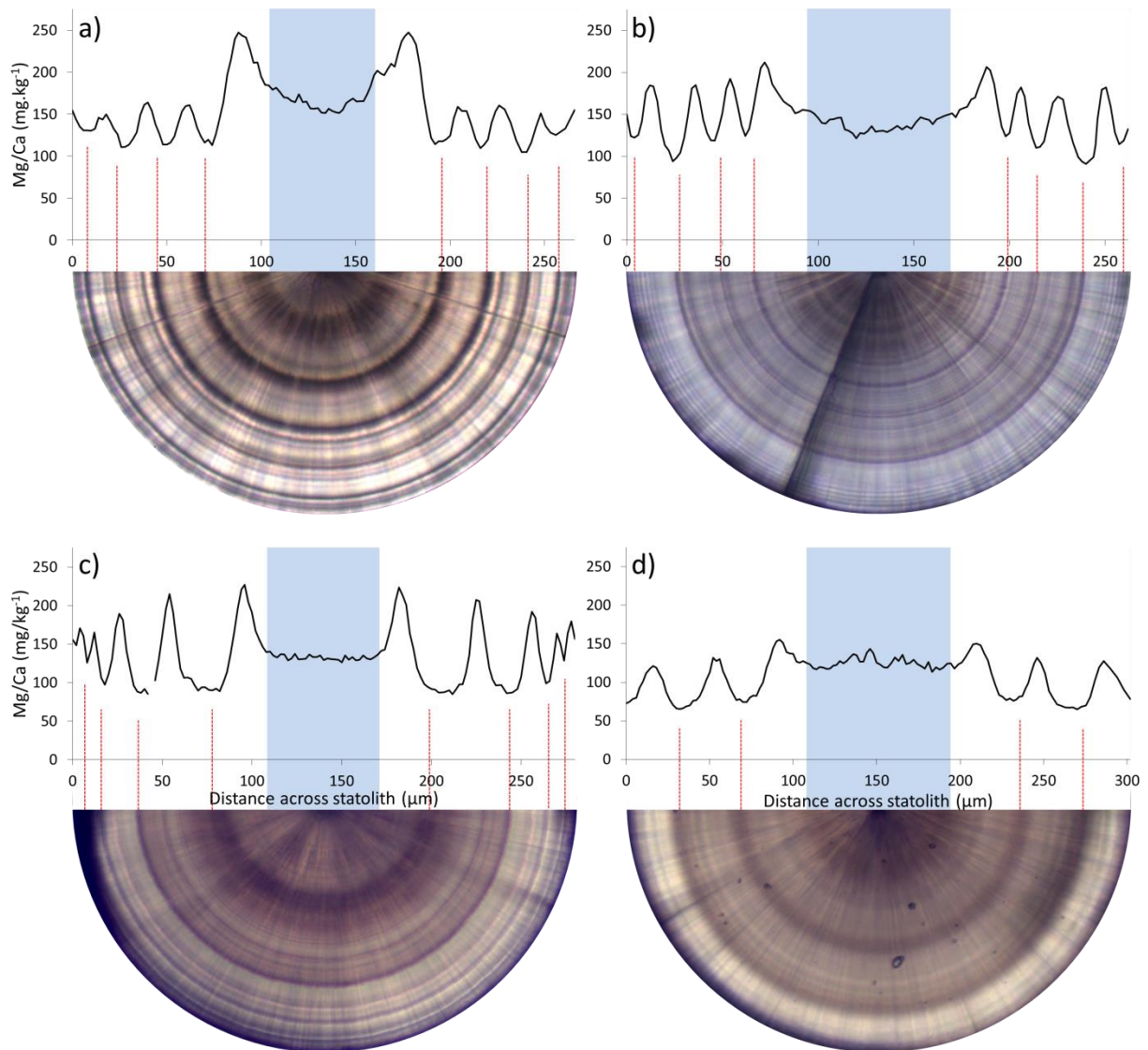


Figure 6.12. Photomicrographs of ground and polished statoliths from field collected *Buccinum undatum* from Jersey, overlaid with profiles of the Mg/Ca ratios determined using SIMS, a & b) are statoliths from mature male whelks whilst c & d) are statoliths from mature female whelks. Blue areas represent larval growth inside the hatching ring. Vertical red lines above the statolith indicate the positions of the growth rings.

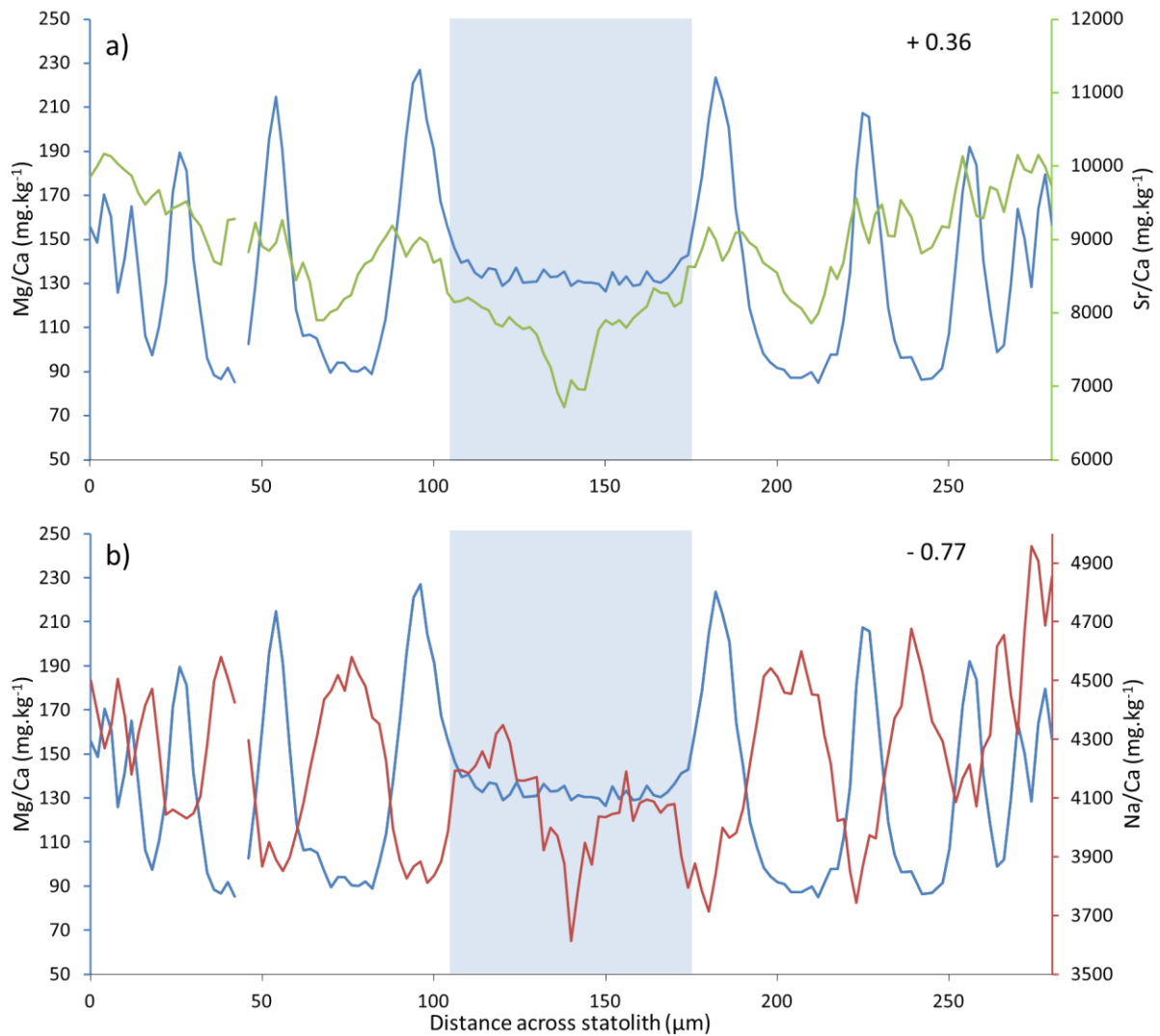


Figure 6.13. a) Mg/Ca (blue) and Sr/Ca (green) profiles across a ground and polished statolith from a *Buccinum undatum* from Jersey. b) overlaid Mg/Ca (blue) and Na/Ca (red) profiles from the same statolith in a). The blue boxes represent larval growth inside the hatching ring and these data were not included in the calculation of the Pearson's correlation coefficients. Mg/Ca and Sr/Ca are correlated in a) = +0.36 and Mg/Ca and Na/Ca show a negative correlation in b) = -0.75. Both of these correlations were significant ($P < 0.001$).

The central portion of each statolith (within the hatching ring) showed inconsistent elemental ratios between samples with little or no obvious pattern. It has been demonstrated (above) that the (Mg/Ca) concentrations in the statolith centre i.e. the period of larval growth inside the hatching ring, varied both between and within the laboratory and field collected whelks. When the relationship between Na/Ca and Mg/Ca ratios were compared in the pre-hatching and post-hatching portions of the statolith from a single whelk (JF4-8) (Figure 6.14), a clear negative correlation exists for the post-hatching portion of the statolith with no significant correlation in the pre-hatching portion. The likely reasons are that 1) during larval development elemental incorporation into the statolith is controlled in the egg capsule and this is likely to be different in different capsules produced by different female whelks and 2) the centre of the statolith is the area most likely to show cracks and fracture lines (see statoliths in Figures 6.8, 6.9 & 6.10 for examples) and this may result in anomalous spikes in the elemental signals if the analytical beam falls along a crack. When the various permutations of correlations between the Na/Ca, Mg/Ca and Sr/Ca ratios for the statolith without the hatching ring elemental data included were calculated, a series of 24 correlations were produced (see Figure 6.15 for male whelks and Figure 6.16 for female whelks). The Pearson correlation coefficients of each relationship are summarised in Table 6.1. The strength of the correlations (based on Fowler *et al.*, 1998) is as follows: 0 – 0.19 = very weak, 0.2–0.39 = weak, 0.4–0.69 = moderate, 0.7–0.89 = strong, 0.9–1 = very strong. The data in Table 6.2 present summary elemental data from the combined element ratios in statoliths from each site.

There are clear variations in elemental relationships both between and within sites. Whilst there are general negative relationships between Na/Ca and Mg/Ca, these relationships do vary within sites. This variation appears to relate to the concentrations of Na, rather than Mg. Much smaller relationships are seen between Mg/Ca - Sr/Ca and Na/Ca – Sr/Ca. No clear patterns are visible between these elemental comparisons with both positive and negative relationships being seen between sites and within a single site. Statistical comparisons of elemental concentrations between sites were attempted (ANOVA). However, due to the highly variable data, normality could not be achieved (even with transformations) as the data were skewed. Non-parametric equivalents (Kruskal-Wallis) were investigated, but the requirement for equal sample sized made them unsuitable for this particular dataset.

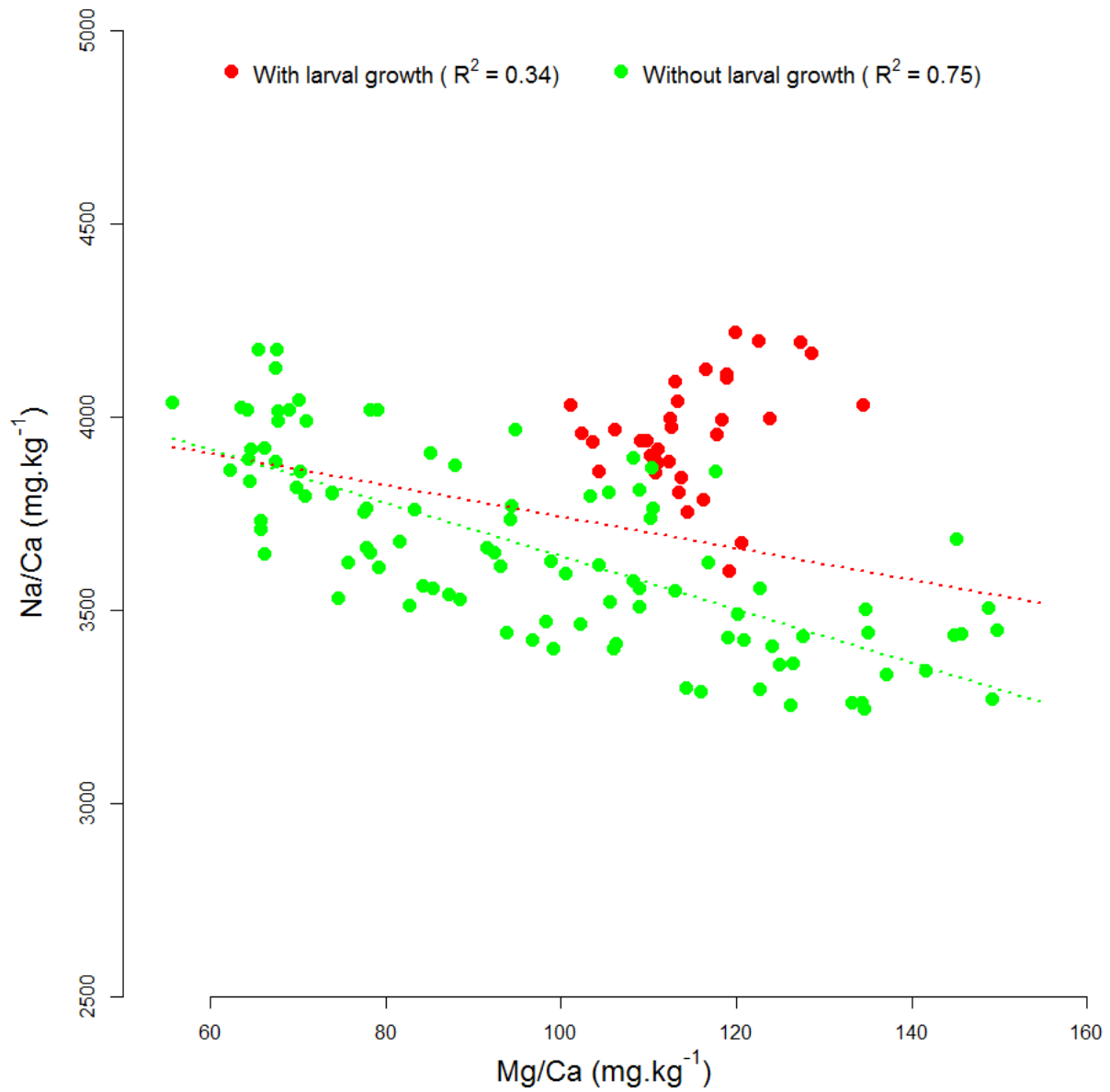


Figure 6.14. Scatter plot of Na/Ca against Mg/Ca for a single statolith from whelk JF4-8. The green dots represent data from the post hatching period of growth and the red dots represent data from within the hatching ring (larval growth). The green dotted line shows the linear relationship between the two element ratios without the larval element data included. The red dotted line is the linear relationship between the two elements including the larval statolith elemental data.

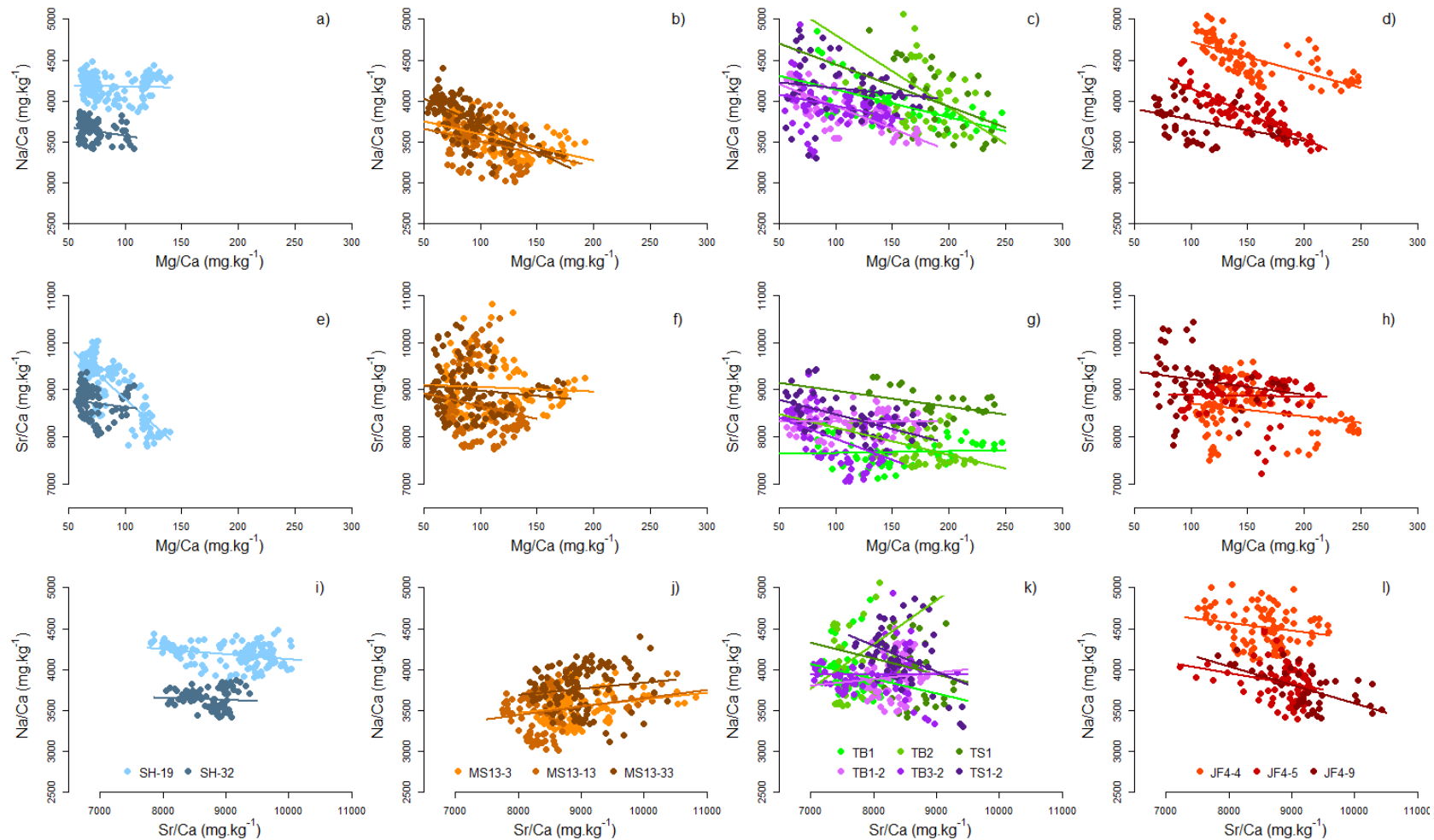


Figure 6.15. Male *Buccinum undatum* statoliths. Scatter plots showing relationships between elemental concentrations in statoliths from individual whelks determined using SIMS. Sodium vs. magnesium (a, b, c & d). Strontium vs. magnesium (e, f, g & h). Sodium vs. strontium (i, j, k & l). The samples from Shetland (SH-19 & SH-32) are shown with blue markers (a, e & i), samples from the Menai Strait (MS13-3, MS13-13 & MS13-33) are shown with brown markers (b, f & j), samples from laboratory reared animals are shown with green (TB1, TB2, TS1) and purple (TB1-2, TB3-2 & TS1-2) markers (year 1 and year 2 respectively, c, g & k) and samples from Jersey (JF4-4, JF4-5 & JF4-9) are shown with red markers (d, h & l). Coloured lines represent linear relationships between datasets of the same colour. Sample SH-31 was not included in the Shetland data as it was anomalous.

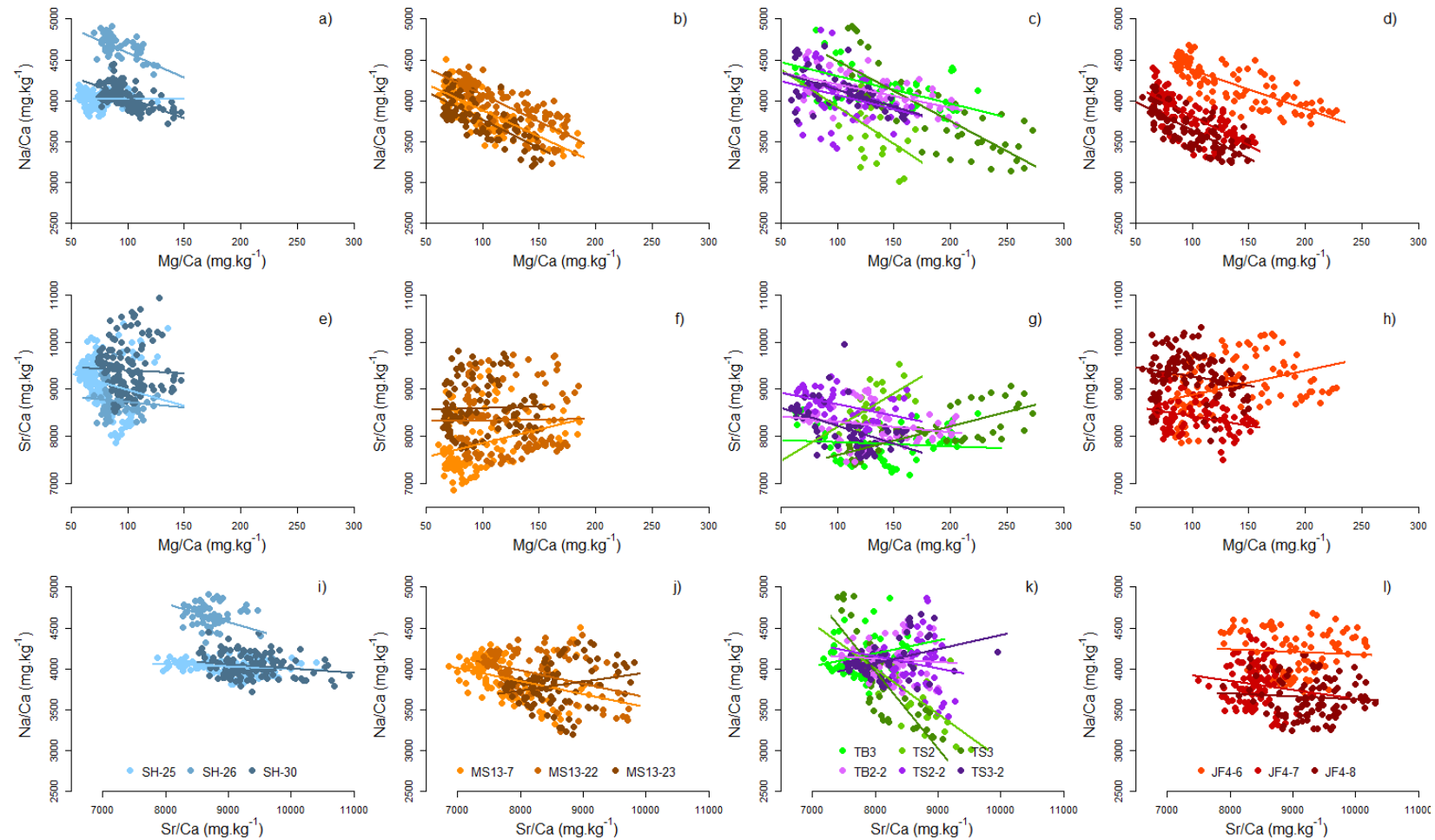


Figure 6.16. Female *Buccinum undatum* statoliths. Scatter plots showing the relationships between elemental concentrations in statoliths from individual whelks determined using SIMS. Sodium vs. magnesium –a, b, c & d. Strontium vs. magnesium e, f g & h. Sodium vs. strontium i, j, k & l. The samples from Shetland (SH-25, SH-26 & SH-30) are shown with blue markers (a, e & i), samples from the Menai Strait (MS13-7, MS13-22 & MS13-23) are shown with brown markers (b, f & j), samples from laboratory reared animals are shown with green (TB-3, TS2 & TS3) and purple (TB2-2, TS2-2 & TS3-2) markers (year 1 and year 2 respectively, c, g & k) and samples from Jersey (JF4-6, JF4-7 & JF4-8) are shown with red markers (d, h & l). Coloured lines represent linear relationships between datasets of the same colour.

Table 6.1. Pearson's correlation coefficients of the relationships between elemental concentration ratio profiles in statoliths from male and female *Buccinum undatum* reared in the laboratory and from the Menai Strait, Jersey and Shetland. Correlation strength is shown by colour, grey = 'weak', yellow = 'moderate' and orange = 'strong'. Significance, ** = $p < 0.001$, * = $p < 0.05$.

	Laboratory year 1 Male			Laboratory year 1 Female			Laboratory year 2 Male			Laboratory year 2 Female		
	TB1	TB2	TS1	TB3	TS2	TS3	TB1-2	TB3-2	TS1-2	TB2-2	TS2-2	TS3-2
Na/Ca vs. Mg/Ca	-0.61**	-0.51**	-0.4*	-0.45**	-0.44*	-0.79**	-0.7**	-0.32*	-0.14	-0.52**	-0.29*	-0.55**
Na/Ca vs. Sr/Ca	-0.2	0.2	-0.14	0.33*	-0.66**	-0.83**	0.06	0	-0.39*	-0.07	-0.14	0.35*
Sr/Ca vs. Mg/Ca	0.06	-0.09	-0.34	-0.48**	0.58*	0.74**	0.01	-0.48**	-0.51**	-0.22	-0.43**	-0.49**
	Menai Strait Male			Menai Strait Female			Jersey Male			Jersey Female		
	MS13-3	MS13-13	MS13-33	MS13-7	MS13-22	MS13-23	JF4-4	JF4-5	JF4-9	JF4-6	JF4-7	JF4-8
Na/Ca vs. Mg/Ca	-0.59**	-0.27*	-0.69**	-0.81**	-0.77**	-0.74**	-0.67**	-0.84**	-0.36**	-0.77**	-0.71**	-0.75**
Na/Ca vs. Sr/Ca	0.22*	0.25*	0.13	-0.34*	-0.4**	0.225	-0.2*	-0.23*	-0.57**	-0.06	-0.13	-0.07
Sr/Ca vs. Mg/Ca	-0.05	-0.16	-0.12	0.32*	0.01	0.03	-0.15	-0.02	-0.18	0.36**	-0.31*	-0.2*
	Shetland Male			Shetland Female								
	SH-19	SH-25	SH-26	SH-30	SH-31	SH-32						
Na/Ca vs. Mg/Ca	-0.04	-0.01	-0.43**	-0.62**	0.67**	-0.24*						
Na/Ca vs. Sr/Ca	-0.28*	-0.17	-0.37**	-0.19	0.81**	-0.06						
Sr/Ca vs. Mg/Ca	-0.78**	-0.19*	-0.1	-0.04	0.5**	-0.13						

Table 6.2. Summary of concentrations of three elemental ratios determined across *Buccinum undatum* statoliths from laboratory reared and field collected whelks from Shetland, Menai Strait and Jersey. Sample SH-31 was not included in the Shetland data as it was anomalous. All data presented are in mg.kg⁻¹.

	Laboratory year 1			Laboratory year 2			Shetland			Menai Strait			Jersey		
	Na/Ca	Mg/Ca	Sr/Ca	Na/Ca	Mg/Ca	Sr/Ca	Na/Ca	Mg/Ca	Sr/Ca	Na/Ca	Mg/Ca	Sr/Ca	Na/Ca	Mg/Ca	Sr/Ca
Mean	4052.7	158.2	7974.6	4035.3	108.9	8276.3	4065.1	84.5	9001.6	3716.3	111.6	8570.5	3966.0	122.5	8911.5
Max	5629.5	272.21	9520.5	4937.8	204.4	9944.2	4912.9	147.4	10932.8	4507.2	266.4	10818.0	5037.7	247.3	10424.9
Min	3004.4	62.7	6740.4	3297.6	55.4	7050.6	3414.1	56.1	7808.2	3008.9	53.4	6857.2	3245.5	55.6	7218.0
Range	2625.0	209.4	2780	1640.2	148.9	2893.6	1498.7	91.3	3124.6	1498.3	212.9	3960.7	1792.1	191.7	3206.8

6.3.3 Crystal structure and composition of statoliths

To develop the elemental compositional study using MRS, μ XRD was used to investigate micro-scale changes in statolith calcium carbonate polymorphs as well as differences in crystal structure. To ensure that no damage was done to the samples during analysis, a 120 second exposure to the X-ray beam was carried out at both the outer edge and centre of a single statolith. No change over time was seen in the diffraction peaks, indicating that the X-ray beam caused no structural damage, the full results of this analysis can be seen in [Appendix K](#) (Figure K.1). Figures 6.17 and 6.18 show stacked intensity traces from each sample spot taken within a single statolith ($n = 110$) overlaid with the intensity trace for calcite (Figure 6.17) and aragonite (Figure 6.18). It is clear that none of the sample peaks correspond to the characteristic peaks for calcite and instead all of the 110 sample spots were identified as aragonite. This was carried out on every one of the 18 statoliths sampled, regardless of sample origin or whelk gender. μ XRD traces acquired from broken, unprocessed statoliths (the same statoliths analysed via MRS) showed a diffraction pattern identical to that of the processed statoliths ([Appendix K](#), Figure K.2). The crystal structure of the statoliths appeared to change along their growth axes. Figure 6.19, shows how a selection of peaks changes across the statolith of a laboratory reared (a) and field collected Menai Strait (b) statolith. The number of high-intensity peaks increases with proximity to the central nucleus. Whilst all of the peaks were present in almost all of the samples, they were often obscured by the same highly intense peak towards the outer edge.

Following μ XRD analysis, the statolith crystal structure was investigated using SEM of mounted broken statoliths. The overall crystal structure appears as crystals radiating from the central nucleus across much of the structure with a clear hourglass shaped structure at the centre (Figures 6.20 & 6.21). The ends of the crystals can be seen displaying clear planes in the structure along which several layers appear to have sheared (Figure 6.22).

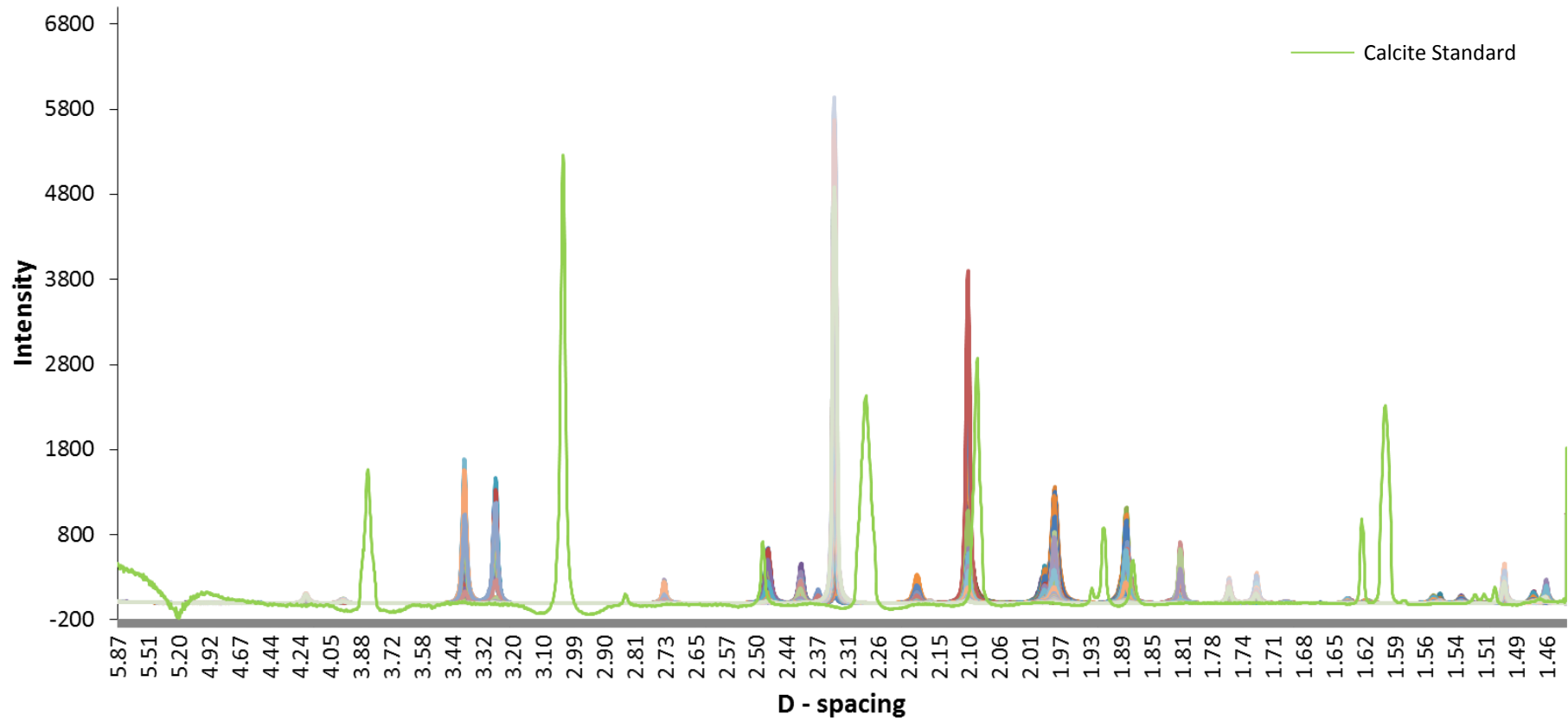


Figure 6.17. A stacked plot of 110 successive diffraction patterns from a line profile across the centre of a single *Buccinum undatum* statolith overlaid with the trace from the calcite standard (green trace).

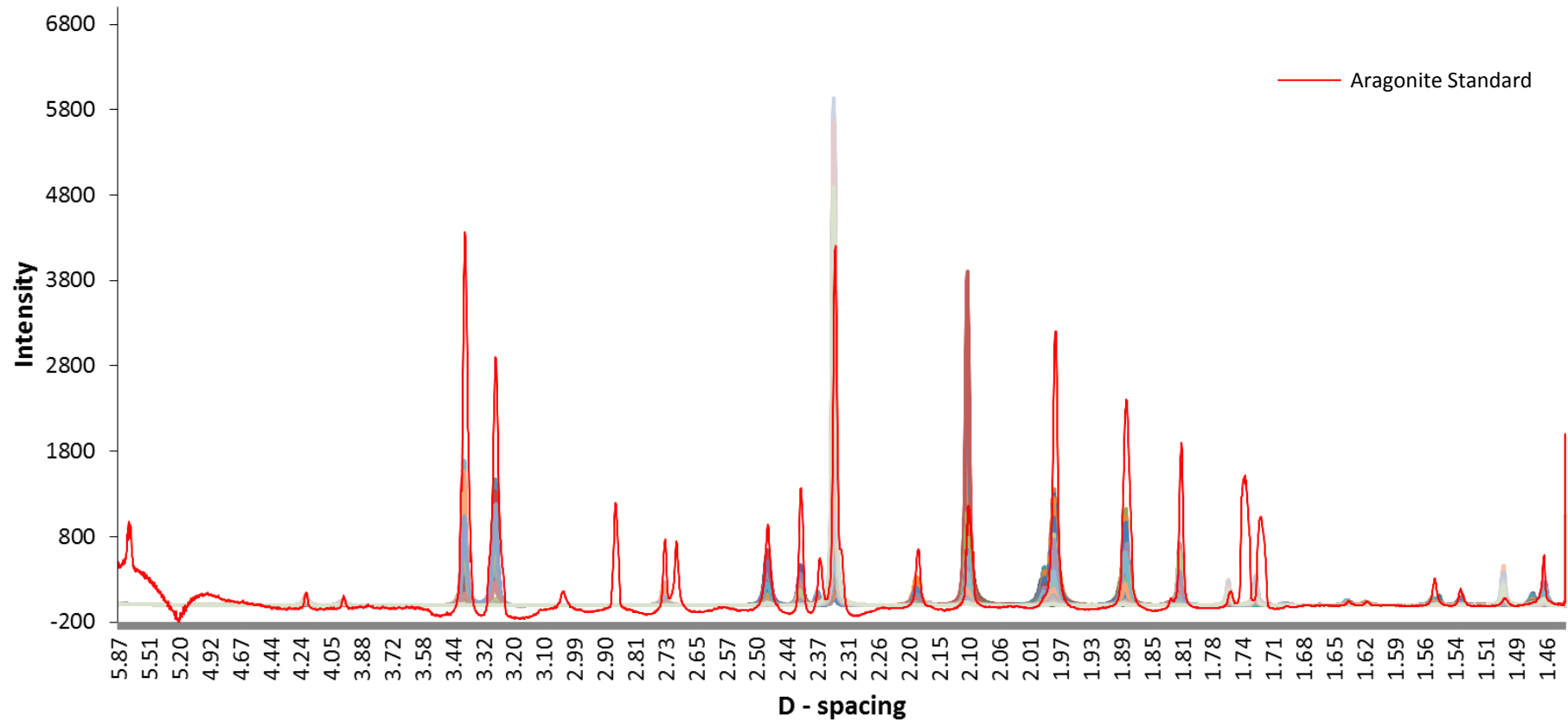


Figure 6.18. A stacked plot of 110 successive diffraction patterns from a line profile across the centre of a single *B. undatum* statolith, overlaid with the trace from the aragonite standard (red trace).

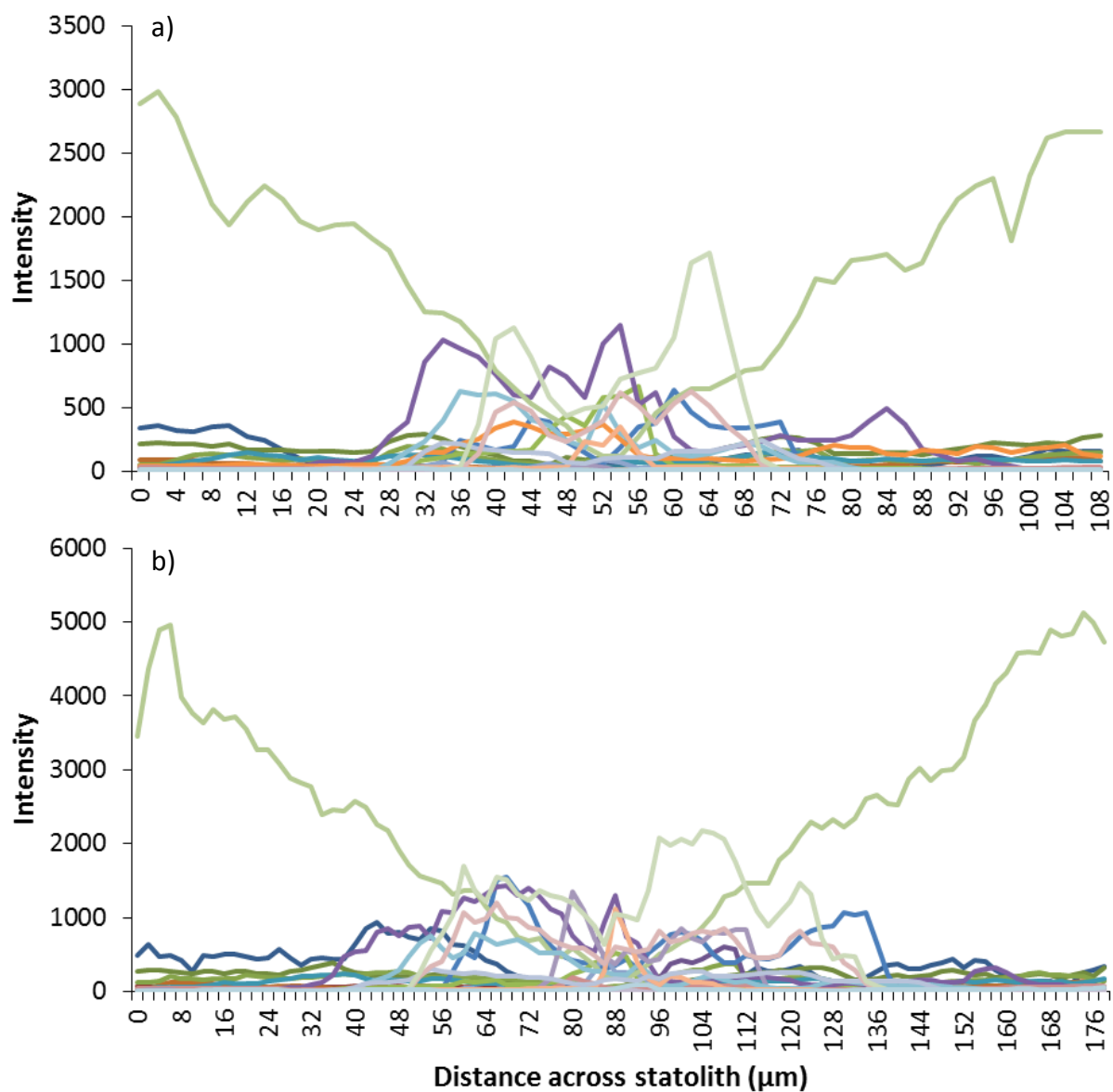


Figure 6.19. The intensity of a selection of XRD peaks across the diameter of two statoliths, a juvenile laboratory reared specimen (a - TB-1) and a field collected adult specimen (b - MS13-13).

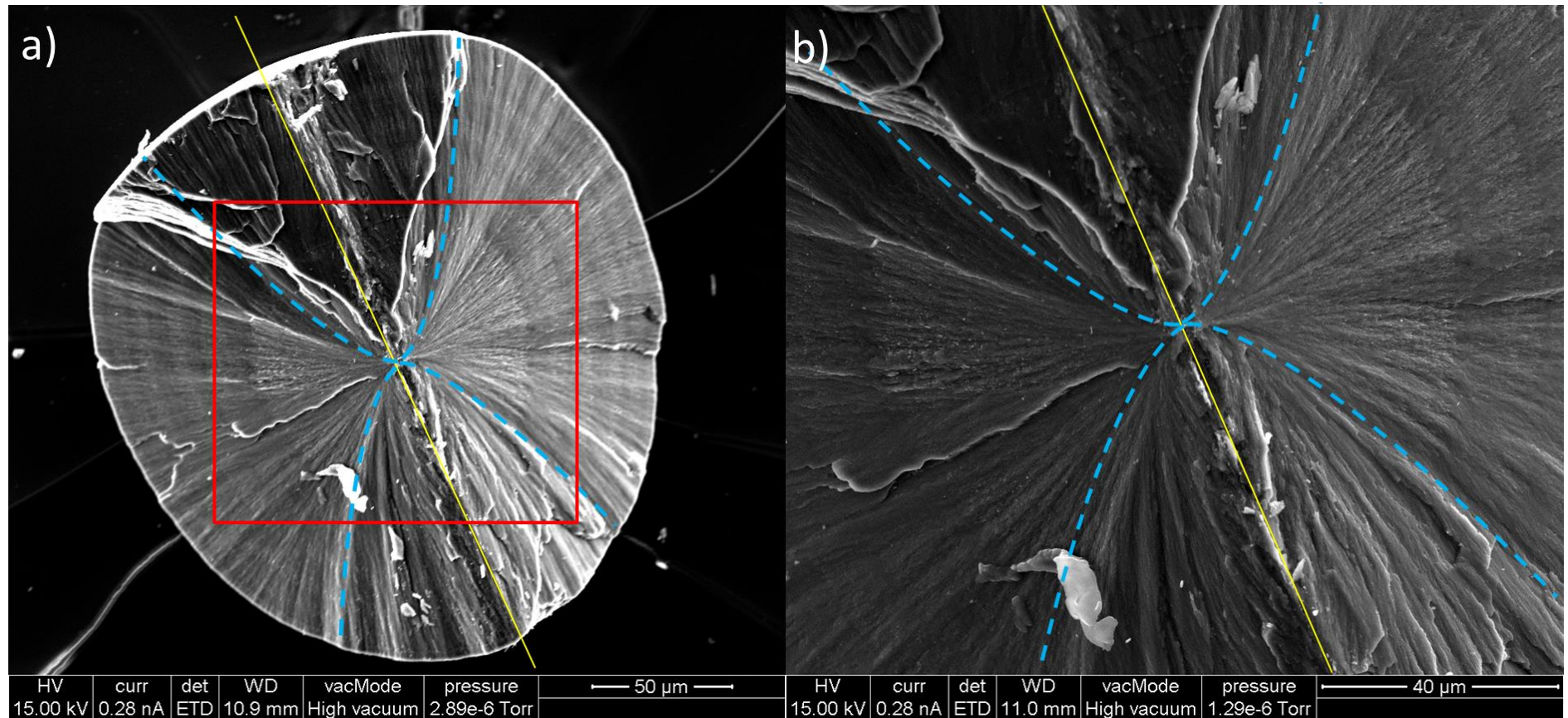


Figure 6.20. SEM images of a fractured statolith segment. The dorso-ventral axis is highlighted with a yellow line, a) growth rings can clearly be seen within the exposed surfaces and b) a magnified image of the nucleus area highlighted by the red box in a) showing a clear 'hour glass' shape in the crystal structure within this region. The blue dotted line highlights the hourglass shape of the crystal structure.

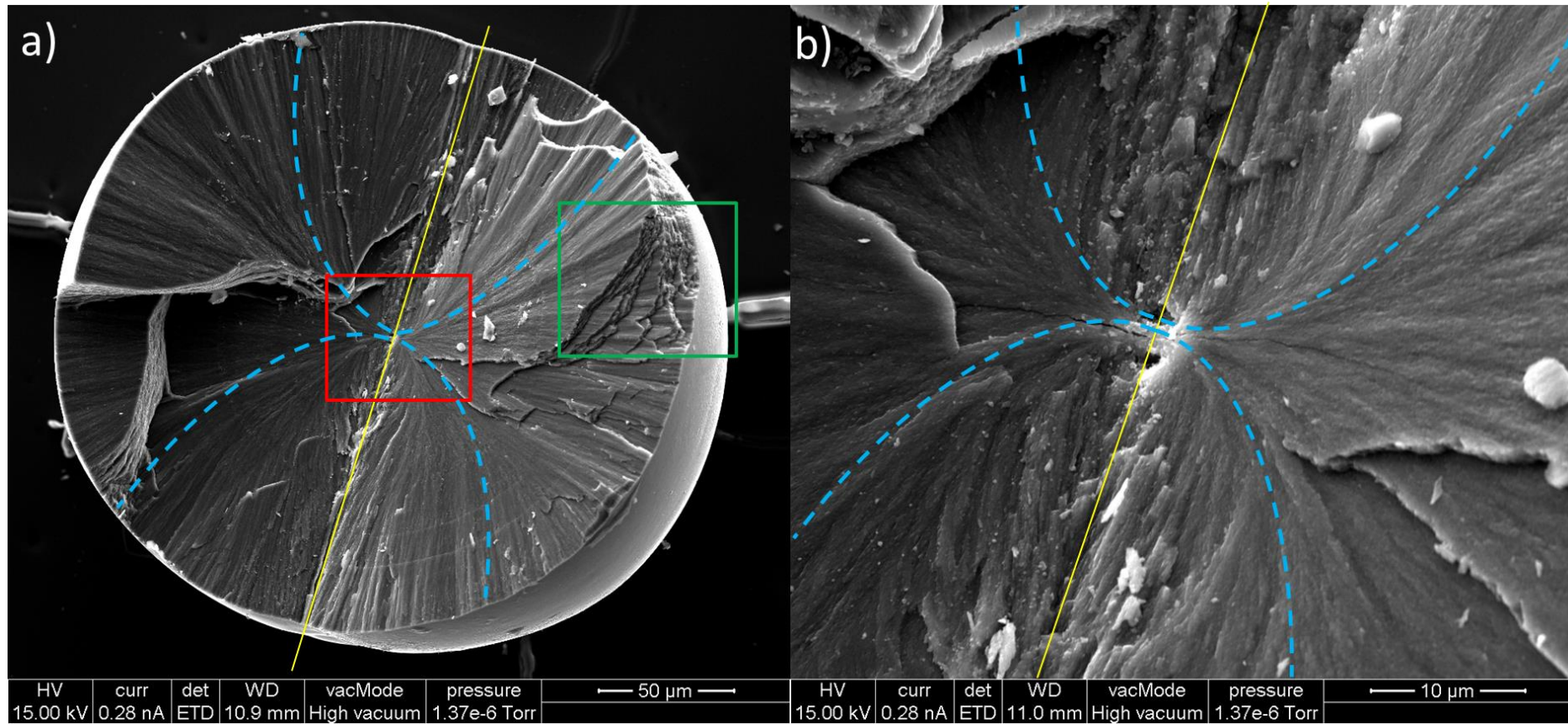


Figure 6.21. SEM images of the fractured surface of half a *Buccinum undatum* statolith mounted on a stub (grey area underneath the statolith), a) the dorso-ventral axis is highlighted with a yellow line. Growth rings can be clearly seen within the exposed surfaces and a radial crystal structure is evident and b) a magnified image of the nucleus area, highlighted by the red box in a). A clear 'hour glass' shape can be seen in the crystal structure within this region and similar to that shown in Figure 6.20b. The green square marks an area of the statolith that is shown in Figure 6.22. The blue dotted line highlights the hourglass shape of the crystal structure.

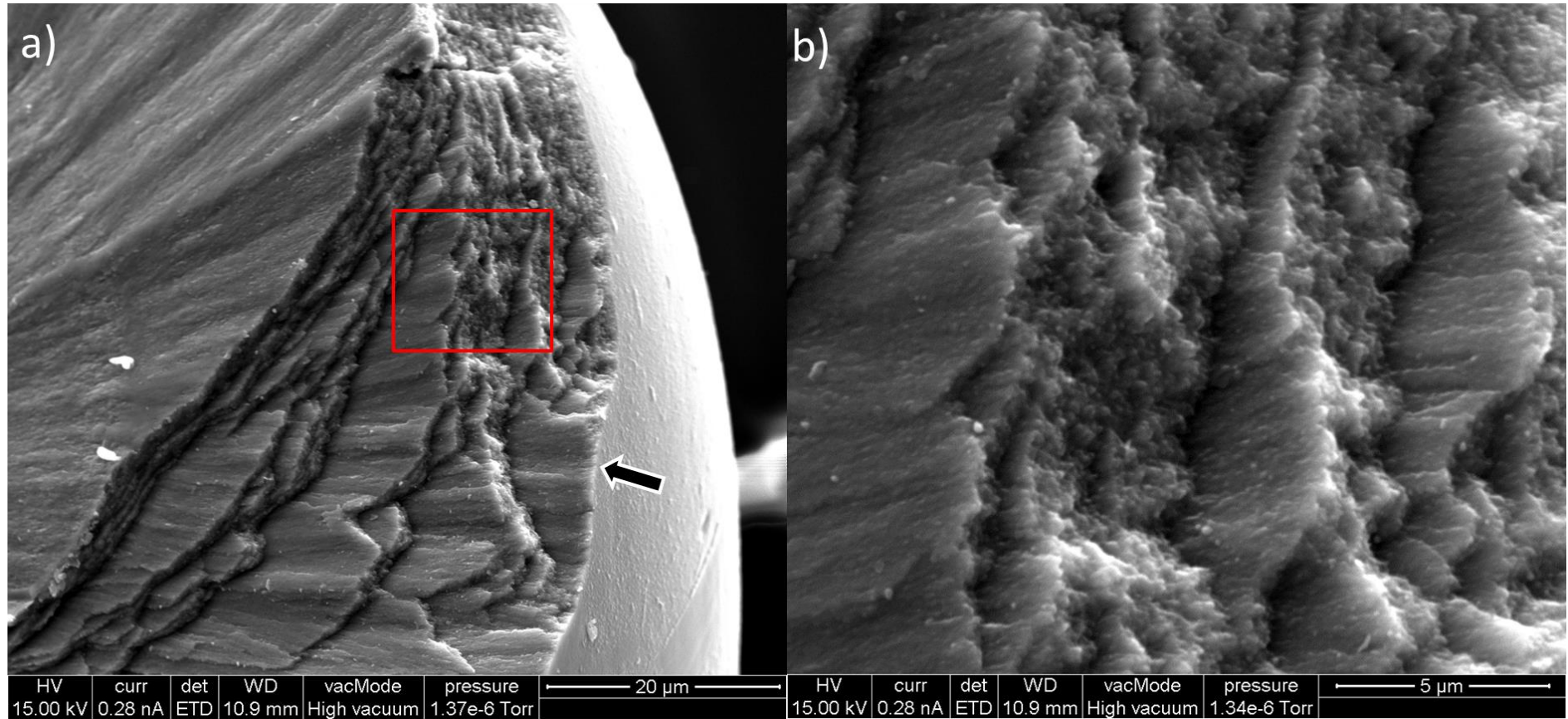


Figure 6.22. A magnified image of the section highlighted in green in Figure 6.21a. a) the radial crystal structure can be seen reaching the edge of the statolith and the smooth outer surface (arrow) is also visible and b) a magnified image of the section highlighted in red in (a) to show broken ends of the crystal structure following fracturing and indicating that the crystals point outward from the central statolith nucleus in all directions.

6.3.5 Anomalous sample

During the SIMS analysis statolith SH-31 from a female whelk from Shetland (Figure 6.23) stood out as anomalous from the other statoliths investigated. The appearance of this statolith was different to the other statoliths and appeared to be crystallised (see Chapter 5). The Sr concentrations within this statolith were roughly 15 times lower than other specimens from the same site and from other sites (mean – 556 mg.kg⁻¹). The concentration of Na was also less than half of that measured in all the other statoliths (mean – 1366 mg.kg⁻¹), finally the concentration of Mg was almost 30 times higher than all the other analysed statoliths (mean – 3900 mg.kg⁻¹). Initially thought to be a software or instrumental error, this sample was re-analysed a second time with identical results. The relationships between the trace elements were also markedly different to all of the other statoliths samples. There was a strong positive correlation between Na and Sr (Pearson's correlation coefficient – 0.82) and a weak negative correlation between Mg and Sr (-0.51). This statolith was the only one to show a positive correlation between Na and Mg (0.68), although this relationship appeared to be inverse over parts of the statolith (Figure 6.23). μ XRD analysis of the right hand statolith from the same whelk found it to be wholly aragonitic and identical to all other samples.

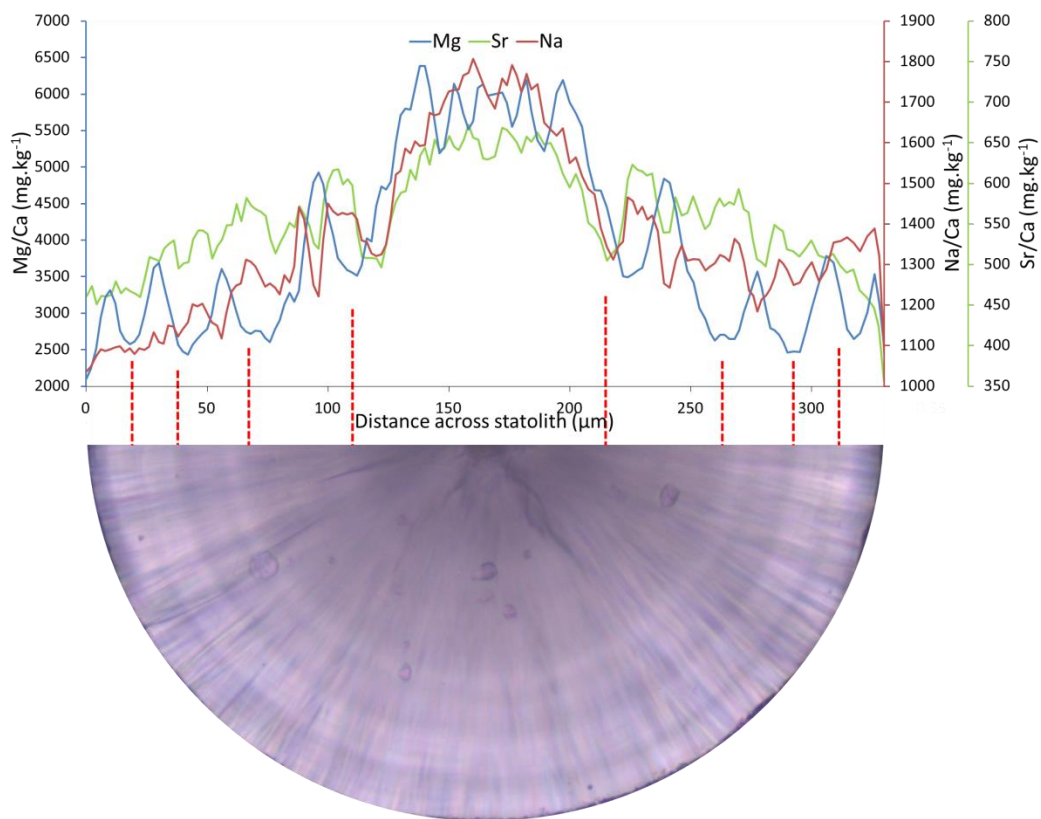


Figure 6.23. Lower part - a photomicrograph of *Buccinum undatum* statolith SH-31 with elemental profiles (above): Mg/Ca (blue line), Na/Ca (red line) and Sr/Ca (green line) profiles overlaid.

6.3.6 Comparison of shell isotopes and statolith chemistry

Once all geochemical analyses were complete for the statoliths and shells, the data from specimens which had both structures analysed were compared. Figures 6.24 and 6.25 show statoliths from male and female whelks respectively, overlaid with reconstructed seawater temperature, determined from the shell oxygen isotopes (Chapter 4) and the statolith Mg profiles (this chapter). Whilst disturbance rings are visible in both statoliths, it is clear that the strongest and most visible annual rings correspond with the number of chemical cycles found within both the shells and statoliths. Table 6.3 summarises all comparisons from the 14 dual-sampled whelks, between the number of geochemical cycles (Mg) in the statolith and ($\delta^{18}\text{O}$ cycles) in the shell with the number of visible statolith rings and operculum rings. Three out of the 14 samples had 1 less Mg cycle than shell isotope cycles, however in all cases, the number of statolith rings matched the number of shell isotope cycles when weak disturbance rings were excluded. The operculum rings both over- and underestimated age in 12 out of the 14 whelks examined, this was likely due to the poor clarity of the rings in 8 out of the 14 opercula.

Table 6.3. Comparison of age and chemistry data for all dual sampled *Buccinum undatum* specimens. Grey boxes denote a miss-match between the highlighted value and the number of shell oxygen isotope cycles. * indicate that the statolith sample contained 1 or more disturbance rings. ? indicate where an operculum has poor clarity.

Location	Sample	No. of d18O cycles in shell	No. of Mg cycles in statolith	No. of statolith rings	No. of operculum surface rings
Laboratory reared animals	T1	2	2	2	0
	T2	2	2	2	3
	T3	2	2	2	2
Menai Strait Female	Pilot shell	3	n/a	3	4
	MS13-7	3	3	3*	2?
	MS13-23	4	3	4	3?
Menai Strait Male	MS13-3	5	5	5*	3
	MS13-13	4	3	4	2?
	MS13-33	4	4	4	4
Jersey Male	JF4-4	5	5	5*	4?
	JF4-5	5	4	5*	4
	JF4-9	5	5	5*	3?
Shetland Male	SH-19	6	6	6	3?
	SH-31	5	5	5	3?
	SH-32	5	5	5	4?

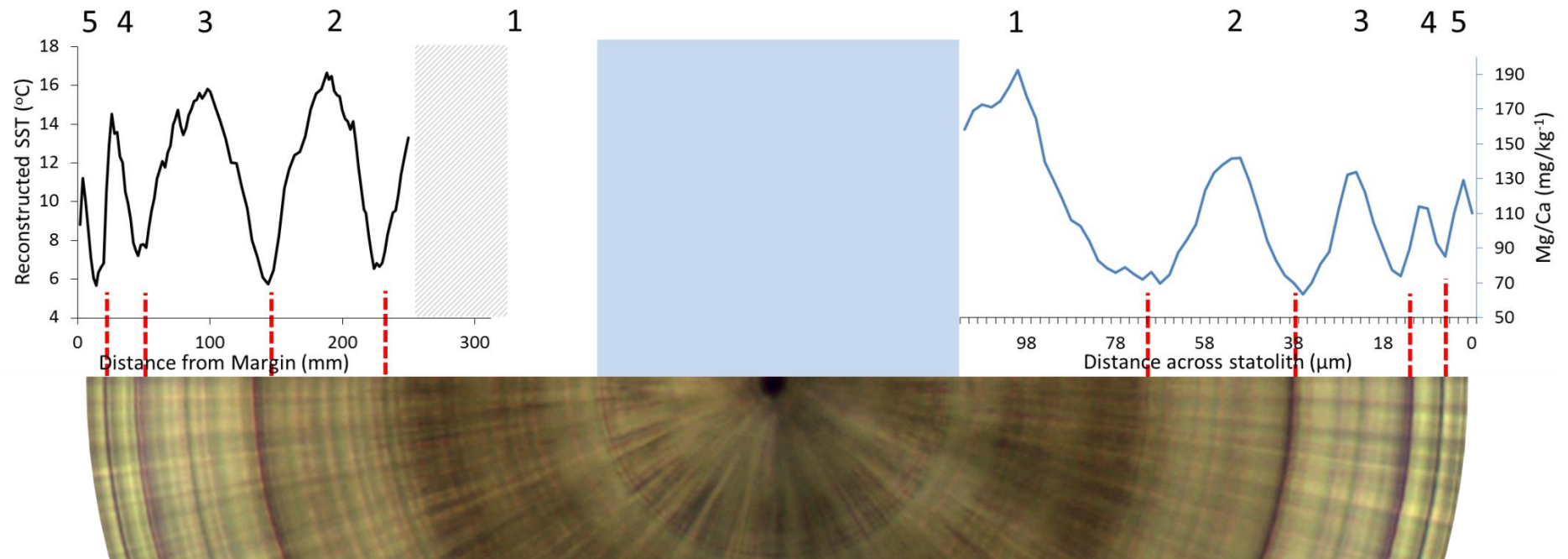


Figure 6.24. The reconstructed SST profile from the shell (black line) and statolith magnesium profile (blue line) of a male specimen (MS13-3), overlaid on a photomicrograph of the matching statolith. The numbers at the top represent matching numbers of cycles found within each analysis. The grey hatched area on the oxygen isotope plot represents the un-sampled section at the apex of the spire. The blue box represents larval growth within the hatching ring.

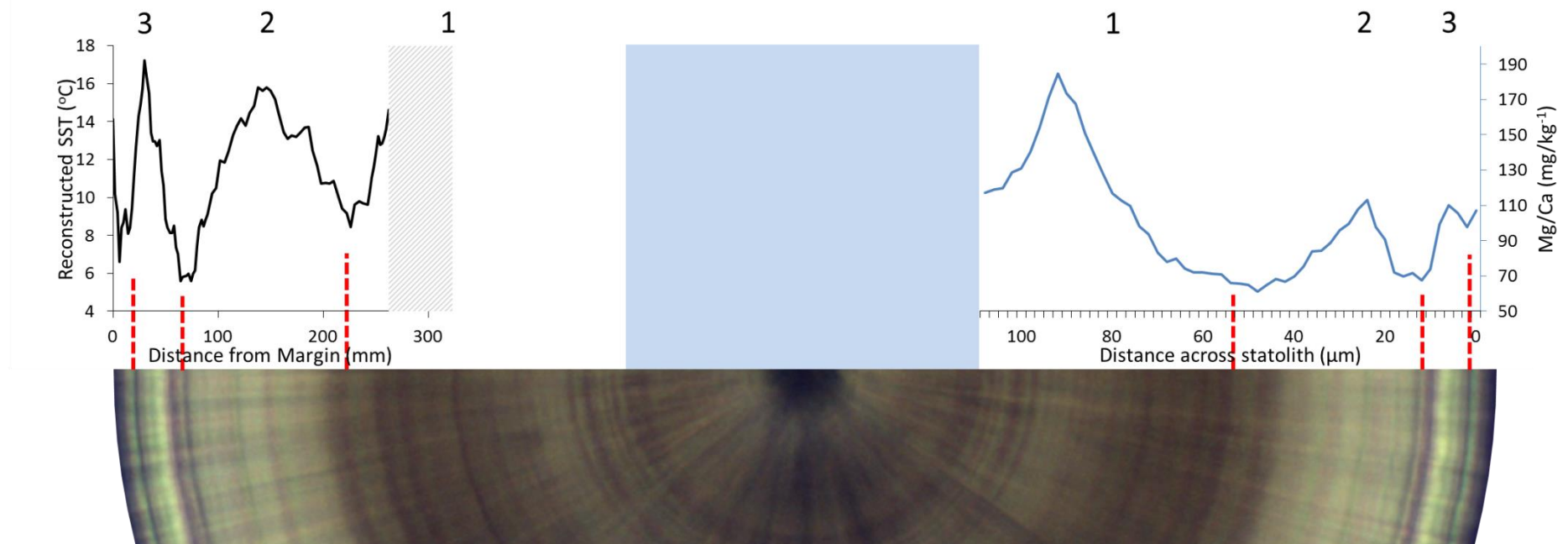


Figure 6.25. The reconstructed SST profile from the shell (black line) and statolith magnesium profile (blue line) of a female specimen (MS13-7), overlaid on a photomicrograph of the matching statolith. The numbers at the top represent matching numbers of cycles found within each analysis. The grey hatched area on the oxygen isotope plot represents the un-sampled section at the apex of the spire. The blue box represents larval growth within the hatching ring.

6.4 Discussion

The results from this chapter represent a novel investigation into the structure and composition of *Buccinum undatum* statoliths using a combination of high precision, cutting-edge techniques which were used to geochemically validate the annual periodicity of statolith growth rings. The results presented here highlight the suitability of techniques such as SIMS and μ XRD for analysing these small and previously difficult to study structures.

6.4.1 Statolith structure

Using SEM the internal structure of *B. undatum* statoliths was shown to vary along the growth axis with differential etching of the statolith surface. Optical microscope observations of the statoliths showed a diffuse area associated with a characteristic colour change that denotes the first annual growth ring. Within this diffuse area clear disturbance rings were observed that could clearly be seen in SEM images, although these rings were always weaker than the annual rings and had a greater definition in ground and polished thin sections prepared for SIMS analyses. The statolith was shown to be composed of aragonite with characteristic peaks in Raman spectra although the number of sampled statoliths was low. There was close agreement between the aragonite standard and the sample spots taken from the statolith, although several of the reported Raman spectra peaks differed by $1\text{--}3\text{ cm}^{-1}$ compared with those reported in the literature (see Parker *et al.*, 2010).

It is probable that the difference between the observed statolith spectra peaks and the published spectra is the presence of trace elements such as Mg^{2+} and Sr^{2+} substituting for Ca^{2+} within the lattice and distorting it (see Smith & Carabatos-Nédelec, 2001; Parker *et al.*, 2010). The difference in elemental composition likely explains why the synthetic calcite standard exhibited all of the expected peaks, whereas the sample spots and the speleothem aragonite standard (which can contain trace elements, Finch *et al.*, 2001) did not. The Raman spectra of the sample spots on the statolith did not display any of the characteristic pigment bands observed in the *B. undatum* shells in Chapter 3 (section 3.3.5). However, a diffuse band was noted between 2850 and 3000 cm^{-1} which likely indicates the presence of structural organic matter within the CaCO_3 matrix (Smith & Dent, 2005). All 3 of the spot samples from the *B. undatum* statolith showed a peak in the spectra that likely indicates the presence of organic matter in the entire statolith matrix, although the most intense peak was observed when a growth ring was analysed. A similar conclusion was reached by Galante-Oliveira *et al.* (2014)

who observed similar spectra in the statoliths of *Nassarius reticulatus*. If the Raman peaks represent differences in the concentration of organic matter present in different parts of the statolith then this will aid significantly in interpreting the distribution of elements such as Sr and Mg in the statolith. Galante-Oliveira *et al.* (2014) also showed using MRS of polished statolith sections that there was a calcite component to the statoliths of *N. reticulatus* with both aragonite and calcite likely present in a homogenous matrix within the statolith. Amorphous Calcium Carbonate (ACC), may have been present on the sample surface of the *N. reticulatus* statoliths following sample preparation. ACC can convert to the metastable polymorph of calcite under certain conditions, such as exposure to water and heat (Radha *et al.*, 2010; Gong *et al.*, 2012), making it possible that if any ACC were present, the heating caused during polishing or the MRS itself over time may have changed this surface material to calcite. However ACC itself was not found by Galante-Oliveira *et al.* (2014) or in this study as the characteristic spectra for ACC has a broad hump between ≈ 100 and ≈ 350 cm^{-1} rather than a discrete peak (Wehrmeister *et al.*, 2010). Galante-Oliveira *et al.* (2014) discounted any possibility of ACC conversion to calcite by using short sample acquisitions for the MRS (to avoid unnecessary heating of the sample) and they also analysed a fractured, unprocessed statolith similar to the samples processed in this study. They found that in all *N. reticulatus* statoliths the peak at ≈ 155 cm^{-1} was more intense than the peak at ≈ 207 cm^{-1} as well as a potentially smaller peak at 711 cm^{-1} . This combination of peaks possibly indicates the presence of a calcite fraction although not all of the characteristic calcite peaks (e.g. 281 cm^{-1}) were seen. None of these issues were seen with the MRS spectra from the *B. undatum* statoliths aside from the possibility of a very small characteristic calcite peak at 711 cm^{-1} in spot 3. It is therefore likely that the statoliths of *B. undatum* are composed solely of aragonite.

More detailed structural analysis of the statoliths using μXRD also found no trace of calcite within the structure of 18 whole statoliths at 2 μm resolution. The μXRD analysis also gave indications about the radial crystal structure of the statoliths which was later confirmed using SEM. The crystal structure was not found to be explicitly radial but rather had an 'hour glass' shape in the central nucleus. A similar crystal structure was found by Galante-Oliveira *et al.* (2014) in the statoliths of *N. reticulatus*. This is the likely reason for the statoliths not being perfectly spherical and instead being slightly flattened on the top and bottom. The changing crystallinity uncovered with the μXRD analyses is likely accounted for by the 'hour glass' structure and the thin statolith sections themselves. Figure 6.26 explains this in more detail, illustrating how a seemingly more complex crystal structure was found in the centre of each

sample. It can be seen that X-rays (green arrows in Figure 6.26b) passing through and close to the centre of the thin section encounter more crystal orientations than the X-rays passing through the outer edge.

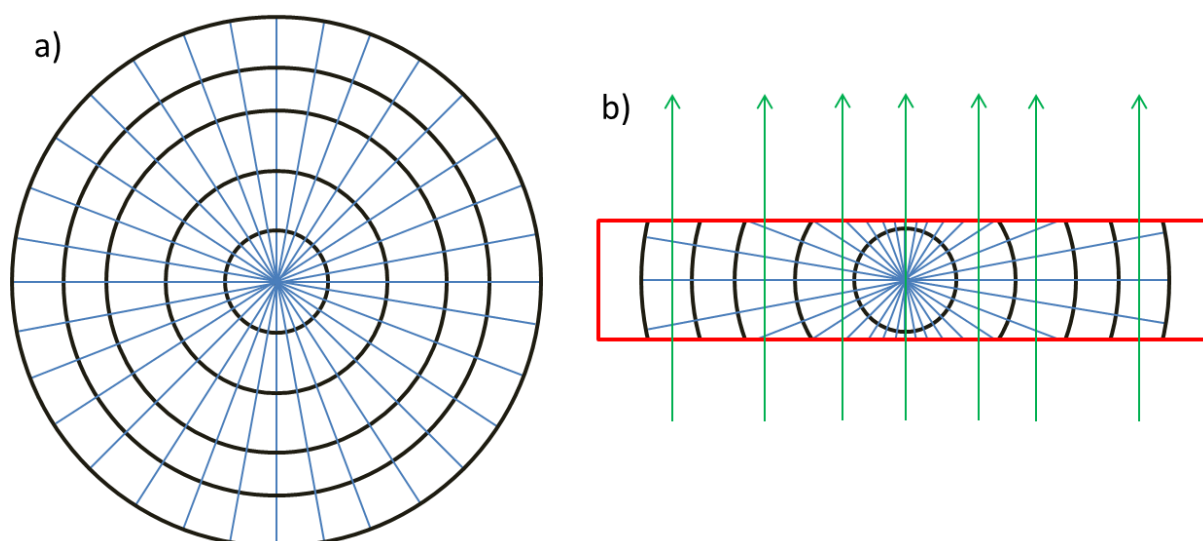


Figure 6.26. a) diagrammatic representation of the 'radial' structure of a *Buccinum undatum* statolith. The black circles represent statolith growth ring and the blue lines represent crystal orientations and b) a diagrammatic representation of a thin section (red box) of the *Buccinum undatum* statolith shown in (a) indicating the crystals sampled during μ XRD. The green lines represent the passage of X-rays.

6.4.2 SIMS analysis

All analysed statolith samples revealed Mg cycles with minimum values corresponding to the visible statolith growth rings. Any disturbance rings that were visible were not revealed by changes in Mg concentration. As the annual periodicity of statolith growth rings had already been validated for juvenile laboratory reared specimens (see Chapter 5) this implied an annual periodicity would be present in cycles in the Mg/Ca profiles and in the Na/Ca profiles also. This was confirmed with the elemental analysis of statoliths from laboratory reared animals of known age. The analysis of statoliths from 1 and 2 year old animals revealed 1 and 2 Mg cycles respectively, which correspond to the visible annual statolith growth rings. These Mg cycles were strongly related to the seasonal seawater temperature cycle. Several clear patterns in Mg incorporation were evident, firstly the maximum concentrations of Mg in the first annual cycle were higher than all subsequent cycles in all statoliths. Whilst this was not as pronounced in some whelks, the innermost cycle was always higher irrespective of location of the whelks or their gender. Secondly, more Mg was incorporated into the statoliths from Jersey in comparison to those from the Shetlands. The mean Mg/Ca values at each site decreased with latitude from the coldest site (Shetland) to the warmest (Jersey), demonstrating a latitudinal seawater

temperature control of Mg incorporation. Evident in several statoliths, the annual Mg cycles from the oldest whelks were lower in amplitude with ontogeny. This is due to two possible factors, firstly a physiological control related to growth rate may lower Mg incorporation with time as shell and statolith formation slows. Secondly the constraints of sampling resolution result in time averaging of portions of the Mg annual cycle between the narrower older growth rings, effectively smoothing out the amplitude of the cycles. Considering the seasonal patterns in the Mg profiles together suggests a combination of both thermodynamic and physiological controls over the incorporation of Mg within the statoliths, with physiological controls likely playing a more important role within the first year of growth. Mg concentrations within the shells (Chapter 4) were roughly equivalent to the concentration of Mg within the matching statoliths. There was some variation in shell and statolith Mg concentrations resulting in average values that were 30-100% higher in the shells.

Sodium concentrations in many statoliths showed strong and moderate negative relationships with Mg. The stronger negative relationships were more often seen in the Menai Strait and Jersey whelk statoliths. Unlike Mg, no clear pattern of increased Na incorporation was seen in the first annual cycle, although, like Mg in older statoliths, the amplitude of the cycles decreased with age. The incorporation of Na into the statoliths is likely controlled by the annual seasonal seawater temperature cycle and a level of physiological control. Interestingly the cycles in Na concentrations in the whelk shells from Shetlands (Chapter 4) are inverse to those seen in shells from the Menai Strait and Jersey. However, the Shetland statoliths displayed similar patterns to the statoliths from the Menai Strait and Jersey. This also means that the Na cycles within the shells and statoliths are inverse to each other for samples from the Menai Strait and Jersey but not for Shetland. At the right hand edge of each adult whelk statolith the Na/Ca profiles rose unexpectedly, likely as a result of an edge effect caused by the low incidence angle of the ion beam (30°). It is unclear why Na concentrations were affected when Sr and Mg concentrations were not. Statolith Na concentrations were comparable between all sites, with a mean value (≈ 4000 mg/kg) similar to the shell Na concentration for all Jersey and Menai Strait. The concentrations of Na within the shells from Shetland differed to the concentrations of Na within the statoliths from the same specimens. This means that the statolith Na concentrations are far more consistent and reliable between sites than Na concentrations in the shell.

The incorporation of Sr into the statoliths is likely under greater physiological control by the whelk than the other elements analysed. Some statoliths showed weak seasonal cycles that

approximately matched the Mg cycles and growth ring formation. However the Sr cycles were often unclear and extra cycles of Sr were apparent when compared to the growth rings. One of the striking features of the Sr cycles in all the adult statoliths was the clear ontogenic increase in Sr concentrations towards the outer edge of the statolith. This was the same for both male and female specimens from all sites. It is likely this control may be related to growth rate, due to the clear ontogenic change. Whilst physiological control on Sr incorporation in the statoliths is clear, this was not seen to the same extent in the shells which displayed no ontogenic change. The mean statolith Sr concentrations were 4 times higher than levels in the shells (Chapter 4) and they were also fairly consistent between sites. The laboratory reared specimens showed lower mean concentrations than the field collected adult specimens, this is accounted for by the lack of any ontogenic increase in concentrations as the whelks were young (1 and 2 years old). However, on average the 2 year old whelk statoliths contained more Sr than the 1 year olds.

The anomalous statolith from whelk SH-31 contained vastly differing concentrations of all 3 elements and displayed values of Mg and Sr which would be expected in a biogenic calcite structure, with higher concentrations of Mg than Sr (Dietzel *et al.*, 2004; Schöne *et al.*, 2010). μ XRD analysis of the corresponding statolith showed it was similarly composed of aragonite like the other statoliths, although its appearance and classification as 'crystallised' suggests it is different from the other statoliths analysed. No other obvious explanation(s) can be found to explain the anomalous results. It is possible that the crystallised structure has different amounts of organic matter, resulting in differences in the incorporation of different elemental concentrations. Further work is required to confirm this and is outside the scope of the current project.

Published accounts of the chemical analyses of molluscan statoliths have frequently focussed on cephalopods (e.g. cuttlefish - Zumholz *et al.*, 2007a; Gillanders *et al.*, 2013; squid - Arkhipkin *et al.*, 2004; Zumholz *et al.*, 2007b and octopods - Ikeda *et al.* 1999) as opposed to gastropods. The relationships found within these species are comparable to the results presented here. Sr/Ca concentrations in the statoliths of *B. undatum* ($\approx 7000 - 10000 \text{ mg/kg}^{-1}$) fall within the range of reported concentrations for cephalopod statoliths ($7000 - 14000 \text{ mg/kg}^{-1}$, (e.g. Ikeda *et al.*, 1999; Ikeda *et al.*, 2003 and Gillanders *et al.*, 2013)). However, they are higher than those found in fish otoliths ($\approx 1750 - 2200 \text{ mg/kg}^{-1}$, Campana, 1999) and mollusc shells ($\approx 700 - 1400 \text{ mg/kg}^{-1}$, e.g. Waring *et al.* 2000 and this study, $1200 - 3000 \text{ mg/kg}^{-1}$). Galante-Oliveira *et al.* (2015) reported periodic cycles of Sr in the statoliths of the gastropod *Nassarius reticulatus* with

maximum concentrations corresponding with the statolith growth rings in 92% of cases. This suggests an inverse relationship with seawater temperature. Zacherl *et al.* (2003b) also reported an inverse correlation between Sr and seawater temperature in the larval statoliths from the marine gastropod *Kelletia kelletii*. Such a relationship was not found in the pre-hatching area of the statolith of *B. undatum*. Interestingly, Zacherl *et al.* (2003b) also reported a positive correlation between Sr and seawater temperature in the protoconch (larval shell) of the same samples, the opposite was found in *B. undatum*. One observation which is strikingly similar in the findings of Zacherl *et al.*'s (2003b) study and this study is the difference in Sr concentrations between the statolith and shell. Sr concentrations were 3-4 times higher in the statoliths than the shell in both species. Ontogenic trends in trace elements across cephalopod statoliths are commonly seen for elements such as Mg (Zumholz *et al.*, 2007b; Arbuckle & Wormuth, 2014). It is believed that this is due to an ontogenic decrease in the organic matter within the matrix of the statolith as a result of the slowing of growth (Bettencourt & Guerra, 2000; Zumholz *et al.*, 2007b). It is therefore likely that if the organic matter content of *B. undatum* statoliths decreases with age as growth slows, this could be the cause of the ontogenic increase in Sr/Ca. The organic matrix of the aragonite shell of the long-lived bivalve *Arctica islandica* has been shown to be depleted in Sr (Schöne *et al.*, 2010). This may explain the observed ontogenetic increase in Sr in *B. undatum* statoliths over time if the organic content of the statolith is greater in the centre part of the statolith than at the edge. Currently there is no evidence of the organic composition of the statoliths that might support this idea and further work should therefore focus on this important aspect of statolith structure and elemental incorporation.

Currently only one paper has investigated the presence of Mg in gastropod statoliths. Lloyd *et al.* (2008) reported on the effect of temperature and egg source effects (the effect of the larval food source and the egg on trace element incorporation) in larval *Kelletia kelletii* enclosed within their egg cases. They found no effect of temperature on Mg incorporation although an inverse relationship between Sr and seawater temperature was found. A strong relationship between the concentrations of Mg in the egg source and the statolith was observed suggesting tight control of magnesium incorporation from the food source in this species. The period of larvae growth within the egg capsule demonstrated higher concentrations of Mg than during the juvenile growth period. As juvenile *B. undatum* develop directly from the egg capsule and have a similar life cycle to *K. kelletii*, it is possible that this may be the reason behind the increased concentrations of Mg seen in this study in the central portions of each statolith. Zumholz *et al.*, (2006) also found that food source had a strong control on the incorporation of

elements such as Sr into the statoliths of the cuttlefish *Sepia officinalis*. They also found elevated levels of Mg in the core of the statoliths. Whilst this is not a direct gastropod example, it does show the potential of a food source to impact upon trace element incorporation within molluscan statoliths. No literature could be found relating to the incorporation of Na into gastropod statoliths, however, Zumholz *et al.* (2007c) found putative daily cycles of Na/Ca in the statoliths of the squid *Gonatus fabricii* using nanoSIMS. It was concluded that these cycles corresponded with daily growth rate changes as a result of a diurnal feeding cycle and were inversely correlated to Sr/Ca concentrations. The findings from this study and those of Zumholz *et al.* (2007c) have demonstrated and confirmed the suitability of high sensitivity, high resolution techniques such as SIMS and nanoSIMS for studying the geochemistry of small biogenic carbonate structures.

6.4.3 Geochemical validation of statolith growth rings

The confluence between the numbers of shell isotope cycles, statolith Mg cycles and visible growth rings strongly supports the validation of an annual periodicity of statolith growth ring formation in *B. undatum*. The numbers of visible growth rings in the opercula rarely matched and generally underestimated whelk age. Taken together these findings give confidence to the use of *B. undatum* statoliths as an age determination tool within the context of fisheries management.

There were several limitations to this work which should be considered when interpreting the results. In several samples the Mg cycles and shell isotope cycles did not match although the number of statolith rings did match the shell isotope cycles. This likely suggests that the weakly defined growth rings at the edge were not fully analysed using SIMS, this was possibly due to a combination of extremely narrow outer growth rings and edge effects arising from resin embedding (which either had a comparatively very high Mg content or contributed significant ^{12}C - ^{12}C dimer interference) masking the elemental cycles. There were also several instances of the correct number of Mg/Ca cycles within the statoliths however the spacing between the cycles did not quite match the widths of the visible growth rings. This was most likely due to the sample preparation. If the central plane of the statolith was not reached during the grinding process then the spherical nature of the statolith would cause the distortion of the available exposed statolith annual ring widths for analysis, causing a miss-match between the Mg/Ca cycles and the visible statolith ring widths (which are not affected by the preparation process and can be viewed in a whole statolith, Figure 6.27). The problem only occurred due to the low

impact nature of the SIMS technique which did not leave identifiable sampling craters that could be matched post-analysis with the elemental data points (Figure 6.28). This meant that when it came to overlaying the trace element profiles on statolith images, instead of matching up each data point to an individual sample spot, the overall width of the calcium signal was used to distinguish the edge of each side of the statolith. This was possible due to the set sampling resolution across each statolith. Whilst this was not problematic for statoliths that had been sectioned through the central plane (Figure 6.27a), in those statolith sections where the central plane had been missed during preparation, the position of the elemental cycles, especially towards the centre of the structure may have been distorted (Figure 6.27b). However, due to the very careful sample preparation, this is unlikely to have caused any misleading interpretation of the elemental concentration data.

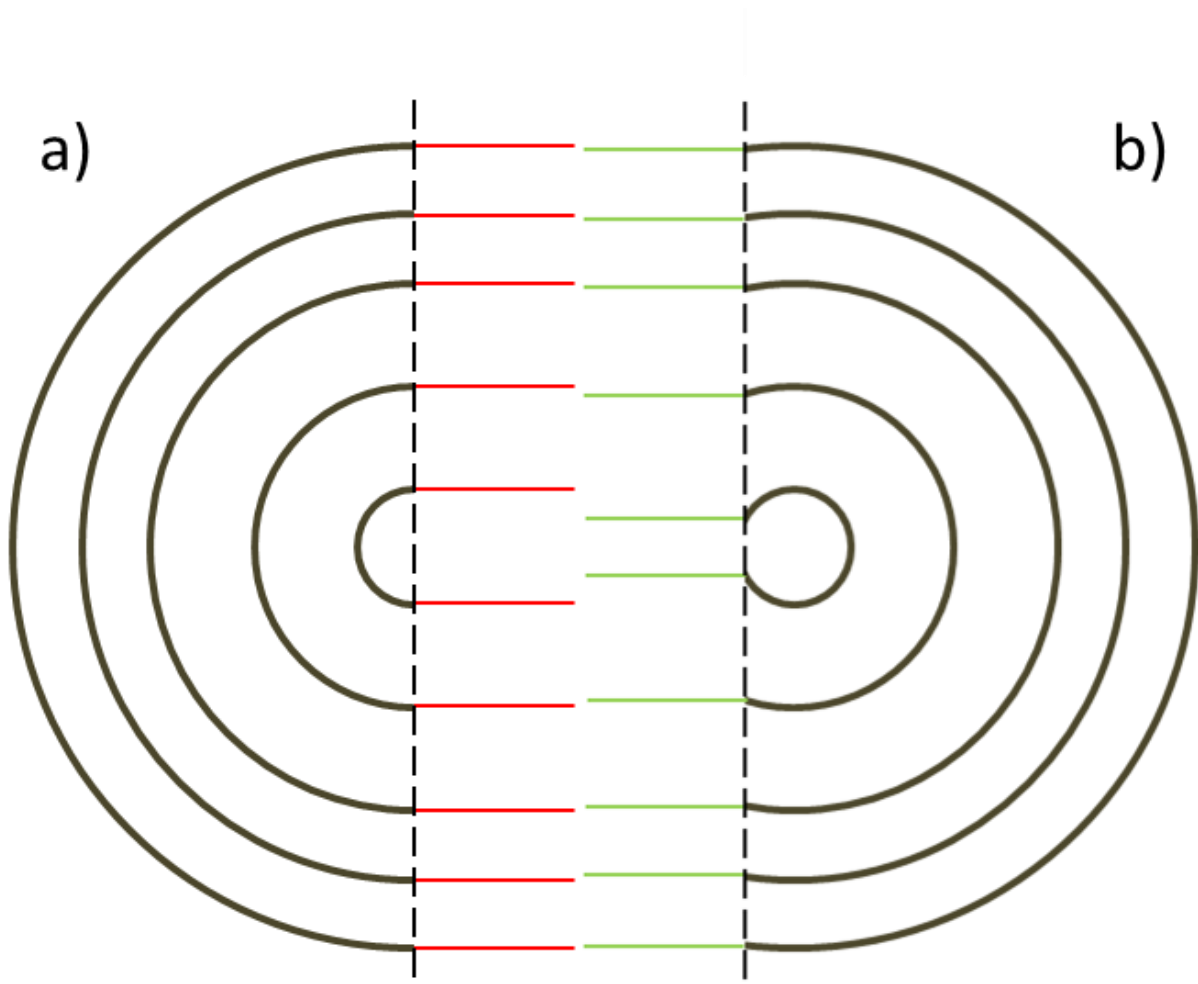


Figure 6.27. Diagrammatic representation of the potential causes of miss-match between the visible and analysed statolith rings. a) a perfectly prepared statolith which has been sectioned to the exact centre leaving an exposed surface (dotted line) that allows the sampling of the growth rings (red lines) and b) the identical statolith shown in a) not properly prepared. The exposed surface for analysis does not reach the central plane and this causes slight distortion of the outer growth ring widths (green lines).

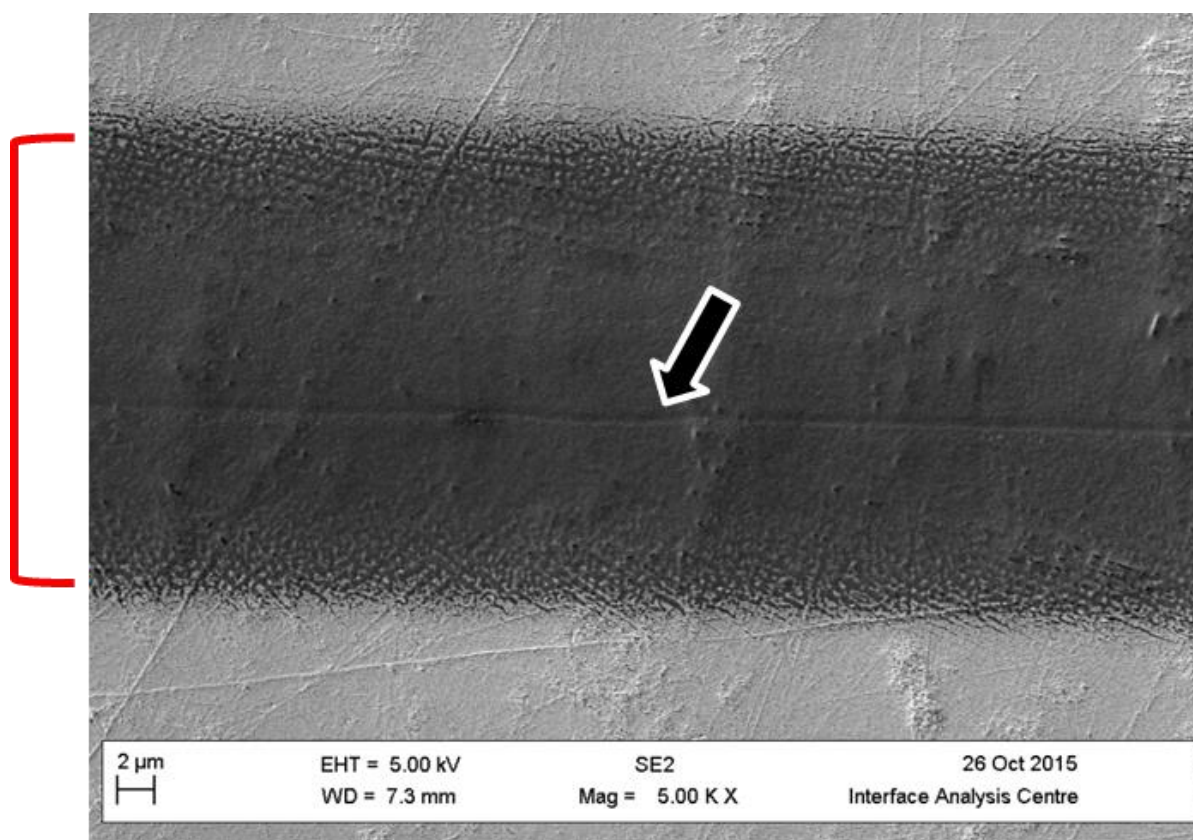


Figure 6.28. An SEM image of a SIMS sampling track across a statolith. The red bracket highlights the area cleared before sampling by the high current beam. The small track highlighted by the arrow is the low current SIMS sample track.

Matrix effects may also be an issue when utilising any surface analytical technique such as SIMS. ‘Matrix effects’ is a generic term in analysis referring to perturbations from expected results caused by some sample compositional control. Those discussed here are specific to the SIMS analysis of the statoliths. Matrix effects are caused when changes in the structure of a sample (such as a change in the organic matter content) cause observed differences in trace element profiles as opposed to absolute changes in trace element concentrations within the CaCO_3 matrix due to environmental or physiological factors at the time of incorporation. Due to the heterogeneous nature of the CaCO_3 matrix within the statoliths, there was a possibility that some of the variation in trace element profiles may have been caused by matrix effects. To check this, raw elemental profiles were compared to the raw profiles of Ca across each statolith. If variation in the Ca profiles matches (with either a positive or negative relationship) a trace element profile then it is possible that the trace element variation is due to increased organic matter within the structure causing a change in the Ca concentration and the trace element concentration (Meibom *et al.*, 2004; Zumholz *et al.*, 2007c). Whilst there was some weak correlation in discreet parts of a few statoliths ([Appendix L](#)), there was no overall pattern of Ca variation affecting trace element profiles for any measured element, discounting matrix effects

on the resulting data. This effect is also diminished by presenting the elemental concentrations as ratios to Ca and also by using a range of calcium based standards with similar compositions for SIMS analysis.

In conclusion, this study investigated the microstructure and microchemistry of *B. undatum* statoliths for the first time. The data presented here represent the first time that any analytical analyses have been performed on *B. undatum* statoliths, and the first time that several high precision techniques (μ XRD and SIMS) have been applied to gastropod statoliths in general. The results emphasise the applicability and usefulness of these techniques for investigating the structural and chemical composition of small carbonate structures on a sub-annual, micro-meter scale.

The growth rings within the statoliths were found to contain clear, negatively correlated cycles in Mg and Na at all three sites and within laboratory reared animals, likely controlled by a combination of environmental and physiological factors. These findings are unique within the literature, not just for gastropod statoliths but for all mollusc statoliths. The cycles in Sr also displayed an ontogenetic increase, something which has never before been uncovered at sub-annual resolution in mollusc statoliths. A clear disconnect between trace element incorporation in the shells (presented in Chapter 4) and statoliths of *B. undatum* was also shown with different average concentrations of each element in each structure. This has been demonstrated previously in the statoliths of larval *K. Kelletii* (Zacherl *et al.*, 2003b). This suggests differing physiological controls at each incorporation site for each element.

The numbers of Mg and Na cycles matched the number of shell oxygen isotope cycles in almost all shells, these findings greatly strengthen the validation of the annual periodicity of growth line formation outlined in Chapter 4. The suitability of statolith growth rings as an age determination tool in comparison to the operculum rings is investigated in the next chapter (Chapter 7) and will be a basis for improving the monitoring practices for this commercially important species.

6.5 References

- Arbuckle NSM, Wormuth JH (2014) Trace elemental patterns in Humboldt squid statoliths from three geographic regions. *Hydrobiologia* 725:115–123
- Arkhipkin AI, Campana SE, FitzGerald J, Thorrold SR (2004) Spatial and temporal variation in elemental signatures of statoliths from the Patagonian longfin squid (*Loligo gahi*). *Can J Fish Aquat Sci* 61:1212–1224
- Basham M, Filik J, Wharmby MT, Chang PCY, Kassaby BE, Gerring M, Aishima J, Levik K, Pulford BCA, Sikharulidze I, Sneddon D, Webber M, Dhesi SS, Maccherozzi F, Svensson O, Brockhauser S, Na'rayc G, Ashton AW (2015) Data Analysis WorkbeNch (DAWN) J Synchrotron Rad 22:853–858
- Bettencourt V, Guerra A (2000) Growth increments and biomineralization process in cephalopod statoliths. *J Exp Mar Biol Ecol* 248:191–205
- Brinza L, Schofield PF, Mosselmans JFW, Donner E, Lombi E, Paterson D, Hodson ME (2014) Can earthworm-secreted calcium carbonate immobilise Zn in contaminated soils? *Soil Biol Biochem* 74:1–10
- Campana SE (1999) Chemistry and composition of fish otoliths: pathways, mechanisms and applications. *Mar Ecol Prog Ser* 188:263–297
- Dietzel M, Gussone N, Eisenhauer A (2004) Co-precipitation of Sr^{2+} and Ba^{2+} with aragonite by membrane diffusion of CO_2 between 10 and 50°C. *Chem Geol* 203:139–151
- Finch AA, Shaw PA, Weedon GP, Holmgren K (2001) Trace element variation in speleothem aragonite: potential for palaeoenvironmental reconstruction. *Earth and Planet Sci Lett* 186:255–267
- Freitas P, Clarke LJ, Kennedy H, Richardson C, Abrantes F (2005) Mg/Ca, Sr/Ca, and stable-isotope ($\delta^{18}\text{O}$ and $\delta^{13}\text{C}$) ratio profiles from the fan mussel *Pinna nobilis*: seasonal records and temperature relationships. *Geochem Geophys Geosyst* 6:Q04D14
- Galante-Oliveira S, Marçal R, Espadilha F, Sá M, Abell R, Machado J, Barroso C (2015) Detection of periodic Sr Ca^{-1} cycles along gastropod statoliths allows the accurate estimation of age. *Mar Biol* 162:1473–1483
- Galante-Oliveira S, Marçal R, Guimarães F, Soares J, Lopes JC, Machado J, Barroso CM (2014) Crystallinity and microchemistry of *Nassarius reticulatus* (Caenogastropoda) statoliths: towards their structure stability and homogeneity. *J Struct Biol* 186:292–301
- Galante-Oliveira S, Marçal R, Ribas F, Machado J, Barroso CM (2013) Studies on the morphology and growth of statoliths in Caenogastropoda. *J Mollus Stud* 79:340–345
- Gillanders BM, Wilkinson LM, Munro AR, de Vries MC (2013) Statolith chemistry of two life history stages of cuttlefish: Effects of temperature and seawater trace element concentration. *Geochim Cosmochim Acta* 101:12–23
- Gomes I, Peteiro LG, Albuquerque R, Nolasco R, Dubert J, Swearer SE, Queiroga H (2016) Wandering mussels: using natural tags to identify connectivity patterns among Marine Protected Areas. *Mar Ecol Prog Ser* 552:159–176

- Gong YUT, Killian CE, Olson IC, Appathurai NP, Amasino AL, Martin MC, Holt LJ, Wilt FH, Gilbert PUPA (2012) Phase transitions in biogenic amorphous calcium carbonate. *P Natl Acad Sci USA* 109(16):6088-6093
- Higson SPJ (2004) *Analytical Chemistry*. Oxford University press, Oxford, UK.
- Ikeda Y, Arai N, Kidokoro H, Sakamoto W (2003) Strontium: calcium ratios in statoliths of Japanese common squid *Todarodes pacificus* (Cephalopoda: Ommastrephidae) as indicators of migratory behaviour. *Mar Ecol Prog Ser* 251:169–179
- Ikeda Y, Arai N, Sakamoto W, Mitsuhashi M, Yoshida K (1999) Preliminary report on PIXE analysis for trace elements of *Octopus dofleini* statoliths. *Fish Sci* 65:161–162
- Lloyd DC, Zacherl DC, Walker S, Paradis G, Sheehy M, Warner RR (2008) Egg source, temperature and culture seawater affect elemental signatures in *Kelletia kelletii* larval statoliths. *Mar Ecol Prog Ser* 353:115–130
- Matta ME, Orland IJ, Ushikubo T, Helser TE, Black BA, Valley JW (2013) Otolith oxygen isotopes measured by high-precision secondary ion mass spectrometry reflect life history of a yellowfin sole (*Limanda aspera*). *Rapid Commun Mass Spectrom* 27:691–699
- Meibom A, Cuif J-P, Hillion F, Constanz BR, Julliet-Leclerc Am, Dauphin Y, Watanabe T, Dunbar RB (2004) Distribution of magnesium in coral skeleton. *Geophys Res Lett* 31:L23306
- O'Connor DJ, Sexton BA, Smart RStC (2003) *Surface analysis methods in materials science*. Springer-Verlag, Berlin
- Parker JE, Thompson SP, Lennie AR, Potter J, Tang CC (2010) A study of the aragonite–calcite transformation using Raman spectroscopy, synchrotron powder diffraction and scanning electron microscopy. *Cryst Eng Comm* 12:1590–1599
- Pourang N, Richardson CA, Chenery SRN, Nasrollahzadeh H (2004) Assessment of trace elements in the shell layers and soft tissues of the pearl oyster *Pinctada radiata* using multivariate analyses: a potential proxy for temporal and spatial variations in trace elements. *Environ Monit Assess* 186:2465–2485
- Radha AV, Forbes TZ, Killian CE, Gilbert PUPA, Navrotsky A (2010) Transformation and crystallization energetics of synthetic and biogenic amorphous calcium carbonate. *PNAS* 107(38):16438–16443
- Schöne BR, Zhang Z, Jacob D, Gillikin DP, Tütken T, Garbe-Schönberg D, McConnaughey T, Soldati A (2010) Effect of organic matrices on the determination of the trace element chemistry (Mg, Sr, Mg/Ca, Sr/Ca) of aragonitic bivalve shells (*Arctica islandica*) – Comparison of ICP-OES and LA-ICP-MS data. *Geochem J* 44:23-37
- Smith DC, Carabatos-Nédelec C (2001) *Raman Spectroscopy Applied to Crystals: Phenomena and Principles, Concepts and Conventions*. In: Lewis IR, Edwards HGM (Eds.), *Handbook of Raman Spectroscopy*. Marcel Dekker, New York
- Smith E, Dent G (2005) *Modern Raman Spectroscopy – A Practical Approach*. John Wiley & Sons, Ltd, England

- Sosdian S, Gentry DK, Lear CH, Grossman EL, Hicks D, Rosenthal Y (2006) Strontium to calcium ratios in the marine gastropod *Conus ermineus*: growth rate effects and temperature calibration. *Geochem Geophys* 7(11):1525–2027
- Speer JA (1983) Crystal chemistry and phase relations of the orthorhombic carbonates. *Rev Mineral Geochem* 11:145–190
- Sturrock AM, Hunter E, Milton AJ, EIMF, Johnson RC (2015) Quantifying physiological influences on otolith microchemistry. *Methods Ecol Evol* 6:806–816
- Sturrock AM, Trueman CN, Milton JA, Waring CP, Cooper MJ, Hunter E (2014) Physiological influences can outweigh environmental signals in otolith microchemistry research. *Mar Ecol Prog Ser* 500:245–264
- Thomas R (2011) Practical guide to ICP-MS, a tutorial for beginners. CRC press, Taylor and Francis group. Boca Raton, Florida
- Waring CP, Trueman CN, Vander Putten E, Dehairs F, Keppens E, Baeyens W (2000) High resolution distribution of trace elements in the calcite shell layer of modern *Mytilus edulis*: Environmental and biological controls. *Geochim Cosmochim Acta* 64:997–1011
- Wehrmeister U, Jacob DE, Soldati AL, Loges N, Häger T, Hofmeister W (2010) Amorphous, nanocrystalline and crystalline calcium carbonates in biological materials. *J Raman Spectrosc* 42:926–935
- White LK, Szabo P, Carkner P, Chasteen NDJ (1977) An electron paramagnetic resonance study of manganese (II) in the aragonite lattice of a clam shell, *Mya arenaria*. *Phys Chem* 81:1420–1424
- Zacherl DC (2005) Spatial and temporal variation in statolith and protoconch trace elements as natural tags to track larval dispersal. *Mar Ecol Prog Ser* 290:145–163
- Zacherl DC, Manriquez PH, Paradis G, Day RW, Castilla JC, Warner RR, Lea DW, Gaines SD (2003a) Trace elemental fingerprinting of gastropod statoliths to study larval dispersal trajectories. *Mar Ecol Prog Ser* 248:297–303
- Zacherl DC, Paradis G, Lea D (2003b) Ba and Sr uptake into larval protoconchs and statoliths of the marine neogastropod *Kelletia kelletii*. *Geochim Cosmochim Acta* 67:4091–4099
- Zumholz K, Hansteen T, Hillion F, Horreard F, Piatkowski U (2007c) Elemental distribution in cephalopod statoliths: NanoSIMS provides new insights into nano-scale structure. *Rev Fish Biol Fisheries* 17:487–491
- Zumholz K, Hansteen TH, Klugel A, Piatkowski U (2006) Food effects on statolith composition of the common cuttlefish (*Sepia officinalis*). *Mar Biol* 150:237–244
- Zumholz K, Hansteen TH, Piatkowski U, Croot PL (2007a) Influence of temperature and salinity on the trace element incorporation into statoliths of the common cuttlefish (*Sepia officinalis*). *Mar Biol* 151:1321–1330
- Zumholz K, Klugel A, Hansteen T, Piatkowski U (2007b) Statolith microchemistry traces the environmental history of the boreoatlantic armhook squid *Gonatus fabricii*. *Mar Ecol Prog Ser* 333:195–204

Chapter 7:

A comparison of growth curve estimations from the statoliths and opercula of the whelk *Buccinum undatum*.

7.1 Introduction

7.1.1 Stock assessment of *Buccinum undatum*

The ability of fisheries scientists to model stock dynamics is the keystone for all fishery management (Hilborn & Walters, 1992). For this to be possible, reliable estimates of growth are required for the target species and populations, to allow the estimation of important parameters such as reproductive output and response to changes in fishing pressure (Beamish, 1990; Day & Flemming, 1992; Troynikov *et al.*, 1998). Stock assessments have been attempted on *Buccinum undatum* previously. Valentinsson *et al.* (1999) endeavoured to undertake a stock assessment in Swedish waters by sampling several areas at regular intervals to evaluate the Catch Per Unit Effort (CPUE) and the stock size, as well as collecting samples for a maturity study. The age of a small sample of whelks (≈ 100 each at two sites) were assessed using a standard method of reading the opercular rings. Unfortunately due to the poor clarity of the opercular rings the age structure of the two populations were not discussed at length. Instead, the CPUE was used as a measure of the stock structure. A crude estimate of stock size was determined at 45,000 – 225,000t of whelks. These estimated figures have an exceptionally high degree of uncertainty with respect to catch management. The variability in estimates arose from wide variability of pot attraction areas (range between 18m^2 – 585m^2) that had been taken from previously published research (i.e. Gros and Santarelli, 1986; Himmelman, 1988; McQuinn *et al.*, 1988). The conclusions of the study indicated that further work was needed to determine aspects of the whelks' life history such as fecundity and mortality that would assist in improving stock estimates. A recent paper by Laptikhovsky *et al.* (2016), for the first time calculated the mortality of several *B. undatum* populations using dead collected shells, something which was not possible until now. This gives confidence that future assessments will be able to overcome some of the previous obstacles to *B. undatum* stock assessment.

Other examples of published whelk stock assessments also used CPUE, such as the Outer Hebrides study of whelks by Jacklin (1998). It was concluded that, due to the predominance of large fouled shells, the population was too old to withstand a sustained fishing effort, although no direct ageing of the whelks was incorporated in the assessment. A similar study was undertaken around Jersey and the Channel Isles (Morel & Bossy, 2004), after a fishery was started in 1996 to satisfy the growing demand from East Asia for whelks. It similarly concluded that more work was needed to better understand individual whelk populations and that further

management options should be considered to ensure its sustainability, should the fishery grow. In the 18 years following these three studies (i.e. Jacklin, 1998; Valentinsson *et al.*, 1999 and Morel & Bossy, 2004) there has been little relevant research to enable robust stock estimates to be made.

For *B. undatum*, the problems with the existing age determination techniques have been discussed at length in the introduction, namely the use of surface rings on the operculum. These focus largely on the poor clarity of the opercula leading to the omission of large portions of the sample set (only 41% - 52% classed deemed as readable by Kideys, 1996; Lawler, 2013 respectively). An additional problem regarding the use of opercula arises from the presence of an additional set of growth lines on the underside of each operculum, known as the adventitious layers.

7.1.2 Growth of the operculum

The growth of the operculum is complex with several areas of growth present on a single operculum (Checa & Jiménez-Jiménez, 1998; Vasconcelos *et al.*, 2012). In a concentric operculum (like those found on *B. undatum*), growth is added to the dorsal (outer) layer via a groove in the foot, in the form of regular additions of thin layers of protein. The operculum is also strengthened and thickened over time with the addition of adventitious layers to the ventral side of the operculum (Figure 7.1).

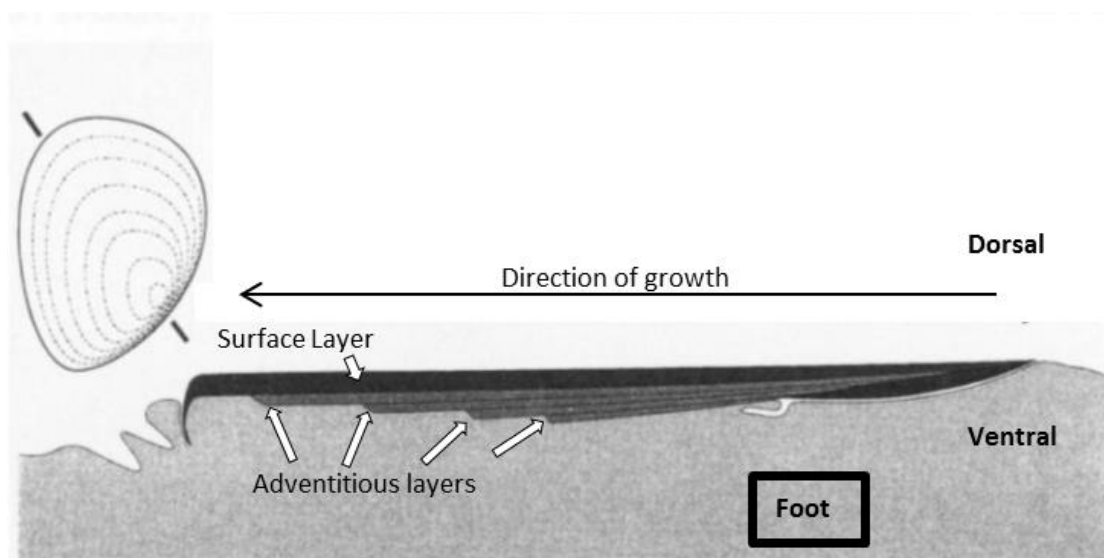


Figure 7.1. Growth of the concentric gastropod operculum. A whole operculum is shown on the left of the figure and in section in the main part of the figure. Adapted from Vovelle, (1967) and Checa and Jiménez-Jiménez (1998).

Once the operculum has been removed from the foot of the animal, the adventitious layers on the ventral surface of the operculum become visible in reflected light and appear similar to the external growth rings viewed with transmitted light (Figure 7.2). However the difference in number of rings on the external surface and on the internal operculum surface and a possible confusion between operculum surface rings (OSR) and adventitious layers (AdL) could lead to errors in estimating a whelk's age. This may have led to confusion in several studies where the adventitious layers of the operculum have been counted as annual growth lines (e.g. Shelmerdine *et al.*, 2007). The relationship between external operculum rings and inner adventitious rings has not been fully investigated for most gastropod species. In one study the relationship between the OSRs and the AdLs in the neogastropod *Hexaplex trunculus*, which has a similar concentric operculum to *Buccinum undatum*, were investigated (Vasconcelos *et al.*, 2012). They found that neither surface of the operculum provided a reliable estimation of age, with the adventitious layers underestimating, and the outer surface layer overestimating, the age of this gastropod. Although a different species to *B. undatum*, their work on *H. trunculus* highlights the importance of validating the deposition of growth rings or lines in accreting structures to determine their age. The periodicity of the outer surface layers on the operculum were validated by Santarelli and Gros (1985) (see Chapter 1), but validation of the adventitious layers as an age estimation tool for *B. undatum* has not yet been authenticated.

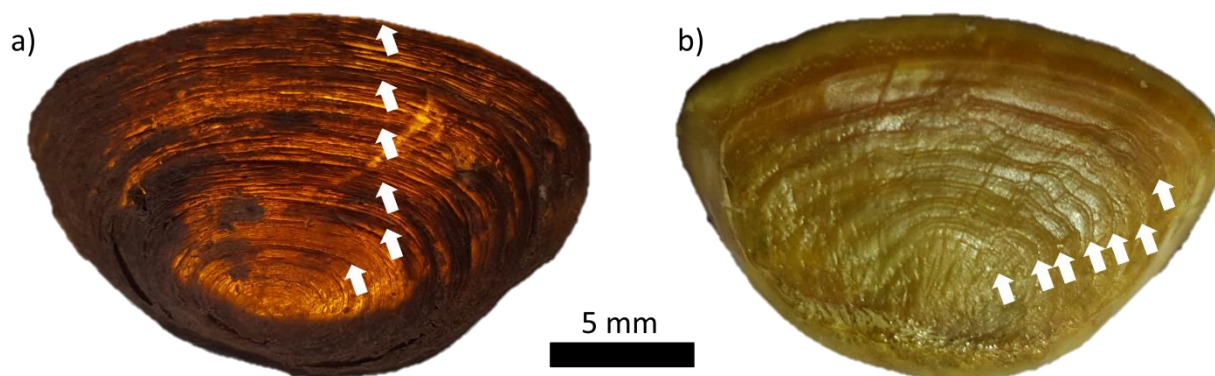


Figure 7.2. An operculum from *Buccinum undatum*. a) external surface of the operculum imaged with transmitted light displays four growth rings (white arrows) and b) inner operculum surface imaged with reflected light shows 7 adventitious layers (rings). (white arrows indicate each ring/layer).

The annual periodicity of statolith growth rings has been unequivocally validated in the preceding chapters of this thesis. The aim of this final results chapter is to assess the viability of three different types of accreted growth lines that occur in *B. undatum* (statolith growth rings - StR, OSR and AdL) for determining a whelk's age and reconstructing the age structure of wild

populations. It was hypothesised that the statoliths would display the greatest clarity and produce the most accurate growth curves compared to the operculum (OSR & AdL) derived ages.

7.2 Materials and methods

Following reproductive assessment (Chapter 2) all *Buccinum undatum* collected from the various sites were re-frozen with the operculum attached to the whelk foot tissue for further analysis.

7.2.1 Statolith sampling and ageing

Upon thawing (5 hours) the statoliths from *Buccinum undatum* collected from all the sample sites (see Chapter 5) were extracted, mounted and imaged using the methodology described in Chapter 5. The resulting statolith photomicrographs were analysed and the number of growth rings counted from the hatching ring outwards. Statoliths of whelks from Amlwch were excluded from the analysis as a high proportion were opaque (59% - Chapter 5, Table 5.2). With the exception of two large whelk statoliths, nearly all of the whelks in a size distribution that was already heavily skewed to the smaller size classes were opaque (Chapter 2, Figure 2.12). Inclusion of age estimates from this population would have greatly biased the data and as such the results for this site are not presented. Much like the reproductive studies outlined in Chapter 2, the large 18 month sample set from the Menai Strait was split into 4 seasons for the following analysis, spring, summer, autumn and winter (January, February & March – winter; April, May & June – spring; July, August & September – summer; October, November & December – autumn). This was done as some of the individual monthly samples had poor size distributions, resulting in skewed data sets.

7.2.2 Operculum growth ring formation

At the same time that the statoliths were extracted, the operculum was removed, rinsed with tap water and left to dry overnight on paper towels at room temperature. The operculum growth lines were visualised using transmitted light from either a lamp or a dissecting microscope. Adventitious layers were counted under a dissecting microscope using reflected light as they were often more difficult to count without magnification. The timing of operculum growth ring formation was studied using laboratory reared *B. undatum* at the same time as the

statolith growth ring formation study described in Chapter 5. The number of OSR and AdL were counted in the opercula of whelks whose statoliths had been assessed (above) and the number compared with the corresponding statolith rings.

7.2.3 Assessment of growth ring and adventitious layer clarity

The clarity of each of the three different growth structures (StR, OSR and AdL) was assessed using a modified methodology adapted from Kideys (1996) where he used a 3 tier scoring system to classify the clarity of opercular surface rings: 1) Unclear – opercular striae were not distinguishable, 2) reasonably clear – opercular striae were distinguishable but the numbers could vary based upon the reader and 3) Clear – opercular striae were well defined.

Following assessment of the whelk opercula, only the ‘reasonably clear’ and ‘clear’ samples were used in subsequent analysis with the ‘unclear’ samples being discarded (Kideys, 1996). In this study this system of scoring was modified so that it could be applied generically to all the growth rings and the adventitious layer equally with the following amendments: 1) No growth rings discernible, 2) Two or more growth rings unclear, 3) One growth ring unclear and 4) All growth rings clear.

A comparison between whelk opercula from each of the clarity rankings can be seen in Figure 7.3. A similar approach to the discarding of unclear specimens was used with only specimens ranked 3 and 4 used in the subsequent analysis. Any samples that were missing were classed as n/a, for statoliths this often constituted the loss of the statolith by the researcher during extraction, for opercula this meant that the sample was lost during potting and collection of the whelk. Importantly to avoid/quantify operator bias, the methodology was tested with a second reader using a random sample of 150 specimens from the Menai Strait for all three sets of growth structures. The clarity rankings from both readers were then compared to establish the inter-reader variance.

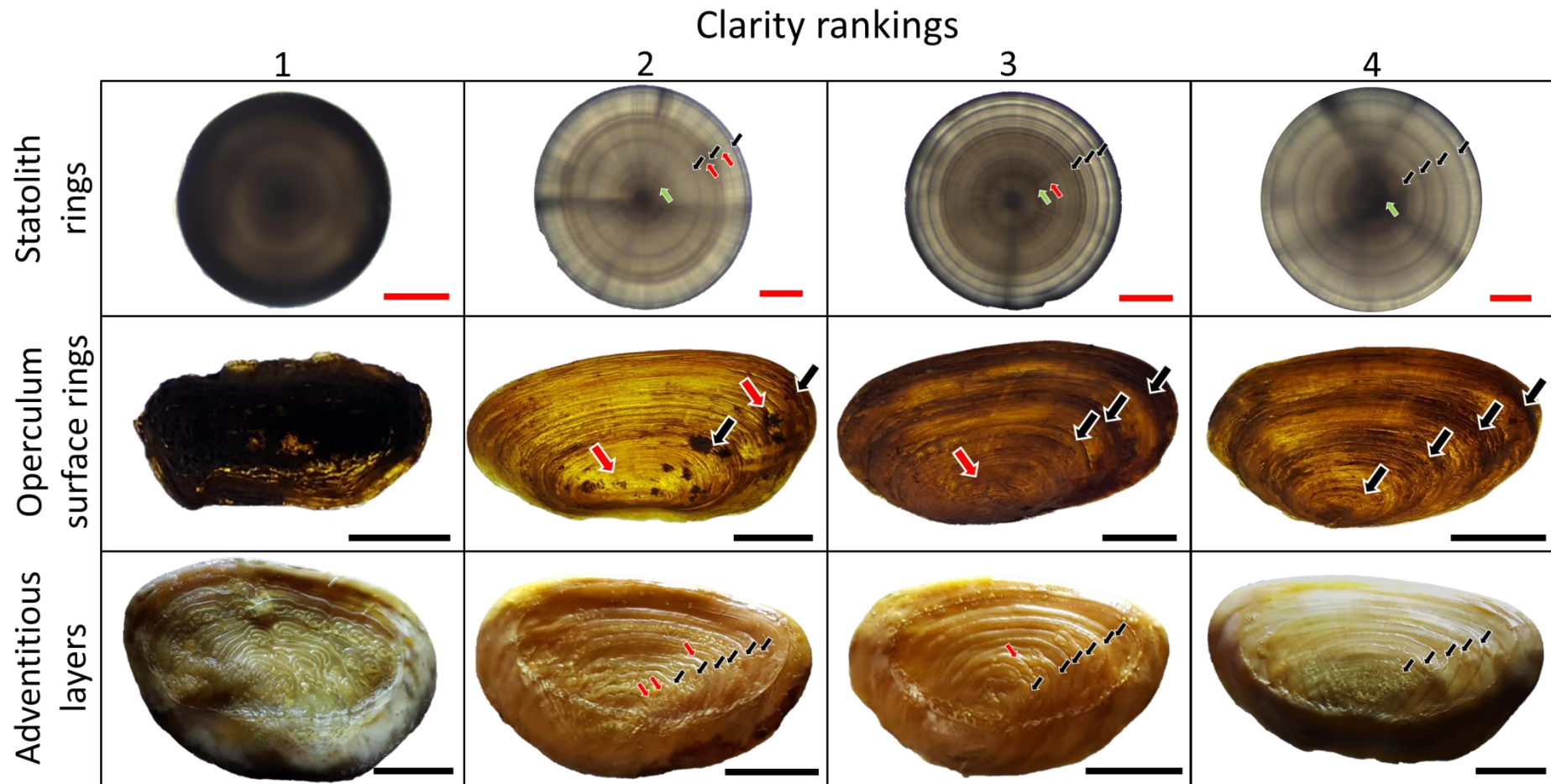


Figure 7.3. *Buccinum undatum* statoliths and opercula. A comparison of four levels of clarity of statolith rings (top row), operculum rings viewed in transmitted light (middle row) and operculum adventitious layers viewed in reflected light (bottom row). Red lines indicate 50 μm scale bars, black lines represent 5 mm scale bars. Black arrows represent clear growth lines, red arrows represent unclear growth lines and green arrows represent the hatching ring of the statoliths.

7.2.4 Growth curve construction

Estimation of the age of whelks from each site using statoliths, operculum rings and adventitious layers generated size at age data. Three commonly used fisheries growth curve equations were fitted to each dataset, using Fishparm (Prager *et al.*, 1994). The von Bertalanffy equation was chosen as it has been used in past studies that have investigated the growth of *B. undatum* (e.g. Shelmerdine *et al.*, 2007). The logistic and Gompertz equations were chosen as some studies investigating the growth of marine gastropods have found sigmoidal growth (Miranda *et al.*, 2008), which is best modelled by these equations (Windsor, 1932).

(1) von Bertalanffy (1934):

$$L_t = L_{\infty}(1 - \exp^{-k(t-t_0)})$$

Where L_t is the length at age t (mm), t is age (years), L_{∞} is the maximum asymptotic length (mm), t_0 is the origin of the growth curve at time zero and K is the rate at which L_{∞} is attained (day^{-1}) (Moreau, 1987; Rodriguez-Sánchez *et al.*, 2009)

(2) Gompertz (1825):

$$L_t = L_0 \exp^{(G(1 - \exp(-gt)))}$$

Where L_t is the mean length (mm) at age t , t is age (years), L_0 is the length at time zero (t_0). G is the instantaneous growth rate at t_0 and g describes the decrease in the rate of G (Prybylski & Garcia-Berthou, 2004). Gg is therefore the specific instantaneous rate of growth at t_0 (Prager *et al.*, 1994).

(3) logistic (Verhulst, 1838):

$$L_t = \frac{K}{1 + (\frac{K - L_0}{L_0})\exp(-rt)}$$

Where L_t is the mean length (mm) at age t . L_0 is the mean length at t_0 , r is the growth rate and K is the asymptotic length (mm) (Prager *et al.*, 1994).

The fit of each growth curve was compared by calculating the R^2 value, the mean squared residual error (MSR_e) and Akaike Information Criterion (AIC) which is a measure of the relative goodness of fit of a particular statistical model to a dataset (Akaike, 1973). The AIC calculation

takes into account both the complexity of the model (i.e. how many parameters are estimated) as well as the residual sum of squares:

$$AIC = n * \ln\left(\frac{SS_{error}}{n}\right) + 2k$$

Where n is the number of observations, SS_{error} is the sum of squares of the residual of the model output and k is the number of parameters fit within the model. The AIC value was then divided by the number of observations to give a value that is comparable between whelk populations. Once the best fit model had been chosen, the resulting growth parameters for each site were compared both between sites and between age estimates within a specific population at each of the sites.

One limitation of the sampling which has already been discussed in Chapter 2 was the absence of juvenile *B. undatum* from most of the sample sites. This resulted in a poor fit for most of the growth curves for each set of age estimates as no juvenile data were available to ‘pin’ the lower age/size estimates for each curve, resulting in unrealistic asymptotic estimates. One option considered was to force the fitted growth curve through zero, this was not appropriate as *B. undatum* is a direct developer and hatches as fully formed juveniles with a size at t_0 that varies depending on a range of factors, such as egg capsule size and mother size (Nasution *et al.*, 2010; Smith & Thatje, 2013). Instead, the size at hatching and at 1 year old were reconstructed for each site by measuring the width of the hatching and year 1 ring in ImageJ for a random sample of 20 statoliths from each site. These measurements were then converted into estimated Total Shell Length (TSL) measurements using the relationships between statolith width and shell height for each site, described in Chapter 5 (see Figure 5.6). The reconstructed TSL measurements were then added to the data set from each population to improve the growth curve estimation. Unfortunately this was not possible for the opercula (due to the poor clarity of the early year growth rings). The estimates from the statolith growth rings were also used in the growth curve estimation for both OSR and AdL. For the Menai Strait site growth curve construction, the measured TSL from laboratory reared *B. undatum* of known age (months) were used to ‘pin’ the lower estimates of size at age. The rationale for this was that the egg masses which the juvenile specimens originated from came from similar conditions to the wild Menai Strait population and the juveniles were grown in constantly flowing Menai Strait seawater.

7.3 Results

7.3.1 Statolith and operculum growth line formation

In Chapter 5 a clear annual seasonal cycle in statolith growth ring formation was demonstrated in laboratory reared *B. undatum*. Figure 7.4 shows the appearance of the annual growth rings in 2, 3, 4 and 5 year old wild collected whelks from the Menai Strait. The clarity of the rings can be seen in these whole mounted statoliths and indicate the variation in clarity and definition of the rings, particularly the 1st growth ring. Whilst the statolith rings are clear and unequivocal the rings on the operculum surface and the adventitious layers rarely corresponded with the number of statolith rings. The examples shown in Figure 7.5 are from two 2.3 year (27 month) old laboratory reared juvenile *B. undatum* and illustrate the lack of correspondence between the rings in both these structures. The statoliths show two annual rings (Figure 7.5a & d), albeit with several disturbance lines visible (a common problem in juvenile statoliths). The corresponding opercula (Figure 7.5b & c and 7.5e & f) have many more rings. The operculum surface rings (Figure 7.5b & e) have respectively, two and three clear rings with two and one possible (disputed) rings. The inner surface adventitious layer rings similarly over estimate the number of rings. Figure 7.5c & f display respectively, four and four rings with an additional possible (disputed) ring in Figure 7.5e.

In a sample of thirty 2.3 year old laboratory reared juvenile whelks, 84% displayed two clear statolith rings (the remaining 16% displayed at least two with one or more prominent disturbance rings). By contrast when the corresponding opercula were examined, only 20% displayed two operculum surface rings. Many of the opercula displayed considerable operculum growth after the second ring which likely represents more than 4 months growth (e.g. Figure 7.5b). Forty percent of opercula had no discernible operculum surface rings and none of the 30 opercula displayed the expected two adventitious layers with the minimum number of layers being three and the maximum number being six.

7.3.2 Growth ring clarity

When statoliths and opercula from whelks from all the sites were examined clear differences in the clarity of the growth rings were seen. Figure 7.6 compares the clarity scores of growth rings from each structure at each site. The statolith rings were clearest at all sites with high percentages scoring 3 and 4 on the clarity scale. The second clearest structure (score 3 & 4) was

the AdL in the opercula with the least clear being the OSR. Both these structures had a frequency of $\approx 25\%$ for the clarity score of 1, i.e. no growth rings visible. From a sample of 150 randomly selected statoliths and opercula the agreement in age between two readers was 89.2% agreement for counting the statolith rings, 45.1% agreement in counting the operculum surface rings and 75.7% agreement in counting the adventitious layers.

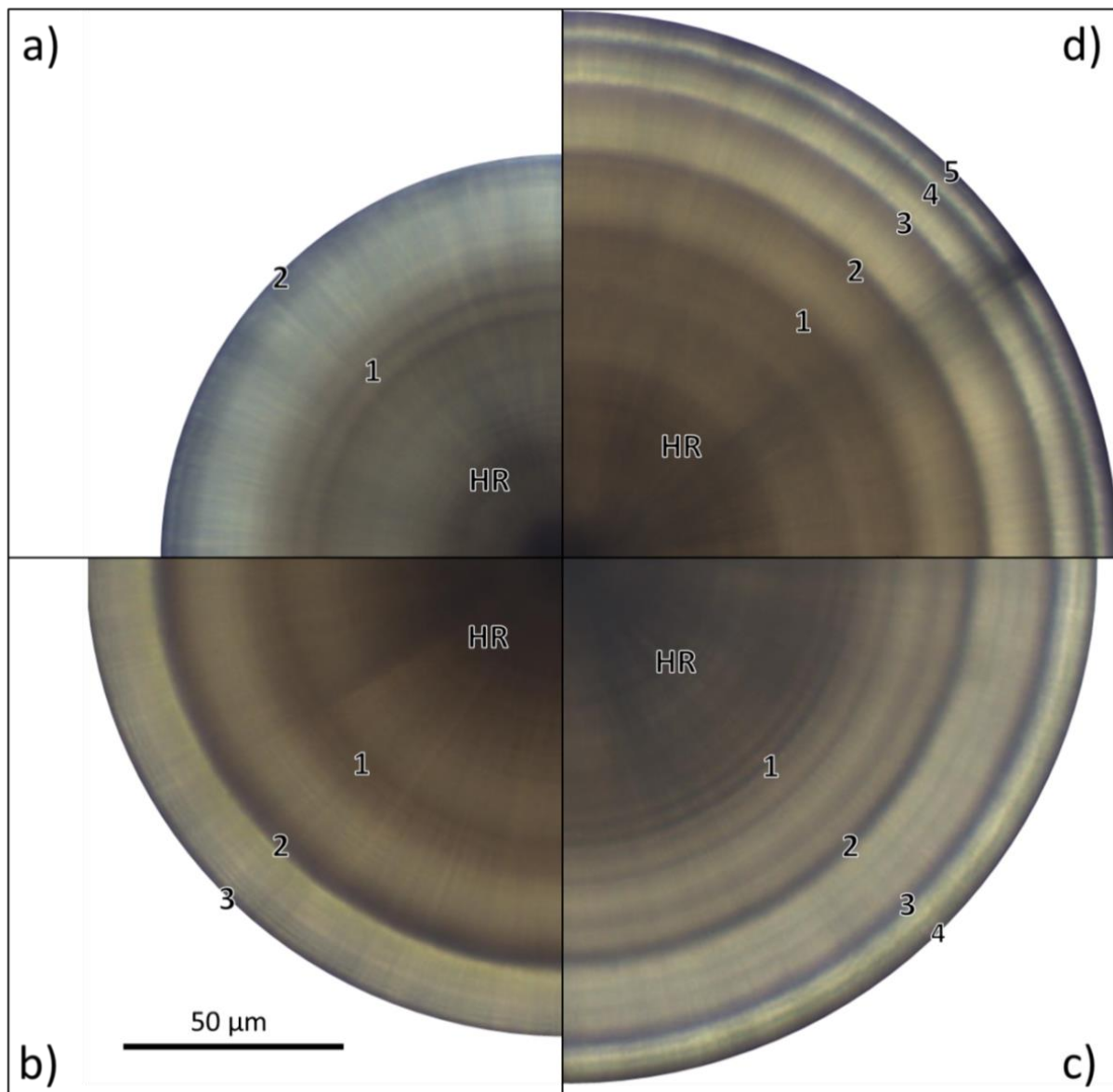


Figure 7.4. A composite image of statolith photomicrographs to show variations in the appearance of the annual rings from a) a 2-year old, b) 3-year old, c) 4-year old and d) 5-year old field collected *Buccinum undatum* from the Menai Strait. HR – hatching ring.

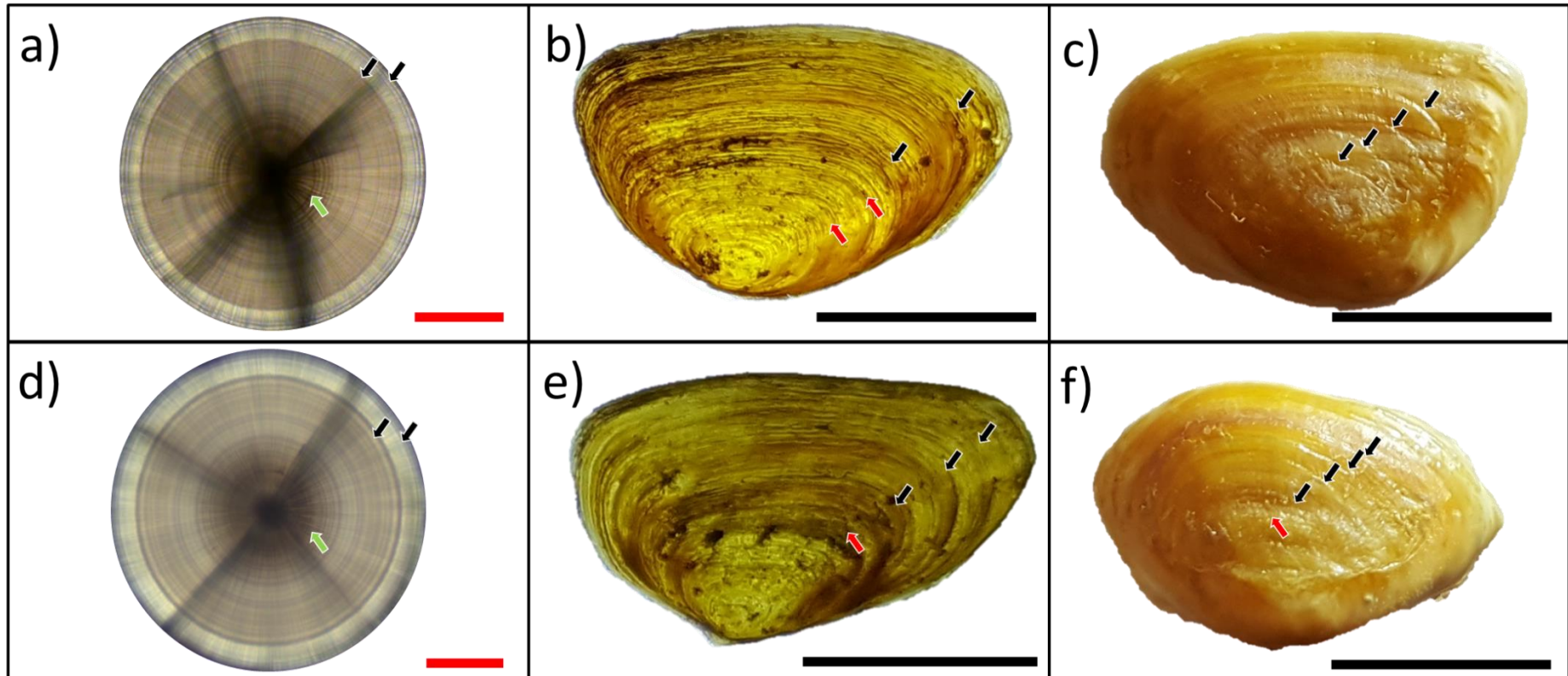


Figure 7.5. Photomicrographs of two 2.3 year old laboratory reared *Buccinum undatum* statoliths (a & d) with corresponding operculum, external surface (b & e) and operculum inner surface showing the adventitious layers (c & f). Hatching rings are represented by green arrows (a & d), clear growth rings by black arrows and disputed rings by red arrows. The statolith rings and operculum surface rings (a & d and b & e respectively) were imaged with transmitted light whereas the adventitious layers on the inner surface of each operculum (c & f) were imaged using reflected light. Red lines indicate 50 μm scale bars, black lines represent 5 mm scale bars.

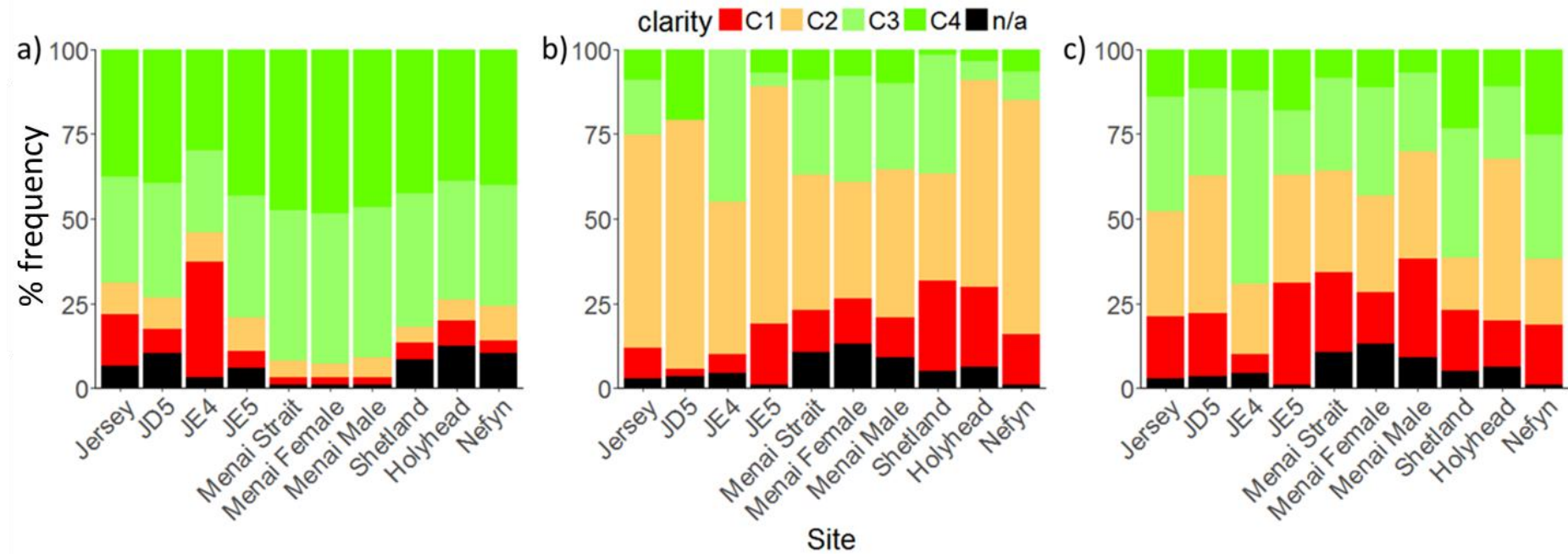


Figure 7.6. Comparison of stacked bar plots showing the % frequency of clarity scores for a) statoliths, b) operculum surface rings and c) adventitious layers from *Buccinum undatum* collected from all sites. n/a represents samples where one or more structures were lost or were not collected during sampling processing.

7.3.3 Growth curve equation choice

The results displayed in Table 7.1 show that for the statolith size at age data, for all sites, Gompertz growth curves with the highest R^2 and the lowest MSR_e and AIC values best described the data. The one exception was the growth curve for whelks from Nefyn that was best described by the von Bertalanffy growth equation. For all sites, the Gompertz and logistic equations resulted in a similar goodness of fit, this is unsurprising since both equations model sigmoidal growth (Windsor, 1932), which *B. undatum* displays. Therefore for all subsequent analyses the Gompertz growth equation was applied.

7.3.4 Site growth curve construction

The clarity of the statolith rings was generally clear so it was relatively easy to estimate the age of whelks from all the sites and then fit the three growth curves to the size at age data (Table 7.1). However the clarity of the OSR quickly became an issue when growth curves were initially fitted to all the data. To improve the growth modelling, age estimates based on the OSR and AdL, where there was uncertainty in the data because of the clarity of the rings, were removed. However, when opercula with a clarity of '1' and '2', were removed from the data the number of age estimates dropped to unusable levels as some of the sites were only left with sample sizes of between 10 and 25 estimates – insufficient to model the operculum growth curve data. To improve this, data where the opercula had a clarity of '2' were also included in order to produce growth curves that could be compared with the statolith growth curves. Summary tables of growth model outputs for operculum derived ages without the '2' clarity specimens and also without the statolith derived juvenile sizes are tabulated in [Appendix M](#).

Table 7.1. Goodness of fit indicators for the three growth models (Gompertz, von Bertalanffy and Logistic) applied to the statolith growth ring size at age data from each site. Bold text indicates the best fitting model for each site.

Model	Parameter	Jersey	JD5	JE4	JE5	Menai Strait (All)	Menai Strait Female	Menai Strait Male	Shetland	Holyhead	Nefyn
Gompertz	R^2	0.90	0.93	0.94	0.94	0.94	0.97	0.97	0.99	0.95	0.93
	MSR_e	26.9	24.75	22.31	21.29	27.18	28.88	25.9	20.67	41.04	73.96
	AIC	3.3	3.25	3.15	3.1	3.3	3.37	3.26	3.05	3.75	4.34
Von Bertalanffy	R^2	0.88	0.91	0.93	0.90	0.93	0.95	0.96	0.98	0.95	0.93
	MSR_e	30.03	30.05	29.43	36.32	31.13	38.23	29.84	24.85	42.49	68.49
	AIC	3.42	3.44	3.42	3.62	3.44	3.65	3.4	3.24	3.78	4.26
Logistic	R^2	0.89	0.93	0.94	0.94	0.4	0.96	0.96	0.98	0.95	0.92
	MSR_e	27.78	24.89	23.75	21.45	29.44	30.44	29.31	24.71	46.77	80.96
	AIC	3.34	3.26	3.25	3.1	3.38	3.42	3.38	3.23	3.88	4.43

Figure 7.7 compares the variance associated with the size at age data and the fitted Gompertz growth curves for the Menai Strait StR, OSR and AdL data. The OSR and AdL data variance is larger than the variance around the statolith data and reflects the greater accuracy of age estimates using statolith rings. Fitted Gompertz growth curves using both the statolith and opercula generated size at age data for each site are shown in Figure 7.8, a) using StR, b) using OSR and c) using AdL. For ease of plotting and clarity of the growth curves the standard error bars have been omitted in the plots. The growth curves fitted to the statolith growth ring data demonstrate that the growth rate of whelks is similar in the Isle of Anglesey Menai Strait and Holyhead populations. The whelks from Jersey were the slowest growing whilst the Shetland whelks reached the largest size. The Nefyn population appeared to grow larger than the other North Wales populations. However the growth curve for this population is based on a small sample compared with the other locations and this population had an unusual size distribution compared to the other populations so that the growth curve for Nefyn may not be representative of the North Wales populations. A similar pattern of site specific growth rates was seen in the OSR and AdL although the shapes of the sigmoidal curves were different.

Growth curves constructed using the OSR displayed a steeper rise than those constructed by either the StR or AdL, with 3 of the curves demonstrating an asymptotic maximum by 6 years of age. This suggests that the distance between the first few rings is wider and that the OSR underestimate the age of each whelk in its early years. Whelks from Jersey had a very slow rate of growth compared to the other populations with the growth rate estimate from the statoliths. None of the plotted growth curves based on the AdL attained their asymptote by the end of the 10 year period. This suggests that the AdL likely overestimate the age of the whelks and underestimate annual shell growth. Figure 7.9a interrogates the growth of the Jersey populations further by investigating their growth from the 3 individual sites and compares this with the combined population statolith ring shell growth data. There are visible differences in the growth curves from the three populations with whelks from JE5 attaining the smallest size of $\approx 60\text{mm}$ whilst those from JE4 reached $\approx 72\text{mm}$ by their 6th year. Whelks at sites JE4 and JD5 display similar growth curves and are geographically closer together than the most distant site JE5 (see Chapter 2, Figure 2.3). Figure 7.9b shows separate growth curves for males, females and a combined growth for the population from the Menai Strait generated from the statolith growth ring data. The differences between males and females is negligible during the first 4-5 years and it is only later that the male whelks appear to attain a greater size than the females, although the difference is only marginal and unlikely to be significant given the variance around

the data. The Menai Strait was chosen to investigate differences in growth between male and female whelks as it had the largest sample size which allowed a comprehensive comparison. A Summary of the calculated growth curve parameters together with the goodness of fit for each model are shown in Table 7.2 for each site for the three growth structures. At every site the Gompertz curves fitted the size at age data generated from the statoliths more closely and with less variability than the OSR and AdL data. The calculated L_0 values also appear to be more realistic using the STR with most sites (excluding JE5 and Nefyn) ranging between 1.2 mm and 5 mm TSL at the time of hatching which is within the range of TSL's observed at emergence from the egg capsules (Chapter 5). In Table 7.3, the calculated L_∞ values are compared to the maximum TSL measured in whelks collected from each site. The data show that for all whelks except those from Holyhead and Nefyn, the statolith growth rings produced L_∞ values that were closest to the maximum specimen TSL within the sample.

7.3.5 Direct comparison of statolith rings and operculum growth lines

The scatter plots shown in Figures 7.10 and 7.11 show the agreement between the statolith and operculum derived ages for each whelk at each site. There is an overall pattern showing that the operculum surface rings underestimate whelk age when compared to the statolith rings and the adventitious layers overestimate whelk age when compared to the statolith rings. This is supported further in summary Table 7.4 which presents the average relationships between the ages from each structure at each site (sum of (StR / operculum derived age) / n). A number >1 indicates an underestimation of age when compared to the statolith rings, values <1 indicate an underestimation of age. All sites except the combined Jersey site show an underestimation of age using the operculum surface rings and an overestimation of age using the adventitious layers.

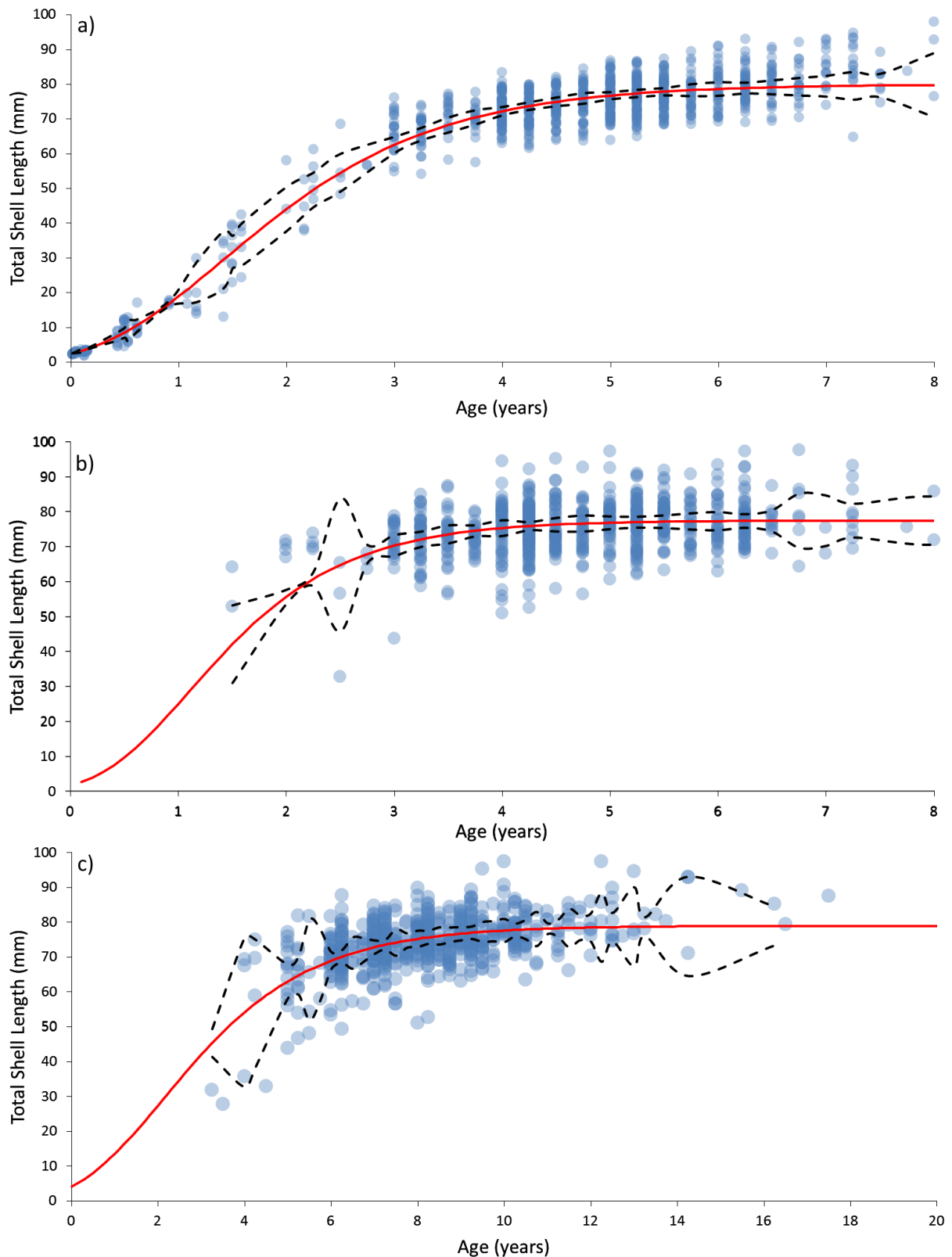


Figure 7.7. Gompertz growth curves for *Buccinum undatum* from the Menai Strait (red lines) for statolith ring data (a), operculum surface rings (b) and adventitious layers (c). Note that the x-axis for graph c) is almost twice the size of a) and b) due to the high age estimations of adventitious layers. Dotted lines represent 95% confidence intervals.

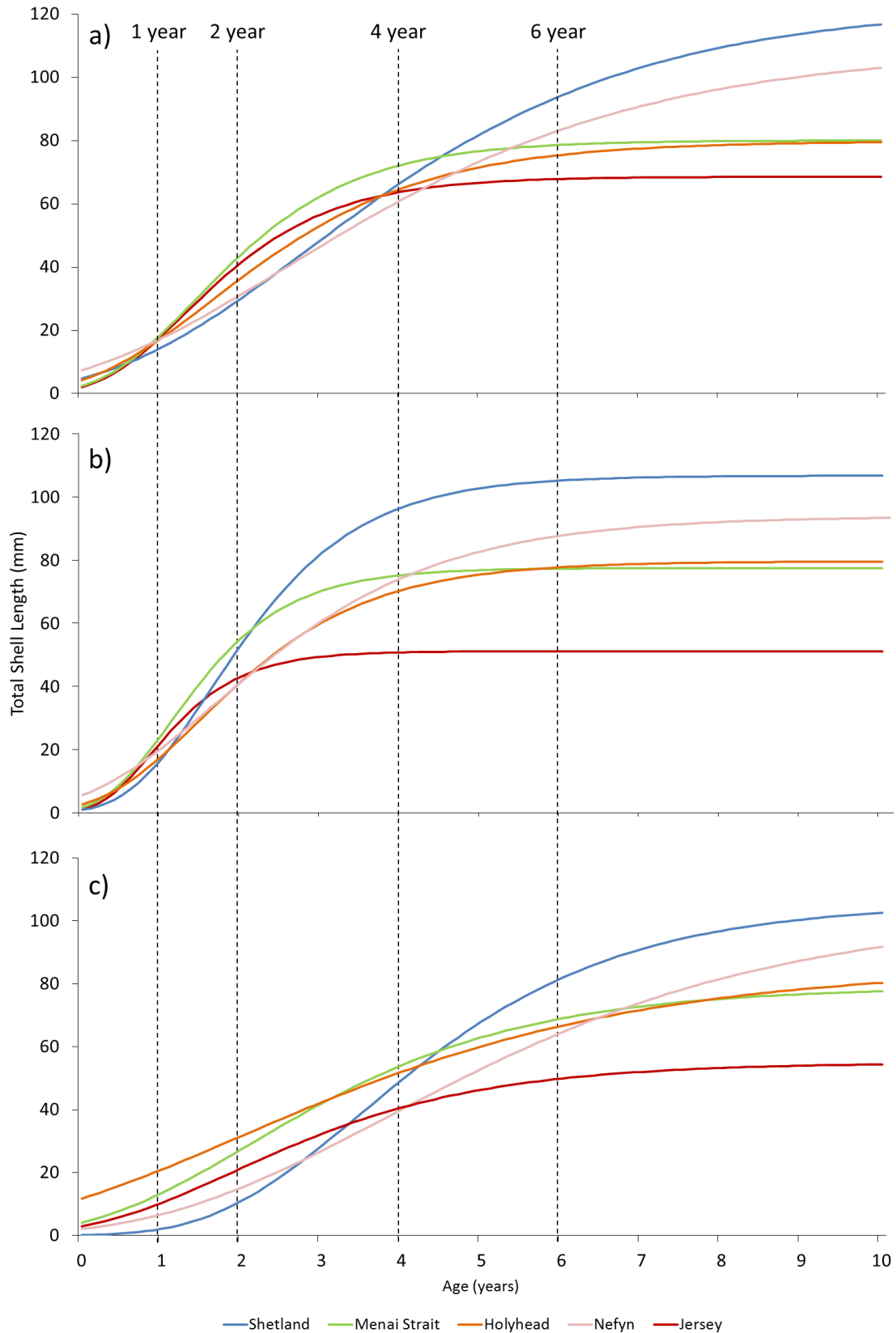


Figure 7.8. Fitted Gompertz growth curves for *Buccinum undatum* from the Shetland Isles (blue lines), the Menai Strait (green lines), Holyhead (orange lines), Nefyn (pink lines) and Jersey (red lines). The data in a) were fitted using data generated from statolith rings, the data in b) were fitted using operculum surface rings and the data in c) were fitted using adventitious layers. Vertical dotted black lines represent 1, 2, 4 and 6 year marks.

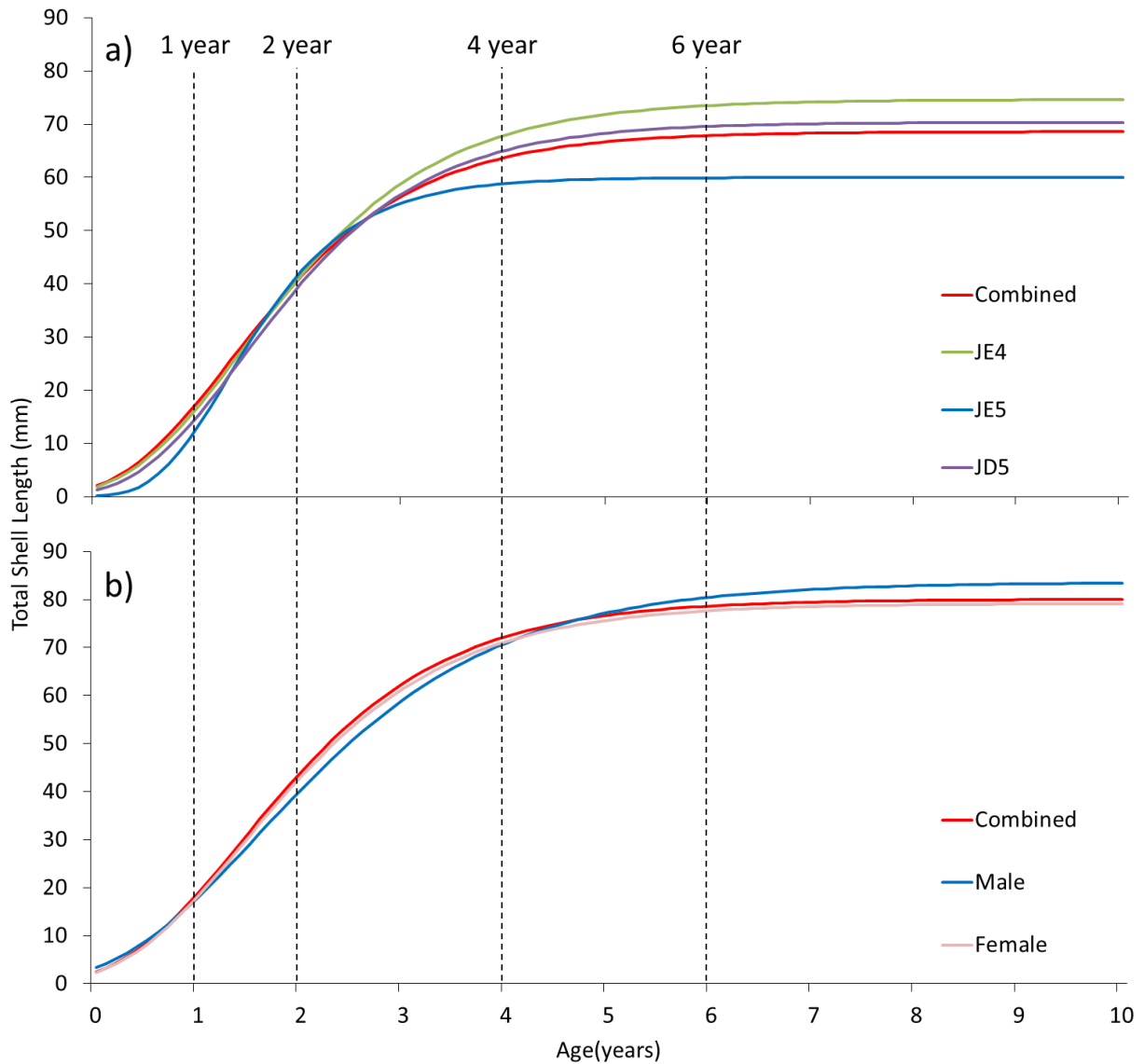


Figure 7.9. a) Fitted Gompertz growth curves for three separate Jersey populations of *Buccinum undatum* (JD5, JE4 and JE5) and combined StR size at age data for Jersey and b) fitted Gompertz growth curves for male and female whelks and combined StR size at age data for the Menai Strait whelks. Vertical dotted black lines represent 1, 2, 4 and 6 year marks.

Table 7.2. Parameter outputs and goodness of fit indicators from Gompertz growth curves fitted to size at age data generated using statolith age data (top table), operculum surface age data (middle table) and adventitious layers (bottom table) for all sites. Bold text indicates the best fitting model at each site.

Statolith Rings										
	Jersey	JD5	JE4	JE5	Menai Strait	Menai Strait female	Menai Strait male	Shetland	Holyhead	Nefyn
L0 (mm)	2.07 ±0.55	1.21 ±0.52	1.88 ±0.53	0.1 ±0.08	2.45 ±0.33	2.35 ±0.29	3.31 ±0.3	4.85 ±0.56	4.29 ±0.87	7.43 ±1.21
L_{∞} (mm)	68.57	70.32	74.59	59.63	80.04	79.14	83.57	122.2	79.77	109.63
K	0.97 ±0.06	0.99 ±0.09	0.92 ±0.07	1.45 ±0.1	0.88 ±0.02	0.87 ±0.02	0.74 ±0.01	0.55 ±0.02	0.66 ±0.04	0.39 ±0.03
R ²	0.89	0.93	0.94	0.94	0.94	0.97	0.97	0.98	0.95	0.93
MSR _e	26.90	24.75	22.31	21.29	27.18	28.88	25.90	20.67	41.04	73.96
n	217	71	64	89	871	398	473	153	89	92
Operculum surface rings										
	Jersey	JD5	JE4	JE5	Menai Strait	Menai Strait female	Menai Strait male	Shetland	Holyhead	Nefyn
L0 (mm)	1.02 ±0.81	0 ±0.03	0.46 ±0.63	0.02 ±0.04	1.66 ±0.41	0.51 ±0.25	1.59 ±0.38	0.9 ±0.59	2.62 ±1.01	5.56 ±1.71
L_{∞} (mm)	51.10	47.15	55.26	50.76	77.45	75.43	79.34	106.71	79.56	93.82
K	1.58 ±0.2	2.17 ±0.48	1.55 ±0.31	1.96 ±0.28	1.22 ±0.05	1.37 ±0.09	1.07 ±0.04	0.97 ±0.08	0.62 ±0.07	0.62 ±0.08
R ²	0.72	0.82	0.81	0.87	0.89	0.94	0.94	0.91	0.92	0.85
MSR _e	69.17	62.97	69.80	48.63	52.50	51.44	44.82	131.14	71.56	140.29
n	244	81	82	81	646	251	395	121	78	90
Adventitious layers										
	Jersey	JD5	JE4	JE5	Menai Strait	Menai Strait female	Menai Strait male	Shetland	Holyhead	Nefyn
L0 (mm)	2.92 ±1.65	2.18 ±1.68	3.29 ±1.55	2.28 ±1.33	4.15 ±0.52	3.33 ±0.45	4.33 ±0.56	0.13 ±0.29	11.74 ±2.24	2.16 ±1.68
L_{∞} (mm)	54.92	47.59	86.00	50.48	78.79	75.38	79.73	105.55	85.46	102.70
K	0.57 ±0.08	0.82 ±0.14	0.36 ±0.07	0.71 ±0.09	0.51 ±0.02	0.66 ±0.04	0.49 ±0.02	0.42 ±0.08	0.35 ±0.07	0.35 ±0.05
R ²	0.71	0.85	0.84	0.90	0.92	0.97	0.95	0.89	0.76	0.88
MSR _e	66.19	57.43	58.97	36.32	40.30	26.60	38.15	122.83	202.72	103.62
n	218	67	82	69	553	245	308	136	89	87

Table 7.3. Summary of the Total Shell Length (TSL) data for each site along with a comparison between the maximum TSL values and the L_{∞} value produced by the Gompertz equation using each of the 3 structures at each site. Bold text indicates the best fit at each site. Maximum differences were calculated by subtracting the maximum Total Shell Length (TSL) measurement at each site from the L_{∞} calculated at each site.

TSL (mm)	Jersey	JD5	JE4	JE5	Shetland
Mean	44.40	43.56	43.17	45.71	92.26
Max.	70.56	66.03	70.56	66.81	115.30
Min.	22.84	27.92	22.84	30.52	44.25
Maximum difference from L_{∞} (statolith rings)	1.99	-4.29	-4.03	7.18	-6.90
Maximum difference from L_{∞} (operculum surface rings)	19.46	18.88	15.30	16.05	8.59
Maximum difference from L_{∞} (adventitious layers)	15.64	18.44	-15.44	16.33	9.75

TSL (mm)	Menai Strait	Menai Strait female	Menai Strait male	Holyhead	Nefyn
Mean	75.05	74.00	75.98	69.95	69.50
Max.	97.87	97.51	97.87	92.46	104.51
Min.	27.82	34.74	27.82	27.87	30.41
Maximum difference from L_{∞} (statolith rings)	17.83	18.37	14.30	12.69	-5.12
Maximum difference from L_{∞} (operculum surface rings)	20.42	22.08	18.53	12.90	10.69
Maximum difference from L_{∞} (adventitious layers)	19.08	22.13	18.14	7.00	1.81

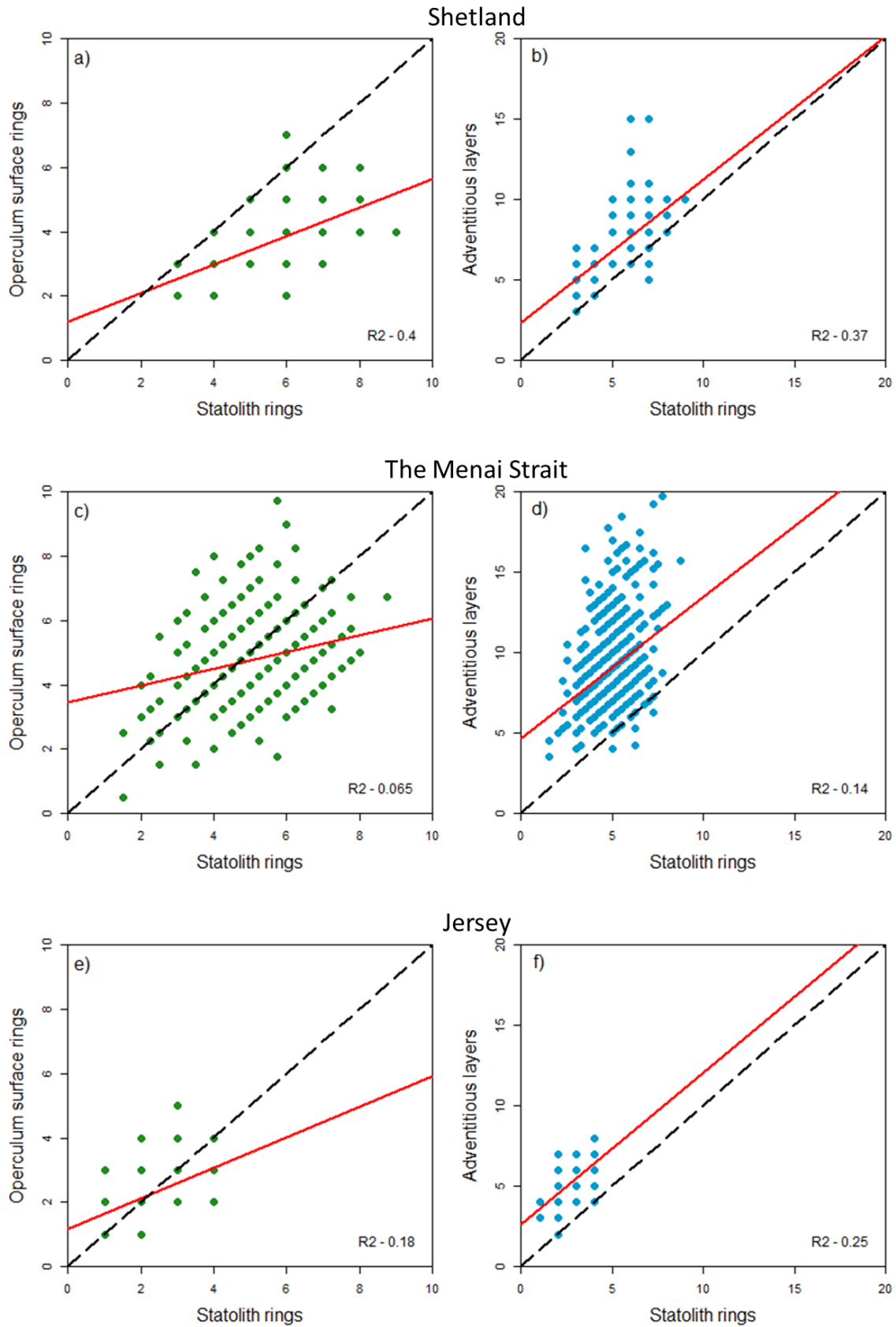


Figure 7.10. Scatter plots of the number of operculum surface rings (a, c, d) and adventitious layers (b, d, f) against the number of statolith rings for individual *Buccinum undatum* from Shetland (a, b), the Menai Strait (c, d) and Jersey (e, f). Red lines represent the fitted linear regression lines to the data. Dotted black lines represent a relationship of 1:1.

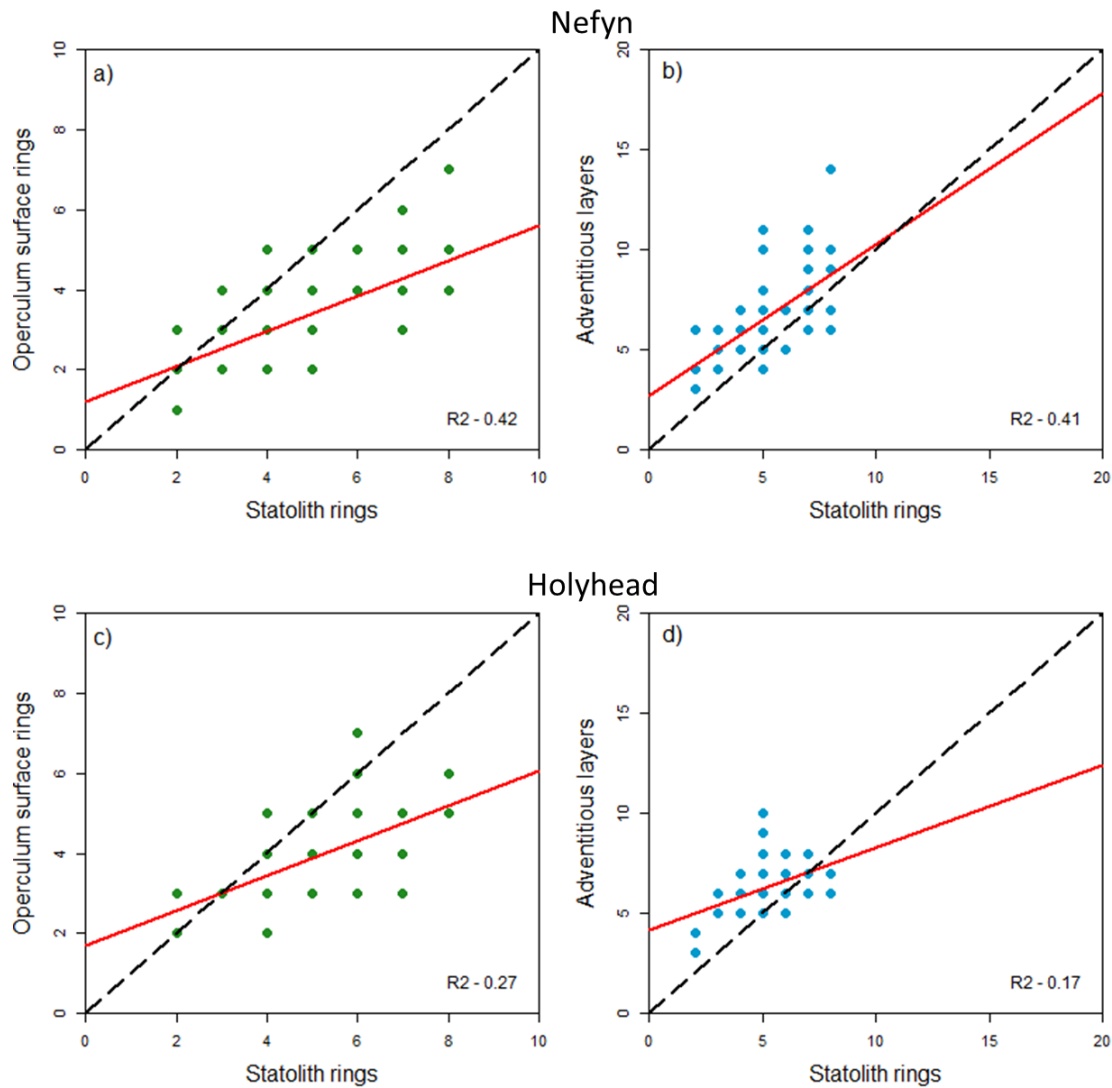


Figure 7.11. Scatter plots of the number of operculum surface rings (a, c) and adventitious layers (b, d) against the number of statolith rings for individual *Buccinum undatum* from Nefyn (a, b) and Holyhead (c, d). Red lines represent the fitted linear regression lines to the data. Dotted black lines represent a relationship of 1:1.

Table 7.4. The average differences between corresponding statolith ring ages and operculum derived ages for each site.

	Adventitious layers	Operculum surface rings
Shetland	1.31	0.66
Menai Strait	1.03	0.54
Jersey	0.89	0.40
Nefyn	1.30	0.68
Holyhead	1.18	0.73

7.4 Discussion

Using a variety of criteria it has been demonstrated that the StR provide a more accurate and reliable estimation of age than either the OSR or AdL.

7.4.1 Clarity of growth rings

The clarity and readability of all 3 sets of growth rings varied between sites, however, the statoliths were the clearest to read at all sites. The statolith growth rings from the juvenile laboratory reared animals were also the clearest when directly compared with the opercula. Two readers were used to assess the number of rings in this part of the research and reliability was only checked at one site, one of the readers (PH) had extensive experience in mollusc ageing techniques whilst the other reader (Devaney Werrin, MMBiol Student), was not versed in statolith ring identification. It is therefore encouraging to find that there was 89.2% agreement between both readers when the statolith rings were counted, however poor, (45.1%), agreement was achieved in counting the operculum surface rings.

In future it is recommended that when statoliths from gastropod populations are investigated, an initial assessment of the accuracy of reading is undertaken routinely so that confidence can be placed around the accuracy of age estimates. The clarity of operculum surface rings from the whelks that were investigated in this study was found to be worse than that in the published literature (41% - 52% readable, Kideys, 1996; Lawler, 2013). Here using the clarity values of '3' and '4', clarity values that were considered to be reasonable to analyse, the reliability ranged between 10 and 40%. In order to provide enough data for constructing growth curves, age estimates from opercula with a clarity of '2' were also included.

7.4.2 Growth modelling

In several previous studies, *B. undatum* growth curves were constructed using OSR ages, modelled growth using the von Bertalanffy equation (e.g. Hancock, 1963; Santarelli & Gros, 1985; Fahy *et al.*, 1995; Kideys, 1996; Shelmerdine *et al.*, 2007; Heude-Berthelin *et al.*, 2011; Lawler, 2013). In this study, it was apparent that the growth of *B. undatum* is sigmoidal and that the von Bertalanffy equation did not fit the growth data as well as the Gompertz growth equation. Using the Gompertz equation resulted in a growth curve with a much better goodness of fit to the data from all the sites except Nefyn. The likely explanation for the difference between previous studies and the current study is a combination of a lack of juvenile whelks

from samples coupled with the poor clarity and inaccurate estimates of age from the operculum growth rings. The lack of juvenile whelks is something that was discussed by Shelmerdine *et al.* (2007), who found no whelks < 3 years of age (i.e. no whelks below 30 mm TSL) for sample sites around Shetland. Lawler, (2013) also had minimum sizes of between 20 mm and 30 mm for most of his sampled sites around England and Heude-Berthelin *et al.* (2011), seemingly had no samples below ≈ 45 mm TSL from west Cotentin, near Jersey. The lack of juvenile (<20 mm) whelks was overcome in the current study by the inclusion of growth data from laboratory reared whelks over the first two years of growth. This adds support to the theory outlined in Chapter 5 about the presence of nursery grounds for *B. undatum* populations.

The poor clarity of the juvenile opercula and definition of the rings was highlighted in this study with only 20% of laboratory reared juveniles displaying the correct age after 2.3 years. During the course of the research it was observed that OSR formed during the first few years of growth from field collected adults were the most difficult to read. It is entirely possible that they may be degraded over time as the operculum is composed of organic material which is exposed throughout the life of the animal. The combination of a lack of juveniles and poor clarity of the early age growth rings on the operculum surface likely masked the characteristic initial bend at the lower end of the sigmoidal Gompertz growth curves. The poor clarity of the early growth rings also likely resulted in a proportion of larger incorrectly aged whelks in the lower size classes (i.e. the first one or two annual rings were not counted because they were not visible). This effect can clearly be seen in the growth curves created by Kideys (1996) who had a TSL range of between ≈ 10 mm and ≈ 55 mm for whelks that he placed in an age class of 0.5 years. The widest variation in a single age class reported by Kideys was seen at year 3 which spanned from ≈ 25 mm to ≈ 120 mm TSL. Although the growth of *B. undatum* does appear to be widely variable within a single population, this finding does seem extreme. The choice of the Gompertz growth equation is in line with several other studies that have found sigmoidal growth and fitted Gompertz growth curves to marine gastropod populations (e.g. Troynikov *et al.*, 1998 - *Haliotis rubra*; Rodriguez *et al.*, 2001 – *Concholepas concholepas*; Chen & Soon, 2002 – *Coralliophila violacea*; Bigatti *et al.*, 2007 - *Odontocymbiola magellanica*; Miranda *et al.*, 2008 – *Neptunea arthritica*).

7.4.3 Growth curve comparisons

The StR derived growth curves were shown to have the best goodness of fit in comparison to the OSR and AdL derived growth curves from all sites. The AdL appear to greatly overestimate the age, something that was also seen in the laboratory reared animals. The OSR derived curves displayed faster rates of growth (K) than StR at all sites (except Holyhead), however the L_{∞} values were lower for all sites. This likely suggests that inaccurately aged whelks are creating an artificial increase in K between one and three years of age for OSR data and this leads into an under-estimation of L_{∞} . The underestimated L_{∞} is likely due to the difficulty in distinguishing between OSRs that are compressed together at the edge of the opercula in older whelks. OSRs are formed from a decrease in the distance between layered organic matter (which forms the growth ring during periods of slow growth), as the growth lines get closer together (through ontogeny) the ability to differentiate between these layers decreases. Alternatively, whilst the growth rings at the edge of statoliths become closer together, they still appear to be discernible in the oldest statoliths as they are not comprised of stacked layers of organic material but significantly are a continuously forming structure. The values of the growth constant K estimated from the adventitious layers are the lowest at all sites, this is due to the overestimation of age resulting in slow rises in the growth curves.

It is of note that the growth curves constructed for whelks from individual sites from Jersey did display some differences indicating that statolith age estimations are sensitive to small differences between geographically close populations. However, the variance surrounding the growth curve estimations would likely mask much of this variance. No clear differences were seen between the growth of male and female whelks from the Menai Strait due to the variance surrounding the Gompertz curves.

Reported values of L_{∞} and K from OSR in the literature are comparable with those calculated during this project. Shelmerdine *et al.*, (2007) calculated values for L_{∞} between 99 mm and 157 mm for sites around Shetland, which is comparable with the L_{∞} values for the Shetland site found in this study (StR – 122.2 mm, OSR – 106.71 mm, AdL – 105.55 mm). The values of K differed from the values of 0.09 and 0.4 day⁻¹ reported by Shelmerdine *et al.*, the StR and AdL estimations were very close to these values (0.42 and 0.55 day⁻¹ respectively) however, the OSR value was much higher (0.97day⁻¹).

7.4.4 Comparison of statolith and operculum ages

Through direct comparison of the statolith ages with the operculum ages taken from the same animals, it appears that the AdL consistently overestimate the age of the animal. For Shetland, the Menai Strait and Jersey, an offset linear relationship is seen when compared to the 1:1 lines plotted. The relationships between the OSRs and StRs appears to change with ontogeny with linear relationships showing underestimation of age in older specimens and overestimation in younger whelks. This could again be linked to the clarity of low age OSRs discussed earlier. With the knowledge of how adventitious layers are formed, it appears that their function is to thicken and strengthen the operculum over time. If so, then it is unlikely that the adventitious layers would have a clear annual pattern and are simply a weak proxy for increased thickening during periods of shell growth. However, in similar species they do appear to show an annual periodicity e.g. *Coralliophila violacea* (Chen & Soon, 2002), *Buccinum isaotakii* (Ilano *et al.*, 2004) and *Neptunea antiqua* (Richardson *et al.*, 2005).

There were minor limitations throughout this project that need to be taken into account when interpreting the age estimation data. Aside from small differences in inter-reader comparison that has already been discussed, the value of adding statolith derived age data to all sample sets and the inclusion of low clarity operculum data should be considered. The addition of TSL data from year 0 and year 1, derived from StR measurements represents a novel way of retrospectively adding crucial size data for often missing size classes. Without these data, the Gompertz nature of the growth curves may have been overlooked. Whilst it is conceivable to undertake this practice for the StR data sets (provided the relationship between statolith diameter and TSL for a particular site is known), in this case the year 0 and year 1 statolith data were also included in operculum derived growth curves. Without it the growth curves for operculum derived ages gave unrealistic estimates of most parameters at all sites (see [Appendix M](#), Table M.1). Therefore to enable a comparison, the juvenile statolith data were included in the operculum analyses. Likewise, the '2' clarity opercula were also included in the analyses due to the extremely low sample numbers at several sites following their removal and again for the sake of comparison they were included in the analysis (data without the '2' clarity opercula in [Appendix M](#), Table M.2). In short, the analysis of the opercula from several sites would not have been possible without the use of statolith derived size at age data and the inclusion of low-clarity operculum specimens. This is more evidence in the preferential use of statoliths in age determination of *B. undatum*. One drawback to the use of statoliths in comparison to opercula

is the time taken to extract and process the specimens. It takes on average 5 minutes to extract and mount a single statolith with practice, this time is significantly less with the use of opercula (possibly 1-2 minutes per specimen). However, some or all of this is negated because the failure rate of reading opercula is considerably higher. The clear advantages to the use of statoliths described here undoubtedly outweigh the collection and processing time needed for their use. Additionally, it is also likely that the subsequent analysis and interpretation of statolith growth rings will be faster.

One issue with the sites from Jersey also needs to be addressed. Many statoliths from all of the three sample sites displayed extra weaker growth rings between the annual growth lines (see Figure 7.12).

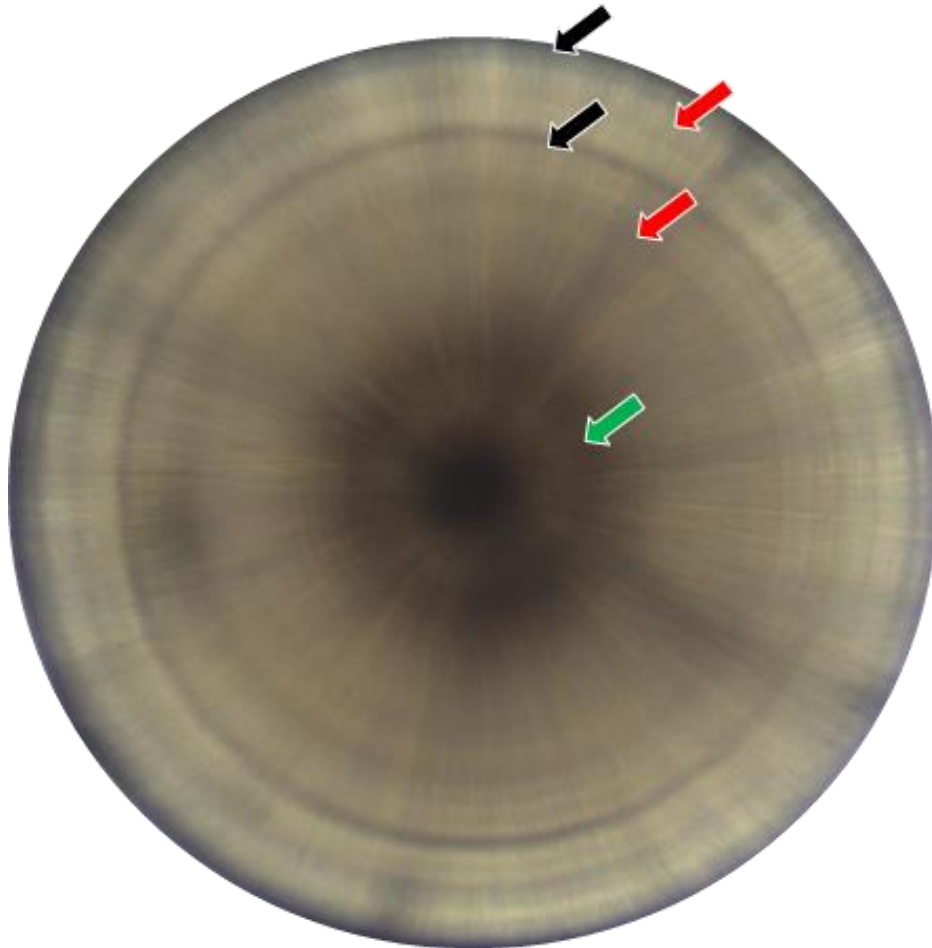


Figure 7.12. A *Buccinum undatum* statolith from a 2 year old male specimen from JD5. The hatching and annual growth rings are clearly visible (green and black arrows respectively). The weaker mid-annual lines are shown with red arrows.

The initial inclusion of these extra weak growth rings in age estimations led to an overestimation of the age resulting in values for size at age roughly half of those observed in the Menai Strait

population. As the SST ranges at these two sites are similar, this finding was a clear anomaly that led to further investigation of the weaker growth rings. With practice it is simple to discount these extra lines, which often do not remain clearly visible as disturbance lines around the whole circumference of the statolith (Figure 7.12). Their formation is likely due to a slowing of growth during the summer maximum temperatures at this site. The extra lines were more of an issue in samples from Jersey (JD5) that were collected from a shallower depth (and therefore were potentially more susceptible to seawater temperature changes) than statoliths from whelks from the other two sites in Jersey (JD5 – 7 m, JE4 – 14 m, JE5 – 13 m). This adds more support to the theory that *B. undatum* has an optimum growth temperature range, discussed earlier in Chapter 4, and that whelks in Jersey may experience deviations from both the temperature minima and maxima during the annual cycle. This issue raises the importance of understanding the environmental setting of locations from which whelk samples are collected to better aid in the interpretation of their statolith rings.

In conclusion, the statoliths of *B. undatum* provide a more reliable method of age estimation than the currently used operculum surface rings. The statolith rings are superior in both their clarity and the variability of the resulting growth curves. The growth of *B. undatum* was shown for the first time to follow a sigmoidal development that is most accurately modelled using a Gompertz growth function. With further refinement and observation the statolith ageing techniques presented here hold great promise for improving the feasibility of stock and population structure assessments for the currently difficult to assess yet commercially important *B. undatum* populations around the U.K and from European waters.

7.5 References

- Akaike H (1973) Information theory and an extension of the maximum likelihood principle. In: Petrov BN, Csáki F (eds.) 2nd International Symposium on Information Theory, Tsahkadsor, Armenia, USSR, September 2-8, 1971, Budapest: Akadémiai Kiadó
- Beamish RJ (1990) The importance of accurate ages in fisheries sciences. In: Hancock DA (ed.) The Measurement of Age and Growth in Fish and Shellfish. Proceedings No. 12. Bureau of Rural Resources, Canberra, Australia
- Bertalanffy V L (1938) A quantitative theory of organic growth. Hum Biol 10(2):181-213
- Bigatti G, Penchaszadeh PE, Cledón M (2007) Age and growth in *Odontocymbiola magellanica* (Gastropoda: Volutidae) from Golfo Nuevo, Patagonia, Argentina. Mar Biol 150:1199-1204
- Checa AG and Jiménez-Jiménez AP (1998) Constructional Morphology, Origin, and Evolution of the Gastropod Operculum. Paleobiology 24(1):109-132
- Chen MH, Soong K (2002) Estimation of age in the sex-changing, coral-inhabiting snail *Coralliophila violacea* from the growth striae on the opercula and a mark-recapture experiment. Mar Biol 140:337-42
- Day RW, Fleming AE (1992) The determinants and measurement of abalone growth. pp. 141-168. In: Shepherd SA, Tegner MJ, Guzman del Praso SA (eds.) Abalone of the World: Biology, Fisheries, and Culture. Fishing News Books, Oxford, UK
- Fahy E, Yalloway G and Gleeson P (1995) Appraisal of the whelk *Buccinum undatum* fishery of the Southern Irish Sea with proposals for a management strategy. Ir Fish Invest Ser B 42
- Gompertz B (1825) On the Nature of the Function Expressive of the Law of Human Mortality, and on a New Method of Determining the Value of Life Contingencies. Phil Trans Roy Soc 115:513-585
- Gros P, Santarelli L (1986) Methode d'estimation de la surface de pêche d'un casier á l'aide d'une filiere experimentale. Oceanologica Acta 9:81-87
- Hancock DA (1963) Marking experiments with the commercial whelk (*Buccinum undatum*). ICNAF Spec Publ 4:176-187
- Heude-Berthelin C, Hégron-Macé L, Legrand V, Jouaux A, Adeline B, Mathieu M, Kellner K (2011) Growth and reproduction of the common whelk *Buccinum undatum* in west Cotentin (Channel), France. Aquat living resour 24:317–327
- Hilborn R, Walters CJ (1992) Quantitative fisheries stock assessment: choices, dynamics and uncertainty. Chapman and Hall, New York
- Himmelman JH (1988) Movement of whelks (*Buccinum undatum*) towards a baited trap. Mar Biol 97: 521-531
- Ilano AS, Fujinaga K and Nakao SJ (2004) Reproductive cycle and size at sexual maturity of the commercial whelk *Buccinum isaotakii* in Funka Bay, Hokkaido, Japan. J Mar Biol Assoc UK 83:1287–1294
- Jacklin, M (1998) Exploratory fishing trials for *Buccinum undatum* around the islands of Barra and South Uist in the Western Isles. SEAFISH consultancy report

- Kideys AE (1996) Determination of age and growth of *Buccinum undatum* L. (Gastropoda) off Douglas, Isle of Man. *Helgolaender Meeresun* 50, 353–368
- Laptikhovsky V, Barrett C, Firmin C, Hollyman P, Lawler A, Masefield R, McIntyre R, Palmer D, Soeffker M, Parker-Humphreys M (2016) A novel approach for estimation of the natural mortality of the common whelk, *Buccinum undatum* (L.) and role of hermit crabs in its shell turnover. *Fish Res* 183:146-154
- Lawler A (2013) Determination of the size of maturity of the whelk *Buccinum undatum* in English waters – Defra Project MF0231
- McQuinn IH, Gendron L, Himmelman JH (1988) Area of attraction and effective area fished by a whelk (*Buccinum undatum*) trap under variable conditions. *Can J Fish Aquat Sc.* 45:2054-2060
- Miranda RM, Fujinaga K, Nakao S (2008) Age and growth of *Neptunea arthritica* estimated from growth marks in the operculum. *Mar Biol Res* 4:224-235
- Morel GM and Bossy SF (2004) Assessment of the whelk (*Buccinum undatum* L.) population around the Island of Jersey, Channel Isles. *Fish Res* 68:283-291
- Moureaux J (1987) Mathematical and biological expressions of growth in fishes: Recent trends and further developments. In: Summerfelt RC, Hall GE (eds.), *The age and growth of fish*. Iowa State University Press, Iowa: 81–113
- Nasution S, Roberts D, Farnsworth K, Parker GA, Elwood RW (2010) Maternal effects on offspring size and packaging constraints in the whelk. *J Zool* 281:112-117
- Prager MH, Saila SB, Recksiek CW (1994) Fishparm: A microcomputer program for parameter estimation of non-linear Models in fishery science. *Univ Ocean Tech Rep* 1:87–90
- Przybylski M, García-Berthou E (2004) Age and growth of European bitterling (*Rhodeus sericeus*) in the Wieprz-Krzna Canal, Poland. *Ecohydrol Hydrobiol* 4(2):207–213
- Richardson CA, Saurel C, Barroso CM and Thain J (2005) Evaluation of the age of the red whelk *Neptunea antiqua* using statoliths, opercula and element ratios in the shell. *J Exp Mar Biol Ecol* 325: 55–64
- Rodriguez L, Daneri G, Torres C, Leo'n M, Bravo L (2001) Modeling the growth of the Chilean loco, *Concholepas concholepas* (Bruguere, 1789) using a modified Gompertz-type function. *J Shellfish Res* 20:309–315
- Rodriguez-Sánchez V, Encina L, Rodríguez-Ruiz A, Sánchez-Carmona (2009) Largemouth bass, *Micropterus salmoides*, growth and reproduction in Primera de Palos' lake (Huelva, Spain). *Folia Zool* 58(4):436-446
- Santarelli L, Gros P (1985) Age and growth of the whelk *Buccinum undatum* L. (Gastropoda: Prosobranchia) using stable isotopes of the shell and operculum striae. *Oceanol Acta* 8:221–229
- Shelmerdine RL, Adamson J, Laurenson CH, Leslie B (2007) Size variation of the common whelk, *Buccinum undatum*, over large and small spatial scales: Potential implications for micro-management within the fishery. *Fish Res* 86:201-206
- Smith KE, Thatje S (2013) Nurse egg consumption and intracapsular development in the common whelk *Buccinum undatum* (Linnaeus 1758). *Helgoland Mar Res* 67:109-120.

- Troynikov VS, Day RW, Leorke AM (1998) Estimation of seasonal growth parameters using a stochastic Gompertz model for tagging data. *J Shellfish Res* 17(3):833-838
- Valentinsson D, Sjödin F, Jonsson PR, Nilsson P, Wheatley C (1999) Appraisal of the potential for a future fishery on whelks (*Buccinum undatum*) in Swedish waters: CPUE and biological aspects. *Fish Res* 42:215–227
- Vasconcelos P, Gharsallah IH, Moura P, Zamouri-Langar L, Gaamour A and Missaoui H (2012) Appraisal of the usefulness of operculum growth marks for ageing *Hexaplex trunculus* (Gastropoda: Muricidae): Comparison between surface striae and adventitious layers. *Mar Biol Res* 8:141-53
- Verhulst PF (1838) Notice sur la loi que la population suit dans son accroissement. *Corr Math Physics* 10:113
- Vovelle J (1967) Sur l'opercule de *Gibbula magus* L. gastéropode Prosobranch: édification, nature protéique et durcissement par tannage quinonique. *C R Acad Sci* 264:141-144
- Windsor CP (1932) The Gompertz curve as a growth curve. *P Natl Acad Sci* 18(1):1-8

Chapter 8:

General discussion

Throughout the six experimental chapters presented in this thesis I have detailed a broad range of findings that relate to the overarching title ‘Age, growth and reproductive assessment of the whelk, *Buccinum undatum*, in coastal shelf seas’. Whilst all of these findings have their own significance within their respective fields, many of them have wider implications and are of direct relevance for the management of commercial whelk fisheries and understanding shell growth. Figure 8.1 shows a diagrammatical representation of how each chapter is related to the three main overarching themes: age determination, growth and reproductive assessment. An overview of the main findings from each chapter will now be presented. This will then be followed by a synthesis of the results within the context of three main themes.

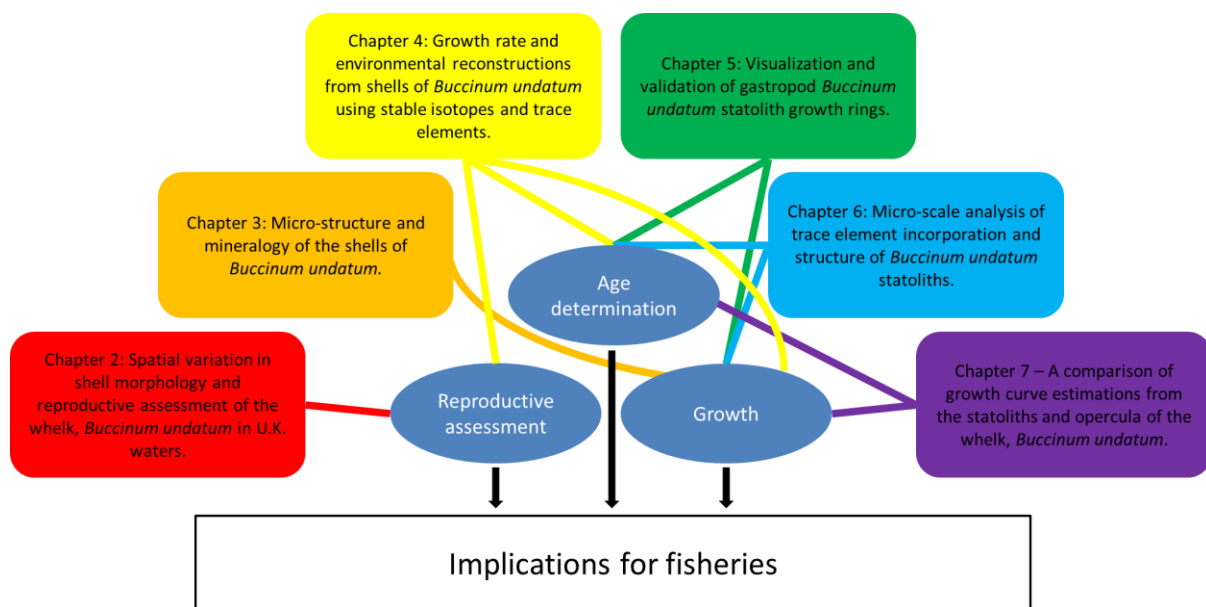


Figure 8.1. A flow chart highlighting the connection of each chapter to the three main themes of the thesis.

8.1 Overview and integration of findings

8.1.1 Chapter 2 - Spatial variation in shell morphology and reproductive assessment of the whelk, *Buccinum undatum* in U.K. waters

In Chapter 2 I investigated spatial differences in the reproductive and morphological characteristics of *B. undatum* populations from various locations around the U.K. The size at maturity of *B. undatum* is an important metric for fisheries scientists to determine, as it has clear implications relating to the sustainability of a fishery such as allowing fisheries scientists to determine catch limits and minimum landing sizes, depending on the size at maturity of the

population. This has been the focus of several recent papers (e.g. Heude-Berthelin *et al.*, 2011; Haig *et al.*, 2015; McIntyre *et al.*, 2015). A comprehensive review of non-dissective methods for estimating size at maturity was achieved during this study as the non-dissective methods are far more time-effective than dissection based (e.g. Martel *et al.*, 1986) or histology based assessments (e.g. Heude-Berthelin *et al.*, 2011). The visual inspection of the digestive gland for percentage volume of gonad tissues resulted in the simplest method that could be applied to *B. undatum* from all sites and sexes equally. An improved version of the Gonado-Somatic Index (GSI) was developed by incorporating gonad volume measurements to create a new metric called the adjusted GSI (aGSI). The aGSI measurements resulted in a more accurate representation of the reproductive cycle over an 18 month period in whelks collected from the Menai Strait than the standard GSI. A peak in gonad development was found in September for both sexes at around the same time as the suspected copulation period. This is the first occasion that the timings of the reproductive cycle of *B. undatum* have been described in whelks from the Menai Strait. Without adjusting the GSI, the peak in gonad development was estimated to occur around 3 months earlier, seemingly unrelated to any reproductive event. This raises the question of the accuracy of the standard GSI method used in earlier studies of whelk reproduction. This may be due to the inclusion of the digestive gland weight (which likely varies in weight seasonally) being incorporated into the standard GSI calculation.

The calculations of L_{50} obtained using visual gonad inspection produced results similar to the published literature for several of the samples sites, however some overestimated L_{50} in comparison to the literature (e.g. Jersey – Heude-Berthelin *et al.*, 2011). A clear annual cyclicity in L_{50} was found over an 18 month period in the Menai Strait. Therefore a recommendation from this study is that, for the most conservative assessment of L_{50} , whelk samples should be collected in the spring when the L_{50} estimates for female whelks in the Menai Strait are markedly smaller than during the rest of the year. However, this is likely tied to the reproductive cycle and may change depending on location. Several calculations of male maturity using penis length, a metric that has been used previously (e.g. Santarelli, 1985; Gendron, 1992; Haig *et al.*, 2015; McIntyre *et al.*, 2015), were investigated. All three trialled methods (P_{50} , 50%PL and inflection point) produced similar sizes at maturity to the visual gonad inspection data. However, certain methods proved to be more accurate for specific sites with size at maturity values close to those calculated using visual gonad inspections. One of the main drawbacks of using penis length as opposed to visual gonad inspection is that only male maturity can be determined. Males were also shown to develop to larger sizes than females at all sites, further

complicating the picture of size and maturity. It is recommended that for any future assessments of maturity, a combination of visual inspection and aGSI should be used to assess the timing of reproduction and L_{50} .

There were several months where there was a clear bias towards male specimens as witnessed from the monthly whelk catches from the Menai Strait (October and November especially during the approximate period of egg laying). It is likely that any heavy fishing pressure during this period will bias the fishing related mortality towards males within this population.

In chapter 2 I also investigated whether there were any differences in shell morphology of whelks collected from different sites. Clear drivers in the statistical differences between the sites were found to be Total Shell Length (TSL), Minimum Shell Width (MinSW), aperture shape and the angle of the spire. The relationships of TSL and shell weight also varied between sites. There were differences between males and females within a single site relating to the shape of the aperture. It is hypothesised that this is due to the extra room required to house the penis within the shell. This finding has also been reported in previous studies (Gendron, 1992; Kenchington & Glass, 1998). Several other clear differences between the shell dimensions were observed over the course of the project such as highly variable pigmentation of the inner shell layers. As this was difficult to quantify, it was not investigated in depth. It is unclear whether these morphological differences are due to environmental or genetic factors, future work could address this question with transplant experiments growing juvenile whelks from different populations under set environmental regimes.

8.1.2 Chapter 3 - Micro-structure and mineralogy of the shells of *Buccinum undatum*

The findings presented in Chapter 3 revealed that the overall structure of *B. undatum* shells are the same at all studied sites (Jersey, the Menai Strait and Shetland). A four layer structure was demonstrated with clear crystalline differences shown using optical and Scanning Electron Microscopy (SEM). Using Micro-Raman Spectroscopy all four of these layers were found to be composed of aragonite although some compositional differences were found. Some of these differences were shown to originate from the pigments within the shell layers (Hedegaard *et al.*, 2006), other differences found in the higher wavelength regions of the Raman spectra are assumed to be due to differences in organic matter content (Socrates, 2002). Organic matrixes are used in mollusc shells to determine many aspects of the shell micro-structure such as the shape of crystal growth, the initial nucleation and placement/alignment of crystals (Weiner &

Traub, 1980; Mann *et al.*, 1989; Addadi & Weiner, 1997; Levi-Kalisman *et al.*, 2001). With the vastly different observed crystal structures it is highly likely that the organic matter differences found within the Raman spectra are due to the different organic matrix structures, required for the mineralisation of the differing crystal formations.

Several 'parasitic' species were found to contribute to the weakening of the shells at different sites, such as suspected fungal or micro-algal infestations in shells from Shetland and boring sponge infestations in shells from Jersey. The presence of these species may affect the crystal structural analyses and the geochemistry of the shell so examination of the shell structure prior to analyses is a priority to avoid skewing and misinterpretation of results.

Shell damage and repair were shown to thicken the shell structure in experimentally damaged animals, confirming the theory of Thomas & Himmelman (1988) who suspected that increased damage incidences increased the thickness and weight of the shells. This suggests that damage incidences (derived from predatory attacks and mobile fishing gear) may be a driving factor of shell weight differences between sites found in Chapter 2.

8.1.3 Chapter 4 - Growth rate and environmental reconstructions from shells of *Buccinum undatum* using stable isotopes and trace elements

Once the structure and composition of the *B. undatum* shells had been established, Chapter 4 investigated the usefulness of *B. undatum* shells as environmental proxies using geochemical analyses (Isotope Ratio Mass Spectrometry, IRMS for stable isotope analysis and solution Inductively Coupled Plasma Mass Spectrometry (solution ICP-MS) for trace element analysis). The oxygen isotope ($\delta^{18}\text{O}$) profiles provided by far the clearest environmental proxy as they closely reflected changes in seawater temperature. Importantly, a species specific palaeotemperature equation was calculated using laboratory reared specimens of *B. undatum* to allow the conversion of $\delta^{18}\text{O}$ values to seawater temperatures. This equation then allowed the retrospective calculation of seawater temperatures from field collected *B. undatum* specimens from three separate sites (Jersey, the Menai Strait and Shetland). The accuracy of the reconstructed temperature profiles was high for the Menai Strait and Jersey but lower in Shetland. The reason for this could have been due to several factors but was likely due to differences between the observed SST from the available logger data and the deeper depths of 18-20 and the *in-situ* temperatures calculated from the shells from the whelk habitat. The ability to accurately reconstruct seawater temperatures from *B. undatum* shells could greatly aid

archaeologists who regularly find *B. undatum* shells in shell middens and shell deposits during palaeoecological studies.

None of the investigated trace element profiles had any consistent patterns between sites and often within single sites the patterns were liable to vary. This clearly highlights the problems with the use of trace element proxies within mollusc carbonates. It was concluded that strong physiological (vital) effects were controlling the incorporation of every studied element to varying extents. Profiles of strontium (Sr) showed the most promise within specimens from the Menai Strait displaying an inverse relationship to SST. However, even though this was the clearest pattern found, this still varied between male and female specimens, with females showing a significant disassociation of Sr/Ca and $\delta^{18}\text{O}$ profiles around the time that sexual maturity was reached. Uranium also displayed the same disassociation patterns in the female specimens suggesting a similar physiological control over its incorporation. Whilst the concentrations of most elements were comparable between the three studied sites, sodium (Na) was shown to vary dramatically. Samples from Shetland had up to 62% higher concentrations of Na within their shells than in the other shells. The pattern of Na incorporation, which was positively correlated in specimens from Jersey and the Menai Strait, was reversed in shells from Shetland. This highlights the inter-site differences in incorporation patterns. It is advised that future studies should avoid trace element profiles within *B. undatum* shells for use as environmental proxies due to their variability. However, the controls and sources of this variability present an exciting area for future research into trace element incorporation in mollusc carbonates as *B. undatum* are easy to rear and maintain within the laboratory and are fast growing.

The $\delta^{18}\text{O}$ profiles from the shell carbonate samples not only allowed the reconstruction of seawater temperature but also enabled the assignment of accurate ages to individual animals and subsequently the analysis of growth rates at different sites. The growth rates varied significantly between sites, with the Menai Strait and Shetland showing faster growth than Jersey where the whelks are likely at their most southerly distribution. Seasonal growth also varied between sites, with samples from Jersey showing more growth between the summer maximum temperature and the winter minimum whilst samples from Shetland showed the majority of their growth was completed between the winter minimum and the summer maximum. It is concluded that these growth differences are likely due to the existence of an

optimum growth temperature with a maximum somewhere below the Jersey maximum temperature.

8.1.4 Chapter 5 - Visualisation and validation of gastropod *Buccinum undatum* statolith growth rings.

The results presented in Chapter 5 outlined an introduction to the use of statoliths, from the most effective methods of extraction, to the best way to visualise growth rings and highlighted problems with statolith use such as the interpretation of 'disturbance' rings. The use of whole, unground resin mounted statoliths was found to be the most effective method for growth line visualisation, as well as minimising sample preparation time. The statoliths themselves were found to have a strong size relationship with the TSL of the animals from which they were extracted. The most important outcome from this chapter was the initial validation of the annual periodicity of statolith growth ring formation. This was achieved by monitoring statolith ring formation in two cohorts of laboratory reared *B. undatum* of known provenance over a period of 2 years. The results from this validation have clear fisheries implications as this is the first step to the full validation of statolith ring formation and the implementation of their use as a fishery monitoring tool.

8.1.5 Chapter 6 - Micro-scale analysis of trace element incorporation and structure of *Buccinum undatum* statoliths.

Chapter 6 took the validation of growth ring periodicity even further through the use of cutting edge analytical techniques such as Secondary Ion Mass Spectrometry (SIMS) and transmission micro-X-Ray Diffraction (μ -XRD) to investigate the structure and chemical composition of statoliths at a micron-scale. Clear cycles in trace elements (magnesium - Mg and sodium - Na) were found within visible annual growth rings of statoliths from 3 wild populations (Jersey, the Menai Strait and Shetland). The annual periodicity of the trace element (and therefore growth line) formation was further constrained with the analysis of 1 and 2 year old laboratory reared specimens which contained 1 and 2 trace element cycles and growth rings respectively. It was also noted that the annual Mg and Na cycles were not affected by the visible 'disturbance' growth rings that have been demonstrated and discussed in Chapter 5. All of the elements within the statoliths were shown to be under some kind of physiological control. Strontium was shown to display clear ontogenic increases whereas Mg displayed increased concentrations in the first year of growth. Magnesium also displayed a decreasing pattern of incorporation in

whelk statoliths from the warmest sampled site (Jersey) to the coldest site (Shetland). This finding supports the theory that the Mg cycles between the growth rings are annual and reflect a temperature cycle with the minima matching the visible growth rings. Although indications of physiological control were found for trace element incorporation, the patterns displayed by the trace elements (i.e. their relationships to one another and coincidence with the growth rings) were comparable between all sites. This coupled with the clear differences in the concentrations of the sampled elements between the shells and the statoliths at each site led to the conclusion that there is a disconnect between the mineralisation sites of the shells and statoliths. This is likely due to the increase in the number of biological membranes permeated by the seawater source to reach the statocyst and possibly the source of the elements themselves, i.e. to the statoliths via the diet and haemolymph rather than transport across the mantle epithelium to the mineralising shell.

The composition of the statoliths was shown to be wholly aragonite at a 2 μm resolution (using $\mu\text{-XRD}$), discounting any effect of CaCO_3 polymorph changes on trace element incorporation. A combination of techniques (SEM, Micro-Raman Spectroscopy and $\mu\text{-XRD}$) uncovered the crystalline structure of the statoliths in which the crystals radiated towards the central nucleus in a hourglass shape, giving an indication of how these structures form over time. It was also highlighted that they contained organic matter, likely indicating that an organic matrix is incorporated in the statolith structure which is used to control deposition, much like the shells of molluscs.

Following the chemical validation of the statolith growth rings, the shells analysed in Chapter 4 were compared with their matching statoliths which were analysed in Chapter 6. Clear agreements were seen between the number of statolith rings, the number of statolith Mg cycles and number of annual shell $\delta^{18}\text{O}$ cycles. This was a final comparative analysis to conclusively confirm the annual formation of statolith growth rings. The operculum growth rings of the animals analysed in Chapter 4 were also compared to the number of shell $\delta^{18}\text{O}$ cycles and showed much poorer matches.

8.1.6 Chapter 7 - A comparison of growth curve estimations from the statoliths and opercula of the whelk *Buccinum undatum*.

Once the annual periodicity of statolith growth rings had been validated using laboratory rearing experiments (Chapter 5) and chemical analyses (Chapter 6) their usefulness as a fishery

monitoring tool was investigated in Chapter 7. Statoliths were compared to the existing age determination tool for *B. undatum* i.e. the operculum (Santarelli & Gros, 1985). Both sets of growth lines found on the operculum (operculum surface rings (OSR) and adventitious layers (AdL)) were compared to statolith rings to determine which was the best structure to use overall. This demonstrated that the statolith rings displayed far superior clarity to both sets of the operculum rings and produced far less variability and a better fit for the growth curves. The best fitting growth curves were created using the Gompertz growth equation and this study is the first example of this growth equation being used for *B. undatum* populations. It is likely that earlier studies mistakenly preferred to use the von Bertalanffy growth equation (e.g. Heude-Berthelin *et al.*, 2011; Lawler, 2013) as they were missing important juvenile size classes from their samples; thus highlighting the need for carefully constructed study protocols to minimise bias. It appeared that the OSRs overestimated the earlier year classes causing a fast initial growth rate and underestimated subsequent year classes, leading to an underestimated L_{∞} . The AdLs greatly overestimated the age of the animals leading to similar values of L_{∞} seen using statolith growth rings but much lower estimates of growth rate as the specimens reached L_{∞} at a much larger estimated age. Whilst juvenile size classes were missing from many populations in this study, the use of validated statolith growth rings allowed the estimation of size at age for year 0 and year 1 juveniles from all populations. It was these retrospectively calculated sizes at ages 0 and 1 that constrained the lower estimates of the growth curves to produce the best population growth estimates.

8.2 Synthesis of Findings

The three major themes running throughout this project were related directly to the initial thesis title: reproductive assessment; growth and age. Each one will now be discussed with wider implications for fisheries research.

8.2.1 Reproductive assessment

Several aspects of the reproductive cycle of *B. undatum* have been investigated throughout the course of this PhD, the majority of these were undertaken in Chapter 2 and related to the estimation of reproductive timings and key maturity assessment tools. This resulted in the development of a set of suggestions for future research that will hopefully reduce the time and

cost of maturity assessments whilst producing accurate and reliable estimates of L_{50} and reproductive cycle timings. Patterns of trace element incorporation were also found in Chapter 4 that likely highlight a reproductive cycle based control on elemental incorporation within the shells of female *B. undatum*. There were several findings of the maturity studies that are of direct relevance to fisheries scientists, aside from the suggested use of visual gonad inspection and aGSI for population assessments. Firstly, there was a clear seasonal bias in the sex ratio of field collected whelks. This could have large impacts on population structure if heavy fishing pressure is applied during the egg laying season when the females are largely absent from the catch. This should be taken into consideration should any seasonal fishery closures be suggested as a potential management strategy. The most pertinent finding of the maturity assessments was that none of the sample sites were properly protected by their regional Minimum Landing Size (MLS). This raises grave concerns about the sustainability and genetic health of whelk populations if a large proportion of the population do not make it to the first mating season. This is a concern that has been raised by several previous studies (e.g. Haig *et al.*, 2015; McIntyre *et al.*, 2015) although the only available solutions consist of an increase of the MLS across the UK or on a region by region basis. A generic increase in MLS would likely be unpopular; many populations with generally smaller size structures and later maturity will instantly become financially untenable as insufficient legally sized whelks will be landed. This would cause disruption for many fishermen who will be disproportionately discriminated against based on the population structure of their fished populations. Regional increases in MLS based on local population structures would in theory result in the most sustainable fisheries, both financially and ecologically. However, the realities of individually assessing each population to set MLS and catch limits presents a huge financial and temporal undertaking which is unlikely to be authorised for relatively low value shellfish stocks. It is also unlikely that regional differences in MLS could be effectively enforced by fishery monitoring agencies on a population by population basis.

8.2.2 Growth

Many aspects of the growth of *B. undatum* have been investigated during this PhD, which fall into three clear categories. The morphological differences observed between populations (Chapter 2), the growth and structure of the shells and statoliths (Chapters 3 and 5) and the analysis of individual and population growth rates (Chapters 4 and 7).

The morphological differences between sites represent the possibility that either environmental or genetic drivers are causing population level variation in shell morphology. Within the context of fisheries regulations, differences in the relationship between TSL and MinSW between populations represents a worrying finding as this relationship is used to set riddle bar spacings based on the MLS, as the MinSW is the narrowest part of the shell. With this finding it must be stressed that the relationship between these two measurements must be accurately established on a regional basis before riddle spacing byelaws are established by local fishery authorities.

Whilst the growth and structure of the shells and statoliths have been discussed in detail down to the composition and crystal structure, there are several findings of the structural studies that have a wider application. The mechanisms of damage repair outlined in Chapter 3, indicate that a thickening of the shell takes place underneath remaining areas of shell following a damage incidence, which is expected to increase the weight of the shells. Damage of *B. undatum* shells is thought to occur through two main mechanisms, failed predator attacks and mobile fishing gear damage (Thomas & Himmelman, 1988; Mensink *et al.*, 2000). This means that the differences in shell weight seen between sites seen in Chapter 2 may in fact be an indication of predator abundance or bottom trawling intensity rather than genetic differences in shell growth. In future studies of *B. undatum* it is suggested that an accurate damage index is developed to allow the quantifiable comparison of population shell damage between sites. In juvenile *B. undatum* shells, damage incidences have been shown to be repaired at rapid rates (Colvin, 2015), making *B. undatum* an ideal candidate for the investigation of kinetic effects on isotope and trace element incorporation during periods of fast growth, presenting an exciting avenue for future research.

The analysis of individual growth rates is something which is of direct and important relevance to fisheries scientists who are trying to estimate population growth rates. The isotopic data presented in Chapter 4 revealed that there are clear growth differences between sites which vary from year to year. There is also close agreement between the isotopic data and the growth curves calculated in Chapter 7. No Samples from the Menai Strait or Shetland had their year of maximum growth in year 1, this often came in year 2 or 3 (aside from Jersey which had comparable fast growth in years 1 and 4). The seasonal growth of laboratory reared animals also showed slower growth in season 1 - year 1 and this is likely due to the cold water temperatures at the time of hatching. These two findings of the isotopic analyses strongly support the finding

of Chapter 7 stating that *B. undatum* follows a sigmoidal growth pattern with slow initial growth.

The reconstructions of site growth rates also indicated that the Menai Strait and Shetland had faster rates of growth than Jersey, this is likely due to an optimal temperature range for growth. Figure 8.2 illustrates how an optimal temperature window might appear when overlaid on the SST records from Chapter 4. It is clear from this figure that portions of both the minimum and maximum temperature extremes for Jersey fall outside this hypothetical range. This would in principle result in growth rings being formed in the statoliths during both the winter minimum temperatures and summer maximum temperatures. This is exactly what was found in Chapter 7 for samples from Jersey which led to the initial overestimation of age at sites from this location. The effect was more pronounced in specimens from site JD5 which was in shallower water. This explanation of an optimal temperature range still does not fully explain the increased growth seen in Shetland compared to the Menai Strait after the second year of growth. This is likely due to either genetic factors or that the site in Shetland is at a depth of ≈ 19 m and possibly under different temperature conditions to those displayed by the SST logger. This probably explains the poor reconstruction of SST from shell $\delta^{18}\text{O}$ values at this site and raises the need for careful interpretation of statolith rings at individual sites, taking all environmental factors into account. A clear recommendation to rectify this issue is the need for accurate logging of key environmental variables such as water temperature, within the micro-environment of the whelk populations.

The absence of juvenile size classes from most of the sampled wild populations, coupled with the mortality observed in laboratory reared juveniles and field collected adults kept in aquaria discussed in Chapter 5, suggests that juveniles may reside in nursery grounds away from the main populations. These nursery grounds likely exist in shallower, warmer waters as the immature laboratory reared juveniles appeared to be more resistant to high water temperatures ($\approx 24^\circ\text{C}$). They may also act as a refuge from predation. This has been anecdotally supported by several fishermen who note that populations of small whelks exist that may well be juveniles residing in nursery grounds. This theory warrants further investigation as it possibly describes an important aspect of whelk population dynamics which has not been previously described. The knowledge of nursery ground locations would be crucial for fishery management as these locations should be avoided altogether as they would likely be comprised of a majority of immature animals. The avoidance of nursery grounds has the potential to be a crude method for avoiding the landing of immature specimens in lieu of ineffective MLS restrictions. Future

work should focus on identifying the differences in thermal tolerances of adult and juvenile whelks and also pinpointing the locations of several nursery grounds in an attempt to better understand the flow of animals between nursery grounds and adult populations.

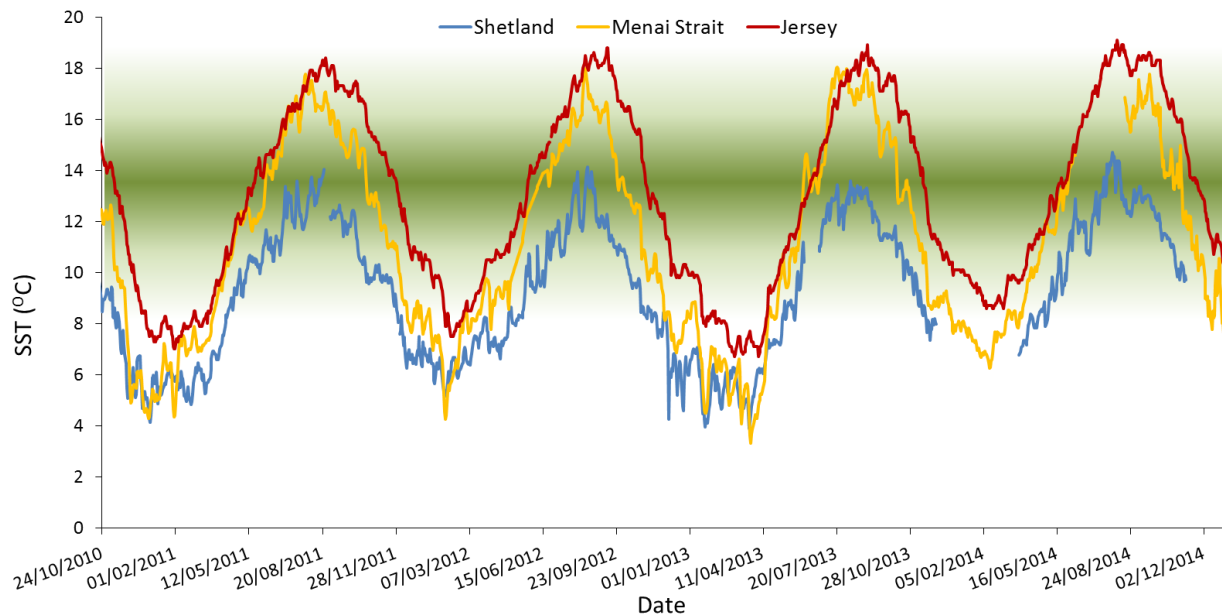


Figure 8.2. SST profiles from the 3 main sample sites from October 2010 to February 2014. The green bar represents a theoretical optimum temperature range for *B. undatum* growth.

8.2.3 Age

The final theme of the thesis was age determination of *B. undatum*. The application of age determination to the assessment of a fished stock that displays wide geographic variation in size at age and maturity cannot be overstated. As detailed in Chapter 7, the ability to model stock dynamics is crucial to fisheries management (Hilborn & Walters, 1992). The results described in this thesis have spanned from the introduction of statoliths and the interpretation of their several types of growth rings (Chapter 5) to the conclusive validation of annual growth rings (Chapters 5 and 6) and finally to their use as an age determination tool of wild populations with applications for fisheries monitoring (Chapter 7). This comprehensive overview of the use of statoliths for *B. undatum* ageing represents a body of work that can be applied directly to current fisheries monitoring programs. Several aspects of statolith use need further development, such as the use of several readers to monitor inter-reader reliability and the disentanglement of annual rings and disturbance rings. These problems could be addressed with further laboratory studies to induce statolith ring development and close work with fishery

monitoring organisations to develop multi-reader methods. The methods outlined in this thesis have already been presented to several organisations within the UK (several Inshore Fishery and Conservation Authorities, IFCAs) at a training workshop organised in conjunction with the Centre for Environment, Fisheries and Aquaculture Science (CEFAS) who were co-funders of this PhD. A standard operating procedure for statolith removal was developed for this workshop which can be seen in [Appendix G](#). A further 4 day training workshop is currently being organised for the 8th of May, 2017, in conjunction with Fisheries and Oceans Canada in St. Johns Newfoundland. This workshop will be advertised to research groups throughout North America who are currently struggling with the monitoring of *B. undatum* fisheries. Initial work into statolith growth ring validation has been written into an article for publication which is comprised of aspects from several of the presented chapters (it is currently 'accepted pending minor changes' for a special issue of Marine Ecology Progress Series that I am co-editing with several colleagues from CEFAS. The submitted version of the paper manuscript is available in [Appendix N](#)).

In conclusion, this thesis has reported on a wide range of aspects of the age, growth and reproductive assessment of the whelk *B. undatum*. Several of these findings have raised the possibility of exciting research into many aspects of *B. undatum* growth, especially related to geochemical analyses of shells and statoliths. Many of the findings throughout the 6 experimental chapters have direct relevance to the management of *B. undatum* populations by fishery scientists, primarily of which is the development of statoliths as a novel age determination tool. These developed methods will enable fishery scientists to improve the assessment and monitoring of *B. undatum* populations and hopefully lead to a more sustainable future for many fisheries.

8.3 References

- Addadi L, Weiner S (1997) Design Strategies in mineralized biological materials. *J Mater Chem* 7:689-702
- Gendron L (1992) Determination of the size at sexual maturity of the waved whelk *Buccinum undatum* Linnaeus, 1758, in the Gulf of St Lawrence, as a basis for the establishment of a minimum catchable size. *J Shellfish Res* 11:1–7
- Haig JA, Pantin, JR, Murray LG, Kaiser MJ (2015) Temporal and spatial variation in size at maturity of the common whelk (*Buccinum undatum*). *ICES J Mar Sci* 72 (9):2707-2719
- Hedegaard C, Bardeau J-F, Chateigner D (2006) Molluscan shell pigments: an in situ resonance Raman study. *J Molluscan Stud* 72:157–162
- Heude-Berthelin C, Hégron-Macé L, Legrand V, Jouaux A, Adeline B, Mathieu M, Kellner K (2011) Growth and reproduction of the common whelk *Buccinum undatum* in west Cotentin (Channel), France. *Aquat living resour* 24:317–327
- Hilborn R, Walters CJ (1992) Quantitative fisheries stock assessment: choices, dynamics and uncertainty. Chapman and Hall, New York
- Kenchington E, Glass A (1998) Local adaptation and sexual dimorphism in the waved whelk (*Buccinum undatum*) in Atlantic Nova Scotia with applications to fisheries management. *Can Tech Rep Fish Aquat Sci* 2237:1–42
- Lawler A (2013) Determination of the size of maturity of the whelk *Buccinum undatum* in English waters – Defra Project MF0231
- Levi-Kalisman Y, Falini G, Addadi L, Weiner S (2001) Structure of the nacreous organic matrix of a bivalve mollusk shell examined in the hydrated state using cryo- TEM. *J Struct Biol* 135:8–17
- Mann S, Webb J, Williams RJP (1989) Biomineralization: Chemical and Biochemical Perspectives. VCH, Weinheim
- Martel A, Larrivée DH, Himmelman JH (1986a) Behaviour and timing of copulation and egg-laying in the neogastropod *Buccinum undatum* L. *J Exp Mar Biol Ecol* 96:27-42
- McIntyre R, Lawler A, Masefield R (2015) Size of maturity of the common whelk, *Buccinum undatum*: Is the minimum landing size in England too low? *Fish Res* 162:53–57
- Mensink BP, Fischer CV, Cadée GC, Fonds M, Ten Hallers-Tjabbes CC, Boon JP (2000) Shell damage and mortality in the common whelk *Buccinum undatum* caused by beam trawl fishery. *J Sea Res* 43:53-64
- Santarelli L (1985) Les pecheries de Buccin (*Buccinum undatum* L.: Gastropoda) du Golfe Normand-Breton. Eléments de gestion de la ressource. PhD thesis, L'Universite d'aix-Marseille

- Santarelli L, Gros P (1985) Age and growth of the whelk *Buccinum undatum* L. (Gastropoda: Prosobranchia) using stable isotopes of the shell and operculum striae. *Oceanol Acta* 8(2):221–229.
- Thomas MLH, Himmelman JH (1988) Influence of predation on shell morphology of *Buccinum undatum* L. on Atlantic coast of Canada. *J Exp Mar Biol Ecol* 115:221–236
- Weiner S, Traub W (1980) X-ray diffraction study of the insoluble organic matrix of mollusk shells. *FEBS Lett* 111:311–316

Appendix list

A: Dispensation for the landing of undersized whelks

B: Statistical analysis outputs from shell morphology analysis in Chapter 2.

C: Overview of analytical techniques

1. Raman Spectroscopy
2. Solution Inductively Coupled Plasma – Mass Spectrometry (Solution ICP-MS)
3. Isotope Ratio Mass Spectrometry (IRMS)
4. Secondary Ion Mass Spectrometry (SIMS)
5. Micro-X-Ray Diffraction (μ XRD)

D: List of elemental standards used for Solution ICP-MS analysis

E: NERC Isotope Geosciences Facility Steering Committee (NIGFSC) application for stable isotope support. Successful - £87,500 in analyses awarded

F: Elemental relationship plots from *Buccinum undatum* shell analyses presented in Chapter 4.

G: Custom MATLAB script used to create average oxygen isotope profiles from multiple individual shell profiles.

H: Whelk statolith removal and mounting Standard Operating Procedure (SOP), written for statolith workshop at CEFAS.

I: NERC Edinburgh Ion Microprobe Facility (EIMF) application. Successful, resulted in 8 days of access to the Cameca IMS-4f Ion microprobe - £15,000 in analyses.

J: Rapid access request to the I-18 beamline at the Diamond Light Source synchrotron facility. Resulted in 24 hours of I-18 beam time with access to Raman microscope and support labs.

K: X-Ray Diffraction (XRD) profiles from quality control sampling during Micro-XRD analysis

L: Plots of raw magnesium and calcium measurements from statoliths analysed using SIMS.

M: Outputs from Gompertz growth equations calculated for operculum growth lines at each site without juvenile statolith and '2' clarity operculum data.

N: Journal article validating the periodicity of statolith growth line formation. In review with Marine Ecology Progress Series. Title - 'Statoliths of the whelk *Buccinum undatum*: a novel age determination tool'

Appendix A:

Dispensation for the landing of undersized whelks

**Is-adran Môr a Physgodfeydd /
Marine & Fisheries Division**



**Llywodraeth Cymru
Welsh Government**

Mr P Hollyman,
School of Ocean Sciences,
Bangor University,
Menai Bridge,
Anglesey,
LL59 5AB

31 January 2014

Dear Mr Hollyman,

**Scientific Research Project:
Fishing for and retention of undersize common whelks with pots**

Thank you for your application regarding the proposed scientific research project, to collect undersized (i.e. below 45mm) common whelks (*Buccinum undatum*) with pots (as described in your application dated 13 November 2013).

After due consideration of the details of the proposed research (as set out in the documents you have provided) and all other relevant factors, the authorisations below ("The Authorisations") are issued under authority of Alun Davies, the Minister for Natural Resources and Food, one of the Welsh Ministers, for the purposes of the various legislation set out below, in order to gather data regarding the growth and fecundity of the common whelk.

The Authorisations:

1. are valid for the period **00:01 on 1 February 2014 to 23:59 on 31 August 2016**;
2. only apply in relation to activities undertaken from one boat at a time owned by Bangor University;
3. only extend to the activities set out in your application dated 13 November 2013 ("the Activities"); and
4. are subject to the Conditions set out below.

Uned Pysgodfeydd / Fisheries Unit
Llywodraeth Cymru / Welsh Government
Ystafell 3 • Suite 3
Cwrt Cedrwydden • Cedar Court
Parc Busnes Havens Head • Havens Head Business Park
Aberdaugleddau, • Milford Haven,
Sir Benfro • Pembrokeshire
SA73 3LS

Ffôn/Tel 01646 693412
Phil.marshall@wales.gsi.gov.uk
Gwefan/Website www.wales.gov.uk

The Authorisations

1. Byelaws of the former North Western and North Wales Sea Fisheries Committee ("NWNWSFC").

The Activities which would otherwise be prohibited by Byelaw 19 (Specified Fish Sizes) and Byelaw 30 (Permit to Fish for Lobster, Crawfish, Crab, Prawn and Whelk) of the former NWNWSFC are hereby authorised to the extent provided in this letter and subject to the Conditions below, pursuant to Byelaw 1 of the former NWNWSFC (as being fishing operations conducted for scientific purposes).

For information, those Byelaws of the former NWNWSFC now have effect, pursuant to Article 13(3) of and Schedule 4 to the Marine and Coastal Access Act 2009 (Commencement No. 1, Consequential, Transitional and Savings Provisions) (England and Wales) Order 2010 (S.I. 2010/630 (C.42)) as if made by the Welsh Ministers in a statutory instrument.

2. Council Regulation (EC) No 850/98 of 30 March 1998 for the conservation of fishery resources through technical measures for the protection of juveniles of marine organisms ("Council Regulation 850/98").

The Activities which would otherwise be prohibited by Article 19 of Council Regulation 850/98 are hereby authorised, subject to the Conditions below, pursuant to Article 43(1) of that Regulation (as being fishing operations conducted solely for the purpose of scientific investigations).

For information, in accordance with Article 43(1) of Council Regulation 850/98, the UK Government and the Commission have been informed in advance of the proposed scientific investigations and the authorisation given under Article 43 of that Regulation.

Conditions

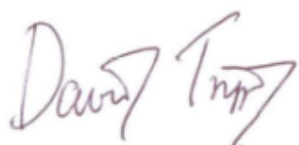
1. These Authorisations may only be exercised whilst onboard a boat owned by Bangor University. [Only one boat at a time may be used in exercise of these Authorisations].
2. A Test of Likely Significant Effect has been undertaken in connection with this scientific sampling work, pursuant to Article 6(3) of the Habitats Directive (Council Directive 92/43/EEC) and Regulation 61 of the Conservation of Habitats and Species Regulations 2010 (SI 2010/490).
3. Any fish, apart from Whelks (*Buccinum undatum*) which are to be retained as part of the Activities, caught whilst undertaking the Activities must be returned to the sea as soon as possible, alive wherever possible, at a location as near as possible to the location from which they were taken. For the avoidance of any doubt, any fish (including Whelks (*Buccinum undatum*)) caught as a result of undertaking the Activities may not be retained or offered for sale.
4. No more than six scientific pots may be set to collect Whelks (*Buccinum undatum*) during any calendar month and each pot may only be set to collect Whelks for no more than one period of 48 hours in each calendar month.
5. A signed copy of this letter must be kept onboard the Bangor University boat at all times while that vessel is operating in exercise of these Authorisations.

6. A signed copy of this letter must be presented upon request to any Welsh Government Fisheries Enforcement Office and/or any Marine Enforcement Officer.
7. The Master of the Bangor University boat and all crew onboard must comply with all demands and instructions issued by the Welsh Government's Fisheries Enforcement Officers and/or any Marine Enforcement Officer.
8. The Master of the Bangor University boat and all crew onboard must comply with all other relevant legislation (i.e. each Authorisation set out in this letter only relates to the legislation mentioned in the same).
9. The Welsh Government's Fisheries Enforcement Operations room must be notified at the beginning and again at the end of each day upon which activities will be undertaken in exercise of these Authorisations.

The Fisheries Enforcement Operations room can be contacted by telephone on 01646 693412 or email sent to milfordhavenfisheryoffice@wales.gsi.gov.uk

10. These Authorisations will expire automatically, if not terminated or withdrawn before that date, at 23:59 on 31 August 2016.
11. The Welsh Ministers may in their absolute discretion withdraw these Authorisations at any time. Where possible prior notice of withdrawal will be given, but in any of the following instances, these Authorisations may be withdrawn without notice:
 - (a) in the case of emergency;
 - (b) if any of the Conditions set out in this letter are breached;
 - (c) if the Activities permitted by this Authorisation result or are likely to result in a significant effect to any European Marine Site (as defined by regulation 8(4) of the Conservation of Habitats and Species Regulations 2010 (S.I. 2010/490)).

Yours Sincerely



David Tripp
Head of Fisheries Strategy

Appendix B:
Statistical analysis outputs from shell morphology
analysis in Chapter 2.

Table B.1. Normality test outputs for all transformed variables used in the PCA and LDA analyses in Chapter 2 from all sites.

Measurement	site	Tests of Normality					
		Kolmogorov-Smirnov ^a			Shapiro-Wilk		
		Statistic	df	Sig.	Statistic	df	Sig.
Total shell length	Amlwch	0.135	13	.200*	0.936	13	0.401
	Holyhead	0.152	45	0.01	0.967	45	0.226
	Jersey	0.148	23	.200*	0.971	23	0.708
	Menai	0.036	271	.200*	0.997	271	0.898
	Nefyn	0.074	42	.200*	0.992	42	0.994
	Shetland	0.06	115	.200*	0.992	115	0.73
Minimum shell width	Amlwch	0.129	13	.200*	0.936	13	0.408
	Holyhead	0.107	45	.200*	0.981	45	0.65
	Jersey	0.124	23	.200*	0.977	23	0.844
	Menai	0.041	271	.200*	0.994	271	0.387
	Nefyn	0.115	42	0.189	0.967	42	0.269
	Shetland	0.052	115	.200*	0.988	115	0.381
Maximum shell width	Amlwch	0.158	13	.200*	0.915	13	0.213
	Holyhead	0.082	45	.200*	0.991	45	0.977
	Jersey	0.124	23	.200*	0.952	23	0.319
	Menai	0.042	271	.200*	0.994	271	0.334
	Nefyn	0.095	42	.200*	0.968	42	0.276
	Shetland	0.068	115	.200*	0.989	115	0.445
Lip Thickness 1	Amlwch	0.144	13	.200*	0.949	13	0.579
	Holyhead	0.096	45	.200*	0.962	45	0.146
	Jersey	0.132	23	.200*	0.961	23	0.49
	Menai	0.05	271	0.096	0.968	271	0.063
	Nefyn	0.117	42	0.163	0.949	42	0.062
	Shetland	0.055	115	.200*	0.99	115	0.57
Aperture length	Amlwch	0.121	13	.200*	0.965	13	0.834
	Holyhead	0.1	45	.200*	0.979	45	0.566
	Jersey	0.1	23	.200*	0.961	23	0.49
	Menai	0.041	271	.200*	0.995	271	0.551
	Nefyn	0.103	42	.200*	0.966	42	0.249
	Shetland	0.05	115	.200*	0.986	115	0.277
Aperture width	Amlwch	0.16	13	.200*	0.968	13	0.876
	Holyhead	0.088	45	.200*	0.988	45	0.915
	Jersey	0.127	23	.200*	0.934	23	0.132
	Menai	0.049	271	.200*	0.991	271	0.094
	Nefyn	0.086	42	.200*	0.984	42	0.801
	Shetland	0.046	115	.200*	0.993	115	0.838
Siphonal canal length	Amlwch	0.174	13	.200*	0.903	13	0.148
	Holyhead	0.062	45	.200*	0.982	45	0.711
	Jersey	0.1	23	.200*	0.972	23	0.743
	Menai	0.038	271	.200*	0.994	271	0.304
	Nefyn	0.086	42	.200*	0.991	42	0.982
	Shetland	0.06	115	.200*	0.986	115	0.28

*. This is a lower bound of the true significance.

a. Lilliefors Significance Correction

Table 1 continued.

Measurement	Site	Tests of Normality					
		Kolmogorov-Smirnov ^a			Shapiro-Wilk		
		Statistic	df	Sig.	Statistic	df	Sig.
Body whorl width	Amlwch	0.136	13	.200 [*]	0.97	13	0.893
	Holyhead	0.076	45	.200 [*]	0.983	45	0.726
	Jersey	0.141	23	.200 [*]	0.949	23	0.275
	Menai	0.044	271	.200 [*]	0.994	271	0.41
	Nefyn	0.09	42	.200 [*]	0.979	42	0.616
	Shetland	0.095	115	0.053	0.981	115	0.093
Spire angle	Amlwch	0.174	13	.200 [*]	0.915	13	0.215
	Holyhead	0.098	45	.200 [*]	0.967	45	0.229
	Jersey	0.186	23	0.039	0.904	23	0.061
	Menai	0.028	271	.200 [*]	0.994	271	0.38
	Nefyn	0.096	42	.200 [*]	0.959	42	0.136
	Shetland	0.08	115	0.069	0.968	115	0.059

*. This is a lower bound of the true significance.

a. Lilliefors Significance Correction

Table B.2. PCA loading outputs from shell morphology analysis presented in Chapter 2.

	PCA Loadings							
	Comp.1	Comp.2	Comp.3	Comp.4	Comp.5	Comp.6	Comp.7	Comp.8
Total shell length	-0.37	-0.22	-0.17	0.14	0.41	-0.25	0.66	0.25
Minimum shell width	-0.41	0.21	0.03	0.04	0.31	0.04	-0.06	-0.81
Maximum shell width	-0.4	0.02	-0.01	0.06	0.42	0.22	-0.62	0.45
Lip Thickness 1	0.39	-0.28	0.33	0.33	0.08	0	-0.08	-0.07
Aperture length	-0.33	-0.52	-0.34	0.4	-0.54	-0.48	-0.27	-0.03
Aperture width	0.24	0.16	-0.8	-0.27	0.03	0.22	0.01	-0.03
Siphonal canal length	-0.22	-0.09	0.12	-0.75	-0.13	-0.18	-0.12	-0.08
Body whorl width	-0.37	-0.16	0.07	0.12	-0.44	0.74	0.25	0.03
Spire angle	-0.17	0.71	0.31	-0.26	-0.22	-0.18	0.15	0.24
Standard deviation	2.16	1.17	1	0.81	0.71	0.61	0.53	0.38
Proportion of variance	0.52	0.15	0.11	0.07	0.06	0.04	0.03	0.02
Cumulative variance	0.52	0.67	0.78	0.86	0.91	0.95	0.98	1

Table B.3. Normality test outputs for principal component outputs for each site.

Measurement	site	Tests of Normality					
		Kolmogorov-Smirnov			Shapiro-Wilk		
		Statistic	df	Sig.	Statistic	df	Sig.
Comp1	Amlwch	0.174	13	.200 [*]	0.926	13	0.3
	Holyhead	0.094	45	.200 [*]	0.975	45	0.427
	Jersey	0.152	23	0.184	0.956	23	0.385
	Menai	0.053	271	0.065	0.99	271	0.06
	Nefyn	0.07	42	.200 [*]	0.98	42	0.652
	Shetland	0.061	115	.200 [*]	0.991	115	0.618
Comp2	Amlwch	0.132	13	.200 [*]	0.924	13	0.282
	Holyhead	0.065	45	.200 [*]	0.983	45	0.76
	Jersey	0.127	23	.200 [*]	0.971	23	0.707
	Menai	0.034	271	.200 [*]	0.995	271	0.555
	Nefyn	0.095	42	.200 [*]	0.984	42	0.818
	Shetland	0.038	115	.200 [*]	0.994	115	0.887
Comp3	Amlwch	0.153	13	.200 [*]	0.956	13	0.695
	Holyhead	0.094	45	.200 [*]	0.979	45	0.566
	Jersey	0.228	23	0.003	0.877	23	0.072
	Menai	0.041	271	.200 [*]	0.992	271	0.146
	Nefyn	0.136	42	0.05	0.977	42	0.546
	Shetland	0.094	115	0.014	0.984	115	0.193

Table B.4. Linear discriminant weightings from the Linear Discriminant analysis presented in Chapter 2.

	Coefficients of linear discriminants				
	LD1	LD2	LD3	LD4	LD5
Total shell length	-10.24	54.2	-32.64	18.36	-5.19
Minimum shell width	3.76	-20.7	54.1	21.31	48.08
Maximum shell width	-2.27	-15.09	-9.23	-0.67	-5.76
Lip Thickness 1	-0.72	-0.57	-1.34	-0.52	2.69
Aperture length	-8.16	1.79	20.73	0.01	-26.87
Aperture width	-2.25	-5.44	1.86	5.06	-6.15
Siphonal canal length	-6.93	5.76	0.47	-15.32	3.49
Body whorl width	-17.5	-9.4	8.36	-34.37	-11.89
Spire angle	23.14	10.02	-7.09	-4.11	-6.62
Proportion of trace	0.62	0.3	0.07	0.01	0

Appendix C:

Overview of analytical techniques

C.1. Raman Spectroscopy

C.2. Solution Inductively Coupled Plasma – Mass Spectrometry
(Solution ICP-MS)

C.3. Isotope Ratio Mass Spectrometry (IRMS)

C.4. Secondary Ion Mass Spectrometry (SIMS)

C.5. Micro-X-Ray Diffraction (μ XRD)

C.1. Raman Spectroscopy

Raman spectroscopy is a technique widely used to analyse the structure and properties of molecules from their vibrational state (Ferraro & Nakamoto, 1994). A laser (or other high intensity light source) is focused onto the surface of a sample, light which is not absorbed is scattered either elastically without any change in its wavelength, or inelastically, resulting in a change in wavelength of the scattered photons. Elastic or Rayleigh scattering is of no significance analytically, however, the change in wavelength of the small amount of inelastically scattered photons ($\approx 0.001\%$) can be measured (Higson, 2004). Inelastic scattering results in the wavelength of scattered photons becoming either longer or shorter from losing or gaining energy. This is known as the Raman effect and results from Stokes or anti-Stokes transitions respectively. Figure C.1 outlines the scattering processes during Raman analysis.

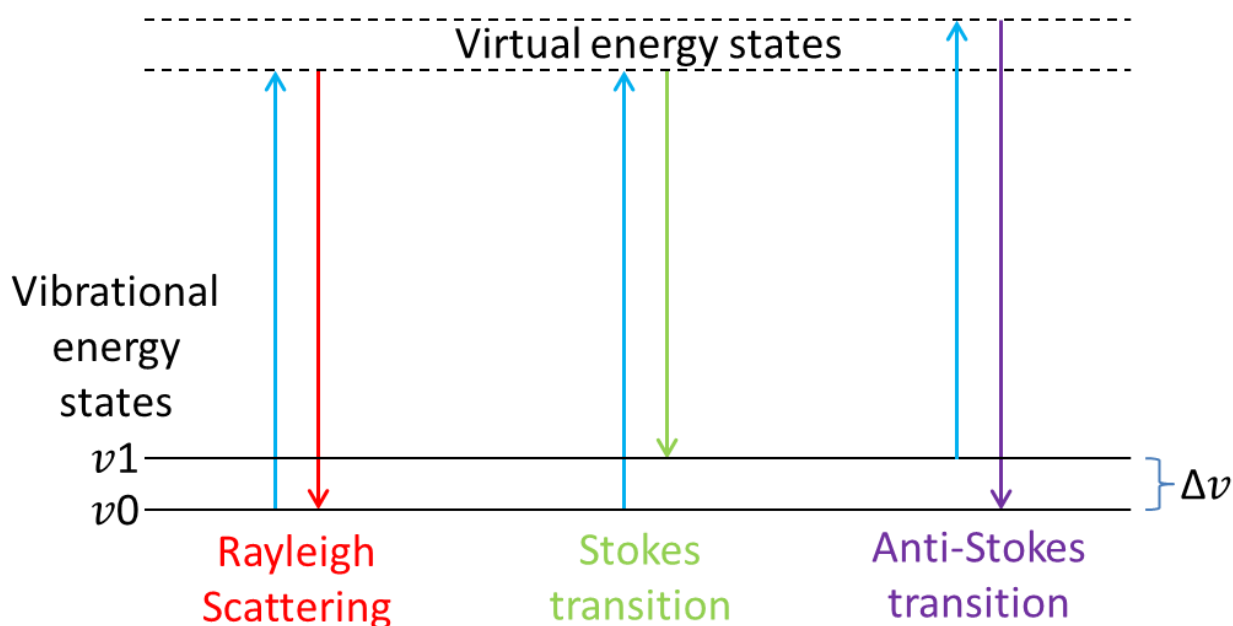


Figure C.1. A diagrammatic representation of the excitation states of molecules during Raman spectroscopy and the resulting energy states of the molecules. As Rayleigh scattering returns to the same state the photon causing the excitation is scattered with the same wavelength. Different photon wavelengths result from Stokes and Anti-Stokes transitions as a transfer of energy takes place and the molecule returns to a different energy state (Adapted from Lewis & Edwards 2001).

When a molecule at an initial energy state (v_0) is hit by a photon, its excitation level rises to a theoretical virtual energy state and then falls back down. If the molecule returns to its original energy state then elastic (Rayleigh) scattering has occurred and the photon is scattered with the same incident wavelength. If the molecule returns to a higher energy state (v_1 , i.e. it gained energy from the photon) the photon will be scattered with a longer wavelength. If the molecule

returns to a lower energy state (i.e. the photon gained energy from the molecule) then the scattered photon will have a shorter wavelength. These changes in wavelength are known as Stokes and anti-Stokes scattering respectively and result in shifts in the wavelength of the scattered photons (the Raman shift) which can be measured (Naife, 2001; Higson, 2004). These shifts are often unique to molecules as the interaction between photons and molecules is determined by the electrochemical properties and polarity of the molecular structure (Nafie, 2001). A spectra of Raman shifts can be made with a spectrometer, with bands of Raman light appearing depending on the molecular structure and vibrations interacted with. These wavelengths from an unknown sample, when compared to those from compounds of known structure, can be used to identify the unknown substance.

Figure C.2 outlines how a Raman spectrometer operates. The Raman spectrometer used in this study was a Reinshaw InVia Raman-Microscope located at the Diamond Light Source facility in Didcot, Oxfordshire.

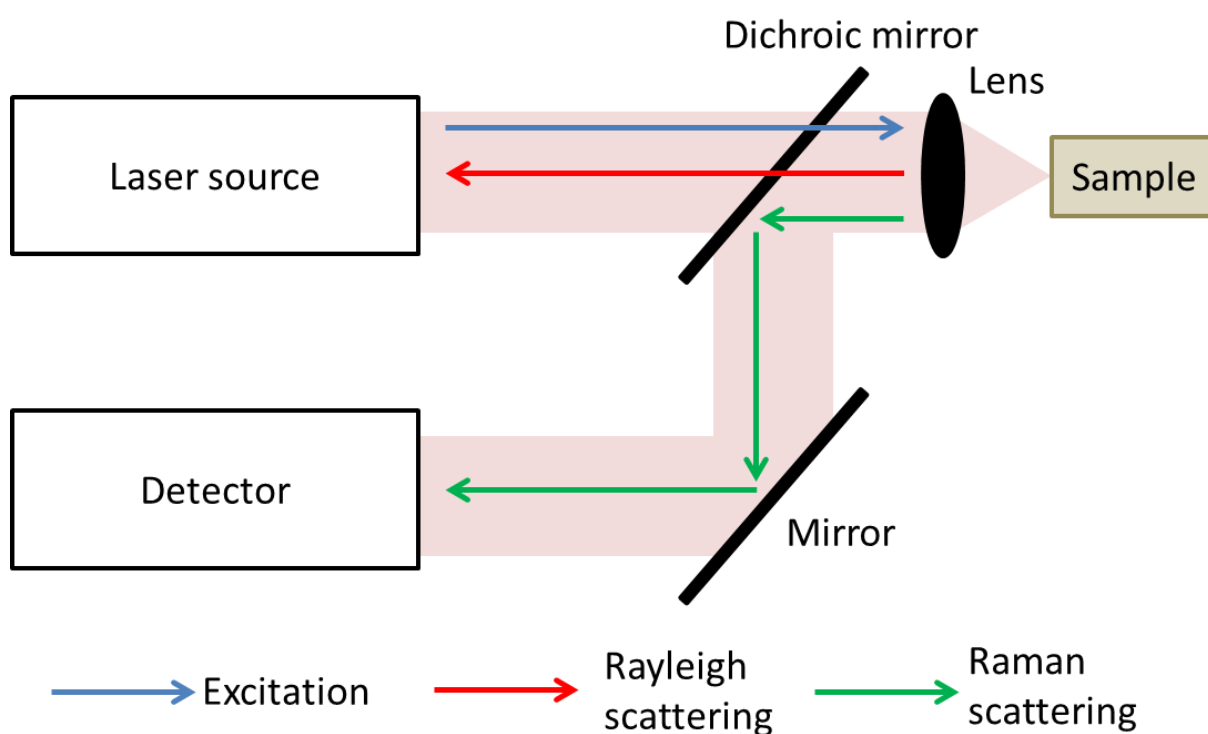


Figure C.2. A simplified diagrammatic representation Raman microscope (adapted from Li *et al.*, 2014).

C.2. Solution Inductively Coupled Plasma – Mass Spectrometry (Solution ICP-MS)

This technique allows high accuracy and precision analysis of trace element concentrations contained within a liquid sample. For mollusc shell analysis, it is generally used when less labour intensive techniques (such as Laser Ablation – Inductively Coupled Plasma – Mass Spectrometry, LA-ICP-MS or SIMS) are unsuitable. Where LA-ICP-MS takes *in-situ* measurements from a shell, solution ICP-MS requires the samples to be collected beforehand, generally via drilling to produce a powder. These powder samples are then digested in acid and diluted to produce a liquid sample which is analysed using combination of three devices: an auto-sampler, a nebuliser, and a mass spectrometer. All of the solution ICP-MS work for this project was undertaken at the British Geological Survey (BGS) using a Teledyne Cetac MVX-7100 low volume auto-sampler (LVA) coupled to a Teledyne Cetac Agilent II desolvating nebulizer which fed into a SPECTRO MS ICP mass spectrometer. The combination this equipment allowed the sampling of very small amounts of shell powder ($\approx 100\mu\text{g}$).

2.1 MVX-7100 μl workstation:

This auto-sampler is capable of taking small volumes of liquid from a sample vial down to $5\mu\text{l}$ (in this instance $100\mu\text{l}$). This is achieved using an automated glass needle programmed to sequentially sample a rack of vials (up to 108 in one run) (Figure C.3). Once the needle enters the vial, a syringe pump removes an accurate volume into a capillary tube. A 6 port rotational valve then turns to connect the capillary tube containing the sample to the nebulizer and the syringe pump pushes the sample out. Between each sample the needle and capillary tube is washed using 1% HNO_3 solution to avoid cross contamination.

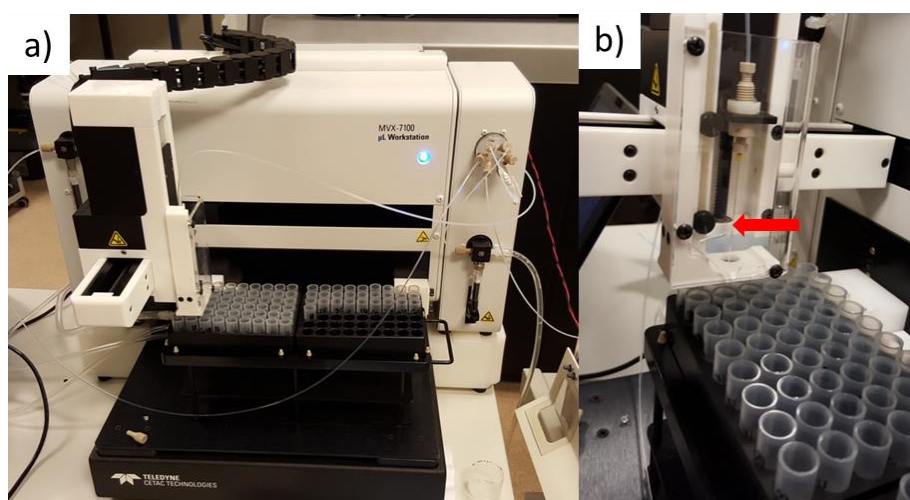


Figure C.3. a) the MVX-7100 autosampler, sample vials can be seen laid in racks to be sequentially sampled. b) a close-up of the glass needle used to extract $100\mu\text{l}$ from each sample vial (highlighted with red arrow).

2.2 Aridus II desolvating nebulizer:

A nebulizer is used to transform a liquid sample into a gaseous one. Conventional nebulisers setups use a concentric nebuliser (Figure C.4).

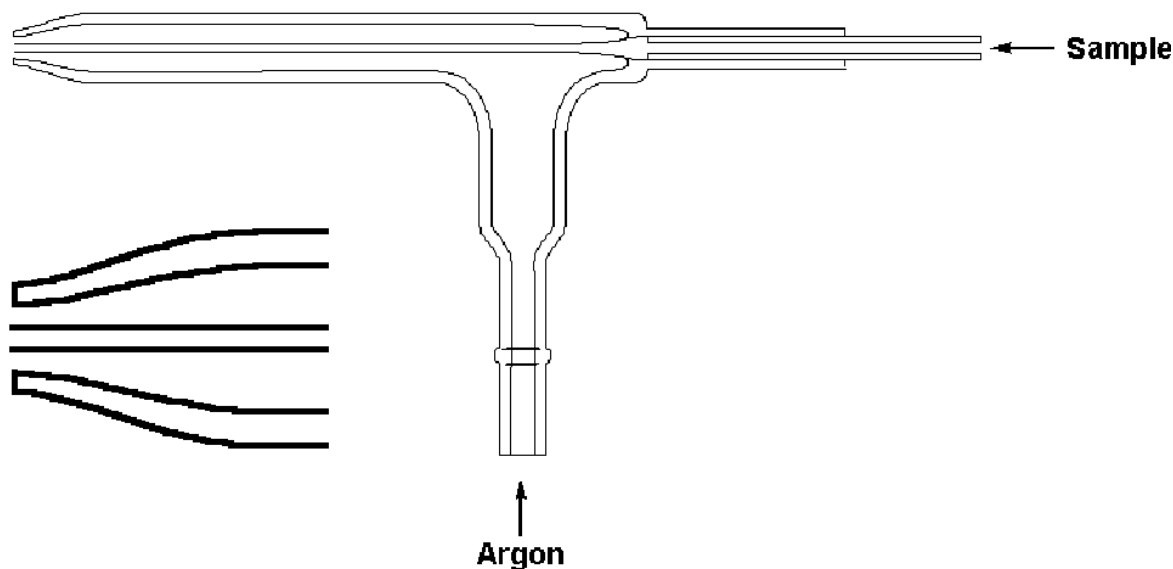


Figure C.4. A diagram of a conventional concentric nebulizer with a close-up diagram of the tip, to show where the argon gas is compressed, creating the Venturi effect upon exit from the nebulizer and contact with the sample liquid. (<http://analyticalprofessional.blogspot.co.uk>, 2016)

Liquid is passed down a capillary tube to an opening that is surrounded by a flow of inert gas (such as Argon), the Venturi effect causes the gas to expand once it has passed the tapered tip of the nebulizer where it meets the sample, this pulls on the surface of the liquid and causes it to split into a mist of big and small droplets. This mist is passed into a spray chamber with the aim of siphoning off the big droplets and drying some of the dilution medium (usually a solvent such as water) out of the small droplets. If too much liquid is passed into the mass spectrometer at any one time it may cause the plasma torch to be extinguished or the sample to not be fully ionised before being passed into the vacuum. Desolvating nebulisers use a concentric nebuliser but much emphasis is placed on drying the water (or other solvent) from the sample so that more can be passed into the MS. This is achieved by having a spray chamber that is heated to 160°C which dries many of the small droplets and begins to dry the larger droplets. The partially dried sample is then passed to the desolvating portion of the nebuliser which consists of a heated tube made from a porous fluoropolymer membrane. Outside this membrane a counter current flow of pure (and therefore dry) argon is constantly flowing (Figure C.5). This causes much of the remaining water vapour to be drawn through the membrane and the remaining

sample is then passed into the MS. The nebuliser used in this project was the Aridus II from CETAC Technologies.

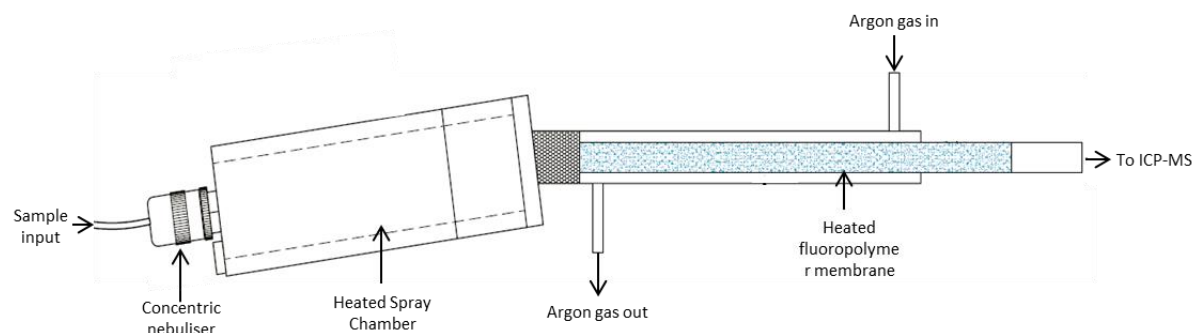


Figure C.5. A diagram of a the Aridus II desolvating nebuliser, used to increase sample introduction efficiency when analysing liquid samples (CETAC technologies, 2009).

2.3 SPECTRO MS:

The SPECTRO MS is a double focussing sector field ICP-MS that is currently unique in its ability to analyse a spectrum of elements from Li^6 to U^{238} simultaneously. The design of the SPECTRO MS is based on Mattauch-Herzog geometry which makes the simultaneous analysis possible. It does this by utilizing both an electrostatic sector field and a magnetic sector field to separate ions onto a 120 mm faraday strip array detector on a single plane (Figure C.6) (Resano *et al.*, 2012).

The initial stage of the ICP-MS analysis is the interface between the low pressure (close to ambient) of the nebulizer and the vacuum of the mass spectrometer. This interface is comprised of the plasma torch and the sampling and skimmer cones (Figure C.7). Firstly the sample passes into the plasma torch where it is heated, vaporised and ionized. The plasma torch is comprised of a coil surrounding a glass tube which emits radio-frequency (RF) energy (creating a field of ionising electromagnetic energy); through this tube Ar gas is passed at a speed of $\approx 15\text{L/min}$. After an initial spark is introduced to ionize some of the argon an electron cascade occurs and the RF energy from the coil keeps the torch in a state of ionization equilibrium (Higson, 2004; de Hoffmann & Stroobant, 2007). As the sample is passed through the argon plasma it is ionized through the interaction of the sample atoms with the Ar ions. The ionised sample and Ar mix is then passed through the sampling cone which peels off most of the Ar by only allowing the central portion of the beam through, into a region of transitional vacuum. The sample ion beam then passes through a skimmer cone which refines the beam further, and directs it into the full vacuum of the MS (Higson, 2004; de Hoffmann & Stroobant, 2007).

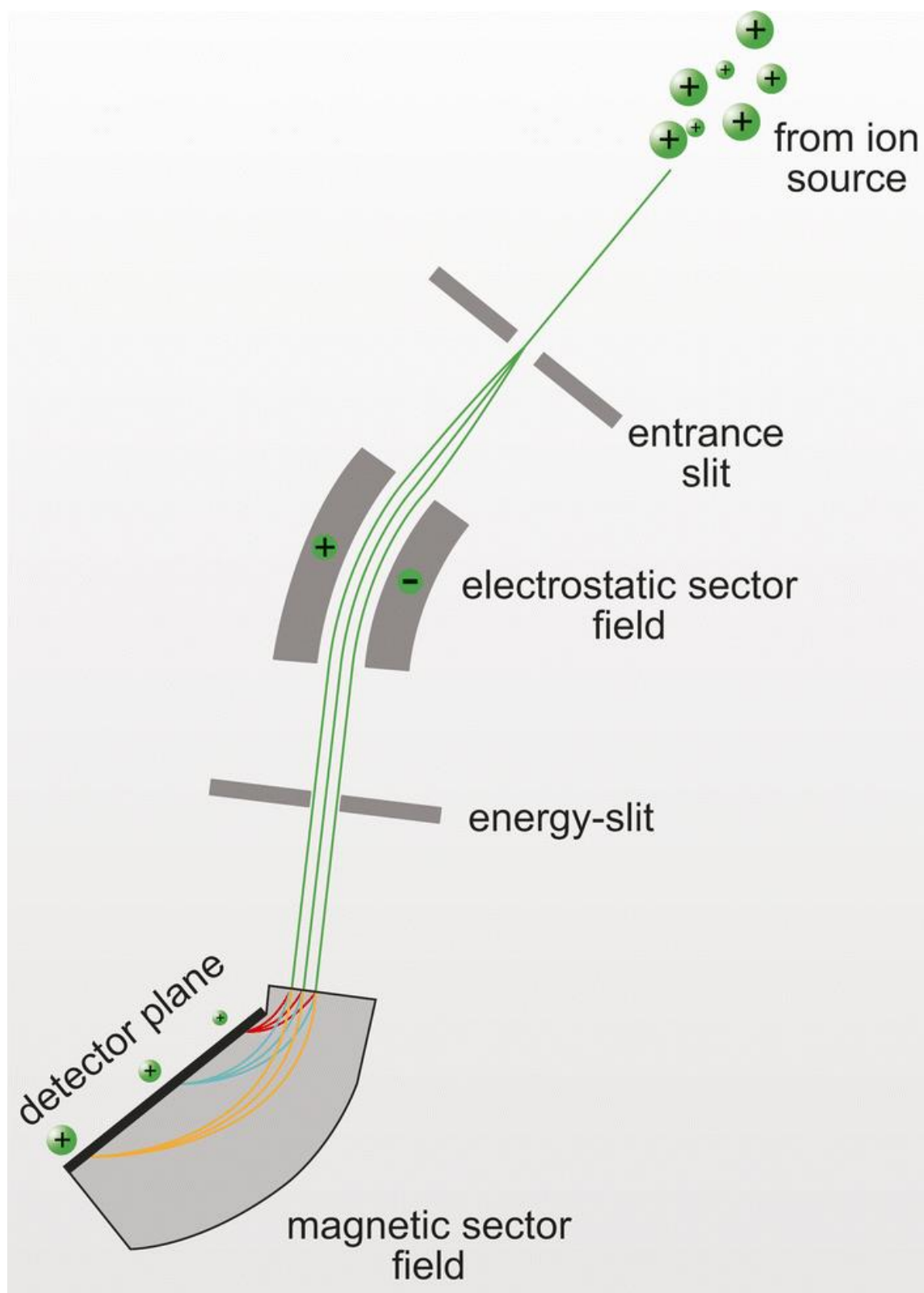


Figure C.6. A diagrammatic representation of the Mattauch-Herzog geometry of the SPECTRO MS, outlining how the beam is split to allow detection of a range of elements at one time (Ardelt *et al.*, 2013).

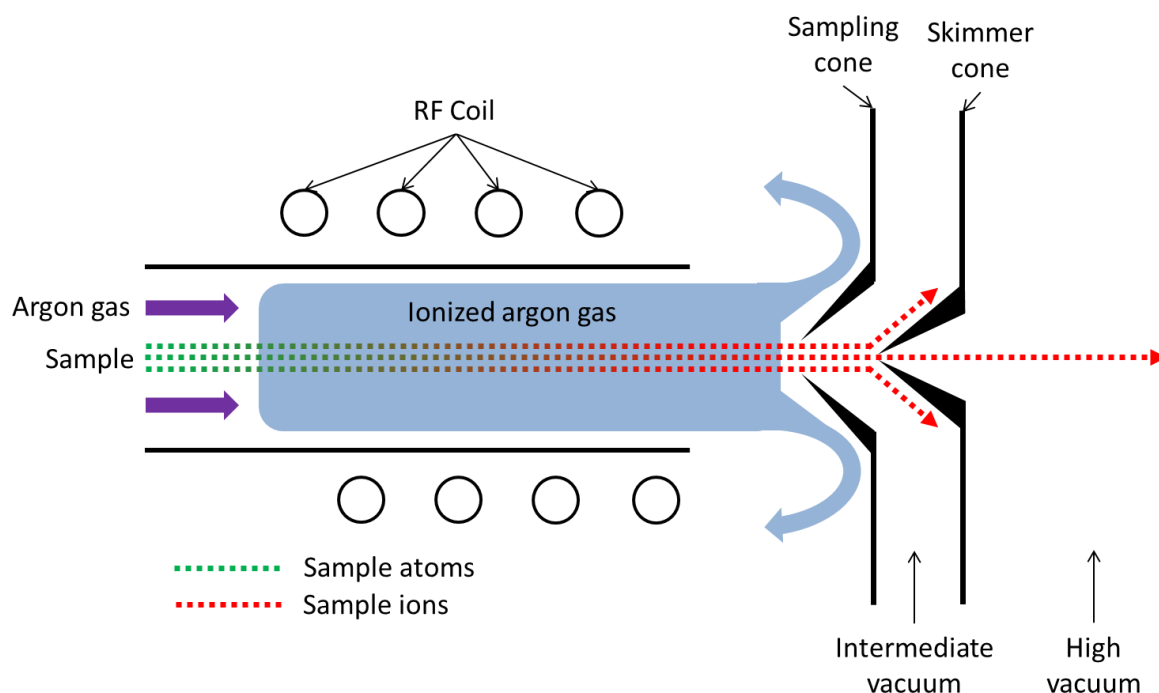


Figure C.7. A diagrammatic representation of a cross section through the sample ionization and introduction area of a mass spectrometer (adapted from Thomas, 2011).

After entering the vacuum of the mass spectrometer (Approximately 10^{-6} mbar), the sample is then passed through an entrance slit into the electrostatic analyser (ESA)/prism. This ESA filters the sample ions by energy, essentially homogenizing the energy of all of the sample ions to a single energy removing any ions that do not possess the required energy through a grid. This is to allow for the subsequent sorting of the ions by mass. The ESA works by having a difference in voltage on the inner and outer surface of the prism and a selector slit at the exit of the prism. Upon leaving the ESA, the sample is passed through two quadrupole filters, the sole purpose of which is to change the profile of the beam from circular to a flat line. The beam is then passed to the magnetic sector where the beam is split by mass and directed onto the detector plate. The detector is a Faraday strip array which is comprised of 4800 separate detectors covering the mass range from Li to U, lighter elements such as Li^6 have up to 20 dedicated detectors whilst heavier elements such as U^{238} only have 4-5 (SPECTRO, 2011). The combination of equipment used for this analysis has never before been used to analyse shell carbonate samples (Chenery *et al.*, 2015).

C.3. Isotope Ratio Mass Spectrometry (IRMS)

This technique, like solution ICP-MS and the Ion-probe, is a mass spectrometer based method. In the case of carbon and oxygen isotope analysis, instead of analysing the abundance of individual elements (via their isotopes) the relative abundance of ionized CO_2 molecules with differing masses is determined. This technique is performed by using an instrument called a gas source mass spectrometer.

Firstly, the weighed sample is dissolved in anhydrous phosphoric acid (H_3PO_4) at a temperature of 90°C to liberate CO_2 gas. After 15 minutes, sufficient time to isotopically equilibrate the gas, the expressed gas is extracted and cryogenically cleaned using a liquid nitrogen trap to remove any moisture from the sample. The sample gas is moved through the system using a series of pumps and bellows. Before entering the mass spectrometer (at vacuum) the sample gas is ionised by a high current filament, this produces ions with differing masses, dependent on the isotopic composition of the molecule ($44-^{12}\text{C} + ^{16}\text{O} + ^{16}\text{O}$; $45-^{13}\text{C} + ^{16}\text{O} + ^{16}\text{O}$ and $46-^{12}\text{C} + ^{16}\text{O} + ^{18}\text{O}$) (Figure C.8).

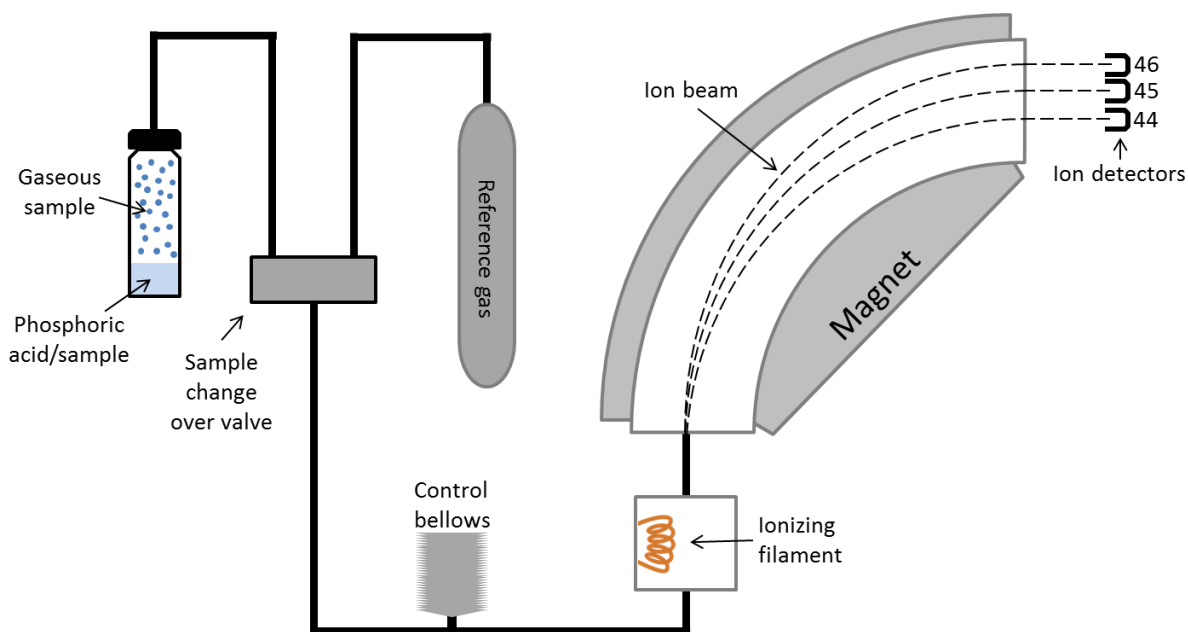


Figure C.8. A simplified diagrammatic representation of a dual inlet gas source mass spectrometer.

Once inside the mass spectrometer, the electromagnet splits the ion beam by mass and the resulting beams of mass 44, 45 and 46 pass through selection slits and are then collected and counted using Faraday cup detectors (Figure 8). The data are calculated as an isotope ratio, this being more precise than individual isotope concentrations. A reference gas of pure CO_2 is also

used to calibrate the signal and the data are reported relative to this on the delta scale i.e. $\delta^{18}\text{O}$. To ensure the highest levels of precision and accuracy, firstly the pressures of the sample and reference gas are matched using a set of bellows and secondly the sample and reference gases are alternately and measured for a number of cycles (standard-sample-standard bracketing).

Faraday cup detectors are less sensitive than electron multipliers (described in section C.4), making them unsuitable for applications requiring very low count rates, however, they are suitable for techniques such as IR-MS which have high ion signals (Thomas, 2011). The ion beam enters the Faraday cup and hits the charge collection cup (Figure C.9). As the charged ions hit the metal of the cup a current is induced which is discharged through an electrical connection. The current measured will be proportional to the number of incident ions, allowing the calculation of ionic abundance of the known mass.

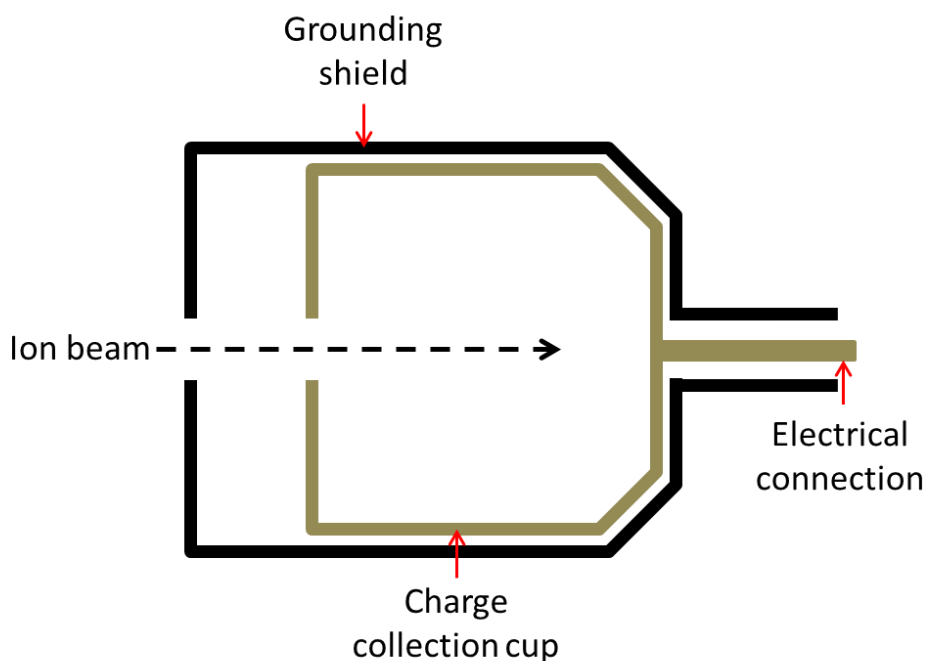


Figure C.9. A diagrammatic representation of a Faraday cup detector (adapted from Higson, 2004)

By doing this the ratio of the isotopes of each of these elements, in this case carbon ($^{12}\text{C}/^{13}\text{C}$) and Oxygen ($^{16}\text{O}/^{18}\text{O}$) is calculated. This is achieved by analysing the abundances of the three masses to calculate the abundance of each carbon and oxygen isotope in the sample. For this project, all IRMS was undertaken at the NERC Isotope Geosciences Unit at the British Geological Survey using a multiprep device coupled with a GV Isoprime dual inlet mass spectrometer were used to analyse the samples.

C.4 Secondary Ion Mass Spectrometry (SIMS)

Secondary Ion Mass Spectrometry (SIMS) is a high resolution, high sensitivity technique, carried out using a instrument, typically called an Ion Microprobe when used for quantitative analysis of solid samples. A beam of negatively charged primary ions (O^-) is used to bombard the surface of a sample at an angle of 30° (interaction angle), which is held under ultra-high vacuum. The result of this bombardment is the desorption of sample atoms, some of which gain enough energy to be ionized due to an exchange of energy (Higson, 2004) (Figure C.10). This creates the secondary ion beam, comprised of ions from ablated sample surface material. Using this technique, micro-scale analyses can be undertaken down to diameters of $1\ \mu m$ (Craven, 2006; Higson, 2004), with an ablation depth of under $3\ \mu m$ (Hinton, pers comms). The depth being primarily a function of analysis time i.e. the longer the sample is analysed the greater the erosion.

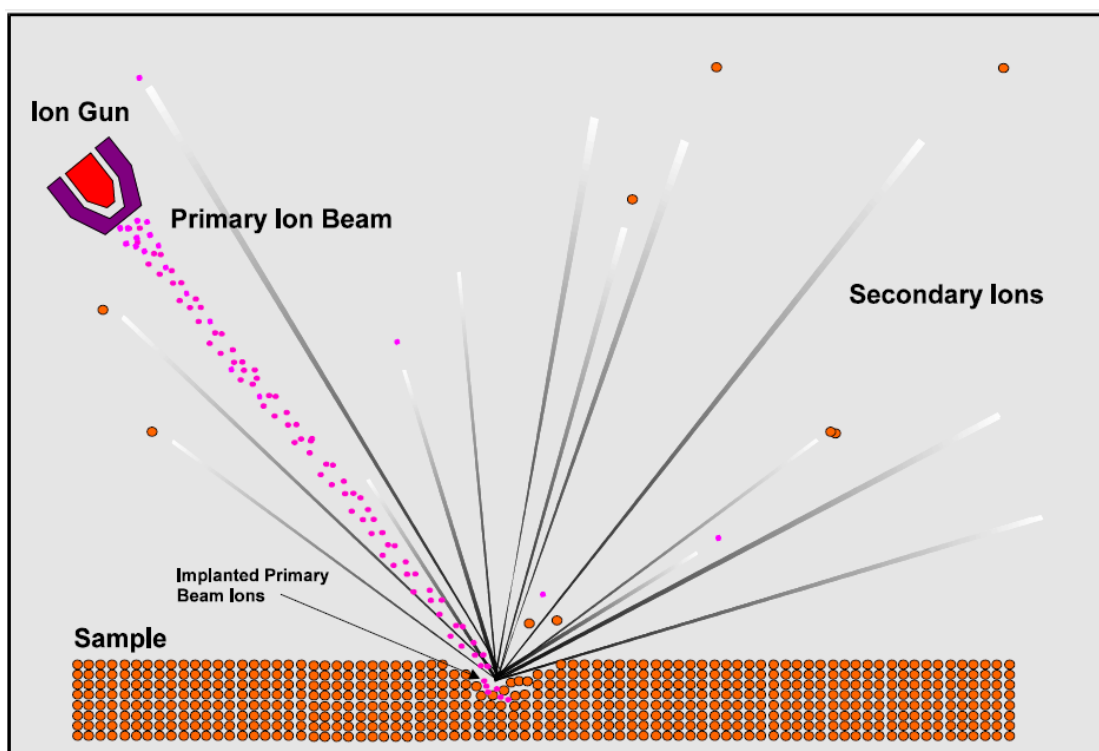


Figure C.10. A diagrammatic representation of the surface ablation undertaken during SIMS, oxygen ions (pink) can be seen interacting with the sample and releasing sample ions (orange). (Craven, 2006)

All of the SIMS analyses undertaken for this project were conducted at the Edinburgh Ion Microprobe Facility (EIMF) using a Cameca IMS-4f which contains a double focussing sector field mass spectrometer, using an O^- primary beam (Figure C.11).

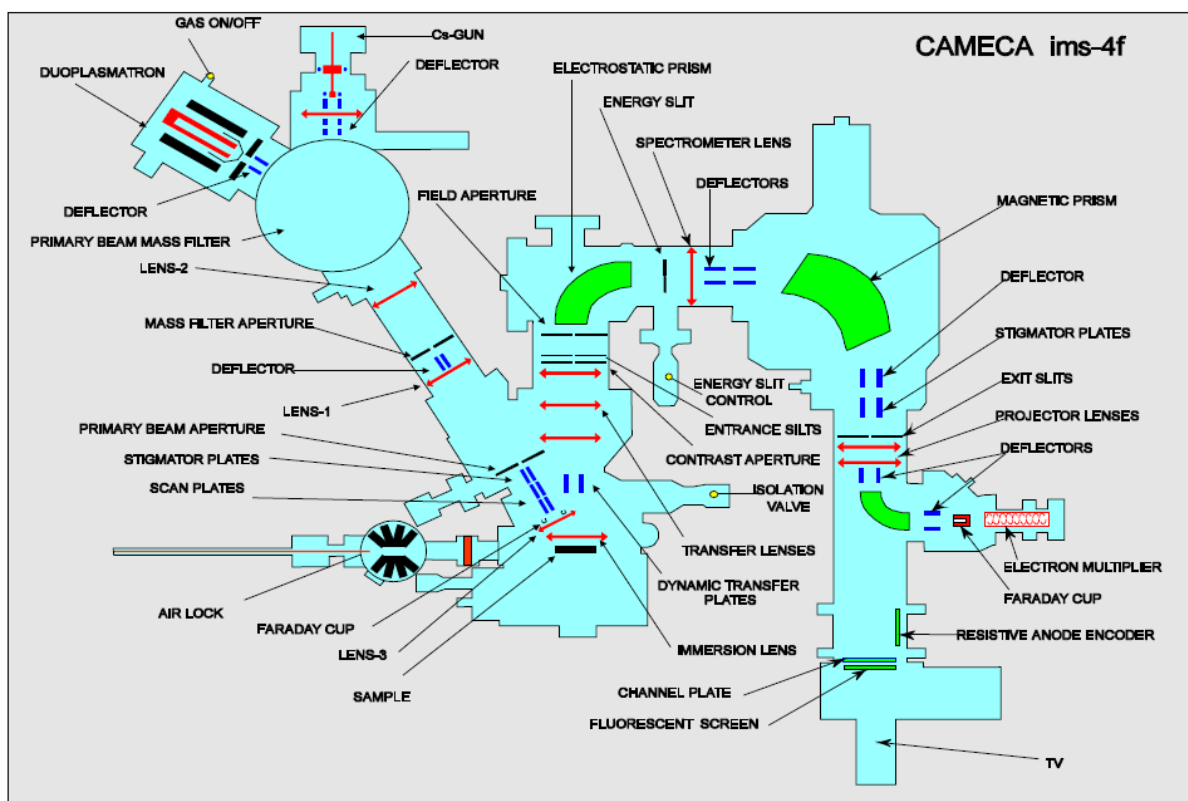


Figure C.11. A schematic diagram of the Cameca IMS-4f Ion Microprobe (Craven, 2006)

The primary ion beam is produced using a duoplasmatron (Figure C.12) which passes high purity oxygen gas through a nickel cathode where it is ionised, forming a plasma. This shapeless plasma is then passed through an extraction electrode which changes it to an rough shaped ion beam. The beam is passed down through the primary ion column where a series of lenses and apertures focus the beam shape and size then direct it to the desired location on a sample (Craven, 2006).

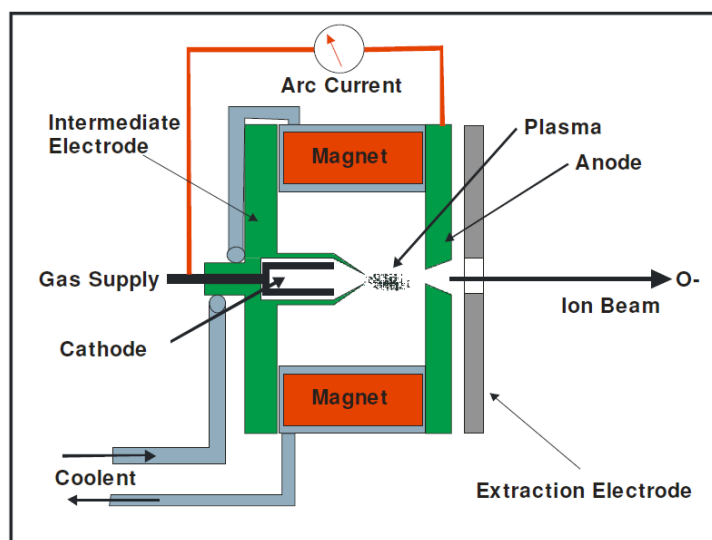


Figure C.12. A diagram of a duoplasmatron, used for creating the O^- ion beam (Craven, 2006).

Once the secondary ions have been produced, due to the angle of interaction they are passed into a high sensitivity double focussing mass spectrometer. This mass spectrometer uses both an electrostatic and a magnetic prism to focus the sample onto the detector. An energy filter in the electrostatic sector (an electrostatic prism) is used to split the beam into different energies by having voltages of differing polarity on the inner and outer surface of the prism, a portion of the split ion beam can then be selected using an energy window slit to filter the beam by energy (Higson, 2004; de Hoffmann & Stroobant, 2007). The selected beam is then passed into the magnetic sector of the mass spectrometer where a magnetic prism is used to filter the beam by mass. This mass filtering splits the beam again, allowing the selection of a single elemental and isotopic mass which is passed to the detector to count the number of instances of this isotope in the beam (Higson, 2004; de Hoffmann & Stroobant, 2007).

The detector used for this project was a discrete dynode electron multiplier (Figure C.13) which amplifies the signal to a detectable limit with a background count rate of down to 0.01 counts per second (Higson, 2004). Electron multipliers are more sensitive than the previously described Faraday cups (Thomas, 2011). This is achieved by directing the ions onto a series of electrodes (called dynodes), as an ion hits the first dynode (kept at grounding potential) between 1 and 3 secondary electrons are produced and directed to the second dynode (held at a slightly higher positive potential) where yet more secondary electrons are produced. This process continues down the length of the electron multiplier with each dynode at a higher potential than the last (with the last being between +1500V and +3500V), this results in an electron pulse or cascade which is then sent through a pulse amplifier and counted (Craven, 2006; Higson, 2004).

Using this method, only one isotope can be analysed at any one point in time, this means that for each sample spot sufficient time must be given to sequentially analyse each desired element. For the analysis of biogenic carbonates, Ca^{44} is always analysed as it is relatively constant, the ratio of all trace element signals are taken against the calcium signal to give the abundance of the trace element within the CaCO_3 .

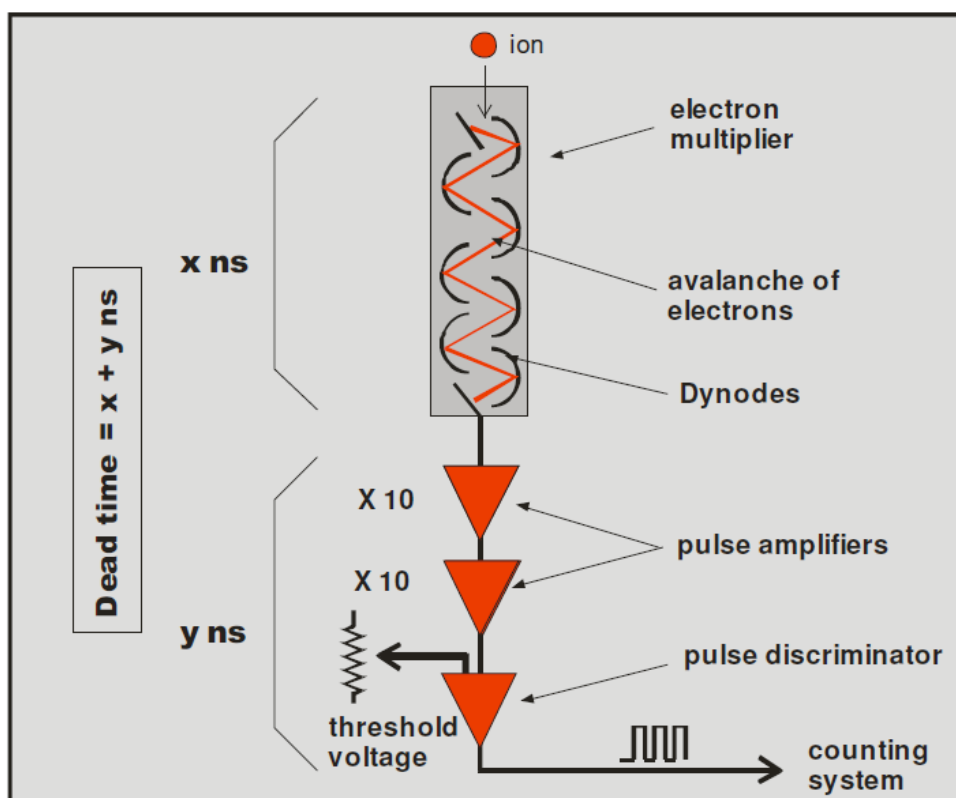


Figure C.13. A diagram of an electron multiplier detector (Craven, 2006).

C.5 Micro-X-Ray Diffraction (μ XRD)

Conventional X-ray diffraction (XRD) uses relatively large amounts of powdered sample to determine the crystal composition of a substance. It does this by utilizing a phenomenon known as diffraction whereby X-rays are directed through the sample where they are scattered or diffracted in a measureable and comparable way by a crystal lattice. The diffracted X-rays are then collected and software is used to produce a diffraction pattern which is comprised of peaks in locations relating to specific crystal planes and structures. Diffraction patterns for unknown compounds or mixtures can be compared to a database of known compounds to determine what crystalline substances are present (Hammond, 2015). The basis of XRD is Bragg's law which allows the calculation of angles within a crystal lattice from scattered X-rays. When incident X-rays have a comparable wavelength to the atomic spacing (d) of the crystalline structure, constructive interference can occur which results in Bragg diffraction (Figure C.14).

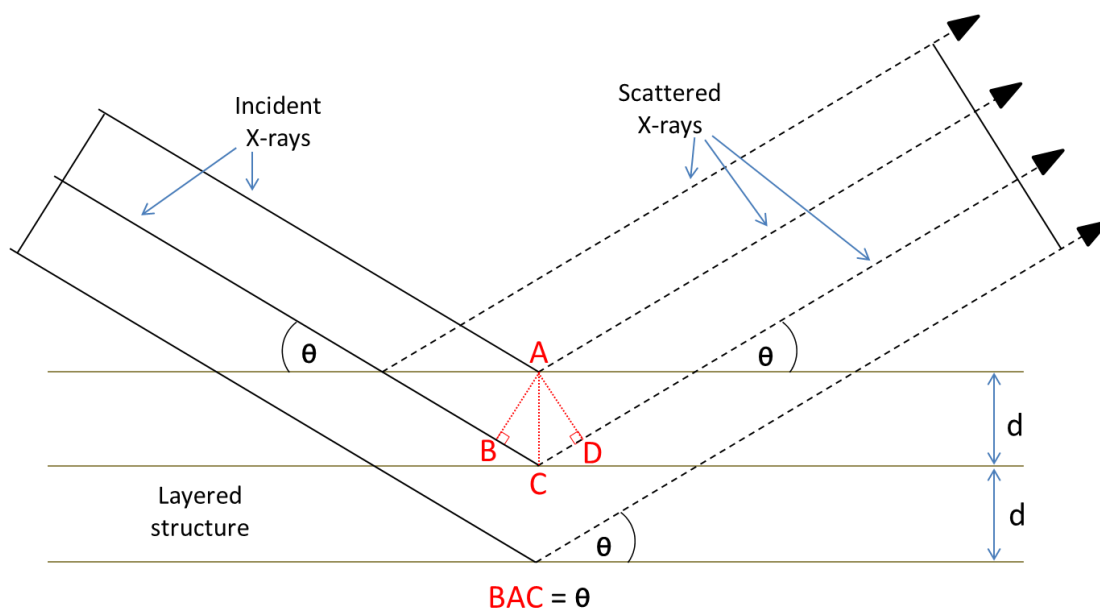


Figure C.14. A diagrammatic representation of Bragg diffraction from a crystalline structure. θ is the angle of incidence of the X-rays (modified from Wilson, 1987).

Bragg's law is described as follows:

$$2d \sin \theta = n\lambda$$

Where d is the spacing between lattice planes, θ is the angle of incidence and λ is the wavelength of the incident beam. Incident rays hitting inner lattice planes travel further (Figure C.14 B-C). When constructive interference of the x-rays occurs, the waves scattered from different lattice planes remain in synchronisation as the value of d is an integer multiple of λ . As

the angle of incidence and the wavelength (λ) of the x-ray are known, the lattice spacing (d) of the unknown crystalline structure can be determined using Braggs law.

μ XRD uses the same principles as conventional XRD, however a much smaller x-ray beam is used, allowing in-situ detection, providing the beam can be transmitted through the sample. The micro X-ray beam is produced using a synchrotron facility which is a type of particle accelerator. The synchrotron used in this study was the Diamond Light Source (DLS) in Didcot, Oxfordshire, where the work was undertaken on the I-18 micro-diffraction beamline. The synchrotron at the DLS produces intense beams of X-rays, infrared beams and ultraviolet light for a range of experimental applications using an electron gun (Figure C.15). The electrons produced by the electron gun are accelerated to close to the speed of light using three particle accelerators, the linear accelerator (linac), the booster ring and the storage ring (Figure 15)(Diamond Light Source, 2017).

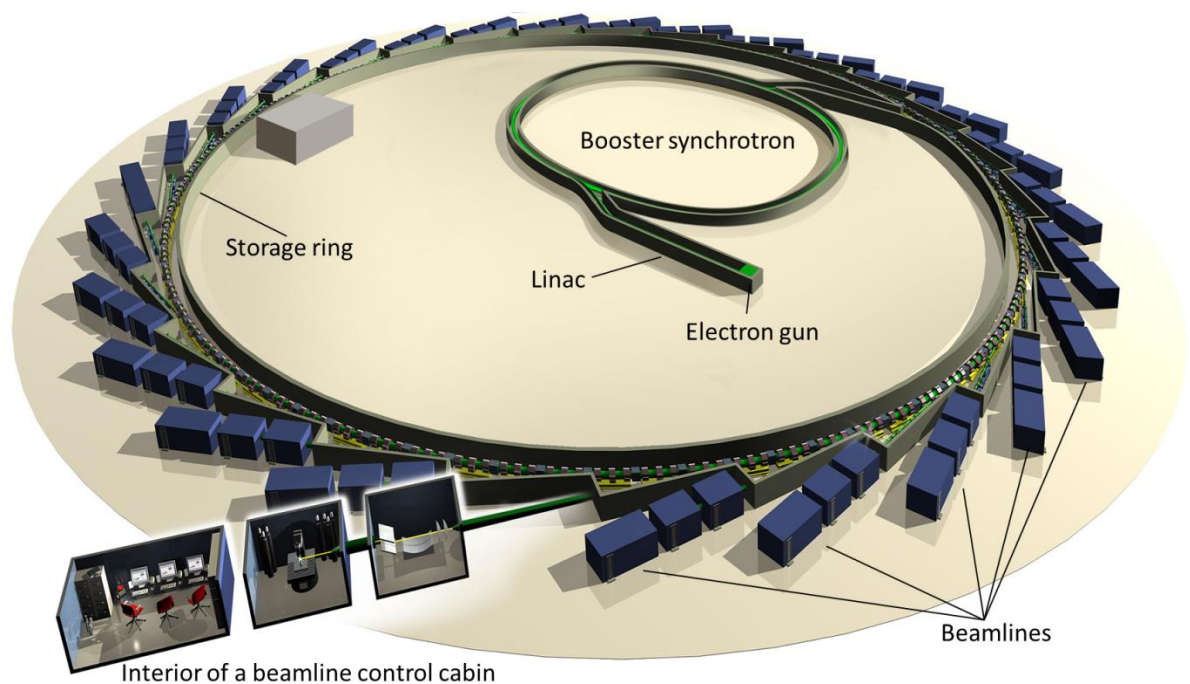


Figure 15. A diagram of the Diamond Light Source facility (Diamond Light Source, 2017).

The electrons are accelerated using a series of large electromagnets that control the direction and speed of the electron beam. As the path of the electrons is bent using both the main storage ring electromagnets and the smaller undulators, the electron beam loses energy in the form of electro-magnetic radiation (light in the broadest sense) which is then transferred to the beamline cabins for experimental work (Diamond Light Source, 2017). The I-18 microfocus spectroscopy beamline used in this study contains an array of apertures, slits and mirrors to produce a concentrated x-ray beam with an energy range from 2.0 – 20.7 ke V (Figure C.16).

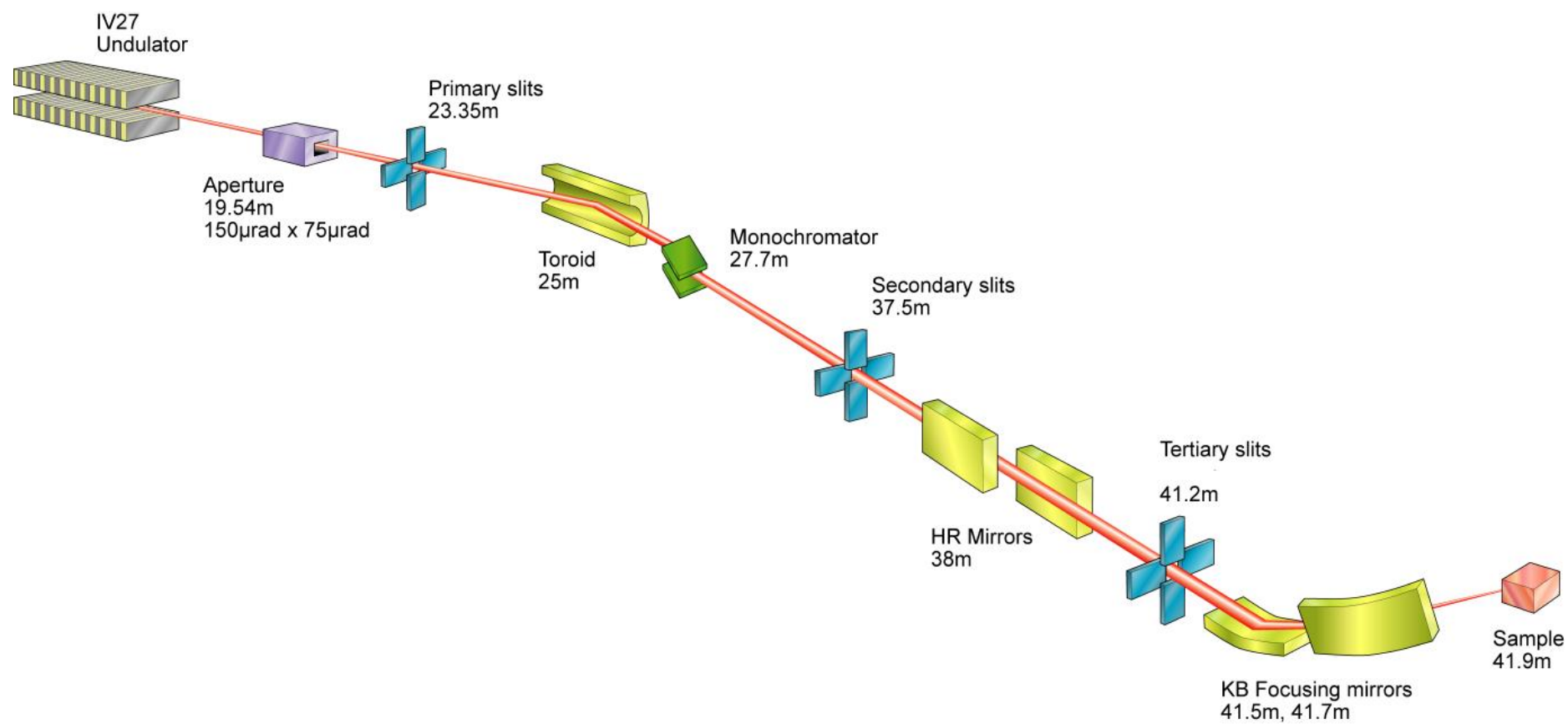


Figure C.16. A schematic diagram showing the I-18 microfocus spectroscopy beamline at the DLS (Mosselmans *et al.*, 2009).

References

- Analytical Instruments (2016) <http://analyticalprofessional.blogspot.co.uk> (accessed 10/10/2016)
- Ardelt D, Polatajko A, Pimm O, Reijnen M (2013) Isotope ratio measurements with a fully simultaneous Mattauch-Herzog ICP-MS. *Anal Bioanal Chem* 405(9):2987-2994
- CETAC technologies (2009) CETAC Aridus II™ desolvating nebulizer system. Operator's manual CETAC Technologies
- Chenery SR, Tye A, Hollyman PR, Clarke D, Winship P, Reijnen M (2015) Analysis of Small Sample Volume Geochemistry Samples by Array Detector ICP-MS. Teledyne CETAC technologies application note: MVX7100-004
- Craven J (2006) Secondary Ion Mass Spectrometry (SIMS) (2006) Edinburgh Ion Microprobe Facility guidebook
- de Hoffmann E, Stroobant V (2007) Mass Spectrometry, principles and applications, third edition. John Wiley and Sons Ltd, Chichester, England
- Diamond Light Source (2017) <http://www.diamond.ac.uk/> (accessed 5/2/2017)
- Ferraro J, Nakamoto K (1994) Introductory Raman Spectroscopy. Academic Press, Inc., New York
- Hammond C (2015) The basics of crystallography and diffraction, fourth edition. International union of crystallography, Oxford University press, Oxford, UK
- Higson SPJ (2004) Analytical Chemistry. Oxford University press, Oxford, UK
- Lewis IR, Edwards HGM (2001) Handbook of Raman Spectroscopy, from the research laboratory to the process line. Marcel Dekker, Inc. New York
- Li Z, Deen MJ, Kumar S, Selvaganapathy PR (2014) Raman spectroscopy for in-line water quality monitoring — instrumentation and potential. *Sensors* 14:17275-17303
- Mosselmans JFW, Quinn PD, Dent AJ, Cavill SA, Moreno SD, Peach A, Leicester PJ, Keylock SJ, Gregory SR, Atkinson KD, Rosella JR (2009). I18 – the microfocus spectroscopy beamline at the Diamond Light Source. *J Synchrotron Radiat* 16:818-824
- Nafie LA (2001) Theory of Raman scattering. In: Lewis IR, Edwards HGM (eds)(2001) Handbook of Raman Spectroscopy, from the research laboratory to the process line. Marcel Dekker, Inc. New York
- Resano M, McIntosh KS, Vanhaecke F (2012) Laser ablation-inductively coupled plasma-mass spectrometry using a double-focusing sector field mass spectrometer of Mattauch–Herzog geometry and an array detector for the determination of platinum group metals and gold in NiS buttons obtained by fire assay of platiniferous ores. *J Anal At Spectrom* 27:165-173
- SPECTRO (2011) SPECTRO MS fully simultaneous ICP-mass spectrometer booklet. SPECTRO analytical instruments. AMETEK materials analysis division
- Thomas R (2011) Practical guide to ICP-MS, a tutorial for beginners. CRC press, Taylor and Francis group. Boca Raton, Florida
- Wilson, M.J., 1987, X-ray powder diffraction methods, in Wilson, M.J. (ed.) A handbook of determinative methods in clay mineralogy, Chapman and Hall, New York

Appendix D:

List of elemental standards used for Solution ICP-MS analysis

Table D.1. A list of all analytical standards used during solution ICP-MS analysis and the contents of each one

Standard name	Concentration (parts per billion)					
	Na	Mg	K	Ca	Fe	Sr
75 CaMaj	750	750	750	75	750	750
50 CaMaj	500	500	500	50	500	500
25 CaMaj	250	250	250	25	250	250
10 CaMaj	100	100	100	10	100	100
	All other elements 0 ppb					
CaQualityControl	500	500	500	50	500	500
	All other elements 5 ppb					
50 ppb Spex	All elements 50 ppb					
25 ppb spex	All elements 25 ppb					
10 pp Spex	All elements 10 ppb					
2.5 ppb spex	All elements 2.5 ppb					
1 ppb spex	All elements 1 ppb					

Appendix E:

NERC Isotope Geosciences Facility Steering Committee (NIGFSC) application for stable isotope support.

Successful - £87,500 in analyses awarded

NIGFSC Use

APPLICATION FOR ISOTOPE GEOSCIENCE SUPPORT

Geochronology & Tracers Facility (NIGL), Stable Isotope Facility (NIGL)
Argon Isotope Facility (AIF), Isotope Community Support Facility (ICSF)

Read the Guidance Notes before completing this form. Submit applications by email to the
NIGFSC Secretary (ilm@bgs.ac.uk) by Wednesday 1st April 2015.



1 Nature of Proposal New ☐ Resubmission ☒ Follow-up ☐ Collaborative ☒ Analysis Only ☐ Previous # IP15071114

2 The Research Project (of which the proposed isotope study forms a part)

2.1 Project Title

Assessing the growth rate of the common whelk in order to help fishery management strategies.

2.2 Principal Investigator (Must be eligible to hold NERC award)

Name: Christopher Richardson Department: School of Ocean Sciences, Bangor University.
Current Post: Professor Address 1: Anglesey
Date Started: 1 May 2011 Phone: 01248 382855 Address 2: UK
email: c.a.richardson@bangor.ac.uk City / Town: Menai Bridge Post Code: LL59 5AB

2.3 Summary of overall research project, including relevant current and recent research

The UK fishery of the common whelk (*Buccinum undatum*) is facing concerns about sustainability (Fahy *et al.*, 2005). The main problem is the inability to accurately age *B. undatum*, which have differing size at age depending on location (Shelmerdine *et al.*, 2007). This has led to difficulties with stock assessments. Current methods of aging focus on the operculum which has been shown to be unusable (Kideys, 1996), the shell is also unusable as it does not show annual growth increments. This study is focused on the statoliths which are small calcium carbonate structures analogous to fish otoliths, which exhibit clear growth rings that appear to have annual periodicity. The aim of this project is to validate the periodicity of statolith ring formation using the geochemistry of the shell to confirm that statoliths are suitable as an aging tool. Several geochemical analyses (e.g. microprobe analysis) are being used to validate the 'annual' increments found in the statolith. The isotope work on the shells of whelks from which the statoliths have been extracted is integral to the project as it forms the basis of the geochemical validation. Trace element sampling of the shell is being undertaken concurrently with Dr. Simon Chenery (BGS).

2.4 Which of the following sources support the investigators and students participating in the project?

NERC Institute Research ☐ NERC Studentship award code: _____
University - Student Research ☒ NERC Grant award code: _____
University - Academic Research ☐ Other awarding body (Name / award code: Bangor University/CEFAS - Award code n/a

3 The Isotope Project

3.1 Personnel (PI, Co-investigators, Students, facility staff etc.) A: Will be involved in sample analysis. T: Will require training.

Name	Position	Institute	Role in Project	A	T
Prof. Chris Richardson	Head of School	Bangor University	Principal Investigator	<input checked="" type="checkbox"/>	<input type="checkbox"/>
Prof. Melanie Leng	Head of Stable Isotope Facility	NIGL	Facility Staff	<input checked="" type="checkbox"/>	<input type="checkbox"/>
Dr. Simon Chenery	Senior analytical Geochemist	BGS	Co-investigator	<input checked="" type="checkbox"/>	<input type="checkbox"/>
Mr. Philip Hollyman	PhD Student	Bangor University	Student	<input checked="" type="checkbox"/>	<input checked="" type="checkbox"/>
				<input type="checkbox"/>	<input type="checkbox"/>

3.2 Project timing

PhD / grant start date: Samples available: If timing is critical, why?
Finish date: Results required:

3.3 Objectives of the isotope project

The objective of the isotope analyses is to reconstruct seawater temperature profiles from samples drilled systematically around ten shells from three locations with differing seawater temperature profiles, this will be coupled with the reconstruction of trace element profiles from the same samples. The aim of these analyses is to directly relate the growth and ring formation in the statoliths with the growth (via the temperature reconstructions assuming equilibrium carbonate precipitation) in the shell. Owing to the small size of the statoliths (~300µm), stable isotope analysis cannot be undertaken with the required resolution, therefore trace elements will be used instead using Secondary Ion Mass Spectrometry (SIMS). The reasoning for undertaking both isotope and trace element analysis on the shell is to allow the oxygen isotope profiles to act as a calibration for the trace elements, which will be directly compared with the statoliths. This will allow a comparison of the periodicity of line formation in the statoliths to the reconstructed temperature profiles of the shell, allowing us to confidently validate the periodicity of the statolith growth increments.

3.4 Working hypothesis or model to be tested

We hypothesize that samples drilled at a high resolution around the whorl of the shells will allow us to reconstruct and identify temperature cycles using $\delta^{18}\text{O}$ as a temperature proxy (assuming equilibrium precipitation). This will allow us to quantifiably assess the seasonal (annual) cycles present in the growth of the shell and the winter and summer temperatures between our three chosen sites. These samples will also be used to reconstruct trace element profiles alongside the isotope based temperatures. SIMS will be subsequently employed to analyse the trace elements along a growth transect inside a statolith from the same whelk, this trace element profile will be compared with trace elements from the shell. We hypothesize that there will be an agreement between the trace element profiles from the statolith and shell which can be directly compared to the seawater temperature reconstruction, allowing us to directly validate the number of growth increments present in the statolith. $\delta^{13}\text{C}$ data gathered will be a proxy for productivity and source of ingestible carbon.

3.5 Manner in which the isotope data are expected to contribute to the objective

The isotope data produced will form the groundwork of the entire geochemical portion of the project. All of the subsequent trace element analysis will be referred back to the isotope work for validation. Without the isotope work, the trace element work would have to rely on existing proxies for seawater temperature in shell material (e.g. Sr:Ca) which would not be as robust as a full reconstructed temperature profile.

3.6 Information to be provided in a preparatory report as a prerequisite to commencing analytical work

The trace element data will be produced ahead of the stable isotope analysis which will confirm preservation and provide some indication of age.

3.7 PhD students - outline the significance of the support requested to the overall thesis

The aim of my PhD project is to develop methods which will enable fisheries scientists to use whelk statoliths for age determination, allowing for comprehensive stock assessment and fishery management. The project is at the midway point and the monthly sampling effort looking to pinpoint the timing of line formation is almost complete (two months remain). Whilst these samples will allow the timing of the growth line to be established they can only cover one annual cycle in the timescale of the project. Whilst this is useful, the ability to retrospectively show that all of the growth lines are a result of a cessation of growth at the same point of an annual cycle will be invaluable. It will lend unquestionable credibility to the field and laboratory experiments. Once the geochemical validation is completed, the aging methods developed will then be employed on several different populations to test the reliability of the developed methods. The PhD is a collaborative project between Bangor University, BGS and CEFAS with supervisors in each of these institutions (Dr. Simon Chenery from BGS). From the initial concept of this project, geochemical analysis was clearly identified to be a necessary and major component, which relies on the ability to solidly reconstruct the temperature from the shells.

3.8 Analyses requested

Type of isotope analysis	Describe sample material	No. of analyses
$\delta^{18}\text{O}$ (and $\delta^{13}\text{C}$)	shell carbonate	10 x c. 100

3.9 NERC Science Themes (enter decimal fractions)

<input type="checkbox"/> Earth System Science	<input type="checkbox"/> Technologies
<input type="checkbox"/> Biodiversity	<input type="checkbox"/> 1 Sustainable use of natural resources
<input type="checkbox"/> Climate Systems	<input type="checkbox"/> Environmental pollution and health
<input type="checkbox"/> Natural Hazards	

3.10 NERC Research areas (enter decimal fractions)

<input type="checkbox"/> Atmospheric Science	<input type="checkbox"/> Polar Science
<input type="checkbox"/> Earth Science	<input type="checkbox"/> 0.2 Science-based Archaeology
<input type="checkbox"/> Earth Observation	<input type="checkbox"/> Terrestrial and Freshwater Science
<input type="checkbox"/> 0.8 Marine Science	

3.11 Project Description

The Project Description should be a largely self-contained justification of the proposed isotope project and must not exceed three sides of 11 point (minimum), single spaced text including references, tables and figures. Colour may be used if desired. The Project Description should be prepared in Microsoft Word, or a compatible word processor, and submitted by email along with the application.

4 Research experience of Principal Investigator**4.1 Relevant research experience including recent publications**

I have extensive experience and I have published >50 papers on the Sclerochronology of molluscs and I have developed methodologies for interpreting growth in molluscs using shell sectioning. I have investigated the elemental composition of shells using Laser-ablation Inductively Coupled Plasma Mass Spectrometry (LA-ICP-MS) and reconstructed seawater temperature in mollusc shells using stable oxygen isotopes. I have validated annual and tidal patterns in mollusc shells using laboratory and field experiments and studied the structure of statoliths using light microscopy and scanning electron microscopy. I have supervised 22 PhD students to completion and currently I am supervising 4 PhD students.

Selected publications:

SAUREL, C., BARROSO, C.M. & THAIN, J. 2005. An evaluation of the age of the red whelk *Neptunea antiqua* using operculum striae, statolith growth rings and elemental ratios in the shell. *J EXP MAR BIOL ECOL*, 325, 55-64.
 CHATZINIKOLAOU, E. & RICHARDSON, C.A. 2007. Evaluating the growth and age of the netted whelk *Nassarius reticulatus* (gastropoda: nassaridae) from statolith growth rings. *MAR ECOL-PROG SER*, 342, 163-176.
 WANAMAKER, A.D. Jr, BUTLER, P.G., SCOURSE, J.D. HEINEMEIER, ERIKSSON, J., KNUDSEN, K.L. & RICHARDSON, C.A. 2012. Surface changes in the North Atlantic meridional overturning circulation during the last millennium. *NAT COMMUN*, 3:899.
 RICHARDSON, C.A., KINGSLEY-SMITH, P., SEED, R. & CHATZINIKOLAOU, E. 2005. Age and growth of the naticid gastropod *Polinices pulchellus* (Gastropoda: Naticidae) based on length frequency analysis and statolith growth rings. *MAR BIOL*, 148, 319-326.

4.2 Applications made to NIGFSC during the last five years.

Application No.	Progress made, publications and other outputs

5. Authorisation

Submitted forms must be approved by the PI, Head of Department, and any Student involved. Facility Staff who have seen the proposal should also note this below.

By checking the box below, you confirm that you agree to the following conditions of access to the isotope facility. For full terms and conditions see guidance notes.

- The support provided through NERC should at least be acknowledged in all relevant publications; co-authorship with NERC Isotope Geosciences facility staff will often be more appropriate.
- Results arising from a NERC isotope allocation are not the sole property of the applicant, but are jointly owned by NERC and the applicant.
- Investigators in receipt of a NERC isotope allocation are required to supply bibliographic references and/or copies of publications (including PhD theses and non refereed publications), which discuss or describe NERC isotope data.

	Name	Approved	Date
Principal Investigator:	Professor Chris Richardson	<input checked="" type="checkbox"/>	19/02/2015
Head of Department:	Professor Chris Richardson	<input checked="" type="checkbox"/>	19/02/2015
Student (if applicable):		<input type="checkbox"/>	

	Name	Seen / discussed	Date
Facility Staff:	Melanie Leng	<input checked="" type="checkbox"/>	24/03/2015
Facility Staff:		<input type="checkbox"/>	

Section 3.11 – Project description

Assessing growth rate of the common whelk in order to help fishery management strategies

Buccinum undatum (the common whelk) is of commercial interest in several countries throughout Northern Europe including the UK. The UK is the largest producer of whelks in Europe (Heude-Berthelin *et al.*, 2011). In 2013 20,000 tonnes of *B. undatum* were landed in the UK with a market value of £13.7 million, accounting for roughly 9% of the total UK shellfish landings by weight and 3% of the total UK shellfish landings by value (MMO, 2014). There has been a dramatic rise in the landings of whelks in the UK due to an increase in the export market to places such as South Korea and Japan (Fahy *et al.*, 2005). Whilst an increase in foreign exports is favourable from an economic standpoint, it has drastically increased pressure on a species which is vulnerable to overexploitation. Currently there are overly simplistic fisheries regulations in place in the UK, the only widespread enforcement being a MLS (Minimum Landing Size) of 45mm shell height. The 45mm shell height came from an EU regulation which has been shown to be wholly inadequate in several studies (Shelmerdine *et al.*, 2007; Heude-Berthelin *et al.*, 2011). The reason that the MLS is inadequate is that *B. undatum* has been shown to have differing size at age and age at maturity with geographical location (Shelmerdine *et al.*, 2007). Whilst the species can reach the MLS within 3 years, at this age the whelks may often have not yet reached maturity.

Several key characteristics of the biology and behaviour of *Buccinum undatum* makes them vulnerable to overfishing. They live a largely sedentary life style and also have direct larval development which can lead to 'closed' populations (Shelmerdine *et al.*, 2007). This coupled with a variable growth rate results in a species that is potentially at risk when exposed to fishing pressure. Fishery declines due to fishing pressure especially in Ireland (Fahy *et al.*, 2005), England (Nicholson and Evans, 1997) and the southern North Sea (Ten Hallers-Tjabbes *et al.*, 1996) have been reported and all show clear declines in stock through reductions in CPUE (Catch Per Unit Effort). Several previous attempts at stock assessment of whelk populations have been undertaken, however, none of these have successfully established the scale of the fishable stock of whelks present in a population (e.g. Morel & Bossy, 2004). The methods used to assess whelk stocks lack the ability to incorporate reliable ageing techniques to determine the population structure and size at age, which is critical for assessing the impact of fishing activities on the immature portion of a population. Current ageing methods focus on growth increments found in the operculum of the whelk (Kideys, 1996; Shelmerdine *et al.*, 2007), as the shell does not exhibit annual rings. Current literature suggests that the visible lines on the operculum form due to the cessation of feeding during the reproductive cycle which also occurs during the summer months. Unfortunately, the operculum is often unclear and unreliable causing many studies to discount a large proportion of the sample which could potentially bias the data. For example Kideys (1996) only classed 16% of opercula as 'clear'. The use of growth rings on the operculum for estimating the age of whelks is currently supported by only one study by Santarelli and Gros (1985) who reconstructed the temperature of three whelk shells by drilling samples at regular intervals and analysing the oxygen isotope composition. The number of annual cycles (which were unclear) matched the number of visible growth lines on the operculum and this was seen as confirmation of an annual periodicity. No recent work has been undertaken to improve on this study, benefiting from the use of modern techniques to match the temperature records in the shell with temperature records in the operculum for clear validation.

A more recent addition to the field of gastropod ageing is the use of statolith microstructures, which contain high resolution archives of growth histories. The gastropod statolith is a small structure of calcium carbonate found within the statocysts, located in the foot of the gastropod in the locality of the pedal ganglion (Fretter & Graham, 1994; Richardson, 2001). They are used for equilibrium and help the animal to determine the direction of gravity

much like the otoliths of a fish. Several studies have highlighted the annual periodicity of growth rings contained within the statoliths of marine gastropods which resemble tree rings (Chatzinikolau & Richardson, 2007). To date, no research has been undertaken to investigate the suitability of *B. undatum* statoliths for age determination. The aim of the current study is to investigate the statoliths of *B. undatum* and assess their potential use as an ageing method for use in stock assessment. This will be undertaken using several different approaches to validate the periodicity of the growth lines exhibited within the statoliths. Field and laboratory experiments are underway to pinpoint the timing of line formation by collecting monthly samples of 50 individuals from a single population in the Menai Strait (North Wales, UK) and assessing the appearance of growth rings during statolith development month by month (i.e. marginal increment analysis - MIA). Simultaneously, juvenile whelks have been hatched and reared from egg capsules and the deposition of the statoliths in the first year of growth is being investigated through regular sampling and assessment of statolith development. In this proposal we aim to investigate the periodicity of the rings within the statolith carbonate using trace element microchemistry, calibrated through the trace element and isotope variability in the whole shell carbonate:

Geochemical validation of seasonality of shell growth: There are no apparent growth rings on the surface of the whelk shell that can be used to determine their age. The aim of the proposed study is to investigate whether there is seasonality of shell growth. Using oxygen and carbon isotope ratios in the shell carbonate of *B. undatum*, seasonal seawater temperature/productivity cycles will be reconstructed and linked with trace element variations (in particular Sr/Ca) in the shell and seasonal seawater temperature records. A relationship between shell growth and reconstructed seawater temperature will be demonstrated and verified following a comparison with the recorded seawater temperature at the time of shell deposition. Three sites covering a range of annual temperature regimes have been chosen for comparison, the Shetland Isles (as a northern latitude colder water example), the Menai Strait (as an intermediate site) and Jersey (as a warmer water southern latitude site). A successful application has been made to the NERC Ion Microprobe facility to investigate the seasonal variation in carbonate geochemistry in the statoliths removed from the whelks whose shells will be analysed in this application. This will allow a comparison of the age of the whelks to be determined from the shell (this application) and from the statolith (Ion microprobe application).

Together with Professor Melanie Leng (NIGL) we have developed the methodology for drilling shell carbonate samples for geochemical analyses. 100 shell carbonate samples of $\approx 1\text{mm}$ width every 2mm will be drilled from around the shell using a hand drill (Fig.2a). Approximately 30 samples per year assuming an average life span of 3 years will be obtained. These samples will be split into two aliquots (≈ 500 micrograms). One part will undergo trace element analysis (primarily for the most abundant elements e.g. Sr, Mg, Ba, Mn) by solution ICPMS, whilst the other aliquot will be used for stable isotope analysis. Assuming precipitation of the carbonate in equilibrium with seawater we will be able to calculate seawater temperature at the time of deposition of the shell through time. In the pilot study utilising the shell of a mature female from the Menai Strait (intermediate site)(Fig. 1) we measured a $\delta^{18}\text{O}$ variation of 2.5 per mil (between winter and summer cycles), using the established relationship between oxygen isotopes of shell carbonate and oxygen isotopes of water (which in this marine setting we assume does not change seasonally and is distant from freshwater inputs) this equates to a seasonality of $c.10^\circ\text{C}$, which is in line with known seasonal temperature changes in the Menai Strait. There is also a clear relationship between $\delta^{18}\text{O}$ and ^{88}Sr meaning that we can potentially derive temperatures from the shell Sr data via an equation: $\delta^{18}\text{O} = -1.0548 + 0.0009 \times ^{88}\text{Sr}$.

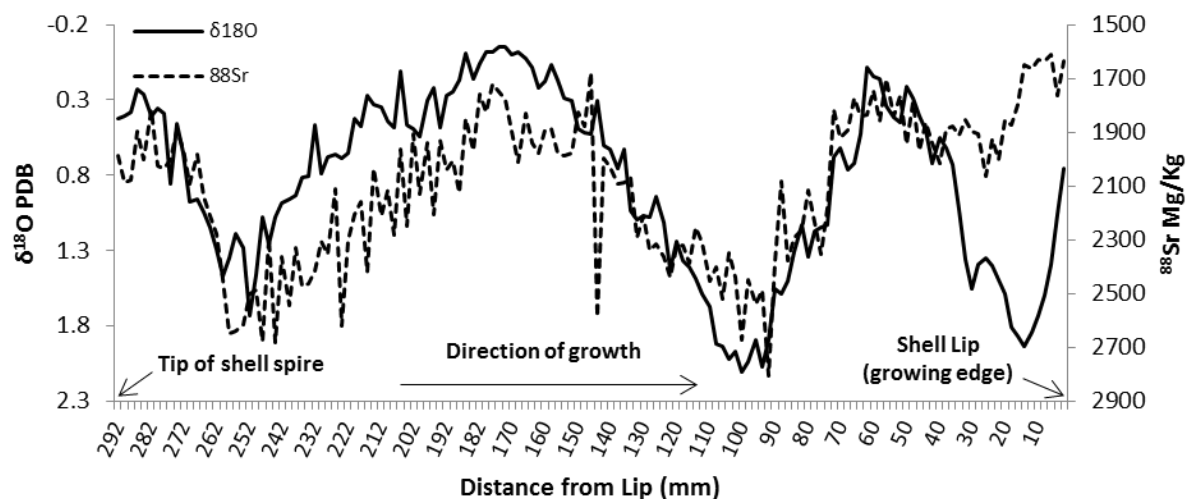


Fig. 1. The results of the pilot study showing a clear relationship between $\delta^{18}\text{O}$ and ^{88}Sr . The clear cyclicity in the data is indicative of a strong annual temperature signal. The $\delta^{18}\text{O}$ signal also has a good agreement with SST (not shown) at the sample site. The offset in $\delta^{18}\text{O}$ and ^{88}Sr in the most recent part of the shell is thought to be due to the onset of sexual maturity, this will be investigated further with this application.

To expand on the pilot study and strengthen the findings, a further four *B. undatum* shells will be analysed from the Menai strait alongside three shells from both the Shetlands and Jersey, using the same techniques. The five shells from the Menai strait will allow us to investigate the observed offsets between ^{88}Sr and $\delta^{18}\text{O}$ during differing maturity stages whilst also allowing the establishment of a chronology for shell $\delta^{18}\text{O}$ profiles in the Menai Strait (after Gentry *et al.*, 2008). Alongside the pilot shell from a mature female, the Menai Strait shells will consist of one further mature female, two mature males and an immature animal. The three shells from the Shetlands and Jersey will allow for smaller chronologies to be created from mature animals allowing for a comparison of the growth rates in the differing temperature regimes at the three sites. Subsequently, statoliths from the same whelks will be analysed for TE using Ion Microprobe analysis (NERC Microprobe application has been accepted, analyses booked for April 2015) as the statoliths are too small to be analysed directly via standard techniques. Sr will be targeted within the statoliths as the pilot study has highlighted a strong relationship between shell ^{88}Sr and $\delta^{18}\text{O}$.

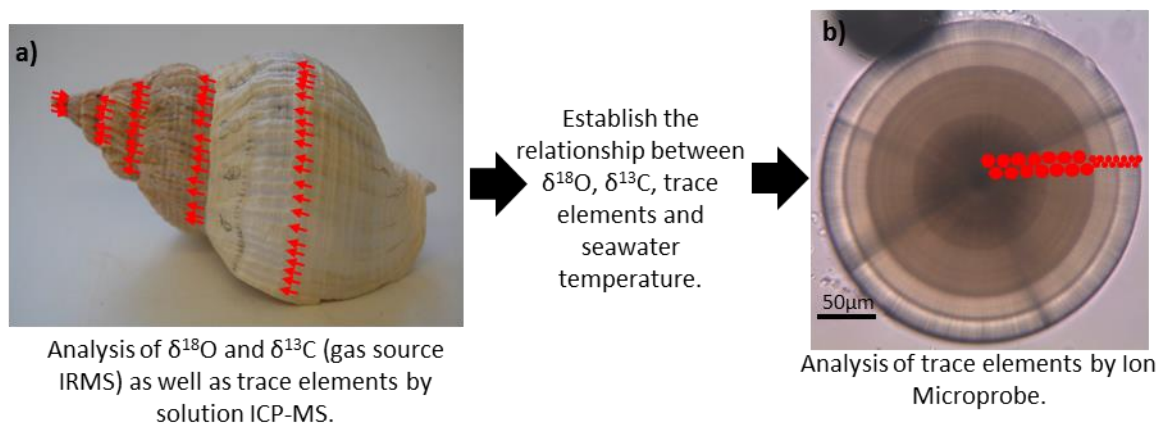


Fig. 2. The proposed sampling methodology. **a)** A Photograph of a whelk shell with drill sampling tracks marked with red arrows around the whorl of the shell. **b)** Photomicrograph showing the growth rings in the statolith of *B. undatum*, as well as the proposed sampling techniques. The black arrows indicate the growth increments. The red dots represent the proposed 5-10 micron pits for abundant trace elements (successful application to the NERC Ion Microprobe facility).

Statoliths have never before been used to determine seasonal changes in geochemistry to understand growth cycles of the shell of gastropods. We anticipate that seasonal trace element profiles in the shells will reflect those found in the statolith and validate an annual

periodicity between the statolith growth rings and shell growth. The statolith growth rings will then be used to assess seasonality of shell growth and formation. The rationale behind using the Stable Isotope Facility is to receive scientific support from Professor Leng who has worked on mollusc shells from a variety of environments. The trace element analyses will take place at BGS with Dr Simon Chenery, a long term collaborator with the PI and co-supervisor of the student Phil Hollyman. Thus, all analytical work will be undertaken by a team within the same institution. Assessing seasonality in the common whelk could also be used in archaeological research as these gastropods are found extensively in midden structures.

References:

- Chatzinikolaou, E. and Richardson, C.A.** (2007) Evaluating growth and age of netted whelk *Nassarius reticulatus* (Gastropoda: Nassariidae) using statolith growth rings. *Marine Ecology Progress Series* 342, 163-176.
- Fahy, E., et al.** (2005) Fishery associated changes in the whelk *Buccinum undatum* stock in the southwest Irish Sea, 1995-2003. *Irish Fisheries Investigations*, 15, 26pp.
- Fretter, V. and Graham, A.** (1994) British Prosobranch Molluscs: their functional anatomy and ecology. Printed for the Ray Society, London. Revised and updated edition, 820pp.
- Gentry, D. K., et al.** (2008) Stable Isotope and Sr/Ca profiles from the marine gastropod *Conus ermineus*: Testing a multiproxy approach for inferring paleotemperature and paleosalinity. *Palaios* 23, 195-209.
- Hancock, D.A.** (1963) Marking experiments with the commercial whelk (*Buccinum undatum*). *ICNAF Special Publication* 4, 176-187.
- Heude-Berthelin, C., et al.** (2011) Growth and reproduction of the common whelk *Buccinum undatum* in west Cotentin (Channel), France. *Aquatic living resources* 24, 317-327. DOI: 10.1051/alr/2011048.
- Kideys, A.E.** (1996) Determination of age and growth of *Buccinum undatum* L. (Gastropoda) off Douglas, Isle of Man. *Helgolander Meeresuntersuchungen* 50, 353-368.
- Morel, G.M. and Bossy, S.F.** (2004) Assessment of the whelk (*Buccinum undatum* L.) population around the Island of Jersey, Channel Isles. *Fisheries Research* 68, 283-291.
- Nicholson, G.J. and Evans, S.M.** (1997) Anthropogenic impacts on the stocks of the common whelk *Buccinum undatum* (L.). *Marine Environmental Research* 44, 305-314.
- Radford, L.** eds. (2014) UK sea fisheries statistics 2013. *Marine Management Organisation*, 178pp.
- Richardson, C.A.** (2001) Molluscs as archives of environmental change. *Oceanography and Marine Biology - An Annual Review* 39, 103-164.
- Santarelli, L. and Gros, P.** (1985) Age and growth of the whelk *Buccinum undatum* L. (Gastropoda: Prosobranchia) using stable isotopes of the shell and operculum striae. *Oceanologia Acta* 8, 221-229.
- Shelmerdine, R.L., et al.** (2007) Size variation of the common whelk, *Buccinum undatum*, over large and small spatial scales: Potential implications for micro-management within the fishery. *Fisheries Research* 86, 201-206.
- Ten Hallers-Tjabbes, C.C., et al.** (1996) The decline of the North Sea whelk (*Buccinum undatum* L.) between 1970 and 1990: a natural or human-induced event?. *PSZN I: Marine Ecology* 17, 333-343.

Appendix F:

Custom MATLAB script used to create average oxygen isotope profiles from multiple individual shell profiles.

Date to day of the year function – necessary for main script

```
function [doy,fraction] = date2doy(inputDate)

%DATE2DOY Converts the date to decimal day of the year.

% [doy,fraction] = date2doy(inputDate)

% Descriptions of Input Variables:

% inputDate: Input date as a MATLAB serial datenum

% Descriptions of Output Variables:

% doy: Decimal day of the year. For instance, an output of 1.5 would
%     indicate that the time is noon on January 1.

% fraction: Outputs the fraction of a year that has elapsed by the input
%     date.

% Example(s):

% >> [doy,frac] = date2doy(datenum('1/25/2004'));

% See also:

% Author: Anthony Kendall

% Contact: anthony [dot] kendall [at] gmail [dot] com

% Created: 2008-03-11

% Copyright 2008 Michigan State University.

%Want inputs in rowwise format

[doy,fraction] = deal(zeros(size(inputDate)));

inputDate = inputDate(:);

%Parse the inputDate

[dateVector] = datevec(inputDate);

%Set everything in the date vector to 0 except for the year

dateVector(:,2:end) = 0;

dateYearBegin = datenum(dateVector);

%Calculate the day of the year
```

```
doyRow = inputDate - dateYearBegin;

%Optionally, calculate the fraction of the year that has elapsed
flagFrac = (nargout==2);
if flagFrac
    %Set the date as the end of the year
    dateVector(:,1) = dateVector(:,1) + 1;
    dateYearEnd = datenum(dateVector);
    fracRow = (doyRow - 1) ./ (dateYearEnd - dateYearBegin);
end
%Fill appropriately-sized output array
doy(:) = doyRow;
if flagFrac
    fraction(:) = fracRow;
end
```

Main profile averaging script – ‘tpred’ function can be changed to alter interpolation resolution

```
function [tpred,out]=Hollyman;
% Interpolate data onto the first day of each
% calendar month using cubic splines then average
OUTFILE='T3 Out.csv';
FILE='T3.xlsx'; % Data file name
nsheet=2; % Number of sets of data
tpred=2013:1/365:2017; % Dates that data is interpolated to
% 1/12 is step size (e.g. change to 1/52 to weekly)
nt=length(tpred);
```

```
out=zeros(nsheet,nt);

for SHEET=1:nsheet;

[NUM,TXT,RAW]=xlsread(FILE,SHEET);

z=NUM;

% Converting the date to decimal
inputDate=datenum(TXT(2:end,2),'dd-mm-yy');

[y,m,d]=datevec(inputDate);

[doy,fraction] = date2doy(inputDate);

t=y+fraction;

save test

% Interpolate using splines
yinterp = interp1(t,z,tpred,'spline');

% Removes interpolation outside bound of data
yinterp(tpred<min(t))=NaN;
yinterp(tpred>max(t))=NaN;

out(SHEET,:)=yinterp;

end

% average interpolations
out=nanmean(out);

% save average
dlmwrite(OUTFILE,[tpred' out'], 'precision',8);
```


Appendix G:

Elemental relationship plots from *Buccinum undatum* shell analyses presented in Chapter 4.

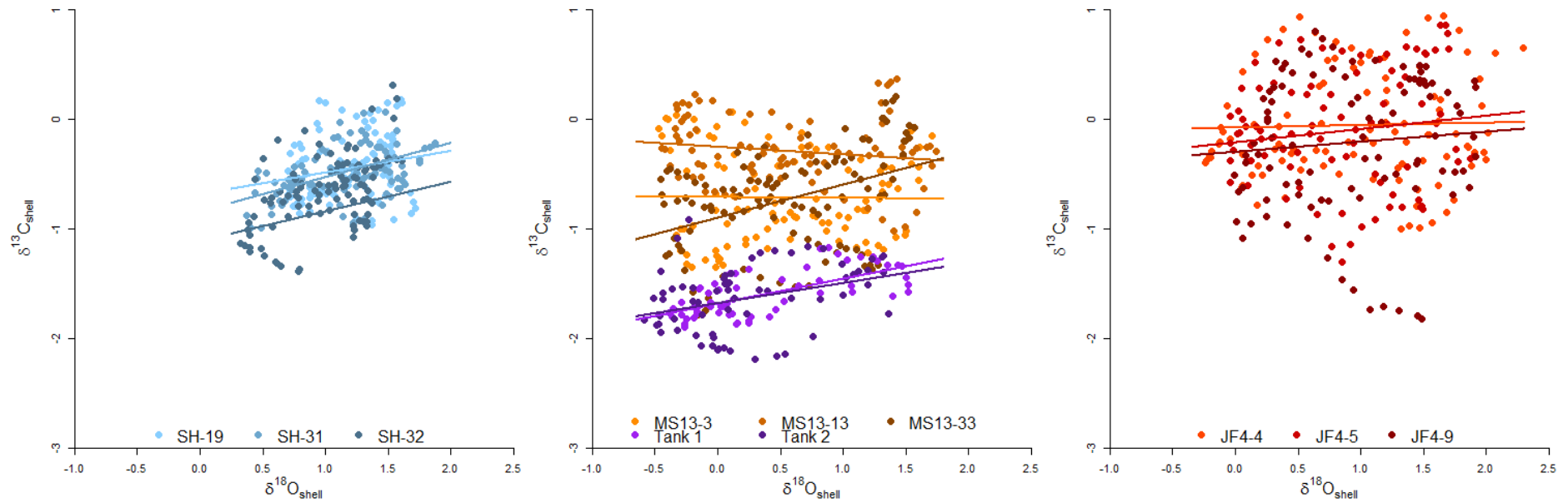


Figure G.1. Scatter plots of $\delta^{13}\text{C}$ against $\delta^{18}\text{O}$ for each shell from Shetland (a), male adults from the Menai Strait and laboratory reared juveniles (b) and Jersey (c). The data from each shell are fitted with a linear line of best fit of the matching colour.

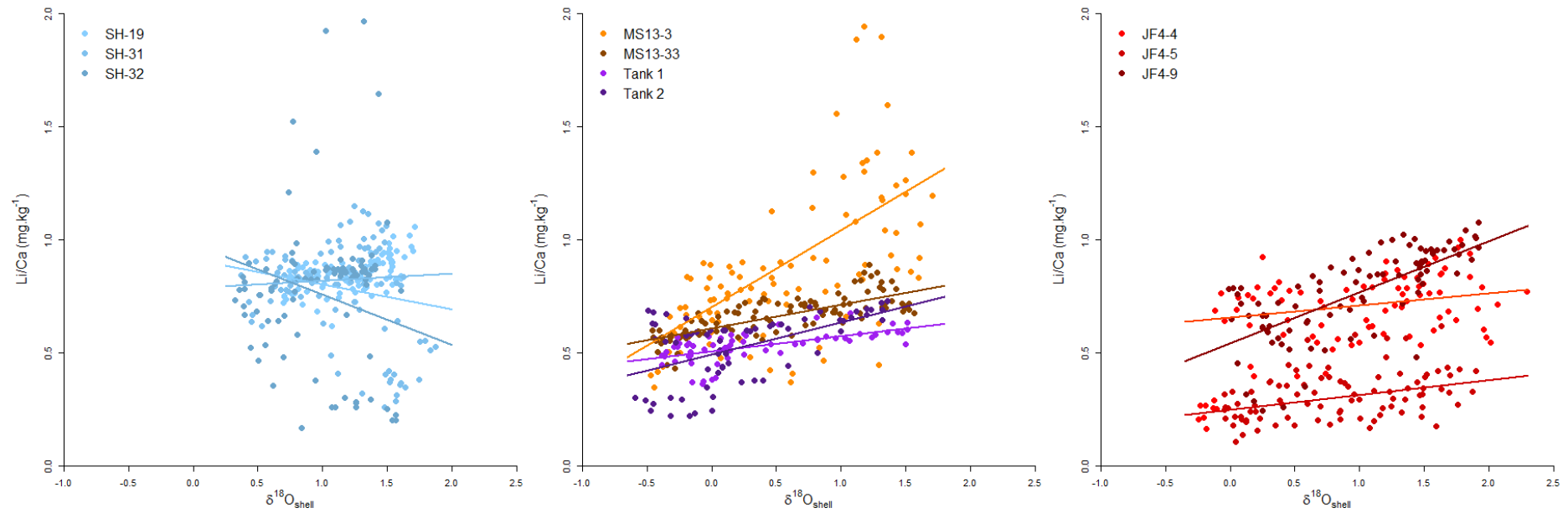


Figure G.2. Scatter plots of Li/Ca against $\delta^{18}\text{O}$ for each shell from Shetland (a), male adults from the Menai Strait and tank grown juveniles (b) and Jersey (c). The data from each shell are fitted with a linear line of best fit of the matching colour.

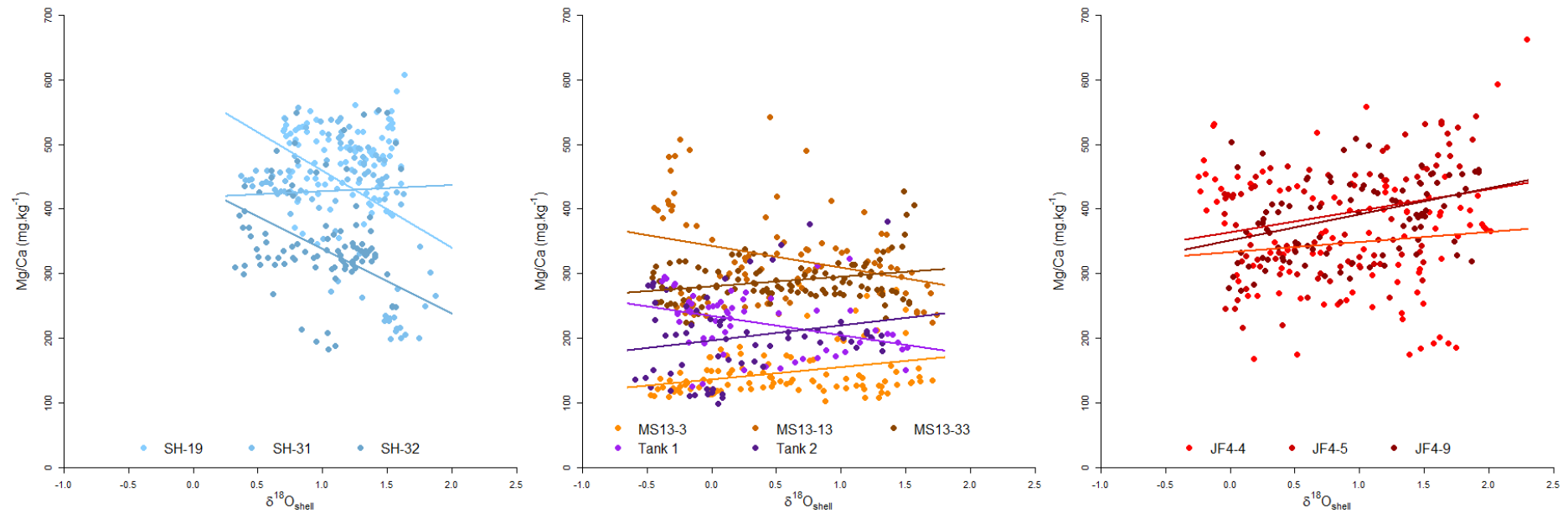


Figure G.3. Scatter plots of Mg/Ca against $\delta^{18}\text{O}$ for each shell from Shetland (a), male adults from the Menai Strait and laboratory reared juveniles (b) and Jersey (c). The data from each shell are fitted with a linear line of best fit of the matching colour.

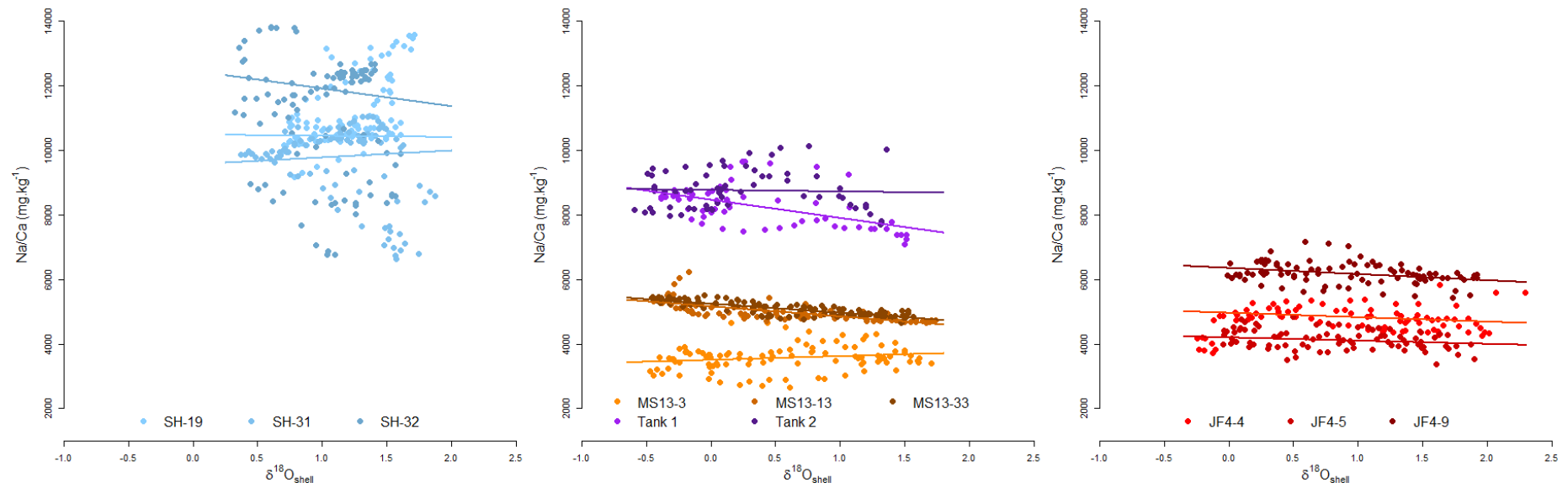


Figure G.4. Scatter plots of Na/Ca against $\delta^{18}\text{O}$ for each shell from Shetland (a), male adults from the Menai Strait and laboratory reared juveniles (b) and Jersey (c). The data from each shell are fitted with a linear line of best fit of the matching colour.

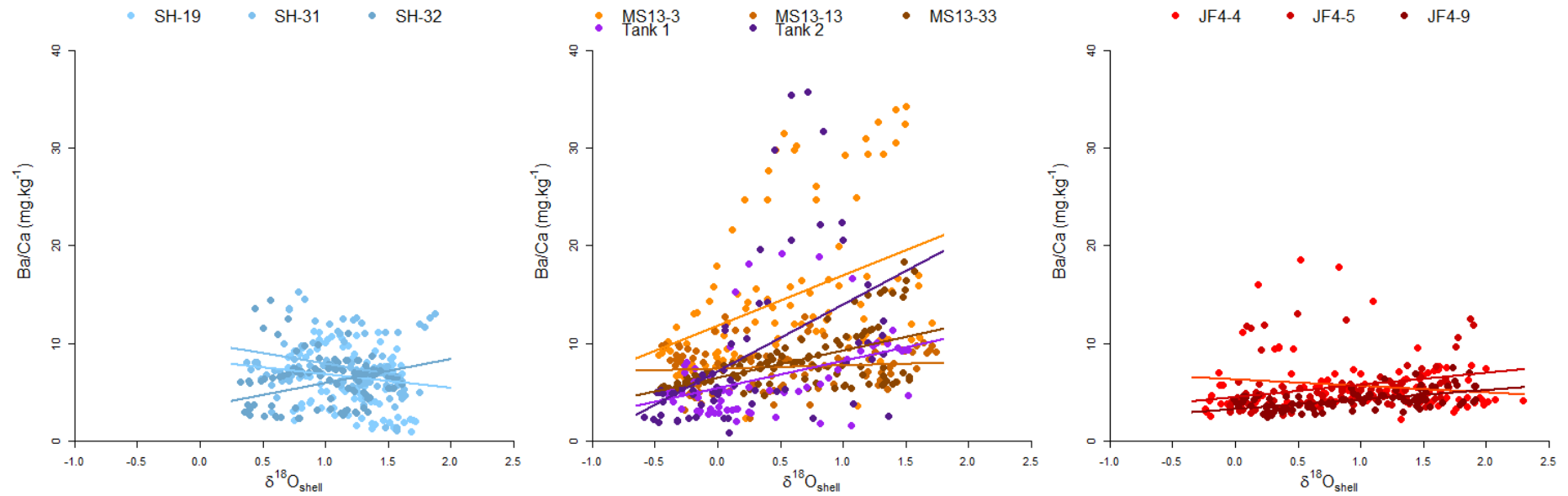


Figure G.5. Scatter plots of Ba/Ca against $\delta^{18}\text{O}$ for each shell from Shetland (a), male adults from the Menai Strait and laboratory reared juveniles (b) and Jersey (c). The data from each shell are fitted with a linear line of best fit of the matching colour.

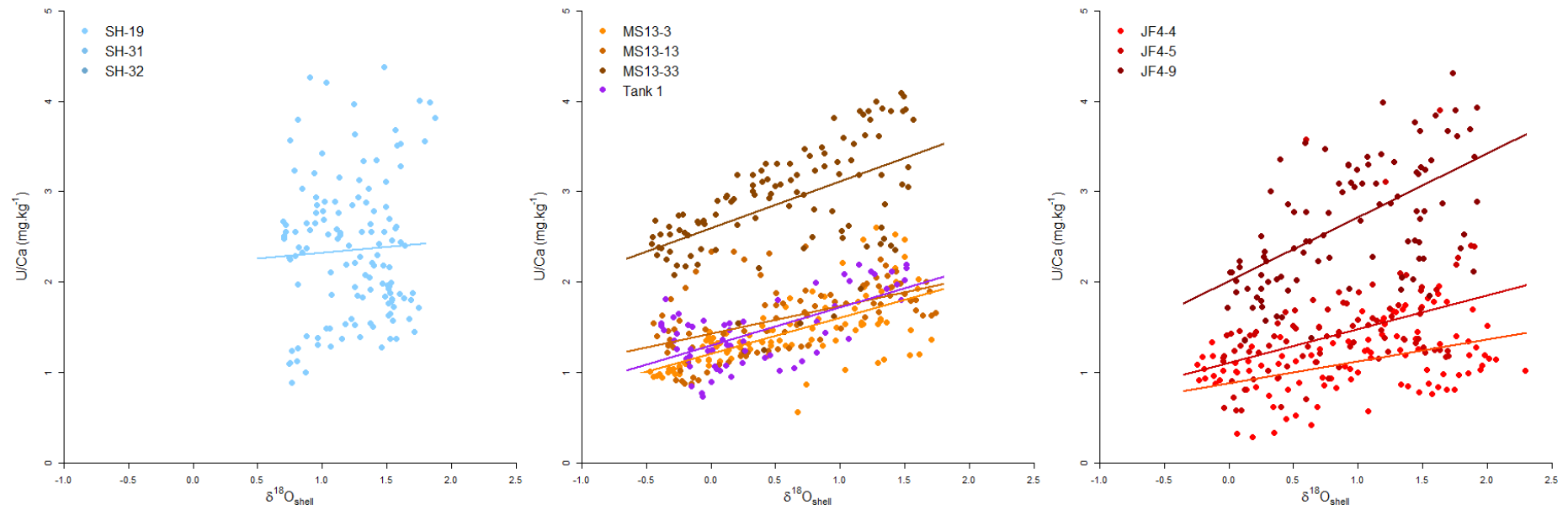


Figure G.6. Scatter plots of U/Ca against $\delta^{18}\text{O}$ for each shell from Shetland (a), male adults from the Menai Strait and laboratory reared juveniles (b) and Jersey (c). The data from each shell are fitted with a linear line of best fit of the matching colour.

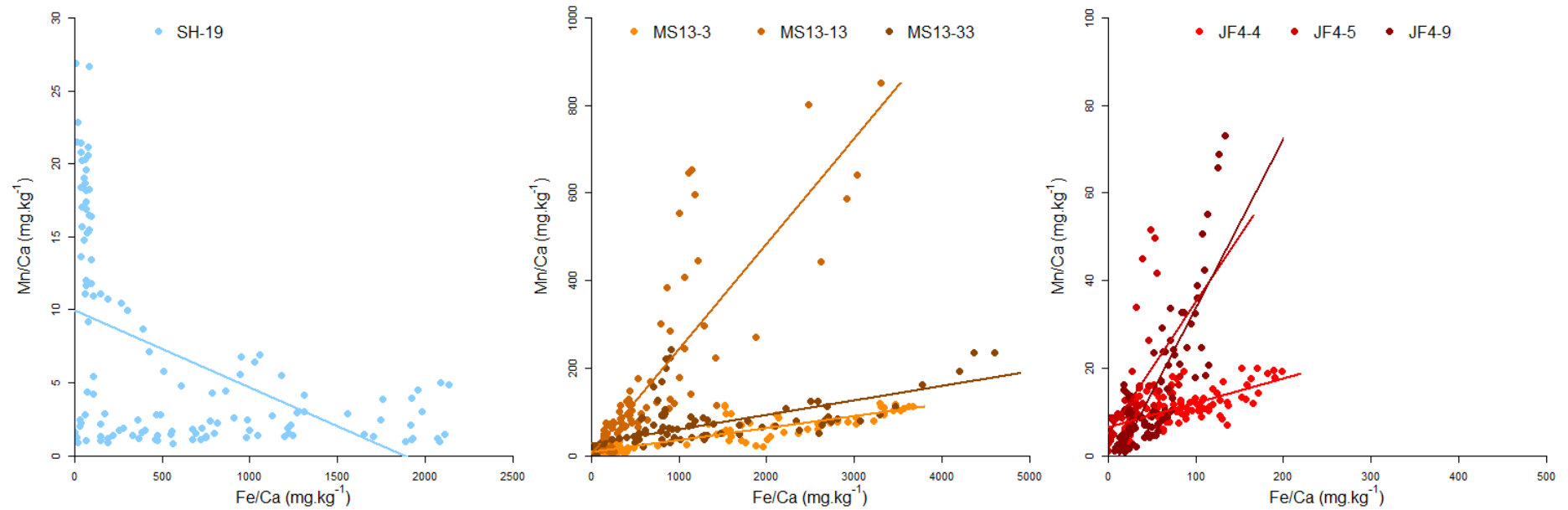


Figure G.7. Scatter plots of Mn/Ca against Fe/Ca for each shell from Shetland (a), male adults from the Menai Strait and laboratory reared juveniles (b) and Jersey (c). The data from each shell are fitted with a linear line of best fit of the matching colour.

Appendix H:

Whelk statolith removal and mounting Standard Operating Procedure (SOP), written for statolith workshop at CEFAS.

*****Whelk statolith removal and mounting laboratory protocol*****

Phil Hollyman - Last updated: 13/7/16

Before statolith removal takes place, whelks should have been processed for maturity assessment (see whelk lab protocol). At the end of this initial assessment you should be left with a labelled shell and matching (frozen) ziplock bag containing the foot of the whelk and operculum but not the gonads/digestive tract. For other species, some people use sodium hydroxide to dissolve the tissue and expose the statoliths, *B. undatum* is too big to do this easily. Even if you do find the statoliths in the dissolved tissue, the outer surface is often tarnished making them difficult to read. For this reason, dissection will be used. Using this method I collect both statoliths from a single animal and place them in a watch glass. If you only require one of the statoliths, it is much easier and less time consuming to dissect them onto microscope slides instead.

Equipment:

- Two small shallow plastic containers (Tupperware or plastic takeaway boxes are perfect)
- A couple of large plastic trays (white lab trays are fine)
- Dissection kit including – Scalpel, small scissors, large forceps, superfine needle nose forceps and a second pair of fine forceps (not required to be as fine as the first)
- Hypodermic needle
- 0.5ml Eppendorf tubes (one for each whelk)
- 70% IMS or Ethanol
- Microscope slides (one for each whelk)
- Fine permanent marker
- Blue roll
- Several watch glasses (number will vary depending on how many samples you want to process at once, 5 works well, if you don't have any just use microscope slides)
- Stick of Crystalbond 509-3 thermoplastic resin (available from Agar - AGB7312)
- Small ziplock bags
- A dissecting microscope
- A compound microscope (with camera-computer interface if possible)
- Alcohol burner
- Disposable plastic pipette
- Fine glass pipette

Before starting, label small ziplocks with the sample code of each whelk (1 bag per whelk). Also, create reference labels containing basic info such as the sample code, whether the operculum is present and the number of statoliths removed and mounted, see example below. This can be modified to whatever you need.

P. Hollyman	OSP20B
Sample date:	12.3.2014
Sample Location:	Menai Strait site
Sample number:	
Whelk Number:	
Shell Height (mm):	
Operculum:	
Statoliths:	
Notes:	

There are several steps to remove and mount the statoliths, it is easier to process several whelks to the same stage in batches of around 5.

Step 1: Removal of the statoliths from the foot of each whelk.

Begin by removing the first batch of whelks from the freezer in their labelled bags (you can remove as many as you would like to dissect that day, but it will be best to start with 1 or two). Place them in a large tray and fill tray with water to speed up defrost.

Remove the first sample (foot and operculum) from the bag and place in a large tray, using forceps remove the operculum (if required) dry with blue roll and set to one side on top of the prepared reference label. Using scissors, remove the penis (if present) and mantle which can both be disposed of (Fig. 1), a large portion of the foot can also be removed at this point as it does not contain the statolith but it is better to keep the foot whole to begin with to help with orientation.

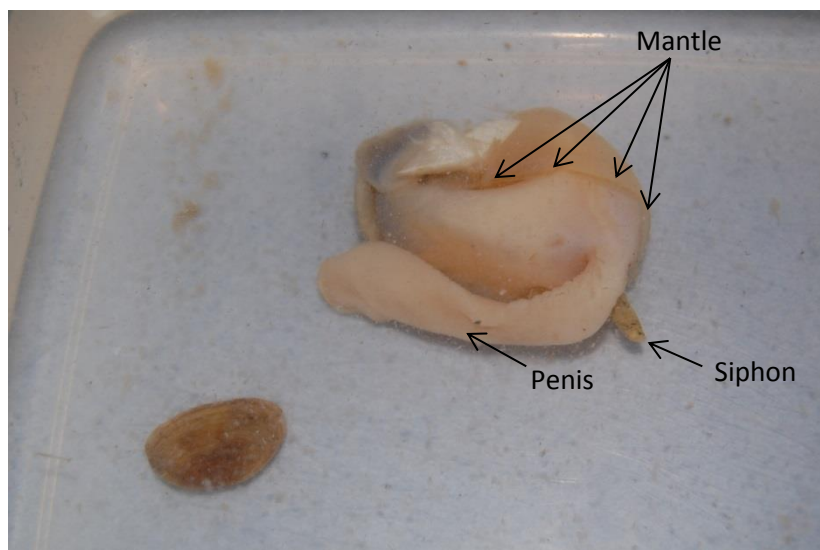


Fig. 1 - A defrosting whelk with the removable parts highlighted

Next, holding the whelk with the forceps, cut the whelk in half along the anteroposterior axis directly between the tentacles (Fig. 2). This is easiest if you insert the lower blade of your scissors underneath and between the tentacles where the proboscis may be showing, for the first cut.

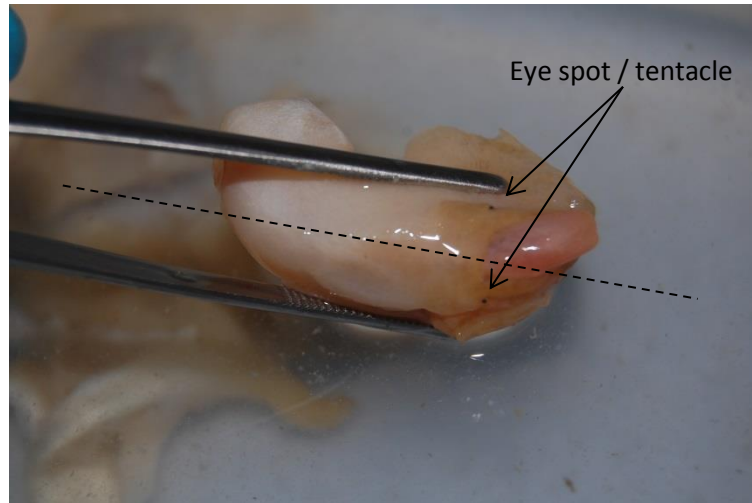


Fig. 2 – A dorsal view of a whelk highlighting the correct incision line

Next, transfer to a transparent container (takeaway container) which can then be placed under the dissection microscope, now switch to both pairs of fine forceps, with the finest pair in your dominant hand.

This entire process will use transmitted light NOT reflected.

With a bit more experience you will be able to tell which half is more likely to contain a statolith or in most cases both of them. Firstly start with the bigger half (this is normally the Right Hand Side (RHS)), orientate yourself with the tentacle at the top of your field of view. You will be able to see a distinction between the thick muscular outer layers of the whelk and the 'cavity' containing the nerves which is typified by soft connective tissue (Fig. 3)(I will refer to this as the nerve cavity from now on).

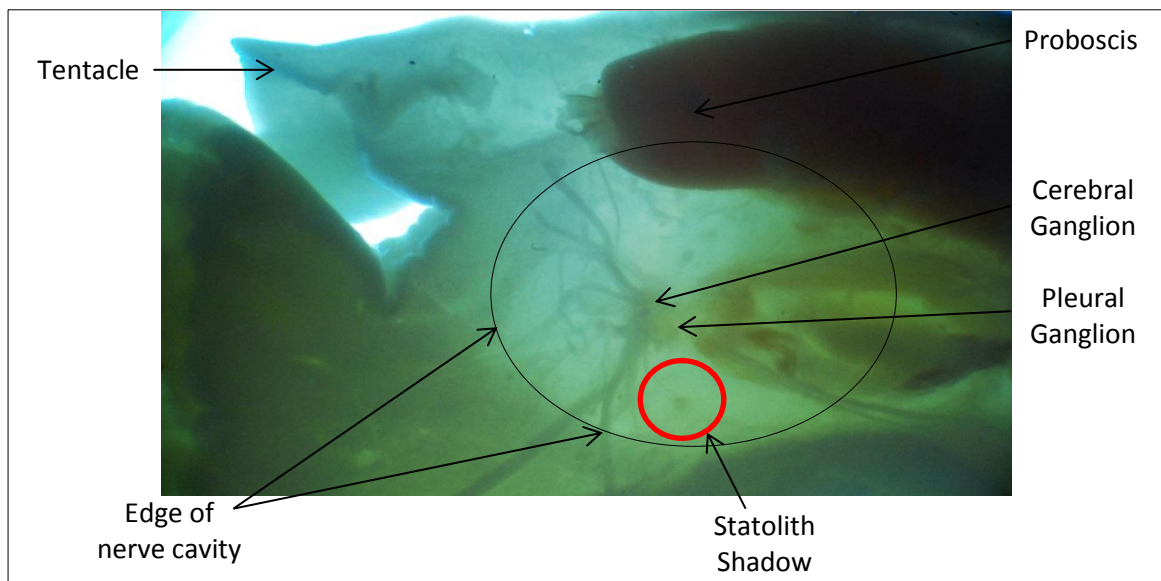


Fig. 3 – A cross section of a whelk (RHS) highlighting the visible internal structures as well as the normal position of the statolith.

The position of the Statoliths:

Follow the base of the tentacle down to the orange mass of nerve ganglia. This mass is basically the brain, containing the cerebral and pleural ganglia. The statolith is located within a sack called the Statocyst, on an offshoot nerve of the cerebro-pedal connective nerve which connects the cerebral ganglion to the pedal ganglion. You don't need to know what is what, just the general position of the ganglia (if you are interested, read Fretter and Graham – British Prosobranch Molluscs, pp269-289). The statolith is normally located between these ganglia and the bottom of the nerve cavity (Fig. 3).

There will be two statoliths in each whelk, a left and right. I always aim to collect both but mount the Left Hand Side (LHS) for consistency. I have found slight size differences (non-significant) between the LHS and RHS, but the pattern of growth rings is always identical. When dissecting out the statoliths, I would normally label the watch glass with R and L to signify which statolith is which. However, you do not need to collect both if it's not necessary.

Identifying the Statolith:

The statoliths will appear as a subtle shadow within the connective tissue, it is best to first try and identify and remove the statoliths in-situ (Fig. 3).

You may find the statolith very close to the cut surface, when this happens on the largest 'half' of the whelk (containing most of the nerve cavity), it is a good indication that the second statolith is in the same section and the statolith on the surface is from the other smaller 'half'. If this happens in the smaller 'half' of the whelk, it is a good indication that the second statolith is in the adjacent 'half'. Using this method you can keep track and identify whether the statolith is the left or right.

DO NOT DIRECTLY GRAB THE STATOLITH WITH FORCEPS!! This will normally result in the statolith shattering. Instead remove the chunk of connective tissue and nerves that surround the statolith and place it in your watch glass (you can also dissect them out directly onto microscope slides if you do not have watch glasses).

If the statolith is not immediately obvious, still using the fine forceps dig down to the area where you think the statolith should be located and carefully look for it. You can use a plastic pipette at this point to clean out the water in the cavity as it can become cloudy and obscure the search.

If you cannot find the statolith, using the fine scissors and forceps, carefully cut out the contents of the nerve cavity taking some of the outer muscle wall with it to ensure you don't leave the statolith behind. Then systematically search through the connective tissue from all angles to find the statoliths.

You should now have a watch glass or microscope slide marked L R with two sections of tissue containing statoliths if you collected both (Fig. 4). Do not leave the statoliths too long at this stage as once the tissue dries, they are difficult to remove, it is a good idea to place a small drop of water over the tissue once it is removed from the whelk.

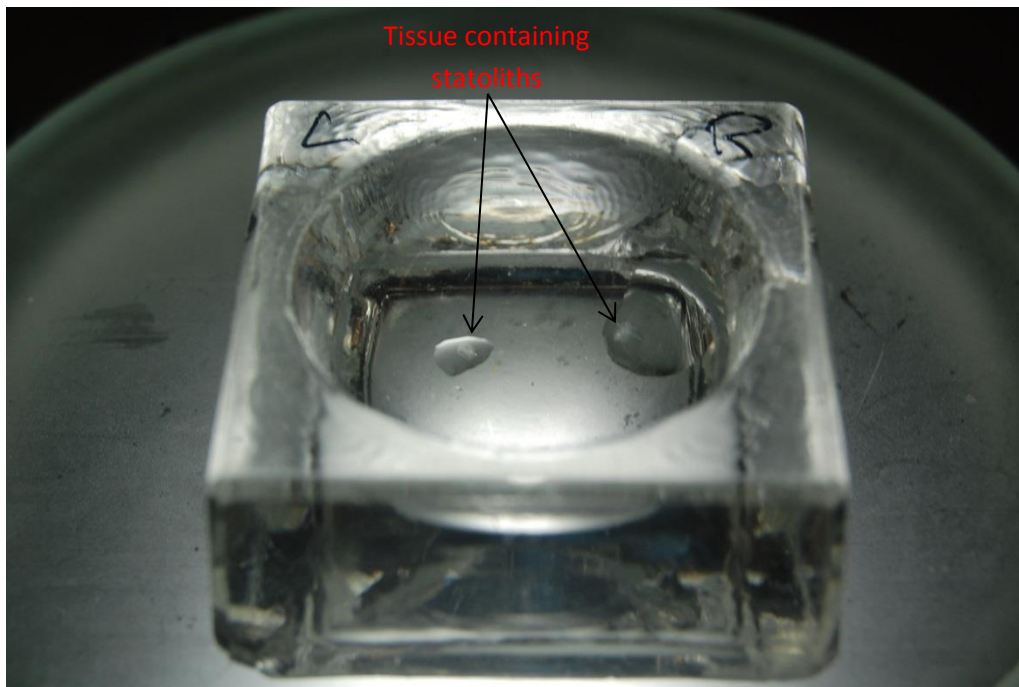


Fig. 4 – The statoliths inside a watch glass, still contained within tissue.

Step 2: Removing the statoliths from the statocysts.

Still under the dissecting scope, increase the magnification, and put in your watch glass, focus on one of the statoliths to see the structures shown in Fig. 5.

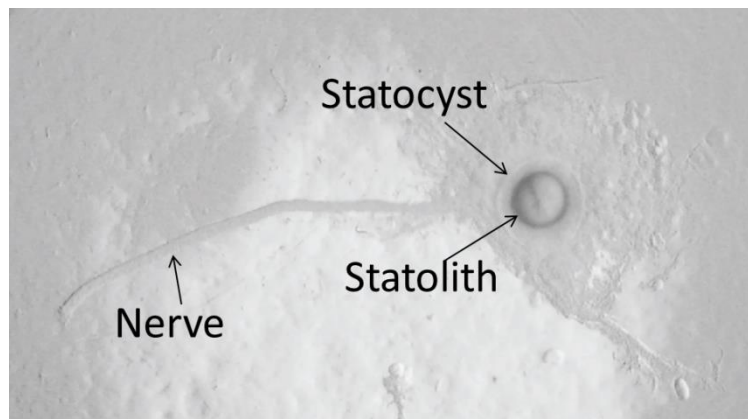


Fig. 5 – a statolith contained within a Statocyst, showing the connecting nerve.

This part is fiddly. Grip the Statocyst as close to the nerve as possible with the superfine forceps. Again be careful to not grab the statolith itself, using the edge of the hypodermic needle in your dominant hand, cut down the tip of your forceps and across the statolith to break open the statocyst. Once removed and free of any tissue, carefully manoeuvre the statolith around in the water to clean it and then up onto the side of the glass out of the water. Alternatively just move it out of the water to where you want to mount it if you have used a microscope slide (Fig. 6). Be careful not to push too hard as the needle might snag on the glass and flick the statolith out of the watch glass, never to be seen again....seriously. Do this for both statoliths and using blue roll,

carefully remove the remaining tissue and dry out the watch glass. At this point, you can leave the statoliths as long as you like before mounting, but be warned, they are VERY easy to lose.

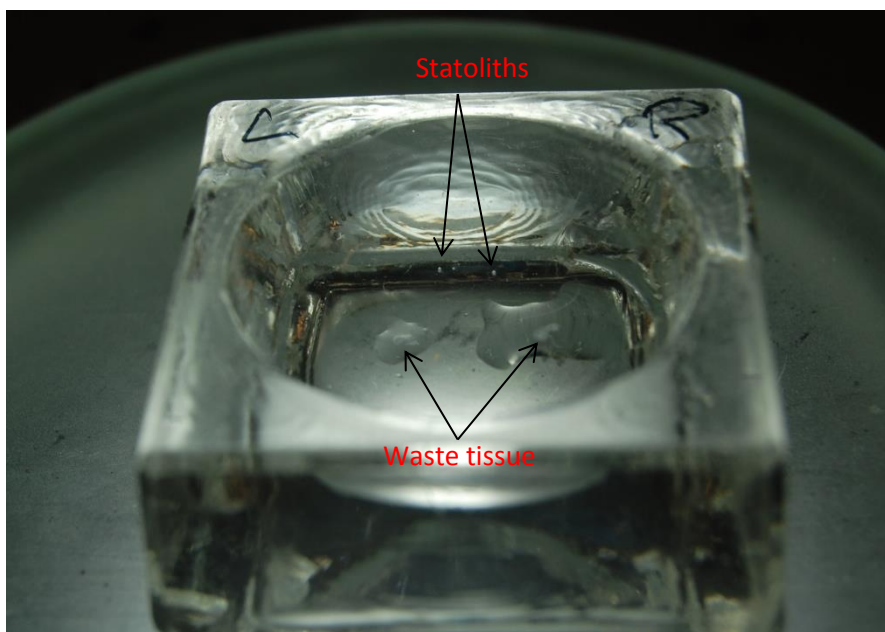


Fig. 6 – The position of the statoliths after removal from statocysts.

Step 3: Mounting the statolith

I normally mount the LHS statolith, if you could not find it, don't worry the RHS will work fine.

Before starting, carefully chip some resin from the end of the resin stick into a small container, you are looking for chips about 4mm long/wide, too small or big and they will be difficult to use. Wipe a microscope slide clean with blue roll and prepare a second small container with clean water. Also, label a 0.5ml Eppendorf tube for each sample where you retrieved both statoliths, this will be used to store the un-mounted one (THIS IS NOT NESSECARY IF YOU ONLY COLLECTED ONE).

Now comes the fun part...

If you used watch glasses to collect statoliths

Place the watch glass under the dissecting microscope and find the statolith you want to mount. Next, light the alcohol burner (or tealight). Hold the end of your slide over the flame, angled upwards, touch the tip of the resin stick to the end of the slide and move in a circular motion until a small circle (1-2cm) of resin is left on the slide (Fig. 7a). As quickly as possible, holding the slide in your non-dominant hand, dip the forceps in the water and use the water tension to pick up the statolith and place in in the warm resin (it is sometimes easier to place the statolith on the slide by eye over the watch glass in case you drop it. When you think it has stuck, look for a small black dot in the resin (Fig. 7b)).

Next move the watch glass out of the way (remember this still has the second statolith in it!) and focus on the statolith in the resin. Using your superfine forceps, pick up a chip of resin and gently melt it over the top of the statolith (Fig. 7c). There should be enough residual heat in the slide to do this, if not, heat it over the flame again. If you hold it over the flame for too long the resin will boil

and the bubbles will obscure the statolith. About 2-3 seconds from cold seems to work depending on the thickness of the slide.

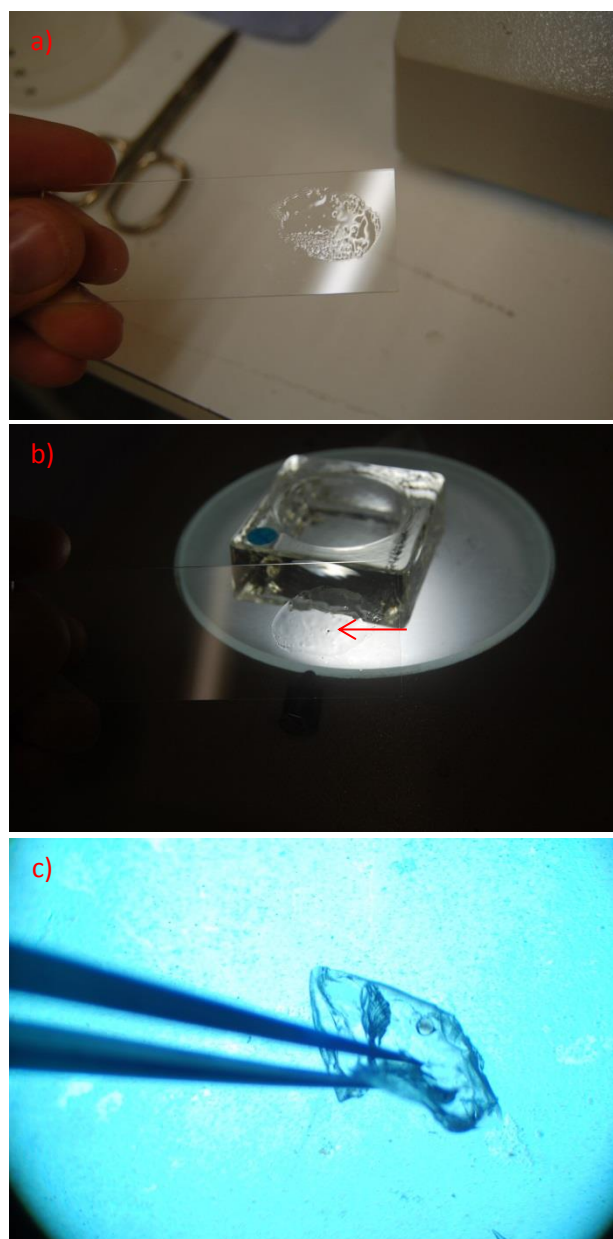


Fig. 7 – Several steps involved in the mounting of the statoliths. a) Position and size of resin needed on the slide. b) A statolith stuck to resin as visible by the naked eye. c) Melting a chip of resin over the statolith to properly mount it.

If you used microscope slides to collect statoliths

Much like the above, however, there is no need to transfer the statolith between slides. Locate the statolith under the microscope, carefully place a chip of resin over the top using forceps and then heat over a flame. Place the heated slide back under the scope to orientate the statolith in the melted resin.

You should now have a statolith in resin on a slide. However, the statolith needs to be in the correct orientation to be readable. The shape of the statolith is not entirely spherical, is it flatter on the top and bottom. Fig. 8 will show you what a correctly mounted and incorrectly mounted statolith will look like. The aim is to orientate the axis of the nucleus perpendicular to the glass. The more accurate this is, the easier it will be to read. This is because the cracks in the statolith (present in most statoliths, possibly a result of the freezing process) run along the nucleus line, when this is perpendicular to the slide, they become far less visible.

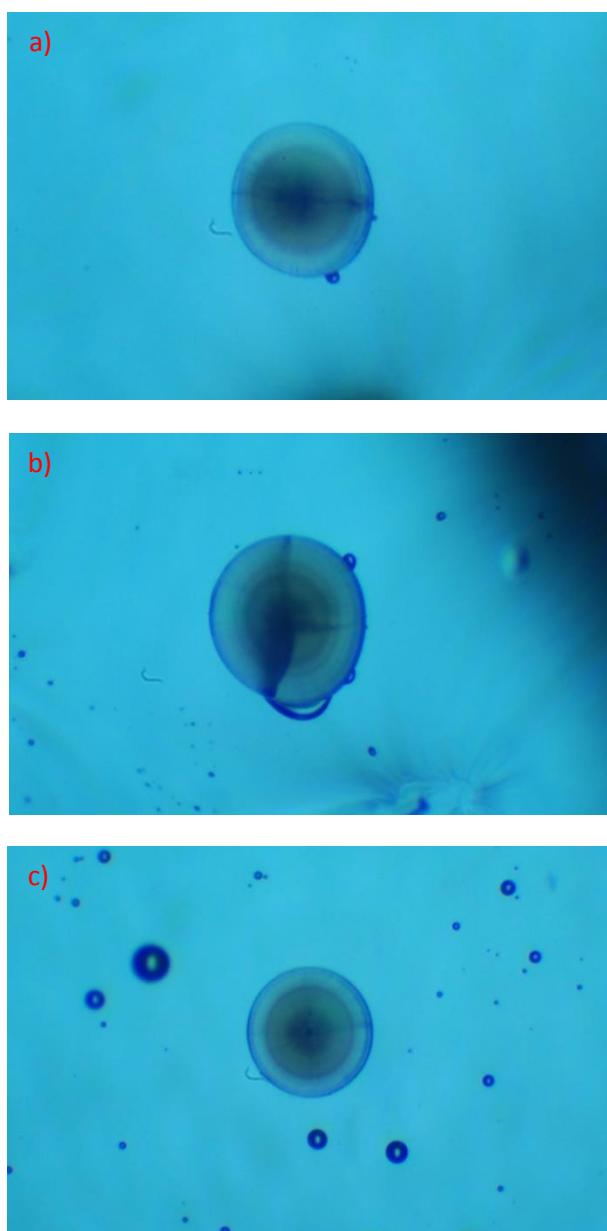


Fig. 8 – a) an incorrectly mounted statolith, this statolith is mounted on its side, this is identifiable by the slightly elongated appearance and the heavy black line through the centre (nucleus line). b) a second incorrectly mounted statolith, the dark marks visible on the statolith are due to the nucleus line (visible in a)) not being perpendicular to the slide, the cracks in the statolith become far more visible as they create a shadow. c) a correctly mounted statolith. Whilst the cracks are still visible, they are only faint lines.

To do this, heat the slide over the flame if it is cold again and use the superfine forceps or the hypo needle to manipulate the resin around the statolith (do not touch the statolith itself) to get the correct orientation. The resin can be heated and cooled as many times as needed, however the less you heat it, the fewer bubbles you will have.

Once the orientation is fixed, let it cool and label the slide with the sample code using a permanent marker or scratch it into the glass.

If you collected both statoliths

Next go back to the watch glass and find the second statolith. Using the glass pipette, take a small amount of 70% IMS and dislodge the statolith from the side of the watch glass. Suck up the statolith along with the alcohol and deposit it inside the labelled Eppendorf tube. Check under the microscope that the statolith is in the tube.

Lastly, if you want to keep them, you can reunite the shell (which should now be dry) with the operculum and spare statolith in the Eppendorf tube. They can all be placed inside the labelled ziplock bag along with the reference label for storage. The slides are best kept in a plastic slide box, stacking them will damage the resin.

The slides can now be imaged using the compound scope and computer (20x or 40x is usually best) and the lines can be analysed.

Once the dissections become faster with practice, you can get more whelks out to defrost at a time and process them in batches. You can cut several in half at one time (about 20 fit into a tray) as long as you work through them in order. Then do all the dissections at once, then remove all of the statoliths from the statocysts at once (make sure there isn't too long between these two so that the tissue doesn't dry out on the slide/watch glass) and finally mount them all.

Appendix I:

NERC Edinburgh Ion Microprobe Facility (EIMF) application. Successful, resulted in 8 days of access to the Cameca IMS-4f Ion microprobe - £15,000 in analyses.



NATURAL ENVIRONMENT RESEARCH COUNCIL SCIENTIFIC SERVICES

Application for Ion Microprobe Analysis

Ion Microprobe Facility
School of GeoSciences
Edinburgh University
EDINBURGH
EH9 3JW

For Office Use Only	
Date received:	
Application No:	IMF
Application Type	<input checked="" type="checkbox"/> Full Application
	<input type="checkbox"/> Pilot (1-day) Application
IMF Grade	

e-Mail: ionprobe@ed.ac.uk

1. Applicants Name (PI):	Professor Chris Richardson
--------------------------	----------------------------


2. Project Title:	Assessing the timing of growth increment formation in the statoliths of the common whelk <i>Buccinum undatum</i> .
-------------------	--

3. Principal investigator <i>N.B. PI must be eligible to hold a NERC award (See www.nerc.ac.uk)</i>	
Name:	Professor Chris Richardson
Position:	Head of School, Bangor University, School of Ocean Sciences
Date current post started:	1 st May 2011
Gender:	<input checked="" type="checkbox"/> Male <input type="checkbox"/> Female
Address:	School of Ocean Sciences, College of Natural Sciences, Bangor University, Menai Bridge, Anglesey, LL59 5AB
Tel:	01248382855
e-Mail:	c.a.richardson.bangor.ac.uk

4. Nature of proposal:
<input checked="" type="checkbox"/> New Proposal
<input type="checkbox"/> Re-Submission
<input type="checkbox"/> Pilot (1-Day) Application

5. Project abstract: <i>Maximum 100 words</i>
The UK fishery for the common whelk (<i>Buccinum undatum</i>) is over-exploited and its future long term sustainability is of concern. A difficulty in assessing whelk populations is that the growth and age of individuals is largely unknown. We are developing a methodology for estimating age using growth rings in statoliths, (cf. fish otoliths) <~0.3mm diameter calcium carbonate structures, in the foot tissue. We propose to use ion microprobe to reconstruct trace elements and stable isotopes across transects of several sectioned statoliths to validate the seasonal periodicity of the growth rings and confirm that statoliths are suitable as an aging tool.

6. Personnel: Other investigators involved in the project including Co-investigators, Research Students, Assistant or Fellows. Please include all persons attending the IMF laboratory.				
Name (and e-mail Address)	Position	Institute	Role in Project	Attending Facility (Yes/No)
Dr. Simon Chenery (srch@bgs.ac.uk)	Senior Analytical Geochemist	The British Geological Survey	Co-investigator	Yes
Philip Hollyman (osp20b@bangor.ac.uk)	PhD Student	Bangor University	Research Student	Yes

7. PhD Studentship. If this applications forms part of a student's PhD, then the student must complete and sign the following section. Please explain the significance of this application to the overall aims of your thesis. (max 100 words)	
<p>The current PhD project is focussing on the development of a tool for estimating the age of <i>Buccinum undatum</i>, using statolith growth rings. We are validating the timing of growth ring formation in statoliths taken from monthly samples of juvenile whelks reared in controlled laboratory experiments and collected seasonally from the Menai Strait. This will allow determination of the seasonal timing of growth ring formation in statoliths, and using microprobe techniques, relate changes in trace elements and stable isotopes across transects of the ~0.3mm diameter spherical statoliths to growth ring formation and seawater temperature.</p>	
PhD Title: The growth and fecundity of the whelk <i>Buccinum undatum</i> in coastal shelf seas	PhD Start Date: 1.8.13
Student Signature: 	Signature Date: 25.9.14

<p>8. Project Description: These should be succinct and self-contained and should explain adequately the following aspects:</p> <p>a) The background to the project.</p> <p>b) Objectives, aims and hypotheses to be tested (these should be clear to all members of the Steering Committee and not just to experts in your field).</p> <p>c) The relevance of, and justification for, ion microprobe analyses (as distinct from other techniques).</p> <p>d) Indicate how the results will be used to test the hypothesis or achieve the objectives and aims.</p> <p>f) For large scale projects please outline the research strategy, and how the project may be expected to develop.</p> <p>NOTE: For a Full Application, please keep to a maximum of two pages using 11 point Arial font and single line spacing. An additional 2 pages (maximum) of legible and appropriate images, diagrams or tables are acceptable. Colour figures are encouraged.</p> <p>NOTE: For a Pilot (1-day) Application, please keep to a maximum of one page using 11 point Arial font and single line spacing. An additional 1 page (maximum) of legible and appropriate images, diagrams or tables is acceptable. Colour figures are encouraged.</p> <p>a) Background to the project: <i>Buccinum undatum</i> (the common whelk) is of commercial interest in several countries throughout Northern Europe including the UK. The UK is the largest producer of whelks in Europe (Heude-Berthelin <i>et al.</i>, 2011). In 2011, 13,800 tonnes of <i>B. undatum</i> were landed in the UK with a market value of £8.9 million, accounting for roughly 9% of the total UK shellfish landings by weight and 3% of the total UK shellfish landings by value (UK Sea Fisheries Statistics 2011). There has been a dramatic rise in the landings of whelks in the UK due to an increase in the export market to places such as South Korea and Japan (Fahy <i>et al.</i>, 2005). Whilst the increase in foreign exports is favourable from an economic standpoint, it drastically increased pressure on a species which is vulnerable to overexploitation. The basic fisheries</p>

regulation in place in the UK is a Minimum Landing Size (MLS) of 45mm shell height. This size (45mm) arose from an outdated EU regulation which has been shown to be wholly inadequate in several studies (Shelmerdine *et al.*, 2007; Heude-Berthelin *et al.*, 2011) as *B. undatum* has been shown to have differing size at age and age at maturity with geographical location (Shelmerdine *et al.*, 2007). Whilst in some populations whelks can reach the MLS within 3 years, at this age the whelks have often not yet reached maturity.

Several key characteristics of the biology and behaviour of *Buccinum undatum* make them vulnerable to overfishing. They live a largely sedentary life cycle and also have direct larval development which can lead to 'closed' populations (Shelmerdine *et al.*, 2007). This, coupled with a varying growth rate, results in a species that is potentially at risk when exposed to fishing pressure. Fishery declines due to fishing pressure in Ireland (Fahy *et al.*, 2005), England (Nicholson and Evans, 1997) and the southern North sea (Ten Hallers-Tjabbes *et al.*, 1996) have been reported and all show clear reductions in Catch Per Unit Effort (CPUE). Several previous attempts at stock assessment of whelk populations have been undertaken, however, none of these have successfully established the scale of the fishable stock of whelks present in a population (e.g. Morel & Bossy, 2004). The methods used to assess whelk stocks lack the ability to incorporate reliable ageing techniques to determine the population structure and size at age, which is critical for assessing the impact of fishing activities on the immature portion of a population. Current ageing methods focus on growth increments found in the operculum of the whelk (Kideys, 1996; Shelmerdine *et al.*, 2007), as the shell does not exhibit annual growth rings. Unfortunately, the operculum is often unreliable causing many studies to discount a large proportion of the sample which could potentially bias the data. For example, Kideys, (1996) only managed to reliably age 16% of operculae he sampled. The use of growth lines in the operculae is supported by a study by Santarelli and Gros (1985), which reconstructed the temperature of 3 whelk shells by drilling samples at regular intervals and analysing the oxygen isotope ratios. The number of annual cycles (which were unclear) matched the number of visible growth lines on the operculum; this was seen as confirmation of an annual periodicity. No recent work has improved on this study using the range of available modern techniques.

A more recent addition to the field of gastropod ageing is the use of statolith micro-structures, which appear to contain high resolution archives of growth histories. The gastropod statolith is a small structure of calcium carbonate found within the statocysts, located in the foot of the gastropod in the locality of the pedal ganglion (Fretter & Graham, 1994; Richardson, 2001). They are used for equilibrium and help the animal to determine the direction of gravity much like the otoliths of a fish. Several studies have highlighted the annual periodicity of growth rings contained within the statoliths of marine gastropods which resemble tree rings (e.g. Chatzinikolaou & Richardson, 2007) (Fig. 1). To date, no research has been undertaken to investigate the suitability of *B. undatum* statoliths for age determination.

b) Objectives, aims and hypotheses to be tested: The aim of the PhD study is to determine the periodicity of growth rings in the statoliths of *B. undatum* and assess their potential use as an ageing method for use in stock assessment. This is being undertaken using several different approaches to validate the periodicity of the statolith growth lines. Field and laboratory experiments are in progress to pinpoint the timing of ring formation by analysing statoliths taken from whelks collected in monthly samples from a single population in the Menai Strait, North Wales and assessing statolith ring development month by month using marginal increment analysis (MIA). Simultaneously, the first year of statolith growth in juvenile whelks that have been hatched from egg capsules and reared under controlled laboratory conditions is being investigated through regular sampling and MIA to determine the timing of seasonal ring formation in relation to seawater temperature. In this application we propose to investigate the relationship between seawater temperature, statolith ring formation and statolith carbonate chemistry using ion probe analysis of trace element and stable isotope microchemistry. In a parallel study (an application currently in submission to the NERC Isotope Geoscience Facility Steering Committee (NIGFSC) at the British Geological Survey (BGS)) the variation in trace element and $\delta^{18}\text{O}$ ratios in the shells of whelks, from which the statoliths in this proposed study have been extracted, are being determined to estimate the age of the shell and then to compare the geochemistry of both the shell and statolith.

Specific hypotheses that will be tested in this proposal are:

H1: The deposition of narrow (winter) and wider (summer) growth rings in statoliths of *Buccinum undatum* will correlate with variations in trace element and $\delta^{18}\text{O}$ ratios in transects taken across the diameter of a statolith.

H2: Variations in trace element and $\delta^{18}\text{O}$ ratios in statoliths will correlate with environmental variations in seawater temperature and verify that narrow growth rings are deposited during the winter.

H3: Patterns of trace element and stable isotope variation in the statolith will mirror the trace element and stable isotope variation in the shell, (NIGFSC application).

c) The relevance of, and justification for, ion microprobe analyses (as distinct from other techniques): Since the statoliths are $\sim 300\mu\text{m}$ in diameter they are therefore too small to sample at high resolution using conventional micromilling or drilling techniques. Laser ablation inductively coupled plasma mass spectrometry (LAICPMS) is also unsuitable, even though the technique may give sufficient spatial resolution for trace element analysis, the depth of the ablation craters ($\sim 20\mu\text{m}$) will cause damage and ingress and analyse underlying areas of the statolith, however this technique may be used to obtain some preliminary data. An Ion Microprobe beam size of $25\mu\text{m}$ is of sufficient width and resolution to allow initially for isotope measurements and then for trace element analysis along transects across the statolith. At this beam size sufficient sample resolution will be achieved to highlight seasonal cycles of trace elements and stable isotopes (hypotheses H1&H2). We anticipate a seasonal seawater temperature variation of $\sim 11^\circ\text{C}$ which equates to a $\delta^{18}\text{O}$ variation of 3.5 per mil.

The proposed sampling strategy for the Ion Microprobe will be to use "stepped" sampling, using a $25\mu\text{m}$ spot size for trace element analysis (e.g. Sr) and for isotope analysis across the full growth axis of each of five sectioned statoliths (Fig. 1a). Stepped 5-10 μm spots may be used to analyse for the heavier trace elements at a higher resolution (e.g. Sr). Each statolith will be mounted in Buehler EpoxiCure-2 resin on a microscope slide and ground using successive grit papers and lapidary pastes to a final polish of $0.25\mu\text{m}$. The appearance of a polished and etched statolith section is shown in Fig. 2a.

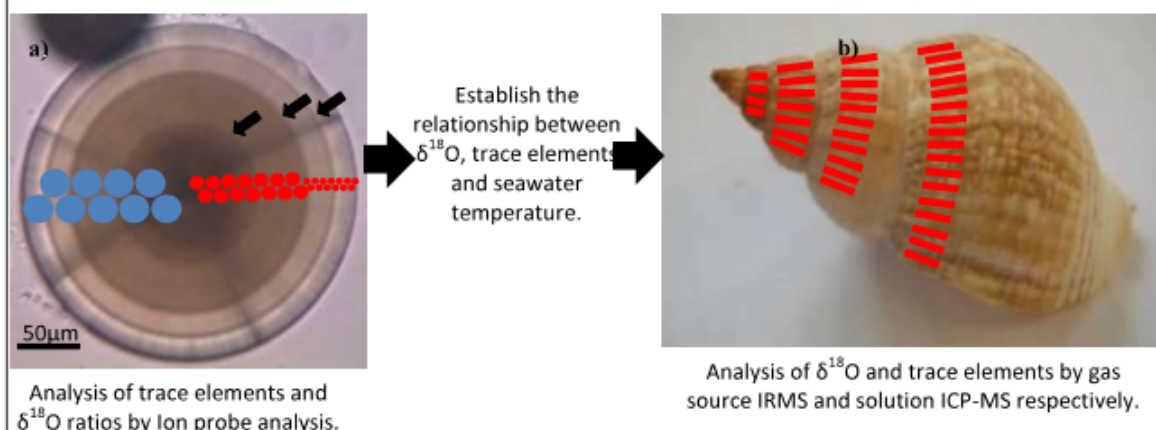


Fig.1, a) Photomicrograph showing the growth rings in the statolith of *B. undatum*, as well as the proposed sampling techniques. The black arrows indicate the growth increments. The red dots represent the proposed 5-10 micron pits for abundant trace elements. The blue dots indicate a proposed 25 track of sample pits across the growth axis of the statolith. **b)** Photograph of a whole shell with the proposed sampling areas marked with red blocks around the whorl of the shell

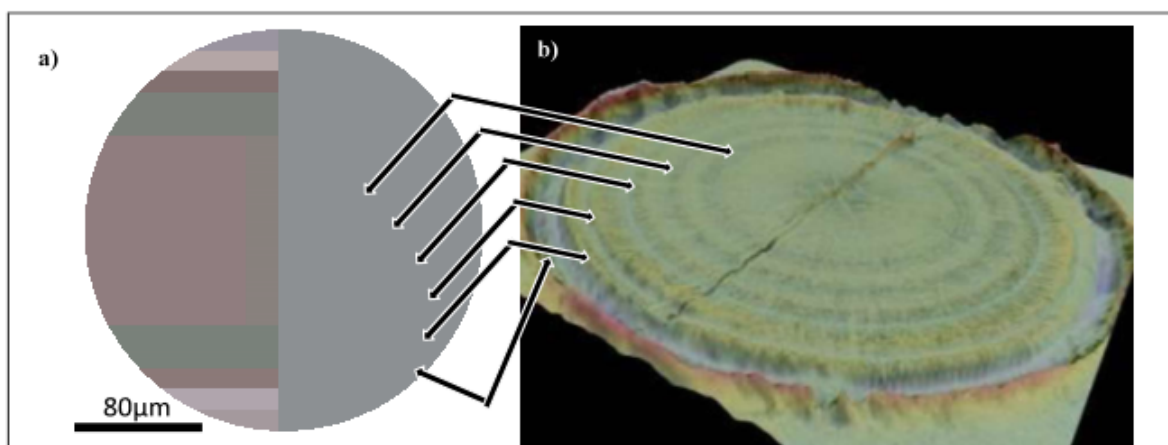


Fig.2 a) A split image of a *B. undatum* statolith, the left side was obtained with transmitted light microscopy, the right hand side is a scanning electron microscope image of the same statolith. The increments are highlighted with arrows. **b)** A 3D reconstruction of the etched statolith surface (same statolith as Fig. 3a), clear distinctions between the increments can be seen. The matching increments between Fig. 3a & b are highlighted with joined arrows.

The data from the Ion Microprobe analyses will be related to analyses of samples drilled from the surface of the shell (see figure 1b) (separate October application has been made to NIGFSC with Co-I's Professor Melanie Leng and Dr Simon Chenery). High resolution drilling (5x1mm drilled samples every 2 mm for the full length of the shell will allow the variation in shell trace element and stable isotope ratios to be measured using a conventional gas source IRMS (isotopes) and solution ICP-MS (Trace elements). A pilot study using this methodology has already been undertaken at BGS where a single shell was sampled at high resolution and a further 4 shells will be drilled and analysed. Once both the shells (NIGFSC application) and statoliths (this NERC Ion Microprobe application) have been analysed the trace element and isotope profiles will be compared to identify any common patterns (Hypothesis H3), see figure 3 for diagrammatic summary.

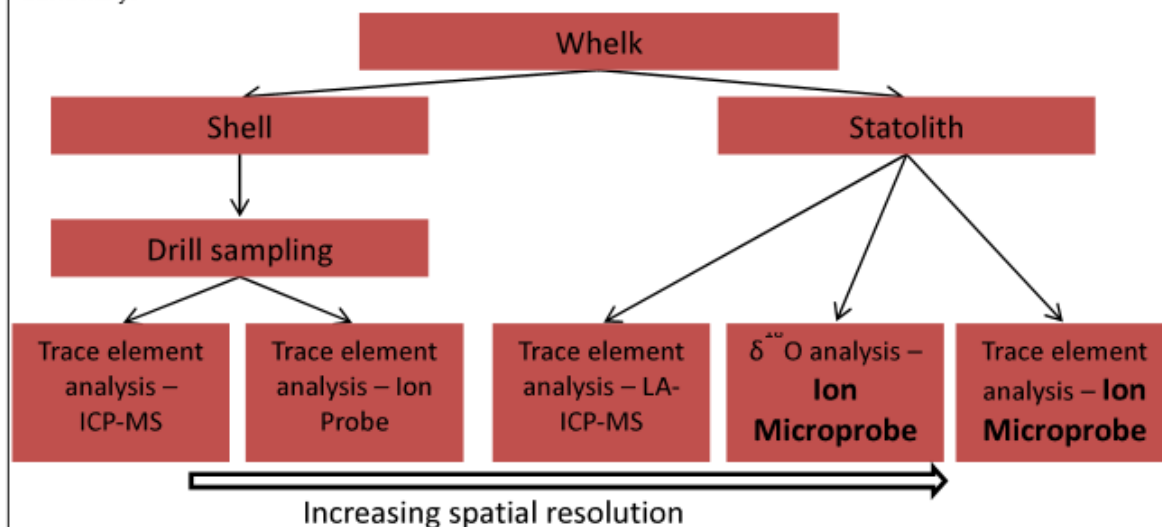


Fig. 3. A diagrammatic representation of all proposed geochemical analyses.

References: Chatzinikolaou, E. and Richardson, C.A. (2007) Evaluating growth and age of netted whelk *Nassarius reticulatus* (Gastropoda: Nassariidae) using statolith growth rings. *Marine Ecology Progress Series* 342, 163-176. Fahy, E., Carroll, J., O'Toole, M., Barry, C. and Hother-Parkes, L. (2005) Fishery associated changes in the whelk *Buccinum undatum* stock in the southwest Irish Sea, 1995-2003. *Irish Fisheries Investigations*, 15, 26pp. Fretter, V. and Graham, A. (1994) British Prosobranch Molluscs: their functional anatomy and ecology. Printed for the Ray Society, London. Revised and updated edition, 820pp. Galante-Oliveira, S., Marçal, R., Guimarães, F., Soares, J., Lopes, J.C., Machado, J., Barroso, C. (2014) Crystallinity and Microchemistry of *Nassarius reticulatus* (Caenogastropoda) statoliths: towards their structure stability and homogeneity. *Journal of Structural Biology* 186, 292-301. Hancock, D.A. (1963) Marking experiments with the commercial whelk (*Buccinum undatum*). *ICNAF Special Publication* 4, 176-187. Heude-Berthelin, C., Hégron-Macé, L., Legrand, V., Jouaux, A., Adeline, B., Mathieu, M. and Kellner, K. (2011) Growth and reproduction of the common whelk *Buccinum undatum* in west Cotentin (Channel), France. *Aquatic living resources* 24, 317-327. DOI: 10.1051/alr/2011048. Kideys, A.E. (1996) Determination of age and growth of *Buccinum undatum* L. (Gastropoda) off Douglas, Isle of Man. *Helgoländer Meeresuntersuchungen* 50, 353-368. Morel, G.M. and Bossy, S.F. (2004) Assessment of the whelk (*Buccinum*

undatum L.) population around the Island of Jersey, Channel Isles. *Fisheries Research* 68, 283-291. **Nicholson, G.J. and Evans, S.M.** (1997) Anthropogenic impacts on the stocks of the common whelk *Buccinum undatum* (L.). *Marine Environmental Research* 44, 305-314. **Richardson, C.A.** (2001) Molluscs as archives of environmental change. *Oceanography and Marine Biology - An Annual Review* 39, 103-164. **Santarelli, L. and Gros, P.** (1985) Age and growth of the whelk *Buccinum undatum* L. (Gastropoda: Prosobranchia) using stable isotopes of the shell and operculum striae. *Oceanologia Acta* 8, 221-229. **Shelmerdine, R.L., Adamson, J., Laurenson, C.H. and Leslie B.** (2007) Size variation of the common whelk, *Buccinum undatum*, over large and small spatial scales: Potential implications for micro-management within the fishery. *Fisheries Research* 86, 201-206. **Ten Hallers-Tjabbes, C.C., Everaarts, J.M., Mensink, B.P. and Boon, J.P.** (1996) The decline of the North Sea whelk (*Buccinum undatum* L.) between 1970 and 1990: a natural or human-induced event?. *PSZN I: Marine Ecology* 17, 333-343.

Appendix J:

Rapid access request to the I-18 beamline at the Diamond Light Source synchrotron facility. Resulted in 24 hours of I-18 beam time with access to Raman microscope and support labs.

User Office		Doc No: SCI-USO-DOC-0062.doc Issue: 1 Page: 1 of 2
-------------	---	--

Rapid Access Proposal

Completed application should be emailed to useroffice@diamond.ac.uk

Experiment Title	Determination of calcium carbonate phases within the statoliths of the gastropod <i>Buccinum undatum</i> .
Beamline Requested	I18
Proposal No	User Office to assign
Number of shifts requested	3
Principal Investigator Name	Dr. Simon Chenery
Principal Investigator Establishment	The British Geological Survey
Principal Investigator Email	srch@bgs.ac.uk
Date Proposal Submitted	
List of Samples	12 thin sections, calcium carbonate in resin.
Brief Science Case	
<p>Gastropod statoliths are small (~250µm) calcium carbonate spheres contained within the nervous system for the purpose of gravity perception. In many species they contain a series of clear growth rings suspected to be annual. We are currently investigating the potential use of common whelk (<i>Buccinum undatum</i>) statoliths as an ageing tool for fisheries research. The validation of annual statolith growth rings would greatly improve current practice by enabling age-structured assessments akin to those used for finfish, and thereby improve the setting of sustainable exploitation rates. We have recently used the Edinburgh Ion Microprobe facility to analyse trace element profiles within the statoliths using Secondary Ion Mass Spectrometry (SIMS). The results of the analyses highlighted clear cycles in ^{24}Mg with minimum values corresponding to the observable growth rings (Fig.1). ^{88}Sr was also analysed but did not show the same cyclicity, possibly because the calcium carbonate phase (i.e. aragonite or calcite) could significantly influence its elemental incorporation (Schone <i>et al.</i>, 2010). We aim to quantify the type of calcium carbonate present within the statoliths as well as the position of any phase changes across the growth axis in relation to the growth rings using the diamond light source. This would represent an advance over previous work in this area as previous attempts to use Electron Back Scatter Diffraction (EBSD) to visually resolve the types of calcium carbonate within <i>B. undatum</i> statoliths have been unsuccessful due to the small crystal size (~80nm). Galante-Oliveira <i>et al.</i>, (2014) analysed the calcium carbonate composition of statoliths from another gastropod species (<i>Nassarius reticulatus</i>) using XRD and micro-Raman spectroscopy. They found both aragonite and calcite present within the same area, seemingly within a spatially homogenous matrix. However the sample resolution was uncontinuous and low (10-20µm). Using high resolution microdiffraction, we would aim to greatly improve the current understanding of statolith calcium carbonate structure and composition which, in turn, will allow a greater understanding of the elemental signals present. This would be achieved by using a 2µm microdiffraction line profile to visually analyse the whole width of 12 statoliths which have been analysed using SIMS. The statoliths will be</p>	

User Office



Doc No: SCI-USO-DOC-0062.doc

Issue: 1

Page: 2 of 2

embedded in EpoThin2™ resin and then ground and polished on both the superior and posterior surfaces to create a thin section of $\sim 20\mu\text{m}$ exposing the central plane for microdiffraction analysis.

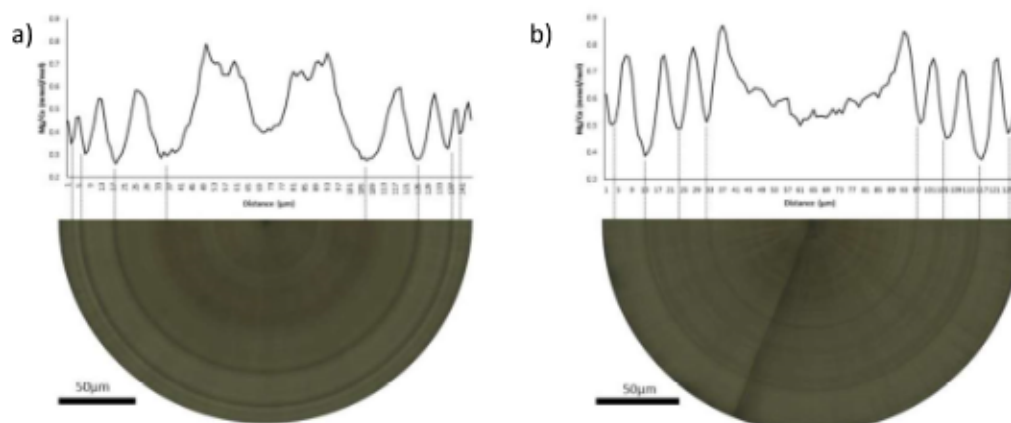


Fig. 1, examples of Ca/Mg ratio cycles across a statolith from a) the Menai Strait and b) Jersey.

Select the science areas (please indicate one choice per column)

Science Area	1	2	3
Biology and Biomaterials	1		
Chemistry			
Energy			
Engineering			
Environment		2	
Materials			
Medicine			
Physics			
Technique Development			3
Food Science			
Archaeological and Cultural Heritage			

Appendix K:

X-Ray Diffraction (XRD) profiles from quality control sampling during Micro-XRD analysis

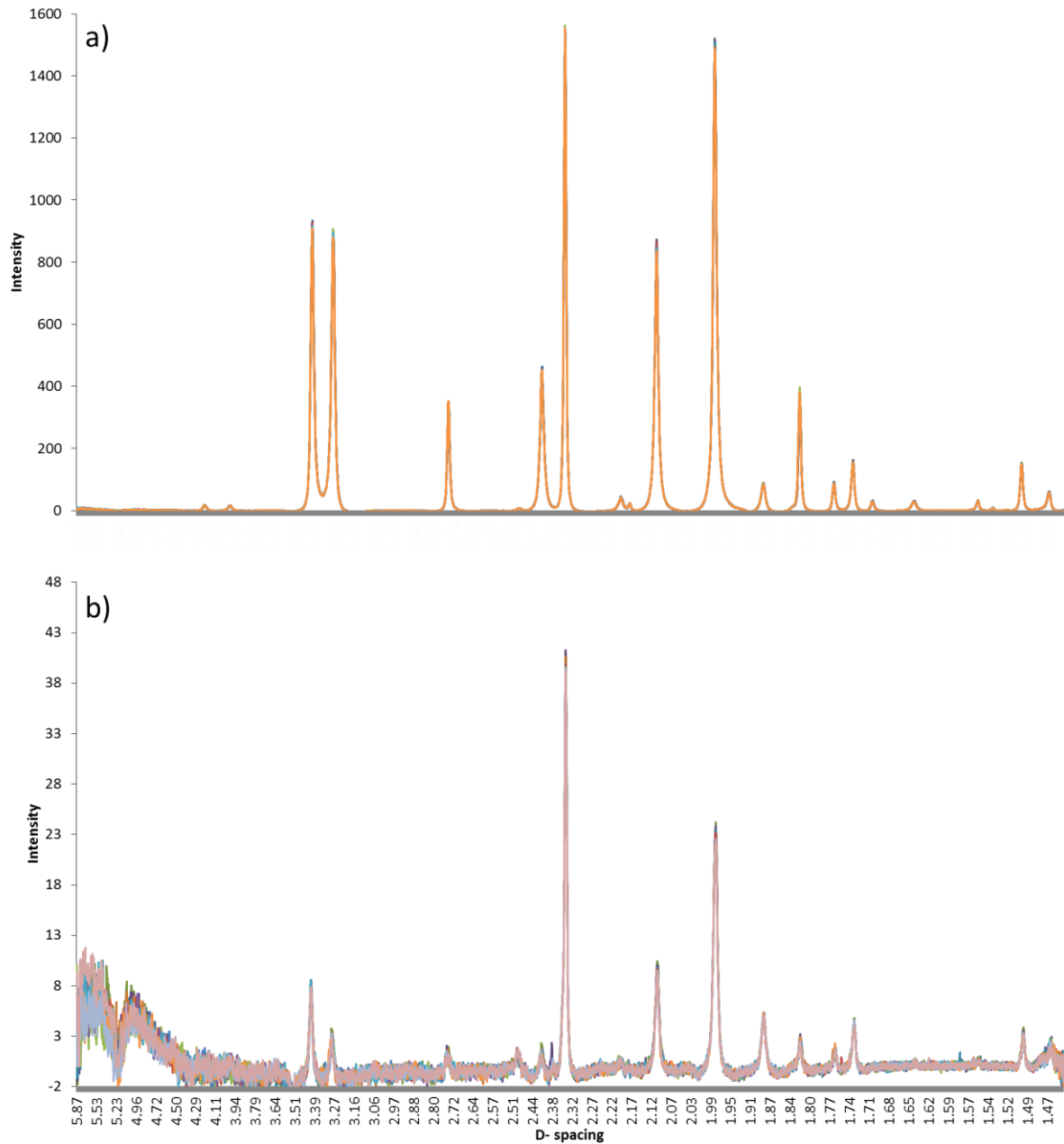


Figure K.1. Stack plots of 12 successive XRD profiles taken at 10 second intervals at the same location. a, shows data from the centre of a statolith from the Menai Strait and b, shows data from close to the edge of the same statolith.

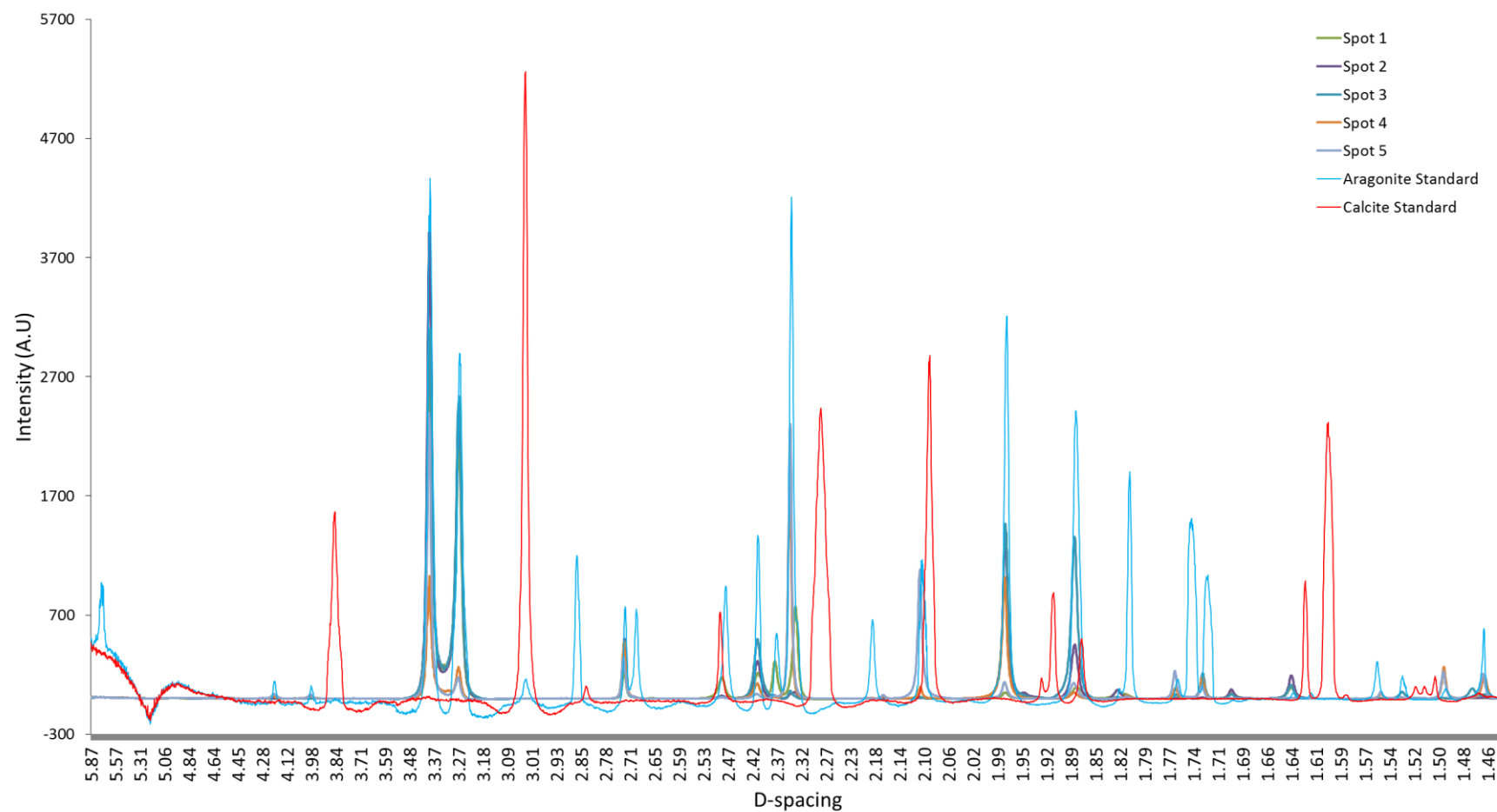


Figure K.2. Stack plot of XRD profiles taken at $\approx 20\ \mu\text{m}$ spacing along the growth axis of the same statolith presented in the Raman microscopy analysis in Chapter 6. The stacked sample profiles are overlaid with profiles from aragonite (blue) and calcite standards (red) (the same standards described in chapter 6).

Appendix L:

Plots of raw magnesium and calcium measurements from statoliths analysed using SIMS.

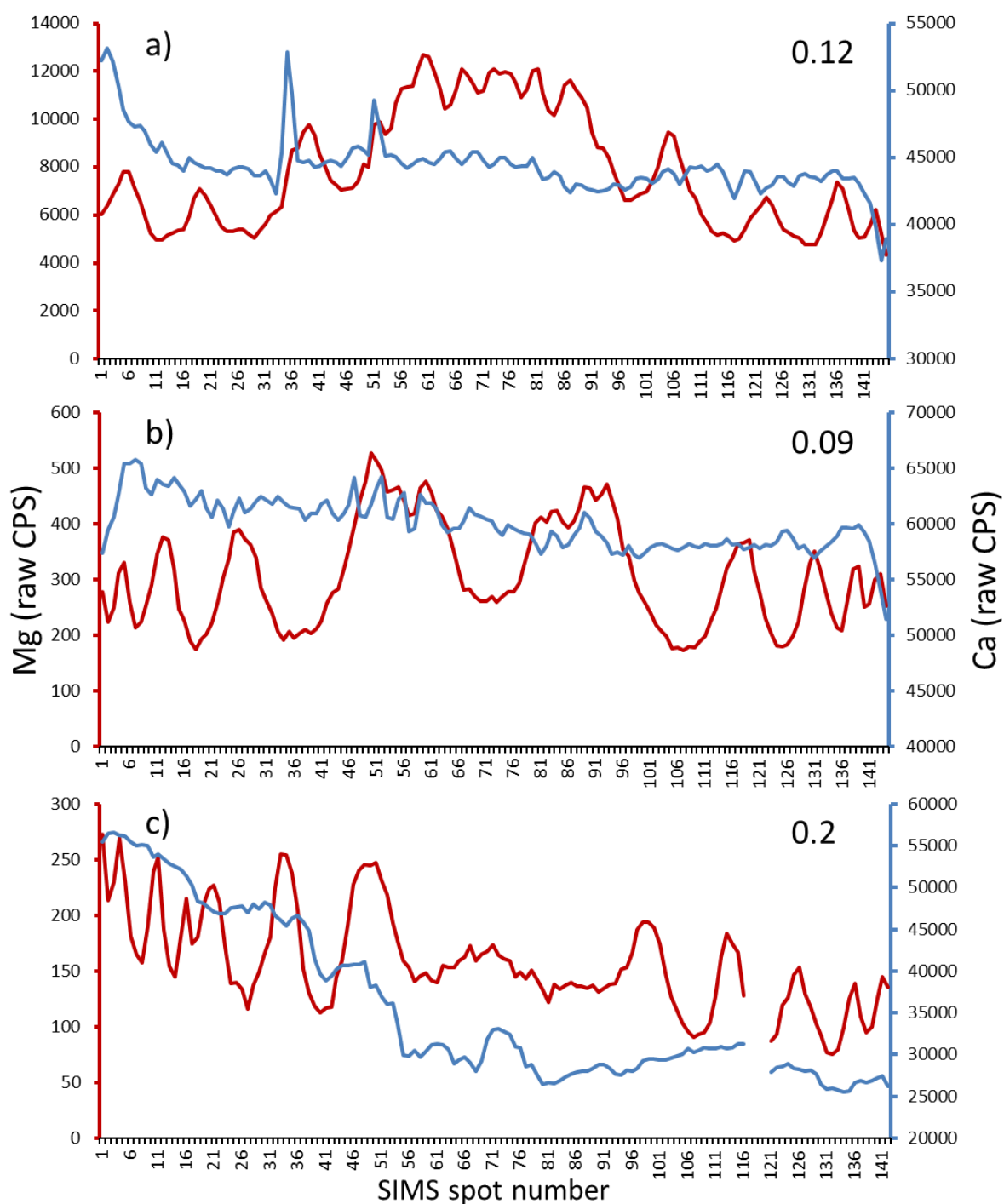


Figure L.1. Raw magnesium (red lines) measurements from SIMS analysis , overlaid with raw calcium measurements (blue lines). a) a sample from Shetland. b) a sample from the Menai Strait and c) a sample from Jersey. The Pearson's correlation coefficients are inset, none of the values presented were statistically significant.

Appendix M:

Outputs from Gompertz growth equations calculated for operculum growth lines at each site without juvenile statolith and '2' clarity operculum data.

Table M.1. Gompertz growth model outputs for Adventitious layers for datasets without '2' clarity samples (top table) and statolith derived juvenile age class samples (bottom table).

Adventitious layers without '2' clarity samples										
	Jersey	JD5	JE4	JE5	Menai Strait	Menai Strait female	Menai Strait Male	Shetland	Holyhead	Nefyn
L0 (mm)	2.91 ±1.65	2.18 ±1.68	2.52 ±1.48	2.12 ±1.19	4.11 ±0.56	3.15 ±0.48	4.29 ±0.53	0 ±0	6.59 ±1.21	2.15 ±1.67
L ∞ (mm)	54.92	47.59	84.42	49.74	78.56	74.42	79.44	104.13	82.73	102.27
K	0.57 ±0.07	0.81 ±0.13	0.38 ±0.07	0.69 ±0.1	0.51 ±0.02	0.69 ±0.05	0.48 ±0.02	0.65 ±0.09	0.39 ±0.05	0.35 ±0.05
R ²	0.71	0.85	0.87	0.93	0.95	0.97	0.97	0.91	0.93	0.88
MSR _e	67.77	47.75	53.14	29.08	40.47	27.44	34.10	110.09	61.89	103.62
	15.64	18.44	-13.86	17.07	19.31	23.09	18.43	11.17	9.73	2.24
n	104	32	35	37	299	148	151	109	36	66

Adventitious layers without juvenile statolith data										
	Jersey	JD5	JE4	JE5	Menai Strait	Menai Strait female	Menai Strait Male	Shetland	Holyhead	Nefyn
L0 (mm)	9.92 ±6.93	28.66 ±18.17	10.56 ±6.2	30.11 ±10.41	7.64 ±6.44	48.73 ±18.66	5.36 ±4.14	0.1 ±0.27	55.61 ±6.18	1.65 ±3
L ∞ (mm)	61.56	75.4	231.59	n/a	80.45	78.85	79.92	105.4	n/a	103.5
K	0.36 ±0.16	0.12 ±0.55	0.13 ±0.15	0 ±1.35	0.43 ±0.07	0.25 ±0.19	0.49 ±0.05	0.55 ±0.08	0 ±3.19	0.36 ±0.11
R ²	0.30	0.07	0.53	0.24	0.35	0.00	0.31	0.58	0.07	0.59
MSR _e	71.86	74.13	71.50	44.43	44.71	33.01	46.57	140.71	138.24	128.01
	9.00	-9.37	-161.03	n/a	17.42	18.66	17.95	9.90	n/a	1.01
n	218	67	82	69	553	245	308	136	89	87

Table M.2. Gompertz growth model outputs for operculum surface rings for datasets without '2' clarity samples (top table) and statolith derived juvenile age class samples (bottom table).

Operculum surface rings without '2' clarity samples										
	Jersey	JD5	JE4	JE5	Menai Strait	Menai Strait female	Menai Strait Male	Shetland	Holyhead	Nefyn
L0 (mm)	0 ±0	0.18 ±0.22	0 ±0	0 ±0	1.81 ±0.45	1.1 ±0.4	1.85 ±0.38	0.73 ±0.55	2.81 ±0.77	3.88 ±1.32
L ∞ (mm)	47.06	49.53	49.10	46.82	78.00	75.72	81.50	105.00	81.40	89.80
K	2.45 ±0.68	1.46 ±0.21	2.59 ±1.48	3.43 ±1.37	1.03 ±0.05	1.13 ±0.08	0.9 ±0.04	1.02 ±0.1	0.82 ±0.09	0.74 ±0.11
R ²	0.81	0.92	0.82	0.95	0.93	0.95	0.97	0.93	0.97	0.92
MSR _e	70.02	20.57	72.98	14.53	51.96	49.44	34.95	123.38	19.74	66.87
	23.50	16.50	21.46	19.99	19.87	21.79	16.37	10.30	11.06	14.71
n	70	18	41	11	310	134	176	65	10	16
Operculum surface rings without juvenile statolith data										
	Jersey	JD5	JE4	JE5	Menai Strait	Menai Strait female	Menai Strait Male	Shetland	Holyhead	Nefyn
L0 (mm)	9.03 ±4.17	23.71 ±12.55	4.44 ±4.21	34.6 ±5.59	36.69 ±4.84	62.72 ±18.03	23.03 ±6.32	1.55 ±2.57	0 ±0.04	19.99 ±8.74
L ∞ (mm)	52.14	51.98	55.87	n/a	79.4	76.88	80.5	107.4	76.5	128.3
K	1.11 ±0.24	0.65 ±0.67	1.21 ±0.4	0.04 ±0.35	0.62 ±0.08	0.38 ±0.65	0.7 ±0.09	0.91 ±0.18	1.23 ±0.34	0.29 ±0.15
R ²	0.32	0.08	0.49	0.18	0.18	0.01	0.25	0.56	0.38	0.48
MSR _e	66.87	68.07	79.35	42.93	48.67	57.76	47.37	172.29	104.85	184.69
	18.42	14.05	14.69	n/a	18.47	20.63	17.37	7.90	15.96	-23.79
n	244	81	82	81	646	251	395	121	78	90

Appendix N:

Journal article validating the periodicity of statolith growth line formation. In review with Marine Ecology Progress Series. Title -

‘Statoliths of the whelk *Buccinum undatum*: a novel age determination tool’

Statoliths of the whelk *Buccinum undatum*: a novel age determination tool

P. R. Hollyman^I, M. J. Leng^{II}, S. R. N. Chenery^{III}, V. V. Laptikhovsky^{IV} and C. A. Richardson^I.

^ISchool of Ocean Sciences, College of Natural Sciences, Bangor University, Menai Bridge, Anglesey, LL59 5AB, UK.

^{II}NERC Isotope Geosciences Facilities, British Geological Survey, Nottingham, NG12 5GG, UK.

^{III}Centre for Environmental Geochemistry, British Geological Survey, Nottingham, NG12 5GG, UK.

^{IV}Centre for Environment, Fisheries and Aquaculture Science (CEFAS), Pakefield Road, Lowestoft, Suffolk, NR33 0HT, UK.

Abstract

The sustainability within the fisheries of the commercially important European whelk, *Buccinum undatum*, has become a major concern through over-exploitation and increased landings in many European coastal shelf seas due to the expansion of export markets to East Asian countries.. Current management of *B. undatum* populations is difficult to achieve as several life history traits make them problematic to accurately monitor. The current method of age determination for stock assessment has a low success rate and focuses on the use of putative annual rings on the surface of the organic operculum. Here we validate an annual periodicity of growth ring formation in *B. undatum* statoliths that provides an alternative, reliable and accurate method for determining a whelk's age. Laboratory reared juvenile *B. undatum* of known provenance and age deposited a hatching ring at the time of emergence from their egg capsule and a clearly defined growth ring during February of their first and second years. Stable oxygen isotope profiles around the shells of two adult whelks confirmed annual growth ring deposition by demonstrating seasonal cycles of $\delta^{18}\text{O}$ in the shell that matched the relative position and number of visible growth rings in the statolith. Validation of annually-resolved statolith growth rings will for the first time, provide fisheries scientists with a tool to determine the age structure of *B. undatum* populations and allow analytical stock assessments that will enable informed decisions for future management practices of whelk fisheries.

Keywords: *Buccinum undatum*, statoliths, age determination, fisheries monitoring, oxygen isotope, Raman Spectroscopy, Sclerochronology

Introduction

The common whelk *Buccinum undatum*, is a commercially important species of marine gastropod fished in the coastal waters of the U.K. and across Northern Europe. In 2015 the UK landings of *B. undatum* by UK vessels totalled 20,900 tonnes with a value at first sale of £18.7 million (MMO, 2016). A large proportion of the whelk landings in the UK and Ireland supply an export market to East Asia that has grown steadily since the mid-1990s (Fahy *et al.*, 2000) in response to recent increases in consumer demand which has driven the expansion of the fishery. However, declines in the number of whelks caught have been noted across European waters (Jersey - Shrives *et al.*, 2015; Ireland - Fahy *et al.*, 2005; North Sea/Netherlands - Ten Hallers-Tjabbes *et al.*, 1996) and have caused several local Inshore Fishery and Conservation Authorities (IFCA's) recently to implement restrictions such as pot and/or catch limits and the number of permits issued (Devon & Severn IFCA, 2016, Eastern IFCA, 2016 and Kent & Essex IFCA, 2016).

The reliable assessment of age and longevity of *B. undatum* is problematic for fisheries scientists, due to *B. undatum* having several life history traits which make them difficult to monitor at a population level. The lack of a planktonic larval stage and a relatively inactive adult lifestyle with no apparent migration (Pálsson *et al.*, 2014) has led to the formation of geographically discrete stocklets which are then vulnerable to overexploitation (Fahy *et al.*, 2000). In many studies these stocklets have been observed to show clear genetic and morphological differences (e.g. Weetman *et al.*, 2006; Shelmerdine *et al.*, 2007; Magnúsdóttir, 2010), including size at maturity which can also differ markedly between sites (McIntyre *et al.*, 2014; Haig *et al.*, 2015; Shrives *et al.*, 2015).

To resolve this conundrum a reliable ageing method needs to be established for *B. undatum* so that accurate population age assessments and analytical stock assessments can be undertaken. The currently accepted method used by fisheries scientists, and validated by Santarelli and Gros (1985), determines the age of whelks by reading growth rings on the operculum, an organic 'shield' that is used to protect the shell aperture when the animal withdraws into its shell. This was achieved by matching cycles in oxygen isotope composition from the shell to the numbers of growth rings

observed on the opercula. However, this method traditionally has had a low success rate owing to the poor clarity of the rings, a problem highlighted by Kideys (1996), who reported that only 16%, from a total of 10,975 opercula examined in whelks from the Isle of Man, U.K., having 'clear and readable' rings, with a further 32% having 'readable' rings, leading to 48% of the samples being discarded. More recently, similar low levels of readability were found in several sites around the UK (Lawler, 2013). The exclusion of large portions of samples due to poor clarity of the rings is likely to have biased the data; the constructed population growth curves were highly variable, presumably due to the ambiguity of the opercular readings.

Since whelks are becoming increasingly exploited there is an urgent scientific need to underpin the fisheries stock assessment of their populations with accurate data concerning the age of individuals and their growth rates. For many mollusc species, the age of an individual can be determined by counting the annual growth lines present in longitudinal shell sections (See Richardson, 2001, for review). This is particularly applicable to bivalve molluscs, but in gastropods this is not possible because there are often no obvious annual growth rings on or contained within their shells.

Mollusc shells are repositories of information about the past environmental history of shell growth and contain within the carbonate of their shells biogenic trace elements and oxygen isotope ratios ($^{18}\text{O}/^{16}\text{O}$, described as $\delta^{18}\text{O}$) which are incorporated into the shell matrix at equilibrium during mineralisation (Wilbur & Saleuddin 1983; Wheeler 1992). Seawater temperature at the time of shell formation can be reconstructed from the gastropods shell throughout ontogeny by determining $\delta^{18}\text{O}$ along the growing axis of the shell e.g. *Rapana venosa* (Kosyan & Antipushina, 2011) and *Conus ermineus* (Gentry *et al.*, 2008). The empirical fractionation of oxygen isotopes in seawater with changes in temperature (Epstein *et al.*, 1953) are well known, a more negative value of $\delta^{18}\text{O}$ reflects warmer seawater temperatures whilst a more positive value is indicative of cooler seawater temperatures (Grossman & Ku, 1986) at a constant $\delta^{18}\text{O}$ of seawater. Sampling the shell carbonate at known intervals along the whorled axis of the shell and determining seasonal changes in $\delta^{18}\text{O}$

allows the age (seasonality) of the shell to be determined. This approach is not suitable for large scale ageing of whelk due to the cost of analysing the potentially huge numbers of samples needed to accurately reconstruct the seasonality across a significant number of shells.

In lieu of being able to directly use the shells or opercula to estimate age, whelks contain an accretory hard structure which is the focus of this paper, the statolith. Statoparticles (such as statoliths) are structures that are integral to the nervous system of a diverse range of animal groups including the Polychaeta (Beesley *et al.*, 2000), Holothuroidea (Ehlers, 1997), Crustacea (Espeel, 1985) and several classes of the Mollusca e.g. the Bivalvia (Morton, 1985), Gastropoda (Barroso *et al.*, 2005; Chatzinikolaou & Richardson 2007; Galante-Oliveira *et al.*, 2013) and Cephalopoda (Arkhipkin, 1997). They are used in gravity perception and are contained within a nerve sac, the statocyst, which detects movement of the statoparticle, indicating a change in orientation (Chase, 2002). Commonly composed of calcium carbonate they have a wide ranging morphology across the phylum in which they are found. The statoparticles of gastropods are often singular, roughly spherical granules called statoliths (collections of multiple smaller granules, see Fretter & Graham, 1994; Richardson, 2001). Gastropod statoliths can contain rings that are deposited annually e.g. *Nassarius reticulatus* (Barroso *et al.*, 2005), *Neptunea antiqua* (Richardson *et al.*, 2005b) and *Polinices pulchellus* (Richardson *et al.*, 2005a) and are an archive of biota life history, containing information about the age and the seasonal temperature cycles (Richardson *et al.*, 2005a, Galante-Oliveira *et al.*, 2015) and their transition from a planktonic pelagic larval lifestyle to a benthic existence (Barroso *et al.*, 2005; Richardson *et al.*, 2005a; Chatzinikolaou & Richardson 2007). Once the rings in the statolith have been deciphered, information about a gastropod's life history can be extracted to understand their ontogenic growth. Thus they are potentially an invaluable resource for fisheries scientists who could use this information to assess population structure of commercially important gastropod species such as *B undatum*.

Here we demonstrate for the first time that growth rings in the statoliths of *B undatum* are annually deposited like those within the opercula and can be used for the reliable age estimation of the species. The timing of statolith growth ring formation was determined in whelks of known age and life history that had been reared in the laboratory under ambient seawater temperatures for two years following their emergence from egg capsules. The structure of the statoliths was also investigated to determine their general morphology and mineralogical composition. We then used shell $\delta^{18}\text{O}$ profiles drilled from around the whorl and compared these data with the matching whelk statoliths growth lines.

Materials and methods

Field collection: Approximately 200 whelks (>25mm shell length) were trapped and collected in February 2015 from a site in the Menai Strait (North Wales, U.K., 53.235556, -4.141835 – decimal degrees, depth 10-11.5m) using a string of 3 baited scientific inkwell pots laid for 24 hours. The drainage holes in the pots were covered with 3mm mesh and the whelk catch was not riddled (the process used by fishermen to remove undersized whelks) to ensure all size classes were retained for analysis. Dispensation for the landing of undersized whelks (<45mm) was granted by the Welsh Government (disp#004). Once collected, whelks were frozen until required, whereupon they were thawed and the body removed from their shells using forceps by gently pulling on the foot to detach the collumellar muscle. Shell height (aperture to spire length) was measured to the nearest 1mm using Vernier callipers, total body weight was recorded to the nearest 0.1g and reproductive maturity assessed using the scale of Haig *et al.* (2015). The bodies of each whelk were re-frozen for later statolith extraction.

Laboratory experiment: This experiment was designed to study the formation of the whelk statolith during ontogeny and to determine the timing of growth ring formation. Seven whelk egg masses that had been laid naturally in an intertidal location at Tal-y-Foel (53.158512, -4.279493 – decimal degrees), in the Menai Strait were collected in November 2013 and 2014. Egg masses were

transported to the laboratory and held in aquaria supplied with flowing ambient seawater from the Menai Strait. Approximately 2 months later juvenile whelks hatched directly from the egg capsules and were reared for 1 year (2014 hatching) and 2 years (2013 hatching) under an approximate 10:14hr light/dark cycle and fed regularly thrice weekly with small pieces of frozen and thawed mackerel *Scromber scrombus*. Each month for 24 months, ten whelks were removed and frozen for later statolith extraction.

Stanolith extraction and ageing: Selected individuals of both frozen field caught adult and laboratory reared juvenile whelks were thawed (3hrs) and the body bisected (Figure 1a). Each half of the whelk body was examined under a low power binocular microscope to locate, dissect and then remove, using fine forceps (0.10 x 0.06mm tip), a pair of statocyst sacs (left and right side) each containing a statolith (Figure 1b). Incident illumination as well as transmitted light were used during the dissections and highlighted the statoliths as small shadows beneath the cerebral ganglion (Fig. 1c). The <0.75mm statocysts were transferred to a watch glass with a drop of Milli-Q® ultrapure water (Merck Millipore), torn open and the statoliths removed using a hypodermic needle (0.5 mm diameter). Where necessary, each statolith was cleaned of any adhering tissue by immersion in 20% sodium hydroxide (NaOH) for 30 minutes and rinsed in Milli-Q® quality water. Once the statoliths had air-dried they were mounted on a microscope slide using Crystalbond™ 509 thermoplastic resin and imaged under a Meiji Techno MT8100 microscope with a Lumenera Infinity 3 microscope camera at 40x magnification. This allowed the visualisation of the statolith growth rings that could then be counted and statolith diameter measured using ImageJ (version 1.48, Ferreira & Rasband 2012; Fig. 2).

Scanning Electron Microscopy (SEM): Several statoliths from the right and left side of small and large whelks were selected for structural analysis. Each statolith was mounted in Crystalbond™ 509 on an aluminium SEM stub and imaged as above. The statolith was ground by hand to the central plane using progressively finer 400, 1200, 2500 & 4000 silicon carbide grinding papers lubricated with

Milli-Q® quality water. Each statolith was finally polished with a 1 µm diamond suspension gel and thoroughly cleaned with detergent and water and dried before submersion in 0.1M hydrochloric acid for 2 minutes to etch the exposed statolith surface. The exposed and etched statolith surfaces were then imaged using a FEI QUANTA 600 environmental scanning electron microscope (SEM) operated in low vacuum mode, with an electron beam accelerating voltage of 12.5 - 15 kV, a beam probe current of 0.14 - 0.26 nA, and a working distance of 10.6-10.9 mm.

Micro-Raman Spectroscopy (MRS): Raman spectroscopy allows differentiation between the polymorphs of CaCO₃ (amorphous CaCO₃, calcite, aragonite and vaterite) by focusing a laser light onto the statolith surface. Inelastic scattering of the incident light occurs after interacting with the sample structure due to interaction with the vibrational levels of the composite molecules causing a shift in the wavelength of the measured scattered photons (Raman shift) (Higson, 2006). The wavelength shifts of the spectra are predictable in position and intensity for different substances. For CaCO₃, two main wavelength regions of the spectra are of interest, peaks in the 100–350 cm⁻¹ range pertain to interaction with features of the external lattice structure whereas peaks in the 600–1800 cm⁻¹ relate to interactions with the internal molecular planes (Parker *et al.*, 2010). To determine the statolith composition, individual statoliths were fractured using fine tipped forceps (0.10 x 0.06mm tip) to reveal the inner growth axis and analysed with MRS (Reinshaw InVia Raman-Microscope) at the Diamond Light Source, Harwell, UK. The MRS consisted of a 473 nm laser at a power of 15 mW and focussed using a lens with a magnification of 20x; a grating with 2400 lines/mm⁻¹ and a pinhole size of 100 µm were used for spectra acquisition. The spectra were acquired between 100 and 3200 cm⁻¹. Three sample spots were taken approximately equidistant along the interior growth axis of three statoliths from the central nucleus to the outer edge. Synthetic calcite and speleothem aragonite standards (Brinza *et al.*, 2014) were analysed prior to and after statolith analyses and the resulting Raman spectra adjusted using a polynomial background correction. Following MRS, the fractured statolith surface was imaged using SEM to obtain a detailed image of the sampled surface.

Isotope Ratio Mass Spectrometry (IRMS): The outer periostracum and any adhering material were cleaned from the shells of an adult male and female whelk collected from the Menai Strait using a stiff bristled brush and tap water and air-dried. The shell surface was abraded using a 1mm diamond burr attached to a Dremel® 4000 to remove any contamination from the shell surface. A sampling axis around the entire whorled growth was marked out close to the shoulder of the shell whorl with 1mm notations along its length. 1x10mm tracks were drilled at a resolution of 2 mm at the apex and most recently formed whorl, the oldest and youngest parts of the shell, then at 4mm for the central portion where growth is fastest, in line with the visible growth striations. Care was taken to only sample the outer nacreous layer of the shell and not drill into the inner nacreous layers which are deposited at a later time. The drilled CaCO_3 samples were collected on small square (2x2 cm) sheets of greaseproof paper transferred to a labelled 0.5ml Eppendorf tube. This sampling strategy was extended as close to the tip of the shell as possible, however, in all cases the earliest shell growth (top 1-1.5cm) could not be sampled owing to shell damage and resolution of drilling.

Approximately 50 – 100 μg of powdered carbonate sample were used for isotope analysis using an IsoPrime dual inlet mass spectrometer plus Multiprep device (at the British Geological Survey, Keyworth, UK). Weighed samples were added to glass vials which were then evacuated and anhydrous phosphoric acid (H_3PO_4) was added to each sample at 90°C . The samples were left to digest for 15 minutes and the expressed gas collected, cryogenically cleaned to remove any moisture and passed into the mass spectrometer. Isotope values ($\delta^{13}\text{C}$, $\delta^{18}\text{O}$) are reported as per mille (‰) deviations of the isotopic ratios ($^{13}\text{C}/^{12}\text{C}$, $^{18}\text{O}/^{16}\text{O}$) calculated to the VPDB scale using a within-run laboratory standard (KCM) calibrated against NBS-19. The aragonite-acid fractionation factor applied to the gas values was 1.00855 (Sharma & Clayton, 1965). A drift correction is applied across the run, calculated using the standards that bracket the samples. The Craig correction was also applied to account for the influence of $\delta^{17}\text{O}$ within the sample (Craig, 1967). The average analytical reproducibility of the standard calcite (KCM) is 0.05‰ for $\delta^{13}\text{C}$ and $\delta^{18}\text{O}$. The resulting ($^{18}\text{O}/^{16}\text{O}$ ratio)

data were treated with a 5-point Savitsky-Golay smoothing filter (Steiner *et al.*, 1972). The $\delta^{13}\text{C}$ data is not presented here.

Results

Statolith location and morphology: Each whelk contains two statocysts in the tissues of its foot each containing a single roughly spherical statolith (st) (<0.75mm in diameter) (Fig. 1b). Each statolith appears as a small shadow visible in cross section of the whelk body indicating its position. Bisected down the middle of the whelk (dotted line Fig. 1a), a single statolith is revealed in each half of the body. Orientation of the statolith in resin in a dorsal/ventral position shows a circular outline shape and is the optimum position to view and measure the visible growth rings (Fig. 2a). Laterally the statolith has an oval shape (Fig. 2b) and has a dorso-ventrally compressed spherical shape where the rings are less clear. Thus to maintain consistency and to maximise the visibility of the rings all analyses/images were undertaken from statoliths orientated in a dorsal-ventral view.

Figure 3a shows that shell length (SL) has a strong relationship with statolith diameter (StD) and relative statolith diameter (RStD), $R^2 = 0.96$ and 0.97 respectively). The latter relationship shows that smaller whelks have relatively larger statoliths compared with large whelks. Statoliths grow with negative allometry in respect to the SL with smaller animals having relatively large statoliths, the character of this allometry changes at $SL \approx 5\text{-}15\text{ mm}$. The data closely fit the line for whelks <60mm allowing estimates of shell length to be determined from the diameter of the rings. However, above this size there is wide variation in statolith diameter. By measuring the statolith diameter at successive rings for whelks <60mm it is feasible to reconstruct shell length at each ring. Figure 3b, shows the relationship between StD and age (ascertained from statolith rings in field caught whelks) has a polynomial relationship ($R^2 = 0.91$). Although there is a strong relationship, there are large amounts of overlap between ages. The clarity of the statoliths was also very high with the vast majority of samples included in the analysis ($n=800$). 48.6% of the samples were classed as 'clear and

readable' and a further 43% as 'readable (using the same criteria as Kideys, 1996), thus only 8.4% of samples were excluded.

Statolith Structure: The broken statolith shown in Figure 4a is composed of aragonite. The Raman spectra extracted between 100 and 750 cm^{-1} demonstrate a coincidence of peaks at 151 cm^{-1} , 183 cm^{-1} , 206 cm^{-1} and a wide peak at 702-706 cm^{-1} for both sample spots 1-3 from the statolith and the aragonite standard (Figure 4b). A shoulder is also visible on the 151 cm^{-1} peak at 143 cm^{-1} . By contrast the calcite standard peaks at 155 cm^{-1} , 281 cm^{-1} and 712 cm^{-1} indicate that this statolith contains no trace of calcite. Figure 4c shows an additional peak between 2850 and 3000 cm^{-1} for the three sample spots. Peaks in this range are thought to be indicative of C-H functional groups found within organic matter (Smith & Dent, 2005) thus likely indicative of the presence of an organic component within the crystal matrix. Figure 5 shows the agreement between the visible rings in the optical microscope (OM) image of a whole statolith (Fig. 5a) and the exposed acid etched SEM image of the central plane of the paired statolith (Fig. 5b). The clarity of the rings in Figure 5b suggests that a clear structural change has occurred during the formation of a growth ring.

Hatching ring and growth ring formation: The inner opaque area seen in Figure 5a signifies the period of development in the egg culminating in the formation of a hatching ring (HR). The hatching ring can also be seen and appears in January when these animals hatched (Figure 6a, b, c & d). For the 2013 juvenile cohort the hatching ring was deposited at a statolith diameter of $53.6 \pm 4\mu\text{m}$ ($\pm 1\text{SD}$, $n=30$) and for the 2014 cohort at $55.1 \pm 6\mu\text{m}$ ($\pm 1\text{SD}$ $n=30$). The data from the two cohorts were not significantly different (paired t-test, $p = 0.15$). The central opaque area (larval growth) seen in Figure 5a is followed by a less opaque region containing weak and diffuse rings. This pattern is also mirrored in Figure 6 which shows the ontogenetic development of statoliths removed from laboratory reared animals of different ages between 2 weeks and 2 years. Clear disturbance rings can be seen in the increment following hatching ring deposition and are a common feature of adult statoliths. The clear year 1 ring in the statolith in Figure 6d marks a colour change from brown to

light brown and was deposited in February during the coldest part of the annual temperature cycle. A similar positioned ring can be seen in Figure 5a, signifying the first annual ring formation. The colour change is regularly seen in statoliths taken from 'field caught' adult whelks and is a good indicator of the position of the first annual growth ring. Following deposition of the slightly unclear first annual ring, subsequent annual rings are clearly delineated in both the optical microscope and SEM images of Figure 5a & b. Disturbance rings, that are a common feature of the statoliths in younger whelks, are typically much weaker in definition than the clear annually-resolved rings.

Annual growth ring validation: Figure 7 shows the coincidence between the statoliths ring position (7c & f) and maximum values in the shell $\delta^{18}\text{O}$ cycles (7a & d). Maximum $\delta^{18}\text{O}$ represents minimum seawater temperatures. The three $\delta^{18}\text{O}$ minima in the female shell (a) match the position of the three statolith rings (c) and the four maxima seen in the male shell (d) match the four statolith rings (f). In both shells the tip of the apex was not sampled, represented by the grey hatch area in Figure 7a & d, and the point at which sampling ceased is indicated by a black arrow (Fig. 7b and e).

Discussion

This study validates for the first time the annual periodicity of growth rings found within the statoliths of the common whelk, *Buccinum undatum*; as well as investigating their structure and composition. This was achieved using a combination of laboratory rearing of juvenile specimens and geochemical analysis of both statoliths and shells from wild collected adults. The validation of the annual growth lines as a reliable ageing tool will provide an alternative to the currently used and often unreliable operculum.

Visualization, interpretation and timing of statolith ring formation: In a previous study following extraction and statolith cleaning, Richardson *et al.* (2005a) hand-ground and polished the statoliths of the neogastropod *Neptunea antiqua* to observe the growth rings. However in the current study when *B. undatum* statoliths were hand-ground (using the above described methods for SEM

preparation) and observed in the optical transmitted light microscope, weaker disturbance rings became more apparent and often obscured the earliest annual growth rings due to the removal of the overlying statolith structure which often masked them. However, when a whole statolith was observed weaker lines were less apparent and this approach was adopted throughout the study.

A single, clear growth ring was deposited annually within the statoliths of the laboratory reared juveniles during February and March when seawater temperatures were minimal in the Menai Strait. Female *B. undatum* lay egg capsules in which larvae develop and juveniles hatch directly leaving their egg capsules without a planktonic larval stage. The first discernible weakly defined statolith ring deposited can be termed a 'hatching ring', formed as the juveniles emerge from their capsules. The hatching ring has a similar position in the statolith to the settlement ring in statoliths from *Polinices pulchellus* (Richardson *et al.*, 2005b) and *Nassarius reticulatus* (Barroso *et al.*, 2005; Chatzinikolaou & Richardson 2007)) that hatch from egg capsules and undergo a planktonic larval existence prior to settlement. Thus importantly, these two kinds of juvenile rings in gastropods with different early life strategies represent the same life history event i.e. the transition from larvae to juvenile. Whilst hatching ring diameters in reared *B. undatum* juveniles are fairly constant (53.6 to 55.1µm), it has been shown that maternal size directly influences egg capsule size and subsequently juvenile hatching size, which in turn can also be mediated by intra-capsular cannibalism (Nasution, 2003; Nasution *et al.*, 2010, Smith & Thatje, 2013). Therefore, in a population with larger than average sized whelks, the hatching ring will be larger than the average observed here. A strong relationship exists between statolith diameter and shell length, however with wide variation in statolith diameters in large (>60mm) and older whelks means that it is not possible to estimate an older whelk's age solely from statolith size. The age of each whelk must be determined by counting the number of annually-resolved statolith rings. The annual periodicity of the growth rings was further validated with the reconstruction of $\delta^{18}\text{O}$ profiles from shells (Fig. 7). This is the same method used by Santarelli & Gros (1985) to validate the observable growth rings in the opercula. However, in this study a higher sampling resolution was used, producing more clearly

defined $\delta^{18}\text{O}$ cycles that are directly overlaid on the visible growth rings of the statolith. Santarelli and Gros (1985) did not demonstrate the ages of the animals from the opercula.

Statolith composition: The statoliths of *B. undatum* are aragonite as shown by Raman spectra with no visible trace of calcite. There was close agreement between the aragonite standard and the sample spots taken from the statolith, several of the reported Raman spectra peaks differed by 1-3 cm^{-1} compared with those reported in the literature (see Parker *et al.*, 2010). It is probable that the difference between the observed statolith spectra peaks and the published spectra is the presence of trace elements such as Mg^{2+} substituting for Ca^{2+} within the lattice and distorting it (Parker *et al.*, 2010). This would explain why the synthetic calcite standard exhibited all of the expected peaks whereas the sample spots and the speleothem aragonite standard (which can contain trace elements, Finch *et al.* 2001) did not. The Raman spectra of the sample spots also exhibited a diffuse band between 2850 and 3000 cm^{-1} which likely indicates the presence of structural organic matter within the CaCO_3 matrix. All three of the spot samples showed a peak in the spectra likely indicating the presence of organic matter throughout the statolith matrix, although the most intense peak was observed when the structure of a growth ring was analysed (spot 3 on the statolith). A similar conclusion was reached by Galante-Oliveira *et al.*, (2014) who observed similar spectra in the statoliths of *Nassarius reticulatus*. If the Raman peaks represent differences in the concentration of organic matter present in different parts of the statolith then this will aid in interpreting the distribution of elements such as Sr and Mg in the statolith. In *N. reticulatus* annual cycles of Sr-Ca ratios were found to correspond with the visible growth rings (Galante-Oliveira *et al.*, 2015) with minimum ratios associated with the rings and maximum concentrations present in the increments between adjacent rings. Schöne *et al.* (2010) has demonstrated the role of organic material in bivalve shells in regulating the control of biogenic element incorporation into the shell structure, highlighting that insoluble organic matter present aragonitic shell of *Arctica islandica* is significantly enriched in Mg and depleted in Sr.

Absence of Juveniles from field collected samples: Small (<25mm) *B. undatum* were completely absent from the baited scientific inkwell pots deployed in the Menai Strait despite every effort to entice, trap and retain the smaller whelk size classes. Shelmerdine *et al.* (2007) similarly were unable to catch small-sized whelks in traps deployed at two sampling sites around the Shetlands (Scotland, East Shetland – landed in Scalloway, West Shetland – landed in Whalsay) and one in southern England (landed in Deal). In order to study the relationship between statolith diameter and shell length and the number of statolith rings (age) and shell length, data were therefore obtained from field-caught whelks and small juvenile laboratory-reared juveniles. The absence of small juvenile whelks in the study of Shelmerdine *et al.* (2007) was attributed to predation pressure from shore crabs who targeted the juvenile whelks. However, more plausible explanations are that juvenile whelks, following emergence from their egg capsules congregate in nursery grounds distant from the main adult fished populations. We are of the opinion and from anecdotal conversations with local whelk fishermen that for some populations, egg laying, juvenile development and growth of *B. undatum* likely takes place in inshore nursery areas from where the juveniles move and recruit into the adult fished populations. Further exploration of this topic is beyond the current study. Understanding differences in the age, growth rate and distributions of whelks in coastal waters will add immeasurably to understanding how to manage and conserve these important scavengers in coastal zones.

Implications for fisheries: With the development of this ageing technique for such a commercially important species, the construction and comparison of population growth curves can be easily implemented on a potentially large scale. Vast improvements over the operculum age determination method have been shown, with a decrease in discarded samples from 48% down to 8.4% and an increase in useable samples from 52% to 91.6%. Whilst the methodology for statolith extraction and analysis is potentially more time consuming than the use of opercula, the huge increase in reliability and decrease in potential sample bias (from large discards) is clear.

Summary

Here, an annually-resolved periodicity of growth ring formation in whole resin-mounted statoliths from *Buccinum undatum* was validated by comparison with seasonally-collected and laboratory-reared juvenile whelks of known age and from similarities between growth rings and the $\delta^{18}\text{O}$ cycles in their shells. This validated novel age determination tool (using the statoliths) can be used to accurately reconstruct the population structure and population growth rates of *B. undatum* and the technique will now be available for fisheries scientists to undertake stock assessments of whelk populations European-wide to determine both size at age, and age at reproduction. These are both metrics that will aid in future management decisions. The statoliths present a viable alternative to the 'difficult to use' opercula. *Buccinum undatum* statoliths are composed of aragonitic calcium carbonate and their structure determined by Raman-Microscopy has revealed variations in organic matter throughout the statolith that might have implications for the way in which biogenic elements are incorporated into the organic lattice of the statolith. Overall we conclude understanding differences in the age, growth rate and distributions of whelks in coastal waters will add immeasurably to understanding how to manage and conserve these important scavengers in coastal zones.

Acknowledgements

This work was supported through a Bangor University/CEFAS partnership PhD scholarship to PH. We are grateful to Gwynne Parry-Jones for collecting the *Buccinum undatum* from the Menai Strait. The IRMS analyses were supported by a NERC Isotope Geosciences Facilities Steering Committee (IP-1527-0515) award and thanks to Hilary Sloane for technical support. Access to the Reinshaw Raman-Microscope was made possible through a rapid access request to the Diamond Light Source (SP13616-1). Production of the SEM micrographs would not have been possible without the help of Dr Lorraine Field (BGS) and Dr. Andy Marriott (BGS). A number of colleagues and students, Richard Patton, Charlotte Colvin, Helène Bonici, Anton Antonov and Devaney Werrin are acknowledged for

their invaluable help with animal husbandry. We also thank Dr. Ewan Hunter and Dr. Andy Marriott, whose comments improved the manuscript greatly.

M. Leng and S. Chenery publish with the permission of the Director British Geological Survey and PH is registered as a BUFI student within BGS.

References

- Arkhipkin AI (1997) Age of the micronektonic squid *Pterygioteuthis gemmata* (Cephalopoda: Pyroteuthidae) from the central-east Atlantic based on statolith growth increments. *J Mollus Stud* 63: 287-290
- Barroso CM, Nunes M, Richardson CA, Moreira MH (2005) The gastropod statolith: a tool for determining the age of *Nassarius reticulatus*. *Mar Biol* 146: 1139–1144
- Beesley PL, Ross GJB, Glasby CJ (eds) Polychaetes & Allies: The Southern Synthesis. Fauna of Australia. Vol. 4A Polychaeta, Myzostomida, Pognophora, Echiura, Sipuncula. CSIRO publishing, Melbourne.
- Brinza L, Schofield PF, Mosselmans JFW, Donner E, Lombi E, Paterson D, Hodson ME (2014). Can earthworm-secreted calcium carbonate immobilise Zn in contaminated soils? *Soil Biol Biochem* 74: 1-10.
- Chase R (2002) Behaviour & its neural control in gastropod molluscs. Oxford University Press, New York
- Chatzinikolaou E, Richardson CA (2007) Evaluating the growth and age of the netted whelk *Nassarius reticulatus* (gastropoda: nassaridae) from statolith growth rings. *Mar Ecol Prog Ser* 342: 163-176.
- Craig H (1957) Isotopic standards for carbon and oxygen & correction factors for mass spectrometric analysis. *Geochim. Cosmochim. Acta* 12: 133-149.
- Devon & Severn IFCA (2016) <http://www.devonandsevernifca.gov.uk/> (accessed 1/7/16)
- Eastern IFCA (2016) <http://www.eastern-ifca.gov.uk/> (accessed 1/7/16)
- Ehlers U (1997) Ultrastructure of the Statocysts in the Apodous Sea Cucumber *Leptosynapta inhaerens* (Holothuroidea, Echinodermata). *Acta Zool – Stockholm* 78 (1): 61-68
- Epstein S, Buchsbaum JR, Lowenstam HA, Ukey HC (1953) Revised carbonate-water isotopic temperature scale. *Bull Geol Soc Am* 64: 1315-1326
- Espeel M (1985) Fine structure of the statocyst sensilla of the mysid shrimp *Neomysis integer* (Leach, 1814) (Crustacea, Mysidacea). *J Morphol* 186: 149-165

- Fahy E, Carroll J, O'Toole M, Barry C, Hother-Parkes L (2005) Fishery associated changes in the whelk *Buccinum undatum* stock in the southwest Irish Sea, 1995-2003. Irish Fisheries Investigations 15, Marine Institute, Dublin.
- Fahy E, Masterson E, Swords D, Forrest N (2000) A second assessment of the whelk fishery *Buccinum undatum* in the southwest Irish Sea with particular reference to its history of management by size limit. Irish Fisheries Investigations 6, Marine Institute, Dublin.
- Ferreira T, Rasband W (2012) ImageJ User Guide.
- Finch AA, Shaw PA, Weedon GP, Holmgren K (2001) Trace element variation in speleothem aragonite: potential for palaeoenvironmental reconstruction. Earth and Planet Sci Lett 186: 255-267
- Fretter V, Graham A (1994) British Prosobranch Molluscs. The Ray Society, London.
- Galante-Oliveira S, Marçal R, Espadilha F, Sá M, Abell R, Machado J, Barroso CM (2015) Detection of periodic Sr Ca⁻¹ cycles along gastropod statoliths allows the accurate estimation of age. Mar Biol 162: 1473-1483. doi 10.1007/s00227-015-2684-y
- Galante-Oliveira S, Marçal R, Guimarães F, Soares J, Lopes JC, Machado J, Barroso CM (2014) Crystallinity and microchemistry of *Nassarius reticulatus* (Caenogastropoda) statoliths: towards their structure stability and homogeneity. J Struct Biol 186:292–301. doi:10.1016/j.jsb.2014.03.023
- Galante-Oliveira S, Marçal R, Ribas F, Machado J, Barroso CM (2013) Studies on the morphology and growth of statoliths in Caenogastropoda. J Mollus Stud 79:340–345. doi:10.1093/mollus/eyt028
- Gentry DK, Sosdian S, Grossman EL, Rosenthal Y, Hicks D, Lear CH (2008) Stable isotope and Sr/Ca profiles from the marine gastropod *Conus ermineus*: testing a multiproxy approach for inferring paleotemperature and Paleosalinity. Palaios 23: 195-209. doi: 10.2110/palo.2006.p06-112r
- Grossman EL, Ku T (1986) Oxygen and carbon isotope fractionation in biogenic aragonite: Temperature effects. Chem Geol 59: 59-74. doi: 10.1016/0168-9622(86)90057-6
- Haig JA, Pantin, JR, Murray LG, Kaiser MJ (2015) Temporal and spatial variation in size at maturity of the common whelk (*Buccinum undatum*). ICES J Mar Sci 72 (9): 2707-2719. doi:10.1093/icesjms/fsv128
- Higson SPJ (2006) Analytical Chemistry. Oxford University Press, New York.
- Kent & Essex IFCA (2016) <http://www.kentandessex-ifca.gov.uk/> (accessed 1/7/16)
- Kideys AE (1996) Determination of age and growth of *Buccinum undatum* L. (Gastropoda) off Douglas, Isle of Man. Helgol. Meeresunters. 50 (3), 353–368.
- Kosyan AR, Antipushina ZA (2011) Determination of *Rapana venosa* individuals' ages based on the $\delta^{18}\text{O}$ dynamics of the shell carbonates. Oceanology 51: 1021-1028. doi:10.1134/S0001437011060075

- Lawler A (2013) Determination of the size of maturity of the whelk *Buccinum undatum* in English waters – Defra Project MF0231.
- Magnúsdóttir H (2010) The common whelk (*Buccinum undatum* L.): Life history traits and population structure. Master thesis. University of Iceland, Reykjavik.
- Marine Management Organisation (2016) UK Sea Fisheries Statistics 2015. Office for National Statistics, London. 156 pp.
- McIntyre R, Lawler A, Masefield R (2015) Size of maturity of the common whelk, *Buccinum undatum*: Is the minimum landing size in England too low? Fish Res 162: 53–57. doi:10.1016/j.fishres.2014.10.003
- Morton B (1985) Statocyst structure in the Anomalodesmata (Bivalvia). J Zool 206: 23–34. doi:10.1111/j.1469-7998.1985.tb05633.x
- Nasution S (2003) Intra-capsular development in marine gastropod *Buccinum undatum* (Linnaeus 1758). Jurnal Natur Indonesia 5: 124–128.
- Nasution S, Roberts D, Farnsworth K, Parker GA, Elwood RW (2010) Maternal effects on offspring size and packaging constraints in the whelk. J Zool 281: 112–117. doi:10.1111/j.1469-7998.2009.00681.x
- Parker JE, Thompson SP, Lennie AR, Potter J, Tang CC (2010) A study of the aragonite–calcite transformation using Raman spectroscopy, synchrotron powder diffraction and scanning electron microscopy. Cryst Eng Comm 12: 1590–1599. doi: 10.1039/b921487a
- Pálsson S, Magnúsdóttir H, Reynisdóttir S, Jónsson ZO, Örnólfsdóttir EB (2014) Divergence and molecular variation in common whelk *Buccinum undatum* (Gastropoda: Buccinidae) in Iceland: a trans-Atlantic comparison. Biol J Linn Soc Lond 111: 145–159. doi:10.1111/bij.12191
- Richardson CA (2001) Molluscs as archives of environmental change. Oceanogr Mar Biol 39:103–164
- Richardson CA, Kingsley-Smith PR, Seed R, Chatzinikolaou E (2005b) Age and growth of the naticid gastropod *Polinices pulchellus* (Gastropoda: Naticidae) based on length frequency analysis and statolith growth rings. Mar Biol 148: 319–326. doi:10.1007/s00227-005-0072-8
- Richardson CA, Saurel C, Barroso CM, Thain J (2005a) Evaluation of the age of the red whelk *Neptunea antiqua* using statoliths, opercula and element ratios in the shell. J Exp Mar Biol Ecol 325: 55–64. doi:10.1016/j.jembe.2005.04.024
- Santarelli L, Gros P (1985) Age and growth of the whelk *Buccinum undatum* L. (Gastropoda: Prosobranchia) using stable isotopes of the shell and operculum striae. Oceanol Acta 8 (2): 221–229.
- Schöne BR, Zhang Z, Jacob D, Gillikin DP, Tütken T, Garbe-Schönberg D, McConnaughey T, Soldati A (2010) Effect of organic matrices on the determination of the trace element chemistry (Mg, Sr, Mg/Ca, Sr/Ca) of aragonitic bivalve shells (*Arctica islandica*) – Comparison of ICP-OES and LA-ICP-MS data. Geochem J. 44: 23–37.

- Sharma T, Clayton RN (1965) Quoted in: Friedman I and O'Neil JR, 1977. Compilation of stable isotope fractionation factors of geochemical interest. Fleischer (Ed), Data of Geochemistry, 6th Ed. United States Geological Survey, Professional Paper 440-KK.
- Shelmerdine RL, Adamson J, Laurenson CH, Leslie B (2007) Size variation of the common whelk, *Buccinum undatum*, over large and small spatial scales: potential implications for micro-management within the fishery. Fish Res 86:201–206. doi:10.1016/j.fishres.2007.06.005
- Shrives JP, Pickup SE, Morel GM (2015) Whelk (*Buccinum undatum* L.) stocks around the Island of Jersey, Channel Islands: Reassessment and implications for sustainable management. Fish Res, 167: 236–242. doi: 10.1016/j.fishres.2015.03.002
- Smith E, Dent G (2005) Modern Raman Spectroscopy – A Practical Approach. John Wiley & Sons, Ltd, England.
- Smith KE, Thatje S (2013) Nurse egg consumption and intracapsular development in the common whelk *Buccinum undatum* (Linnaeus, 1758). Helgo Mar Res 67: 109-120.
- Steiner J, Termonia Y, Deltour J (1972) Comments on Smoothing and Differentiation of Data by Simplified Least Square Procedure. Anal. Chem, 44: 1906-1909.
- Ten Hallers-Tjabbes CC, Evaraarts JM, Mensink BP, Boon JP (1996) The decline of the North Sea whelk (*Buccinum undatum* L.) between 1970–1990: a natural or a human-induced event? Mar Ecol 17 (1–3): 333–343.
- Valentinsson D, Sjodin F, Jonsson PR, Nilsson P, Wheatley C (1999) Appraisal of the potential for a future fishery on whelks (*Buccinum undatum*) in Swedish waters: CPUE and biological aspects. Fish Res 42: 215–227.
- Weetman D, Hauser L, Bayes MK, Ellis JR, Shaw PW (2006) Genetic population structure across a range of geographic scales in the commercially exploited marine gastropod *Buccinum undatum*. Mar Ecol Prog Ser 317: 157–169.
- Wheeler AP (1992) Mechanisms of molluscan shell formation. In: Bonucci E (ed) Calcification in biological systems. CRC Press, Boca Raton, pp 179–216.
- Wilbur, K. M., Saleuddin, A. S. (1983) Shell formation. In: Wilbur, K. M. (ed.) The Mollusca - physiology. Vol. 4. Academic Press, New York, pp 235-237

Figures

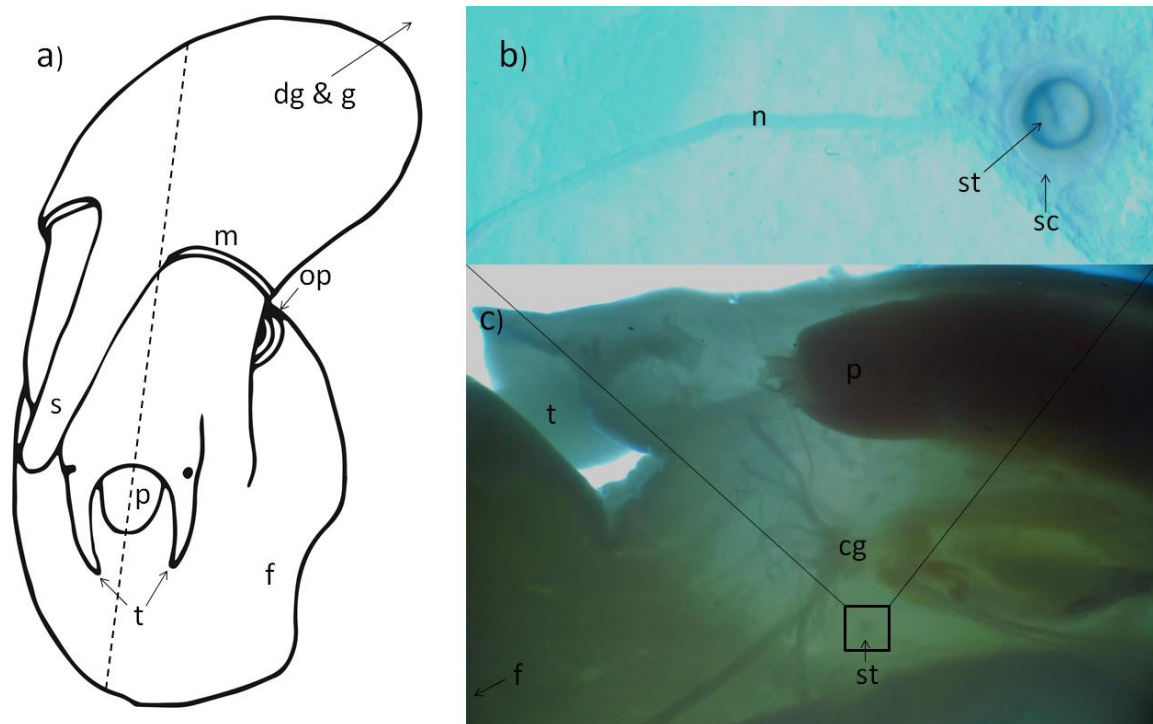


Figure 1a. Ventral view of a female *Buccinum undatum* removed from its shell showing; s - Siphon, m - Mantle, p - Proboscis, op - Operculum, f - Foot and t - Tentacles. dg - Digestive Gland and g - Gonad are out of frame. The dotted line represents the bisection of the whelk. b), A statolith following removal; n - Nerve, st - Statolith and sc - Statocyst. c), half a bisected *B. undatum* illuminated using transmitted light, viewed in a dissection microscope, showing the cg - Cerebral Ganglion and st - Statolith.

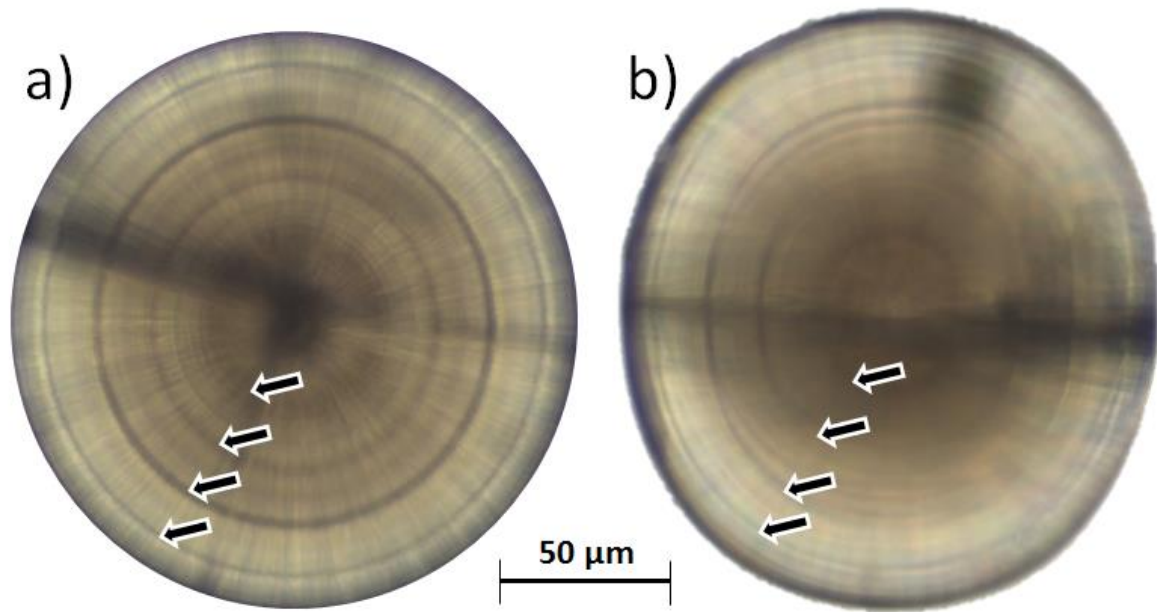


Figure 2. Photomicrographs of two statoliths removed from an individual *Buccinum undatum* from the Menai Strait. a) shows a dorso-ventral view whilst b) shows a lateral view of the statolith. The growth rings are marked with arrows in each statolith orientation.

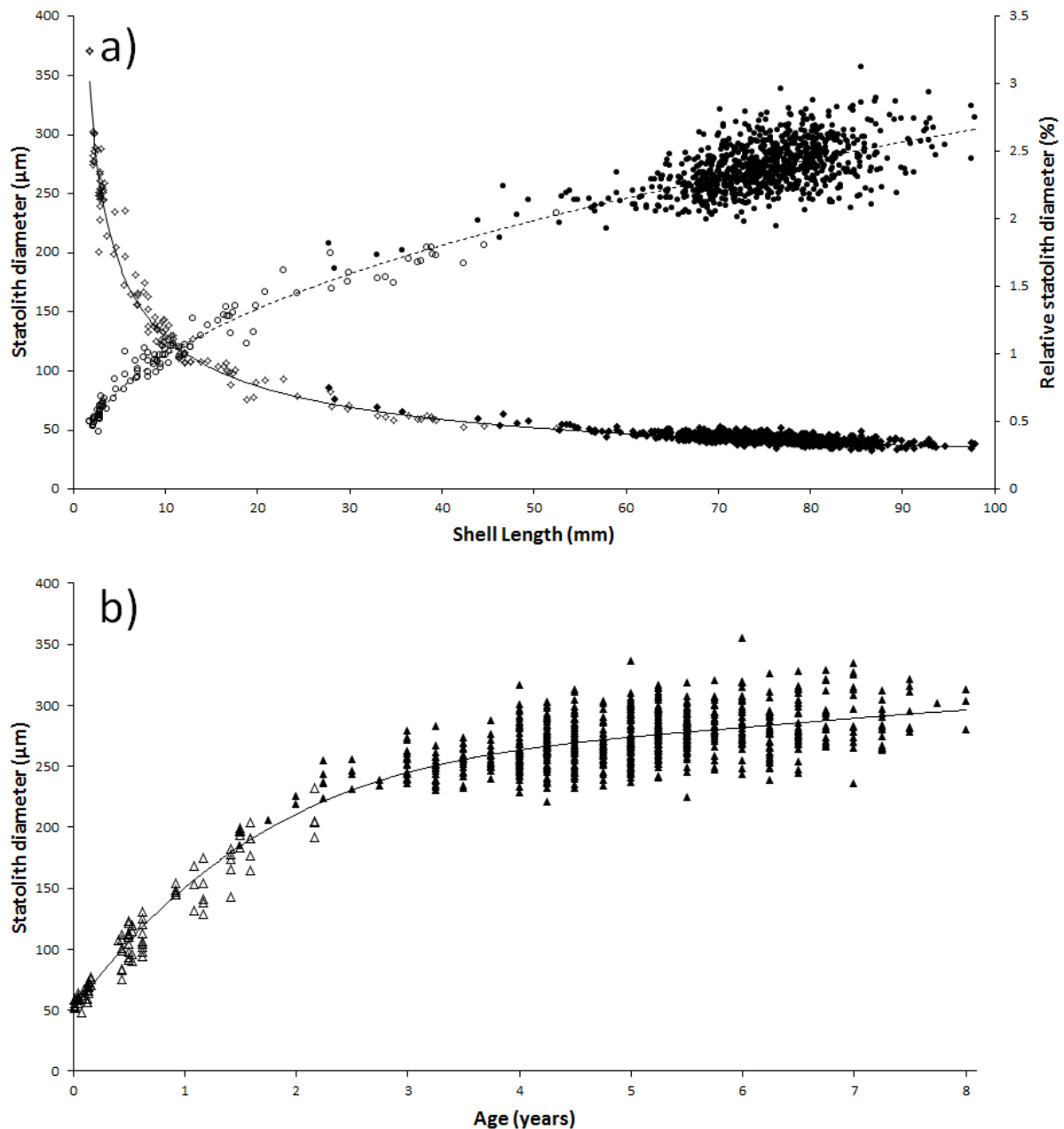


Figure 3a. Scatterplot showing the relationship between statolith diameter (StD) and shell length (SL) of field collected *Buccinum undatum* from the Menai Strait (filled circles), and tank grown juveniles (empty circles), fitted with a power function line (dotted line, $y = 41.38x^{0.4354}$), $R^2 = 0.96$. The relationship between SL and relative statolith diameter (RStD, statolith diameter/shell length*100), showing field collected whelks (filled diamonds), and tank grown juveniles (empty diamonds), fitted with a power function line (solid line, $y = 4.138x^{-0.565}$), $R^2 = 0.98$. $n=953$. Figure 3b) Scatterplot showing the relationship between StD and age, constructed from statolith rings for field collected animals (filled triangles) and known age for tank grown animals (empty triangles), fitted with a polynomial trend line, $R^2 = 0.91$. $n=931$.

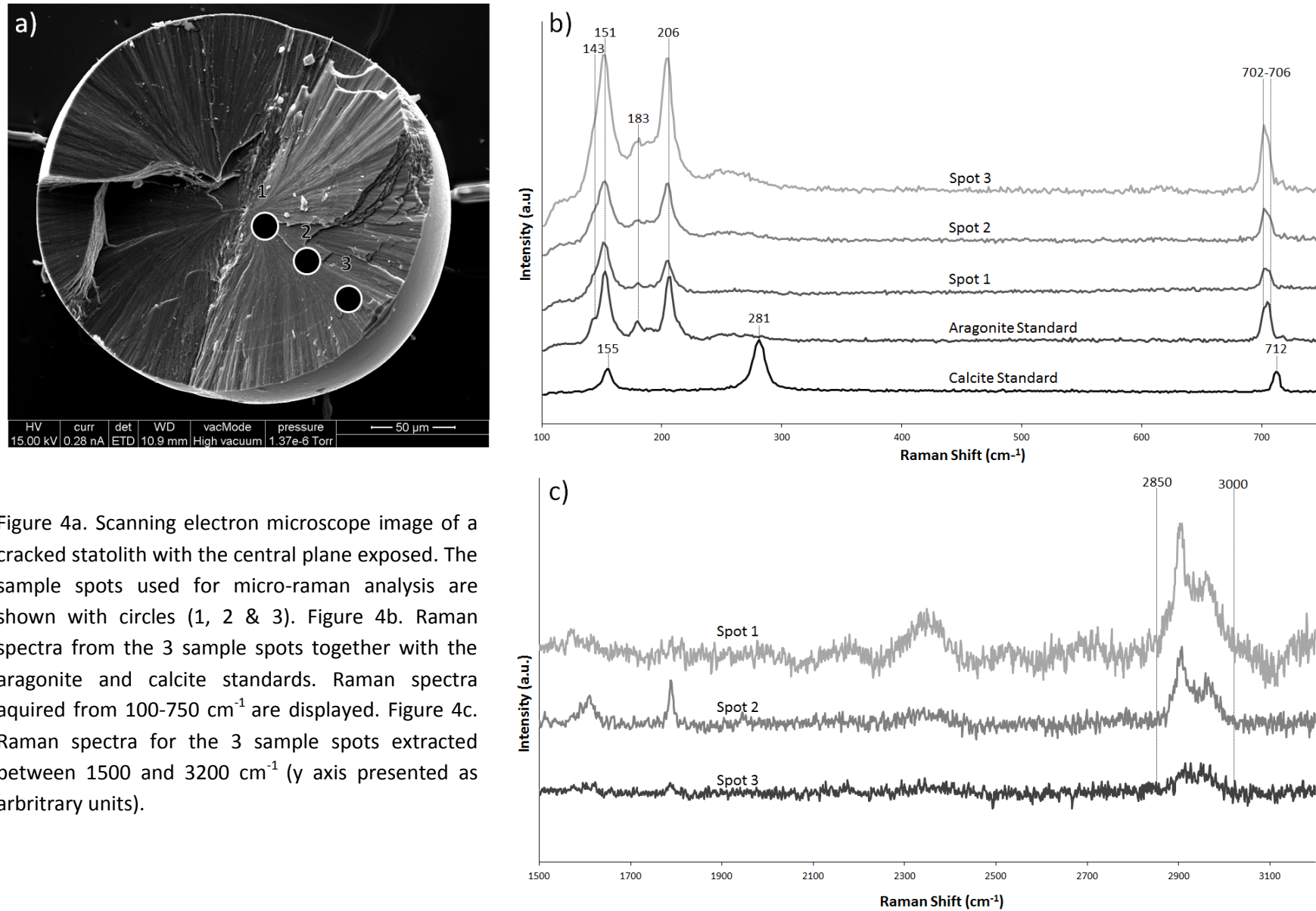


Figure 4a. Scanning electron microscope image of a cracked statolith with the central plane exposed. The sample spots used for micro-Raman analysis are shown with circles (1, 2 & 3). Figure 4b. Raman spectra from the 3 sample spots together with the aragonite and calcite standards. Raman spectra acquired from 100-750 cm^{-1} are displayed. Figure 4c. Raman spectra for the 3 sample spots extracted between 1500 and 3200 cm^{-1} (y axis presented as arbitrary units).

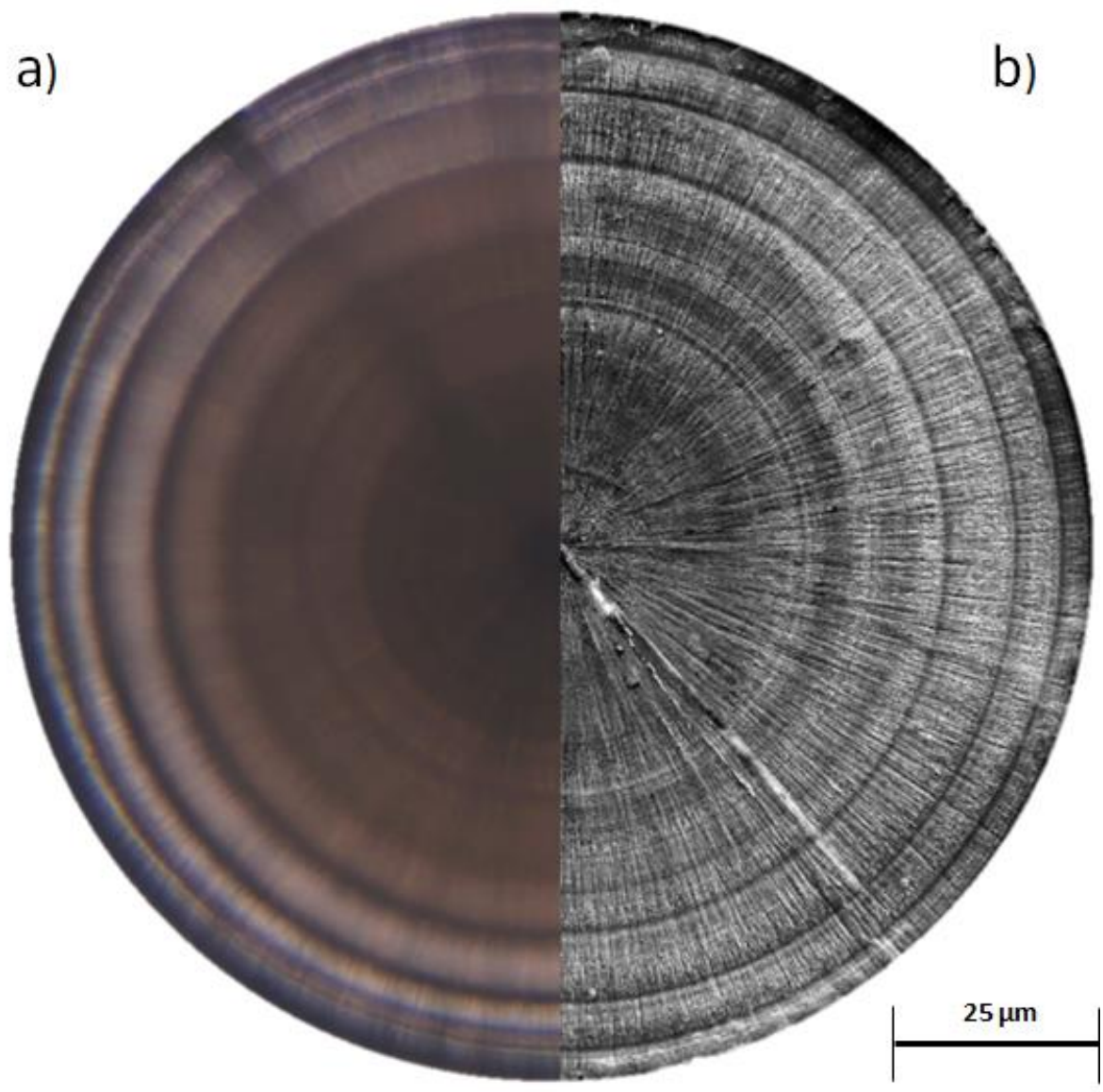


Figure 5. Composite image of two statoliths from the same *Buccinum undatum* specimen. a) a photomicrograph of an extracted and mounted left hand statolith imaged using optical microscopy. b), a Scanning Electron Microscope image of the matching right hand statolith that has been resin-mounted, ground to the central plane, polished and etched.

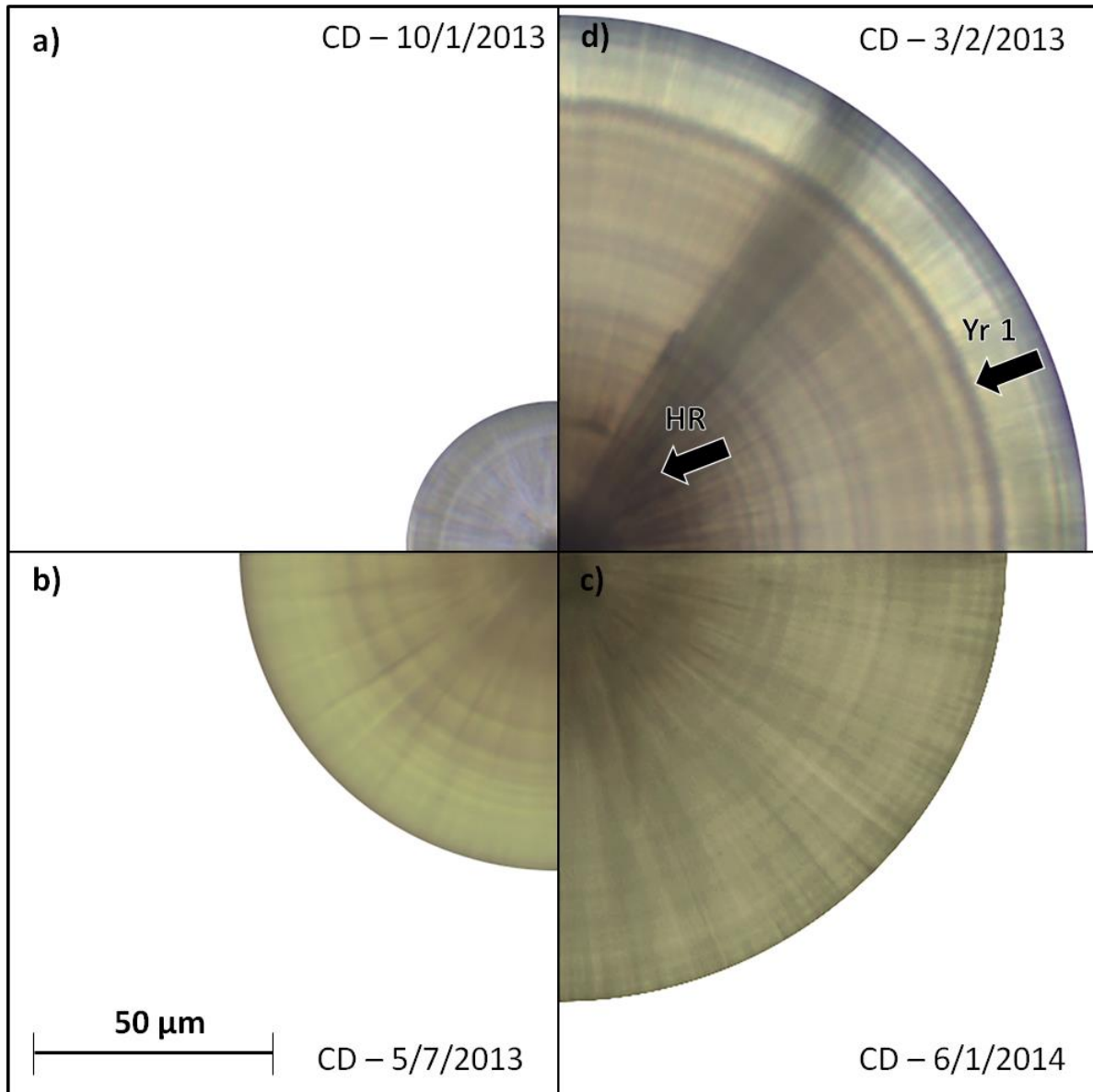


Figure 6. Composite image showing seasonal juvenile statolith development at a) 2 weeks after hatch, b) 6 months after hatch, c) 1 year after hatch and d) 2 years after hatch. In all cases the hatching ring is visible (HR) as are multiple faint disturbance lines. The 1 year ring is also visible in the 2 year old (Yr 1). CD – Collection Date.

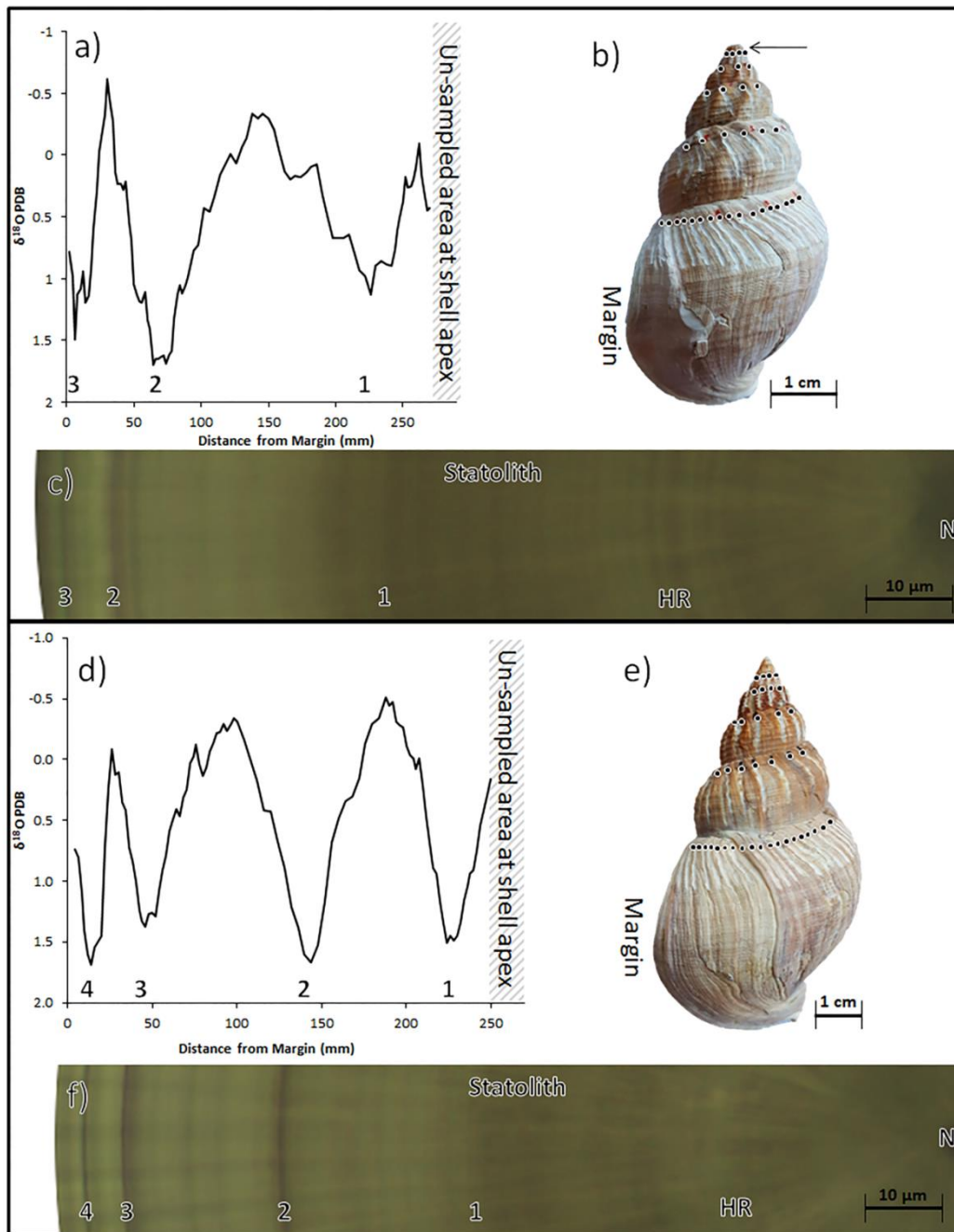


Figure 7. Comparison of the shell $\delta^{18}\text{O}$ profiles with the associated statolith for two *Buccinum undatum*. Figure 7a. $\delta^{18}\text{O}$ profile from the shell of a female *B. undatum*, the y axis has been inverted to show the position along the shell of the positive peaks in the $\delta^{18}\text{O}$ cycles (coldest seawater temperatures, highlighted with numbers). The data have been smoothed using 5 point Savitsky-Golay filter. Figure 7b. The shell drill sampled for the data in 7a, visible drill tracks have been highlighted with red dots and the black arrow denotes where sampling at the apex was ceased. This un-sampled area corresponds to the hatched area in 7a. The very tip of this specimen has been lost due to damage. Figure 7c. Photomicrograph of the matching statolith from the animal in 7a & b, showing the nucleus (N), Hatching ring (HR) and annual bands (numbers). Figure 7d, e & f show the same figures as Figure 7a, b & c respectively for an older male specimen.